

**Scientific Basis for a  
Safety Case of Deep  
Geological Repositories**

## Scientific Basis for a Safety Case of Deep Geological Repositories

Ulrich Noseck  
Dirk Becker  
Christine Fahrenholz  
Judith Flügge  
Sven Hagemann  
Volker Hormann  
Robert Kilger  
Klaus-Peter Kröhn  
Michael Kröhn  
Artur Meleshyn  
Jörg Mönig  
Helge Moog  
André Rübél  
Sabine Spießl  
Jens Wolf

December 2021

### **Remark:**

This report refers to the research project 02E11647 which has been funded by the Federal Ministry for Economics and Energy (BMWi).

The study was conducted by the Gesellschaft für Anlagen- und Reaktorsicherheit (GRS) gGmbH.

The authors are responsible for the content of the report.

**Keywords:**

Analogues, Biosphere, Clay, Crystalline Rock, Geochemistry, Knowledge Management, Permafrost, Radioactive Waste, Rock Salt, Safety Assessment, Safety Case, Scenarios, Sensitivity Analysis, Uncertainty

## Abstract

The assessment of the long-term safety of a repository for radioactive or hazardous waste and therewith the development of a safety case requires a comprehensive system understanding, a continuous development of the methods of a safety case and capable and qualified numerical tools. The objective of the project “Scientific basis for the assessment of the long-term safety of repositories”, identification number 02E11647, was to follow national and international developments in this area, to evaluate research projects, which contribute to knowledge, model approaches and data, and to perform specific investigations to improve the methodologies of the safety case and the long-term safety assessment.

This project, founded by the German Federal Ministry of Economics and Technology (BMWi), was performed in the period from 1<sup>st</sup> April 2018 to 30<sup>st</sup> June 2021. The results of the key topics investigated within the project are published in the following reports:

- GRS-644: Natural Analogues for Repositories in Crystalline Formations.
- GRS-643: Scientific Basis of a Safety Case for Deep Geological Repositories

Moreover, substantial contributions were developed for the following international reports and flyers:

- NEA: International Features, Events and Processes (IFEP) List for the Deep Geological Disposal of Radioactive Waste. NEA/RWM/R(2019)1, July 2019
- NEA: Managing uncertainty in siting and implementation – Creating a dialogue between science and society. Joint FSC-IGSC Workshop, October 2019
- SANDIA: “Sensitivity Analysis Comparisons on Geologic Case Studies: An International Collaboration.” Sandia National Laboratories Technical Report SAND2021-11053
- SANDIA: “Generic FEP Catalogue and Salt Knowledge Archive”. Sandia National Laboratories Technical Report SAND2020-13186.



## Zusammenfassung

Die in diesem Projekt durchgeführten Arbeiten haben zu verschiedenen Aspekten eines Safety Case einen Beitrag geleistet; speziell zu den Nachweisgrundlagen (Prozessverständnis), zu den Methoden und Strategien zur Entwicklung eines Safety Case, zur Langzeitsicherheitsanalyse, zu zusätzlichen Nachweisen, Analysen und Argumenten, die in einem Safety Case verwendet werden, wie auch zu soziotechnischen Aspekten, beispielsweise der Kommunikation mit der Gesellschaft und der Aufbewahrung essentieller Informationen für zukünftige Generationen. Nationale Projekte wie auch Entwicklungen in anderen Ländern und auf internationaler Ebene wurden verfolgt.

Eine aktive Teilnahme erfolgte in internationalen Komitees und Arbeitsgruppen, wie dem Radioactive Waste Management Committee (RWMC), der Integration Group for the Safety Case (IGSC), der Arbeitsgruppe Information, Data and Knowledge Management (IDKM) und zugehörigen Expertengruppen, dem Salt Club, Crystalline Club sowie Aktivitäten der IAEA zur Behandlung der Biosphäre in einem Sicherheitsnachweis. Die dabei erreichte Erweiterung des Wissens trägt auch zur Erarbeitung und Weiterentwicklung entsprechender nationaler Methoden und Vorgehensweisen bei.

Im Hinblick auf Langzeitsicherheitsanalysen wurden Arbeiten zum Thema Ungewissheits- und Sensitivitätsanalysen durchgeführt. Probabilistische Analysen stellen ein wichtiges Werkzeug zur Untersuchung der Ungewissheit der mit einem Computermodell berechneten Ergebnisse (Ungewissheitsanalyse) sowie auch der Bestimmung der Sensitivität der Ergebnisse gegenüber der Variation der Eingangsdaten (Sensitivitätsanalyse) dar. Derartige Analysen gewähren einen tieferen Einblick in das Verhalten von sicherheitsanalytischen Modellen und erhöhen damit das Modellverständnis und das Vertrauen in die Modellergebnisse. Die Arbeiten, die zu diesem Thema vorgestellt werden, umfassen zwei Aspekte. Erstens wurden detaillierte Sensitivitätsanalysen mit hochentwickelten Metamodellen durchgeführt, die speziell den Einfluss von Parameter-Wechselwirkungen im Fokus hatten. Zweitens ist GRS in eine internationale Arbeitsgruppe involviert (Joint Sensitivity Analysis Exercise, JOSA), die ins Leben gerufen wurde, um verschiedene Ansätze zur Sensitivitätsanalyse zu testen und Modellergebnisse auszutauschen. Die hier vorgestellten Ergebnisse können als Zwischenergebnisse aufgefasst werden, da die Forschungsarbeiten noch weitergeführt werden. Generell gehören varianzbasierte Methoden zu den wichtigsten Ansätzen in der Sensitivitätsanalyse; dafür stehen mittlerweile effektive mathematische Verfahren und numerische Algorithmen zur Verfügung. Korrelationskoeffizienten und Regressionsansätze werden

weiterhin verwendet und liefern robuste Informationen. Andere mathematische Ansätze wie etwa dichte-basierte Verfahren liefern in der Regel dazu konsistente Ergebnisse, können aber bei komplexerem Systemverhalten unter Umständen deutlich abweichende Sensitivitäten ermitteln, woraus sich häufig ein vertieftes Systemverständnis ergibt. Graphische Methoden wie beispielsweise CUSUNORO eignen sich besonders für einen schnellen Überblick und erlauben zudem, Einflüsse über den gesamten Wertebereich einer Variablen zu visualisieren.

Generell gute Übereinstimmung wurde in den Rechnungen der verschiedenen Teilnehmer aus JOSA bezüglich der linearisierenden Verfahren der Sensitivitätsanalyse gefunden. Bei varianzbasierten Verfahren ergaben sich dagegen merkbare Unterschiede, obwohl alle diese Verfahren theoretisch dieselben Sensitivitätsindizes berechnen, jedoch auf Basis mathematischer Ansätze, die auf z. T. sehr unterschiedlichen Analysemethoden, Näherungen oder Interpolationen beruhen. Häufig wurde beobachtet, dass die Sensitivitätsanalysen der einzelnen Partner bezüglich der Signifikanz des oder der wichtigsten Parameter übereinstimmten, aber unterschiedliche Reihenfolgen in den weniger relevanten Parametern ermittelten, insbesondere wenn die interessierenden Größen über viele Größenordnungen variieren. Daraus ist zu folgern, dass derart ermittelte Rangfolgen generell nicht überinterpretiert werden sollten. Es besteht auch kein völliger Konsens zwischen den Teilnehmern über die Abgrenzung zwischen Sensitivitätsmesswerten, die auf eine sekundäre Sensitivität hinweisen, und Sensitivitätsmesswerten, die auf eine vernachlässigbare Sensitivität hinweisen. Dies unterstreicht die Notwendigkeit der Entwicklung von Konsensverfahren zum Testen oder zur Begründung von Schlussfolgerungen in Bezug auf Parameter mit niedrigerem Rang.

Hinsichtlich der Biosphärenmodellierung in der Sicherheitsanalyse zeigte ein Vergleich der vom tschechischen und dem deutschen Biosphärenmodell berechneten Biosphären-Dosiskonversionsfaktoren (BDCFs) signifikante Unterschiede, die für einige Radionuklide um mehr als drei Größenordnungen betragen. Um die Gründe für diese Unterschiede zu identifizieren, wurden die Modellansätze und Daten, die in Biosphärenmodellen aus Tschechien und Deutschland verwendet werden, verglichen und die Auswirkungen dieser Unterschiede auf die BDCFs beschrieben. Der Benchmark konzentrierte sich auf die Radionuklidbehandlung im Boden, die Wege vom Boden zur Pflanze und die externe Strahlung vom Boden, die für die meisten Radionuklide entscheidend sind. Allgemein hat sich gezeigt, dass die Transportmodellierung im Boden meist ähnliche Ergebnisse liefert, obwohl unterschiedliche Modellansätze verwendet

werden. Einige Unterschiede in der Beschreibung des Radionuklidtransports im Boden konnten durch unterschiedliche Parameterwerte erklärt werden. Darüber hinaus wurde festgestellt, dass die Modelle für die externe Strahlenexposition recht unterschiedlich sind, und ihr Einfluss auf die BDCFs wurde untersucht. Letztendlich konnten die sehr großen Unterschiede bei den BDCFs jedoch hauptsächlich auf zwei Fehler zurückgeführt werden, einen durch einen Einheitenfehler und einen zweiten durch die Einbeziehung eines unrealistischen Expositionspfades. Beide Fehler sind bei der Übertragung des Biosphärenmodells in das Programm Excel aufgetreten. Darüber hinaus hat die tschechische Organisation UJV die Notwendigkeit erkannt, BDCFs für Radionuklide separat zu berechnen. Dieser Benchmark, der nur zwei Teilbereiche des Biosphärenmodells betrachtet hat, war ein wichtiger Beitrag zur Qualitätssicherung beider Modelle.

Da, wie bereits erwähnt, für die meisten Radionuklide der Transport im Boden mit daran anschließenden Expositionspfaden am stärksten zur Strahlenexposition beiträgt, wurde eine Studie zum aktuellen Kenntnisstand in der Modellierung der Radionuklidsorption in Böden initiiert. Für die entsprechenden Modellrechnungen wurde das UNiSeCs II Modell mit dem Component Additivity Ansatz verwendet, das für gemäßigte klimatische Bedingungen konzipiert und validiert wurde und daher für die meisten deutschen und westeuropäischen Böden anwendbar sein sollte. Es konnte mit Hilfe von Daten aus Batch-Experimenten für die Radionuklide Am, Pu, Se, Ni, Cs, Ra und U validiert werden. In einigen Fällen mussten Parameter geschätzt oder zusätzliche Annahmen getroffen werden. Es ist wünschenswert, das Modell vorzugsweise mit Felddaten weiter zu validieren. Durch Anwendung des Modells wurden für jedes Radionuklid die wichtigsten Parameter der Bodenlösung anhand Parametervariationen für zwei Refesol-Böden ermittelt. Dabei wurden die Parameter der Bodenlösung in Bereichen, die im Boden häufig vorkommen und z.B. auch IAEA-Datensammlungen aufgeführt sind, variiert. Insbesondere für Cs und Ra, wo die Unterschiede zwischen dem tschechischen und dem deutschen Modell am größten sind, ist auch die Bandbreite der Sorptionsberechnungen recht hoch. Auch die in den Biosphärenmodellen zur Sicherheitsanalyse verwendeten Werte liegen in den berechneten Bereichen. Um unter Feldbedingungen auftretende Bandbreiten von  $K_d$ -Werten abzuschätzen, wurden auch probabilistische Rechnungen durchgeführt, bei denen der elementspezifische Verteilungskoeffizient für eine Reihe von Parameterkombinationen berechnet und nach seiner Häufigkeit klassifiziert („ $K_d$ -Verteilungsdichte“) wurde. In den meisten Fällen liegt der Medianwert der Verteilung nahe dem deterministisch berechneten Wert für definierte Referenzbedingungen. Allerdings ist auch hier zu beachten, dass einige Bodenparameter (z.B. pH und  $p_e$ ) in der Regel korreliert sind und somit nicht alle

Kombinationen von Bodenparametern im Feld gleich wahrscheinlich sind, wie in den Berechnungen angenommen. Weitere Einschränkungen des Modells, insbesondere für jedes der betrachteten Elemente, werden ausführlich beschrieben.

Zum Thema Bentonit-Wiederaufsättigung wurden Arbeiten zu zwei verschiedenen Aspekten durchgeführt. Erstens nahm die GRS aktiv an der Task Force on Engineered Barrier Systems teil, was die Arbeit an Task 9 – FEBEX in-situ-Test einschloss. Zweitens wurde ein erster Schritt zur Übertragung des im Code VIPER realisierten Modellkonzepts zur Bentonit-Wiederaufsättigung in den COMSOL Multiphysics Code implementiert.

Der FEBEX-In-situ-Test wurde über mehr als 18 Jahre im Grimsel Felslabor (Schweiz) der Nagra durchgeführt. In den Grimsel-Granit wurde ein 70,4 m langer Stollen mit einem Querschnitt von 2,28 m Durchmesser eingebracht. In den hinteren 17,4 m des Stollens wurden zwei elektrische Heizer und im restlichen Bereich des Stollens verdichtete Bentonitblöcke eingesetzt. Die Testzone wurde mit einem Betonstopfen verschlossen. Das Experiment wurde mit Sensoren ausgestattet, die die thermo-hydro-mechanischen Prozesse in der Tonbarriere und im umgebenden Grimsel-Granit überwachten. Das Experiment war fünf Jahre in Betrieb. Danach wurden die äußeren Heizer abgeschaltet und die äußere Versuchshälfte ausgebaut, wobei an verschiedenen Stellen des Gesteins, des Betons und des Bentonit-Buffers Proben entnommen wurden. Die restliche Versuchshälfte inklusive des zweiten Heizers wurde für weitere 13,2 Jahre in Betrieb gehalten. Danach wurde der Versuch komplett abgebaut und wie zuvor an verschiedenen Stellen Proben entnommen. Aus den Modellrechnungen zum FEBEX-Versuch mit Code VIPER ergeben sich folgende, wesentliche Schlussfolgerungen: Die Simulationsergebnisse stimmen im Großen und Ganzen recht gut mit den Daten und den Ergebnissen anderer Modellierungsteams überein. Dort, wo stärkere Abweichungen festgestellt wurden, hatten auch andere Teams Schwierigkeiten, die Messwerte zu beschreiben. Die Entkopplung der thermischen Berechnungen vom hydraulischen Teil, also die Vernachlässigung der Abhängigkeit der thermischen Parameter vom Sättigungsgrad, scheint einen eher geringen Einfluss auf das Gesamttemperaturfeld sowie auf die relative Feuchteentwicklung im Bentonit-Buffer zu haben. Die gleiche Beobachtung wurde bereits bei den beiden vorherigen nicht-isothermen Modellen gemacht, die von der GRS für Task 1 und Task 2 innerhalb der EBS Task Force erstellt wurden. Die einseitige Kopplung, dass thermische Effekte hydraulische Prozesse beeinflussen aber nicht umgekehrt, hat den Vorteil, dass dies die Modellierung erheblich beschleunigt. Nachteilig ist jedoch, dass eine Erhöhung der Leistungsaufnahme der Heizer durch Änderungen der Wärmeleitfähigkeit aufgrund

eines steigenden Wassergehalts nicht simuliert werden kann. Im Hinblick auf die Wiederaufsättigung konnte nur ein Bruchteil der Fragestellungen, die in der Aufgabenbeschreibung definiert wurden, von Code VIPER beschrieben werden. Wesentlicher Grund dafür ist, dass VIPER entwickelt wurde, um ein alternatives Konzept zur Simulation der Bentonit-Wiederaufsättigung zu testen und zu verfeinern. Dazu war es bisher nicht erforderlich, die Fähigkeit zur vollständigen 3D-Modellierung im Code zu implementieren, die zur Beschreibung der meisten Aspekte des FEBEX-Benchmarks notwendig war. Diese Arbeit hat damit einmal mehr gezeigt, dass eine 3D-Modellierung auf Dauer für konkrete Anwendungen benötigt wird. Als Konsequenz wurde beschlossen, das VIPER-Konzept auf den Code COMSOL Multiphysics zu übertragen. Aufgrund der Komplexität von VIPER ist dies jedoch nur stufenweise sinnvoll. Der erste Schritt zur Übertragung des VIPER-Konzepts auf COMSOL Multiphysics wurde erfolgreich durchgeführt – die Anwendung auf 3D-Probleme ist damit möglich – und anhand einer einfachen Form der isothermen Wiederaufsättigung demonstriert. Sinnvolle nächste Schritte wären zum einen die Erweiterung des COMSOL-VIPER-Modells auf die volle Komplexität der isothermen Sättigung. Dies würde den Import von gemessenen Isothermen sowie die ganze Bandbreite möglicher Randbedingungen beinhalten. Ein weiterer Schritt könnte die Implementierung aller Temperaturabhängigkeiten von sekundären Variablen und Parametern in Vorbereitung auf ein nicht-isothermes Modell sein.

Die Existenz von Permafrost ist ein Thema, das bei einem Sicherheitsnachweis berücksichtigt werden muss, da es sich über mehrere 100 m unter die Oberfläche erstrecken und damit Prozesse insbesondere im Fernfeld eines geologischen Tiefenlagers beeinflussen kann. Unter Permafrostbedingungen können sich völlig andere Grundwasserströmungssysteme im Vergleich zu denen während warmer Klimaphasen entwickeln, da gefrorene geologische Schichten eine effiziente Strömungsbarriere darstellen. Wie stark tiefere Grundwassersysteme vom Einfrieren betroffen sind, hängt jedoch von der Ausdehnung des Permafrosts ab. Die Schwierigkeiten bei der Vorhersage des Grundwasserflusses unter Permafrostbedingungen werden durch das Auftreten von Taliki – nicht gefrorenen Zonen in Permafrostgebieten – verschärft. Während sowohl offene als auch geschlossene Taliki von geringer Bedeutung sind, können durchgehende Taliki hydraulische Fenster zwischen tiefen ungefrorenen Grundwasserleitern und der Bodenoberfläche bilden und damit die Radionuklidmigration im Falle einer Freisetzung von RN aus dem Abfall entscheidend beeinflussen. Für geklüftete Medien, wie sie hier betrachtet werden, existiert noch keine Beziehung, die den von Eis eingenommenen Volumenanteil im Porenraum in Abhängigkeit von der Temperatur beschreibt. Eine solche Kurve, eine

Gefrierkennlinie für die Kluft, ist notwendig, um die sich ändernden hydraulischen Bedingungen während der zeitlichen Entwicklung von Permafrost in geklüfteten Medien zu simulieren.

Daher sollte ausgehend von einem Gefrierexperiment in einer mit einem 3D-Drucker hergestellten, wassergesättigten Kluft ein neuer Ansatz zur Ableitung solcher Daten etabliert und getestet werden. Sofern erfolgreich sollten der Eisgehalt und die dazugehörige Temperatur sowie die relative Permeabilität für Wasser gemessen und diese Messungen dann bei unterschiedlichen Temperaturen wiederholt werden. Ein hoher Aufwand wurde in den Aufbau und die Beobachtung der Experimente, die sich als sehr anspruchsvoll erwiesen, gesteckt. Mehrere unvorhergesehene Schwierigkeiten haben das Experiment schließlich so weit verzögert, dass im Rahmen des Projekts nur die Beobachtung des Einfrierens in einer Kluft mit vereinfachter Geometrie erreicht werden konnte. Verschiedene Schwierigkeiten und Herausforderungen sind bei der Verwendung von farbigen Tracern und der Optimierung der Kühlbox aufgetreten. Eine verbesserte Konstruktion, die eine robustere Installation ermöglicht und gleichzeitig flexibel genug ist, um einen Verlauf in einer natürlichen Kluft aufzunehmen, ist daher in zukünftigen Experimenten ratsam. Die angestrebte Strategie für die weitere Arbeit ist, die Versuche zuerst mit parallelen Klufflächen sowohl hinsichtlich der Technik als auch der Interpretation der Ergebnisse zu verbessern. Nachdem die Tests mit parallelen Klufflächen kontrolliert durchgeführt werden können, sollen gedruckte Nachbildungen von realen Kluffen verwendet werden.

Aus den genannten Gründen konnte die Modellierung der Experimente, die eine Simulation des Gefrierprozesses von Wasser mit den damit verbundenen Veränderungen der thermischen Eigenschaften erfordert hätte, nicht in dieser Art durchgeführt werden. Als Ersatz wurde ein numerisches Modell für Granitformationen erstellt, das das Wachstum der Permafrostdicke mit abnehmender Oberflächentemperatur beschreibt und viele der physikalischen Aspekte des ursprünglich angedachten Modells umfasst. Die Eingabeparameter wurden so gewählt, dass sie dem kanadischen Schild entsprechen, einer der größten und ältesten kristallinen Formationen der Erde. Als Zielgröße wurde die stationäre Dicke des Permafrostbodens in Abhängigkeit von der Oberflächentemperatur berechnet. Das Modell war in der Lage, die Referenzdaten aus dem Feld zu beschreiben. Der nächste Schritt ist die Einbeziehung großer aquatischer Strukturen an der Oberfläche, um den Einfluss solcher Strukturen auf die gefrierenden Schichten zu untersuchen. Darüber hinaus bildet dieses Modell die Basis für Untersuchungen über das vorliegende

Projekt hinaus und dient als Vorarbeit für Forschungsarbeiten zur Grundwasserströmung unter Permafrostbedingungen wie beispielsweise der Ermittlung der Bedingungen für die Talik-Bildung.

Tongestein wird als potenzielle Wirtsgesteinsformation für ein geologisches Tiefenlager in Deutschland betrachtet. Aufgrund des natürlichen Wassergehalts des porösen Tonstein-Wirtsgesteins und der hydrostatischen Randbedingungen ist zu erwarten, dass die verfüllten Einlagerungsflächen eines tiefen geologischen Endlagers innerhalb weniger Jahrhunderte wieder mit Wasser gesättigt werden. Der Kontakt der gusseisernen Behälter und Auskleidungen mit Wasser in Abwesenheit von Sauerstoff führt zu anaerober Korrosion unter Bildung von Wasserstoff. Die entstehenden Gasvolumina sind typischerweise zu groß, um in den Einlagerungsbereichen im Porenraum der Verfüllung gespeichert zu werden und führen daher zu einem Gasdruckaufbau. Die resultierenden Druckgradienten induzieren eine advektive Bewegung von Gas und möglicherweise auch von Wasser im Stollensystem des Endlagers, aber auch im tonigen Wirtsgestein. Aus diesem Grund wurden die Gastransportmechanismen in Tonstein-Wirtsgesteinen lange Zeit untersucht und das Ziel der hier vorgestellten Studie war es, den Stand der Technik zu überprüfen, um die Gastransportprozesse in die integrierte Leistungsbewertungsmodellierung einzubeziehen, seit der letzten Überprüfung im Jahr 2008.

Im Allgemeinen kann der Gastransport in Tongestein durch vier verschiedene Mechanismen beschrieben werden, abhängig von der Menge der gebildeten Gase, nämlich (i) Auflösung und Diffusionstransport durch den Ton, (ii) Zweiphasenströmung (wenn der Gasdruck unter der minimalen Hauptnormalspannung liegt), (iii) Dilatanz-getriebener Gasfluss und (iv) hydraulische Kluftbildung, wenn der Druck auf die Gesteinsmatrix die Bruchfestigkeit des Tongesteins überschreitet. Ein Schwerpunkt der seit 2008 durchgeführten Forschungen war es, den Effekt des Dilatanz-getriebenen Gastransports in verfestigtem Tongestein mit Bohrkernproben in Laborexperimenten und in-situ-Experimenten in Untertagelabors und begleitenden numerischen Modellrechnungen genauer zu untersuchen. Aus der direkten Beobachtung des mechanischen Verhaltens der Tonsteinproben in Laborversuchen kann hinreichend gut geschlossen werden, dass der Dilatanz-getriebene Gastransport im Tongestein eine Tatsache ist. Es existiert jedoch noch keine allgemein akzeptierte Theorie des mechanischen Verhaltens während der dilatanten Gasströmung, die konsistent die Porositäts- und Permeabilitätsänderungen des Tongesteins als Funktion des Gasdrucks beschreibt.

Es soll jedoch darauf hingewiesen werden, dass Aufweitung und Wiederverschluss der Mikrorisse kein großes Problem darstellt. Es ist bekannt, dass Tongestein wieder abdichtet und seine ursprüngliche Permeabilität erreicht, wenn die mechanische Belastung bei vorhandener Hauptspannung abnimmt, selbst wenn Risse entstanden sind. Trotzdem führen die offenen Fragen im prinzipiellen Verständnis des Dilatationsprozesses im Tongestein dazu, dass eine mathematische Beschreibung des phänomenologischen Netto-Gastransfers durch das Tongestein unter dilatanten Bedingungen fehlt. In der Literatur werden häufig klassische van Genuchten Zweiphasen-Strömungscodes verwendet, um den Gastransport zu simulieren, z. g. TOUGH2, die aber nur anwendbar sind, wenn der Gasdruck unter der minimalen Hauptspannung des Gesteins bleibt. Es wird nicht erwartet, dass dieser Ansatz auch für dilatante Druckbedingungen gültig ist, obwohl er hier und da noch angewendet wird. In den TOUGH2-Code wurden verschiedene Modifikationen programmiert, um einen Dilatanz-getriebenen Gasfluss zu modellieren. Ein umfassender Vergleich der verschiedenen Ansätze oder ein Code-Benchmark der resultierenden Codes wurde bisher nicht durchgeführt. Obwohl diese Modellansätze in der Lage waren, die Ergebnisse von Gastransportexperimenten zu beschreiben, scheint aus unserer Sicht keine dieser Modifikationen gerechtfertigt zu sein, um für zuverlässige Langzeitprognosen verwendet zu werden, die für die Langzeitsicherheitsanalyse erforderlich sind. Solange weder die physikalischen Gleichungen des mechanischen Verhaltens beim Gastransport durch Dilatation des Tongesteins hinreichend gut beschrieben sind noch eine validierte phänomenologische Beschreibung des Netto-Gastransports existiert, wird vorgeschlagen, ein Endlagerkonzept zu wählen, das bei der erwarteten Entwicklung des Systems nicht zu einem Dilatanz-getriebenen Gastransport führt, sondern ein Gasdruck entsteht, der immer deutlich unter der minimalen Hauptspannung des Gesteins bleibt. Dies kann entweder durch ein Endlagerkonzept erreicht werden, in dem nur geringe Eisenmengen verwendet werden oder das zu geringen Korrosionsraten des Eisens unter den zu erwartenden chemischen Bedingungen führt.

Ein Sicherheitsnachweis für ein tiefes geologisches Endlager basiert auf einer Langzeitsicherheitsanalyse, berücksichtigt aber auch zusätzliche quantitative und qualitative Argumente, die die Berechnungsergebnisse sowie den Sicherheitsnachweis selbst untermauern. Quantitative Argumente werden eher aus der Anwendung von Sicherheits- und Performanceindikatoren, qualitative Argumente dagegen hauptsächlich aus Beobachtungen archäologischer oder geologischer Prozesse in natürlichen Systemen, die denen ähnlich sind, die in der Entwicklung des Endlagersystems erwartet werden, abgeleitet. Letztere werden als natürliche Analoga bezeichnet. Ein Ziel dieses Projektes war es,

Analoga-Studien zusammenzustellen, die für einen Sicherheitsnachweis für ein potenzielles Endlager in kristallinen Formationen verwendet werden können. Entsprechende Zusammenstellungen existieren bereits für potentielle Endlager in Steinsalz und Ton- bzw. Tonsteinformationen. Aufgrund der Komplexität und des zu berücksichtigenden geologischen Zeitrahmens (Bewertungszeitraum 1 Mio. Jahre) können Einblicke in relevante „natürliche“ geologische Prozesse wesentlich zum Systemverständnis und insbesondere zur Beschreibung und Untermauerung der Features, Events and Processes (FEP) beitragen. Daher wurde hier ein Ansatz entwickelt, Analogastudien basierend auf dem FEP-Katalog, der für kristalline Formationen in Deutschland erstellt wurde, zusammenzustellen und auszuwerten. In einem ersten Schritt wurden Komponenten und Prozesse aus dem FEP-Katalog identifiziert und für diesen Ansatz verwendet, für die ein signifikanter Beitrag von Informationen aus Analogastudien erwartet wurde. Es wurden die Komponenten-FEP „Wirtsgestein“, „Risse und Klüfte im Wirtsgestein“ sowie die Prozess-FEP „Permafrost“, „Mikrobielle Prozesse“, „Metallkorrosion“, „Alteration der Abfallmatrix“ und „Diffusion“ betrachtet. Für jedes FEP wurden die wichtigsten Merkmale aus den FEP-Beschreibungen im FEP-Katalog abgeleitet und in Form eines zusammenfassenden Datenblattes übernommen. Im Anschluss daran wurden für jedes FEP charakteristische Informationen aus NA-Studien aus der Literatur zusammengetragen sowie in Bezug auf die wichtigsten Charakteristika jedes betrachteten FEP zusammengestellt und strukturiert. Beispielhaft wird in dem vorliegenden Bericht der Ansatz für den FEP „Permafrost“ dargestellt, entsprechende Informationen für alle anderen FEP finden sich in einem separaten Bericht /FAH 21/. Für den FEP Permafrost wurden Informationen aus Analogastudien zu (i) Ausdehnung und Tiefen einschließlich der Einflussparameter, (ii) nicht gefrorenen Bereichen innerhalb des Permafrosts (taliki) – die auch in der oben beschriebenen Studie zum Permafrost verwendet wurden –, (iii) Kluftbildung und -füllung sowie zu (iv) Generell hat sich dieser Ansatz als nützlich erwiesen, um die verschiedenen und vielfältigen Informationen aus bestehenden Analogstudien für einen Sicherheitsnachweis vorzubereiten und zu strukturieren. Es wird empfohlen, diese Arbeit fortzusetzen, indem weitere FEP für potenzielle Endlager in kristallinen Formationen einbezogen werden.

Ein zentrales Ergebnis einer aktuellen Studie zu geochemischen Speziationsrechnungen für relevante Radionuklide im Nahbereich eines Endlagers in Steinsalz war, dass insbesondere für die Elemente C, Cl, I, Nb, Ni, Se und Sn hohe Ungewissheiten bezüglich ihres geochemischen Verhaltens und damit auch bezüglich ihrer Löslichkeit unter hochsalinaren Bedingungen bestehen. Da offene Fragen zu Se und I bereits in anderen

Forschungsprojekten bearbeitet werden, war das Ziel der hier beschriebenen Aufgabe, eine Strategie für weiterführende Experimente für die Elemente Cl, Ni, Sn und Nb zu entwickeln, um eine fundierte Grundlage für geochemische Modellrechnungen unter hochsalinaren Bedingungen zu schaffen. Für jedes dieser vier Elemente wird eine Beschreibung seiner Speziation mit relevanten Oxidationsstufen, der Bildung der wichtigsten Komplexe in Lösung mit anorganischen und organischen Liganden, relevanter Mineralphasen sowie des aktuellen Stands der geochemischen Modellierung einschließlich Einschränkungen und offenen Fragen präsentiert. Außerdem wurden für das Element die im EU-Projekt CAST erzielten Ergebnisse zu Kohlenstoff zusammengestellt und bewertet. Schließlich wurden für jedes Element die wichtigsten zukünftigen Forschungsarbeiten zur Erhöhung des Vertrauens in die Speziationsmodellierung und damit in die Bestimmung ihrer Löslichkeit vorgeschlagen.

Für Ni sollten sich zukünftige Arbeiten auf die Untersuchung von Festphasen konzentrieren, die die Löslichkeit von Nickel, insbesondere in alkalischen Lösungen und die Abschätzung von Pitzer-Wechselwirkungskoeffizienten für relevante Nickelspezies zum Inhalt haben. In  $\text{CaCl}_2$ -haltigen Lösungen sollte die Bildung und Relevanz von ternären Calcium-Nickel-Hydroxid-Komplexen untersucht werden, da diese die Löslichkeit von Nickel drastisch erhöhen können. Ein weiteres Thema betrifft die Bildung fester Lösungen mit Magnesium und Eisen(II) die Nickel in Gegenwart dieser Element bildet und über deren Stabilität wenig bekannt ist. Darüber hinaus sollte die Bildung von elementarem Nickel sowie von Nickelsulfid untersucht werden, da die Bildung dieser Phasen die Löslichkeit von Ni auf sehr niedrige Werte senken kann.

Der wichtigste Rückhalte Mechanismus für  $^{36}\text{Cl}$  in einem Endlager in Steinsalz ist wahrscheinlich der Isotopenaustausch zwischen Lösung und Halit, der in Sicherheitsanalysen bisher nicht berücksichtigt wird. Die Kinetik dieses Prozesses sollte untersucht werden. Schwer lösliche chloridhaltige Sekundärphasen, die die Mobilität von  $^{36}\text{Cl}$  beeinflussen, sind eher nicht zu erwarten.

Die Zusammenstellung und Diskussion der verfügbaren Informationen zur Zinnchemie hat eine Reihe von Wissenslücken aufgezeigt, die spezifische, weitere wissenschaftliche Untersuchungen erforderlich machen. Dazu gehören (i) die Relevanz und Stabilität von ternären Calcium- und Magnesium-Zinn(II)-Hydroxo-Komplexen, (ii) die Stabilität des  $\text{Sn}(\text{OH})_4(\text{aq})$ -Komplexes, (iii) die Löslichkeit der Mineralphase Hydroromarchit,  $\text{Sn}_3\text{O}_2(\text{OH})_2$  und Schönfliesit,  $\text{MgSn}(\text{OH})_4$  sowie (iv) Ionenwechselwirkungskoeffizienten der wichtigsten Zinnspezies in alkalischen Lösungen:  $\text{Sn}(\text{OH})_3^-$ ,  $\text{Sn}(\text{OH})_5^-$  und  $\text{Sn}(\text{OH})_6^{2-}$ .

Für Nb wird vorgeschlagen, für zukünftige Arbeiten zwei Untersuchungsstränge zu verfolgen. Zunächst sollte die Löslichkeit von Nb(+V)-Oxid im neutralen bis alkalischen Bereich mit unterschiedlichen Hintergrundkonzentrationen von NaCl, MgCl<sub>2</sub> und CaCl<sub>2</sub> untersucht werden, um zu beurteilen, ob unter bestimmten Bedingungen die Bildung anderer Phasen als Nb<sub>2</sub>O<sub>5</sub>(s) erfolgt. Pitzer-Koeffizienten für Wechselwirkungen zwischen Nb(OH)<sub>6</sub><sup>-</sup> und Na<sup>+</sup> sollen abgeleitet werden. Zweitens muss die Bildung von Hexaniobat-Ionenpaaren untersucht werden. Es wird vermutet, dass die Ausfällung von Nb<sub>2</sub>O<sub>5</sub>(s) zunehmend unterdrückt wird, da die Hexaniobat-Vorstufen als Ionenpaare stabilisiert werden, was schließlich zur Bildung anderer Phasen führt.



## Table of contents

<b>1</b>	<b>Introduction.....</b>	<b>1</b>
<b>2</b>	<b>Safety Case and Safety Assessment.....</b>	<b>5</b>
2.1	Uncertainty and sensitivity analysis .....	5
2.1.1	Introduction.....	5
2.1.2	Methods and approaches .....	6
2.1.2.1	Bayesian Sparse Polynomial Chaos Expansion (BSPCE) .....	8
2.1.2.2	Random Sampling High-dimensional Model Representation (RS- HDMR) method.....	9
2.1.2.3	Pointwise and generalised approach .....	10
2.1.3	Test models.....	10
2.1.3.1	Analytic model – time-dependent Ishigami function .....	10
2.1.3.2	Clay model.....	11
2.1.3.3	LILW model .....	12
2.1.4	Results .....	14
2.1.4.1	Time-dependent Ishigami function .....	14
2.1.5	Clay model.....	18
2.1.5.2	LILW model .....	26
2.1.6	Summary .....	33
2.1.7	Joint sensitivity analysis exercise (JOSA) .....	35
2.1.7.1	Introduction.....	35
2.1.7.2	Software .....	36
2.1.7.3	Calculation cases.....	38
2.1.7.4	Results and conclusions .....	40
2.1.7.5	Summary .....	49
2.2	Biosphere modelling: Czech German benchmark .....	50
2.2.1	Introduction.....	50
2.2.2	Contamination of the soil and pathways to plants .....	50
2.2.2.1	Modelling – Czech model.....	51
2.2.2.2	Modelling – German model.....	55

2.2.2.3	Results .....	57
2.2.3	Discussion .....	60
2.2.4	External irradiation from soil by irrigation .....	64
2.2.4.1	Results and discussion .....	65
2.2.5	Conclusions .....	67
2.3	Biosphere modelling: Radionuclide sorption in soils.....	68
2.3.1	Model description, implementation and validation .....	68
2.3.1.1	Geochemical code and databases.....	68
2.3.1.2	Model structure.....	68
2.3.1.3	Implemented submodels.....	69
2.3.1.4	Model validation.....	71
2.3.2	Calculation of $K_d$ values for two Refesols.....	74
2.3.2.1	Refesol properties.....	75
2.3.2.2	Definition of standard conditions .....	75
2.3.2.3	Modeling assumptions for $K_d$ calculations under field conditions.....	76
2.3.2.4	$K_d$ -values under standard conditions.....	77
2.3.3	Sensitivity analysis.....	79
2.3.3.1	Solution parameters and parameter ranges .....	79
2.3.3.2	Single Parameter Variations .....	81
2.3.4	Range of Variations .....	91
2.3.4.1	Calculation of $K_d$ Matrices.....	92
2.3.4.2	$K_d$ Ranges .....	93
2.3.4.3	$K_d$ Distributions .....	94
2.3.5	Summary .....	101
2.3.5.1	Processes not taken into Account.....	102
2.3.5.2	Parameters not taken into Account.....	102
2.3.5.3	Limitations of the Model.....	102
<b>3</b>	<b>International developments and co-operation.....</b>	<b>105</b>
3.1	RWMC.....	105
3.2	IGSC.....	106
3.3	Salt Club.....	114

3.4	Crystalline Club .....	118
3.5	IDKM .....	123
3.6	Microbial processes MIND .....	126
3.6.1	WP1 – Organic waste forms .....	127
3.6.2	WP2 – Engineered barriers.....	131
3.7	Workshop on Post-closure Criticality Safety.....	133
3.7.1	Introduction and background .....	133
3.7.2	Potential for future co-operation and next steps.....	135
3.8	MODARIA II.....	137
<b>4</b>	<b>Selected topics .....</b>	<b>145</b>
4.1	Bentonite re-saturation.....	145
4.1.1	Task 9 – FEBEX in-situ test .....	145
4.1.1.1	Test case description .....	145
4.1.1.2	Model concept .....	149
4.1.1.3	Thermal model.....	151
4.1.1.4	Water uptake Model.....	159
4.1.1.5	Provisional comparison of modelling results .....	168
4.1.1.6	Summary .....	169
4.1.1.7	Conclusions .....	170
4.1.2	Transferring code VIPER to COMSOL Multiphysics.....	170
4.1.2.1	Motivation .....	170
4.1.2.2	Conceptual model.....	171
4.1.2.3	Mathematical model.....	172
4.1.2.4	Transfer .....	173
4.1.2.5	Verification.....	174
4.1.2.6	Demonstration of multidimensional modelling .....	175
4.1.2.7	Outlook.....	177
4.2	Permafrost.....	178
4.2.1	Motivation .....	178
4.2.3	Observing freezing groundwater in fractures.....	183
4.2.3.1	Test components and preparation .....	183

4.2.3.2	Experimental procedure.....	189
4.2.4	Modelling growth of permafrost.....	209
4.2.5	Conclusions and outlook.....	216
4.3	Gas transport in clay stone .....	218
4.4	Natural analogues for repositories in crystalline rock formations.....	224
4.4.1	Background .....	224
4.4.2	NA information related to FEP Permafrost .....	226
4.5	Uncertainties in geochemical behaviour of relevant fission and activation products in the repository near-field in rock salt .....	240
4.5.1	Nickel.....	241
4.5.1.1	Oxidation states .....	241
4.5.1.2	Hydrolysis.....	241
4.5.1.3	Complex formation with chloride .....	242
4.5.1.4	Complex formation with sulfate .....	243
4.5.1.5	Complex formation with sulfide .....	243
4.5.1.6	Complex formation with carbonate.....	244
4.5.1.7	Relevant solid phases.....	244
4.5.1.8	Speciation model .....	248
4.5.1.9	Modeling in high-saline solutions .....	249
4.5.1.10	Suggestions for further work .....	251
4.5.2	Carbon.....	251
4.5.2.1	Redox and speciation .....	252
4.5.3	Chloride .....	255
4.5.3.1	Oxidation states .....	255
4.5.3.2	Speciation.....	255
4.5.3.3	Relevant solid phases.....	255
4.5.3.4	Suggestions for further work .....	257
4.5.4	Tin .....	257
4.5.4.1	Oxidation states .....	257
4.5.4.2	Speciation of tin(II) in aqueous solutions.....	257
4.5.4.3	Speciation of tin(IV) in aqueous solutions .....	261
4.5.4.4	Solid phases of Tin(II).....	264

4.5.4.5	Solid phases of Tin(IV).....	266
4.5.4.6	Speciation model .....	268
4.5.4.7	Modeling in high-saline solutions .....	268
4.5.4.8	Identification of knowledge gaps .....	270
4.5.5	Niob .....	270
4.5.5.1	Speciation.....	271
4.5.5.2	Relevant solid phases.....	274
4.5.5.3	Speciation model .....	278
4.5.5.4	Modeling in high saline solutions .....	278
4.5.5.5	Suggestions for further work .....	278
<b>5</b>	<b>Summary and conclusions .....</b>	<b>279</b>
	<b>References .....</b>	<b>289</b>
	<b>List of Figures.....</b>	<b>317</b>
	<b>List of Tables .....</b>	<b>325</b>



# 1 Introduction

Within this project strategies and methods to build a safety case for deep geological repositories are further developed. This includes all different aspects of the safety case, namely the assessment basis, methods and strategies, the scientific fundamentals, long-term safety assessment and additional lines of evidence to be used in a safety case. In the international framework the methodology of the safety case is frequently applied and continuously improved. According to definitions from IAEA and NEA the safety case is a compilation of arguments and facts, which describe, quantify and support the safety and the degree of confidence in the safety of the geological repository. The safety of the geological repository should be demonstrated by the safety case. The safety case is the basis for essential decisions during a repository programme. It comprises the results of safety assessments in combination with additional information like multiple lines of evidence and a discussion of robustness and quality of the repository, its design and the quality of all safety assessments including the basic assumptions.

A key element of the safety case is the safety assessment, which represents the evaluation of the performance of a disposal system and the quantification of its potential radiological impact on human health and the environment. The assessment has to demonstrate whether the disposal facility complies with the national regulatory requirements. It is accompanied by an open and adequate addressment of uncertainties. Usually, a comprehensive approach for the handling of the uncertainties is applied including the analysis of the potential evolutions of the repository system and a uncertainty and sensitivity analysis reflecting the uncertainty of model parameters describing the complex repository system. In addition to the quantitative assessment of the repository evolution other arguments are used to support the safety case. One group of arguments are natural analogues, namely processes and features observed in nature with similarity to the processes and conditions expected in the future evolution of the repository system.

The R&D work performed within this project contributes to the improvement of process and system understanding as well as to the further development of methods and strategies applied in the safety case. Emphasis was put on the following aspects:

Regarding the treatment of parameter uncertainty, as part of this project the collaboration with groups from USA, Belgium, Finland, France, Russia and Switzerland was continued to compare the approaches for probabilistic uncertainty and sensitivity analysis and to

learn from each other. Several calculation cases, based on the respective national programmes, were selected for comparison of methods.

In the frame of a co-operation with the Czech organisations SURAO and UJV, biosphere models applied in long-term safety assessment have been compared and similarities and differences identified. A crucial process is the transport and immobilization in the soil. With respect to this process state-of-the-art calculations for selected radionuclides have been carried out to determine the bandwidth of sorption on two representative reference soils in Germany.

The aspect of adequately communicating the safety case to key stakeholders, particularly the wide public is currently receiving raising interest on national and international level. In addition, the topic of information, data and knowledge management (IDKM) has been acquiring an increasingly important role in society, and also in the field of radioactive waste disposal, where key challenges are the transfer of relevant information about the repository to the next generations due to the long timeframe of repository implementation until its closure. Substantial contributions were contributed to the NEA activities on safety case communication, particularly on the joint workshops of the Integration Group for the Safety Case (IGSC) and the Forum of Stakeholder Confidence (FSC) as well as to the new NEA initiative "Information, Data and Knowledge Management (IDKM).

Geochemical data and codes available for solubility calculations in repository near field in rock salt have been analysed in a previous study /MOO 17/. On the basis of the outcomes, namely that particularly for the elements C, Cl, Nb, Ni, and Sn high uncertainties exist with respect to their geochemical behaviour in highly saline conditions and therewith for the determination of solubilities, results for carbon yielded in the European project CAST were evaluated and a strategy for further experiments to derive a substantiated basis for geochemical modelling in high saline conditions for the elements Cl, Ni, Sn und Nb was developed.

Natural analogues are one type of additional arguments, which can be used to support the safety case. One task of the project was devoted to the compilation of analogue studies for radioactive waste repositories in crystalline formations and a systematic analysis, how such studies can support a safety case. A FEP catalogue for repositories in crystalline formations, developed in the project CHRISTA II, FKZ 02E11617, was used for this task.

With regard to bentonite re-saturation two different aspects were addressed within the project. Firstly, an active participation in the Task Force on Engineered Barrier Systems (TF EBS) implied model simulations on Task 9 – FEBEX in-situ test. Secondly, the transfer of the model concept for bentonite re-saturation as previously realised in the 1D code VIPER to the COMSOL Multiphysics code was started.

Under permafrost conditions, radically different groundwater flow systems compared to those prevailing during warm climate stages may evolve as freezing grounds provide an efficient flow barrier. However, the degree to which lower groundwater systems are affected by freezing depends of course on the thickness of the permafrost.



## **2 Safety Case and Safety Assessment**

### **2.1 Uncertainty and sensitivity analysis**

#### **2.1.1 Introduction**

Probabilistic analysis is a well-proven tool for investigating the overall uncertainty of the results of a computational model (uncertainty analysis) as well as its sensitivities against variation of input parameters (sensitivity analysis). In the context of final repository Performance assessment (PA), probabilistic analysis is internationally considered as state of the art for uncertainty management. Moreover, sophisticated sensitivity analysis is suitable for providing deeper insight to the behaviour of PA models and can therefore increase model understanding and confidence.

For some time, going along with the increase of computer capabilities, sophisticated methods of probabilistic sensitivity analysis have been in the focus of mathematical research. Various new approaches have been developed, which look promising but need testing with practical models. Repository PA models, which take into account a number of interacting physical and chemical effects, are often highly non-linear and rather complex and so provide a specific challenge for sensitivity analysis.

The use of investigations on the application of newly developed, sophisticated sensitivity analysis methods on complex PA models is twofold: on the one hand, mathematicians get feedback about the performance of their methods on realistic models, which can trigger improvements and further developments. On the other hand, the performance assessors gain more insight about the behaviour and sensitivities of their own models and learn which sensitivity measures are best appropriate to reflect the specific properties and how sensitivity analysis can contribute to model understanding and parameter prioritisation. This is therefore an essential piece of work in view of a safety case for a deep geological repository in Germany. The work presented in this chapter is therefore focused on this topic.

In the research project MOSEL (02E10941) /SPI 2017/, several modern methods of sensitivity analysis have been investigated using differently complex realistic PA models. In the meantime, the mathematical research has proceeded, now allowing for investigations that could not be performed within MOSEL. Specifically, the role of parameter

interactions remained an open topic. The work presented in this chapter is therefore focused on this topic.

In this chapter, we describe two tasks, which are related to each other. Subsequently to the investigations in MOSEL, some more detailed sensitivity analyses have been made, specifically focused on the influences of parameter interactions, using sophisticated metamodeling methods that could not be applied in MOSEL. Moreover, GRS is involved in an informal international working group (Joint Sensitivity Analysis Exercise, JOSA), which consists of a number of organisations dealing with radioactive waste disposal and was founded in order to exchange model results and to test different sensitivity analysis approaches. In the following, at first a very short theoretical and methodological introduction is given; then we present relevant results and findings from the mentioned investigations. Since both tasks described here are being continued, this should be seen as a report on an interim status.

## **2.1.2 Methods and approaches**

The output of a computational model depends on a number of input parameters, which are subject to a specific uncertainty, typically characterised by a probability density function (pdf). As a result, the model output is also uncertain. Generally spoken, the sensitivity against a parameter or parameter combination is analysed by determining the influence of the uncertainty of that parameter (combination) on the uncertainty of the model output.

Variance-based sensitivity indices are based on the idea to decompose the total unconditional variance of the model output into partial variances corresponding to different terms in the ANOVA decomposition /SAL 04/. The key indices used most often are the first-order index (SI1) and the total-order index (SIT). SI1 refers to the individual impact of one parameter on the model and SIT represents the total effect of one parameter on the output in interactions with all other parameters. The second-order sensitivity indices (SI2) describe the common influence of a set of two model parameters, also higher orders are possible. We will refer to such common influences as parameter interactions.

Different methods for calculating variance-based sensitivity indices are available. Established methodological approaches are the Sobol' method /SOB 01/ or EFAST (Extended Fourier Amplitude Sensitivity Test /SAL 99/). However, despite recent advances in improving formulas for the Sobol' method /KUC 17/, many thousands of model runs may

be required for the convergence of these methods, depending on the model properties. Especially, for calculation of second- or higher-order sensitivity indices, direct variance-based methods of sensitivity analysis generally perform poorly. One of the reasons for that is that from a set of probabilistic model runs the large majority of them are of little relevance for the interaction under investigation, which often leads to unstable and un-sound index values. With the challenging hypothetical but realistic PA model oriented at the features of an existing repository for low- and intermediate-level radioactive waste (LILW), investigated in MOSEL, some of the main findings were:

- High sample sizes up to several tens of thousands, depending on the evaluation method, are needed to achieve stable results.
- The classical Sobol' method does not produce satisfying results with reasonable numbers of model runs. Even with more than 30,000 runs, the calculated time-curves of sensitivity indices are unstable and volatile; for some intervals, total-order indices significantly above 1 were calculated by the method.
- The EFAST method seems to perform marginally better than the Sobol' method. The time-curves of sensitivity indices look a bit smoother and more stable, but still displaying random-looking and implausible oscillations. Moreover, the results are sensitive to the random seed of the sampling sequence. At least, the calculated total-order indices remain below 1.

A major drawback of classic Sobol' as well as EFAST is that they require specifically tailored sampling schemes, which cover the parameter space rather inhomogeneously.

In many cases metamodels can provide accurate representations of the detailed and costly original models. A metamodel (or surrogate model) is a computationally fast mathematical approximation model that is supposed to simulate the output of the original model as accurately as possible, which is reached by adjusting its internal coefficients by a number of original model runs. Metamodels play an important role in the analysis of complex systems. They serve as an effective way of mapping input-output relationships and assessing the impact of the inputs on outputs /BAR 06/. For black-box models or laboratory observations, where mechanistic models do not exist, meta-models can provide a valuable insight into the underlying relationship between inputs and outputs.

In MOSEL /SPI 17/, two PA models, describing hypothetical repositories in salt and clay, were established, which are also used for the investigations in this chapter. While the clay model is a relatively simple and smooth PA model, the salt (LILW) model is more complex, including a discontinuous nature as a result of barrier dissolution depending

upon certain parameters. Further, the model output is skewed and tailed; most of the output values are very low. Several variants of the LILW model, which only differ regarding the number of varied input parameters, are considered. Additionally, as a well-investigated analytic test model the Ishigami function is studied.

For the clay model investigations, we consider sets of computation results achieved with two sampling methods (random and quasirandom LpTau). As meanwhile it can be considered a fact that nearly always quasirandom sampling performs significantly better than random sampling and to avoid confusing variety of results, we exclusively use LpTau for analysing the LILW model.

In the work presented here, two metamodel-based methods (RS-HDMR, BSPCE), which are contained in the SobolGSA software package /SOB 21/ are investigated to determine parameter interactions. These methods are based upon the concept of sparse Polynomial Chaos Expansion (PCE). RS-HDMR is an important subclass of PCE. With PCE, the input/output relations of computer models are expressed with polynomial terms. In such a PCE representation, usually a few terms out of many can already capture the most salient features of the model response within the accounted input space. On this basis, a sparse PCE can be built. After generation of the sparse PCE of the model response, the Sobol' indices for global sensitivity analysis can analytically be computed at negligible additional computational costs on the basis of analytical functions of the polynomial chaos (PC) coefficients generated from the input/output data. Consequently, a higher order sensitivity analysis is possible with a relatively low number of original model runs (/SHA 17/). Some orienting investigations with RS-HDMR were already done in a previous project /NOS 18/; the results looked promising but left some open questions, requiring further investigation.

In the following subsections, the basic ideas of the applied methods and approaches are roughly explained. For details, we refer to the literature.

#### **2.1.2.1 Bayesian Sparse Polynomial Chaos Expansion (BSPCE)**

The BSPCE method uses a Bayesian approach to build the sparse PCE, i.e. the Bayesian model averaging (BMA), which only considers the significant polynomial terms for the data set at hand to catch the main characteristics of the model output. This may only require a small number of basis functions and polynomial chaos (PC) coefficients and thus a small number of simulations to calculate the sparse PC coefficients. More

specifically, BMA, which is a formal statistical approach based on Bayes' theorem, is used to quantitatively compare and rank different alternative models. With the BMA approach, the posterior probability for each individual model is estimated via prior information of each model in combination with the observed/original data to find the best one among the rival models. Thereby, the model selection criterion KIC (Kashyap information criterion) is utilised in such a way that it is evaluated for each competing model. The one model with the smallest KIC is the best model. The KIC criterion decreases the computational effort by considering the most likely parameter set instead of integrating over the entire parameter space. This ensures efficiently finding the best sparse PCE from the available data set. BSPCE provides first and total-order indices. More details on the algorithm and also the different mathematical equations of the PCE and Bayesian approaches can be found in /SHA 17/.

#### **2.1.2.2 Random Sampling High-dimensional Model Representation (RS-HDMR) method**

The RS-HDMR method was already shortly described in /NOS 18/, further details can be found in /ZUN 13/, /SPI 18/ and /SOB 21/. The integrable component functions of the ANOVA-HDMR decomposition built from the input/output data are decomposed into one- and two-dimensional basis functions of orthonormal polynomials and two coefficients of decomposition. This results into a HDMR approximation function of up to second order interaction. The regression method is then used for minimizing the discrepancy between the original model function and its polynomial chaos expansion approximation. By means of the obtained coefficients of the decomposition, the Sobol' indices of first and second order can be determined. Based on the assumption that third- and higher-order interactions are negligible, SIT is approximated as the sum of SI1 and all related SI2. One has to keep in mind that this approach neglects parameter interactions of order 3 or higher.

For the RS-HDMR method, initial guess has to be made for the maximum orders of the polynomial terms ( $k, l$ ) before running the approach. Although in principle, higher maximum polynomial orders allow better approximation of the model behaviour, this is only possible if enough real model results are available. It turned out that one has to choose the polynomial orders with care in order to avoid overfitting artifacts, which can significantly distort the calculated sensitivity indices. According to /SHA 2017/, a high-degree polynomial or a large number of input parameters results in a large number of PCE coefficients. However, a large number of coefficients has the tendency to overfitting when regression-based methods are used to build the sparse PCE for computing the Sobol'

indices. In that case, a large number of simulations is then required to compute the overall set of PCE coefficients.

### 2.1.2.3 Pointwise and generalised approach

For analysis of time-dependent results, one normally investigates each point in time separately by calculating sensitivity indices as relative contributions to the total variance:

$$S_i(t) = \frac{V_i(t)}{V(t)}. \quad (2.1)$$

Such an evaluation can be misleading, as the total variance itself can vary over several orders of magnitude during the model time. This does not become visible in such curves and can lead to misinterpretation of apparently high sensitivities, for instance at late times, where there is often very little variability of the model output at all and consequently nearly no influence from the input parameters.

Therefore, additionally to the *pointwise evaluation*, we apply cumulative approach, which we call *generalised evaluation*. For this approach, the output variance is averaged over all previous time steps in the analysis of the current step, so that the complete history of model variance is included in the calculation of the indices:

$$S_i(t) = \frac{\int_0^t V_i(t') dt'}{\int_0^t V(t') dt'}. \quad (2.2)$$

By using this formula, all previous time steps go into the analysis of the current step. If the total variance decreases by several orders of magnitude towards the end of the model time, which is a typical situation for repository models, these indices become nearly constant at later times. Apart from scaling the variance, /ALE 20/ claims that the above formula also takes care of the temporal correlation structure of the process.

### 2.1.3 Test models

#### 2.1.3.1 Analytic model – time-dependent Ishigami function

The Ishigami function is a simple mathematical function with three parameters, which is often used as a test model for sensitivity analysis. It is specifically appropriate for investigating higher-order effects as it exhibits a strong interaction between the first and third

parameters, while the SI1 of the third parameter is 0. Detailed sensitivity investigations were performed, e.g., in the framework of the EU project PAMINA /PLI 2009/.

*Zaccheus and Kucherenko /ZAC 15/* introduced a time-dependent model, which is defined via the ODE

$$\frac{dY}{dt} = a'_t \sin^2(\pi[2X_2 - 1]) + b'_t (\pi[2X_3 - 1])^4 \sin(\pi[2X_1 - 1]) \quad (2.3)$$

with

$$a'_t = \frac{da_t}{dt}, \quad b'_t = \frac{db_t}{dt}$$

$$a_t = 7 \exp(-t), \quad b_t = 0.1 \exp(t).$$

and the parameters  $X_1, X_2, X_3$  uniformly distributed in the interval (0,1).

The ODE is solved with the initial condition being the original Ishigami function:

$$Y_0 = \sin(\pi[2X_1 - 1]) + a_0 \sin^2(\pi[2X_2 - 1]) + b_0 X_3^4 \sin(\pi[2X_1 - 1]) \quad (2.4)$$

with  $a_0 = 7$  and  $b_0 = 0.1$ .

### 2.1.3.2 Clay model

The clay model describes a generic repository in a Northern German clay formation. It was already investigated in the project TONI /RUE 07/ and was used as a test model in MOSEL /SPI 17/. Six parameters were selected for investigation, which are listed in Tab.

**2.1.**

**Tab. 2.1** Parameters of the clay model

Parameter	Type of pdf	Range
<i>DiffClay2:</i> Diffusion constant clay formation 1	Log-uniform	8.3E-12 - 8.3E-10
<i>DiffClay3:</i> Diffusion constant clay formation 2	Log-uniform	8.3E-12 - 8.3E-10
<i>KdBent:</i> Kd value bentonite (U)	Log-uniform	4 - 400
<i>KdClay2:</i> Kd value clay formation 1 (U)	Log-uniform	2 - 200
<i>KdClay3:</i> Kd value clay formation 2 (U)	Log-uniform	2 - 200
<i>PorClay:</i> Porosity clay formation 2	Uniform	0.06 - 0.24

### 2.1.3.3 LILW model

The LILW model is based on a model for an existing repository site for low and intermediate-level waste in rock salt and reflects a number of its typical properties. It is described in detail in /SPI 17/. Here we repeat only that the model includes a seal failure, which can occur at some point in time, depending on the values of different parameters, and typically leads to a sudden increase of the model output by about two orders of magnitude. At many points in time, the distribution of output values is bimodal, resulting from the overlap of the distributions that represent the cases with and without seal failure.

Tab. 2.2 lists the model input parameters. Originally, four model variants were investigated, which differ by the actually varied parameters while all others were fixed to their standard values. In the work presented here, we investigate only the model variants with 6 and 20 parameters (LILW6 and LILW20).

**Tab. 2.2** Parameters of the LILW model (LILW-6: only red parameters, LILW-7: red and green, LILW-11: red, green and blue, LILW-20: all parameters)

Parameter	Type of pdf	Range / pdf parameters	Standard value
<i>GasEntryP:</i> Gas entry pressure	Uniform	0 - 2.5	2.0
<i>IniPermSeal:</i> Initial permeability of dissolving seal	Log-normal	$\mu=41.0605$ $\sigma=1.9809$	$1.0 \cdot 10^{-18}$
<i>RefConv:</i> Reference convergence rate	Log-uniform	$1.0 \cdot 10^{-5}$ - $1.0 \cdot 10^{-4}$	$4.0 \cdot 10^{-5}$
<i>AEBConv:</i> Factor of local convergence variation in AEB	Log-uniform	0.05 - 5.0	1.0
<i>GasCorrPE:</i> Organics corrosion rate	Log-normal	$\mu=12.6642$ $\sigma=1.1177$	$1.0 \cdot 10^{-5}$
<i>TBrine:</i> Time of brine intrusion	Log-normal	$\mu=8.8857$ $\sigma=0.6933$	7500
<i>BrineMgSat:</i> Relative magnesium saturation of brine	Triangular	0 - 0.1 - 1.0	0.1
<i>RGConv:</i> Factor of local convergence variation in RG	Log-uniform	0.25 - 2.5	1.0
<i>GasCorrFe:</i> Metal corrosion rate	Log-normal	$\mu=-6.6728$ $\sigma=1.1177$	$4.0 \cdot 10^{-3}$
<i>AEBGasProd:</i> Proportion of the material involved in gas production in AEB	Triangular	0.1 - 0.8 - 1.0	0.8
<i>NABGasProd:</i> Proportion of the material involved in gas production in NAB	Triangular	0.1 - 0.8 - 1.0	0.8
<i>RGGasProd:</i> Proportion of the material involved in gas production in RG	Triangular	0.1 - 0.8 - 1.0	0.8
<i>NABConv:</i> Factor of local convergence variation in NAB	Log-uniform	0.05 - 5.0	0.2
<i>MBCConv:</i> Factor of local convergence variation in MB	Log-uniform	0.075 - 0.75	0.2
<i>DiffCoeff:</i> Diffusion coefficient	Log-uniform	$1.0 \cdot 10^{-10}$ - $1.0 \cdot 10^{-8}$	$1.0 \cdot 10^{-9}$
<i>RefPor:</i> Reference porosity	Triangular	0.15 - 0.3 - 0.4	0.3
<i>FacDisp:</i> Longitudinal dispersion length	Triangular	0.5 - 1.0 - 2.0	0
<i>ConvFak:</i> Variation factor for sheeting	Uniform	0 - 2.0	1.0
<i>PorDebris:</i> Porosity of debris from sheeting	Uniform	0.25 - 0.5	0.4
<i>C14Inv:</i> Variation factor for C-14 inventory	Uniform	0 - 2.5	1.0

## 2.1.4 Results

### 2.1.4.1 Time-dependent Ishigami function

In order to get a feeling of how the RS-HDMR and BSPCE methods perform, we start with some investigations on the time-dependent Ishigami function defined in 2.1.3.1. The first- and total-order indices for the parameter  $X_1$ , calculated pointwise in time using the direct Sobol' formula, are presented in Fig. 2.1.

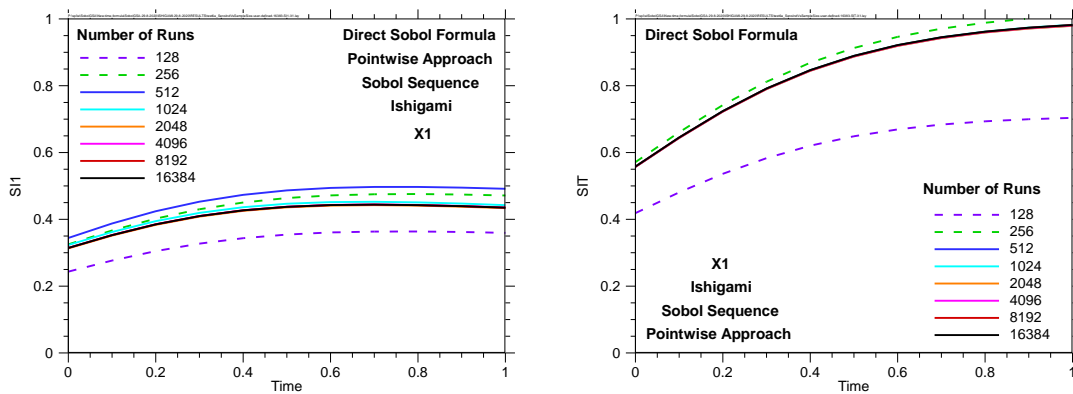


**Fig. 2.1** Pointwise approach: SI1 and SIT of  $X_1$  of the Ishigami function with Sobol' sampling and different number of simulations, calculated using the direct Sobol' formula

Obviously, 128 runs are insufficient but with 1000 or more runs one gets stable results, which can be used as reference for assessing other methods.

The SI1 results calculated by the RS-HDMR method with four different combinations of polynomial orders ( $k-l$ ) are presented in Fig. 2.2. The calculations were made on the basis of the same samples as the Sobol' evaluation. In all cases stable results are reached already with 256 runs, so one can conclude that the method actually reduces the required sample size. However, it poses the challenge of correct choice of coefficients. It appears that with  $k=10$  sufficiently good results are calculated, but  $l=2$  seems to be better than  $l=4$  or  $l=5$  for low sample size. This is due to the mentioned effect of overfitting.

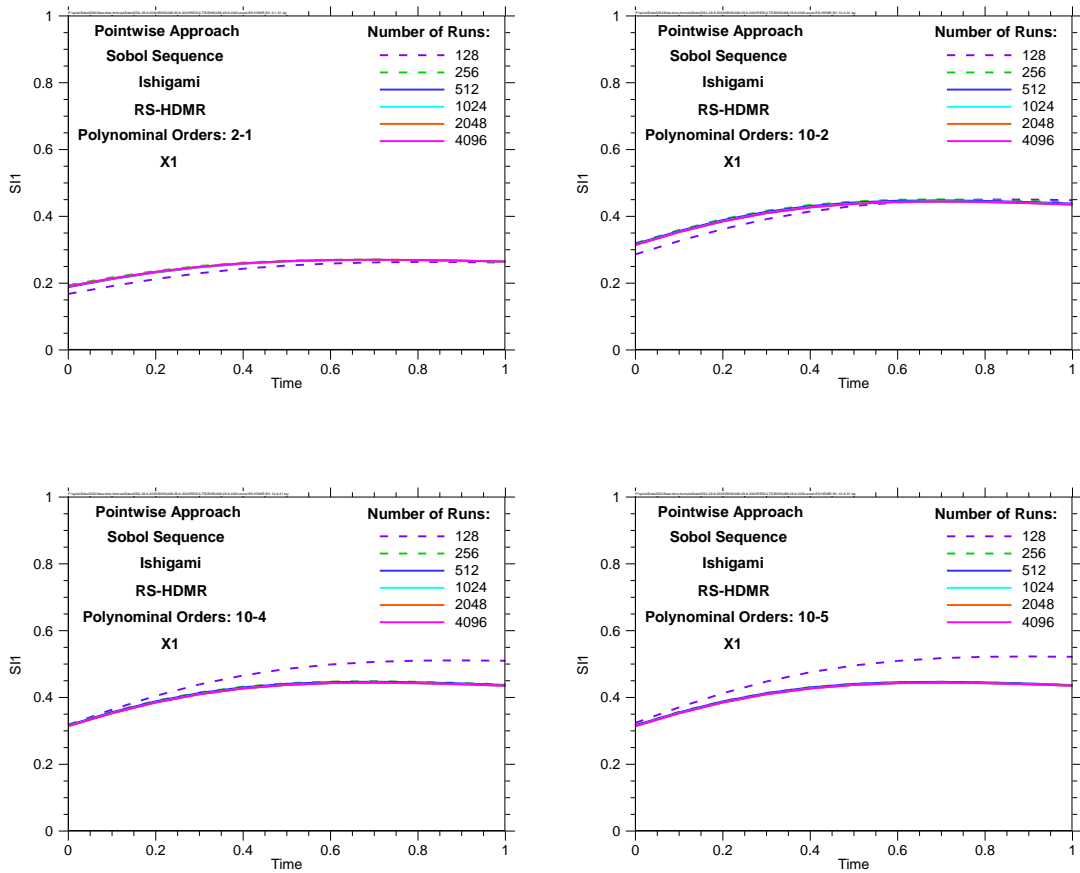


**Fig. 2.2** Pointwise approach: SI1 of X1 of the Ishigami function with Sobol' sampling and different number of simulations and coefficients, calculated using the RS-HDMR method

The RS-HDMR approach is also capable of calculating second-order effects. In the Ishigami function there is a strong interaction between  $X_1$  and  $X_3$ , which is analysed in Fig. 2.3 by presenting the respective SI2. The second order analysis seems to require higher polynomial orders, especially higher  $l$ , to become stable, but if these parameters are well-chosen the method obviously yields reliable results even at a sample size as low as 256.

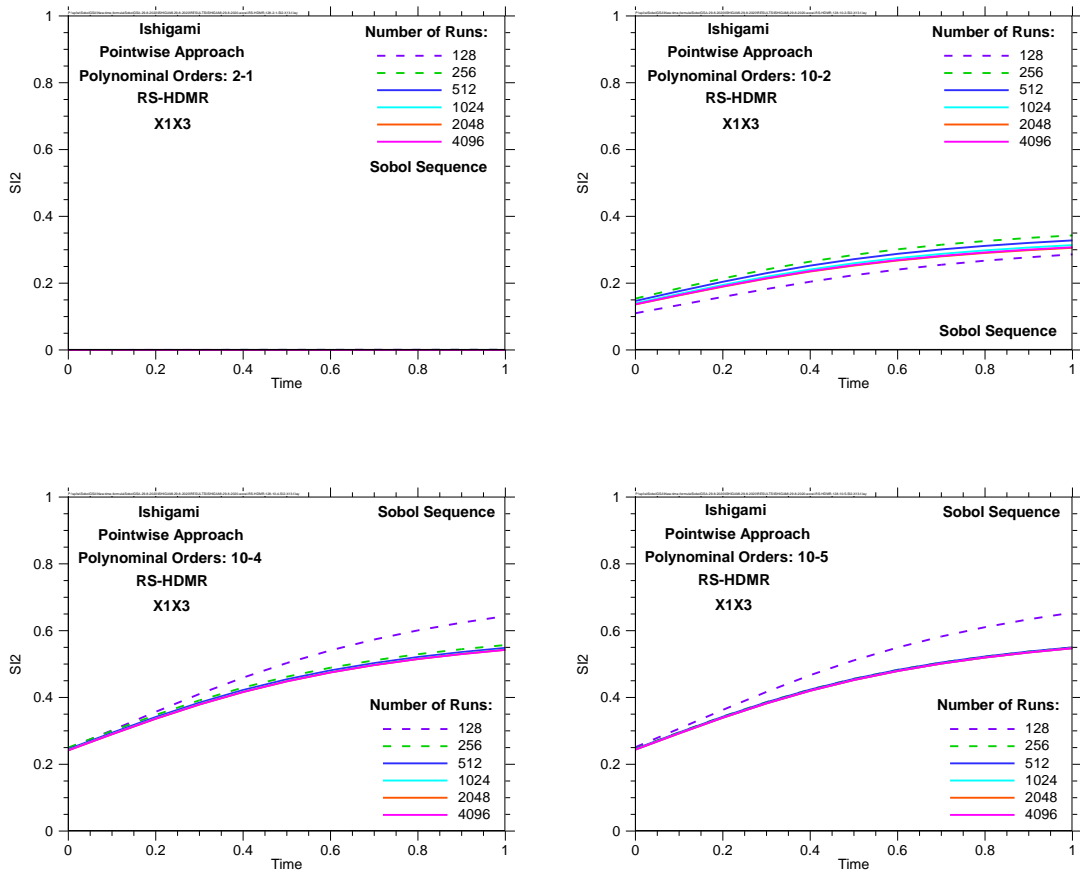


**Fig. 2.3** Pointwise approach: SI2 of the Ishigami function with Sobol' sampling and different number of simulations and coefficients, calculated using the RS-HDMR method

We now have a look at the results for the total index SIT, as presented in Fig. 2.4. By mathematical reasons, the SIT value cannot exceed 1, and if that nevertheless happens, the calculation method has failed. One can conclude from the figures that a sample size of 128 is definitely too low, but for 256 or more runs one gets fairly stable results if appropriate polynomial orders are applied.

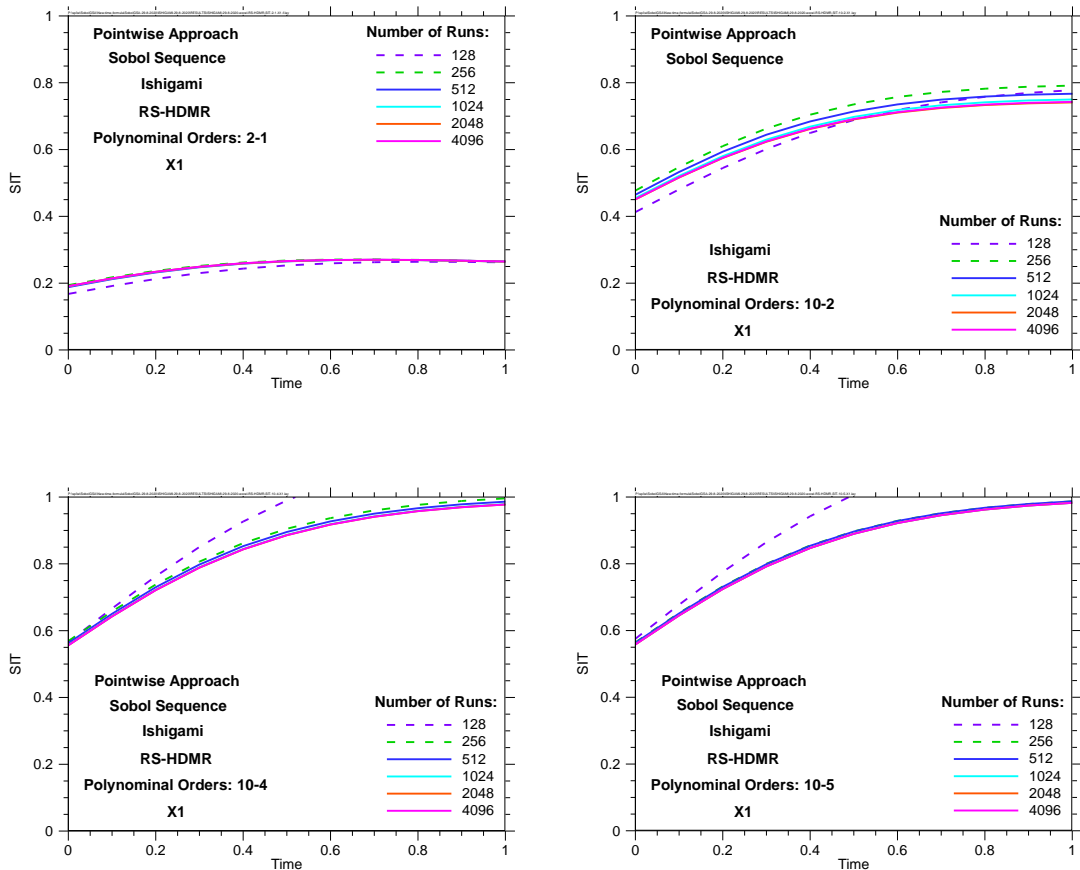


**Fig. 2.4** Pointwise approach: SIT of X1 of the Ishigami function with Sobol' sampling and different number of simulations and coefficients, calculated using the RS-HDMR method

One should keep in mind that RS-HDMR approximates the total-order indices by summing up first- and second-order indices. The third-order interaction between all three parameters is neglected. The fact that the curve nevertheless reaches nearly 1 at the end of time shows that this three-parameter interaction is actually very low.

Finally, in Fig. 2.5 the SI1 and SIT results for X1, calculated using the BSPCE method, are shown. This method yields stable results even with 128 runs. As an additional advantage, it does not require user-choice of additional parameters and calculates "true" SIT. The fact that the SIT curves very much resemble those obtained with RS-HDMR is another indication that there is no relevant third-order interaction.

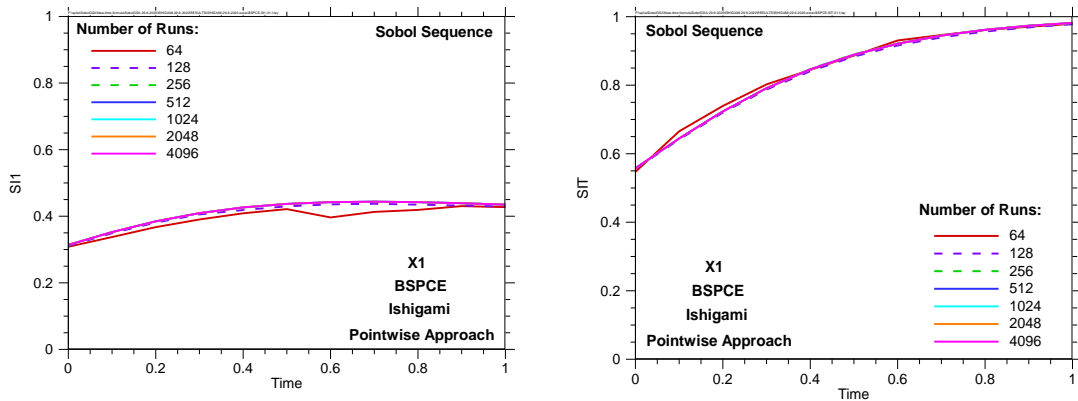


**Fig. 2.5** Pointwise approach: SI1 of and SIT of X1 of the Ishigami function with Sobol' sampling and different number of simulations, calculated using the BSPCE method

### 2.1.5 Clay model

The clay model, although showing some repository-typical properties, is a relatively smooth example model with a fairly high degree of linearity (or at least monotonicity).

#### 2.1.5.1.1 RS-HDMR method - Choice of the coefficients

##### Pointwise approach

In the following we investigate for the pointwise approach how the choice of the two polynomial orders ( $k-l$ ) influences the RS-HDMR results for SI2 (interaction of the parameters *DiffClay2* and *DiffClay3*) and SIT (*DiffClay3*). For training the internal meta-model, we use sets of 8192 (random) and 4096 (LpTau) simulations. The results are presented in Fig. 2.6. In general, it can be seen that LpTau sampling, despite the smaller sample size, produces better consistent curves.

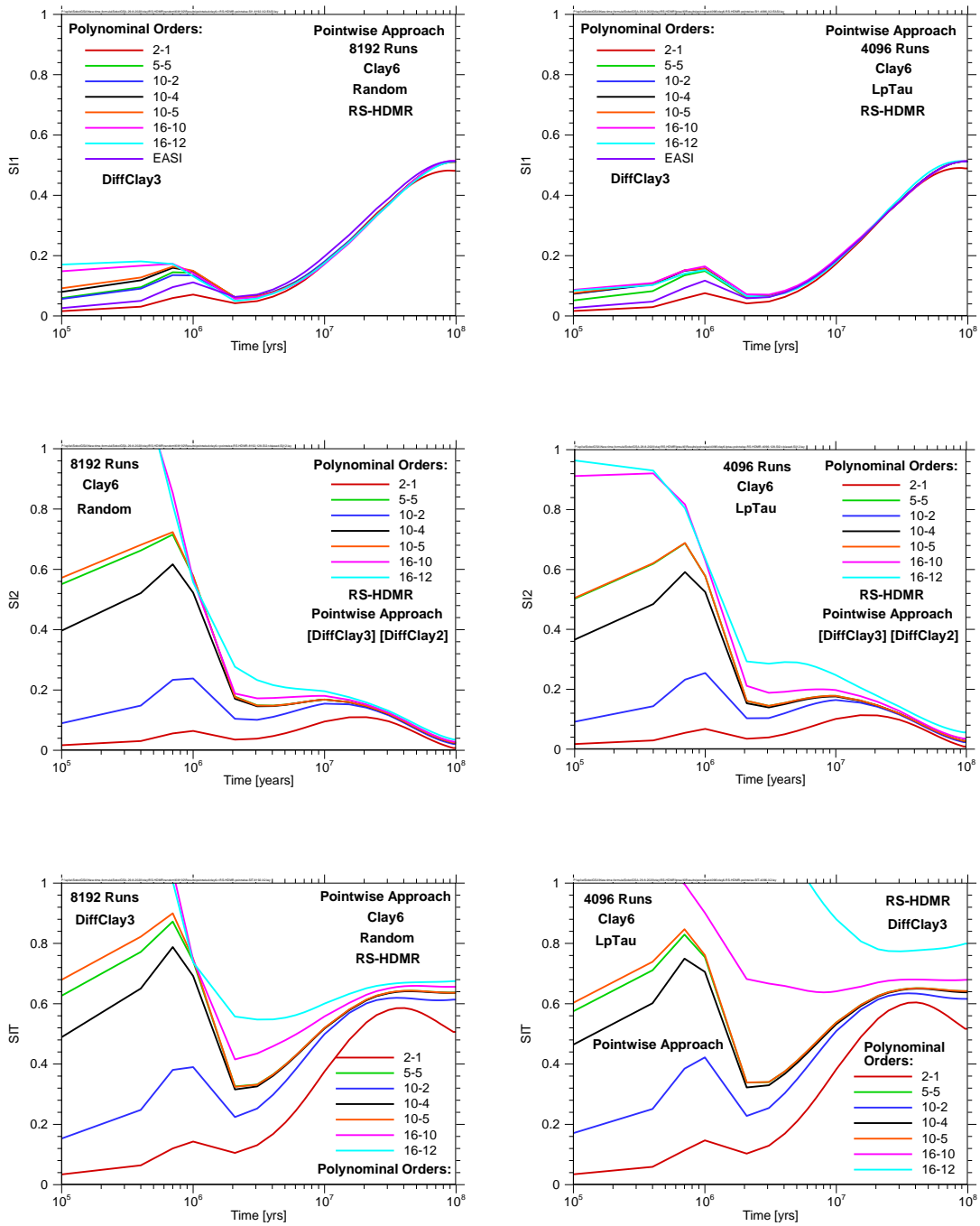


**Fig. 2.6** Pointwise approach: SI1 of *DiffClay3*, SI2 of [*DiffClay3*][*DiffClay2*] and SIT of *DiffClay3* with 8192 runs (random sampling) and 4096 runs (LpTau sampling), calculated using RS-HDMR with different pairs of polynomial orders

The mentioned effect of overfitting leads to calculated sensitivity indices above 1 for  $k=16$ , which is obviously too high. The best results are achieved with 5-5 or 10-5, at lower  $l$  convergence is not reached, at least for early points in time.

The first-order index (SI1) converges quicker with respect to the polynomial coefficients than the SI2 and SIT indices. For comparison, the SI1 curves calculated with EASI are also presented. Under the (not necessarily true) assumption that these represent the "true" values, one can conclude that RS-HDMR systematically calculates too high SI1 at early points in time (which means if the basis of nonzero-results is weak) except if very low  $k$  is chosen.

The figure shows that the pointwise approach calculates relatively low 1<sup>st</sup>-order sensitivities for early times, which increase up to about 0.5 at the end of the model time. In contrast, the 2<sup>nd</sup>-order index starts at high values and decreases to nearly 0. Obviously, the system is dominated by *DiffClay2-DiffClay3*-interaction in the beginning, but the interaction loses importance with time and the system is more controlled by individual parameter influences.

### **Generalised approach**

In contrast to the pointwise approach, the generalised approach as defined in 2.1.2.3 takes account of the total history of sensitivity, so that typically the sensitivity curves reach nearly stable values at some time. Fig. 2.7 presents the same curves as Fig. 2.6, but calculated using this approach. At early times, the curves proceed similarly as those of the pointwise approach but reach medium, nearly constant values at the end. At late times, the total output variance is small, so that the relative contributions of the different parameters or parameter combinations do no longer play an essential role if evaluated in this way.

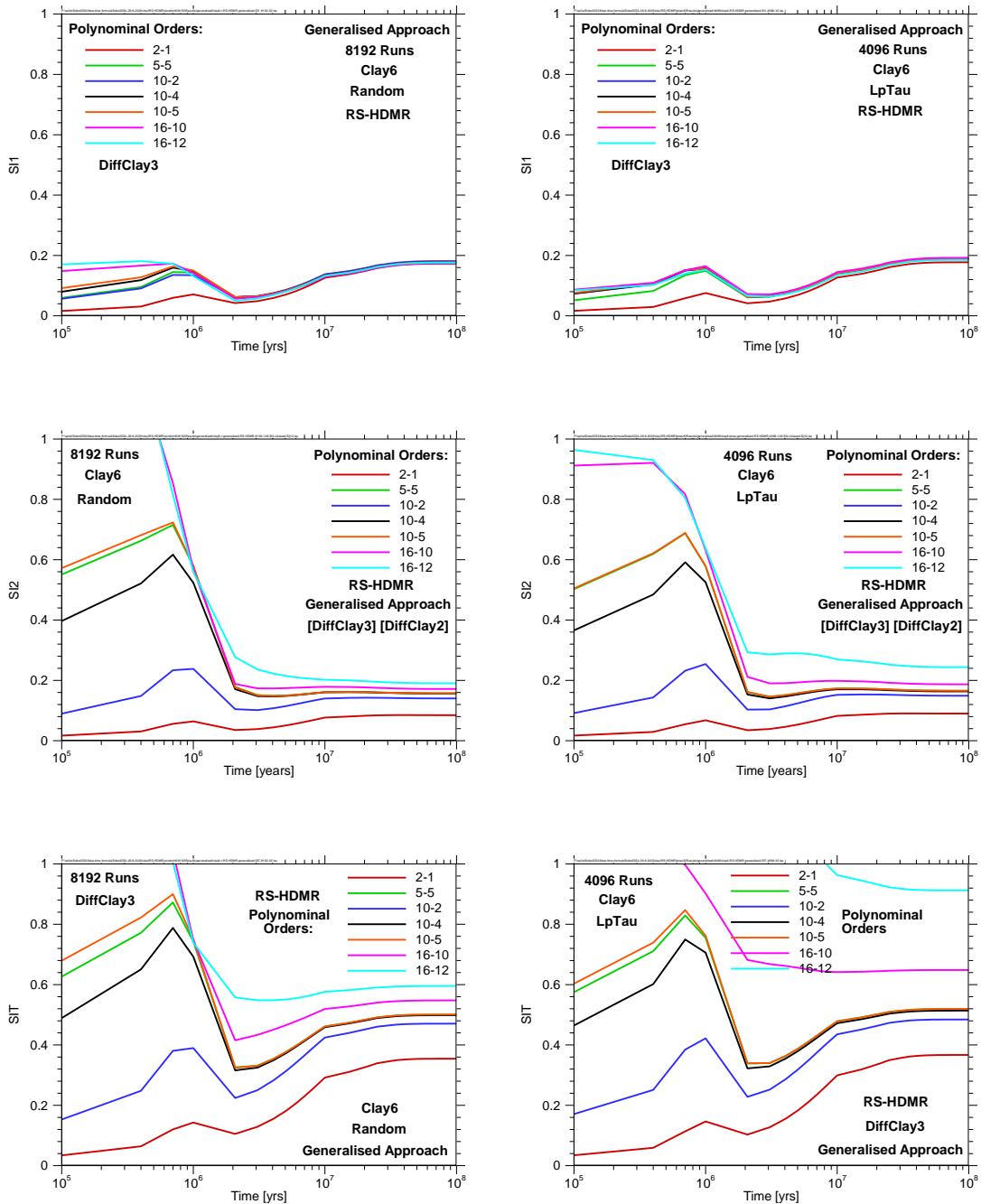


**Fig. 2.7** Generalised approach: Si1 of *DiffClay3*, Si2 of [*DiffClay3*][*DiffClay2*] and SIT of *DiffClay3* with 8192 runs (random sampling) and 4096 runs (LpTau sampling), calculated using RS-HDMR with different pairs of polynomial orders

For the generalised approach, the performance of the RS-HDMR method is the same as for the pointwise approach. As for the pointwise approach, for accurate determination of the indices, polynomial coefficient ( $k-l$ ) combinations of 10-5 or 5-5 yield the most convincing results.

#### **2.1.5.1.2 BSPCE method**

Compared to the RS-HDMR method, the BSPCE method has the advantage that it determines the optimal polynomial orders internally. So, there is no need for the user to experiment with technical parameters and assess the quality of results. Moreover, it calculates "true" total-order indices. On the other hand, it does not provide second-order indices.

#### **Pointwise approach**

In Fig. 2.8 some BSPCE results for the clay model, obtained with different sample sizes and sampling methods are presented. In contrast to the experiences from investigations with other methods, one cannot see a clear superiority of quasirandom LpTau sampling over random sampling. With both sampling schemes, the minimum number of simulations for achieving fairly stable results for total-order indices seems to be about 2000 – 4000.

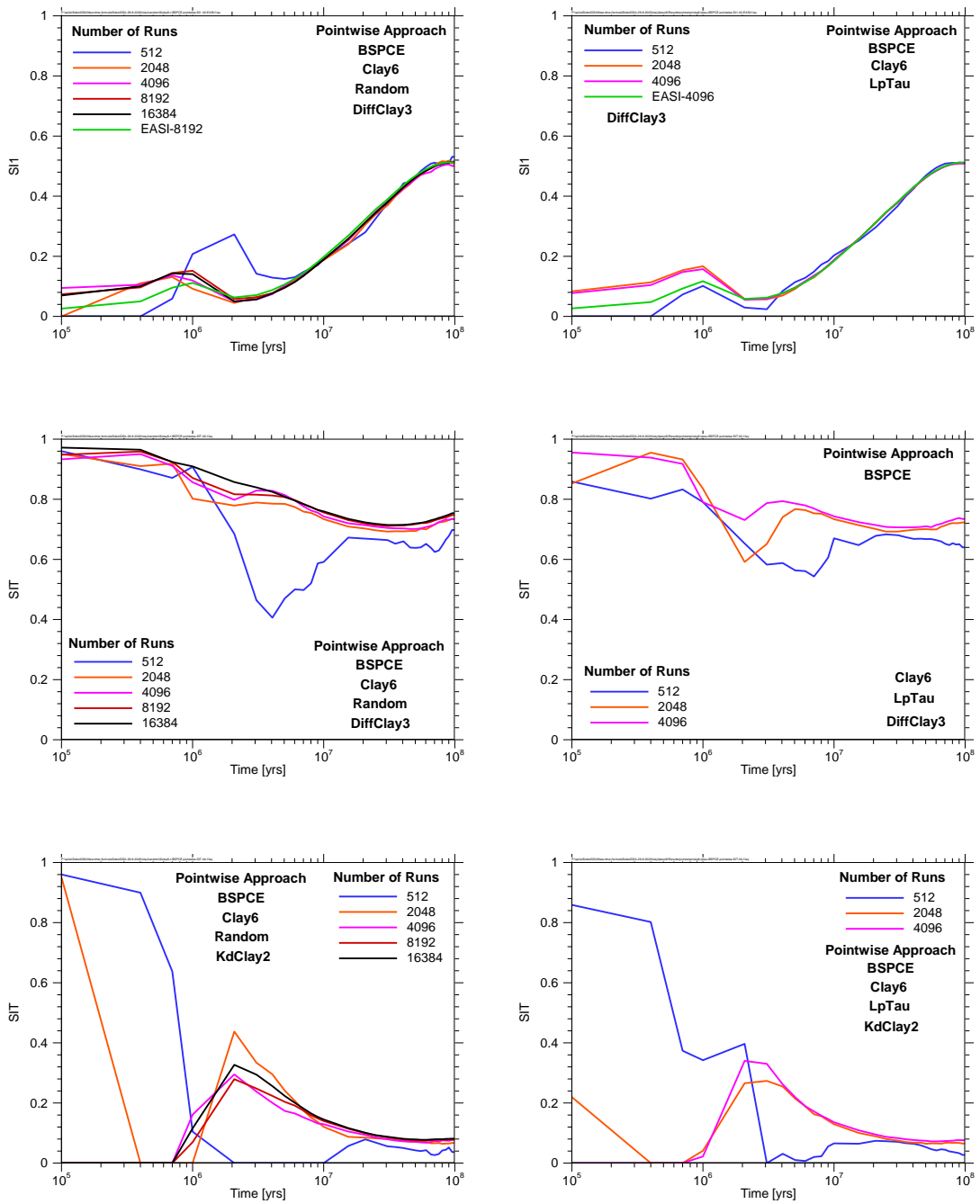


**Fig. 2.8** Pointwise approach: S11 of *DiffClay3* and SIT of *DiffClay3* and *KdClay2* for random and LpTau sampling with different sample sizes, calculated with BSPCE

## Generalised approach

In Fig. 2.9 the equivalent results for the generalised approach are presented. At early times, the curves resemble those of the pointwise approach but reach more or less stable values later.

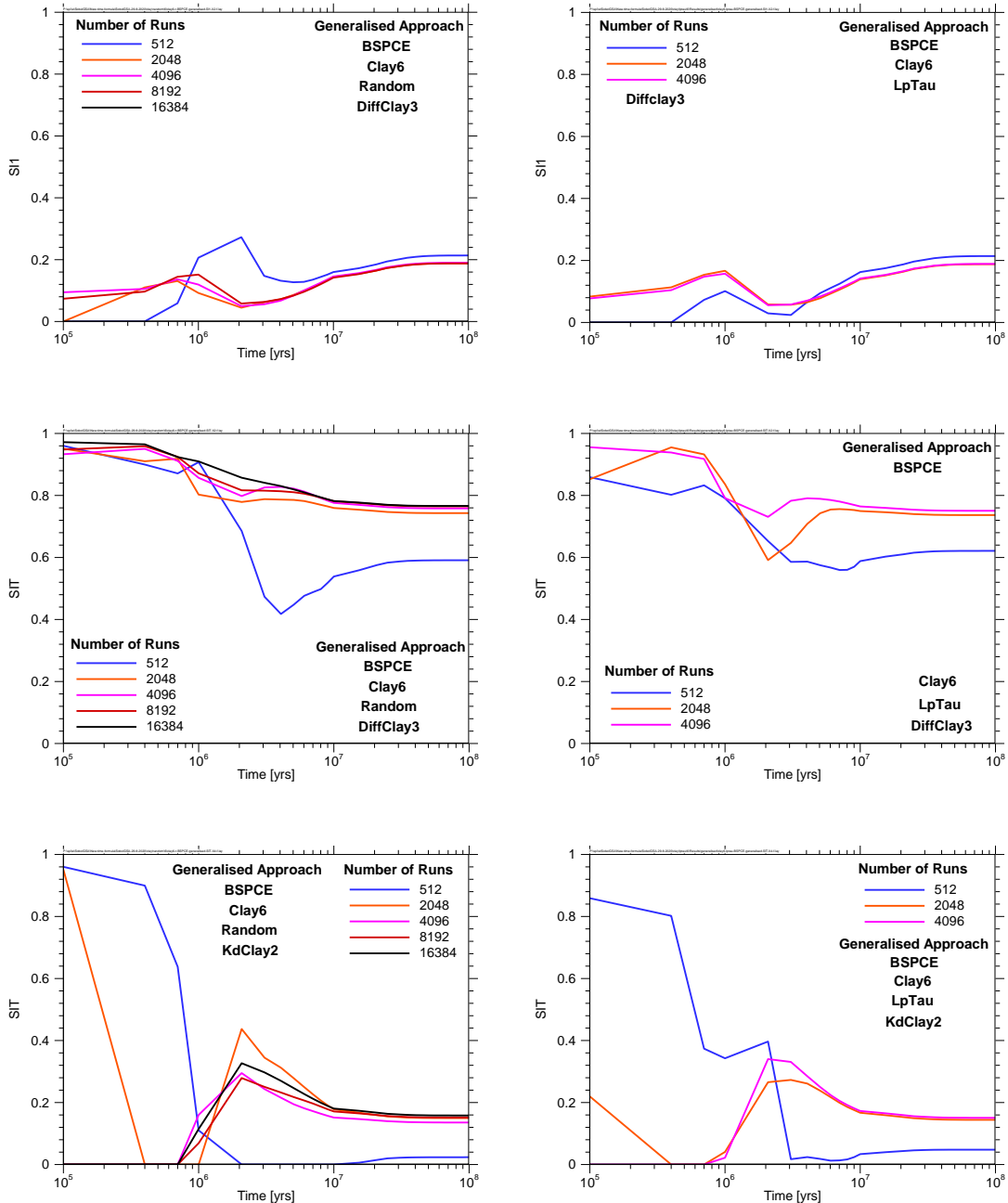


**Fig. 2.9** Pointwise approach: SI1 of *DiffClay3* and SIT of *DiffClay3* and *KdClay2* for random and LpTau sampling with different sample sizes, calculated with BSPCE

### 2.1.5.1.3 Comparison of RS-HDMR and BSPCE

While the SI1 results of BSPCE are in good agreement with those from RS-HDMR and also with the values calculated by EASI, the SIT results differ between BSPCE and RS-HDMR. Although the SIT importance ranking of the different parameters obtained by the two metamodeling methods is the same, the SIT curves differ in shape and magnitude. This might, at least in part, be due to the different behaviour of the numerical approaches, but it can also be a hint to the existence of relevant higher-order interactions, since RS-HDMR neglects all orders higher than 2. Higher order effects between the different parameters with the exception of *KdClay2* may occur especially between  $10^6$  years and  $2 \cdot 10^7$  years as during this time, the BSPCE SIT indices are considerably higher than those from RS-HDMR. This is demonstrated in Fig. 2.10.

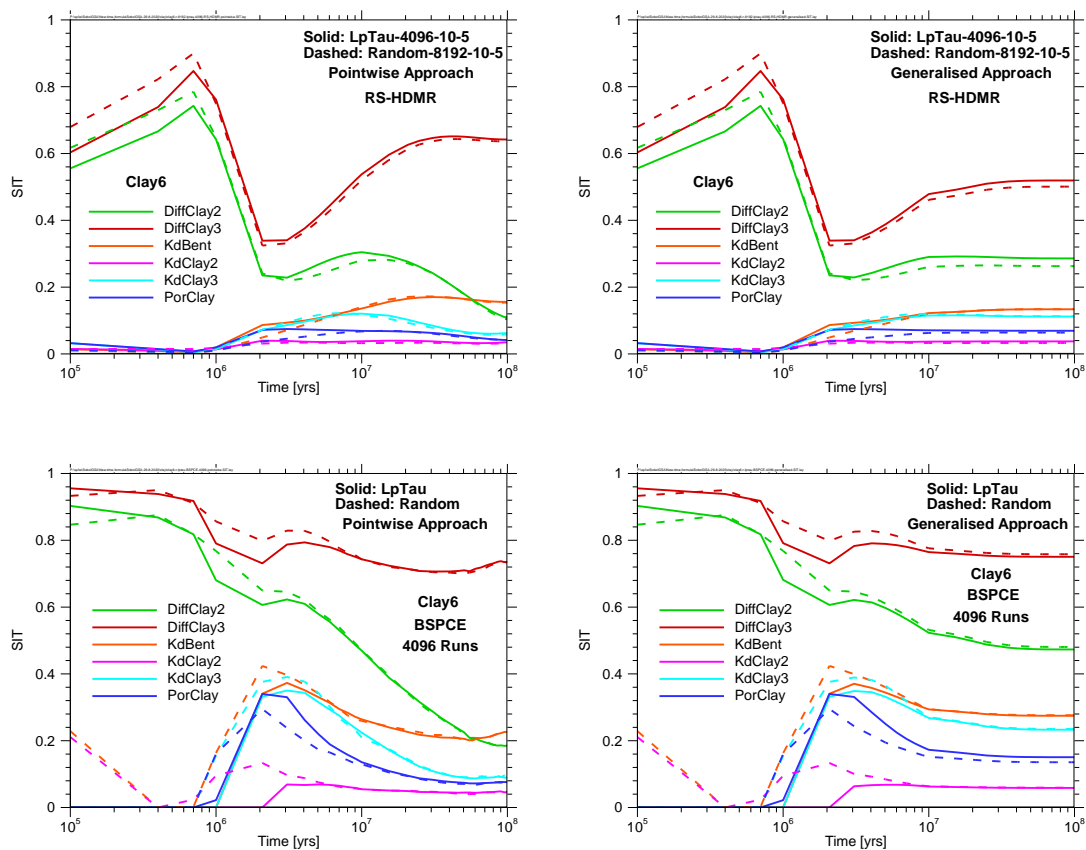


**Fig. 2.10** Pointwise and generalised approach: SIT of the clay system with random and lptau sampling calculated using RS-HDMR and BSPCE

For most direct methods as well as for the RS-HDMR metamodeling method quasirandom LpTau sampling requires fewer runs to provide stable results than random sampling. This, however, does not seem to be the case for BSPCE. At least from the results presented above one cannot deduce a significant superiority of LpTau above random sampling, neither for the pointwise nor for the generalised approach.

### **2.1.5.2 LILW model**

Compared to the clay model the LILW model is much more complex and nonlinear and provides a more challenging test model for metamodeling methods. The investigations with this model are under way; the results achieved so far have not yet been understood in detail and seem to raise new questions. Therefore, in the following we confine ourselves to presenting some preliminary findings. For the investigations, LpTau sampling has been used exclusively.

#### **2.1.5.2.1 RS-HDMR method**

The LILW model has already been analysed with RS-HDMR in /NOS 18/. It is still an open question how the maximum polynomial orders should be chosen in order to get reliable results and at the same time avoid overfitting artifacts. Even if the optimal combination were found, this result would not automatically be transferable to other models.

Fig. 2.11 shows results RS-HDMR for the LILW20 model, calculated using the pointwise and the generalised approach with two different combinations of parameters and number of runs. While for the first-order indices the agreement looks quite well, there are still considerable differences for SI2 and SIT. The comparison between the pointwise and the generalised approach shows that the system becomes more or less stable after  $10^5$  years.

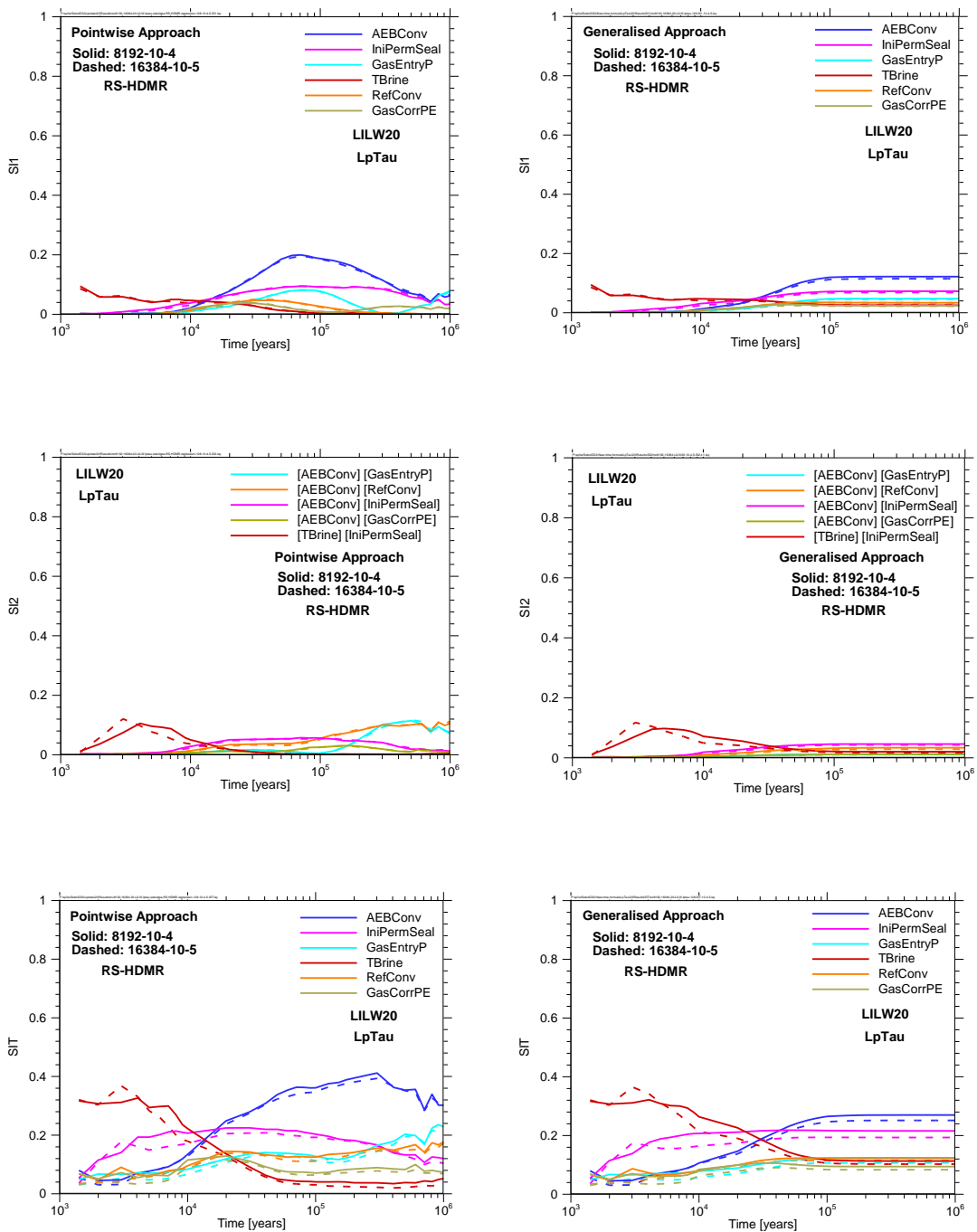


**Fig. 2.11** Pointwise and generalised approach: SI1, SI2 and SIT indices of the LILW20 model with 8192 and 16384 simulations and coefficients of 10-4 and 10-5 using the RS-HDMR method

#### 2.1.5.2.2 BSPCE method

Fig. 2.12 presents SI1 and SIT for the *AEBCov* and *IniPermSeal*, the two parameters that in former investigations turned out to be the most important ones. The results were obtained from the LILW6 model, i.e. the model version with 6 parameters. One can see that the SI1 curves converge satisfyingly for 1000 or more runs. SIT, however, seems to require considerably higher numbers of runs. Even between 8192 and 16384 runs there are still clearly visible differences. This is a general phenomenon of the calculation of total-order indices with BSPCE. The higher the considered order of interaction the less stable and robust sensitivity indices are calculated from a given set of model runs. As total-order indices include all orders of interaction, this phenomenon leads to rather spiky SIT curves at sample sizes that are fully sufficient for SI1.

In Fig. 2.13, the corresponding curves are shown for the generalised approach. With regard to the number of runs the same considerations hold. Although the spikiness of the curves decreases at the end of the model time, the convergence is not better than for the pointwise approach.

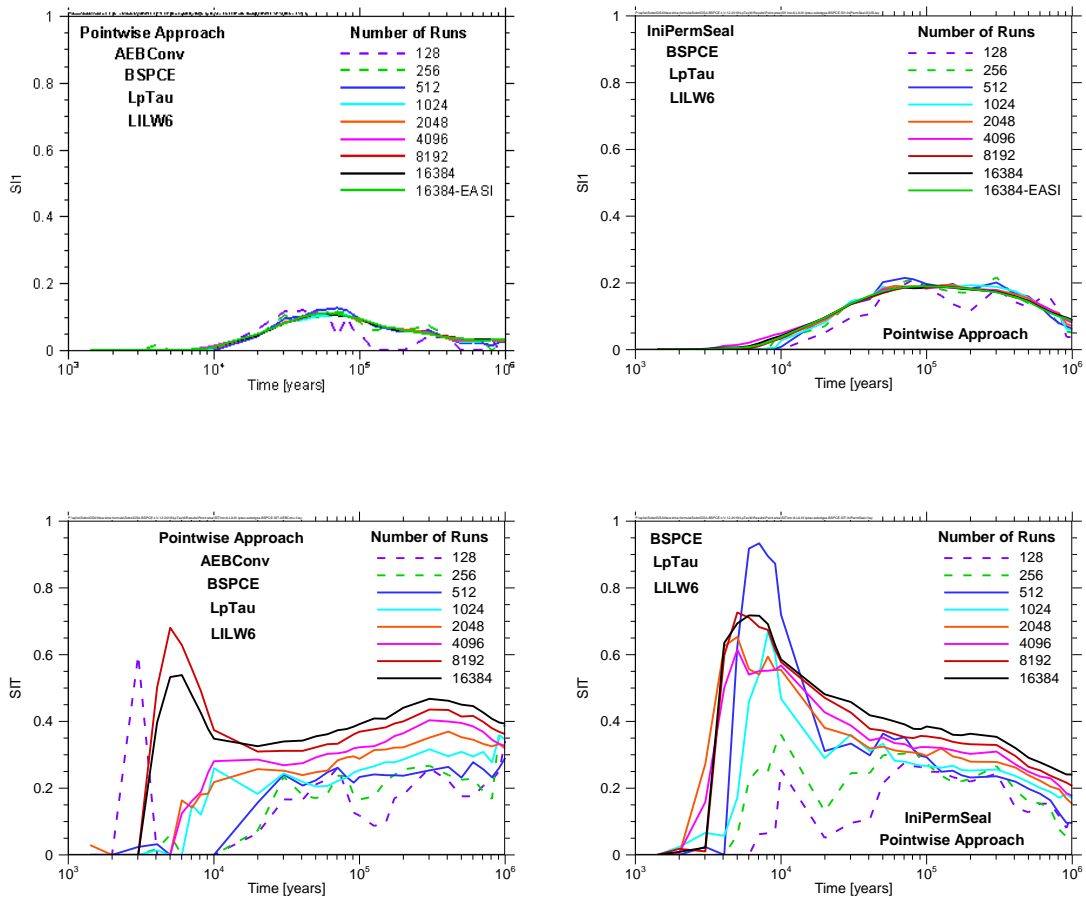


**Fig. 2.12** Pointwise approach: SI1 and SIT of *AEBConv* and *IniPermSeal* with LpTau sampling and different number of simulations, computed using BSPCE

The time curves of SI1 and SIT for all model parameters are shown in Fig. 2.13 for the pointwise and the generalised approach, calculated from different numbers of runs. Specifically for the most important parameters the convergence seems to be unsatisfactory, which can be seen as a hint that there are considerable and uncertain interactions with these.

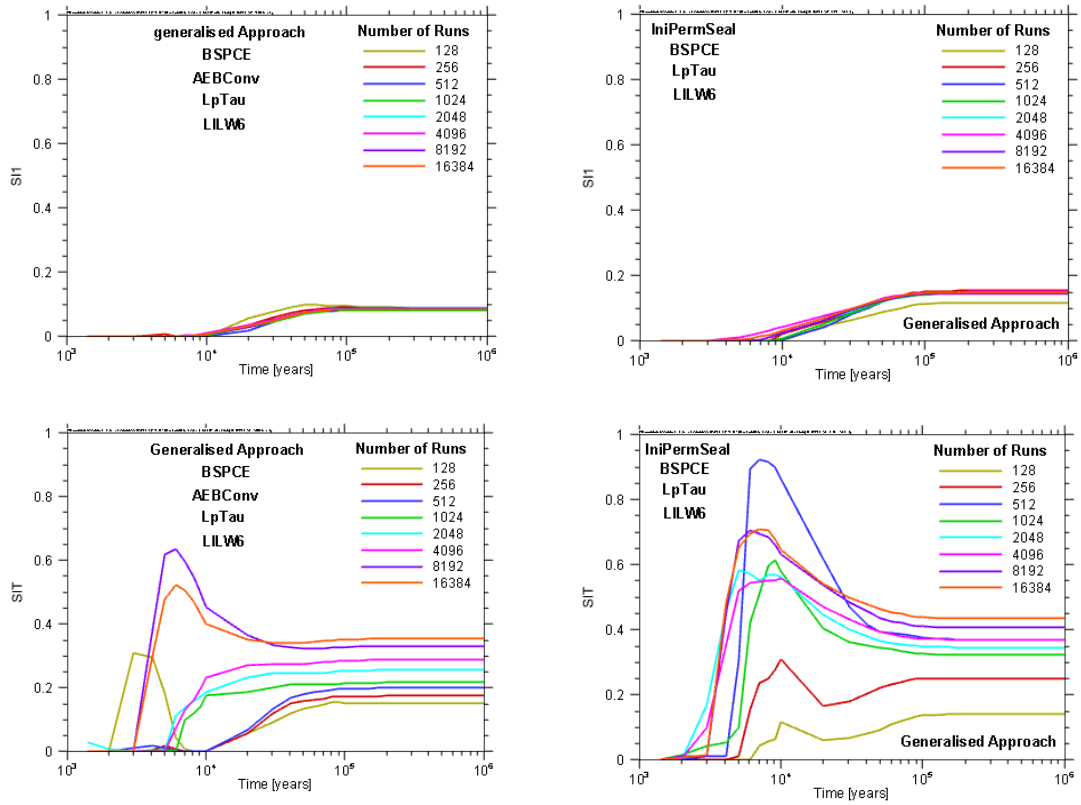


**Fig. 2.13** Generalised approach: SI1 and SIT of *AEBCConv* and *IniPermSeal* with LpTau sampling and different number of simulations, computed using BSPCE

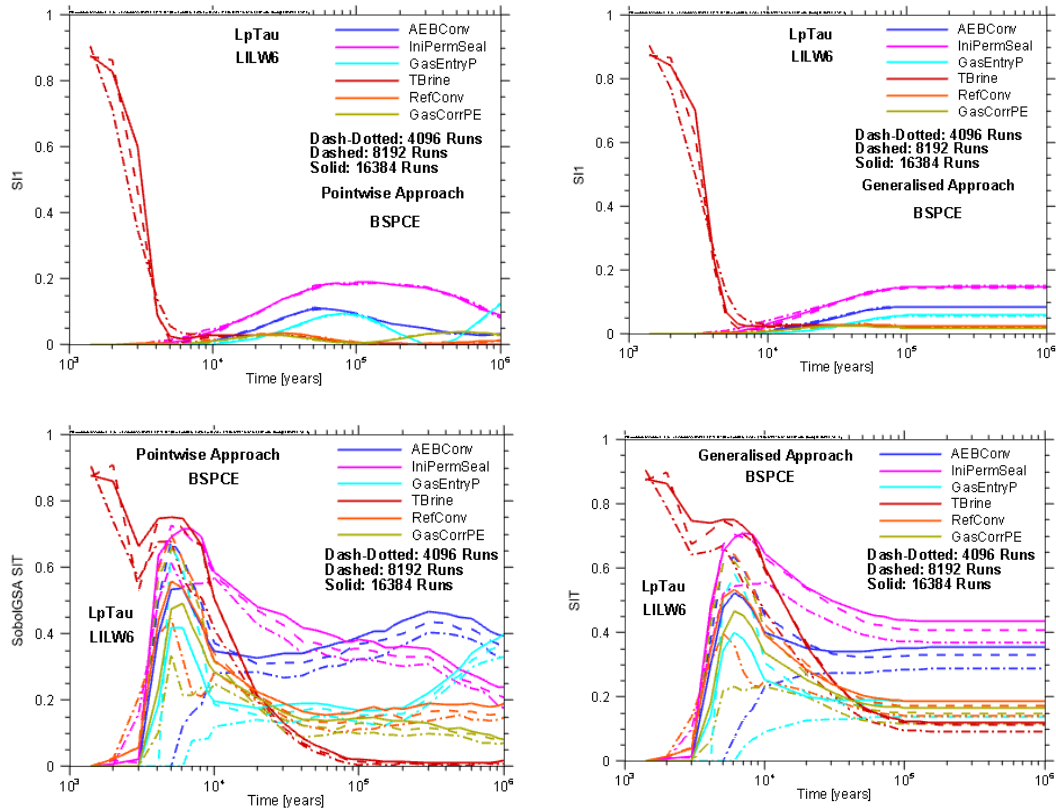


**Fig. 2.14** Pointwise and generalised approach: SI1 and SIT of the LILW6 model with LpTau sampling and 4096, 8192 and 16384 runs calculated using BSPCE

### 2.1.5.2.3 Robustness of the SIT and SI2 results using RS-HDMR

To check the robustness and consistency of the SIT and SI2 results obtained with RS-HDMR, some calculations were performed with a specific version of the LILW model, which only depends on the two parameters that were found most important: *AEBConv* and *IniPermSeal*. Additionally, a dummy parameter with no actual influence on the model output was taken into account. As expected, SI1 of the dummy parameter was calculated to be practically zero over the total model time, and the same holds for SI2 for the combinations of the dummy parameter with any of the other two.

In Fig. 2.15, SI1 of both "real" variables, their sum and SI2 of their interaction are presented. The higher the polynomial orders ( $k, l$ ) are chosen, the closer are the calculated SI1 to those obtained with EASI. Apparently, the metamodel gets actually better with increasing values of  $k$  and  $l$ . While in the case of the LILW6 model the highest

combinations seemed to cause overfitting artifacts, that is not the case here. One can conclude that fewer influential parameters allow for higher polynomial orders to get a well-fitting metamodel.

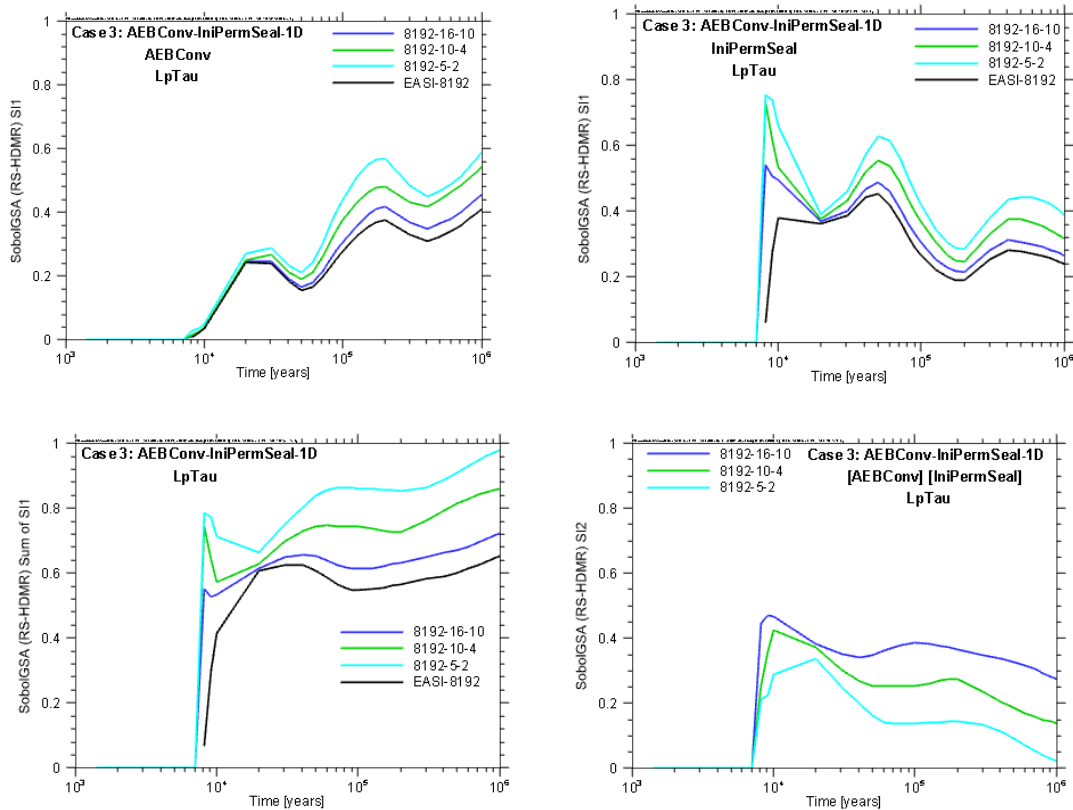


**Fig. 2.15** Pointwise approach: SI1 and SI2 of the influential parameters and sum of SI1 of the case AEBConv-IniPermSeal-1D of the LILW model with 8192 simulations using RS-HDMR with different coefficients and EASI

#### 2.1.5.2.4 Comparison of RS-HDMR and BSPCE

Fig. 2.16 presents a comparison of RS-HDMR and BSPCE with best possible number of simulations and coefficients. The figure shows a good agreement for the first order, but considerable differences for the total order. This may, at least in part, be due to the fact that RS-HDMR does not really calculate the total-order indices but approximates them by summing up the first- and all second-order indices of a parameter, neglecting all higher orders of interaction. Indeed, the total-order indices calculated by RS-HDMR are always below those obtained with BSPCE. With regard to parameter ranking, both methods agree for most of the time. At late times the SIT ranking of *AEBConv* and

*IniPermSeal* is reversed in the generalised approach compared to the pointwise approach, as the higher importance of *IniPermSeal* at earlier times refers to a much higher total variance and therefore keeps dominating till the end in the generalised approach. BSPCE seems to require more simulations to yield stable results than RS-HDMR.

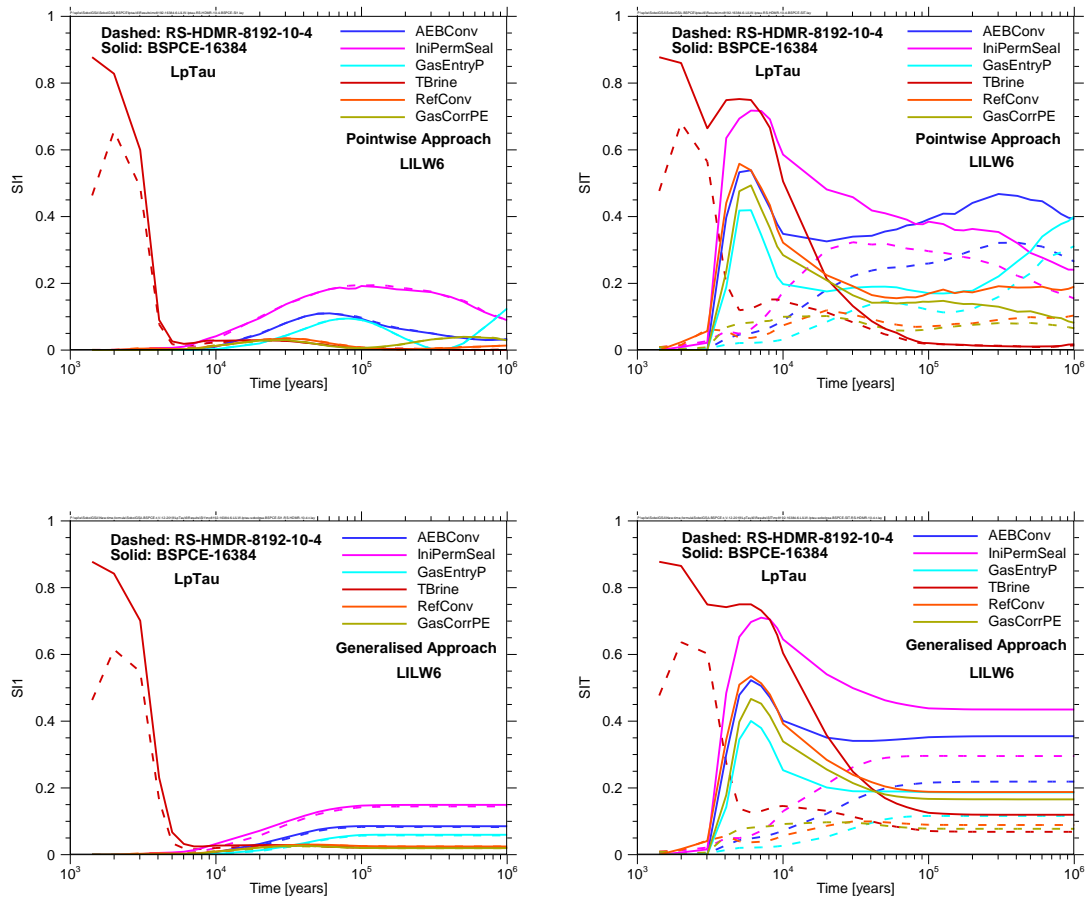


**Fig. 2.16** Pointwise approach: comparison of RS-HDMR and BSPCE methods for SI1 (left) and SIT (right)

### 2.1.6 Summary

The focus of this chapter was the determination of the influences of parameters and parameter interactions on the output of performance assessment (PA) models from available data sets. This was done on the basis of two PA models already investigated in the MOSEL project (clay and LILW case) with two metamodel-based methods (RS-HDMR, BSPCE), which are contained in the SobolGSA software package. Many evaluations were undertaken with these two methods in order to find the required number of original model runs as well as to optimise the choice of the parameters of RS-HDMR, i.e. the

maximal polynomial orders taken into account. The clay model is a simple and smooth PA model while the LILW model has a skewed, non-linear and discontinuous nature. In addition to these two PA model models, an analytic function, the time-dependent Ishigami function, was examined to support understanding and investigate the performance of the methods. To analyse the time-dependent output of the PA models, two time-dependent approaches for sensitivity analysis were utilised. In the pointwise approach, the output at each time step is considered independently. The generalised approach includes averaged output contributions at all previous time steps in the analysis of the current step.

For the Ishigami function, for good convergence of the higher order indices, a few hundred original model runs are sufficient for building good metamodels for both methods. The mathematically defined function seems to allow good approximation by polynomials. Several thousand of simulations, however, are required for satisfying convergence of the SI2 and SIT curves for the clay case, although this case is considered rather smooth. For the complex and nonlinear LILW case, at least twice as many simulations are needed. For the main indices (SI1), however, convergence is reached with significantly fewer simulations, but the same quality can be achieved with direct methods like EASI. So, one can conclude that the strength of metamodeling methods is not so much a reduction of the number of original model runs but the ability to calculate higher- and total-order indices.

For both time-dependent approaches investigated, the same number of simulations is required to build good metamodels.

For the RS-HDMR method, different sets of coefficients were investigated. For both PA models,  $k=10$ ,  $l=5$  work well. This set of coefficients worked also very well for the Ishigami function. So, it can be used for unknown models to start with, but one should keep in mind that there is danger of overfitting, especially if few runs are available. This recommendation is not a mathematical result but an experience from the numerical investigations.

RS-HDMR and BSPCE showed a good agreement for the main effects of both PA models, but the total-order indices calculated by RS-HDMR was always below those obtained with BSPCE. This may, at least in part, be due to the simplifying assumption of RS-HDMR that the total index is the sum of the first- and all second-order indices of a respective parameter.

## **2.1.7 Joint sensitivity analysis exercise (JOSA)<sup>1</sup>**

### **2.1.7.1 Introduction**

Over the past five years, an informal working group has developed to investigate existing sensitivity analysis methods, identify best practices, and examine new sensitivity analysis methods being developed. A series of annual meetings was held starting with a “Workshop on Handling Uncertainties” in September 2015 at Harwell, UK, followed by an “International Workshop on Sensitivity Analysis of Final Repository Systems” in Braunschweig, Germany in October 2016, and then by a “Quantification of Uncertainty Workshop” in August 2017 in Albuquerque, NM, USA. It was at this latter workshop in the U.S. where more collaborative work was initiated among the international participants and organizations, as discussed below.

A follow-on workshop in Brussels, Belgium in October 2018 led to a more formal establishment of this collaboration during the subsequent Integration Group for the Safety Case (IGSC) Symposium on the Safety Case in Rotterdam, The Netherlands in October 2018. The sensitivity analysis group is working under the auspices of Organization for Economic Cooperation and Development (OECD)/ NEA’s Integration Group for the Safety Case (IGSC).

The Uncertainty Quantification workshop held in August 2017 in Albuquerque, USA, led to a joint sensitivity analysis exercise effort initiated in October 2017, with participation from GRS, Posiva, SCK-CEN, SNL, and TUC, and later joined by IBRAE as well as by ENSI, Fortum, IRSN and Nagra as observers. The core group discussed various case studies that could be examined from a safety assessment context for geologic disposal, representing different modelled systems with varying levels of details, complexity, data uncertainty, and spatial extent. The group identified seven test cases ranked in order of complexity and since then has compared analysis methods on progressively more complex models. Four of these case studies which are based on less complex models are presented in this report: the GRS clay case, the SNL shale case, the Dessel case, and the IBRAE groundwater case. Multiple groups examined different sensitivity analysis techniques on each case. Each case study owner provided input and output datasets

---

<sup>1</sup> This chapter summarises in short the work presented in detail in /SWI 21/ and reproduces parts of that report verbatim or in a shortened form

and explanation of the case so that others could use the case to demonstrate their sensitivity analysis approaches.

The concept of the study, the group's work, and interim results were presented on several occasions, e. g. at the Integration Group for the Safety Case (IGSC) Symposium held in Rotterdam in October 2018 (/ROE 19/, /STE 19a/, /MAR 19/). Subsequently, a few members participated in the International High-Level Radioactive Waste Management Conference held in (Knoxville TN, April 2019) (/BEC 19a/, /STE 19b/), the 2019 General Assembly of the European Geosciences Union (Vienna, April 2019) (/SPI 19a/), and at the Ninth International Conference on Sensitivity Analysis of Model Output (Barcelona, October 2019) (/BEC 19b/, /SPI 19b/, /SAV 19/, /PLI 19/).

#### **2.1.7.2 Software**

The partners use different numerical tools for their investigations. While the software coverage for methods based on linear regression is generally good, variance-based and moment-independent sensitivity measures are not generally found in standard software products. Different data-analytic programming languages offer toolboxes and script collections. In Tab. 2.3, we present some software tools and a link to a website where appropriate.

**Tab. 2.3** Toolboxes for sensitivity analysis

Toolbox/Package	Language	Website
UQLab	MatLab / Octave	www.uqlab.com
SAFE (Sensitivity Analysis for Everybody)	Matlab. Also R, Python	www.safetoolbox.info
GUI-HDMR	Matlab	<a href="http://www.gui-hdmr.de">www.gui-hdmr.de</a>
Sensitivity	R	cran.r-project.org/web/packages/sensitivity/index.html
openTURNS	Python	openturns.github.io/www/
SALib	Python	salib.readthedocs.io/en/latest/
mads. Model Analysis and Decision Support	Julia/C	mads.lanl.gov
EcoLego	Set of toolboxes	<a href="http://www.ecolego.se">www.ecolego.se</a>
SobolGSA		www.imperial.ac.uk/process-systems-engineering/research/free-software/sobolgsa-software/
SimLab		ec.europa.eu/jrc/en/samo/simlab
Dakota		dakota.sandia.gov
MUQ: MIT Uncertainty Quantification Library		<a href="http://muq.mit.edu/">http://muq.mit.edu/</a> More UQ focused, Bayesian calibration
NESSUS		<a href="http://www.swri.org/nessus">www.swri.org/nessus</a> More UQ, Reliability and failure estimation focused.
UQtk	C++/Python	<a href="http://www.sandia.gov/UQToolkit/">http://www.sandia.gov/UQToolkit/</a>
PSUADE		github.com/LLNL/psuade computing.llnl.gov/projects/psuade-uncertainty-quantification
SmartUQ		www.smartuq.com/software/sensitivity-analysis/

### 2.1.7.3 Calculation cases

Four case studies which are based on less complex models have been selected for the first step and are presented in this report: the GRS clay case, the SNL shale case, the Dessel case, and the IBRAE groundwater case. The models are described in /SWI 21/. Tab. 2.4 summarises the main features of these models.

**Tab. 2.4** Main features of the model cases

<b>GRS Clay</b>	<b>Description</b>
Waste form	Spent nuclear fuel in specific spent fuel element containers
Engineered barriers	Steel container, bentonite buffer
Repository description	1070 boreholes with 5 containers each, reference depth 400 m
Natural system	Lower Cretaceous Clays, formations Apt and Alb
Far Field	Generic 10-km transport path through a typical rock medium
Biosphere	Exposure pathways considered via pre-defined dose conversion factors, groundwater flow $10^{-5}$ m <sup>3</sup> /yr
Conceptual release pathways	Purely diffusive transport through bentonite, Apt and Alp, stylised far field
Processes modelled	Degradation of waste matrix, radionuclide dissolution, solubility in container water, diffusive transport and retention in buffer and clay layers, 1D advective-diffusive transport through far field
Software codes used	CLAYPOS3, CHETLIN4, EXMAS2
Number of inputs	6
Number of outputs	194 (time series)
Sample size and type	4096 (LpTau) – 8192 (random)
Reference for full description of case	/RUE 10/
<b>SNL Shale</b>	<b>Description</b>
Waste form	Spent nuclear fuel in 12-PWR canisters
Engineered barriers	Bentonite buffer with material properties appropriate for a compacted mixture of 70% bentonite and 30% quartz sand
Repository description	Repository has 515-m depth with 84 drifts, 4 shafts, and an emplacement footprint of 2.6 km <sup>2</sup> . 4200 waste packages emplaced with 50 packages per drift and 20-m center-to-center spacing.
Natural system	450 m thick indurated shale interrupted by a 30 m thick sandstone aquifer; a 75 m thick limestone aquifer; a 585 m thickness of sealing shale including a 90 m thickness of silty shale unit; a 60 m thick sandstone aquifer; 30 m thickness of unconsolidated overburden.
Biosphere	Well water ingestion dose model
Conceptual release pathways	Advection, diffusion, element-based solubility, medium-specific sorption, decay in all phases

Processes modeled	Waste package degradation, waste form (UO <sub>2</sub> ) dissolution, equilibrium-controlled radionuclide sorption and precipitation/ dissolution, radioactive decay and ingrowth in all phases (aqueous, adsorbed, precipitate), coupled heat and fluid flow, and radionuclide transport via advection and diffusion.
Software codes used	PFLOTRAN, Dakota
Number of inputs	10
Number of outputs	6
Sample size and type	50 – 200 (LHS)
Reference for full description of case	/MAR 17/
<b>Dessel Case</b>	<b>Description</b>
Waste form	Steel drums of homogeneously cemented LILW
Engineered barriers	Type I concrete monoliths (with backfill mortar),
Repository description	Near surface disposal facility
Natural system	Not considered
Biosphere	Not considered
Conceptual release pathways	Diffusion in concrete and mortar, advective transport in fracture and conductive sorbing media (inspection room & embankment)
Processes modeled	Advective-dispersive/diffusive transport
Software codes used	Comsol Multiphysics 3.5a
Number of inputs	22
Number of outputs	200 (time series)
Sample size and type	256 -1024 – 24000 (quasirandom)
Reference for full description of case	/PER 18/
<b>IBRAE Groundwater</b>	<b>Description</b>
Waste form	High-level radioactive waste
Engineered barriers	Stainless steel overpack, bentonite buffer
Repository description	450–500 m depth, 75 m deep boreholes containing waste packages
Natural system	500 m thick low permeability rock
Biosphere	Not considered
Conceptual release pathways	Not considered
Processes modelled	Single-phase fluid flow
Software codes used	GERA
Number of inputs	12
Number of outputs	37
Sample size and type	140 - 1400 – 14000 – 28000 (random)
Reference for full description of case	/NEU 20/, /SAV 21/

#### 2.1.7.4 Results and conclusions

In the following, we present summarily some selected results, following the above order of the calculation cases. For further results and details see /BEC 21/.

##### 2.1.7.4.1 GRS clay model

As a start, several partners have calculated classical correlation- and/or regression-based sensitivity measures. As these are well-defined and numerically easy to calculate, the results are in very good agreement. GRS results have been reported in detail in /SPI 17/. In Fig. 2.17 and Fig. 2.18, we show the results obtained by SNL for the PEARSON correlation coefficient and the SPEARMAN rank correlation coefficient (in this kind of presentation each sub-figure highlights one of all curves).

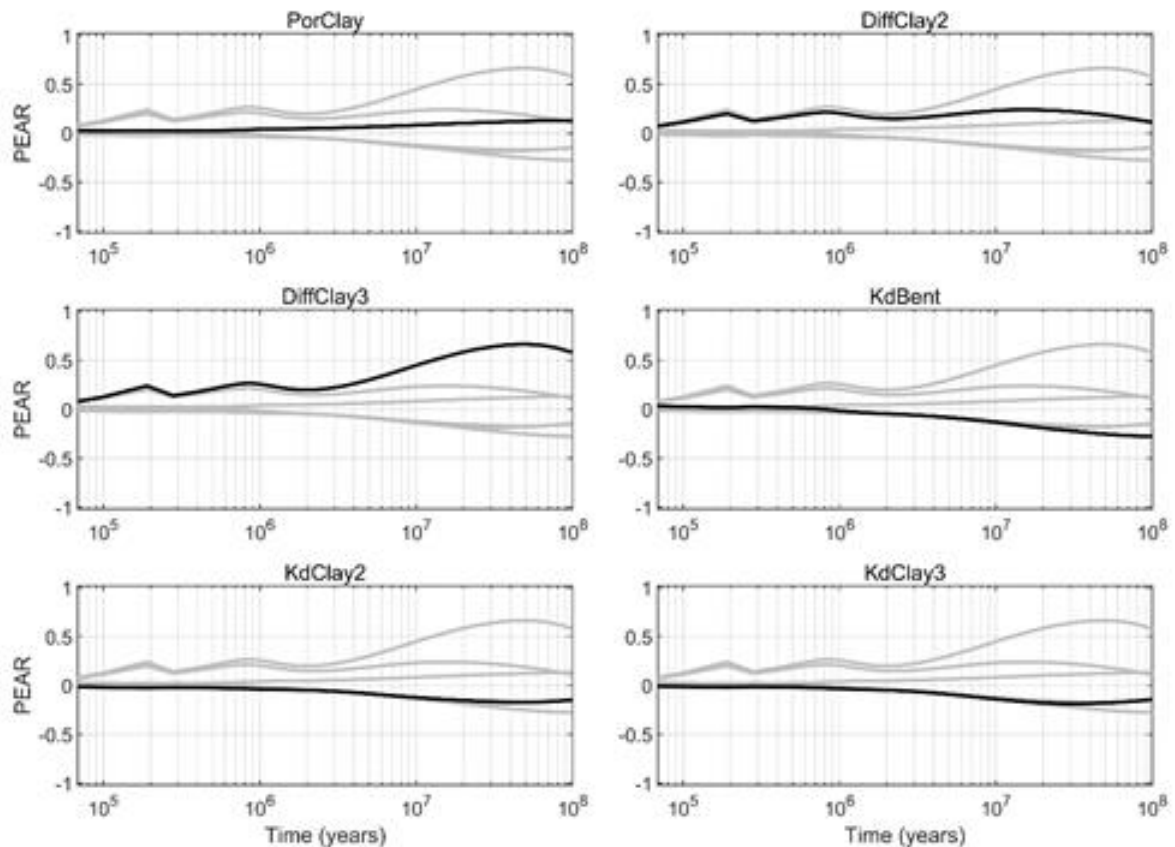
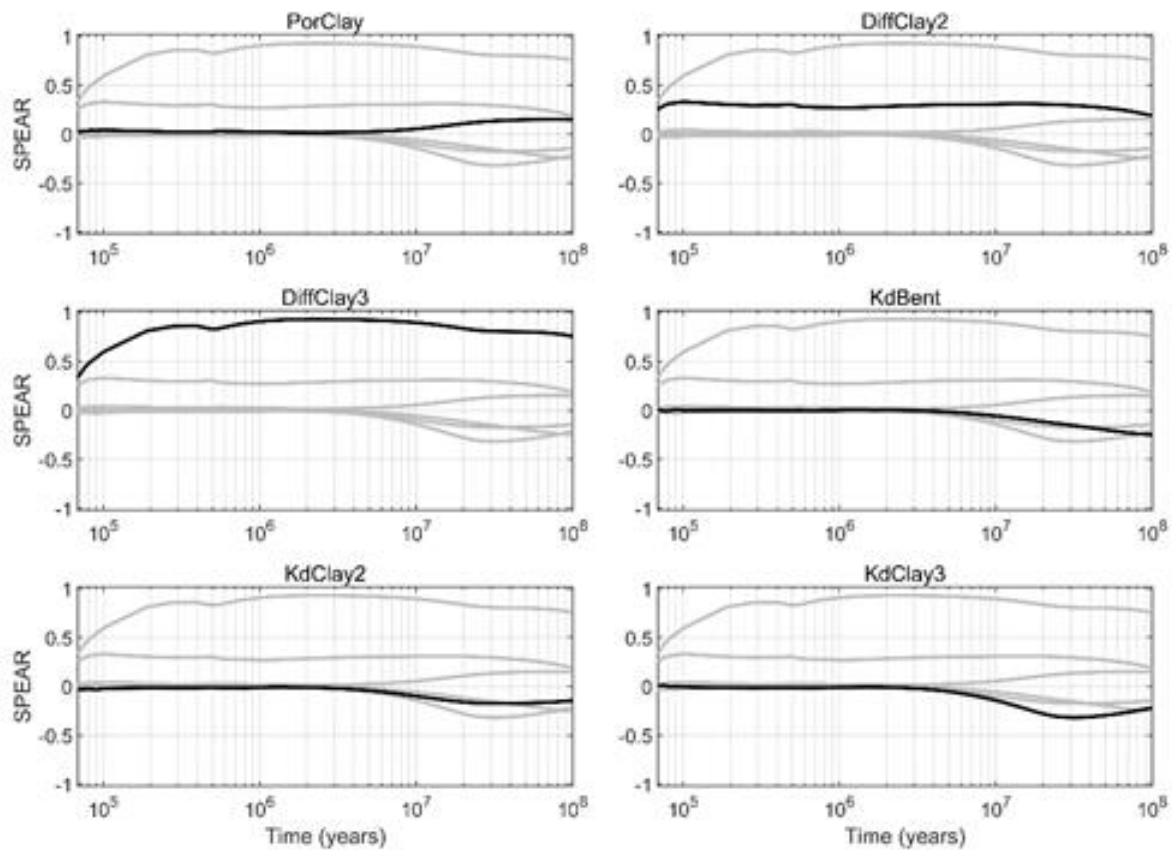


Fig. 2.17 Pearson correlation coefficients of the GRS clay system (SNL results)



**Fig. 2.18** Spearman rank correlation coefficients of the GRS clay system (SNL results)

The main sensitivities can well be seen at these curves: *DiffClay3* dominates nearly over the full time period, and there is also some influence of *DiffClay2* in the early time frame. All other parameters gain considerable importance only at very late times.

IBRAE made some investigations with the PAWN method on the clay model. This is a density-based method, which assesses sensitivities by calculating the maximum difference between the unconditioned and the conditioned output cdf (cumulated density function). The conditioned cdf is obtained by restricting one parameter to a narrow range, and the sensitivity measure is calculated by taking the mean<sup>2</sup> of the maximum cdf difference over the total parameter range /PIA 18/. To reduce the noise one can use a dummy parameter with no influence to the model output and subtract its apparent sensitivity. Results obtained in this way are shown in Fig. 2.19, using the same kind of presentation as in the previous figure.

---

<sup>2</sup> The authors propose also other statistical measures (medium, maximum) but the added value of these is disputable.

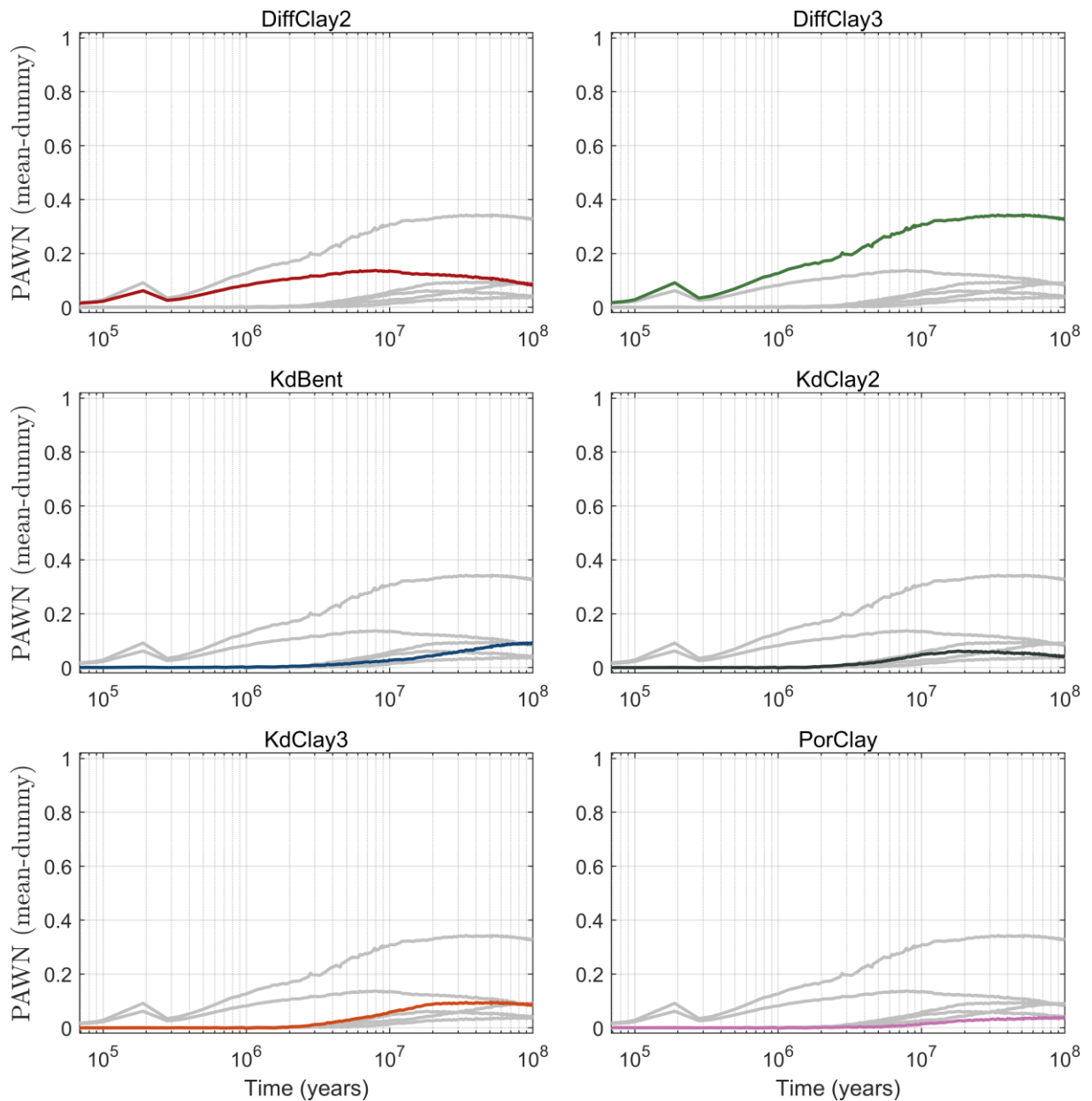


**Fig. 2.19** Sensitivity analysis of GRS Clay case (8192 runs): PAWN method, dummy parameter subtracted (IBRAE results)

The dominance of *DiffClay3* and the second place of *DiffClay2*, specifically in the earlier time frame, can well be seen also in this figure. Qualitatively, there are no major differences to the variance-based evaluations presented in /SPI 17/ since the model is smooth and monotonic. In other cases, however (for instance, with multimodal output distributions), variance may not be fully adequate to describe the output variability, and then, density-based methods like PAWN may reveal other sensitivities.

#### 2.1.7.4.2 SNL shale model

The shale model is not time-dependent but calculates a number of quantities of interest (QoI), six of which were selected for the JOSA investigations. These QoI represent the maximum I-129 concentration over time at six different observation points (three in sandstone and three in limestone) and in the following are denoted as response functions RF1 to RF6. Therefore, time curves cannot be made.

The CUSUNORO analysis by GRS is presented in Fig. 2.20. For RF1 it shows a clear deviation from the horizontal line only for the parameter *pShale*. Although there seems to be a certain bend also in the curves for *kSand* and *rateWP*, this cannot be judged as significant. The situation is similar for RF2 and RF3, except that the influence of *kSand* is clearer and obviously reversed. For RF4 the parameter *rateSNF* seems to gain some importance. For RF5 and RF6, *kLime* is the most conspicuous parameter, but its curves follow more or less straight lines, except a sharp bend around an input contribution of 0.8, corresponding to a permeability value of about  $2.5E-15$  m<sup>2</sup>. This shape of the CUSUNORO curves suggests some change in the model behaviour in a small range of values of *kLime*.

The number of available simulations is too low for clearly identifying less significant sensitivities by using CUSUNORO.

SNL investigated the system using classical methods as well as two different surrogate modelling approaches: a Gaussian process (GP) model and a polynomial chaos expansion (PCE) model. Also log-transformed data were taken into account. These results confirm those achieved with CUSUNORO. The log transformation enhances the dominance of the leading parameters. Specifically for RF6, the log-transformed output seems to be nearly exclusively determined by *kLime*.

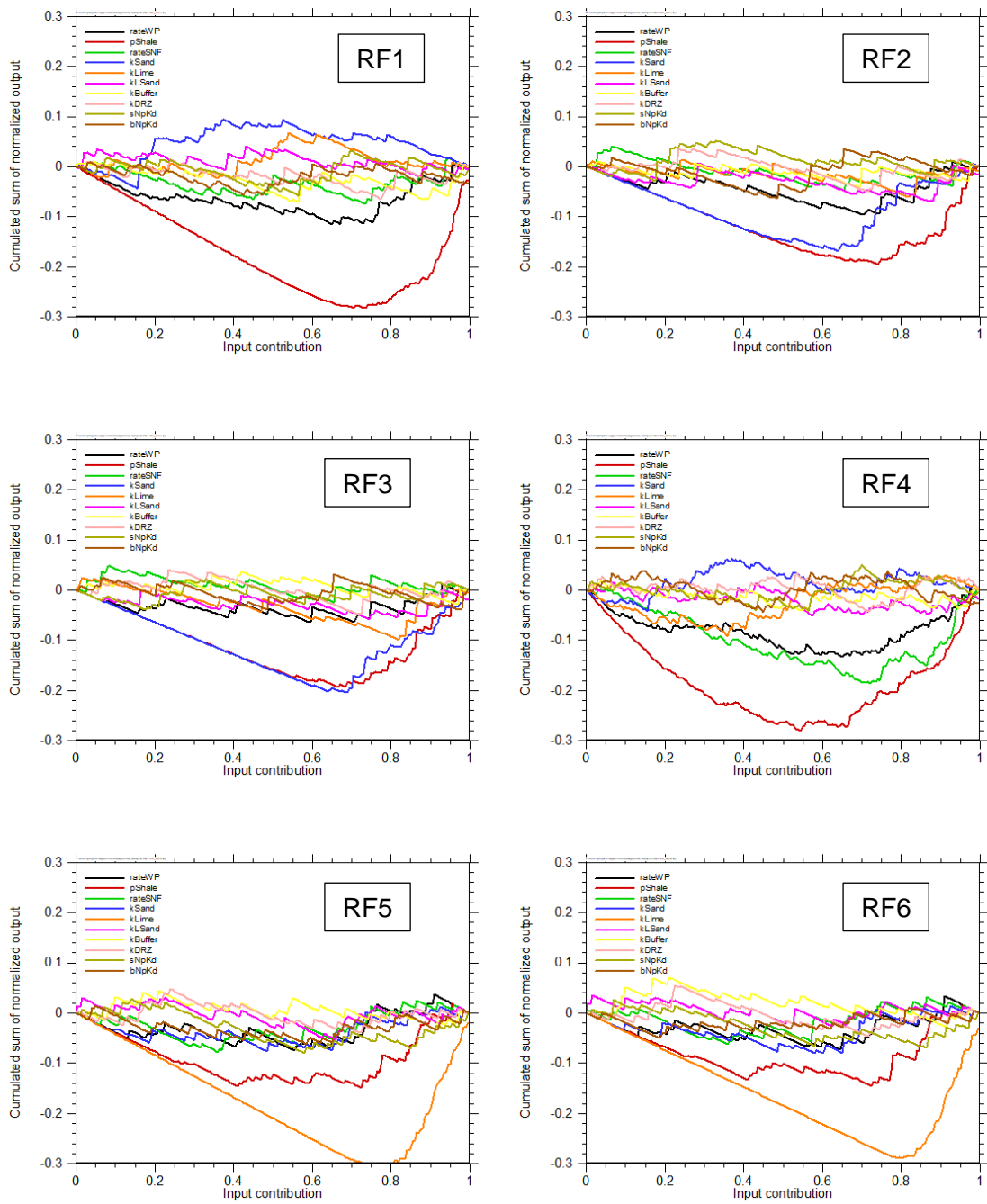


**Fig. 2.20** CUSUNORO analysis of the SNL shale system (GRS results)

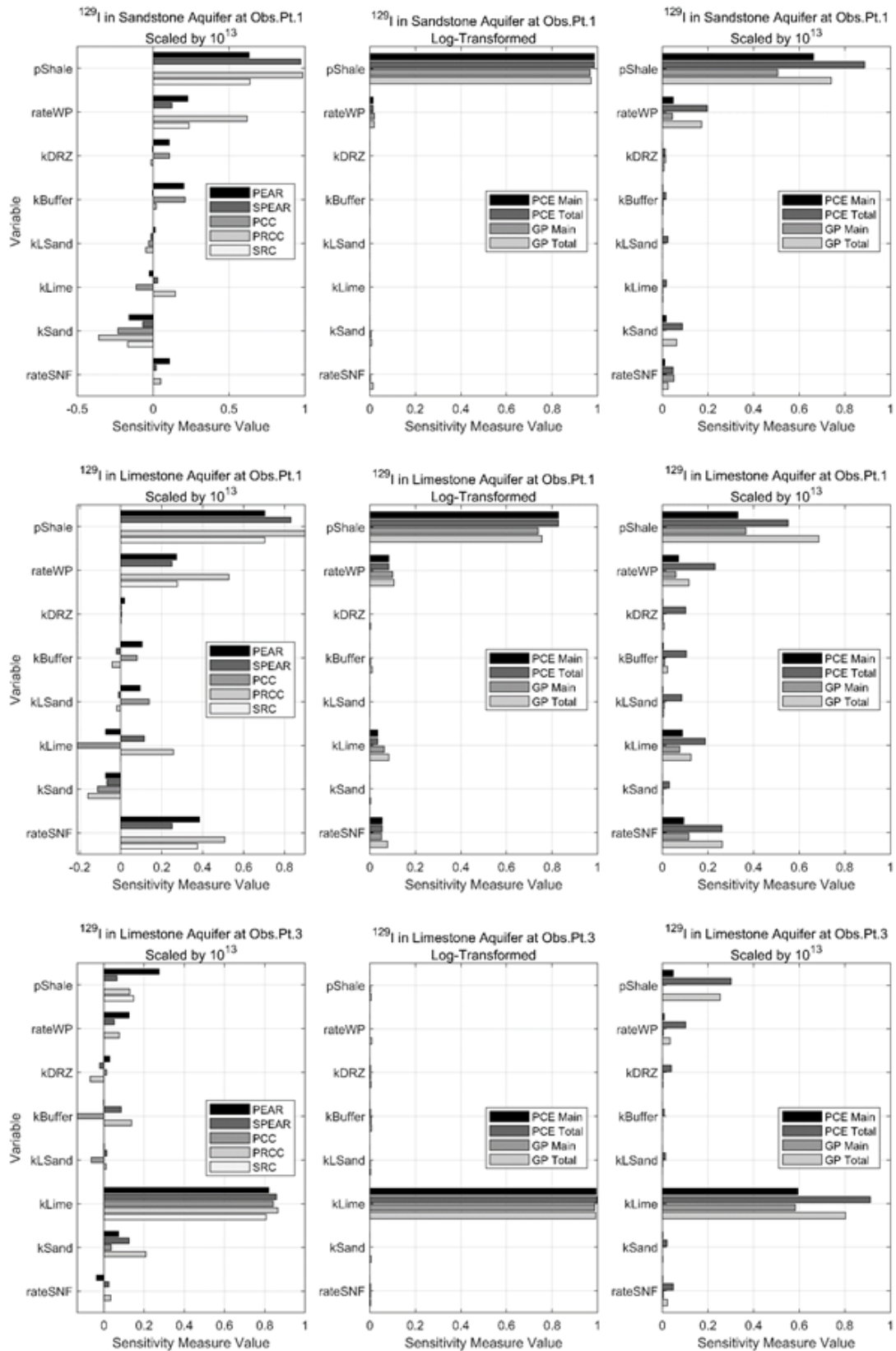


**Fig. 2.21** Sensitivity measures for RF1 (upper), RF4 (middle) and RF6 (lower) of the SNL Shale calculation case (SNL results)

### 2.1.7.4.3 Dessel model

The Dessel model shows some interesting features insofar as at some time between 1000 and 1200 years there seems to be a change of the direction of influence for some of the parameters. GRS has analysed the case using the classical standard regression coefficients. The analysis was performed with the original data as well as after applying the transformation  $y \mapsto \log_2(1 + y/a)$  with different values for  $a$ , see Fig. 2.22.

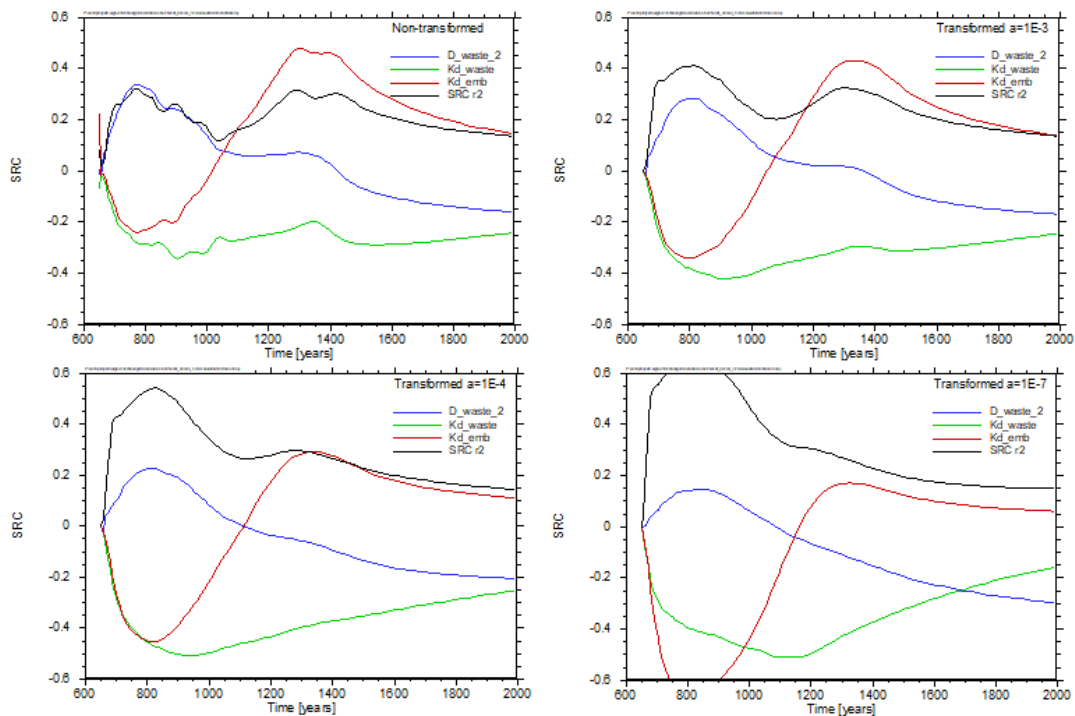


**Fig. 2.22** Sensitivity analysis of the Dessel model with different transformation parameters (GRS results)

The transformation has the effect of a log transformation for high values ( $\gg a$ ) but unlike this, does not overweigh very small values and even allows zeros. It can be seen that the transformation has a smoothing effect and emphasises some sensitivities specifically at early times, where typically many low values occur.

If the functional dependence of the output upon the inputs is not explained by linear or additive functions, then the missing part can be explained by the presence of interactions, which first-order indices are not able to detect. Fig. 2.23 demonstrates this, where, especially for the large output variance in the time span between 680 to 800 years, a

large part remains unaccounted for by first order effects. In this figure, absolute rather than relative contributions to the variance are shown, which reveals additional information when considering sensitivities evolving over time. One may be tempted to screen-out parameters which do not contribute to first order effects but may be important in driving interactions.

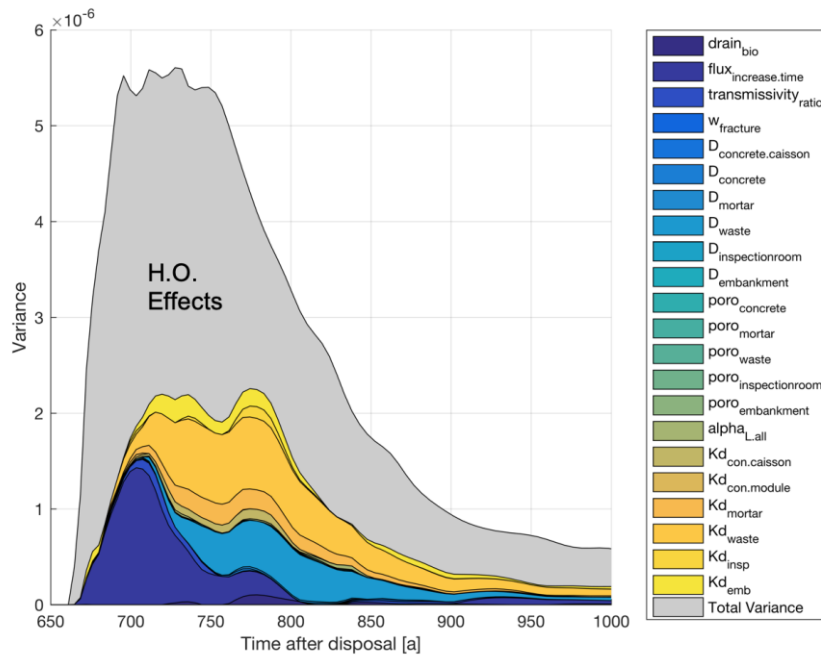
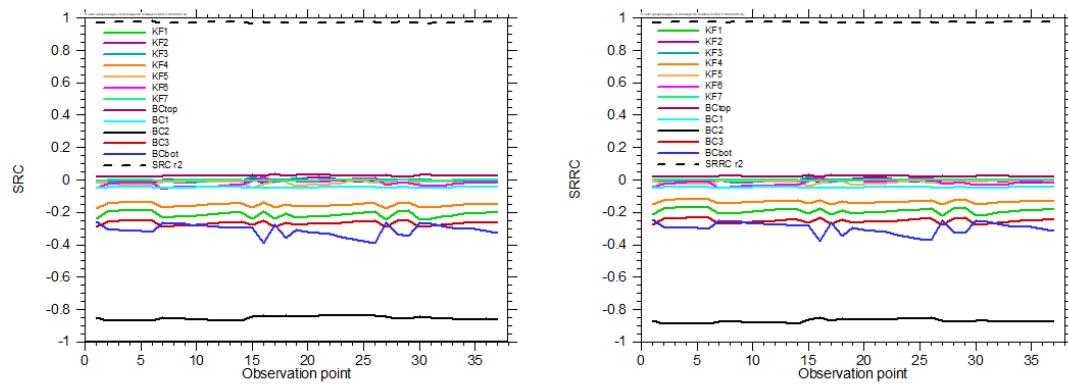


**Fig. 2.23** Sum of first order effects and absolute contribution to total output variance (results of SCK-CEN)

#### 2.1.7.4.4 IBRAE groundwater model

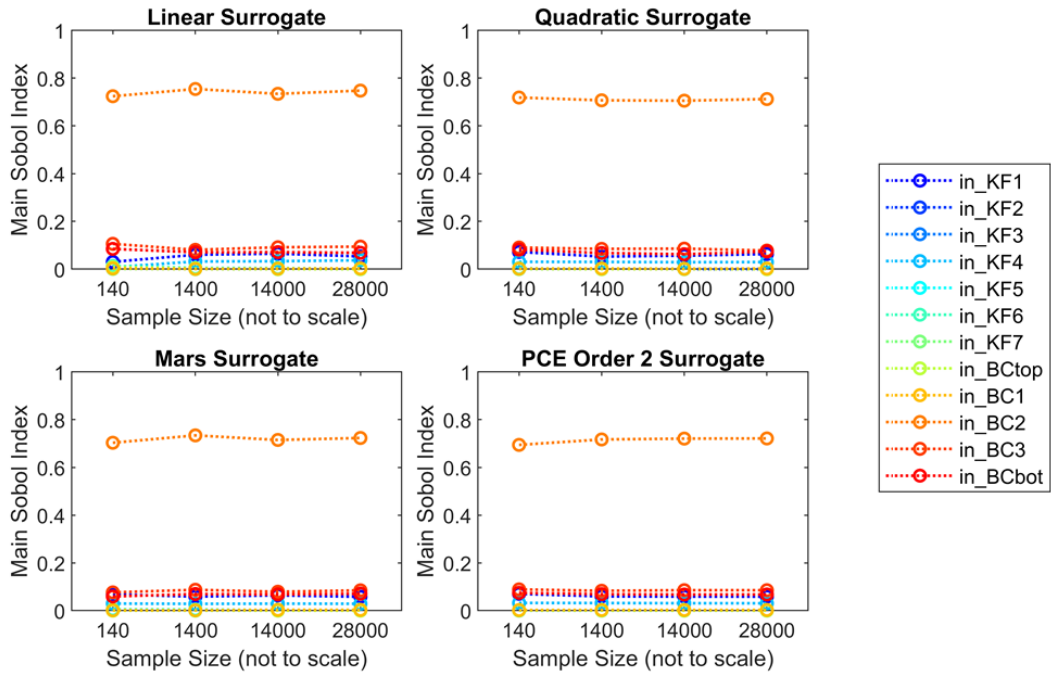
The model does not calculate time-dependent results but 37 values of hydraulic head at different locations which correspond to experimental observation points and are foreseen for model calibration. Sets of 140 to 28000 model runs are available.

Fig. 2.24 shows the results of the direct and rank-based regression analysis for all 37 observation points, calculated from the 28000-set of runs. Both sets of curves look nearly identical, which is a clear hint that the model is highly linear. This is confirmed by the  $r^2$  value, which is nearly 1, no matter if a rank transformation is performed or not.



**Fig. 2.24** Direct (left) and rank-based (right) sensitivity analysis of the IBRAE groundwater model (GRS results)

The first-order sensitivity indices calculated by SNL from linear, quadratic, MARS (multi-variate adaptive regression spline), and PCE (order 2) surrogate models (also for the dataset of 1400 realizations) are shown in Fig. 2.25. The results are essentially identical regardless of model type, indicating that no model is necessarily more appropriate for this data set than the others. Obviously, higher-order surrogate models are not superior to a linear one, which also confirms that the original model is practically linear.



**Fig. 2.25** First-order sensitivity indices of the IBRAE groundwater model, calculated with different surrogate models for all sample sizes (SNL results)

### 2.1.7.5 Summary

In summary, we found that the variance-based methods are now easily generated using a variety of approaches and belong to the main Sensitivity Analysis (SA) approaches. Correlation coefficients and regression approaches continue to be used and are informative. More advanced methods show results mostly consistent with simpler methods but there are important differences. Graphical methods such as CUSUNORO also provide additional visualisation which can show influences over the range of a variable. It might be advisable to start an analysis by applying such methods.

We found consistency between the linear sensitivity measures calculated by the different partners but sometimes the variance-based sensitivity indices did not exactly agree with the linear sensitivity measures. Also, there were more differences in rankings seen across the several variance-based sensitivity indices, such as EASI, EFAST, PCE and RS-HDMR. Generally, variance-based methods involve more complicated algorithms and require more computational costs. The various approximations being made in these approaches may account for some of these differences. For surrogate methods, the surrogate type may play a role in the accuracy of the estimation of variance-based indices. Differences in rankings were also seen depending on the use of data transformations.

The appropriateness of specific transformations is not always obvious, and justification of such transformations may be an opportunity for future study.

We often found that the sensitivity analyses across participants identified the same first most important parameter but differed on the importance of lower ranked parameters. This may be due to differences between methods in detecting variable significance, particularly because the quantities of interest often span many orders of magnitude. Variables of secondary importance may need to be identified by connecting less clear sensitivity analysis results with physical phenomenology. Validation or goodness-of-fit metrics, in the context of surrogate modelling or regression analysis, may help select the most appropriate transformation to use for sensitivity analysis or identify the best surrogate model.

There is also a lack of consensus between participants on the delineation between sensitivity measure values that indicate secondary sensitivity versus sensitivity measure values that indicate negligible sensitivity. This highlights a need for development of consensus methods for testing or justifying conclusions regarding lower-ranked parameters.

## **2.2 Biosphere modelling: Czech German benchmark**

### **2.2.1 Introduction**

A comparison of biosphere dose conversion factors (BDCFs) calculated by UJV with the Czech biosphere model and by GRS with the German biosphere model showed significant differences, for some radionuclides by more than three orders of magnitude. The objective of this benchmark here is to identify reasons for these differences. Therefore, the modelling approaches and data used in biosphere models from Czech Republic and Germany are compared and the impact of differences on the BDCFs are described. The benchmark presented here is focused on the radionuclide treatment in the soil, the pathways from soil to plant and the external radiation from soil.

### **2.2.2 Contamination of the soil and pathways to plants**

This section describes the modelling approaches and data used by UJV and GRS.

### 2.2.2.1 Modelling – Czech model

The Czech conceptual model (see Fig. 2.26) is based on the reference biosphere ERB2A (Agricultural well) presented in the document „Reference Biospheres“ for solid radioactive waste disposal (prepared in the frame of the IAEA project BIOMASS-6).

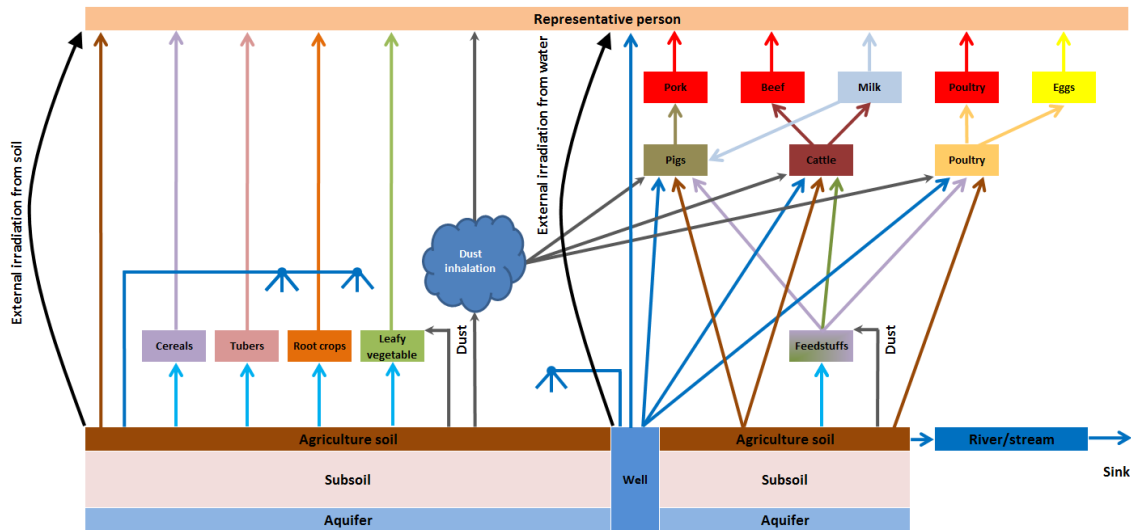


**Fig. 2.26** Czech conceptual biosphere model (local version for the site Kravi Hora)

The simplified assumptions and “stylised” approaches to human behaviour and characteristics have been used due to the uncertainty connected to the future development of the biosphere and human behaviour. The methodology called “Route map” (recommended by IAEA-BIOMASS-6) have been used for the staged development of the biosphere model. The computer model of the biosphere was created in the GoldSim version 12 software environment. The stand-alone model (see Fig. 2.27) simulates the radionuclide concentrations of  $1 \text{ Bq/m}^3$  in groundwater at the output from the geosphere and the same radionuclide concentrations in the well water (dilution in the well is not considered). The model calculates BDCFs that are intended for the representation of the total transport of individual radionuclides through the biosphere and their corresponding contributions to the total annual effective dose for a representative person. (The biosphere model was then transferred into a complex model of the transport of radionuclides from the repository through the geosphere.)

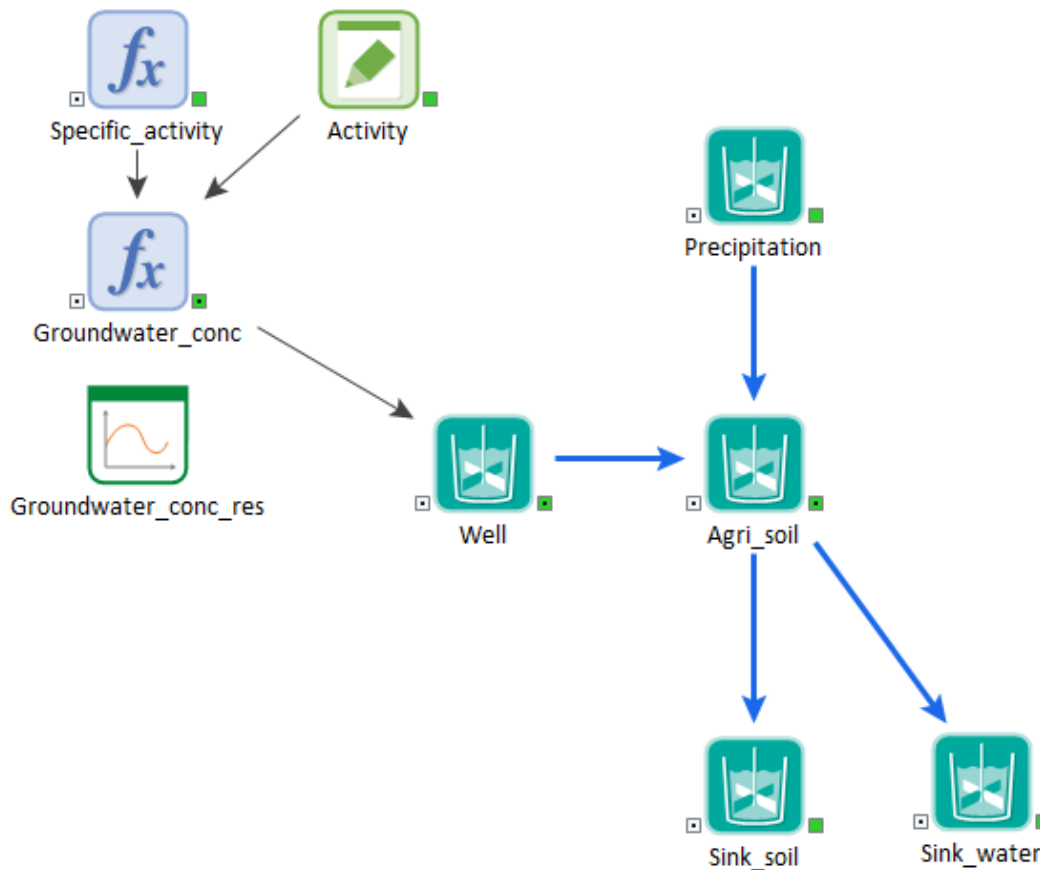


**Fig. 2.27** Czech transport model in GoldSim

The dynamic elements of the model (the concentration of radionuclides in them changes over time) are Well, Agri\_soil, Sink\_soil and Sink\_water. They are modelled by GoldSim elements „Cell Pathway“ (discrete „well-mixed“ environmental compartment). The transfer pathways between dynamic elements (e.g. irrigation, precipitation, infiltration, erosion or other) are based also on equations presented in the mentioned document for the reference biosphere ERB2A. The radionuclide concentration (mass or volume activity) in crops and animal products can be considered as being in equilibrium with the radionuclide concentration (volume activity) in the well water and with the radionuclide concentration in agricultural soil (mass or volume activity).

Cultivated soil is assumed to be ploughed, if not every year then every few years. A “well mixed” (homogenised) layer is assumed associated with the typical ploughing depth of 0.3 m. It is assumed that root intake and other biotic activity occur within the root layer. This means that the detailed soil structure should not be modelled.

The input and output parameters are listed in the following

- Input
  - irrigation water (200 l/year/m<sup>2</sup>, 1 Bq m<sup>-3</sup>) (*Well > Agri\_soil*)
  - atmospheric precipitation (614,1 L yr<sup>-1</sup> m<sup>-2</sup>) (*Precipitation > Agri\_soil*)
- Output
  - evapotranspiration (612,2 L yr<sup>-1</sup> m<sup>-2</sup>) – *without radionuclides*
  - direct outflow (surface run-off + interflow) (63,3 L yr<sup>-1</sup> m<sup>-2</sup>) - *with radionuclides* (*Agri\_soil > Sink\_water*)
  - infiltration (138,7 L yr<sup>-1</sup> m<sup>-2</sup>) - *with radionuclides* (*Agri\_soil > Sink\_soil*)
  - direct mass transport to the lower soil layer (it depends on retardation coefficient) (*Agri\_soil > Sink\_soil*)
- Simulated events (by GoldSim code)
  - mass balance (inflows, outflows – water)
  - partitioning (between solid and fluid fraction in soil compartment)
  - solubility constraints

The plant (crop) contamination via root uptake is calculated by

$$C_{c,root} = \frac{C_s CF_{crop} F_{p2}}{(1 - \theta_t) \rho} \quad (2.5)$$

The parameters are listed in Tab. 2.5 and Tab. 2.6.

**Tab. 2.5** Parameters for calculation of RN uptake via root, Czech model

Parameter	Unit	Value
Activity from root uptake $C_{c,root}$	Bq kg <sub>fm</sub> <sup>-1</sup>	-
Volume activity of radionuclide in irrigated agriculture soil (based on dry weight of soil) $C_s$	Bq m <sup>-3</sup>	-
Soil to plant transfer factor $CF_{crop}$	(Bq kg <sub>fm</sub> <sup>-1</sup> )/ (Bq kg <sub>dm</sub> <sup>-1</sup> )	Tab. 2.6
Fraction of the internal contamination associated with the edible part of the crop at harvest that is retained after food processing $F_{p2}$	-	1 (conservative)
Total porosity of agricultural soil $\theta_t$	-	0.45
Grain density (dry density) of agricultural soil $\rho$	kg m <sup>-3</sup>	2 650

**Tab. 2.6** Soil to plant transfer factors [(Bq kg<sub>fm</sub><sup>-1</sup>)/(Bq kg<sub>dm</sub><sup>-1</sup>)] used in the Czech model

Element	Cereals	Leafy vegetable	Root crops	Tubers (potatoes)	Fodder	Fodder based on
Cl	47	25	11	11	25	Leafy veg.
Tc	2	250	46	0.094	76	Pasture
I	0.00036	0.0041	0.0047	0.0047	0.0037	Pasture
Cs	0.020	0.074	0.030	0.035	0.19	Pasture
Ra	0.029	0.12	0.091	0.012	0.26	Grass
U	0.0077	0.043	0.025	0.028	0.072	Pasture

Note: The values taken from /IAEA 10/ are shown in brown (dark colour - soil type - loam, light colour - all soil types), the values taken from /STA 03/ are shown in green and values taken from /IAEA 03/ in blue. The values given for potatoes (tubers) from values for root vegetables are shown in violet. The final column of the table shows on what kind of transfer factor the values considered for fodder are based.

The plant (crop) contamination via foliar uptake with parameters listed in Tab. 2.7 and Tab. 2.8 is calculated by

$$C_{c,int} = Int_{crop} V_{irr} C_w \frac{(1 - F_{abs})e^{-WT} F_{p3} + F_{abs} F_{p2} F_{trans}}{Y} \quad (2.6)$$

**Tab. 2.7** Parameters for calculation of RN uptake via foliage, Czech model

Parameter	Unit	Value
Radionuclide concentration in the edible part of the crop (interception + foliar uptake + weathering) $C_{c,int}$	Bq kg <sub>fm</sub> <sup>-1</sup>	-
Fraction of radionuclide in the spray irrigation water that is deposited on the surface of the crop $Int_{crop}$	-	Tab. 2.8
Irrigation rate $V_{irr}$	m <sup>3</sup> yr <sup>-1</sup> m <sup>-2</sup>	0.2
Radionuclide concentration in the well water $C_w$	Bq m <sup>-3</sup>	-
Fraction of intercepted radionuclide initially deposited onto the crop surface that is absorbed from external surfaces into crop tissues $F_{abs}$	-	0.5
Removal rate of radionuclide deposited on crop surface by weathering processes (weathering rate) including mechanical weathering, wash-off and leaf fall $W$	yr <sup>-1</sup>	18
Interval between irrigation and harvest $T$ - cereals - leafy vegetables + fodder - root crops + tubers	year	0.075 (27.4d) 0.02 (7.3d) 0.04 (14.6d)
Fraction of external contamination from interception that is retained on the edible part of the crop after food processing $F_{p3}$	-	Tab. 2.8
Fraction of the internal contamination associated with the edible part of the crop at harvest that is retained after food processing $F_{p2}$	-	1
Fraction of absorbed activity that is translocated to the edible part of the crop by the time of harvest (translocated fraction) $F_{trans}$	-	Tab. 2.8

**Tab. 2.8** Interception parameters

Element	Int <sub>crop</sub>	F <sub>p3</sub>					F <sub>trans</sub>				
		Cereals	Leafy veg.	Root crops	Tubers	Fodder	Cereals	Leafy veg.	Root crops	Tubers	Fodder
Cl	0.3	0.01	0.1	0	0	0.1	0.1	1	0.1	0.1	1
Tc	0.1	0.01	0.1	0	0	0.1	0.1	1	0.1	0.1	1
I	0.3	0.01	0.1	0	0	0.1	0.1	1	0.1	0.1	1
Cs	0.3	0	0.1	0.1	0.1	0.1	0.088	0.19	0.3	0.3	0.19
Ra	0.3	0	0.1	0.1	0.1	0.1	0.08	0.18	0.099	0.099	0.18
U	0.3	0	0.1	0.1	0.1	0.1	0.16	0.036	0.43	0.43	0.036

Note: The orange values are taken from /IAEA 03a/ and the violet values from /EPRI 02/.

The external contamination of the surface of crops is calculated by

$$C_{c,dep} = \frac{C_s S_{crop} F_{p1}}{(1 - \theta_t) \rho} \quad (2.7)$$

The parameters are listed in Tab. 2.9.

**Tab. 2.9** Parameters for calculation of external contamination of crops, Czech model

Parameter	Unit	Value
Radionuclide concentration deposited on the crop surface $C_{c,dep}$	Bq kg <sub>fm</sub> <sup>-1</sup>	-
Volume activity of radionuclide in irrigated agriculture soil (based on dry weight of soil) $C_s$	Bq m <sup>-3</sup>	-
External contamination of the crop due to the deposition of re-suspended soil $S_{crop}$	kg <sub>dm</sub> <sup>-1</sup> soil / kg <sub>fm</sub> <sup>-1</sup> crop	0.0002
Fraction of external soil contamination on the edible part of the crop retained after food processing $F_{p1}$	-	0.1

The total radionuclide concentration in the crop is calculated as the sum of root uptake, foliar uptake and external contamination.

### 2.2.2.2 Modelling – German model

A principle scheme for the treatment of the soil and the resulting pathways as required in the German regulations is shown in Fig. 2.28. Two types of soil are considered, namely soil for pasture plants and soil for all other plants. The animals are fed by pasture plants, whereas all other plants are used for nutrition of humans. With respect to the treatment

in the model the plants are divided into three groups, i.e. leafy vegetables, other plants and pasture plants.

### LeafTube

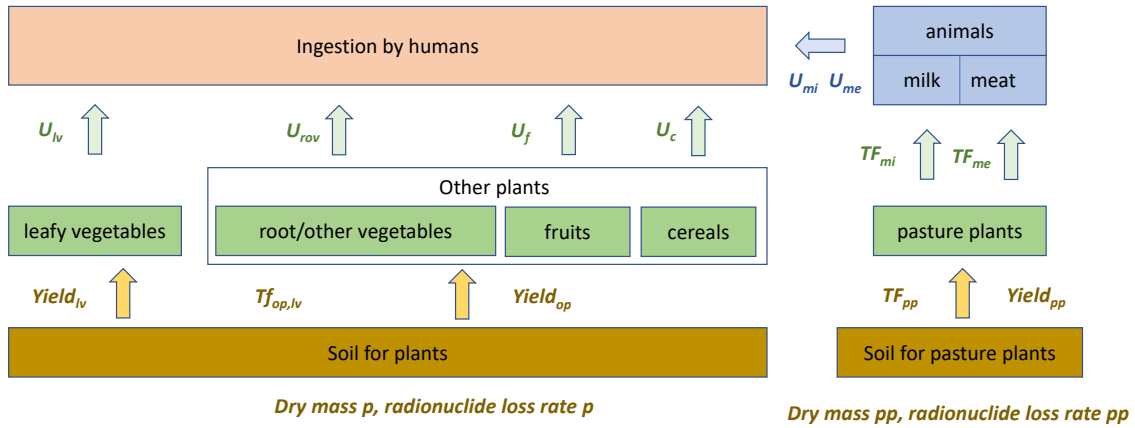


**Fig. 2.28** Scheme for the treatment of contaminated soils and resulting pathways with key parameters differing for the respective components.

The calculation of radionuclide uptake of the plant from the soil via the root has to be calculated by the following formula:

$$C_r^n = C_r^{fließ} \left[ \frac{WT_r^n t_R}{p^m (\lambda_{M,r} + \lambda_r) 365} (1 - \exp(-(\lambda_{M,r} + \lambda_r) t_b)) \right] \exp(-\lambda_r t_v^n) \quad (2.8)$$

Regarding only the concentration in the soil the equation can accordingly be modified to

$$C_r^{n,s} = C_r^{fließ} \left[ \frac{W t_R}{p^m (\lambda_{M,r} + \lambda_r) 365} (1 - \exp(-(\lambda_{M,r} + \lambda_r) t_b)) \right] \quad (2.9)$$

All parameters are listed in Tab. 2.10 and Tab. 2.11.

**Tab. 2.10** Parameters and parameter values used in the German model for root uptake into the plant for the irrigation pathway. Note that values for pasture soil are in brackets.

Parameter	Unit	Value
Specific activity in plants $C_r^n$	Bq kg <sup>-1</sup>	
Specific activity in soil $C_r^{n,s}$	Bq kg <sup>-1</sup>	
Concentration of radionuclide r in the well water $C_r^{fließ}$	Bq m <sup>-3</sup>	1
Irrigation rate $W$	m <sup>3</sup> m <sup>-2</sup> s <sup>-1</sup>	1.2e-8
number of days, at which irrigation occurs $t_R$	d	180
Plane dry mass of soil $p^m$	kg m <sup>-2</sup>	280 (120)
Time during which radionuclides get deposited in soil $t_b$	s	3.1e7 - 3.1e12
Time between harvest and consumption of plant $t_v^n$	s	5.2e6 (60.2d)

**Tab. 2.11** RN-specific parameters and parameter values used in the German model for root uptake into the plant for the irrigation pathway. Note that values for pasture soil are in brackets.

Parameter	Unit	Cl-36	Tc-99	I-129	Cs-135	Ra-226	U-238
Soil to plant transfer factor $T_r^n$	(Bq kg <sub>fm</sub> <sup>-1</sup> )/ (Bq kg <sub>dm</sub> <sup>-1</sup> )	5.0 (5.0)	3.0 (3.0)	2.0e-2 (1.0e-2)	5.0e-2 (5.0e-2)	5.0e-3 (1.0e-2)	3.0e-3 (3.0e-3)
Effective residence constant for RN in the root area of plants $\lambda_{M,r}$	s <sup>-1</sup>	1e-8 (2e-8)	1e-8 (2e-8)	1e-9 (2e-9)	1e-10 (2e-10)	1e-11 (2e-11)	1e-11 (2e-11)
Physical decay constant $\lambda_r$	s <sup>-1</sup>	7.3e-15	1.0e-13	1.4e-15	9.6e-15	1.4e-11	4.9e-18

The accumulation of radionuclides with increasing time in the soil can be considered in the exponential term  $1 - \exp(-(\lambda_{M,r} + \lambda_r)t_b)$ . The time during which radionuclides get deposited on the soil  $t_b$  is set to 50 years in the German regulations. However, for the benchmark calculations it is varied between one year and 10<sup>5</sup> years.

The calculation of plant contamination via foliar uptake is calculated by

$$C_r^n = C_r^{flies} \left[ \frac{Wf_w}{Y^n(\lambda_v + \lambda_r)} (1 - \exp(-(\lambda_v + \lambda_r)t_b^n)) \right] \exp(-\lambda_r t_v^n) \quad (2.10)$$

The parameters not mentioned so far are listed in Tab. 2.12.

**Tab. 2.12** Parameters and parameter values used in the German model for foliar uptake into the plant for the irrigation pathway, s. also Tab. 2.10 and Tab. 2.11.

Parameter	Unit	Value
Specific activity in plants $C_r^n$	Bq kg <sup>-1</sup>	
Interception factor $f_w$		0.3
Product yields $Y_n$		
- Leafy vegetables	kg m <sup>-2</sup>	1.6
- Pasture plants		0.85
- Other plants		2.4
Constant for residence time of RN on vegetation $\lambda_v$	s <sup>-1</sup>	5.7e-7

### 2.2.2.3 Results

The radionuclide concentrations in the soil calculated with the Czech and the German model are shown in Tab. 2.13. In the German model two types of soil, namely soil for pasture plants and soil for all other plants are distinguished (see Fig. 2.28). In both models a concentration of 1 Bq/m<sup>3</sup> for the contaminated well water is considered.

The results in the table show an increase of the radionuclide concentrations with increasing time according to the accumulation in the soil. The bold marked numbers are the ones, which are used in the biosphere calculations of GRS and UJV, respectively. For GRS the consideration of the accumulation time of 50 years is prescribed, in case of UJV (stand-alone model used for BDCF<sub>s</sub> calculation) an accumulation time of 10<sup>5</sup> years is applied in order to consider the complete accumulation even for the strong sorbing radionuclides. This is illustrated in Fig. 2.29.

**Tab. 2.13** Radionuclide concentrations in soil (Bq kg<sub>dm</sub><sup>-1</sup>) calculated by Czech and German biosphere models for different points in time. For GRS concentration values differ for soil (top) and pasture soil (bottom). The bold numbers are the values used in the reference case by UJV and GRS

RN	After 1 yr		After 50 yrs		After 1000 yrs		After 10 <sup>5</sup> yrs	
	GRS	UJV	GRS	UJV	GRS	UJV	GRS	UJV
Cl-36	5.72E-4 1.15E-3	2.13e-4	2.11e-3 2.47e-3	2.90e-4	2.11e-3 2.47e-3	2.90e-4	2.11E-3 2.47E-3	2.90e-4
Tc-99	5.72e-4 1.15e-3	1.91e-4	2.11e-3 2.47e-3	2.43e-4	2.11e-3 2.47e-3	2.43e-4	2.11e-3 2.47e-3	3.43e-4
I-129	6.57e-4 1.51e-3	4.31e-4	1.64e-2 2.34e-2	4.63e-3	2.11e-2 2.47e-2	4.66e-3	2.11e-2 2.47e-2	4.66e-3
Cs-135	6.66e-4 1.55e-3	4.57e-4	2.94e-2 6.39e-2	2.25e-2	2.02e-1 2.46e-1	3.48e-1	2.11e-1 2.47e-1	7.95e-1
Ra-226	6.67e-4 1.56e-3	4.57e-4	3.11e-2 7.21e-2	2.25e-2	4.70e-1 9.58e-1	3.28e-1	8.91e-1 1.46e+0	6.45e-1
U-238	6.67e-4 1.56e-3	4.56e-4	3.15e-2 7.29e-2	2.10e-2	5.72e-01 1.15e+0	1.28e-1	2.11e+0 2.47e+0	1.33e-1
Nb-94	6.67e-4 1.56e-3	4.57e-4	3.29e-2 7.62e-2	2.26e-2	5.63e-01 1.14e+0	3.61e-1	1.91e+0 2.34e+0	9.25e-1

In general, with both models similar shaped curves are calculated with an initial increase and a saturation at a distinct point of time. This point of time is depending on the retardation in the soil, i.e. the higher the retardation coefficient the later saturation is reached. Cl-36 and Tc-99 reach saturation after about 5 years and I-129 after about 50 years, whereas for Cs-135 and Ra-226 saturation is not reached before 10<sup>4</sup> years. The comparison shows that the more mobile radionuclides Cl-36, Tc-99 and I-129 have significantly higher concentrations in the German model compared to the Czech model. This is also true for the values calculated after 50 years (reference value for GRS) compared with the values after 10<sup>5</sup> years (reference value for UJV). For the three other radionuclides the concentrations after 50 years in the German model are lower than the concentrations after 10<sup>5</sup> years in the Czech model.

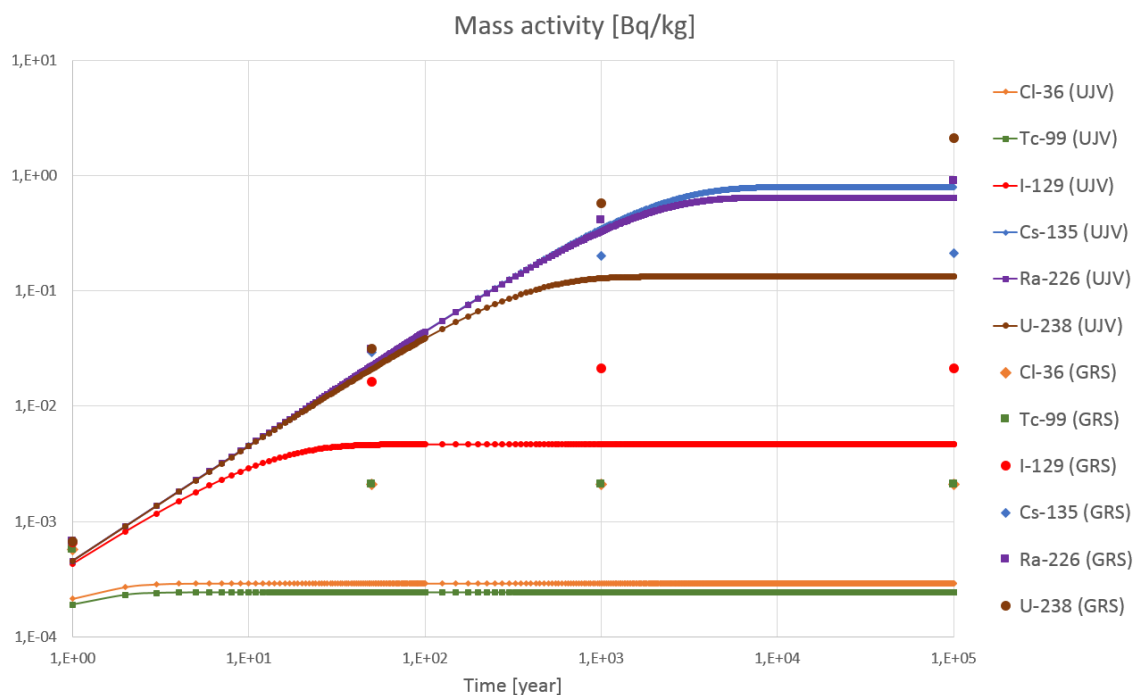


**Fig. 2.29** Time dependence of radionuclide concentration in agricultural soil calculated by UJV and GRS model

**Tab. 2.14** Radionuclide concentrations in plants (Bq/kg fresh mass) calculated by German biosphere model for different points in time

RN	After 1 yr		After 50 yrs		After 1000 yrs		After 10 <sup>5</sup> yrs		type
	root	total	root	total	root	total	root	total	
Cl-36	2.86e-3	5.36e-3	1.06e-2	1.31e-2	1.06e-2	1.31e-2	1.06e-2	1.31e-2	plant
		6.6e-3		1.43e-2		1.43e-2		1.43e-2	Leafy v.
	5.77e-3	1.15e-2	1.23E-2	1.81e-2	1.23E-2	1.81e-2	1.23E-2	1.81e-2	pasture
Tc-99	1.72e-3	4.21e-3	6.34e-3	8.84e-3	6.34e-3	8.84e-3	6.34e-3	8.84e-3	plant
		5.46e-3		1.01e-2		1.01e-2		1.01e-2	Leafy v.
	3.46E-3	9.2e-3	7.40e-3	1.31e-2	7.40e-3	1.31e-2	7.40e-3	1.31e-2	pasture
I-129	1.31e-5	2.51e-3	3.28e-4	2.83e-3	4.23e-4	2.92e-3	4.23e-4	2.92e-3	plant
		3.76e-3		4.08e-3		4.17e-3		4.17e-3	Leafy v.
	1.51e-4	5.89e-3	2.36e-3	8.10e-3	2.47e-3	8.21e-3	2.47e-3	8.21e-3	pasture
Cs-135	3.33e-5	2.53e-3	1.47e-3	4.03e-3	1.01e-2	1.26e-2	1.06e-2	1.31e-2	plant
		3.78e-3		5.28e-3		1.39e-2		1.43e-2	Leafy v.
	7.76e-5	5.82e-3	3.32e-3	9.07e-3	1.23e-2	1.80e-2	1.23e-2	1.81e-2	pasture
Ra-226	3.33e-6	2.50e-3	1.56e-4	2.66e-3	2.35e-3	4.84e-3	4.45e-3	6.95e-3	plant
		3.75e-3		3.91e-3		6.09e-3		8.20e-3	Leafy v.
	1.56e-5	5.76e-3	7.54e-4	6.50e-3	9.58e-3	1.53e-2	1.46e-2	2.04e-2	pasture
U-238	2.00e-6	2.50e-3	9.44e-5	2.59e-3	1.72e-3	4.21e-3	6.34e-3	8.84e-3	plant
		3.75e-3		3.84e-3		5.46e-3		1.01e-2	Leafy v.
	4.67e-6	5.75e-3	2.29e-4	5.97e-3	3.46e-3	9.20e-3	7.4e-3	1.31e-2	pasture

Tab. 2.14 shows the activity concentration of radionuclides in plants (per kg fresh mass) received by root uptake only and the total concentration (including foliar uptake) as calculated by the German model. The concentrations of radionuclides in the different plants calculated for root uptake and contamination by soil with the Czech model are listed in Tab. 2.15.

**Tab. 2.15** Radionuclide concentrations in agriculture crops (Bq/kg fresh mass) calculated by Czech biosphere model for different points in time

Root uptake + external contamination of crops					
RN	After 1 yr	After 50 yrs	After 1000 yrs	After 10 <sup>5</sup> yrs	
Cl-36	1.00e-2	1.36e-2	1.56e-2	<b>1.56e-2</b>	Cereals
	5.33e-3	<b>7.24e-3</b>	8.30e-3	<b>8.30e-3</b>	Leafy vegetables
	2.34e-3	3.19e-3	3.65e-3	<b>3.65e-3</b>	Root vegetables
	2.34e-3	3.19e-3	3.65e-3	<b>3.65e-3</b>	Tubers
Tc-99	3.82e-4	4.87e-4	5.58e-4	<b>5.58e-4</b>	Cereals
	4.78e-2	<b>6.08e-2</b>	6.98e-2	<b>6.98e-2</b>	Leafy vegetables
	8.79e-3	1.12e-2	1.28e-2	<b>1.28e-2</b>	Root vegetables
	1.80e-5	2.29e-5	2.62e-5	<b>2.62e-5</b>	Tubers
I-129	1.64e-7	1.76e-6	2.03e-6	<b>2.03e-6</b>	Cereals
	1.77e-6	<b>1.91e-5</b>	2.20e-5	<b>2.20e-5</b>	Leafy vegetables
	2.03e-6	2.18e-5	2.52e-5	<b>2.52e-5</b>	Root vegetables
	2.03e-6	2.18e-6	2.52e-5	<b>2.52e-5</b>	Tubers
Cs-135	9.15e-6	4.51e-4	7.20e-3	<b>1.82e-2</b>	Cereals
	3.38e-5	<b>1.67e-3</b>	2.66e-2	<b>6.75e-2</b>	Leafy vegetables
	1.37e-5	6.77e-4	1.08e-2	<b>2.74e-2</b>	Root vegetables
	1.60e-5	7.89e-4	1.26e-2	<b>3.19e-2</b>	Tubers
Ra-226	1.33e-5	6.52e-4	9.50e-3	<b>1.87e-2</b>	Cereals
	5.49e-5	<b>2.70e-3</b>	3.93e-2	<b>7.74e-2</b>	Leafy vegetables
	4.16e-5	2.05e-3	2.988e-2	<b>5.87e-2</b>	Root vegetables
	5.50e-6	2.70e-4	3.94e-3	<b>7.75e-3</b>	Tubers
U-238	3.52e-6	1.62e-4	1.12e-3	<b>1.17e-3</b>	Cereals
	1.96e-5	<b>9.03e-4</b>	6.22e-3	<b>6.54e-3</b>	Leafy vegetables
	1.14e-5	5.25e-4	3.62e-3	<b>3.80e-3</b>	Root vegetables
	1.28e-5	5.88e-4	4.05e-3	<b>4.26e-3</b>	Tubers

### 2.2.3 Discussion

The benchmark has been performed to identify reasons for significant differences in BDCFs calculated by each code considering various different exposition pathways. These BDCF values are listed in Tab. 2.16 including the ratio between the UJV and GRS value. The BDCF values are very similar in case of Cl-36 and differ between all other radionuclides by one to more than three orders of magnitude with the highest difference in case of Ra-226. Generally, the values calculated by UJV are higher than those calculated by GRS.

Since a clear identification of selected parameters or processes responsible for the differences, has not been possible, it was assumed that the accumulation of radionuclides in the soil might be the key reason for the differences. The Czech model calculates the transport in the soil and therewith considers a time dependent radionuclide accumulation in the soil. Whereas in the German model an accumulation time of 50 years and no time dependence is considered.

**Tab. 2.16** Biosphere dose conversion factors (BDCF) in [(mSv yr<sup>-1</sup>) / (Bq m<sup>-3</sup>)]

Radionuclide	UJV	GRS	UJV/GRS
Cl-36	7.8e-6	9.2e-6	0.85
Tc-99	2.6e-6	9.4e-8	27.2
I-129	2.0e-4	2.7e-6	74.5
Cs-135	6.2e-5	7.7e-8	801
Ra-226	4.1e-3	8.7e-7	5263
U-238	1.4e-4	5.0e-7	275

As illustrated in Fig. 2.29 for relatively mobile radionuclides like Cl-36, Tc-99 and even I-129 a stationary state is reached after nearly 50 years, i.e. the concentrations in soil do not further increase after 50 years. For less mobile radionuclides as Cs-135, Ra-226 and U-238 the accumulation is not completed after 1000 or even 10000 years. Therefore, for these less mobile radionuclides a higher concentration in the soil is expected in the Czech biosphere calculations.

In order to better understand the mobility of the six radionuclides it needs to be regarded, which parameters are applied to describe the RN retardation. Although the German model is simpler a comparison is possible. A loss rate, which is used in the German model can also be calculated for the Czech model by

$$\lambda_{il} = \frac{I}{R_i \theta d} \quad \text{with} \quad R_i = 1 + \frac{1 - n_{tot}}{n_w} \rho K_d \quad (2.11)$$

The parameters for calculation of a loss rate for the Czech model are listed in Tab. 2.17.

**Tab. 2.17** Parameters for calculation of loss rate in the Czech model

Parameter	Unit	Value
Transfer rate coefficient $\lambda_{il}$ of nuclide $i$	s <sup>-1</sup>	Tab. 2.18
Infiltration rate	m yr <sup>-1</sup>	0.1
Retardation coefficient $R_i$ of nuclide $i$	-	Tab. 2.18
Water-filled porosity of cultivated soil $\theta$	-	0.2
Thickness of cultivated soil layer $d$	m	0.3
Soil grain density $\rho$	kg m <sup>-3</sup>	2650
Total porosity $n_{tot}$	-	0.45
Water-filled porosity $n_w$	-	0.2

Based on the distribution coefficients ( $K_d$  values) applied for radionuclide sorption on soil in the Czech model a loss rate is calculated.  $K_d$  values, corresponding retardation coefficients and loss rates are compiled in Tab. 2.18 and compared to the loss rates used in the German model.

**Tab. 2.18**  $K_d$  values, corresponding  $R_i$  values and  $\lambda_{il}$  for the Czech model compared to  $\lambda_{M,r}$  of the German model (values in brackets are for pasture soil)

Radionuclide	UJV model			GRS model
	$K_d$ [ $\text{m}^3 \text{kg}^{-1}$ ]	$R_i$	$\lambda_{il}$ [ $\text{s}^{-1}$ ]	$\lambda_{M,r}$ [ $\text{s}^{-1}$ ]
Cl-36	3.0e-4	3.19	1.7e-8	1e-8 (2e-8)
Tc-99	2.3e-4	2.68	2.0e-8	1e-8 (2e-8)
I-129	6.9e-3	51.28	1.0e-9	1e-9 (2e-9)
Cs-135	1.2	8 746	6.0e-12	1e-10 (2e-10)
Ra-226	2.5	18 220	2.9e-12	1e-11 (2e-11)
U-238	0.2	1 459	3.6e-11	1e-11 (2e-11)

Concerning the radionuclide loss rates, the values are rather similar for the more mobile radionuclides Cl-36, Tc-99 and I-129 in the Czech and German biosphere model. Consequently, the saturation times are rather similar for these radionuclides. Furthermore, it shows that for similar loss rates the concentrations in soil calculated by the German model are by a factor 5 to ten higher than in the Czech model. Regarding the more strongly sorbed radionuclides, U-238 is slightly more mobile in the Czech model than in the German model. For Cs-135 and Ra-226 the loss rates are by more than one order of magnitude higher in the German model, i.e. they are less mobile in the Czech model.

In Tab. 2.19 the resulting concentrations in soil are compiled. For GRS both, the values after 50 years (as required by the regulations) and the values after complete enrichment, namely after  $10^5$  years are shown. The concentration ratios for the comparison with show clearly highest values for Ra-226 and decrease in the order Cs-135, U-238, I-129, Tc-99 and Cl-36. This is the same order for the BDCFs. However, the concentration ratios in soil are one to three orders of magnitude lower than the ratio of the BDCFs and can therewith not explain the differences in BDCFs.

**Tab. 2.19** Comparison of concentration in soil [ $\text{Bq kg}^{-1}$ ]. For GRS concentration after 50 years (reference value) and after  $10^5$  years are shown.

RN	UJV (after $10^5$ yrs)	GRS (after 50 yrs)	Ratio (UJV/GRS)	GRS (after $10^5$ yrs)	Ratio (UJV/GRS)
Cl-36	2.9e-4	2.1e-3	0.14	2.1e-3	0.14
Tc-99	3.4e-4	2.1e-3	0.16	2.1e-3	0.16
I-129	4.7e-3	1.6e-2	0.29	2.1e-2	0.22
Cs-135	8.0e-1	2.9e-2	27.6	2.1e-1	3.79
Ra-226	6.5e-1	3.1e-2	20.8	8.9e-1	0.72
U-238	1.3e-1	3.2e-2	4.06	2.1e+0	0.06

Tab. 2.19 also shows that the consideration of longer accumulation times in the German model would lead to higher concentrations for Cs-135, Ra-226 and U-238, where the differences in BDCFs are highest.

In order to investigate, whether an additional increase in concentrations occur in the Czech model, which might explain the large differences in BDCFs the uptake in plants is addressed. Exemplarily the concentration of radionuclides in leafy vegetables and the resulting dose for this single pathway is calculated and the results are listed in Tab. 2.20.

**Tab. 2.20** Concentration in leafy vegetables, calculated dose for this single pathway (ingestion of leafy vegetables) and ratio of dose rates for UJV/GRS. For GRS the data are based on soil concentrations after 50 years

RN	Conc. [Bq/kg]		IDC [Sv/Bq]	Dose [Sv/yr]		Ratio (UJV/GRS)
	UJV	GRS		UJV	GRS	
Cl-36	1.8e-2	1.4e-2	9.3e-10	6.7e-10	5.1e-10	1.3
Tc-99	6.4e-2	1.0e-2	6.4e-10	1.7e-9	2.5e-10	6.8
I-129	1.1e-2	4.1e-3	1.1e-7	4.8e-8	1.8e-8	2.7
Cs-135	6.1e-2	5.3e-3	2.0e-9	5.0e-9	4.1e-10	12
Ra-226	8.0e-2	3.9e-3	2.8e-7	9.4e-7	4.3e-8	22
U-238	6.7e-3	3.8e-3	4.5e-8	1.2e-8	6.7e-9	1.8

In general, the dose ratios of UJV and GRS reflects the concentration ratios in soil (column 4, Tab. 2.19). However, for Cl-36, Tc-99 and I-129 the dose ratio (UJV/GRS) is significantly higher. Since the consumption rates (40.4 vs 39.9 kg yr<sup>-1</sup>) and the ingestion dose coefficients (IDC) are very similar, the differences are mainly due to transfer processes from soil to the plant or by contamination of plants via foliar uptake and in the Czech case via external contamination of crops. This cannot be explained by the root uptake, since the transfer factors are by more than two order of magnitude higher in case of Tc-99 for GRS and rather similar for I-129. The additional contribution from plant contamination by soil, considered only in the Czech calculations might play a role. Clearly, a further analysis is needed, including also analyzing the impact of foliar uptake.

These selected benchmark calculations indicate that the concentration of radionuclides in soil, where the accumulation for stronger sorbing radionuclides is not considered in case of GRS, do not explain the observed differences in the biosphere dose conversion factor between GRS and UJV. Some more thorough analysis of the German biosphere model already identified two errors, one caused by a unit error, and a second one by

including a non-realistic pathway. Both have occurred during transferring the new biosphere model into Excel. In addition, the need to calculate BDCFs for radionuclides separately have been identified by UJV. It is caused by the GoldSim code settings. This need to be evaluated in more detail and call for a further benchmarking including the whole branch of pathways to understand the differences.

#### 2.2.4 External irradiation from soil by irrigation

The second part of the benchmark exercise is related to the external irradiation. It is focused on residence time on irrigated agricultural soil. In addition to the calculations for the soil pathways Nb-94, where the overall dose rate is dominated by external radiation, is investigated here, too.

**Tab. 2.21** Parameters for calculation of external radiation from residence time on agricultural soil, Czech model

Parameter	Unit	Value
Contribution of radionuclide <i>i</i> to the dose from external irradiation from soil $D_{i,s-ext}$	Sv yr <sup>-1</sup>	
Concentration of radionuclide <i>i</i> (volume activity) in the agricultural soil (related to the dry soil mass) $C_{i,s}$	Bq m <sup>-3</sup>	
Time spent outdoors in a field with contaminated soil $OT_s$	s yr <sup>-1</sup>	2.0 e7 (14.5 h/d)
Dose coefficient for external irradiation from soil for radionuclide <i>i</i> $DCext_{i,s}$	(Sv s <sup>-1</sup> ) / (Bq m <sup>-3</sup> )	Tab. 2.22

In the Czech model for external irradiation from soil (surface) the following equation is applied

$$D_{i,s-ext} = C_{i,s} OT_s DCext_{i,s} \quad (2.12)$$

The parameters are listed in Tab. 2.21 and Tab. 2.22.

In the German model different pathways for external radiation are foreseen, i.e. residence time on bank sediments, on flooded areas and on dredge discharge pools /BMU 12/. For the benchmark, which considers residence times on irrigated agricultural areas an additional modelling approach is used.

**Tab. 2.22** Dose coefficients for external radiation for Czech and German model

Radionuclide	UJV [(Sv s <sup>-1</sup> ) / (Bq m <sup>-3</sup> )]	GRS [(Sv s <sup>-1</sup> ) / (Bq m <sup>-2</sup> )]
Cl-36	1.3e-20	-
Tc-99	6.7e-22	-
I-129	6.9e-20	2.0e-17
Cs-135	1.57e-22	-
Ra-226	1.7e-19	1.6e-15
U-238	5.5e-22	2.3e-17
Nb-94	5.2e-17	1.5e-15

The radiation exposure for radiation exposure on irrigated agricultural soil is calculated by the equation /PRO 02/

$$H_{a,r} = c_r^{n,s} \rho_s U_r t_a g_{b,r} \quad (2.13)$$

The parameters are listed in Tab. 2.22 and Tab. 2.23.

**Tab. 2.23** Parameters for calculation of external radiation from residence time on agricultural soil, German model

Parameter	Unit	Value
External radiation exposure by irrigated agricultural area $H_{a,r}$	Sv yr <sup>-1</sup>	
Specific activity in soil $c_r^{n,s}$	Bq kg <sup>-1</sup>	
Density of dry soil $\rho_s$	kg m <sup>-3</sup>	1200
Effective soil thickness $U_r$	m	0.05
Time spend on irrigate agricultural soils $t_a$	s	3.6e6 (1000 h yr <sup>-1</sup> )
Dose coefficient for external radiation from soil $g_{b,r}$	s	s. Tab. 2.22

#### 2.2.4.1 Results and discussion

The results for the calculations of external radiation exposition by residence on contaminated agricultural soil calculated by the Czech and German model are compiled in Tab. 2.24 and in addition illustrated in Fig. 2.30. For the German model no dose coefficients for Cl-36, Tc-99 and Cs-135 are listed, since their contribution for the external radiation pathway is considered to be too low to impact the overall dose.

The doses by external radiation are rather similar for Nb-94 and a factor three to ten higher for I-129 in the calculations from GRS. This likely reflects the concentration differences in the soil. The differences are significantly larger for Ra-226 and U-238. The external radiation expositions calculated by GRS are higher by about one to two orders of magnitude for Ra-226 and more than three orders of magnitude for U-238 after longer

accumulation times. Since the concentrations in soil are similar for Ra-226 and only one order of magnitude higher in GRS calculations for U-238 the difference in external radiation exposition is likely to be the fact that in the dose coefficients applied by the German model the impact of daughter nuclides is considered, which is not the case for the dose coefficients applied by the Czech model.

**Tab. 2.24** Dose from external irradiation from the soil (radionuclide contributions) (Sv yr<sup>-1</sup>) calculated by Czech and German biosphere models for different points in time

RN	After 1 yr		After 50 yrs		After 1000 yrs		After 10 <sup>5</sup> yrs	
	GRS	UJV	GRS	UJV	GRS	UJV	GRS	UJV
Cl-36	0.0	7.6e-14	0.0	1.0e-13	0.0	1.0e-13	0.0	1.0e-13
Tc-99	0.0	3.6e-15	0.0	4.5e-15	0.0	4.5e-15	0.0	4.5e-15
I-129	2.8e-12	8.3 e-13	7.2e-11	8.9e-12	9.1e-11	9.0e-12	9.1e-11	9.0e-12
Cs-135	0.0	2.6e-15	0.0	1.3e-13	0.0	2.0e-12	0.0	4.5e-12
Ra-226	2.3e-10	2.2e-12	1.1e-8	1.1e-10	1.6e-7	1.6e-9	3.1e-7	3.1e-9
U-238	3.3e-12	7.0e-15	1.6e-10	3.2e-13	2.8e-9	2.0e-12	1.1e-8	2.0e-12
Nb-94	2.2e-10	6.6e-10	1.1e-8	3.3e-8	1.8e-7	5.2e-7	6.2e-7	1.3e6

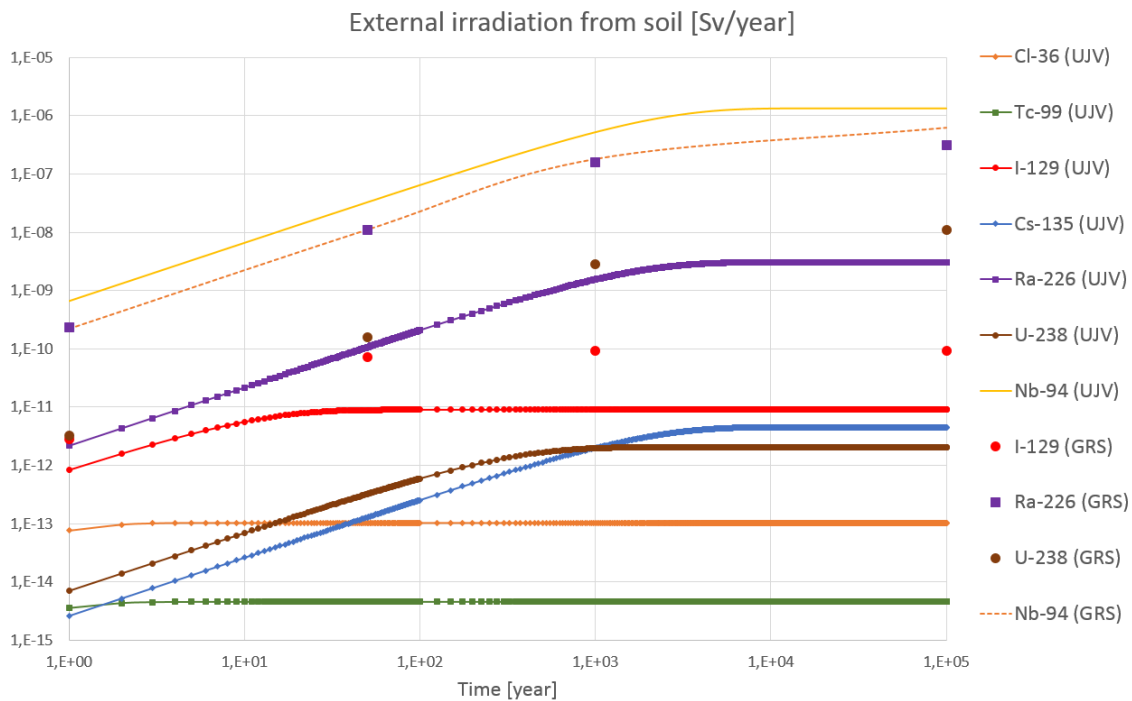


**Fig. 2.30** Time dependence of dose from external irradiation from irrigated agricultural soil calculated by UJV and GRS

Since the external irradiation pathway on irrigated agricultural soil is not considered in the German regulations so far, a comparison of this pathway with the three other external irradiation pathways required in the regulations has been done. The results are shown

in Tab. 2.25. In general, the radiation exposures calculated for the irrigation pathway are lower than those from the other pathways. The difference is low in case of Ra-226 and Nb-94 (for pathways residence on bank sediments and inundation areas). However, large differences are found for I-129 and for Nb-94 (mud disposal areas) with more than two orders of magnitude higher exposures. For U-238 the differences are more than one order of magnitude. This indicates that for the other pathways rather conservative assumptions are made in the German model. The origin of these differences and the reasonability behind need to be investigated further.

**Tab. 2.25** Comparison of radiation exposures [Sv yr<sup>-1</sup>] for different external radiation pathways calculated with the German model (for irrigation on agricultural soils accumulation time of 50 years is considered)

RN	Bank sediments	Inundation areas	Mud disposal areas	Irrigated soils
Cl-36	0.0	0.0	0.0	0.0
Tc-99	0.0	0.0	0.0	0.0
I-129	3.3E-08	1.1E-07	1.4E-07	7.2e-11
Cs-135	0.0	0.0	0.0	0.0
Ra-226	2.6E-08	3.5E-08	6.1E-08	1.1e-8
U-238	2.8E-09	3.0E-09	5.8E-09	1.6e-10
Nb-94	2.5E-08	2.5E-08	8.1E-06	1.1e-8

As a consequence, the contribution of the pathway via external irradiation play a role for several radionuclides to the overall BCDFs calculated with the German model, whereas the contribution of the external irradiation from soil is three or more orders of magnitude lower in case of the Czech model than the total effective dose (from all pathways) and therewith do not significantly contribute to the BCDF.

## 2.2.5 Conclusions

The benchmark has been successfully performed. The reasons assumed for the differences in the BDCFs calculated by UJV and GRS with the respective national biosphere models could not be confirmed. The enrichment of radionuclides in the soil did not explain the much higher BDCFs calculated by the Czech model compared to the German model. Instead, a more thorough analysis of the German biosphere model already identified two errors, one caused by a unit error, and a second one by including a non-realistic pathway. Both have occurred during transferring the new German biosphere model into Excel. In addition, the need to calculate BDCFs for radionuclides separately have been

identified by UJV. It is caused by the GoldSim code settings. This need to be evaluated in more detail and call for a further benchmarking including the whole branch of pathways to understand the differences. And already this first part of the benchmark looking only into two sub parts of the biosphere model was already an important contribution to the quality assurance of both models. Furthermore, differences in the description of the radionuclide transport in the soil as well as differences in the models for external irradiation have been evaluated and their impact on BCFs estimated.

## **2.3 Biosphere modelling: Radionuclide sorption in soils**

In this work package, the soil solid-liquid distributions of the elements Am, Pu, Ni, Tc, Se, Cs, Ra and U are estimated for the conditions that are usually present in agricultural soils. This is carried out by using the UNiSeCs modeling approach /HOR 13, HOR 15/ that has been further developed in the BMBF joint project Trans-LARA, FKZ 02NUK051. Furthermore, the relevant soil parameters are identified by single parameter analyses for each element. Using these results, uncertainty ranges of the distribution coefficients ( $K_d$ ) are estimated by calculating the  $K_d$  for various combinations of the relevant parameters using literature values /BLU 16/ of the respective parameter ranges frequently occurring in agricultural soils. These  $K_d$  ranges are calculated for two reference soils („Refesols“, /KOE 09/). Finally, the limitations of the model are discussed, including soil processes and parameters that are not taken into account.

### **2.3.1 Model description, implementation and validation**

#### **2.3.1.1 Geochemical code and databases**

The geochemical code used for the  $K_d$  calculations is PHREEQC /PAR 13/, Version 3.6.3. The thermodynamical data for solution and solid phase equilibria were drawn from the Thermochemie database /GRI 15/, Version 9b0. The database for the sorption reactions had been compiled by the author from the literature (see chapter 2.3.1.3) and has been extended for this project.

#### **2.3.1.2 Model structure**

The UNiSeCs approach is based on a reduction of the complexity of the mineralogical soil structure. Under the conditions present in middle-European soils, and especially in

Refesols (excluding alkaline and calcite rich soils), three main components have been identified to be most relevant for the sorption of inorganic species in agricultural soils, namely (i) the clay fraction, (ii) hydrous oxides (HO) and (iii) immobile as well as mobile organic matter (IOM resp. DOM). The basic assumption in the UNiSeCs approach is that all other solid soil components can be neglected for solid-liquid distribution calculations. However, if in a special case an additional soil component is relevant, the model can be easily extended as long as the appropriate thermodynamical sorption data are available.

The UNiSeCs II version of the model makes the following approximations:

1. The HO fraction which is mainly composed of hydrous oxides of iron, aluminum and manganese can be represented by ferrihydrite, a mineral that is frequently present in soils because it is usually involved in Fe-precipitation processes. A large number of ferrihydrite sorption data can be found in the literature, e.g. /DZO 90/. The complexation constants for aluminum hydroxides such as gibbsite seem to be generally similar to those for ferrihydrite /KAR 10/. The amount of HO is generally calculated from the results of the respective soil analyses (sum of oxalate extractable iron and aluminum).
2. The clay fraction is represented by the “reference” clay mineral illite, which frequently occurs in agricultural soils and has an intermediate position within the clay minerals with respect to the number of surface sites. It has also been extensively analyzed for its properties with regard to sorption of radionuclides /BRA 17/. However, as hydrous oxides and ca. one half of the IOM is thought to be part of the clay fraction, these components have to be taken into account in the calculation of the amount of illite binding sites /HOR 13/.
3. 80 % of the IOM is humic substance /SCH 97, STE 02/ and can be represented by humic acid, while 38 % of the DOM can bind cations and can be represented by fulvic acid /GRO 10/. The cation binding properties of both humic and fulvic acid have been characterised and quantified by a sophisticated model /TIP 11/, which is used in UNiSeCs II.
4. It is assumed that 50 % of the organic matter is organic carbon (OC) /BLU 16/. The abbreviations for immobile and dissolved organic carbon are IOC resp. DOC.

### **2.3.1.3 Implemented submodels**

In some cases the original model did either not provide sorption constants for a particular element or included only constants that were estimated by so-called linear free energy

relationships (LFER, further explanations can be found in /APP 05/, /DZO 90/ or /BRA 17/). To amend this situation, other submodels from the literature that were based on experimental data were included in UNiSeCs II, if possible. The species that are taken into account in sorption modelling are shown in Tab. 2.26. In some cases, the sorption of an element on a certain compartment is not relevant and has thus not been implemented (e.g. Cs<sup>+</sup> on organic matter in mineral soils /RIG 02, LOF 02/).

There is no model for sorption of anions on OM in the literature.

**Tab. 2.26** Species for which sorption submodels have been implemented in the extended UNiSeCs model

Compartment Element	Illite Bradbury and Bae- yens (2009,2017)	hydrous oxides Dzombak and Morel (1990)	organic matter Tipping (2011) Stockdale (2011)
Americium	Am <sup>3+</sup>	Am <sup>3+</sup> /ZAV 04/	Am <sup>3+</sup> Am(OH) <sup>2+</sup>
Plutonium	Pu <sup>4+</sup> Pu <sup>3+</sup> PuO <sub>2</sub> <sup>+</sup> /BAN 16/	PuO <sub>2</sub> <sup>+</sup> Pu <sup>4+</sup> /ZAV 04/	Pu <sup>4+</sup> Pu(OH) <sup>3+</sup> PuO <sub>2</sub> <sup>2+</sup> PuO <sub>2</sub> (OH) <sup>+</sup>
Uranium	UO <sub>2</sub> <sup>2+</sup>	UO <sub>2</sub> <sup>2+</sup> /MAH 09/ <sup>2</sup>	UO <sub>2</sub> <sup>2+</sup> UO <sub>2</sub> (OH) <sup>+</sup>
Nickel	Ni <sup>2+</sup>	Ni <sup>2+</sup>	Ni <sup>2+</sup> Ni(OH) <sup>+</sup>
Radium	Ra <sup>2+</sup> #	Ra <sup>2+</sup> /SAJ 14/	Ra <sup>2+</sup> # Ra(OH) <sup>+</sup> #
Cesium	Cs <sup>+</sup>	-	-
Technetium	-	TcO <sub>4</sub> <sup>-</sup> § Hormann, Trans-LARA Project	Tc(OH) <sub>2</sub> TcOOH <sup>+</sup> /BOG 11/
Selenium	SeO <sub>3</sub> <sup>2-</sup> /MIS 09/	SeO <sub>3</sub> <sup>2-</sup> , SeO <sub>4</sub> <sup>2-</sup> , (Se <sup>2-</sup> ) §	-
competing ions <sup>1</sup>	Na <sup>+</sup> , K <sup>+</sup> , Ca <sup>2+</sup> , Mg <sup>2+</sup> , Fe <sup>2+</sup> §	Ca <sup>2+</sup> , Fe <sup>2+</sup> , PO <sub>4</sub> <sup>3-</sup> , SO <sub>4</sub> <sup>2-</sup> , CO <sub>3</sub> <sup>2-</sup>	Fe <sup>2+</sup> , Fe <sup>3+</sup> , Al <sup>3+</sup> , Mg <sup>2+</sup> , Ca <sup>2+</sup> and first hydrolysis products

§ Estimated by linear free energy relationships (LFER)

# estimated; values for Ba/Sr used

<sup>1</sup> not in the submodels of /MIS 09/, /ZAV 04/ and /BOG 11/

<sup>2</sup> including two U-carbonate complexes

#### 2.3.1.4 Model validation

The model has been validated for Am, Pu, Se, Ni, U, Ra and Cs using batch experiment data from the literature. For Tc, no appropriate data could be found. The validation for Am, Pu and Se including the modeling procedure has been described in a recent publication /HOR 21b/ and is thus not shown here.

The Cs data are from /GIL 08/, using a selection of 20 soils with clay percentages between 10 and 50 % and  $C_{org}$  contents below 10 %. In 3 cases, the relative deviation of the simulations from the experimental data are higher than a factor of 2.6 (see Fig. 2.31), increasing the average deviation from the experimental values to a factor of 2.0). In two of these cases, the soils had a combination of high Na concentrations in solution and high  $C_{org}$  as well as calcite contents.

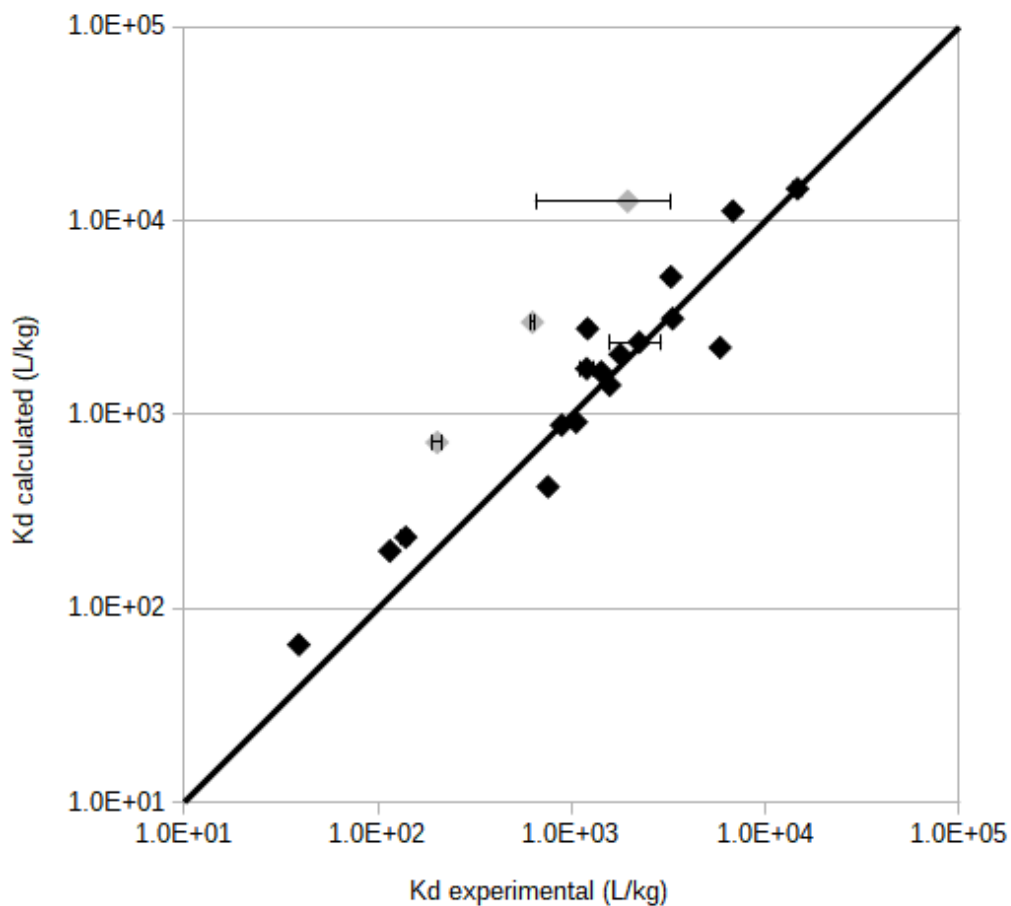


**Fig. 2.31** Simulations vs. experimental data for Cs from /GIL 08/

grey: relative deviations > 2.6

For Ni, the validation was carried out with the data from /STA 04/, with a selection of 10 soils. In this case, the hydrous oxide content was not given and had to be estimated using the data from Refesol 01A. Moreover, also the concentration of Ni in the pre-equilibration solution had to be estimated. As is summarised in /RIN 17/, “concentrations of Ni in natural solutions of surface horizons of different soils vary from 3 to 150  $\mu\text{g L}^{-1}$ , depending on soil types”. We only present here the simulations for the minimum concentration and the geometric mean of the values given above (experimental uncertainties were not given). In both cases, the model tends to overestimate  $K_d$  (see Fig. 2.32); however, using the geometric mean, the deviation from the experimental values is only in three cases higher than a factor of 2 (increasing the average deviation to a factor of 2.5). Moreover, the calculated values may be even lower if low concentrations of cyanide are taken into account, as briefly discussed in chapter 2.3.2.4.

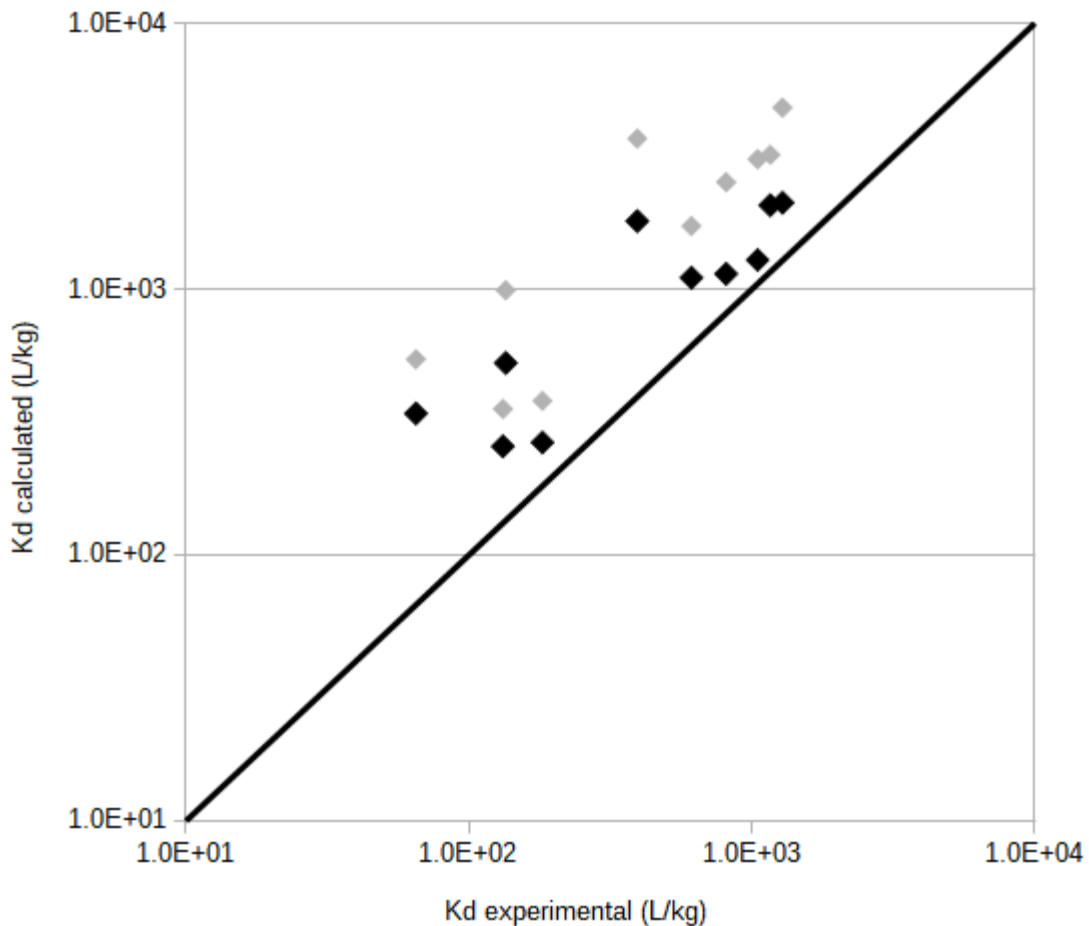


**Fig. 2.32** Simulations vs. experimental data for Ni from /STA 04/  
 Ni concentration at pre-equilibration: grey 0.003  $\text{mg L}^{-1}$ ; black 0.02  $\text{mg L}^{-1}$ .

The validation for Ra was difficult as already pointed out in /URS 19/; the experiment had been carried out using fertilisers after contamination with Ra and most of the  $K_d$  could be explained by coprecipitation with barium sulphate (Ba probably introduced as Ba-phosphate by fertilization). A re-evaluation of the simulations using the data of /VAN 07a/ shows (Fig. 2.33) that only in three cases, sorption was relevant under these assumptions. Taking both processes into account, the deviations of the simulations from the experimental values were in no case larger than 3, with an average of a factor 1.7.

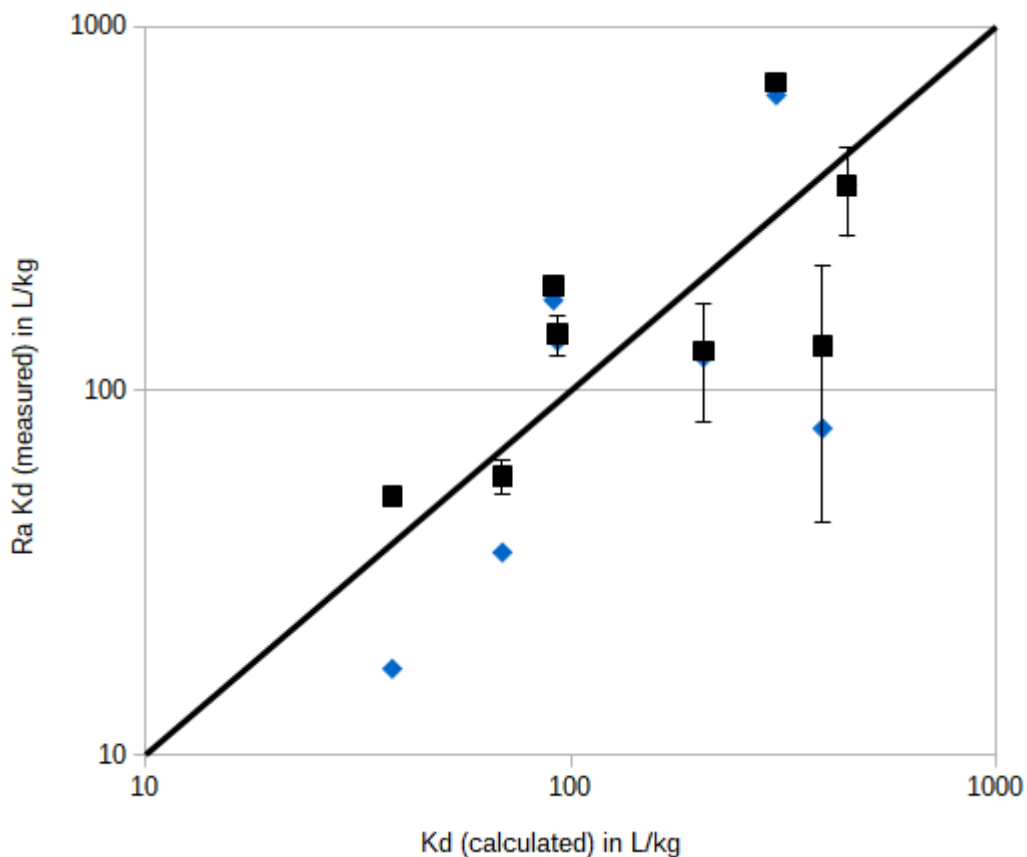


**Fig. 2.33** Simulations vs. experimental data for Ra from /VAN 07a/

blue diamonds: calculations without sorption

Also the U data from /VAN 07b/ (as used in /HOR 12/) have been re-evaluated to validate UNiSeCs II. In all simulations except for the three soils with the highest pH values (> 6.9) depicted in grey in Fig. 2.34, Becquerelite ( $\text{Ca}(\text{UO}_2)_6\text{O}_4(\text{OH})_6 \cdot 8\text{H}_2\text{O}$ ) has been allowed to precipitate in the contaminated solution because the soil had been fertilised after contamination. Here the average deviation of the simulation from the experimental values is by a factor of 1.5 (highest value 2.3).

In summary, the capability of UNiSeCs II predicting results of batch experiments is satisfactory and therefore its use for predicting  $K_d$  values in the field should be applicable. Of course, it is still desirable to further validate the model, preferably with data from the field.

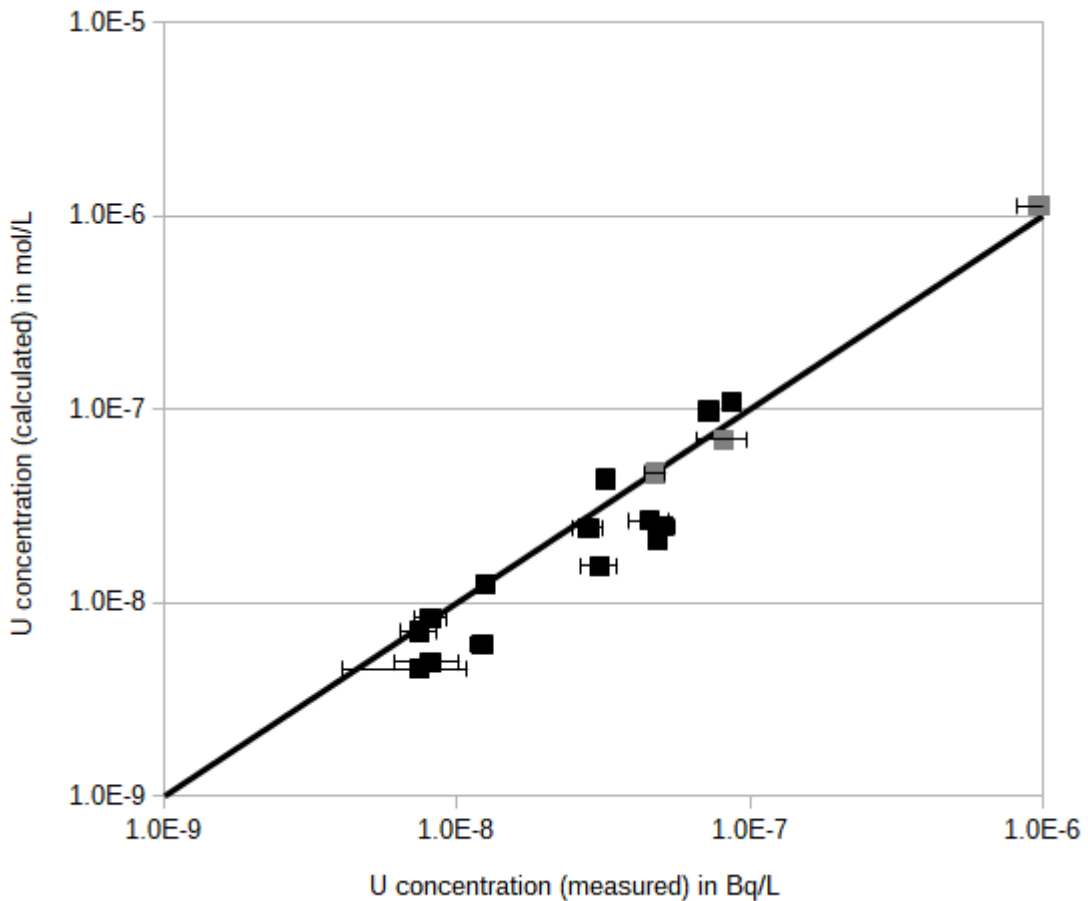


**Fig. 2.34** Simulations vs. experimental data for U from /VAN 07b/

grey: calculations without Becquerelite precipitation in the contaminated solution. Note that in this case, concentrations in solution are given.

### 2.3.2 Calculation of $K_d$ values for two Refesols

In this section,  $K_d$  values are calculated for two Refesols for a defined set of soil solution parameters, approximating conditions that are frequently occurring in soils (“standard conditions”).

### 2.3.2.1 Refesol properties

$K_d$  values were calculated for the Refesols 01A and 03G. These two soils were chosen because they have different sorptive properties. The characteristics listed in Tab. 2.27 are based on the analysis from the IME laboratories (Fraunhofer Institute for Molecular-biology and Applied Ecology, K. Weinfurter) and the results from the analysis for CEC and oxalate extractable hydrous oxides performed at FSU Jena prior to the lysimeter experiments carried out within the Trans-LARA project.

**Tab. 2.27** Characteristics of the two Refesols as far as relevant for PHREEQC modeling (ox = oxalate extractable hydrous oxides)

Refesol Property	01A	03G
Clay %	6.1	24.8
CEC in meq/kg	31.4	153.7
field capacity in g/100g	29.3	73.4
organic C %	0.93	3.01
Fe <sub>ox</sub> in g kg <sup>-1</sup>	1.73	5.48
Al <sub>ox</sub> in g kg <sup>-1</sup>	1.05	2.27
Mn <sub>ox</sub> in g kg <sup>-1</sup>	0.36	0.60
pH (CaCl <sub>2</sub> )	5.6	6.0

Refesol 03G (silty loam) has substantially higher amounts of clay, hydrous oxides and organic C than Refesol 01A (slightly loamy sand). Thus it is to be expected that also the calculated distribution coefficients will be significantly higher.

### 2.3.2.2 Definition of standard conditions

For the simulations, physicochemical conditions were defined that characterise a German average soil in the vegetation period. The temperature was assumed to be 15°C and the soils were taken to be at field capacity. For the soil solution composition, the geometric means of the ranges of “frequently occurring” ion concentrations (Tab. 5.1-2 in /BLU 16/) were chosen, assuming log-normal distributions of the respective populations. The concentrations of Fe and Al, two important competing ions for sorption, were estimated by equilibrating the soil solution with Goethite and Gibbsite, respectively. For inorganic C, a partial CO<sub>2</sub> pressure of 10<sup>-2.0</sup> atm was assumed, a value that is common

in middle European soils /APP 05/. For the redox state, a pe of 10 (Eh = 590 mV) was chosen, a value that is typical for partially saturated soils around a pH of 6 (see Fig. 2.35). The soils are also assumed to be fertilised, which leads to high P concentrations in solution (3.2 mg/L vs.  $\leq 0.1$  mg/L in unfertilised soils).

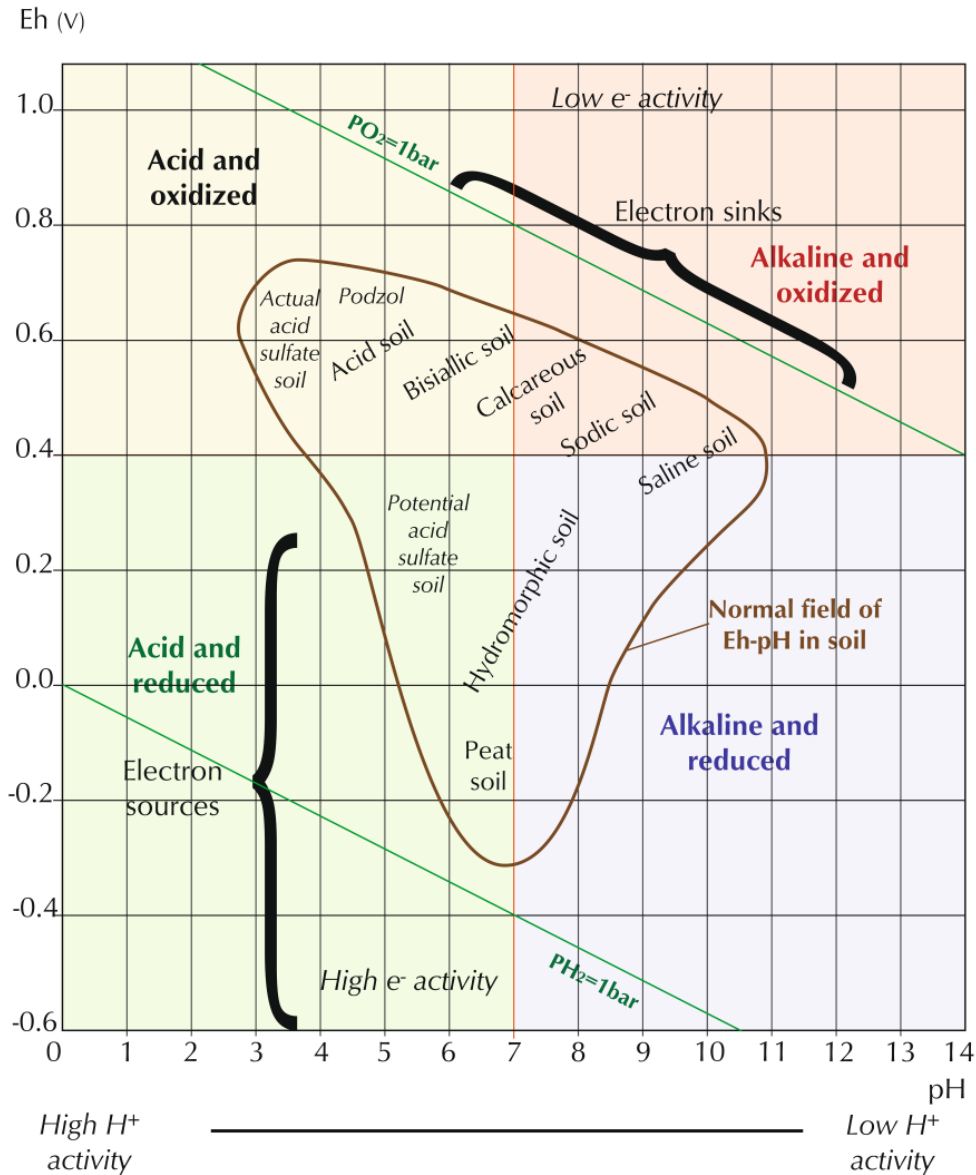


**Fig. 2.35** Normal ranges of Eh-pH in soil (from /HUS 13/)

### 2.3.2.3 Modeling assumptions for $K_d$ calculations under field conditions

For modeling the radionuclide partitioning, it is assumed that the contamination does not change the macroionic composition of the soil solution. Thus, the solution that is taken for pre-equilibration is also used for the advection step, with the modification that is

introduced by adding a trace amount of contaminant. The respective concentrations are calculated from the “proposed maximum concentrations” in mol m<sup>-3</sup> listed in Tab. 2.6 of /NOS 12/. In the case of Ni and Se, the soil solution contains estimated background values for the respective stable nuclides. In the case of Ni, a value of 2 µg L<sup>-1</sup> has been found /DUI 08/; this value has been used in the sensitivity and matrix calculations. However, values between 3 and 150 µg L<sup>-1</sup> are also given in the literature /RIN 17/. For Se, no background value for soil is given in the literature. However, an appropriate approximation may be the “Nationaler Basiswert” for groundwater (90 % percentile), which is reported to be 1.26 µg L<sup>-1</sup> /BLA 15/. Both concentrations are larger than the values given in /NOS 12/ and are therefore used for modeling, assuming isotopic equilibrium after contamination for both elements. In cases where the saturation index for a solid radionuclide mineral phase exceeds zero, it is assumed that the phase stays in solution as a colloid due to the low radionuclide concentration and thus does not change the distribution coefficient.

#### **2.3.2.4 K<sub>d</sub>-values under standard conditions**

Using the standard conditions and the assumptions described in the two previous sections, distribution coefficients have been calculated for Am, Pu, Ni, Tc, Se, Cs, Ra and U. In Tab. 2.28 and Tab. 2.29, the calculated K<sub>d</sub> values (called “standard” K<sub>d</sub> values in the following sections) are compared to the respective ranges given in the IAEA Technical report 472 /IAE 10/ for sand and loam. However, it has to be pointed out that the IAEA values are mostly derived from batch experiments that were often not carried out following a normed procedure (using different solid/liquid ratios and contaminant solutions). For Am, Pu, U, Cs and Ni (Refesol 01A), the results of the simulations are lying well within the ranges given by the IAEA.

**Tab. 2.28** Calculated distribution coefficients for Refesol 01A under the standard conditions defined in chapter 2.3.2.2

For comparison, the experimental ranges and geometric means for sandy soils from /IAE 10/ are given in the right three columns. \* including Tc in the diffuse layer; \*\* no fertilization

Kd in (L kg <sup>-1</sup> ) Element	calculated, Refesol01A	values from IAEA Tecdoc 1616 (sand)		
	standard conditions	minimum	geometric mean	maximum
Americium	1500	67	1000	37000
Caesium	5000	10	530	35000
Nickel	310	3	130	7200
Plutonium	350	33	400	6900
Radium	18	49	3100	40000
Selenium	6 (90)**	4	56	1600
Technetium	0.0002 (0.04)*	0.01	0.04	0.1
Uranium	540	0.7	110	67000

**Tab. 2.29** Calculated distribution coefficients for Refesol 03G under the standard conditions defined in chapter 2.3.2.2

For comparison, the experimental ranges and geometric means for loamy soils from /IAE 10/ are given in the right three columns. \* including Tc in the diffuse layer; \*\* no fertilization

Kd in (L kg <sup>-1</sup> ) Element	calculated, Refesol 03G	values from IAEA Tecdoc 1616 (loam)		
	standard conditions	minimum	geometric mean	maximum
Americium	5800	50	4200	48000
Caesium	8500	39	3500	55000
Nickel	1700	7.0	180	1200
Plutonium	1700	100	950	9600
Radium	73	12	1100	120000
Selenium	6 (220)**	12	220	1600
Technetium	0.0005 (0.09)*	0.01	0.07	0.09
Uranium	2000	0.9	310	39000

For Ra, the model may underestimate sorption on soil particles, which has already been pointed out in /URS 19/. The reason is probably the use of the complexation constants for Barium for the sorption on humic substances. However, simulation of extraction with pure water in a batch experiment (solid/liquid ratio 1:10) leads to considerably higher K<sub>d</sub> values (510 L kg<sup>-1</sup> for Refesol01A and 1300 L kg<sup>-1</sup> for Refesol 03G).

For Se, the distribution coefficients also seem to be comparatively low. If we assume that the soil is not fertilised with P, setting the concentration to  $0.1 \text{ mg L}^{-1}$  (which is the highest P concentration in unfertilised soils /BLU 16/), the calculations for otherwise standard conditions lead to values close to the geometric mean of the IAEA values.

The Tc values are both very small in the experiments. The simulations usually only take into account the sorbed species and not the species present in the diffuse layer because the latter do not contribute significantly to the solid-liquid distribution. This has been verified by tentatively including these species in the simulations for Ra, Ni, U and Se. For Tc however, this contribution is significant as can be seen in the respective table entries. The diffuse layer calculation is carried out using the –donnan option in PHREEQC and is limited to the HO surface (for Tc, all other models are non-electrostatic). This option will be applied in all forthcoming calculations involving Tc.

For Ni, the model overestimates the  $K_d$  in Refesol 03G, which has higher amounts of clay (24.8 %) and IOM (3 %). This is possibly caused by complexants in solution that have not been taken into account in the simulation. Cyanide, for instance, is often present in trace amounts soil due to natural as well as artificial sources /BLU 16/; however, background values for soil solution could not be found anywhere. In seepage water from soil to groundwater, the trigger value (“Prüfwert”) is  $10 \text{ } \mu\text{g L}^{-1}$  /BBO 99/. Simulations with a concentration of  $3 \text{ } \mu\text{g L}^{-1}$  yield  $K_d$  values that are reduced by a factor of about 2.5.

In general, the UNiSeCs II model yields plausible estimations of the  $K_d$  under field conditions for the radionuclides considered in this study.

### **2.3.3 Sensitivity analysis**

Following the definition of standard conditions in the field and testing model plausibility, the sensitivities of the distribution coefficients with regard to the most important soil solution parameters (Tab. 2.30) are analyzed for both Refesols.

#### **2.3.3.1 Solution parameters and parameter ranges**

Apart from pH (and  $p_e$  in case of the importance of redox processes), the most significant parameters that may determine the  $K_d$  are the major cations and anions, because they may either compete for binding sites or act as complexants keeping the radionuclide in solution. For most nuclides, DOM is also important because it usually binds

comparatively large amounts of cations. Fe- and Al cations are both important competitors for complexation, both in solution and on surfaces. However, as their concentration is in first approximation governed by the dissolution of Goethite and Gibbsite respectively, their concentrations are not treated as variables here. Moreover, the experimentally determined concentrations of the free ions of these metals are almost always masked by species that are present as mineral colloids or already bound to DOM in solution. Thus, suitable concentration ranges of free and complexed Fe and Al in solution are not available. However, these quantities will vary with other soil solution parameters, e.g. the dissolution of Fe from Goethite is pH dependent.

Since reactions in solution and on surfaces are temperature dependent, it is to be expected that this is also the case for the distribution coefficients. Unfortunately, the temperature dependences of the intrinsic surface complexation constants cannot be calculated via the van't Hoff equation, because the surface reaction enthalpies are not available. Therefore, it is not reasonable to vary the temperature by using the PHREEQC *temp* parameter, because the results will lead to misconceptions unless the temperature dependence of the intrinsic complexation constants is small.

**Tab. 2.30** Ranges of parameter values used in the sensitivity analysis

\* Cs and Ni, \*\* Cs

Parameter	(concentrations in mg L <sup>-1</sup> )		
	minimum	geometric mean	maximum
pH	4.8	-	8.2
pe	2	-	13
Ca	40	80	160
Mg	5.0	11	25
Na **	2.0	6.3	20
K **	3.0	9.5	30
Mn	0.0	0.027	0.7
NH <sub>4</sub> <sup>+</sup> *	0.20	0.89	4.0
Sulfate	10	35	120
Phosphate	1.0	3.2	10
Nitrate	20	63	200
pCO <sub>2</sub>	-2.5	-	-1.5
DOC	15	28	50

The values for pH, anions, cations and DOC are taken from Tab. 5.2 of /BLU 16/, using the column “frequently occurring values” for agricultural soils. The pH values are measured in soil solution and the range is extended to the whole interval. The pe was assumed to range from 13 (Eh  $\approx$  770 mV, well aerated) to 2 (Eh  $\approx$  120 mV, temporarily waterlogged), see also Fig. 2.35. To better estimate the carbonate content of the soil solution, it is calculated by setting the solution in equilibrium with a certain CO<sub>2</sub> pressure (average: pCO<sub>2</sub> = -2.0, see definition of standard conditions). This will take into account changes of carbonate content with respect to other soil parameters. pCO<sub>2</sub> is varied between -1.5 and -2.5, which is approximately the range of frequently occurring values according to Fig. 5.12 in /APP 05/. The parameter ranges used here are shown in Tab. 2.30.

### 2.3.3.2 Single Parameter Variations

For each element and respective soil, single parameter variations have been performed. In order to maintain charge balance, virtual charged species have been introduced. These species are chemically inert and do not react with solid surfaces although they may accumulate in the diffuse layer.

In the case of pH, PHREEQC predicts a precipitation of calcite in the slightly alkaline region (pH  $\geq$  7.5). This will have effects on K<sub>d</sub>, because a lower concentration of complexing carbonate will keep less cations in solution and competition by Ca<sup>2+</sup> ions decreases also. However, it is known that in soils, Ca<sup>2+</sup> is frequently supersaturated with respect to calcite /MCB 90, SUA 92/. A corresponding saturation index (SI) can be estimated by the IAP (ionic activity product) data given in /SUA 92/ and the solubility product (K<sub>s</sub>) for Calcite given in the data base using the relation  $SI = \log(IAP/K_s)$ . Corrected for temperature, SI  $\approx$  0.25 has been calculated and is used in the calculations.

In Tab. 2.31 and Tab. 2.32 the K<sub>d</sub> value ranges calculated for the respective parameter ranges from Tab. 2.30 are shown for each nuclide. Only significant parameters, where the ratio R between the maximum and minimum K<sub>d</sub> is  $\geq$  1.4 for at least one soil are taken into account. These are candidates to be chosen in the calculation of the respective K<sub>d</sub> matrices (Sect. 2.3.4.1). The last column gives information about the correlation between K<sub>d</sub> and parameter. The ratios of the maximum and minimum K<sub>d</sub> values (M values) in the respective parameter range are almost the same for the two refesols with a tendency to slightly higher values for Refesol 01A, probably because of higher competition effects due to the generally lower amount of surface sites.

**Tab. 2.31** The most significant parameters for Am, Cs, Ni and Pu

$$M = K_d \text{ max} / K_d \text{ min}$$

Parameter (mg/L) <sup>1</sup>	Refesol 01 A			Refesol 03 G			correlation
	K <sub>d</sub> min (L kg <sup>-1</sup> )	K <sub>d</sub> max (L kg <sup>-1</sup> )	M	K <sub>d</sub> min (L kg <sup>-1</sup> )	K <sub>d</sub> max (L kg <sup>-1</sup> )	M	
	<b>Americium</b>						
DOC	7.96e+02	2.65e+03	3.3	3.04e+03	1.01e+04	3.3	negative
pH	1.00e+03	3.43e+03	3.4	3.39e+03	1.04e+04	3.1	local maximum at pH 7.2
	<b>Cesium</b>						
Ammonium	2.12e+03	1.01e+04	4.8	3.58e+03	1.72e+04	4.8	negative
K	2.85e+03	7.94e+03	2.8	4.84e+03	1.34e+04	2.8	negative
pH	5.00e+03	1.05e+04	2.1	8.49e+03	2.01e+04	2.4	constant, positive at pH > 7.6
	<b>Nickel</b>						
Cyanide	3.07e+00	3.11e+02	100	1.89e+01	1.65e+03	87	negative
pH	5.19e+01	1.53e+03	29	1.93e+02	4.89e+03	25	positive
Mn	1.76e+02	3.24e+02	1.8	7.86e+02	1.76e+03	2.2	negative
DOC	2.60e+02	3.48e+02	1.3	1.27e+03	1.92e+03	1.5	negative
Ca	2.52e+02	3.59e+02	1.4	1.39e+03	1.86e+03	1.3	negative
pe	2.22e+02	3.11e+02	1.4	1.26e+03	1.65e+03	1.3	positive pe 5 - 13: ~ constant
	<b>Plutonium</b>						
pH	1.43e+02	5.84e+03	41	5.02e+02	2.50e+04	50	maximum at pH 7.1
DOC	1.91e+02	6.30e+02	3.3	8.95e+02	2.94e+03	3.3	negative
pe	2.20e+02	5.27e+02	2.4	1.05e+03	2.33e+03	2.2	plateau at pe 5 - 11
Ca	3.27e+02	3.99e+02	1.2	1.51e+03	2.15e+03	1.4	positive

**Tab. 2.32** The most significant parameters for Ra, Se, Tc and U

M =  $K_d \text{ max} / K_d \text{ min}$ , M values marked >> are larger than 100

Parameter (mg L <sup>-1</sup> ) <sup>1</sup>	Refesol 01 A			Refesol 03 G			correlation
	Kd min (L kg <sup>-1</sup> )	Kd max (L kg <sup>-1</sup> )	M	Kd min (L kg <sup>-1</sup> )	Kd max (L kg <sup>-1</sup> )	M	
<sup>1</sup> except pH and pe							
	<b>Radium</b>						
pH	5.97e+00	2.77e+02	46	2.54e+01	8.47e+02	33	positive
Ca	1.03e+01	2.78e+01	2.7	6.49e+01	1.22e+02	1.9	negative
Phosphate	1.19e+01	1.85e+01	1.6	5.59e+01	7.32e+01	1.3	positive
	<b>Selenium</b>						
pe	< 1.0e-04	7.37e+00	>>	< 1.0e-03	2.76e+01	>>	plateau at pe 4 - 9
pH	< 1.0e-03	7.45e+00	>>	< 2.0e-03	3.04e+01	>>	negative
Phosphate 0.0 mg/L :	5.18e+00	8.79e+00	1.7	5.02e+00	7.89e+00	1.6	negative
		8.98e+02	>>		5.85e+02	>>	
	<b>Technetium</b>						
pe	3.83e-02	3.96e+03	>>	8.55e-02	1.08e+04	>>	negative, pe 5 - 13: constant
pH	2.67e-02	5.27e-02	2.0	6.81e-02	1.35e-01	2.0	minimum at pH ~ 7.2
DOC, pe 2	2.44e+03	6.00e+03	2.5	7.24e+03	1.47e+04	2.0	negative
Phosphate 0.0 mg/L :	3.26e-02	8.72e-02	2.7	7.37e-02	1.02e-01	1.3	negative
		1.48e-01	4.5		3.14e-01	4.3	
	<b>Uranium</b>						
pH	2.80e-01	5.67e+02	>>	8.60e-01	1.88e+03	>>	maximum at pH 6.0
DOC	3.17e+02	8.44e+02	2.7	1.07e+03	2.95e+03	2.8	negative
Phosphate 0.0 mg/L :	3.97e+02	6.07e+02	1.5	1.51e+03	2.10e+03	1.4	negative
		8.19e+02	2.1		4.70e+03	3.1	

### 2.3.3.2.1 pH

Generally, pH is one of the most important parameters because it determines the protonation and thus the sorptive surface properties. The correlation between  $K_d$  and pH largely depends on which model components determine sorption and on the interplay with available competitors and is therefore not simple to predict. For the binding of Se and Tc, protons in solution are required to generate the sorptive species and thus the correlation is negative. For cations, it will tend to be positive at low pH as the proton concentration and thus the competitive action decreases. At high pH, the situation may be different, e.g. due to increasing complexation of the radionuclide in solution with carbonate. For the example of americium, this behaviour is shown by the curve depicted by the red diamonds in Fig. 2.36.

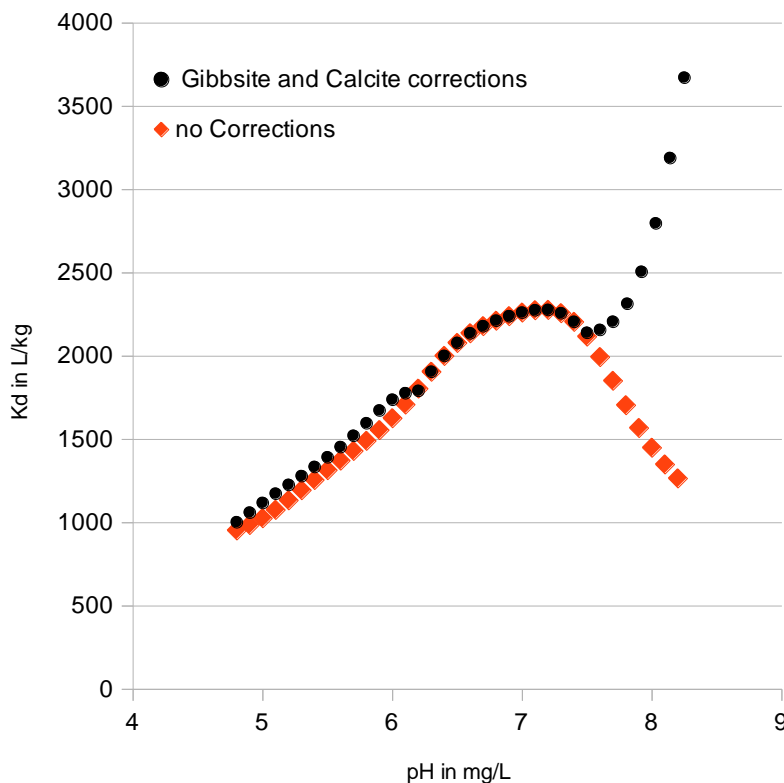


**Fig. 2.36** Calculated pH dependence of  $K_d$  for americium (Refesol 01A)

As described in /HOR 21b/, the solubility index of Gibbsite is set to -1 for pH values below 6.3 because the soil solution tends to be undersaturated with respect to Gibbsite at low pH. On the other hand, the saturation index of standard the soil solution with respect to calcite will exceed zero at higher pH and thus, the calcium concentration in solution will be limited due to precipitation. If both instances are accounted for in the simulation, the

pH dependence of the  $K_d$  is represented by the black bullets in Fig. 2.36. While the Gibbsite correction makes a comparatively small difference, the effect of Calcite precipitation is considerable. This is caused by the drastic reduction of  $\text{Ca}^{2+}$  ions; while at concentrations between 40 and 160 mg/L the variance of  $\text{Ca}^{2+}$  has little effect on the  $K_d$ , at low concentrations (ca. 12 mg/L at pH 8 after precipitation) the effects of competition become visible.

In the case of U on the other hand, the model predicts that  $K_d$  decreases with increasing pH over several orders of magnitude above pH 6.5 (see Fig. 2.37), which is primarily due to the increasing U complexation as  $\text{Ca}_2\text{UO}_2(\text{CO}_3)_3$  in solution.

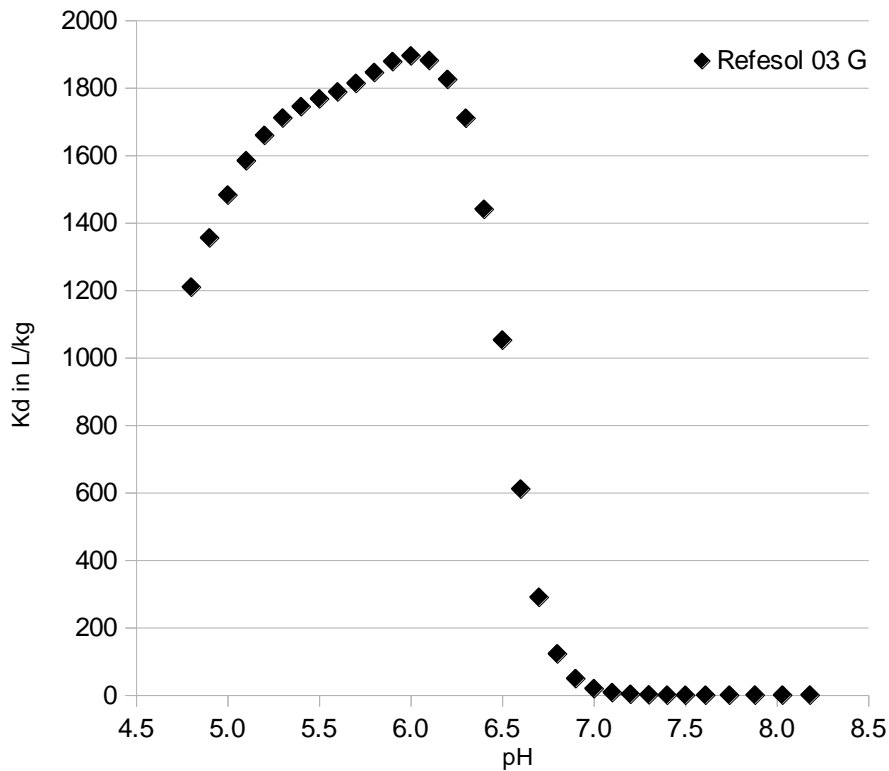


**Fig. 2.37** Calculated pH dependence of  $K_d$  for uranium (Refesol 03G)

However, in /IAE 10/, a geometric mean of  $65 \text{ L kg}^{-1}$  is reported for soils with  $\text{pH} \geq 7$  and a corresponding minimum value of  $0.9 \text{ L kg}^{-1}$ . A value of  $20 \text{ L kg}^{-1}$  for Refesol 03G at pH 7 ( $1.4 \text{ L kg}^{-1}$  at pH 7.3) predicted by the simulation points to a possible underestimation of the  $K_d$  at higher pH values.

### 2.3.3.2.2 Dissolved Organic Matter

For cations, sorption to DOM keeps more of the radionuclide in solution and thus, the  $K_d$  of cations is always negatively correlated with DOM. This effect is most pronounced for actinides like americium because of their strong affinity to organic matter (example for Am shown in Fig. 2.38). On the other hand, the effect of sorption to DOM is negligible in the case of the (weakly binding) radium.

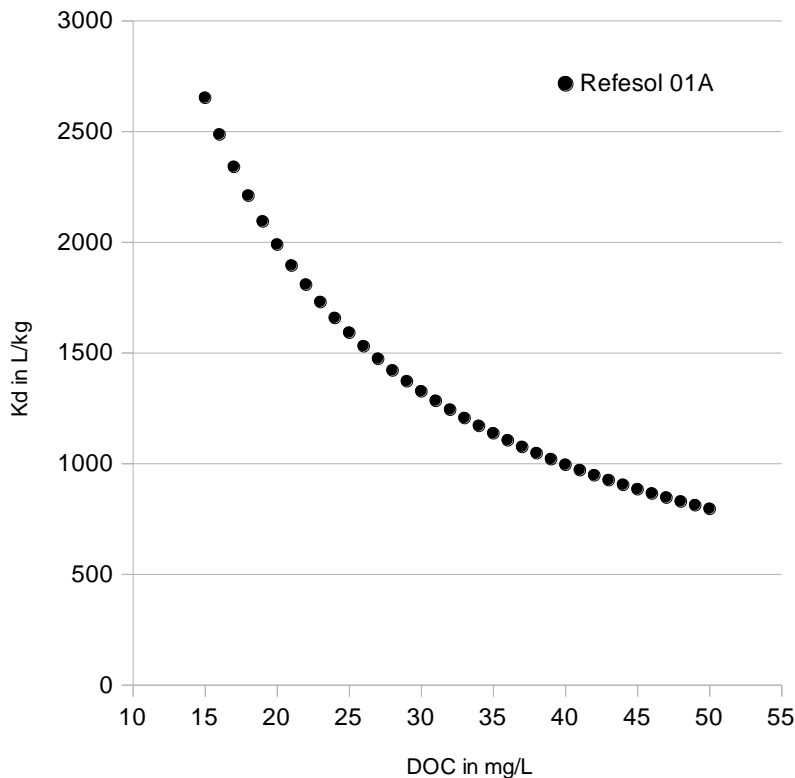


**Fig. 2.38** Calculated DOC dependence of  $K_d$  for americium (Refesol 01A)

### 2.3.3.2.3 Ammonium

Cesium is a special case because its retention is governed by the sorption on the frayed edge sites of clay. This is why the two competitors  $K^+$  and  $NH_4^+$  are most significant, as their exchange constants are larger than  $Na^+$  and  $H^+$ .  $NH_4^+$  has the highest R values, the effect of an increase in  $NH_4^+$  being strongest at low concentrations (Fig. 2.39).

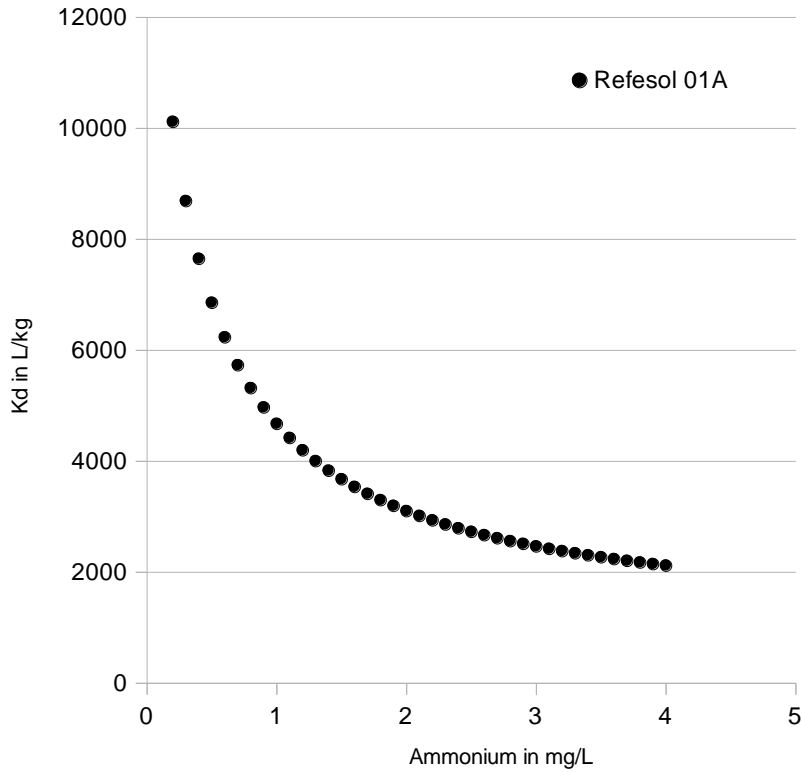


**Fig. 2.39** Calculated ammonium dependence of  $K_d$  for cesium (Refesol 01A)

#### 2.3.3.2.4 Cyanide

As pointed out in Sect. 2.3.2.4, cyanide may play an important role for the  $K_d$  estimation of Ni, due to its strong complexing properties. The effect is predicted to be even larger than that of pH, an increase of  $CN^-$  concentration from 0 to  $4 \mu g\ l^{-1}$  would lead to a  $K_d$  decrease by one order of magnitude (Fig. 2.40).

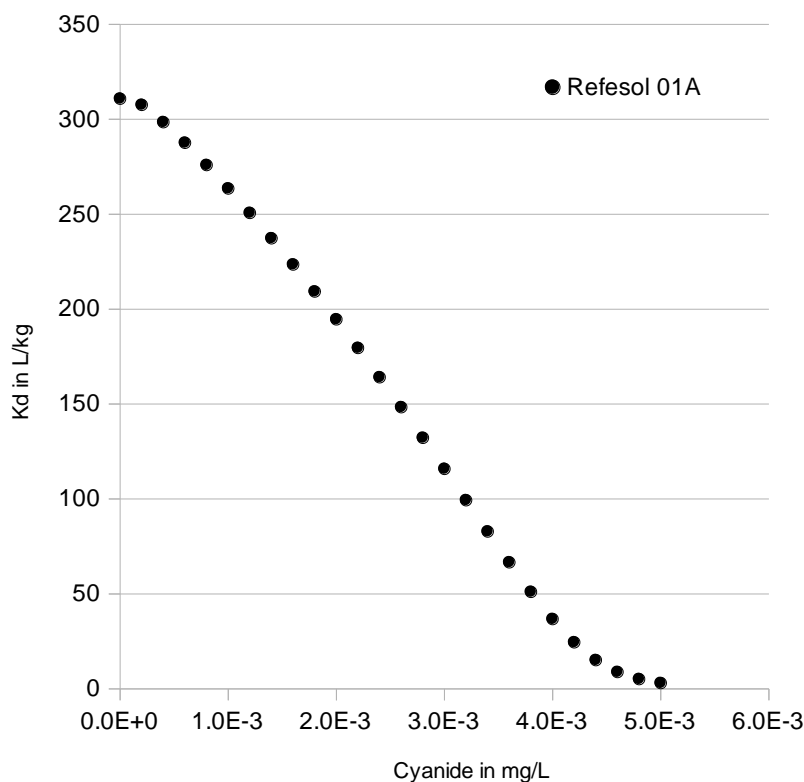


**Fig. 2.40** Calculated cyanide dependence of  $K_d$  for nickel (Refesol 01A)

Unfortunately, this has not yet been confirmed experimentally in agricultural soils; therefore, this result should be treated with caution.

### 2.3.3.2.5 Phosphate

Phosphate is also a competitor for anion sorption at hydrous oxide surfaces as well as a strong complexant of cations and its effects are most distinct at low P concentrations between 0.001 and 0.01 mg l<sup>-1</sup> (Fig. 2.41); this effect is most pronounced for selenium. This is important, because in agricultural soils, P is almost always introduced into the soil solution by fertilization and the minimum P concentration in fertilised soils is around 0.1 mg l<sup>-1</sup>. In unfertilised soils, the  $K_d$  is predicted to be up to two orders of magnitude higher.

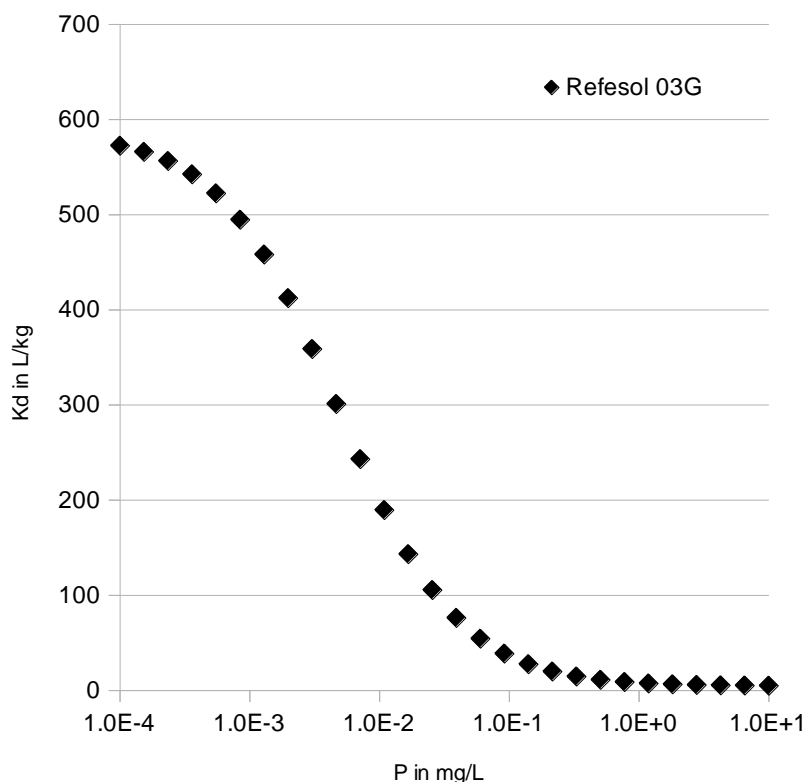


**Fig. 2.41** Calculated phosphate dependence of  $K_d$  for selenium (Refesol 03G)

### 2.3.3.2.6 Redox state

In the case of the elements Pu, Se and Tc, the redox state is very important. For Pu, the  $K_d$  generally exhibits a plateau below  $pe = 11$ , where Pu(IV) is dominant (Fig. 2.42). At very low  $pe$ , Pu(IV) is reduced to Pu(III), which is less complexed by ligands like hydroxyl ions. At higher  $pe$ , the plutonium is oxidised to Pu(V) and Pu(VI).

The plateau of the  $K_d$  for selenium shows the region where selenite is the most stable species. The range of this plateau is shifted to lower  $pe$  values with increasing pH (Fig. 2.43).

According to the Boggs model /BOG 11/, technetium is increasingly bound to organic matter below  $pe$  5 because of the formation of  $TcO(OH)_2$  and  $TcO(OH)^+$  ions. The effects of  $pe$  and pH are strongly interdependent and are shown in Fig. 2.44.

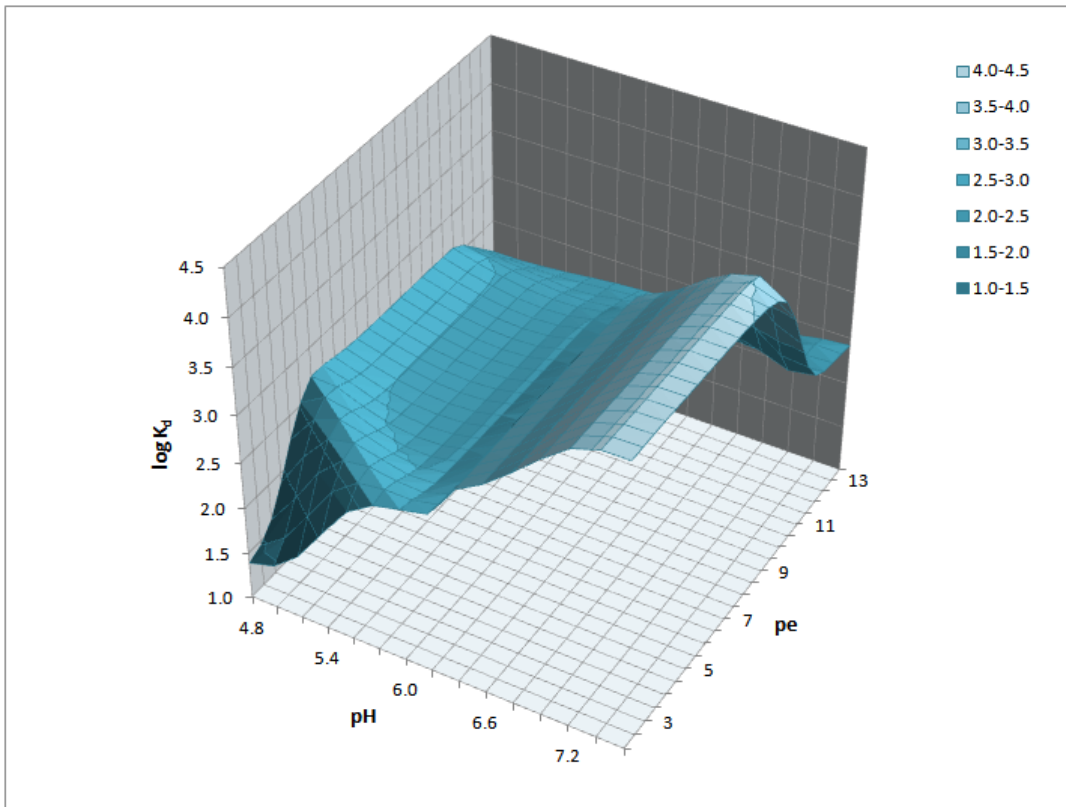


**Fig. 2.42** Dependence of  $\log K_d$  for Pu on pe and pH

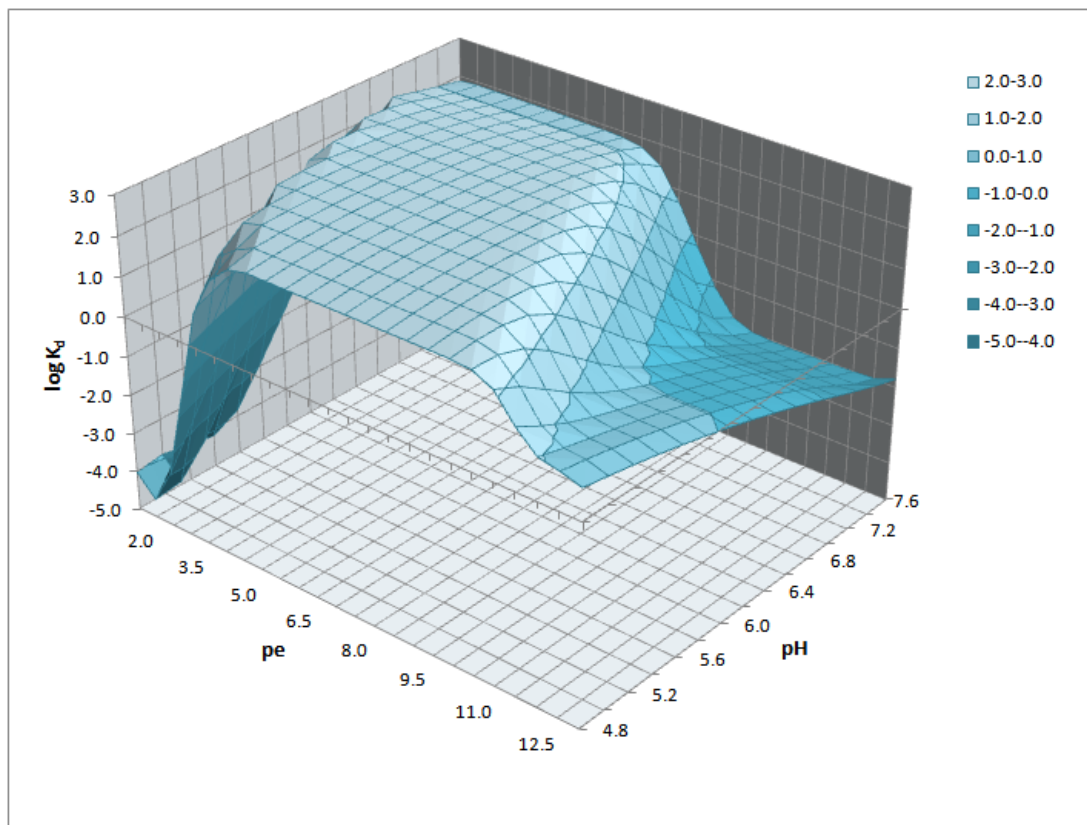


**Fig. 2.43** Dependence of  $\log K_d$  for Se on pe and pH

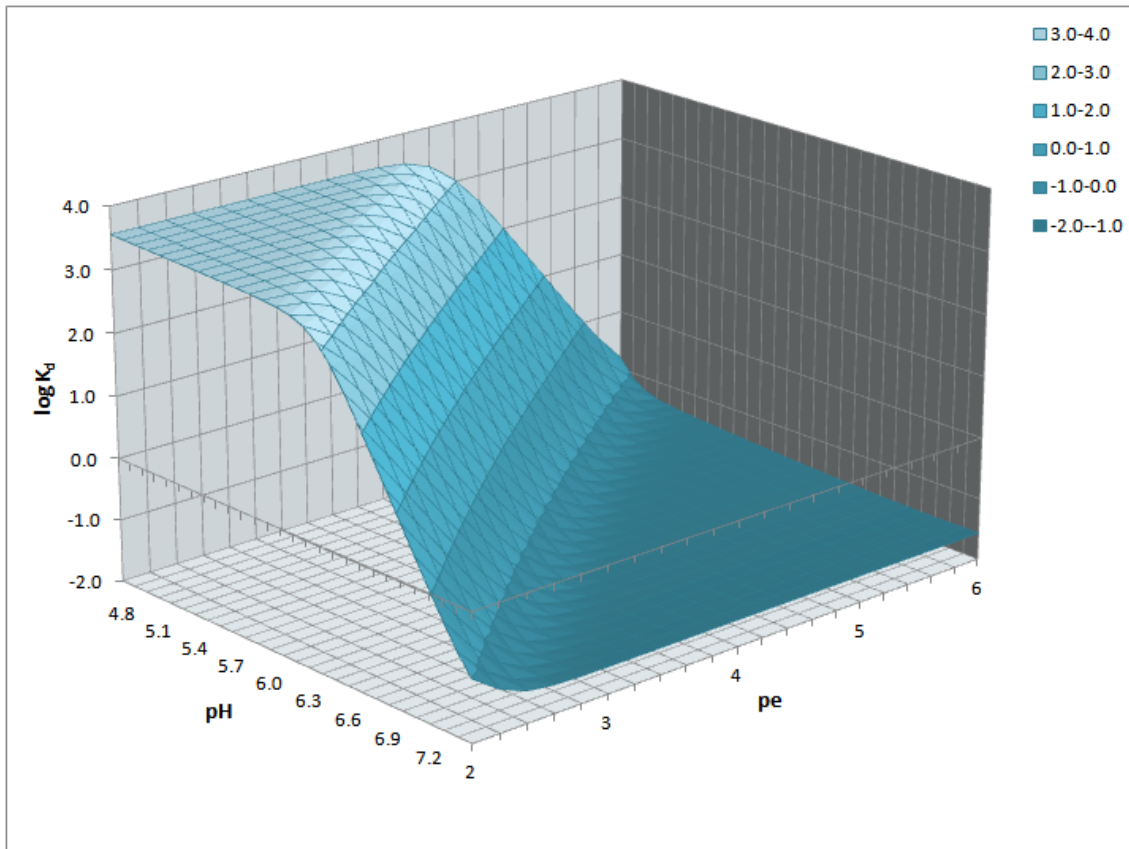


**Fig. 2.44** Dependence of  $\log K_d$  for Tc on pe and pH

### 2.3.4 Range of Variations

Having identified the most relevant soil parameters, the variability of the  $K_d$  values for every nuclide and soil occurring under typical agricultural conditions can be estimated. The ranges of the individual parameters are again taken from Tab. 2.30 used in the sensitivity analysis, with the exception of pH, where the range is 4.8...7.5. At higher pH, calcite is likely to be present in amounts where its properties as a sorbent may not be negligible. As calcite is not represented in the current UNiSeCs approach, the calculated  $K_d$  values would be less reliable and are thus omitted. Moreover, the upper pH value still exceeds the range of the “frequently occurring values” given by /BLU 16/ and in the set of the twelve Refesols /KOE 09/, the pH values of all soils are well below this limit.

In the cases where phosphate is a relevant parameter (Se, Tc, Ra, U), the simulations are also carried out in a P concentration range where the soil is not or only weakly fertilised (0.001 mg/L – 1.0 mg/L). Especially in the low P concentration range the  $K_d$

dependence is most pronounced and the results can be used to compare fertilised and unfertilised soils.

For nickel, the postulated cyanide dependence of  $K_d$  is not taken into account because there is no experimental evidence for this behaviour. Thus, the calculated values will have a tendency to be overestimated, especially for Refesol 03G (see also Tab. 2.29). The pe will also not be varied because in the case of Ni, it is largely constant in the region that is common in soils.

#### **2.3.4.1 Calculation of $K_d$ Matrices**

$K_d$  matrices are spreadsheets where the distribution coefficient is tabulated for a defined set of parameter combinations. For the estimation of  $K_d$  ranges, the spreadsheets have to be calculated for each nuclide and soil for the respective set of relevant parameters given in Tab. 2.31 and Tab. 2.32. The calculations have been performed by a batch program ("KdMultigrid", version 0.1.11, a screenshot is shown in Fig. 2.45), developed by the author within the joint project Trans-LARA. This program basically edits the input PHREEQC file in the lines where parameters have to be varied, calls PHREEQC and writes the calculated  $K_d$  into a text file, along with the varied parameters and some control variables. This process can be repeated for a defined number of combinations and step-sizes in parameter space. More details can be found in the Trans-LARA project report /HOR 21a/.

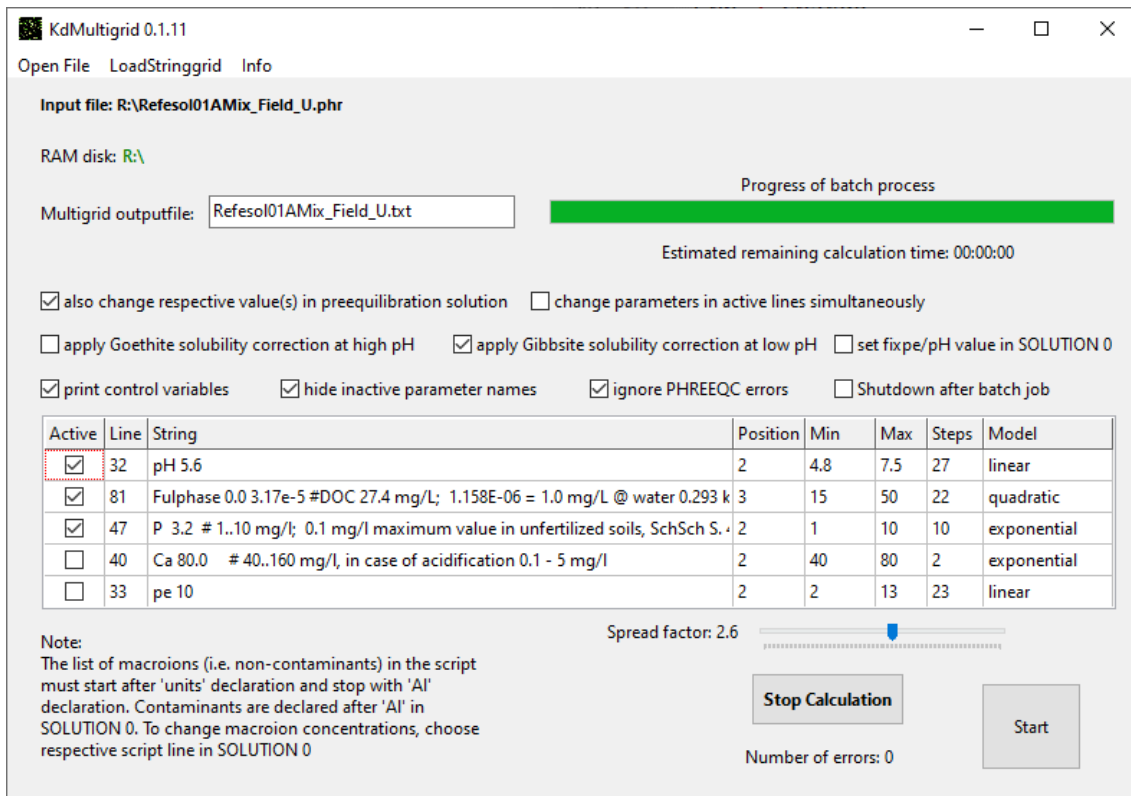


**Fig. 2.45** Screenshot of the batch program „KdMultigrad“

### 2.3.4.2 $K_d$ Ranges

The text files generated by “KdMultigrad” have been imported into Excel sheets for analysis of the maxima, minima and median values of the calculated  $K_d$  matrix. The results are shown in Tab. 2.33. The soils are assumed to be fertilised (phosphate concentrations between 1 and 10 mg/L). In cases where the sensitivity study indicates a significant dependence on phosphate concentration, also ranges for soils with no P fertilization (phosphate between 0.001 and 0.1 mg/L) are shown.

For some parameter combinations, PHREEQC could not compute equilibria for the soil solution and consequently no  $K_d$  was calculated. It is likely that these combinations are also not occurring in the field. This indicates that the remaining combinations may not be equally probable and thus the calculated median  $K_d$  may not be the most probable value for the given soil.

**Tab. 2.33** Ranges of  $K_d$  values calculated by „KdMultigrid“

low P: no phosphate fertilization (P: 0.001 mg L<sup>-1</sup> – 0.1 mg L<sup>-1</sup>), high P: phosphate fertilization (default, P: 1 mg L<sup>-1</sup> – 10 mg L<sup>-1</sup>)

soil state	Refesol 01 A			Refesol 03 G		
	$K_d$ min (L kg <sup>-1</sup> )	$K_d$ max (L kg <sup>-1</sup> )	Median (L kg <sup>-1</sup> )	$K_d$ min (L kg <sup>-1</sup> )	$K_d$ max (L kg <sup>-1</sup> )	Median (L kg <sup>-1</sup> )
	<b>Americium</b>					
	5.50E+02	4.16E+03	1.70E+03	1.78E+03	1.33E+04	5.44E+03
	<b>Cesium</b>					
	1.33E+03	1.88E+04	4.38E+03	2.10E+03	3.20E+04	7.32E+03
	<b>Nickel</b>					
	4.04E+01	1.37E+03	3.18E+02	1.50E+02	4.48E+03	1.13E+03
	<b>Plutonium</b>					
	1.15E+01	1.79E+04	4.83E+02	8.21E+01	7.54E+04	1.81E+03
	<b>Radium</b>					
low P	3.16E+00	5.16E+01	1.40E+01	1.41E+01	1.66E+02	4.95E+01
high P	3.85E+00	5.37E+01	1.60E+01	1.55E+01	1.73E+02	5.53E+01
	<b>Selenium</b>					
low P	4.66E-06	9.64E+02	6.24E+01	1.20E-05	2.44E+03	1.67E+02
high P	5.07E-08	2.05E+01	5.90E+00	1.75E-07	5.82E+01	2.27E+01
	<b>Technetium</b>					
low P	3.58E-02	8.56E+03	1.09E-01	9.14E-02	2.78E+04	2.80E-01
high P	2.33E-02	8.57E+03	3.98E-02	5.59E-02	2.78E+04	1.03E-01
high P, pe=10	2.33E-02	6.64E-02	3.13E-02	5.95E-02	1.70E-01	7.99E-02
	<b>Uranium</b>					
low P	1.63E+00	6.08E+03	5.64E+02	4.17E+00	1.58E+04	1.77E+03
high P	8.77E-02	1.04E+03	3.32E+02	2.55E-01	3.32E+03	1.06E+03

### 2.3.4.3 $K_d$ Distributions

As noted above, it is not to be expected that the  $K_d$  values in parameter space are equally distributed between the minimum and maximum values shown in Tab. 2.33. Although the parameter combinations may not all be equally probable, the “density” of values over the whole  $K_d$  interval may reveal further information. Thus, these (normalised) densities have been calculated for each element and Refesol 01A. The results are shown in the following histograms (the results for Refesol 03G are similar). Note that the  $K_d$  scale is

logarithmic and that it is adapted to the respective ranges for better readability. The vertical red line shows the approximate position of the calculated “standard”  $K_d$  (as defined in Kap. 2.3.2.4) shown in Tab. 2.28. The distributions are not smooth which is mainly due to the limited resolution of the  $K_d$  matrices.

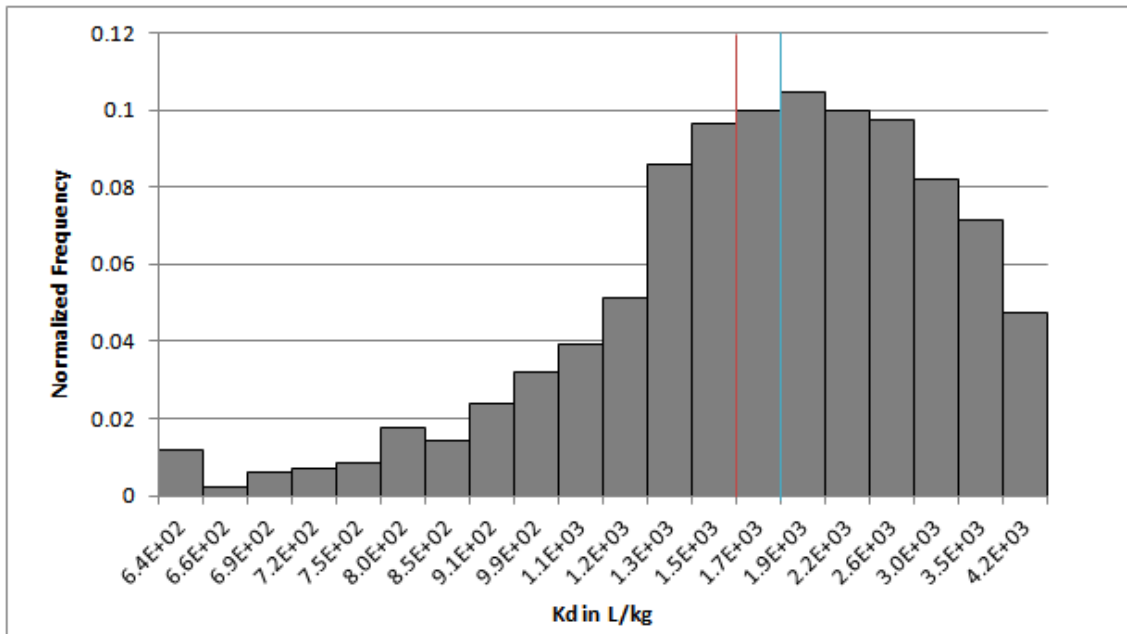


**Fig. 2.46**  $K_d$  distribution of Am for Refesol 01A

$K_d$  given in logarithmic scale; red line: approximate position of the „standard“  $K_d$ ; blue line: approximate position of the median  $K_d$ .

The  $K_d$  range for Am is comparatively small; within this range, the distribution is broad and its maximum is close to the geometric mean ( $1500 \text{ L kg}^{-1}$ ) of the maximum and minimum value which coincides with the “standard” value (Fig. 2.46). The median value of the distribution is slightly higher ( $1700 \text{ L kg}^{-1}$ ). The minimum  $K_d$  values tend to occur at high pH and high DOC concentrations, while the opposite applies to the upper  $K_d$  range.

The situation is similar for Cs, where the maximum of the  $K_d$  distribution is very close to the “standard” value, which is  $5000 \text{ L kg}^{-1}$  (Fig. 2.47). The median value is slightly lower ( $4400 \text{ L kg}^{-1}$ ). As expected, the  $K_d$  is lowest when the ammonium and potassium concentrations are high and vice versa.

The median  $K_d$  for Ni is  $310 \text{ L kg}^{-1}$ , almost equal to the “standard”  $K_d$  ( $320 \text{ L kg}^{-1}$ ), and in the lower range of the  $K_d$  interval (Fig. 2.48). The lowest values occur in cases where DOC and Ca levels are high but pH is low; DOM keeps Ni in solution by complexation and Ca acts as a competitor for sorption to soil solids.

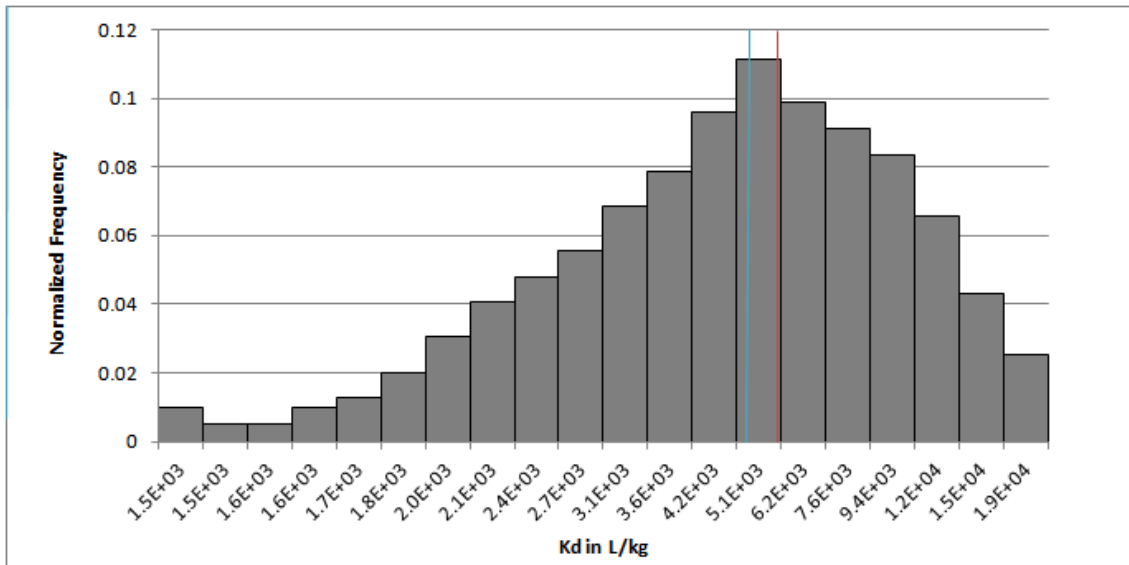


**Fig. 2.47**  $K_d$  distribution of Cs for Refesol 01A

$K_d$  given in logarithmic scale; red line: approximate position of the „standard“  $K_d$ ; blue line: approximate position of the median  $K_d$ .

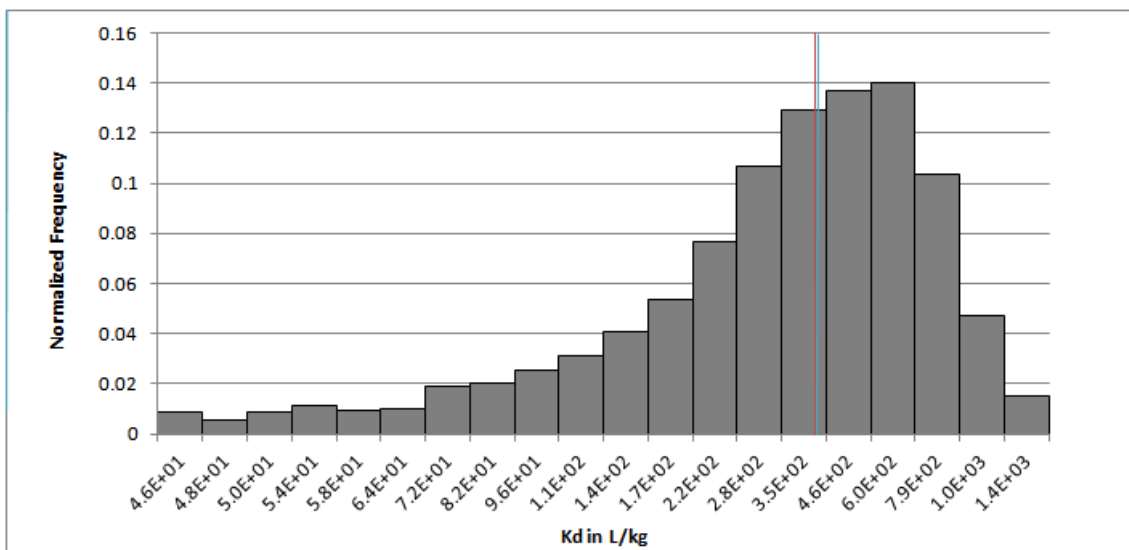


**Fig. 2.48**  $K_d$  distribution of Ni for Refesol 01A

$K_d$  given in logarithmic scale; red line: approximate position of the „standard“  $K_d$ ; blue line: approximate position of the median  $K_d$ .

The distribution for Pu is sharper compared to its range (Fig. 2.49); the maximum values occur in cases where pH is high (low competition by protons) and the DOC concentrations are low (low complexation by DOM in solution). The median value

(480 L kg<sup>-1</sup>) of the distribution is higher than the “standard” value (350 L kg<sup>-1</sup>), but both are in the low range of the interval.

Two regions contribute to this behaviour (see also Fig. 2.42):

- combinations of lower redox voltages with lower pH, where the mobile Pu(III) is prevalent
- pe values > 11, where the Pu(V) and Pu(VI) species dominate, which also have lower affinities to solid surfaces in comparison to Pu(IV)

The redox behaviour of Pu has already been described in chapter 2.3.3.2.6.

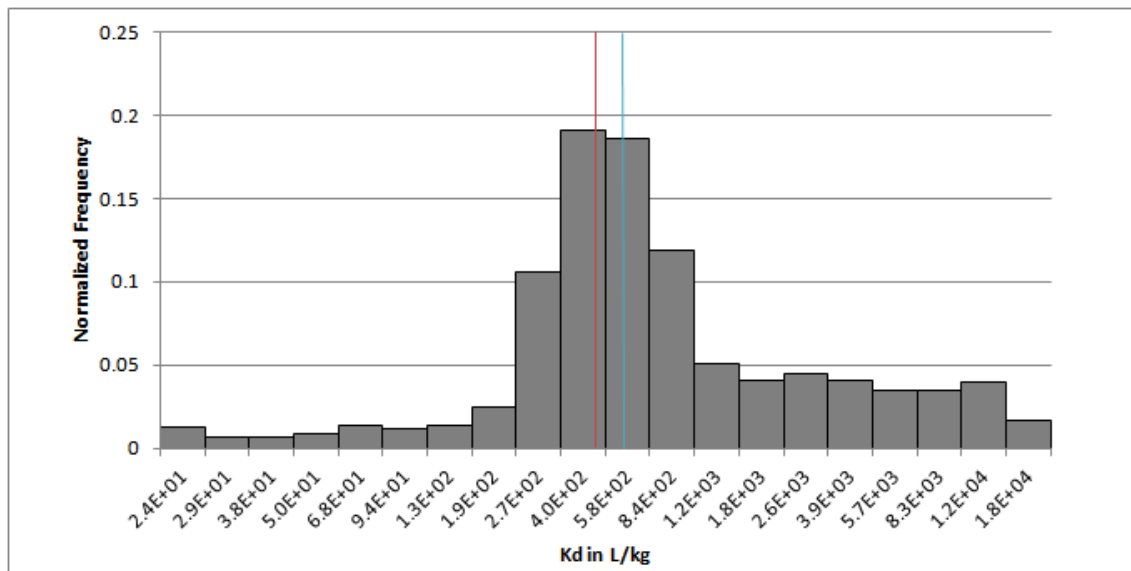


**Fig. 2.49** K<sub>d</sub> distribution of Pu for Refesol 01A.

K<sub>d</sub> given in logarithmic scale; red line: approximate position of the „standard“ K<sub>d</sub>; blue line: approximate position of the median K<sub>d</sub>.

The median and “standard” values for Ra are close (16 resp. 18 L kg<sup>-1</sup>), see also Fig. 2.50. Higher values are associated with pH > 6 and low Ca concentrations (less competition by protons and calcium). For the low P simulations, the results are essentially the same.

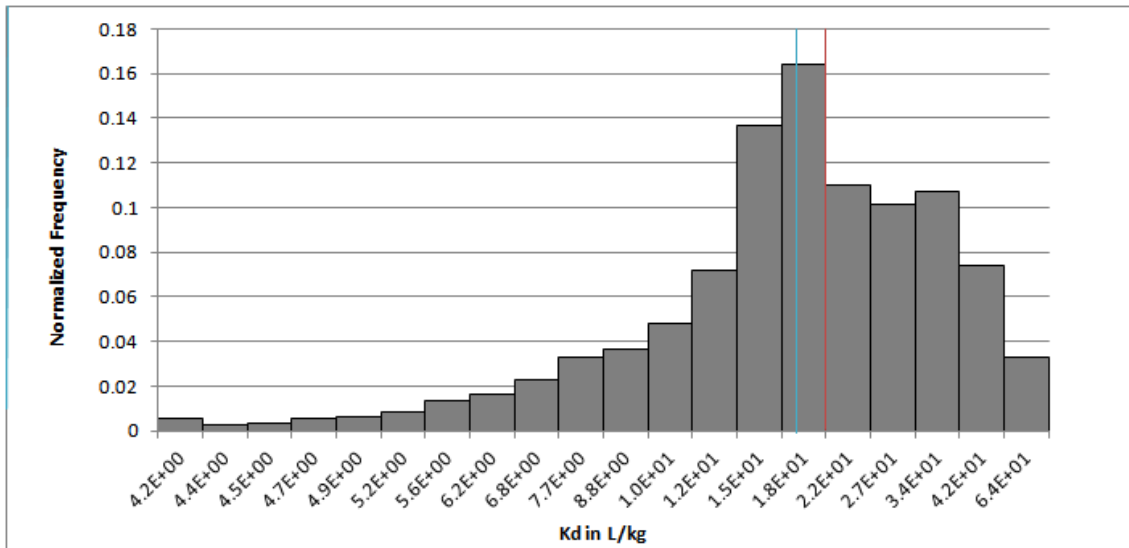


**Fig. 2.50**  $K_d$  distribution of Ra for Refesol 01A.

$K_d$  given in logarithmic scale; red line: approximate position of the „standard“  $K_d$ ; blue line: approximate position of the median  $K_d$ .

The  $K_d$  distribution for Se is shown in a linear scale (Fig. 2.51), where two modes can be clearly separated. About 40 % of the computed values are lower than  $1 \text{ L kg}^{-1}$  (down to very low values close to 0). These correspond to the regions where either selenate (higher pe) or colloidal Se (pe < 4) dominate. The broader second mode is associated with pH-pe combinations where selenite is the dominant species. In this region, generally sorption to illite dominates. However, the median and “standard”  $K_d$  values are the same ( $5.9 \text{ L kg}^{-1}$ ), because the broader mode extends to values over  $10 \text{ L kg}^{-1}$ . Under conditions with no P fertilization the situation is similar (“standard” and median values  $90$  resp.  $62 \text{ L kg}^{-1}$ ), although the second mode is “smeared out” and thus the median value is closer to the low end of the range. Due to the low concentrations of P, sorption to hydrous oxides generally dominates and the  $K_d$  values are higher.

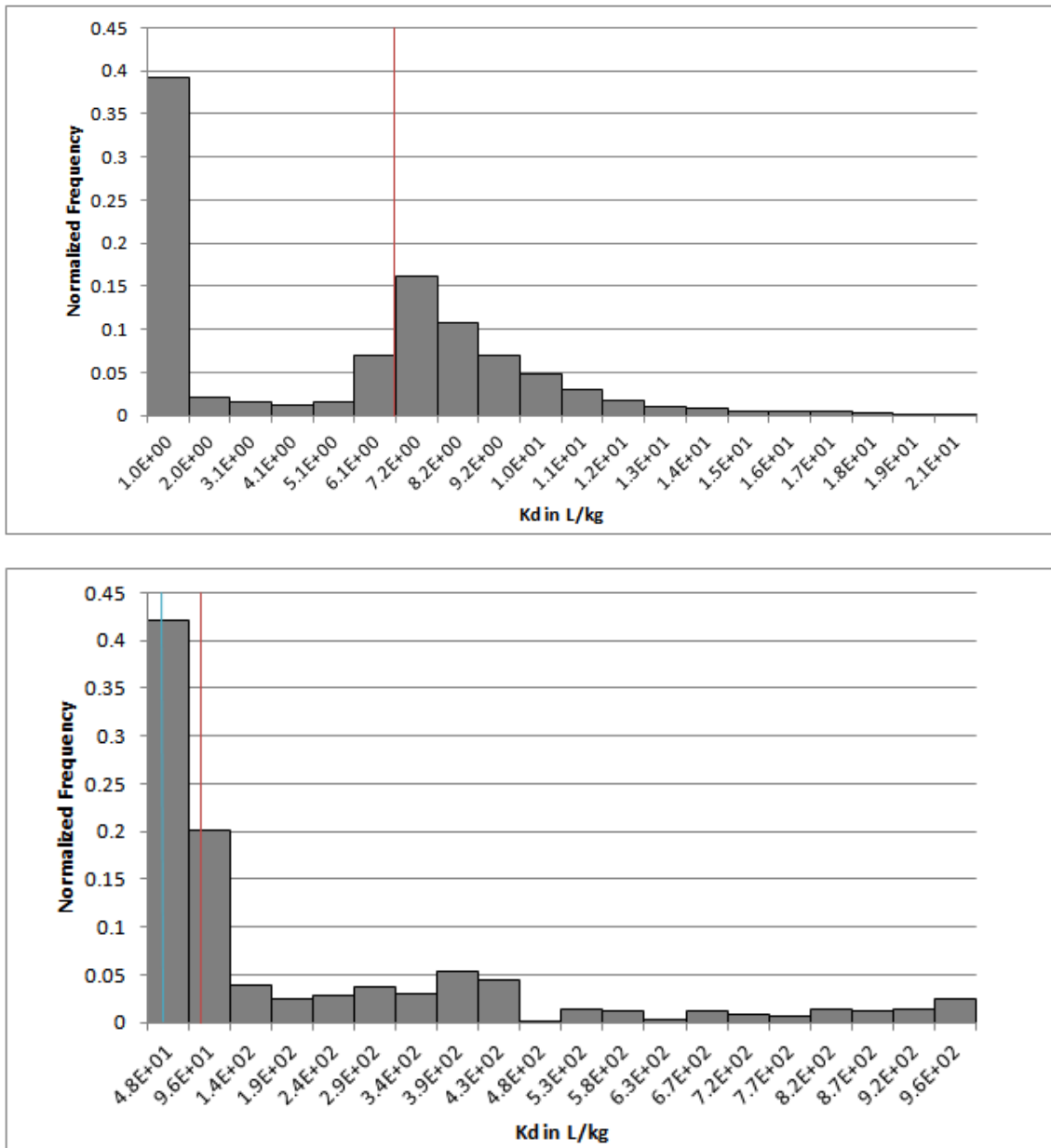


**Fig. 2.51**  $K_d$  distribution of Se for Refesol 01A

Note that  $K_d$  is given in linear scale; red line: approximate position of the „standard“  $K_d$ ; blue line: approximate position of the median  $K_d$ ; top: P fertilization, bottom: no P fertilization.

The  $K_d$  distribution of Tc (both “standard” and median values  $0.04 \text{ L kg}^{-1}$ ) also has two modes (Fig. 2.52). The low  $K_d$  mode is largely due to adsorption in the diffuse layer and pertechnetate sorption on hydrous oxides at  $p_e > 4$ . Towards higher  $K_d$  values, sorption to OM and DOM at lower  $p_e$  becomes increasingly important. The highest  $K_d$  values correspond to the lower  $p_e$  region where the Boggs model predicts high sorption to organic matter. At  $p_e = 10$ , this mode is absent and the maximum  $K_d$  is  $6.64E-02 \text{ L kg}^{-1}$ . In this case, the median value is significantly but not substantially lower at  $0.03 \text{ L kg}^{-1}$ .

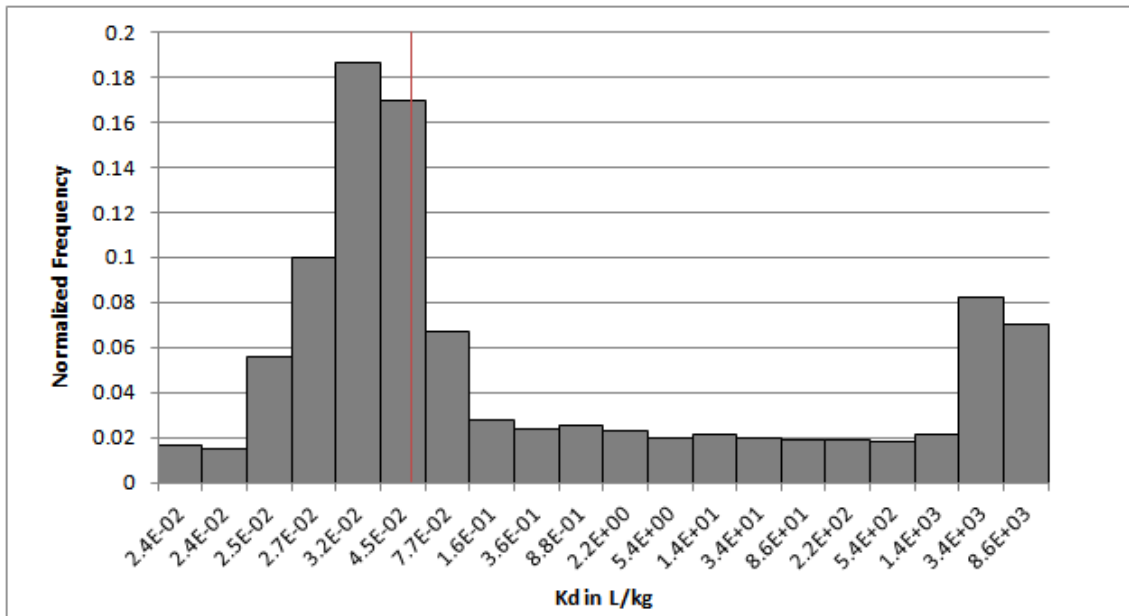


**Fig. 2.52**  $K_d$  distribution of Tc for Refesol 01A

$K_d$  given in logarithmic scale; red line: approximate position of the „standard“  $K_d$  and the median  $K_d$ .

The main portion of the  $K_d$  distribution of U („standard“ and median values 540 resp. 320  $L\ kg^{-1}$ ) is above 100  $L\ kg^{-1}$  (Fig. 2.53). However, about 30 % of the values are at  $< 5\ L\ kg^{-1}$ , which are associated with higher pH values as already shown in Fig. 2.37. This is also the reason why the median value is lower than the “standard” value.

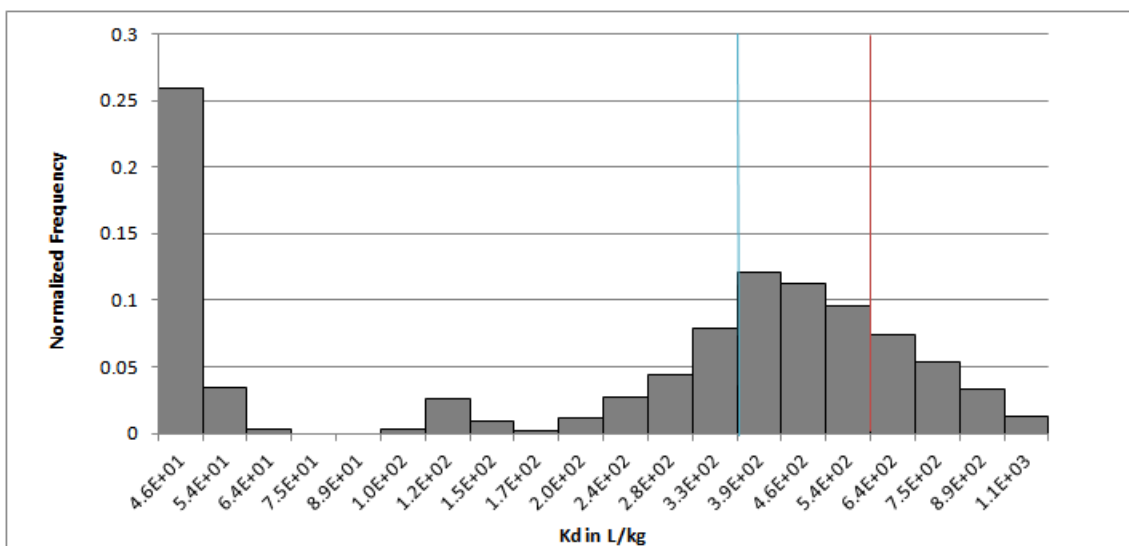


**Fig. 2.53**  $K_d$  distribution of U for Refesol 01A.

$K_d$  given in logarithmic scale; red line: approximate position of the „standard“  $K_d$ ; blue line: approximate position of the median  $K_d$ .

### 2.3.5 Summary

The component additive model UNiSeCs II has been designed and validated for moderate climatic conditions and should be applicable for the majority of the German and Western European soils. It could be validated for the radionuclides Am, Pu, Se, Ni, Cs, Ra and U with the help of data from batch experiments. However, as in some cases, parameters had to be estimated or additional assumptions had to be made, it is desirable to further validate the model, preferably with data from the field. These data should include the composition of the soil with respect to the main sorbents as well as the composition of the soil solution and should cover a wide range of possible occurring soil states.

The most important soil solution parameters have been identified for each radionuclide by single parameter variations for two Refesols within ranges that are frequently occurring in the soil and by monitoring the resulting variation of the distribution coefficient. However, although soil parameters are often correlated, synergistic or antagonistic effects are not considered in the sensitivity study.

$K_d$  values and ranges have been calculated for two Refesols which represent two soil types that are frequently occurring in Germany. Among all 12 Refesols, Refesol 01A has comparatively low contents of the sorbing components clay, OM and HO, while Refesol 03A represents the soils with a large sorbing capacity (see also Tab. 2.27). Thus, it is to be expected that for the range of common soils in Germany, the influence of soil composition on  $K_d$  is more or less reflected by the differences shown in Tab. 2.33.

To estimate ranges of  $K_d$  that may occur under field conditions, the element-specific distribution coefficient has been calculated for a number of parameter combinations and has been classified by its frequency of occurrence (“ $K_d$  distribution density”). In most cases, the median value of the distribution is close to the value calculated under “standard conditions”, see Sect. 2.3.2.4. Again, it has to be noticed that some soil parameters (e.g. pH and pe) are usually correlated and thus not all combinations of soil parameters in the field will be equally probable. In some cases, PHREEQC is not able to calculate an equilibrium and these parameter configurations are thus treated as impossible. The underlying probability distribution for the parameter combinations is unknown and can be expected to depend on external factors like temperature, soil treatment (e.g. fertilization) etc. Thus, the uncertainty of the shape of the  $K_d$  distribution density is not yet clear.

In the following sections, further issues are discussed that limit the application of the model.

#### **2.3.5.1 Processes not taken into Account**

It has to be noted that UNiSeCs II is an equilibrium model, which means that it does not take into account dynamic processes like time dependent or irreversible sorption. The sorption of cations on mineral surfaces is usually a comparatively fast process. Typical time constants are in the order of minutes /APP 05/, but there is also evidence that these processes may take place over days or weeks (e.g. in the case of Pu /ROU 05/). Desorption processes on the other hand tend to be slower than sorption /APP 05/. Diffusion of sorbed particles into the bulk of the sorbent (as is the case with Cs in illite interlayers, see e.g. /FUL 15/) is an irreversible process that is even slower.

#### **2.3.5.2 Parameters not taken into Account**

As already explained in Sect. 2.3.3.1, the effects of temperature have not been calculated. The temperature dependence of the intrinsic complexation constants may be a source of systematic errors.

Although cyanide is a strong complexant for nickel and may be present in soils, it is not used in the calculation of  $K_d$  matrices as no reliable data on concentrations resp. concentration ranges in agricultural soils could be found in the literature.

#### **2.3.5.3 Limitations of the Model**

UNiSeCs II will not be applicable in cases where there are significant amounts of soil components that are known to be sorbents for the radionuclide in question (e.g. calcite and Pu, /ZAV 04/). For alkaline soils in general, the model has not been tested and is possibly not valid.

The composition of immobile organic matter and DOM (approximated by humic resp. fulvic acid using Model VII) is implicitly assumed to be independent of the soil parameters. Under certain conditions however (e.g. low redox potential for a prolonged period), the composition and thus the amount and characteristics of the relevant binding sites may change significantly. To the knowledge of the author, corresponding studies have not yet been carried out.

As has been stated before, the model for technetium could not be validated. In the region where large  $K_d$  values ( $> \approx 1$ ) are predicted, the model validity depends largely on the validity of the Boggs model itself and the validity of the general model assumptions described in Sect. 2.3.2.3.

In the case of cesium, sorption is almost exclusively governed by frayed edge sites on clay minerals and the comparison of simulations with experimental values from the literature gave good results (see Sect. 2.3.1.4). However, the model has been only validated for soils with OC ranges up to  $\approx 10\%$ . At higher contents of OC, the model will increasingly overestimate sorption, probably because a fraction of the binding sites is blocked by aggregates of organic molecules. This has already been discussed in /HOR 02/.

The interaction of selenium with organic matter is discussed and reviewed by /DIN 17/. As the interaction of Se with OM seems to be complex and also depends on microbial action, there is currently no thermodynamical submodel that can be included in UNiSeCs. If there is any significant change of the  $K_d$  caused by these processes, this is probably long-term and thus not reflected in the batch experiment that has been used for validation /HOR 21b/.



### **3 International developments and co-operation**

#### **3.1 RWMC**

The Radioactive Waste Management Committee (RWMC) of OECD/NEA was created in 1975. Ever since it provides a forum of senior representatives from regulatory authorities, radioactive waste management and decommissioning organisations, policy making bodies, and research-and-development institutions from the NEA member countries. The International Atomic Energy Agency (IAEA) participates in the work of the RWMC, and the European Commission (EC) is a full member of the Committee. The RWMC aims at assisting member countries in developing safe, long-term management of radioactive waste while continuing to support adaptive radioactive waste management plans in response to evolving societal expectations and values and changes in public policies. After Bulgaria joined in 2021, NEA has now 34 member countries. In addition, Chinese experts attend plenary meetings as observers since 2019 according to the agreement between NEA and China.

Since January 2019 Ms. Rebecca Tadesse serves as Head of the Division of Radioactive Waste Management and Decommissioning. Prior to joining NEA, Ms. Rebecca Tadesse served as the Chief of the Radiation Protection Branch in the Office of Nuclear Regulatory Research at the United States Nuclear Regulatory Commission.

In 2018 the Committee on Decommissioning and Legacy Management (CDLM) was created. Since 2019 CDLM and RWMC are holding a joint meeting each year to exchange information and discuss topics of mutual interests. The Regulators Forum (RF) and the Forum on Stakeholder Confidence, FSC, support both RWMC and CDLM.

In January 2019 a three-day workshop on Information, Data and Knowledge Management (IDKM) was held in France. Based on the main conclusions from this workshop, RWMC approved the creation of a new Working Party on IDKM in the management of radioactive waste. The mandate of this Working Party was approved in 2020 for 3 years.

In 2019 RWMC approved the creation of an Expert Group on Application of Remote and Robotic Systems in Nuclear Back-End (EGRRS) on the discussions and outcomes of a corresponding NEA Workshop. The RWMC agreed in 2021 with the extension of the

EGRRS for 2022-2023 and endorsed objectives and plan of the development proposed by EGRRS.

In mid-2020 RWMC conducted a survey among member states concerning the prioritization of topics to be addressed in the future resulting in the following list of topics with high priority:

- challenges of extended storage and impacts on disposal,
- development and improvement of radioactive waste matrices,
- methodology to address all hazards of radioactive waste,
- transportation aspects of radioactive waste, and
- strategy to share and maintain large infrastructures as optional for the joint initiative.

RWMC agreed that the two topics of priority, extended storage and transportation of radioactive waste/spent fuel will be studied by a new ad-hoc group, that was established for one year to prepare recommendations on the elaboration of both topics in the RWMC. The ad-hoc group consists of interested RWMC members or delegated experts. The recommendations will be reviewed by RWMC and the decision made in the RWMC meeting in 2022.

RWMC furthermore agreed, that addressing the topic of all hazards in radioactive waste could be discussed within the future initiative between RWMC and CDLM with the involvement of the Regulators Forum. The topic “large infrastructures” will be kept as potential future topic.

The RWMC agreed that the topic on RW matrices could be discussed as part of an activity on new materials application in the RWMC Bureau, taking into account the results of the topical session at the RWMC-54 meeting in 2021 and survey; the recommendations to the RWMC would be developed by the RWMD and RWMC Bureau and proposed at RWMC-55.

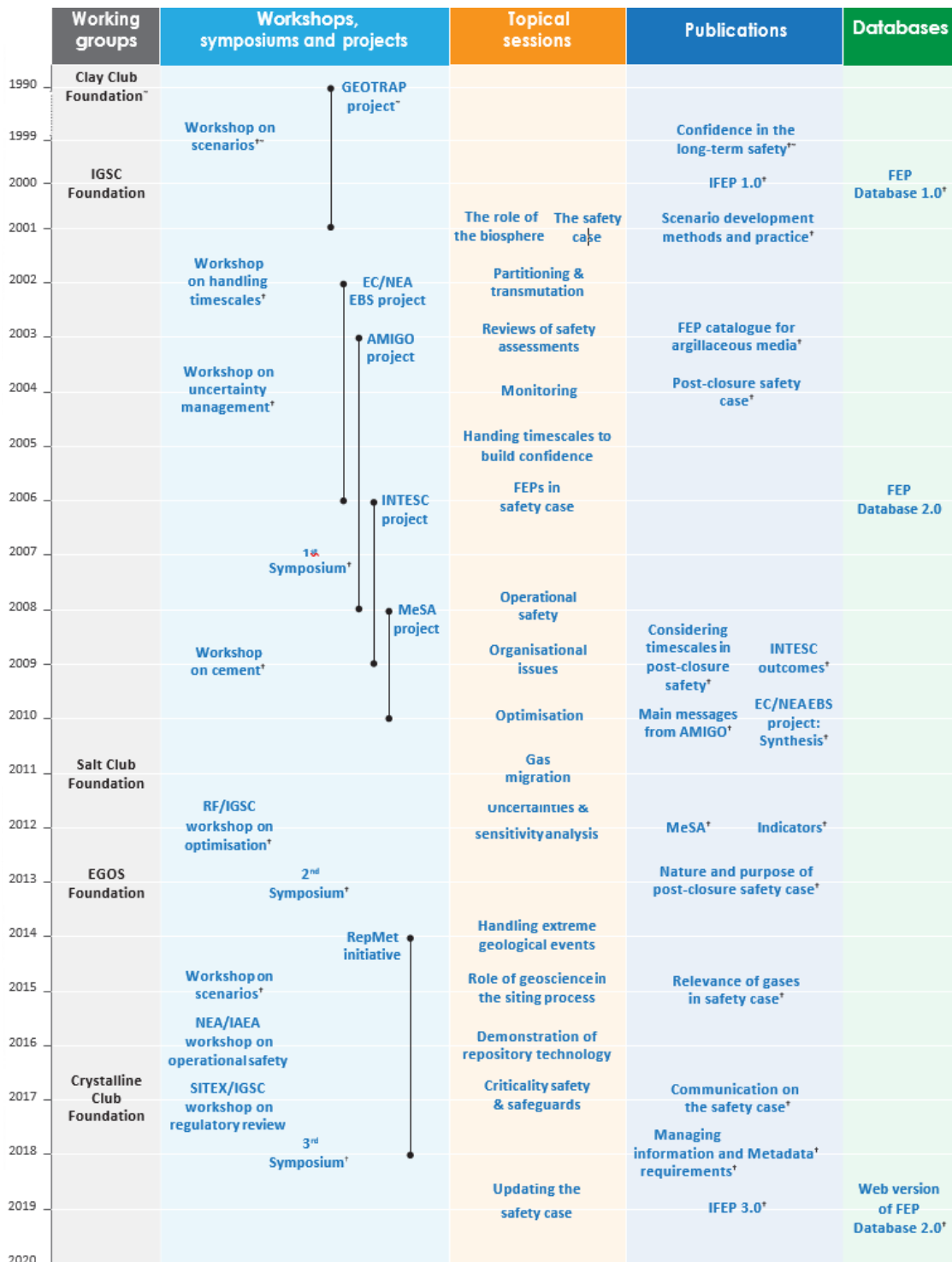
### **3.2 IGSC**

The Integration Group for the Safety Case (IGSC) of the NEA was established in 2000. It is the main technical advisory body to the Radioactive Waste Management Committee

(RWMC, see chapter 3.1) on the deep geological disposal, particularly for long-lived and high-level radioactive waste. It was established in recognition of the need to foster full integration of all aspects of the safety case.

After 20 years work the IGSC was celebrating its 20th anniversary and published a brochure to mark the occasion /NEA 20a/. The brochure reports on work carried out by the IGSC on issues relating to safety case development for geological disposal facilities, and reflects on key safety case activities and challenges. For two decades, the IGSC has taken a leading role in identifying, documenting and evaluating emerging issues and trends, and in establishing consensus on good practices in the development of the safety case. The IGSC has also shown how it is possible to adapt the concept of the safety case in line with the needs, challenges and progress of national programmes at different stages of development. The work of the IGSC has in turn been particularly informed by developments in countries such as Finland, France, Sweden, Switzerland and the United States, which have moved from conceptual safety case studies to various stages of site-specific safety cases for geological repositories, with a new repository in Finland now under construction /NEA 20a/.

The brochure reflects on 20 years of IGSC work in order to trace the evolution of the concept of the safety case overall and as a tool for programme integration, for regulatory decision-making at major project stages, for knowledge transmission and wider communication, and for prioritisation of research, site evaluation and repository design. In the process, this brochure highlights the role and contribution of key IGSC activities and reports, and identifies remaining challenges in these areas. The outcomes of IGSC activities are documented in publicly available technical reports, information flyers and databases and has been presented in a Timeline in Fig. 3.1 /NEA 20a/.



<sup>†</sup> Publications relating to these items are included in the References section.  
<sup>\*</sup> Activity conducted by IGSC predecessor committees.

**Fig. 3.1** Timeline of IGSC activities and selected publications /NEA 20a/

Beside the anniversary brochure important work were presentations to Safety Case Symposium in Rotterdam, to topical sessions and involvement in the cooperation between IGSC and the NEA groups Forum of Stakeholder Confidence (FSC). In the following, key activities of the last three years are briefly reported and summarised.

Every seven years a NEA symposium dealing with new developments in NEA member countries and at international organisations related to the safety case is organised by the IGSC. In October 2018 the symposium “Current Understanding and Future Direction for the Geological Disposal of Radioactive Waste” took place in Rotterdam. The symposium focused on the technical aspects of the safety case for the post-closure phase of Deep Geological Repositories (DGRs) /NEA 22/. The interplay of technical feasibility, engineering design issues, operational and post-closure safety and non-technical challenges such as safety case communication were explored. The main objective of this symposium was to share practical experiences on preparing, developing, documenting and reviewing a safety case from both the implementers' and reviewers' perspectives to learn from national programmes about issues concerning the siting, construction, operation and post-closure phases; to identify potential challenges that may arise as a repository programme matures and the safety case moves to represent an actual facility and inventory; to understand different players' perspectives on safety case communication, i.e. implementers, regulators and communities; to exchange useful information for developing work programmes through international co-operation /NEA 22/.

One important aspect for reaching acceptance of a radioactive waste repository by a society is an appropriate and effective communication of the various and quite complex topics of a safety case to the public. This is a topic raising more and more interest in the IGSC member countries during the last years. As a consequence, IGSC has started to work on this topic and published a first report “Communication on the Safety Case for a Deep Geological Repository” in 2017 /NEA 17/. IGSC recognised the expertise of the Forum on Stakeholder Confidence (FSC) on communication and decided to co-operate with this NEA group to further develop its view on safety case communication.

As a consequence, both groups planned and held a first joint workshop on safety case communication, which took place in 2017. The workshop served as a platform to identify specific topics and working approaches for future collaboration between the working groups. Since “Managing uncertainty” was identified as one key topic both working groups are interested in, a second workshop focussing on this topic was performed. The objectives of the workshop were to develop joint views on ways towards better communicating and addressing uncertainties in repository siting and development and in radioactive waste management governance. In addition, both organisations had individual objectives, (i) IGSC to better understand how uncertainties are perceived by different stakeholders and what role they play in debate, participation, governance and decision-

making and (ii) FSC to better understand what types and areas of technical uncertainties exist and how they are addressed. This second joint workshop took place in 2019 and the key results have been documented in a /NEA 19a/. Beside presentations on the topics (i) How uncertainty is communicated in the media, (ii) Risk perception: perspectives on risk and uncertainty and (iii) Ethical uncertainties and nuclear waste disposal, the workshop performed a world café in four different groups addressing the questions

1. What does the term uncertainty mean to scientists? Especially with regard to siting and implementation?
2. What does the term uncertainty mean to members of civil society? Especially with regard to siting and implementation?
3. What uncertainties is society willing and able to accept and under which conditions?
4. What are good examples of communicating uncertainty and why? What can we learn from these from the disposal of radioactive waste?

In the following some lessons learnt are presented. This and more detailed information about the outcomes can be found in the flyer /NEA 19a/.

Uncertainties and unresolved issues should be addressed openly and competently to build confidence. If stakeholders perceive that uncertainties are being downplayed, they are more likely to interpret the uncertainty as a threat. Stakeholders want to receive information they can trust, to be guided in coming to their own decision (which may include a risk assessment based on the uncertainties). They want to be able to form their own view as to whether risks are acceptable and, where possible, to have some control in mitigating the risks. In order to trust technical information, stakeholders first need to trust the integrity of the information provider.

Uncertainties are part of daily life; in particular they are “business as usual” for scientists. It is worthwhile to communicate that repository development is not an exception in that respect. It is important to distinguish between risks (potential for harm) and uncertainties (lack of knowledge) in communicating about safety.

Not all uncertainties are the same – stakeholders may be willing to accept some uncertainties but not others; hence, it is important to understand stakeholder values and concerns. Uncertainties should always be presented in a context to which the stakeholder

can relate. The more familiar an uncertainty, the more likely it is to be accepted (e.g. uncertainties regarding travel, weather, medical X-rays).

A third workshop with local stakeholders will take place in 2022.

### **Topical session on updating of safety cases**

The objective of the topical session in 2019 was to explore why and when safety cases get updated and what considerations are associated with the updates, from implementers and regulators viewpoint /NEA 19b/. The implementations of repositories are long term endeavors covering several decades. Safety cases evolve at different rates and ways from design stage, through construction & operation, to the post closure period. Safety case development is an iterative process. Beside the continuous evolution of knowledge legislative and regulatory changes may occur and significant changes may need to be considered even after waste operations. In order to elucidate the backgrounds and safety case updates the following key questions have been asked to the presenters:

- What prompts a safety case update (or a PA update)? Who decides?
- What frequency & depth is required for periodic safety case reviews?
- How will “significant” changes be identified? What is “significant”?
- When do several small changes or gradual changes make a “significant”
- What about changes to data, models, computer codes etc.?
- How to ensure all effects of a change are considered, even the unexpected?
- How to ensure a change and its effects are always incorporated throughout the safety case?
- How to maintain safety case knowledge (e.g., of PA) and integrity over time?

The following presentations from the different countries were given:

- Andrey Guskov (IAEA): IAEA, GEOSAF III - “updating the safety case”
- Mihaela Ion (NWMO, Canada): NWMO’s considerations for updating a safety case
- Julie Brown (CNSC, Canada) Canadian considerations for the regulatory review of the safety case
- Allan Hedin (SKB, Sweden): Swedish Operator’s considerations for updating a safety case
- Bo Stromberg (SSM, Sweden): Swedish Regulator’s considerations for updating a safety case
- Sylvie Voinis (Andra, France): Considerations for updating a safety case in France

- Thomas Kämpfer (Nagra, Switzerland): Swiss operator's considerations for updating the safety case in view of the upcoming general licence application
- Alexander Carter (RWM, UK): Digital safety case management – moving towards a 'live' safety case
- Andrew Baker (LLW Repository Ltd., UK): Considerations for updating the safety case of LLWR Site (UK)
- George Basabilvazo (DOE, USA): The 2019 Safety Case for WIPP
- Jürgen Wollrath (BGE, Germany) and Ulrich Noseck (GRS, Germany): Considerations for updating the safety case in Germany

The session chairs have compiled the conclusions of the session, which can be found in /NEA 19b/, and highlighted the following aspects. Safety cases and case studies are driven by the programme and by regulation/legislation. In some cases, regulations and legislation have changed requirements after safety cases have been developed requiring updates. Periodic updates are required for several programmes.

In the pre-operational phase safety cases play an important role in siting. In this respect also their role in discussing with the public was mentioned. In Sweden, for example, after site investigations were completed, a partial safety case for two sites was performed that showed the critical differences between them. This formed part of the licence application showing the motivation in choosing Forsmark. The safety cases were presented to the municipalities and their experts, enabling them to ask more in-depth questions. The partial safety cases used in the decision making clearly laid out the advantages of one site over another, and helped to focus discussions

Safety case used to demonstrate it meets requirements and handles uncertainties, but it should also be a decision-making tool – and thus be a “live” document. As repository construction and preparations for the operational phase are ongoing, the safety case is acquiring and incorporating a wealth of data on the site and engineered barrier design and installation. During operation, it is more of a decision-making tool e.g. for design improvements and it is also a tool to verify that the disposal system is correctly understood.

The needs for an update vary between the pre-licensing period and the various licensed phases. Construction and operation incorporate information such as changes to waste acceptance and protection of workers must ensure operational safety and also long-term safety.

Another driver for updating a safety case is when changes to regulations occur. Disposal projects span long timeframes and elements in some requirements may change, as the state of the art evolves. IT was mentioned by the Swedish regulator, when regulations are changed there needs to be a full assessment of what this means for the implementer, it cannot be changed in an arbitrary fashion.

Updates to the safety case are required at least every 15 years, in several countries in shorter time intervals. An example from a LILW repository that is currently being reviewed illustrates the evolution of the safety case structure and methodology over the years. For safety case updates quality assurance management systems are highly important. The safety case is complex, quality assurance should ensure that consistent data are used, in all disciplines, which is also very important for building confidence with stakeholders. Finland has a data clearance process, which is a way of transferring the correct information between groups aiming to prevent errors. In Belgium, quality assurance measures for modelling, safety assessment, and other processes (such as construction) need very good quality assurance measures; the management system is a key chapter in the safety case. In Canada in the pre-licensing period a regulatory review was undertaken of the NWMO's management system for data acquisition, including contractor procurement and quality assurance programmes that were in place. The data wasn't reviewed, just the processes, which can be seen as a management system review. Quality assurance was reviewed in Sweden – the regulator aimed to reproduce SKB's modelling results using other codes, which was mostly done by external experts. Emphasis was on radionuclide transport, hydrogeology, and some other areas. Differences in assessment results were the focus of discussions. For LLWR (UK) the process of updating the safety case is controlled by procedures in the management system; ensures relevant safety case managers are consulted.

The role of monitoring when transitioning from operational to post-closure safety was mentioned. Post-closure monitoring requirements tend to be country dependent. What is meant by “monitoring”, vs surveillance (in IAEA guidance); there are debates in terms of how they play into each other, and how they can be used to ensure changes in the operational phase do not affect assumptions made in the licence application phase, or post-closure safety.

Key factors / values / assumptions must be identified and checked on a regular basis during construction/operation; to ensure actual outcomes are still within the envelope of what is being assumed in the safety case. One way to assess this is by monitoring of

selected parameters, there are also others e.g. inspections, non-destructive testing. In Canada monitoring or verification activities would be proposed to the regulator in some type of institutional control plan but is no current requirement.

The safety case may have overly conservative assumptions, but there are other techniques / experiences to help with safety case robustness. Or rely on saying that using all the tools employed, releases remain orders of magnitude below regulatory limits.

Belgium has developed a safety statement tree, giving the big picture of RD&D and how it is managed, which helps to derive the safety case argumentation; the argumentation tree is an efficient tool but requires a huge amount of work (connecting data, different software); a digital argumentation tree is really helpful for developing the safety case, for updates, and also for managers – training is necessary at all levels. This is similar to the RWM (UK) Claims-Arguments-Evidence (CAE) structure, which lies at the heart of the developing digital safety case.

With respect to the different safety cases during the pre-licensing period, discussed throughout the meeting, safety cases at other intermediate phases (i) need to be complete enough to be able to support decision-making between the regulator and the waste management organisations, and (ii) must have clarity on what constitutes a ‘complete’ safety case (for different phases). Further, involvement of all stakeholders showing that their views are taken into account could help with both the review and potentially with acceptance.

### **3.3 Salt Club**

The “Expert Group on Repositories in Rock Salt Formations (Salt Club)” was established in 2012 by OECD/NEA. Current member states are the United States, Germany, Netherlands, United Kingdom, Poland and Romania. The key objective of the Salt Club is to promote the exchange of information and share approaches and methods to develop and document an understanding of salt formations as a host rock for a high-level radioactive waste repository. The Salt Club holds regular annual meetings at which its Programme of Work (PoW) are established, updated and reported about. In the current PoW of the Salt Club from 2021 to 2022 the following work activities /NEA 20b/ are listed:

- Common Features, Events and Processes (FEP) catalogue for a HLW repository in rock salt and Salt Knowledge Archive (scope, definition, collection of ideas, available information on state-of-the-art of knowledge management)

- Scenario development for repositories in salt
- State-of-the-art report on important commonalities and differences of repositories in flat-bedded and domal salt
- Geomechanical integrity evaluation, including numerical and experimental work with crushed salt
- Thermodynamic aspects of brine chemistry
- Actinide and Brine Chemistry (ABC) Salt Workshops
- Joint International Pitzer Database (JIPD) and
- Microbial gas generation in saline systems.

In the current period GRS is mainly involved in the FEP data base and scenario development activity. In 2012, the NEA salt club started an activity for developing an international FEP database for repositories in salt, which should include information of available FEP catalogues in salt and which should be available to the public. This data base should provide future scenario developers with information about relevant processes and effects in all compartments of a repository system including a comprehensive reference data base (Salt Knowledge Archive).

The Salt Club FEP Database is a comprehensive catalogue of FEP that are potentially important for the post-closure performance of a repository for high-level radioactive waste (HLW) and spent nuclear fuel (SNF) in salt (halite) host rock. The generic salt repository FEP include consideration of relevant FEP from a number of United States, Dutch, German, and international FEP lists and is supposed to be a suitable starting point for any repository program in salt host rock. Priority is laid on a systematic, comprehensive and clear list of FEP to enable users to get a good overview and to check for completeness of FEP in a future project.

The salt FEP catalogue and database employ a FEP classification matrix approach that is based on the concept that a FEP is typically a process or event acting upon or within a feature. The FEP matrix provides a two-dimensional structure consisting of a Features/Components axis that defines the “rows” and a Processes/Events axis that defines the “columns” of the matrix /FRE 20/. The design of the FEP classification matrix is consistent with repository performance assessment – the Features/Components axis is organised vertically to generally correspond to the direction of potential radionuclide

migration (from the waste to the biosphere) and the Processes/Events axis is designed to represent the common two-way couplings between thermal processes and other processes (such as thermal-mechanical or thermal-hydrologic processes). Related FEP can be easily identified – related FEP will typically be grouped in a single matrix cell or aligned along a common row (Feature/Component) or column (Process/Event).

The development of the matrix-based salt FEP involved two major activities. The first activity was to map the original salt-repository-specific FEP to the salt repository FEP matrix; some of the original salt FEP mapped to a single matrix cell, while some of these FEP mapped to more than one matrix cell and had to be subdivided. For example, the original transport FEP typically applied to most, if not all, of the Features/Components of either the engineered barriers or the geosphere and therefore needed to be subdivided into multiple FEP – one for each Feature and/or Component. From the set of mapped FEP a smaller set of matrix-based FEP were developed for each cell, to eliminate redundancy and to conform to the new classification scheme of the matrix. The second activity was the identification of the Associated Processes. For each Process or Event, a general set of FEP and Associated Processes was developed. These associated processes could generally apply to (i.e., act upon or within) any Feature or Component.

The online Salt FEP Database can be downloaded from [www.saltfep.org](http://www.saltfep.org). It contains the FEP matrix, the FEP, and the associated processes for each FEP. It provides a starting point to create and document site-specific individual FEP. Furthermore, the FEP matrix is connected to the Salt Knowledge Archive, a database of about 20000 references and documents representing the historical knowledge on radioactive disposal in salt. A detailed description of the FEP Database and the underlying concepts is documented in /FRE 20/.

A specific site and the repository system will undergo exactly one evolution, which will be governed both by climatic and geological processes at the site and processes induced by the repository construction and the emplacement of heat-generating waste. Despite a detailed understanding of the various influencing factors, this real evolution cannot be predicted unequivocally in all details. The resulting uncertainty with regard to the future evolution of the repository system can be reduced only marginally by additional research and site investigations. Therefore, a limited number of reasonable possible evolutions are derived in a safety case based on a systematic assessment of relevant influencing factors with the objective to identify and describe in detail relevant scenarios, which allow to assess post-closure repository safety.

The primary goal of a repository system scenario development is to derive a set of scenarios covering key aspects of uncertainties regarding the future evolution of the repository system – specifically the portion of the uncertainty not explicitly treated in numerical models. The safety assessment requires this set of scenarios cover all significant evolutions regarding the safety of the repository. Repository systems are complex. These systems include technical (Engineered Barrier Systems – EBS) and natural features (geological barriers) over long periods of time with limited possibilities for observation and monitoring. For these complex systems it is nearly impossible to derive plausible scenarios only by describing its evolution for the whole system. To reduce complexity of a repository system it is common practice to analyze its components and characteristics (Features) and the influencing Processes and Events. The identification process often entails a comprehensive system of FEP and a related discussion of which FEP are relevant for the repository's safety and which are not (i.e., the FEP screening process).

In a second step, the set of possible future evolutions is reduced and only carried forward for the identified key processes and events and their influence on the safety-relevant components. In step 3, the possible evolutions of processes and events for the various factors are selected and then condensed into scenarios.

Following this approach, the scenario development step is conceptually between FEP development and system-level performance assessment (PA) models development:

Site characterization data → Scenarios → PA models

Scenarios are an option for formalizing and planning a complex decision process that must be made in light of significant uncertainties. Scenarios do not need to all be real evolutions of the expected future in a system; they supply a set of different possible or bounding futures on the basis of geologic system characterization and physical process understanding. Scenario are a single possible future evolution and therefore always implies the possibility of other alternative futures.

The development of scenarios is one of the key elements of a safety case for permanent geologic disposal of radioactive waste /NEA 12/. The approach is typically based on FEP, that are compiled into a FEP catalogue. During the Salt Club meeting in 2019 in Rapid City, it was decided to extend the Salt Club activity on FEP and to go a step further and establish a collaboration on scenario development in salt. In August 2020 an online workshop was held to

- define collaboration goals
- discuss the international status and national perspectives
- regulatory requirements
- general methodology in scenario development
- special features in scenario development in salt
- the importance of Human Intrusion

On the workshop it was decided to create a state-of-the-art report (SOAR) for the NEA salt club on scenario development in salt within the current mandate period 2021-2022.

In June 2019 the sixth workshop on Actinide-Brine-Chemistry (ABC-Salt VI) was held in Karlsruhe. As all previous workshops it was jointly organized by researchers from the U.S. and Germany. More than 40 participants representing research entities, Waste Management Organizations (WMOs) and regulators, respectively, from 8 countries participated in the workshop. Apart from 11 scientific oral presentations and a poster session with 14 contributions discussion panels were organized on the issues “organic complexation” and “actinide redox chemistry” in saline settings. Due to the lively exchange on a good scientific level the discussion panel format turned out to be a very positive experience.

In this topic, the Salt Club will address in the future actinide-organic interactions, data gap assessments and, for the first time, more realistic and mechanistic assessments of microbial gas generation processes in saline systems.

### **3.4 Crystalline Club**

Deep geological repositories use a combination of engineered and natural barriers to safely contain and isolate radioactive waste from people and the environment. Repository development for long-lived radioactive waste is a strategic area in the work programme of the NEA Radioactive Waste Management Committee (RWMC). Among the different geological formations considered suitable for hosting geological repositories, crystalline rocks are characterised by their high strength, thereby providing high rock-stability and a low thermal expansion coefficient. Unfractured crystalline rock shows a low permeability. Crystalline rocks, e. g. granite or gneiss are highly resistant to chemical alteration compared to other host rocks.

Many countries are developing or planning to develop deep geological disposal facilities for radioactive waste or performing research in underground research facilities in crystalline host rocks. Although scientific and geotechnical understanding of crystalline rocks continues to advance from the dedicated research carried out by these countries, there are research areas in which member countries may benefit from the scientific exchange and joint R&D efforts.

Similar to other NEA expert groups, the Crystalline Club (CRC) is composed of technical experts with experience in evaluating or reviewing the understanding of crystalline rock as host rocks for deep geologic disposal projects. Members represent waste management organisations, regulatory authorities, academic institutions, and research and development institutions. The CRC was founded in 2017 with founding members from Czech Republic, Germany, Japan, Russian Federation, Spain and USA. By 2021, CRC has 41 members from eleven member countries. Newer member countries are Canada, Finland, Switzerland, Romania and Republic of Korea.

The CRC's mission is to promote the exchange of scientific evidence/information for demonstrating the safety of developing geological disposal facilities in crystalline rock formations. To fulfil its objectives, the tasks carried by the CRC includes:

- Promoting the exchange of information on approaches, methods, methodologies and technologies in order to understand the characteristics of crystalline rocks and to use their advantages to host a repository;
- Developing and exchanging information specific to certain geological media among countries currently pursuing or considering crystalline rock as a candidate deep geological repository medium;
- Identifying areas of interest for fundamental research, i.e. where understanding is incomplete or improvements are required;
- Developing reports and expert recommendations;
- Promoting common projects and task groups within the CRC; and
- Communicating identified topics of common interest and/or exchange with other working groups or international projects.

Annual plenary meetings are held on a regular basis in order to further the information exchange between the CRC members. The first CRC meeting was held on 05-07 December 2017 in Prague, Czech Republic, the following meetings were held on 13-14

June 2018 in Mizunami, Japan, on 25-27 June 2019 in Krasnoyarsk, Russian Federation and on 01-03 June 2021 online.

The safety assessment of deep geological repositories is based on a complex workflow, commencing with the collection of field and laboratory data and the acquisition of the relevant knowledge and argumentation, and concluding with the final dose calculation for a representative person. The workflow is based on data as well as on assumptions and simplifications in geosphere and safety models. With each step in the siting process and thus an increase in knowledge, ideally the number of assumptions and simplifications is reduced. A comparison of the different safety assessment approaches of the CRC member countries, with respect to the use of data and the application of descriptive models in the final dose evaluation process, will represent a valuable step forward in terms of improving the reliability of the crystalline host rock environment safety assessment process. To reach this goal, the CRC Program of Work (PoW) 2019-2020 included the following tasks:

1. Data: The identification of the key data to be obtained from crystalline rock environments (the geosphere) that is relevant to the safety assessment process.
2. Models: The comparison and evaluation of the transfer of data for the compilation of both descriptive and safety assessment models.
3. Criteria development: The identification of requirements for the development of siting criteria concerning crystalline host rock environments. The definition of the main parameters of crystalline host rocks that are of crucial importance for, and exert an impact on, the safety evaluation process.

The tasks were addressed during topical sessions at the plenary meetings with the participation of different CRC members and guests. The goal of the first topical session during CRC-3 in Krasnoyarsk on “Data acquisition, processing and management for model development” was to identify the key data to be obtained from crystalline rock environments, that is relevant to the safety assessment process and the development of an R&D strategy as well as to evaluate data necessity in different stages of the site selection process. These data will be entered into the site descriptive models, the results of which will then be used as input data for the construction of complex safety assessment models. Six presentations from Russia, Japan, Canada, South Korea, China and the Czech Republic gave an overview of the different national approaches considering availability, acquisition, processing, and management of geo-scientific data, and their

use in the development of the safety case. An international table of parameters that must be considered in the safety assessment process was derived.

The second workshop (“models”) was planned to be held in the course of the planned CRC-4 meeting in Germany in 2020. Due to the global travel restrictions put into force as consequence of the global coronavirus pandemic, the meeting had to be postponed to 2021. Unfortunately, the travel restrictions were still in force in 2021. The CRC-4 meeting as well as the topical session were therefore held in a virtual and comprised format. The goal was to describe the various procedures to be applied for the transfer of the results of geological, hydrogeological, geochemical and transport research, as well as the results of the models of potential sites, to the relevant safety assessment models, with respect to the simplification of the system, the application of the relevant data and the accuracy of the model results. Based on the outcomes of the topical session, a questionnaire for each country is currently being developed, that interrogates which software and safety assessment models are being/will be applied and the procedures employed for the transfer of both the relevant data and the results of the descriptive models to the safety assessment models, while taking into account the various advantages and disadvantages, the accuracy of the data obtained and the associated uncertainties.

The three-staged PoW 2019 – 2020 was extended to the PoW 2021 – 2022 in order to regularly finalise the planned tasks. Therefore, the next topical session to be held in 2022 during the CRC-5 meeting will address the last step of the PoW 2019 – 2020. This topical session will deal with criteria development with the aim to identify and describe in detail the most important parameters of crystalline rock environments that might influence the various stages of the siting process with respect to crystalline host rock and to identify those parameters of key importance with respect to each stage of the site evaluation process.

In 2021, an additional CRC webinar was held on 11, 18 and 25 March 2021 complementing the aims and tasks of the PoW 2019 – 2022. It was entitled “Research methods and modern measuring equipment used for site and rock characterization”. The webinar featured presentations and discussion of fault characterization in crystalline host rock, including geophysical/geotechnical methods for determination of the location and dimensions of fractures and faults. The meeting was well attended by 40 to 50 delegates, both CRC members, delegates from other OECD/NEA organizational units and guests.

The webinar started with a keynote on “Feedback from Safety Assessment on what is important to characterize” by Johan Andersson (SKB, Sweden), presenting on the assessment of post-closure safety and safety functions and requirements. The presentation focused on key safety characteristics of the geosphere and of crystalline rocks as well as key factors affecting safety of KBS-3 design. It was followed by two presentations on fault characterization. Morpho-structural analysis was introduced for the identification of brittle fracture zones using digital terrain models and remote sensing techniques by Zita Bukovská (SÚRAO, Czech Republic). It combines techniques of geomorphology, geology, remote sensing and computer science and makes it possible to depict the real relief and characterize the relief (e.g. slope angle, curvature). A combination of morpho-structural analysis and geological/geophysical data is useful to establish the 3D model of a specific site. Using the example of the Mizunami Underground Research Laboratory in Japan, some geological and geophysical investigations were introduced by Eiji Sasao (JAEA, Japan), but it was also shown, that these might not always be sufficient for a comprehensive hydraulic characterization. Discontinuities may act as pathways for groundwater flow and contaminant transport, but on the other hand, they can also act as hydraulic barriers under certain conditions, i. e. the “main shaft fault” at Mizunami. Therefore, a thorough characterization of those discontinuities affecting groundwater flow and/or mass transport is very important.

The second workshop day focused on geophysical in-situ measurements with two presentations on different exploration techniques at different scales by Aaron DesRoches (NWMO, Canada) and Hartwig von Hartmann (LIAG, Germany). The integrated analysis of geophysical log and core data in a fractured granitoid bedrock is a fast, easy and cost-effective method for identification of hydraulic and fractured bedrock intervals taking into account the lithology, fractures and core logging. A new approach including machine learning in the interpretation of the in-situ measurements is a promising way forward. At a larger scale, fault analysis can be realized by 3D seismic exploration. One example from a deep geothermal project in a granite body in Germany was presented. Using the 3D seismic method, different kind of structures can be detected at a regional scale. Challenges remain in the interpretation of inclined geological boundaries. In order to apply the method to more shallow depth exploration, an adjustment of the method would be needed.

The third session of the webinar focused on the hydraulic in-situ characterization with presentations by Pat Dobson (LBNL, USA) and Jere Komulainen (Posiva, Finland).

Fracture flow is one of the key processes in a crystalline safety case, and many techniques for fracture characterization are available (field & laboratory). A case study from the COSC-1 borehole, central Sweden, served as an example for fracture (and associated flow) characterization of crystalline rock, where fiber-optic sensing and the SIMFIP tool were applied. Based on the hydraulic in-situ characterization, an integrated fracture characterization can be used to create DFN models. Uncertainties remain on fracture lengths, apertures and fracture connectivity. The POSIVA flow log device is a useful technique to characterize (single) fracture flow by analyzing the fracture flow, borehole pressure and resistance. Results are beneficial additional data for modelling hydraulic properties and DGR construction.

It can be summarized that fractures are key safety characteristics of the geosphere and of crystalline rocks. Different methods for fault characterization are available from field scale to laboratory scale, while different questions require different methods of fracture characterization. Challenges are the characterization of bulk data vs. single fracture data, the integration of results into models and uncertainty quantification. New developments of fracture characterization are addressing some of the open issues.

### **3.5 IDKM**

National programmes for radioactive waste management tend to run for decades, as well as the process of safety case development and review in all their phases (i.e. pre-siting, siting, characterization, construction, operation and finally closure). In this time perspective, the Information, Data and Knowledge Management (IDKM) play a fundamental role. Therefore OECD-NEA initiated the project IDKM.

A first workshop to start the IDKM and to establish expert groups for the selected working areas took place in January 2020 in Paris. Based on a draft roadmap in this workshop the ideas and potential tasks of the IDKM project have been discussed and interest of the participants in respective subgroups was raised and identified. A chair of the group and 5 bureau members one of them from GRS, responsible for steering the IDKM work and supporting the chair, have been elected. During the year the bureau finalised the IDKM roadmap and worked on establishing expert groups for the IDKM project. It was decided to found the four expert groups EGSSC, EGKM, EGAR and EGAP, see Fig. 3.2. This figure has been internally used by the WP-IDKM Bureau where GRS is a member and is allowed to use it.



**Fig. 3.2** Structure of the IDKM with the four expert groups. Figure is internally used by the IDKM Bureau

GRS is mainly involved in the expert group EGAR. The EGAR identifies activities to assist WMOs with their procedures and practices leading up to placing the records in an archive (without including the same ones that national or other archives perform receiving such records). EGAR supports RWMOs in their efforts and research in the archiving areas recommending feasible, resource saving standards, methods, tools, and consider various roles under various repository phases in the areas of archiving. The scope of EGAR includes all types of records that a RWMO can place in archives, including paper-based documents, objects such as borehole samples, and digital records, digitized documents and “data born-electronic”, sound recordings, films and similar. The EGAR work includes both archiving of records which are expected to no longer be used during the repository lifetime but could be important in the future (for example, upon decision of future generations to retrieve the waste), and preservation of records that are no longer actively used but will likely be needed in the near future of the repository programme (for example, for the compilation of the next safety case). Moreover, the EGAR work includes all RWMO activities related to archiving, whether these are prescribed by regulators or performed by the RWMO in its best effort to inform future generations.

Each of the IDKM expert group has its own bureau steering the work of the group. The programme of work of the expert group EGAR is divided into two global tasks, namely the “Set of essential records” and “Archiving”.

During the RK&M project an example procedure to select a Set of essential records (SER) for a radioactive waste repository, illustrated by an example application was developed on a generic basis. Within the new SER task, it is intended to test the proposed procedure by applying it to the records of an existing repository, namely the Konrad repository in Germany, which is currently under construction. By the application it is envisaged to:

- concretize the review process for the SER, investigate whether the proposed classification and rating scheme is appropriate and check if additional instruments are needed,
- systematize and underpin the arguments for classification and rating of the records and
- identify and, if possible, rectify any shortcomings and optimise the proposed procedure and tools.

This work is intended to be completed in four steps:

1. Compilation of a comprehensive record list (restricted to the initial example record category: “Site and host rock survey and characterization records”) by respective search tools. The aim is to identify all records related to this category from the archive of the German implementing organization BGE.
2. Perform a two-step categorization process of the identified records by use of the Excel table format and the needs of future generations as proposed in the RK&M project.
  - Two separate multidisciplinary teams from the implementer BGE and the research organization GRS discuss and categorize the complete list of records.
  - Both groups will exchange their individual results and harmonize the categorization results in the Excel table. Specific evidence will be put on the arguments used for characterization of each record. This process might be accompanied by external participants – members from the SER or EGAR group – either by participating in the meetings or afterwards by

reviewing the results. This requires at some stage the translation of the German into the English language.

3. A systematic categorization and selection procedure shall be derived, e.g. a criteria checklist or guidelines. Relevant aspects are related to questions like (i) How much information about the record is needed to decide whether it is relevant for the SER or not (e.g. only title, short summary, others)? (ii) Can the procedure be automatized? (iii) If criteria for categorization are derived, can they be prioritized or weighted?
4. The applied and further developed procedure to all remaining record categories, which have been proposed during the RK&M project, namely “Repository design and realization”, “Waste and waste packages”, “Repository operation records”, “Safety and environmental impact assessments, Licensing documentation” and “Societal and general information”. By application of the procedure the reasoning of the existing categorization will be tested and the necessity to include additional categories will be discussed. All experiences learned will be documented in an updated report describing identification and selection of an SER.

The results from the Konrad programme and experiences from other national cases, which still need to be defined, are planned to be regularly presented and discussed within the EGAR group.

The main purpose of the SER is seen as being to inform future generations in the medium term, several centuries from now. However, the SER might play an additional important role in knowledge transfer in the pre-closure phase of the repository, over a time frame of several decades. Furthermore, addressing the needs encountered in the short-term may lead to the identification of new records that should be mentioned in the record list. This link with the pre-closure needs should also be investigated and might be included into the SER selection procedure by implementing additional need(s).

### **3.6 Microbial processes MIND**

This discussion represents a compilation of main outcomes of the Project MIND based on the publication by Mijndonckx, K., Small, J., Abrahamsen-Mills L., Pedersen, K., &

Leys, N. (2019): Final integration and evaluation report. MIND project, Euratom research and training programme 2014-2018, Deliverable 3.7, 2019.

Microbiology in Nuclear waste Disposal (MIND) was a multidisciplinary project, which was run from 1<sup>st</sup> June 2015 to 31<sup>st</sup> May 2019 and addressed key microbiology issues in support of the implementation of waste disposal across the EU, specifically, concerning organic waste forms (chapter 3.6.1) and performance of repository components (chapter 3.6.2). WP1 addressed key issues concerning intermediate level waste (ILW), including the combined effects of radiolysis and biodegradation of anthropogenic and natural organic polymers on (i) radionuclide speciation and release, and (ii) the potential to fuel microbial processes in ILW and the barrier system. WP2 addressed key issues regarding the effects of microbial activity on the waste containers, buffer, backfill and seals of repositories. WP3 evaluated further the impact of different strategies to identify microbial community in clays using a commercial microbial community standard.

### **3.6.1 WP1 – Organic waste forms**

#### **Bituminised waste**

Belgian disposal concept uses Eurobitum as the reference bituminised waste consisting to 60 % of bitumen Mexphalt R85/40 and 40 % of soluble and insoluble salts. Bitumen degradation studies were done with synthetic Boom Clay water (SBCW) at pH 8.5 or clay-cement water (CCW) at pH 12.5 and with irradiation at anoxic conditions. Water uptake by the bituminized waste resulted in a leaching of large amounts of NaNO<sub>3</sub> and other soluble salts to the Boom Clay. Besides the added acetate, formate and oxalate, the microbial community was able to use organics leaching from Eurobitum for nitrate reduction. The highest nitrate reduction rates were observed in the presence of acetate. A biofilm formation, suggesting an enhanced degradation of Eurobitum, was observed at all conditions except for pH 12.5 which seems to be a limiting value for microbial nitrate reduction. However, the microbial community was not eliminated at this pH as intact cells were present after resuscitation at slightly alkaline pH. It seems further that phosphate can quickly become a limiting nutrient at some experimental conditions, however, it is not expected to be a limiting nutrient *in situ*, as phosphate is bioavailable as, e.g., apatite in Boom Clay.

### **Cellulose containing waste**

At pH between 12.5 and 13.3, cellulose undergoes chemical hydrolysis, to produce mainly isosaccharinic acid (ISA). The latest model proposed that the complete hydrolysis of cellulose would require between 1000 and 5000 years. Neither that model nor the previous models included the effect of radiolytic or biological degradation because of lacking studies on these effects under hyperalkaline conditions. This was addressed in MIND. It was found that irradiation enhances the rate of cellulose hydrolysis at pH 12.7, with the concentration of ISA being around 4 times higher after 5 months reaction, and the bioavailability of (crystalline) cellulose for microbial degradation. The products of the microbial degradation of irradiated cellulose were H<sub>2</sub>, acetate, and presumably CO<sub>2</sub>, whereas no methane was detected. ISA forms water soluble, alkali stable complexes with various radionuclides, thus enhancing their mobility. However, in a beneficial effect, microorganisms can ferment ISA to acetate, and presumably CO<sub>2</sub>.

### **PVC containing waste**

In the UK, halogenated plastics constitute the largest component of the organic-containing waste inventory. PVC in its pure form is a rigid, mainly amorphous material with little flexibility. To be of use in the nuclear industry, it is rendered flexible by a variety of additives, including plasticizers, heat stabilizers, fillers, pigments, flame retardants, UV absorbers, colorants and antioxidants. Of these, plasticizers are typically present in the largest quantities, accounting for between 30% and 50% by volume. Work made in MIND demonstrates that PVC additives are able to fuel microbial metabolism at high pH conditions (pH 10) of an ILW repository. Irradiation renders plasticised PVC less bioavailable at pH 10, but microbial metabolism appears to be supported still. Chemical alkaline and radiolytic degradation of plasticised PVC caused leaching of phthalic acid, triphenyl phosphate and other organics. Phthalate is known to complex with radionuclides, and the results of this study indicate that microbial activity is unlikely to reduce this risk as phthalate was not found to support the tested metabolism.

### **Ion exchange resins waste**

Resins represent the largest single component of the organic material in the inventory of ILW and LLW in Switzerland and Czech Republic. A production of H<sub>2</sub> and a number of gaseous chlorinated aliphatics, such as bromomethane, chloromethane, dichloromethane, and chloroethane, as well as aromatic compounds, such as benzene and

toluene were revealed upon irradiation of resins. Radiolytic yields for benzene and chloromethane show however that their concentrations in the gas phase are very low ( $\sim 10^{-8}$  M). Bacterial proliferation was supported only at low concentrations of 0.2 and 2 g/l of the irradiated exchangers. Differently from non-irradiated resins, irradiated resins proved to be lethal for the microbial population of the anoxic underground water from Josef URL at the concentration of 20 g/l, indicating toxicity of radiolysis products.

### **Radionuclide immobilisation**

Bacterium *Stenotrophomonas bentonitica*, isolated from Spanish bentonites, is able to tolerate mobile Se(IV) by reducing it to Se(0) under aerobic, anaerobic and alkaline (up to pH 10) conditions. Amorphous Se(0) (a-Se) nanospheres are formed initially and transform subsequently to less soluble, one-dimensional trigonal selenium (t-Se) nanostructures with diverse crystallinity, morphology (hexagonal, nanotubes, etc.) and size. These Se nanostructures are associated with sulphur, indicating that sulphur-containing organic compounds are involved in the reduction of Se. This bacterial strain is also able to tolerate up to 200 mM of Se(VI) and to reduce it to Se(0) by forming intracellular monoclinic and trigonal Se nanotubes.

### ***In situ* processes: hydrogen consumption**

Repeated weekly injection of H<sub>2</sub> into an *in situ* borehole in Opalinus clay and repeated replacement of the borehole water with artificial Opalinus clay porewater devoid of sulphate for over 350 days were undertaken to accelerate the transition to methanogenic conditions. However, the microbial community was dominated by sulphate-reducing bacteria, and geochemical indicators such as  $\delta^{34}\text{S}$ -sulphate and  $\delta^{13}\text{C}$ -methane confirmed the biological reduction of sulphate and the lack of methanogenesis despite the decrease of sulphate concentration to  $\sim 4$  mM. Thermodynamic calculations suggested that bicarbonate concentration was likely too low to support methanogenesis.

Methanogens were dominating the microbial community in an *in situ* experiment with a porewater saturated porous medium (80% sand and 20% bentonite, w/w) and H<sub>2</sub> addition. In accompanying microcosm experiments with artificial Opalinus Clay porewater depleted in sulphate and repeatedly injected by H<sub>2</sub> and Opalinus Clay, no methanogenesis was observed. Sulphate reduction and an abiotic release of Fe(II) from Opalinus Clay were observed instead. X-ray absorption spectroscopy analysis of the clay revealed the presence of FeS in the inoculated samples but its absence in the non-inoculated

control. This result suggests that sulphide produced by the sulphate-reducing bacteria reacted with Fe(II) to produce FeS.

### ***In situ* processes: methane generation from organic waste**

The TVO gas generation experiment has been in operation for nearly 20 years studying methanogenic gas generation from cellulose and steel containing LLW from the operation of the Olkiluoto power plants. The MIND project has enabled interpretation and modelling of an 18-year dataset of chemical and gas measurements and microbiological studies have been undertaken of stored and new water samples. The alkaline cellulose degradation processes occurring in waste drums has neutralised the initial alkaline pH conditions (pH 10-11) of tank water buffered by concrete. Microbial sulphate reduction was occurring over the first 2 years, which resulted in peak concentrations of sulphide of ~0.2 mM that slowly declined to micromole concentrations in equilibrium with the Fe sulphide phase mackinawite. Organic carbon initially rose to around 8 mM but since 2006 declined, which was coincident with an increase in the rate of methane gas generation to around 1 m<sup>3</sup> per year from the whole experiment. This was consistent with methanogenesis occurring once the pH had declined to below pH 9. It was also suggested that the increased rate of methanogenesis might have been a consequence of the decline in aqueous sulphide concentration to below  $3 \times 10^{-6}$  M. Hydrogenotrophic methanogens dominated after one year of operation, which was related to the utilisation of hydrogen generated by the anaerobic corrosion of steel. Acetoclastic methanogens were detected for the first time in 2005, which coincided with an increase in the gas generation rate. Several factors influencing the gas generation were identified including the occurrence of competing microbial groups, environmental conditions (especially pH) and high concentrations of inhibitive substances like volatile fatty acids and sulphide. The relative ratio of sulphate reducing bacteria compared to methanogens was shown to decrease considerably during the experiment. Microbiological findings were consistent with the>NNL Generalised Repository Model.

### **Modelling of microbial processes**

Kinetic models of microbial processes relevant to geological disposal have previously been included in the PHREEQC geochemical model. In the case of LLW disposal in the UK, a biogeochemical model (Generalised Repository Model, GRM) has been developed to model the redox evolution and microbial gas generation processes and has been validated using long term experimental data from the TVO gas generation experiment.

Other performance assessment models include the T2GGM developed to examine microbial gas generation in the Canadian deep geological repository. Recently, NAGRA have developed models to assess the sources and sinks of gas generation. Within the MIND project, PHREEQC and GRM were used to assist in the interpretation of microbial experiments and to form the basis of new modelling tools and approaches.

### **Limits of microbial life in an ILW repository**

MIND project studies indicate that pH in the range 10–11 represents a realistic upper limit for microbial nitrate reduction process, including the consumption of ISA and gluconate and organics present in plasticised PVC and bitumen. Still, the high pH adapted nitrate-reducing inoculum collected from a former lime kiln site showed some evidence of survival at pH 12.5. Methanogenesis is the lowest energy yielding process of relevance to ILW disposal and is expected to have the lowest pH tolerance. Studies of the TVO gas generation experiment imply that pH 9 represents a likely upper limit for active methanogenesis, although other toxicity effects and competition with sulfate reduction and fermentation processes may further reduce this threshold to pH 8. It is also evident that heterogeneity of pH and the occurrence of low pH micro-niches, where microbes may thrive, are important to defining such pH thresholds.

### **3.6.2 WP2 – Engineered barriers**

#### **Sulphide availability and its effects on canister corrosion**

Three laboratory experiments were performed at TUL/CV Rez in the anaerobic glove boxes ( $O_2 < 1$  ppm) under sterile and non-sterile conditions at 20°C and 35°C using the anoxic underground water from Josef URL. In the first experiment at 20°C, a strong increase of SRB population in biofilm and water samples was observed after 240 days. These findings coincided with the Electrochemical Impedance Spectroscopy (EIS) data, indicating a presence of a two-layer biofilm on the steel surface, which was confirmed using scanning electron microscopy.

In the second experiment at 35°C, EIS data indicated a presence of only a single protective biofilm layer after 293 days, which reduced the corrosion rate. The biofilm, as well as water samples, were dominated by SRB species *Desulfomicrobium* and *Desulfovibrio* spp. At 20°C and by *Desulfovibrio* spp. At 35°C. Despite different corrosion behaviour at 20°C and 35°C, no significant difference in corrosion rates was observed.

In the third experiment at 20°C, Czech synthetic bentonite pore water (SBPW) was used to simulate the effect of bentonite buffer. The anoxic underground water from Josef URL was used as a microbial inoculum. Under sterile conditions, the corrosion rate decreased with time to a value of 0.4 µm/a after 26 months. In the non-sterile case, the corrosion rate peaked at 5.4 µm/a after 6 months and decreased to 3.5 µm/a after 26 months, and extensive pitting corrosion was observed despite a domination of the nitrate reducing microorganisms in the samples caused presumably by a high nitrate concentration of SBPW.

In an anoxic experiment by EPFL in Opalinus clay with steel coupons embedded in bentonite in an anoxically drilled borehole, an autotrophic sulphate-reducing bacterium and a sulphide-producing organism were identified as primary producers. Their necromass was degraded by fermenting organisms producing low molecular weight organic acids such as acetic acid, which were utilized by heterotrophic sulphate-reducing organisms. Counts of aerobic heterotrophs increased until 1.5 years despite the anoxic conditions and remained viable until the last sampling after 5.5 years. It was suggested that bentonite contained adsorbed molecular oxygen, which was bioavailable. A clear increase in complex organic matter degraders and a decrease in sulphate-reducing organisms after 1.5 years was observed. This suggested that electron donors from the Opalinus clay, which may transiently fuel sulphate reduction, were rapidly depleted. After 5.5 years, the increase in complex organic matter degraders was reversed and the abundance of autotrophic sulphate-reducing primary producers increased again.

### **Microbial activity in bentonite buffer**

In 3- to 4-month experiments with different bentonites compacted to saturated wet densities of 1400 to 2000 kg/m<sup>3</sup>, sulphide-producing bacteria could be cultivated from all samples and for some bentonites a decrease of microbial counts with increasing wet density was observed. Beyond a swelling pressure of ~1000 kPa sulphide production was absent or was at the detection limit. Published data on turgor pressure, which can compensate for external pressure in prokaryotic cells, vary between 80 and 2000 kPa. Results from the MIND project suggest a limit at ~1000 kPa.

Fe(III) in bentonites Asha, MX-80 and Calcigel was reduced by sulphide under formation of elemental sulphur, Fe(II), and FeS, which rendered a sulphide immobilisation capacity of the clays of at least 40 µmol/g clay. Effective diffusion coefficients for sulphide in Asha bentonite compacted to saturated wet densities of 1750 and 2000 kg/m<sup>3</sup> were  $2.74 \cdot 10^{-11}$

and  $6.60 \cdot 10^{-12}$  m<sup>2</sup>/s, respectively. No sulphide breakthrough was observed for Calcigel, which completely immobilised added sulphide.

Irradiation of bentonite showed to a total absorbed dose of 19,656 Gy at a dose rate of 13 Gy/h did not sterilize bentonite under aerobic conditions. Indigenous bentonite microflora reaches even higher abundances under anaerobic conditions, which exemplified a need for further research on the effect of irradiation under anaerobic conditions.

### **Microbial activity in backfill and influence on plugs and seals**

High pH (>12) conditions imposed by the Ordinary Portlandite CEM I inhibited microbial nitrate reduction in the Boom Clay borehole water. However, SEM analysis indicated the presence of intact cells in the supernatants and putative biofilm structures on the cement. Similarly, at sulphate reducing conditions, high pH conditions inhibited microbial activity but did not eliminate microbial population. Alkaline pH > 10 in contact with concrete were suggested to likely inhibit the growth of bacteria. At the same time, microbial activity may decrease pH in high alkaline repository barriers to a certain degree.

### **WP3 – DNA extraction protocols for clay**

In a benchmark experiment, seven laboratories received 10 g of Opalinus Clay rock spiked with the Zymobomics cell mock. Every participating laboratory extracted DNA using their own method. The amount of extracted DNA ranged from 0.66 ng to 418 ng, while in theory ~4.5 µg DNA could be obtained. One method was outstanding in reassembling the mock community, while the other methods over- and underrepresented different operational taxonomic units.

## **3.7 Workshop on Post-closure Criticality Safety**

### **3.7.1 Introduction and background**

Criticality safety over long, post-closure, timescales is unique to geological disposal. Sharing of knowledge and approaches to demonstrating criticality safety will have clear benefits for WMOs. On 10. February 2020 a one-day workshop organized by the British WMO RWM and hosted by Nagra, on the topic criticality safety in the post-closure phase of a repository took place in Wethingen (Switzerland).

19 experts from 12 organizations (WMOs as well as research and technical support organizations) of eight European countries participated. This workshop aimed to allow (i) a transparent exchange of applied methodologies, knowledge gaps and results between the WMOs, which comprised relevant aspects as research, technology, implementation of measures for criticality safety and regulations and (ii) the identification of differences and commonalities between the methods and approaches to demonstrate criticality safety.

The specific objectives of this workshop were for each participating country to provide an update on their progress and plans for post-closure criticality safety. This should include:

- A brief overview of the inventory for disposal (i.e. is it just spent fuel, other types of waste etc)
- A brief overview of the regulation that needs to be demonstrated (i.e. who is the regulator and what do they ask for)
- An overview of the approach taken to demonstrate post-closure criticality safety
- An overview of future activities planned to further development of post-closure criticality safety

This aimed to answer some of the below questions:

- How to ensure that the line of argumentation for the criticality safety case between the different WMOs does not contradict?
- How to ensure that results from different WMOs do not contradict each other or, if they do, how to handle them in a transparent way?
- Which technical issues are similar for each WMO (e.g. uncertainties, assumed parameters etc; deterministic and/or probabilistic approach; consequence analysis yes or no) and where can/should we benefit from each other? What are the different regulatory requirements in each participating nation for post-closure criticality safety?

Presentations about the current status were given and Information from each WMO was collated, including:

- Inventory for disposal.

- Regulatory requirements.
- Approach to likelihood of post-closure criticality.
- If any consequence analysis is performed/planned.
- The time period of assessment.
- The criticality safety criterion used.
- Key assumptions in the approach.
- Identified future work

### **3.7.2 Potential for future co-operation and next steps**

Throughout the workshop, areas of potential collaboration were identified. These may be between the whole community or just a smaller number of participants (depending on applicability/similarities). From the list below, it should be recognised that there is quite a large amount of overlap between different areas, however they are separated to try and identify areas of interest and to potentially prioritise those areas seen as most important. The list below highlights some of the key areas identified:

- Communication of arguments - Public perception will be challenging for all, so clearly describing arguments for various stakeholders is important. This is especially true if the approach is not to completely rule out a criticality or if some consequence analysis is performed. Collaborative work could include discussions of approaches to communicating criticality safety to various stakeholders.
- Scenario development - Most approaches require the development of scenarios that are then assessed. The range of these scenarios could vary quite widely depending on the approach taken. For example, when considering probable geometrical changes to spent fuel there is a wide range of possibilities between intact fuel and fully degraded fuel, with the 'worst-case' not necessarily being straightforward to identify. Scenario development could also include out-of-package scenario development such as consideration of U and Pu migration and mobility behavior. An important area to also consider is the starting point of scenario development, that is what is assumed to happen between packaging and disposal during any interim storage stage. Collaborative work could include agreeing a reasonable approach to scenario selection and sensitivity studies based on these scenarios.

- Approach to burn-up credit (BUC) - It is envisaged that most of the approaches will require some form of BUC to demonstrate post-closure criticality safety of spent fuel. Even though the exact approach might be different, there are a lot of similar areas of development/challenge that could be collaborated on. These include:
  - Loading curve methodology: The methodology for developing loading curves and challenges associated with could be investigated as a group, such as whether a actinide only or actinide plus fission products approach is adopted and how this would be performed. A (somewhat) consistent methodology would assist in other areas such as validation and review.
  - Validation of data and models - It is obvious from the extensive list of required information for BUC that the effort required to validate a depletion code against such measurements is a considerable undertaking. A large source of PIE data is the OECD-NEA SFCOMPO database. However, this has not been 'peer-reviewed' and if various WMOs are reliant upon this data, it would be beneficial to review the data to ensure it is appropriately reported. There are also likely to be other validation requirements on nuclear data etc, that could be collaborated on.
  - Uncertainty approach – The BUC approach requires many uncertainties to be assessed, a methodology for completing this is demanding to complete and there may therefore be benefits in sharing knowledge and resource. Especially if the overall approach to BUC is somewhat consistent across WMOs.
  - Data requirements/compliance challenges – Along with validation of the model and data, there will be the outstanding challenge of demonstrating to the appropriate regulator that the methodology and data record requirements can be robustly complied with. Therefore, identifying the compliance challenges and means to address these will be important.
- Neutron absorber stability/persistence – The presence and stability of neutron absorbers is an important aspect. There has been work in various programmes to look at the formation and stability of beneficial species such as gadolinium and iron corrosion products. As multiple nations may rely on similar arguments, there would be benefit in ensuring 'state-of-the-art' knowledge is captured appropriately, especially if work has already been completed to minimise duplication.
- Approach to consequences assessment – Some WMOs utilise consequences assessments as part of their baseline, some use it as a 'what-if' assessments and

others do not plan to undertake assessments. The methodology/approach to assessing consequences is not straight-forward and therefore

- ISO Standard for fissile waste (ISO 22946) – The recently published ISO standard on fissile waste excludes fuel, however for those WMOs who deal with ILW there is a requirement on developing a lifecycle strategy for fissile wastes. As this is relatively new, there presents an opportunity to share best practice to align approaches.
- Knowledge management – The topic of knowledge management, both in terms of people/corporate knowledge and data/records, was discussed throughout. It was recognized that this is wider than just post-closure criticality safety, however there may be opportunities to identify suitable means to capture knowledge across WMOs so that important information is not lost.
- Waste acceptance criteria – As WMOs progress through siting, they will need to adopt a WAC programme at some point. Demonstration of what is known, and how robust this is will need to be shown to regulators and there may be opportunity to share best practice and approaches.

It has been proposed that the next step is to identify a method for further collaboration on the areas identified above. This will likely involve both WMOs and their supply chain. One potential option is to propose such work as a EURAD second wave project. If this is not accepted, alternative means of collaboration will need to be identified as there was a desire through the whole group to continue collaboration beyond 'update workshops/meetings' every two years.

### **3.8 MODARIA II**

MODARIA until now had two phases. The first phase ran from 2012 to 2015 and updated the BIOCLIM recommendations, particularly in terms of potential patterns of long-term climate change at local, regional and global scales, and sought to develop a common framework for addressing climate change in post-closure safety assessments /IAEA 20/. Following this, a work programme was established in a second phase with the aim of evaluating, updating and clarifying the BIOMASS methodology within the IAEA MODARIA II programme.

The BIOMASS methodology was developed between 1996 and 2001 as part of an overall IAEA programme /IAEA 03/. The methodology has proved very useful, providing a

systematic and transparent approach for biosphere assessment. However, since its publication, there has been considerable experience gained through its practical application, as well as further knowledge and experience gained from international collaborations and from scientific developments.

Several working group meetings have taken place as part of the MODARIA II programme, providing the basis for extensive collaborative work that has underpinned the BIOMASS enhancement programme. Early in the work programme, several fields for refinements for the BIOMASS methodology were identified as given in red in Fig. 3.1.

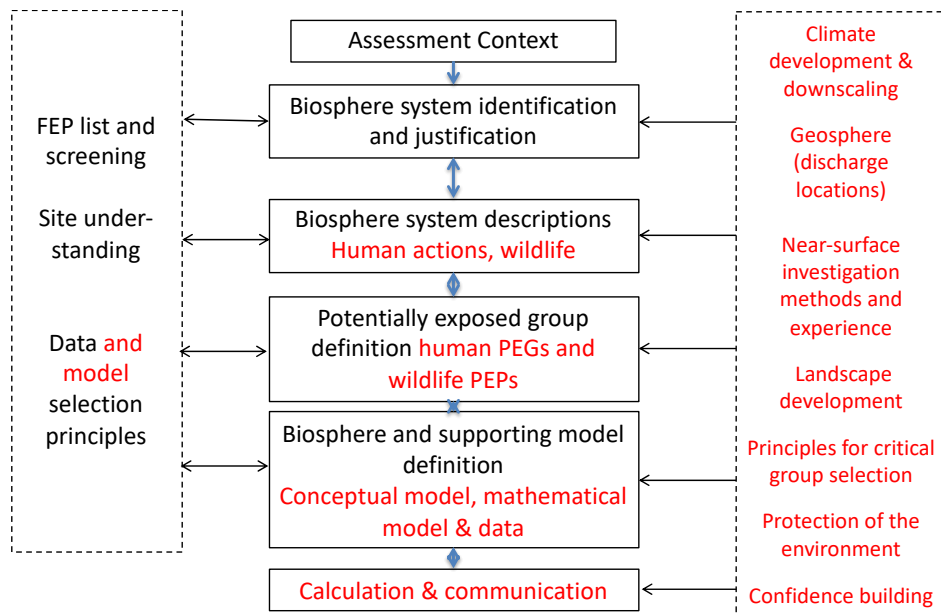


**Fig. 3.1** The BIOMASS methodology with refinements identified in red

The original BIOMASS methodology has been shown to provide useful guidance in helping to ensure consistency in the way in which the surface environment is represented in post-closure safety assessments for solid radioactive waste disposal facilities. There are many areas of important experience gained since 2001 covering:

- site characterisation,
- understanding of key processes that influence the headline assessment results, and hence areas for focussed consideration,
- approaches to addressing environmental change,
- approaches for explicitly demonstrating environmental protection,

- treatment of the geosphere-biosphere interface and
- regulatory developments and regulatory review, and hence, sufficiency of a safety assessment.

A report was drafted during the project period which provides guidance on how to represent the biosphere in post-closure safety assessments and the report will be published by IAEA. The components of the original methodology are retained but have been enhanced and some of the detail restructured based on experience. The report is intended to be suitable for use in various countries at different stages in the development of disposal options for a wide variety of different types of radioactive waste. It is recognised that individual countries have different regulatory regimes. The methodology has the flexibility to accommodate different types of assessment (from initial scoping studies through to inputs to safety cases submitted in support of licence applications) of various types of facility in diverse regulatory contexts.

The enhanced BIOMASS methodology, shown in cyclical form in Fig. 3.2 is consistent with the original. Experience has shown how system understanding plays a central role in safety assessments for radioactive waste disposal, especially for site-specific contexts, together with the associated degree of iteration and feedback. The integral role of the biosphere within the overall safety assessment is also emphasised. The enhanced methodology now recognises more clearly the need for iteration. Furthermore, whilst the structure is similar to the original, it is made clear that it is not a linear sequential methodology; the start point will depend on where you are in a programme.

It is further recognised that the methodology is not standalone, it is an important component of the overall safety assessment and safety case and there needs to be engagement with different aspects of the overall programme. The context for the biosphere assessment is set by that for the overall safety assessment to which it contributes, and the components of the biosphere assessment context are

- the purpose of the assessment, including the regulatory regime within which it is conducted, or which it is intended to inform,
- the endpoints of the assessment (e. g. individual doses to human health),
- the assessment philosophy, including management of uncertainty,
- the disposal system and the site context,

- the source term to the biosphere and associated interface,
- the time frames to be represented and
- the societal assumptions to be made.

The biosphere systems are first identified and justified, and then characterised through development of a high-level, qualitative narrative. A narrative is a text account of the development in time of the biosphere focusing on those aspects that are relevant to post-closure assessment. The narrative then provides the basis for a more detailed quantitative description, sufficient to support the assessment modelling. These biosphere representations are usually compatible with the changing climate and landscape projected to apply to the region of the disposal facility under the scenario being investigated.

After identifying, justifying and describing the biosphere systems adopted for assessment, the next step of the enhanced BIOMASS methodology is to develop associated conceptual and quantitative models of contaminant migration and potential exposure. In the enhanced BIOMASS methodology, which can be applied at any stage of project development, the following basic steps towards model development are identified, building on the biosphere system description:

- Develop a conceptual understanding of contaminant release, migration and potential exposure for each of the biosphere system(s) carried through to the assessment
  - Identify those biosphere components that are to be distinguished as separate features in the representation of mass and contaminant transport (i.e. distinct potentially contaminated environmental media)
  - Identify and characterise the PEGs (Potentially Exposed Group) that need to be explicitly addressed in the assessment
  - Develop conceptual models identifying the processes that result in contaminant transport between the biosphere components and give rise to potential exposure of the PEG
- Develop a mathematical representation for the FEP (Features, Events and Processes) comprising each of the conceptual models, taking account of the extent and quality of input data that will be available when the model is to be used

- Collate and justify the input data required by the mathematical models, drawing on the system description and taking account of the approach defined in the assessment context with regards to treatment of parameter uncertainties
- Implement, verify and validate the models

Given the uncertainties associated with the biosphere on timescales relevant to post-closure safety assessment, the associated models should aim to be no more complex than is necessary. It may be appropriate to assess potential impacts of contaminant releases to the biosphere by modelling a constant input of contaminants to the biosphere through to equilibrium to give constant annual-effective-doses for humans or-dose-rates for biota, or concentrations for non-radioactive materials. The ratios between these measures of impact and the input rates are typically termed biosphere dose conversion factors. Such constant ratios may apply if the biosphere is being modelled independently of other components of an assessment. Two considerations in determining whether such an approach is appropriate are whether inputs to the biosphere change only slowly compared with the timescale to achieve equilibrium and whether the characteristics of the biosphere also change only slowly compared with the timescale to achieve equilibrium.

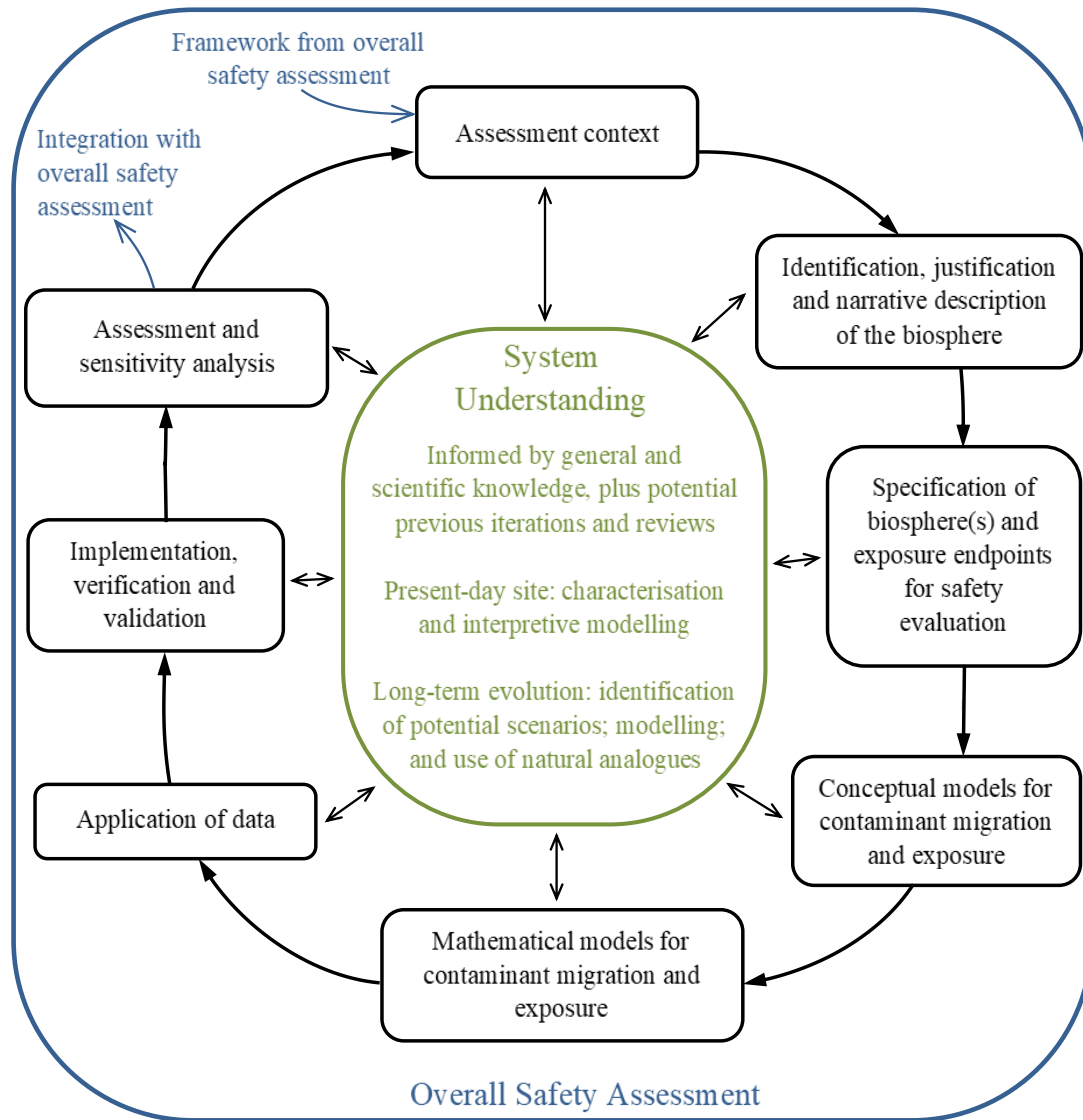


**Fig. 3.2** Schematic illustration of the enhanced BIOMASS methodology (in black) showing integration with the overall safety assessment (in blue) and the central role that is played by understanding of the disposal system (in green)

Experience gained through biosphere assessments conducted following the original IAEA BIOMASS programme has shown that the overall steps in the methodology remain relatively consistent across assessments conducted in a range of different contexts. The detailed structure of assessments undertaken within different programmes can be expected to differ, as appropriate to context, the overall safety case/safety strategy and the structure of the organisations undertaking the studies. Nonetheless, the methodology provides guidance towards robust yet pragmatic approaches to managing the

uncertainties inherent in assessing safety over long timescales. Consistent with the original BIOMASS methodology, the context for each assessment remains as playing a central role in guiding the approach and assumptions that are necessary.

MODARIA II has been strengthened the BIOMASS methodology in many ways, including:

- integrating biosphere assessment within the iterative process of the broader safety assessment and any associated safety case,
- drawing on updated understanding of long-term environmental change in helping to define the biosphere systems to be modelled,
- drawing on experience of contributing to and synthesising site characterisation and associated detailed modelling,
- drawing on experience on defining potential exposure groups and potentially exposed biota populations,
- recognising the importance of stakeholder engagement in helping to define assessments that address their specific interests and concerns.



## **4 Selected topics**

### **4.1 Bentonite re-saturation**

The selected topic "Bentonite re-saturation" has been worked at from two different angles. It comprises firstly of an active participation in the Task Force on Engineered Barrier Systems (TF EBS) that implied working on Task 9 – FEBEX in-situ test, and secondly of a first step for transferring the model concept for bentonite re-saturation realised in code VIPER /KRÖ 11/ to the COMSOL Multiphysics code.

#### **4.1.1 Task 9 – FEBEX in-situ test<sup>3</sup>**

##### **4.1.1.1 Test case description**

The FEBEX (Full-scale Engineered Barriers Experiment in Crystalline Host Rock) in-situ test was a full-scale test conducted over 18.4 years in the Grimsel URL (Switzerland) managed by NAGRA. It was based on the ENRESA AGP Granito (Deep Geological Disposal, Granite) reference concept. A 70.4 m long drift with a circular section 2.28 m in diameter was excavated in the Grimsel granite. In the last 17.4 m of the gallery, two electrical heaters of dimensions and weight equivalent to those considered in the ENRESA and NAGRA concepts were emplaced and in the remaining space compacted bentonite blocks were emplaced. The test zone was closed with a concrete plug (see Fig. 4.1).

The experiment was instrumented with sensors monitoring the thermo-hydro-mechanical processes taking place in the clay barrier and in the surrounding Grimsel granite. The experiment was in operation for five years. Thereafter, the outer heater was switched off and the outer half of the experiment was dismantled, whereby samples were taken from various points of the rock, the concrete and the bentonite buffer. During this first dismantling, the remaining half of the experiment, including the second heater, continued in operation. This remaining half of the experiment was in operation for additional 13.2 years. Thereafter, the experiment was completely dismantled and, as before, samples from various points were taken.

---

<sup>3</sup> Most of the text in this section is copied from the Task Description.

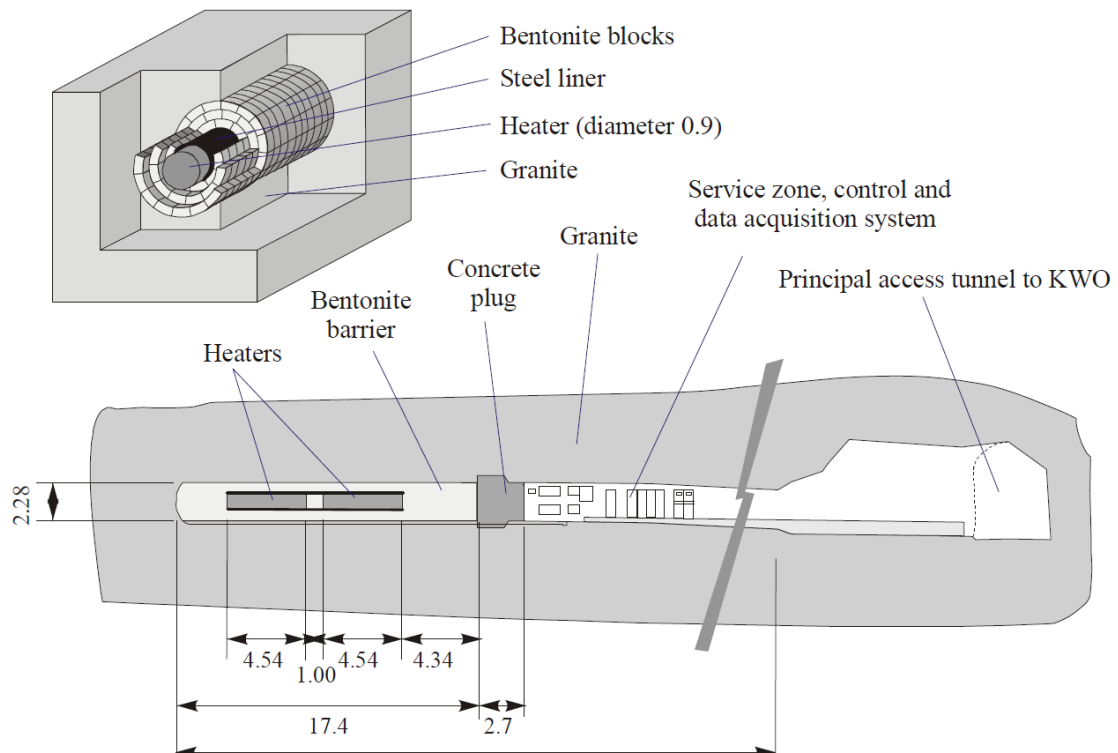


**Fig. 4.1** FEBEX "in situ" test layout; from /ENR 00/

Of interest for Task 9 – FEBEX in-situ test are several cross-sections as well as specific points along the FEBEX-tunnel. They are depicted in Fig. 4.2. (For reasons discussed in the following section, only a few cross-sections could be considered for the present work, though.) The experimental set-up during stage 2 is depicted in Fig. 4.3. Furthermore, the data along two axial segments, depicted in Fig. 4.4 are requested. Characteristic periods of the experiment are listed in Tab. 4.1. The periods that are relevant for the models are compiled in Tab. 4.2. The work described in the following refers to stages 1 and 2 which are defined as the period until dismantling heater 1 and the subsequent period until dismantling heater 2.

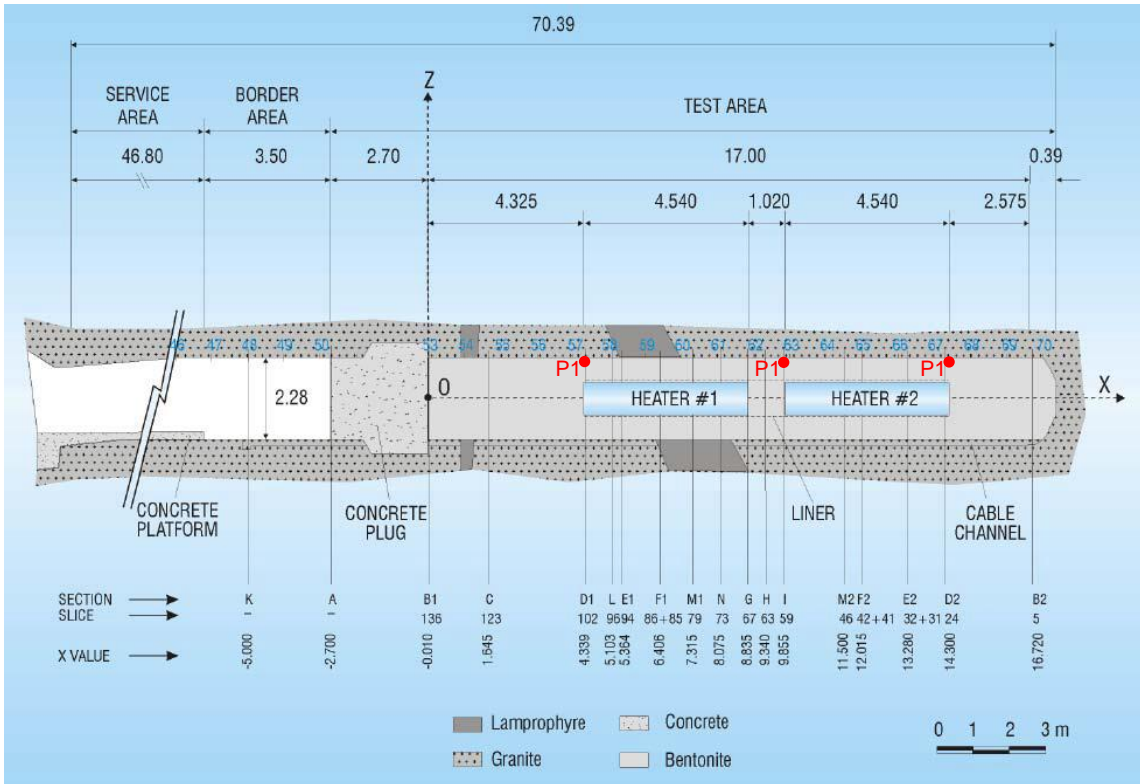


Fig. 4.2 General layout for stage 1 of the FEBEX in situ test; from /BÁR 03/

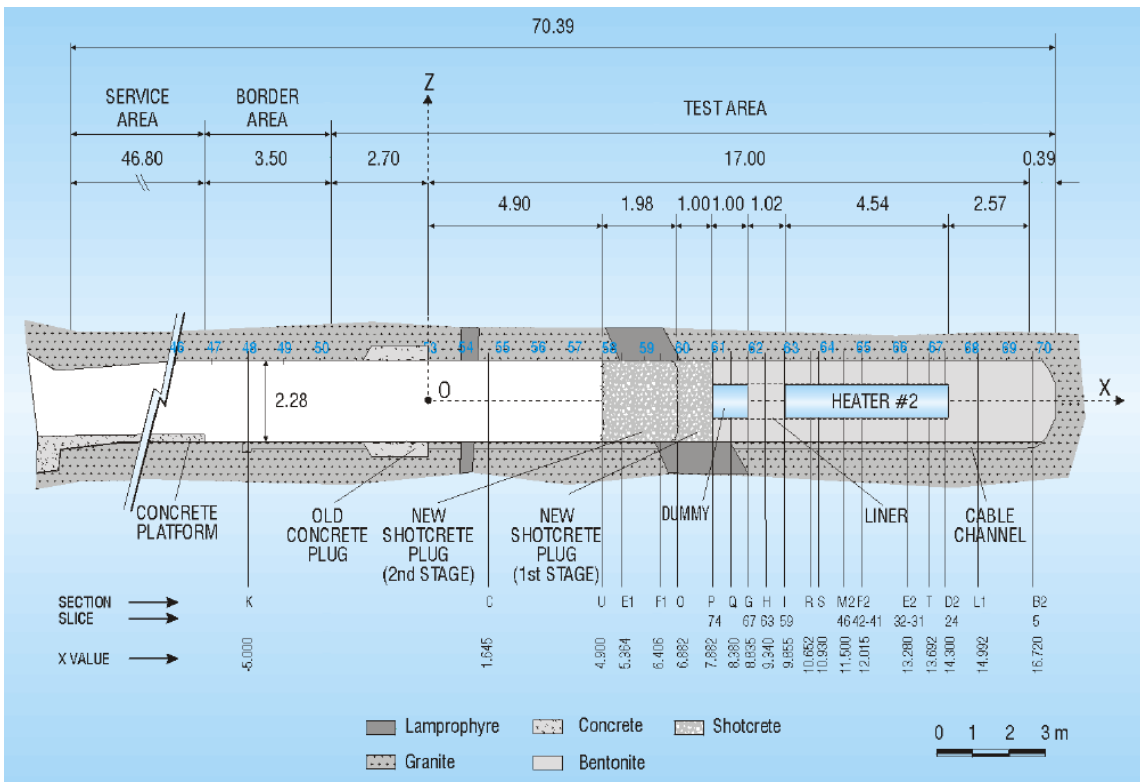
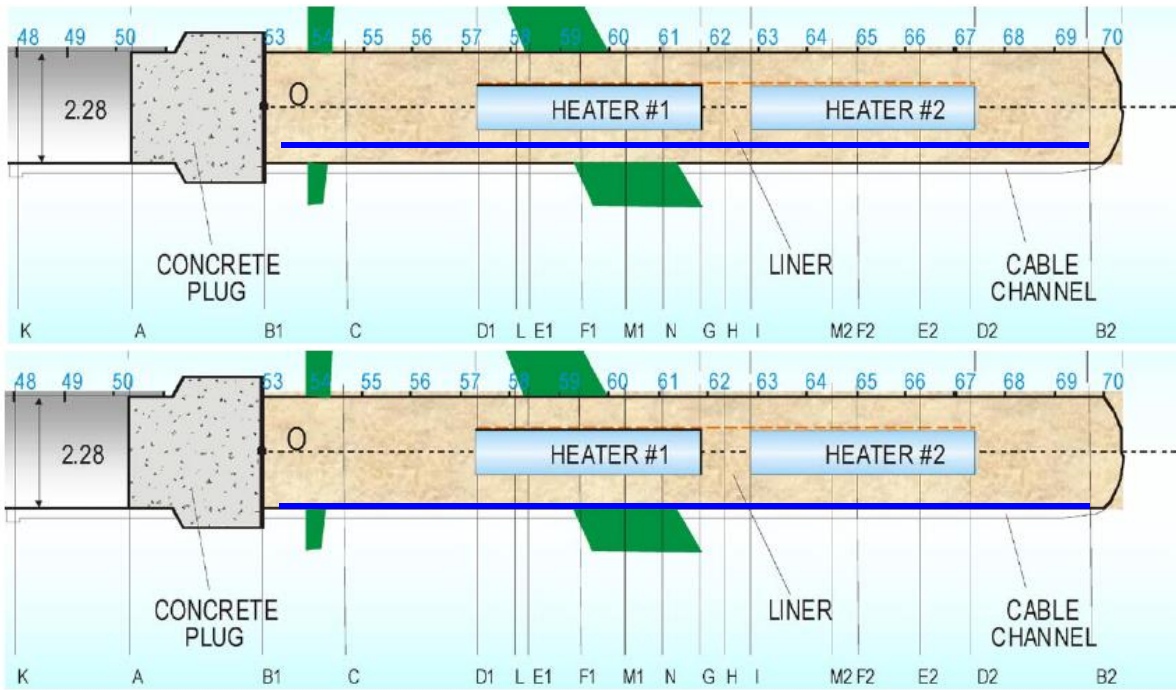


Fig. 4.3 General layout for stage 2 of the FEBEX in situ test; from /BÁR 03/



**Fig. 4.4** Position of axial segments AS1 (left) and AS2 (right) /BÁR 03/

**Tab. 4.1** Characteristic periods of the experiment

Event	Date	Day relative to the start of the heaters
Start of tunnel excavation	25.09.1995	-521
End of tunnel excavation	30.10.1995	-486
Start of installation	01.07.1996	-241
End of installation	15.10.1996	-135
Heaters switch on (day 0)	27.02.1997	0
Heater #1 switch off	28.02.2002	1827
End of first dismantling	19.07.2002	1968
Start demolition of the 1 <sup>st</sup> section of the plug	07.04.2015	6613
End demolition of the 1 <sup>st</sup> section of the plug	17.04.2015	6623
Heater #2 switch off	24.04.2015	6630
Start demolition of the 2 <sup>nd</sup> section of the plug	27.04.2015	6633
End demolition of the 2 <sup>nd</sup> section of the plug	08.05.2015	6644
Start dismantling of buffer until heater #2	18.05.2015	6654
Extraction of heater #2	04.06.2015	6671
End of dismantling	20.07.2015	6717

**Tab. 4.2** Characteristic periods for the models

Event	Day relative to the start of the heaters
Begin of wetting	-135
Begin of power-controlled heating	0
Begin of temperature-controlled heating <sup>4</sup>	51
Heater #1 switch off	1827
Time of post-dismantling data acquisition	1968
Heater #2 switch off	6630
Time of post-dismantling data acquisition	6717

#### 4.1.1.2 Model concept

Contrary to most other contributions to Task 9, no fully coupled THM-approach is used here but only coupling of the temperature calculations to the hydraulic simulation. The influence of water flow on the temperature field is neglected. The thermal calculations are done first with an axisymmetric 2D-model using the resulting temperature fields as input for the calculation of the non-isothermal water uptake

---

<sup>4</sup> See “Initial and boundary conditions“ in section 4.1.1.3 for details

For stage 2 the changes in the system due to excavation and renewed plugging are neglected. Heater 1 is just switched off at the end of stage 1.

The water uptake code allows only for 1D- and axially symmetric 1D-model domains. Possible re-saturation effects in the direction of the system axis can therefore not be covered by this model. Unfortunately, this excludes most of the cross-sections of interest as defined in the task description. Best met by these restrictions are cross-sections that are orthogonal to the system axis and either cutting through the barycentre of the heaters or being located at a certain distance to the heaters as well as to the tunnel ends. This leaves sections C, F1, and F2 for modelling. Section F1, however, is crossing the slanted lamprophyre layer which might have disturbed axial symmetry for the thermal model. It is therefore also skipped for this investigation.

The granite at the Grimsel site has a permeability around  $10^{-18} \text{ m}^2$  which is comparatively high and is assumed to provide as much water as the bentonite can take up. Modelling of the flow field in the rock is thus not required.

The 135 days of isothermal wetting preceding the heating period are also simulated. The resulting humidity distribution is used as initial condition for simulation of the non-isothermal water uptake. Note that this allows for keeping the model time in sync with the beginning of heating.

The following data are acquired from the thermal model:

- (1) Power uptake of heaters 1 and 2 after day 61
- (2) Radial temperature profiles in cross-sections
  - D1, I, and D2 as requested by the task description
  - C and F2 for water uptake calculations
- (3) Axial temperature profiles along segments AS 1 and AS 2
- (4) Evolution of temperature at P1 of sections D1, I, and D2

From the hydraulic model the following data are derived:

- (5) Distribution of relative humidity in sections C and F2
- (6) Evolution of relative humidity at three/two points in sections C and F2
- (7) Distributions of water content and degree of saturation at day 1968

Not calculated because of the model simplifications are evolutions of total stress and distributions of dry density at days 1968 and 6717.

### 4.1.1.3 Thermal model

#### Geometry and numerical grid

Heaters as well as the tunnel have a circular cross-section and there are no relevant anisotropies in the granitic host rock. The model for stage 1 is therefore chosen to be 2D-axisymmetric with a length of 50 m and a radius of 45 m. The radius has been chosen according to a numerical pre-test where the maximum temperature increases at the outer boundary at 45 m did not exceed 1.5°C after 6717 days. This condition is important to ensure that the error by closing the outer boundaries to heat flow remains minimal. A 3D-view of the full model as well as a cut-out in 2D is depicted in Fig. 4.5.

The mesh is chosen in such a way that the highest spatial resolution can be found where the highest temperature gradients are expected. The highest grid density can therefore be found at the heaters with about 5 elements per meter with slightly varying size in the radial direction. In total there are 3793 triangular elements that are expanded into 3D-space by axial symmetry and 13484 nodes. An impression of the mesh is given in Fig. 4.6.

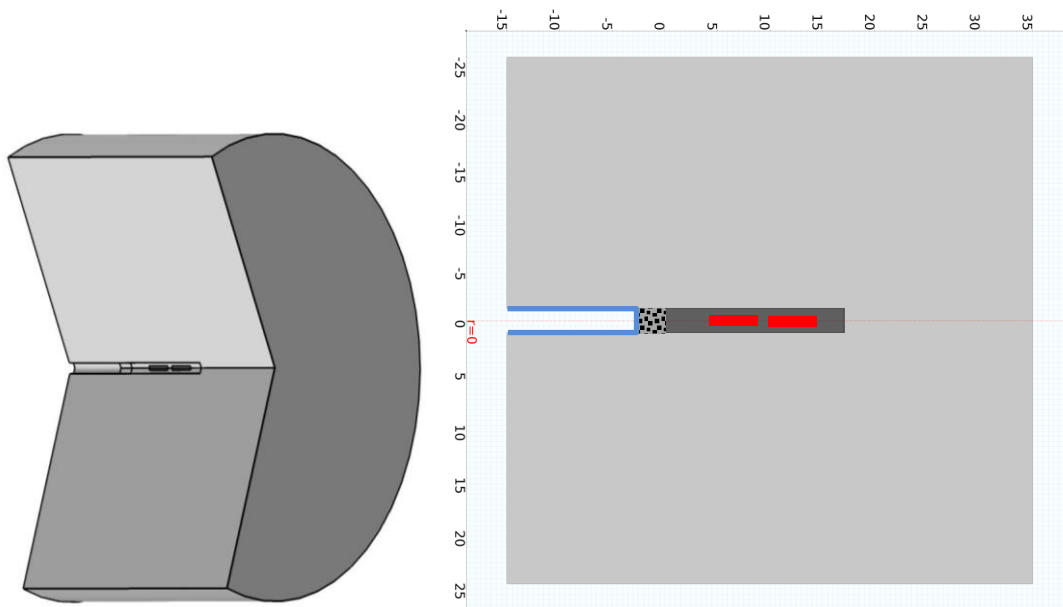


**Fig. 4.5** Domain of the thermal model; left: full model in 3D, right: cut-out in 2D

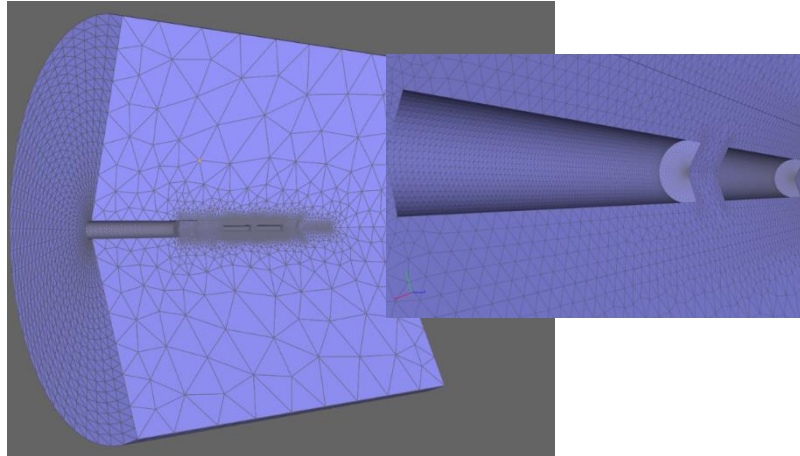


**Fig. 4.6** Numerical grid; left: opened whole domain, right: close-up

### Mathematical model

The heat flow problem is solved with the help of code COMSOL. In the heat transport module, the following equation is numerically solved but the convective term is not active here:

$$(1) \quad \rho C_p \frac{\partial T}{\partial t} + \rho C_p \mathbf{u} \cdot \nabla T = \nabla \cdot (k \nabla T) + Q \quad (4.1)$$

- $\rho$  - density [kg/m<sup>3</sup>]
- $C_p$  - specific heat capacity [J/(kg K)]
- $T$  - temperature [K]
- $t$  - time [s]
- $\mathbf{u}$  - velocity vector [m/s]
- $k$  - thermal conductivity [W/(m K)]
- $Q$  - heat source/sink [W/(m<sup>3</sup> s)]

### Material data

The model comprises four materials which are granite, bentonite buffer, steel heaters and concrete for the tunnel plug. The parameters for granite and concrete could be taken from the COMSOL material data library. The heater materials are approximated by steel AISI 4340, for which the parameters are also available from the COMSOL-library. This material has been envisioned for the steel dummy as well that replaced heater 1 partly after the first dismantling. Buffer data are taken from /GEN 19a/ and /KRI 07/ (see foot-notes). The data are compiled in Tab. 4.3.

**Tab. 4.3** Material parameters for the thermal model

	<b>granite</b>	<b>concrete</b>	<b>buffer</b>	<b>heaters</b>
thermal conductivity [W/(m K)]	3.3	1.8	1 <sup>5</sup>	44.5
specific heat capacity [J/(kg K)]	850	880	800 <sup>6</sup>	475
density [kg/m <sup>3</sup> ]	2600	2300	2780	7850

### **Initial and boundary conditions**

An initial temperature of 12°C is assumed throughout the system. The same temperature is assigned to the surfaces of tunnel and of the plug at all times. The faces and the lateral surface of the cylindrical piece of granite that defines the model domain are assumed to be thermally insulated for the whole modelling time also.

Most complex are of course the boundary conditions for the heaters. From day 1 to day 21 a constant power of 1200 W is fed into each of the heaters. Between days 21 to 53 the power is increased to 2000 W. After that period, the temperature of the canister surface is controlled by varying the heater power and successively switched up to 95°C, 99°C, and 100°C from day 53 to day 61. The surface temperature of 100°C is ascribed further on for the respective running time of the heaters. Heater 1 is switched off on day 1827 in the model, heater 2 on day 6630. Excavation is assumed to be represented by the results for day 6717.

### **Model performance**

Thermal simulations are performed on a grid with 3793 triangular 2D-axisymmetric elements and 13484 nodes. Five elements are assigned to the distance across the buffer. Running time of the model is 24 s including stage1 and stage 2. Note again, that stage 2 is approximated by simply switching off heater 1.

---

<sup>5</sup> Relates to a degree of saturation of S=0.85 according to Annex 2 in /GEN 18/

<sup>6</sup> Chosen erroneously after /KRI 07/; better fitting would have been using 750 J/(kg K) according to the Task Description.

## Results

### Temperature

As mentioned above, the temperature increase at the boundary of the granitic block was checked. According to the results, the temperature increases at the observation point after 6717 days by 1.53°C as indicated in Fig. 4.7.

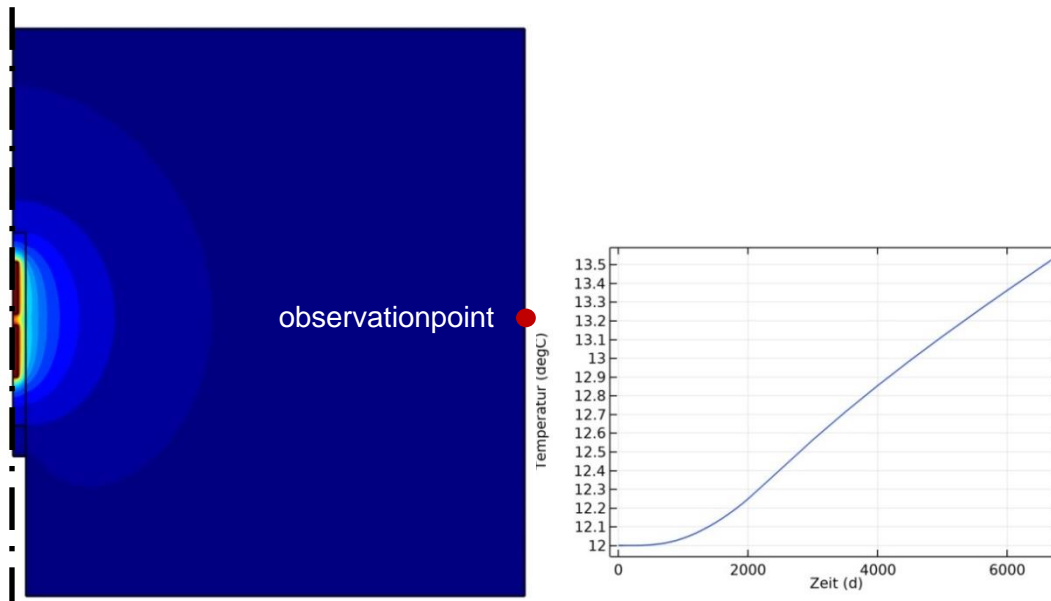


**Fig. 4.7** Temperature field after 18 years of heating;  
left: contour lines and temperature observation point (red dot)  
right: breakthrough temperature at observation point

With respect to temperature, the following data are either requested by the task description or required for the subsequent re-saturation modelling:

Evolution of temperature at P1 of sections D1, I, and D2 (see Fig. 4.8)

Radial temperature profiles in cross-sections D1, I, and D2 (see Fig. 4.9)

Axial temperature profiles along segments AS 1 and AS 2 (see Fig. 4.10)

Radial temperature profiles in sections C and F2<sup>7</sup> (see Fig. 4.11 and Fig. 4.12)

---

<sup>7</sup> for water uptake calculations

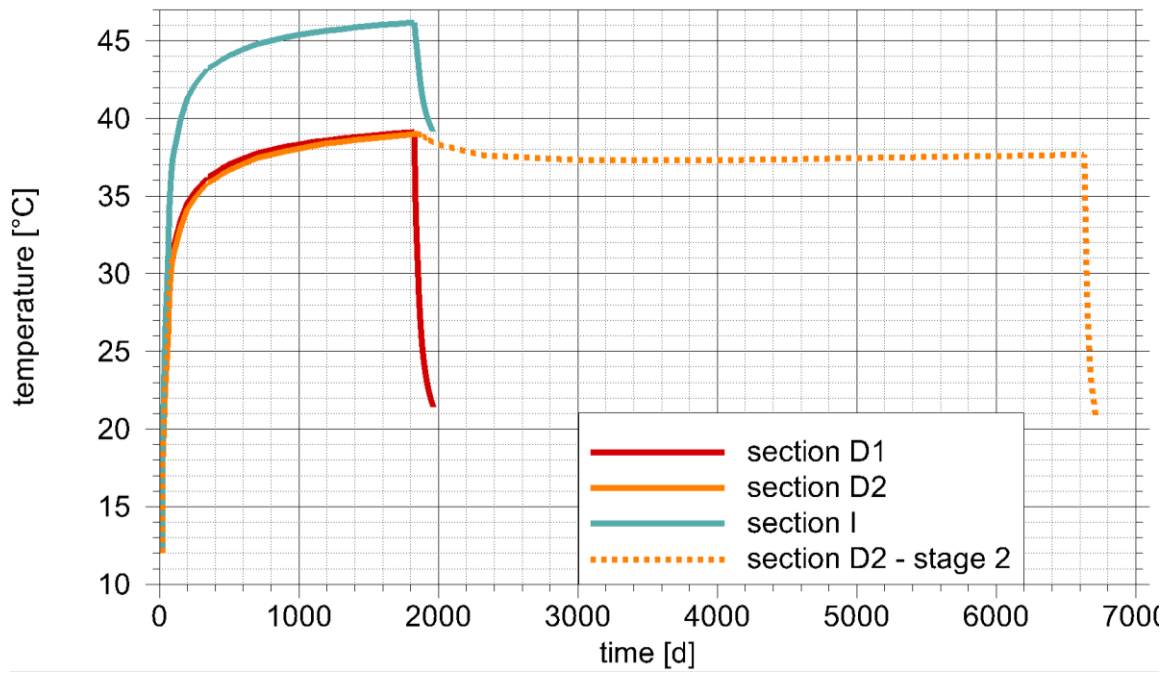


**Fig. 4.8** Temperature evolution at point P1 on sections D1, D2, and I

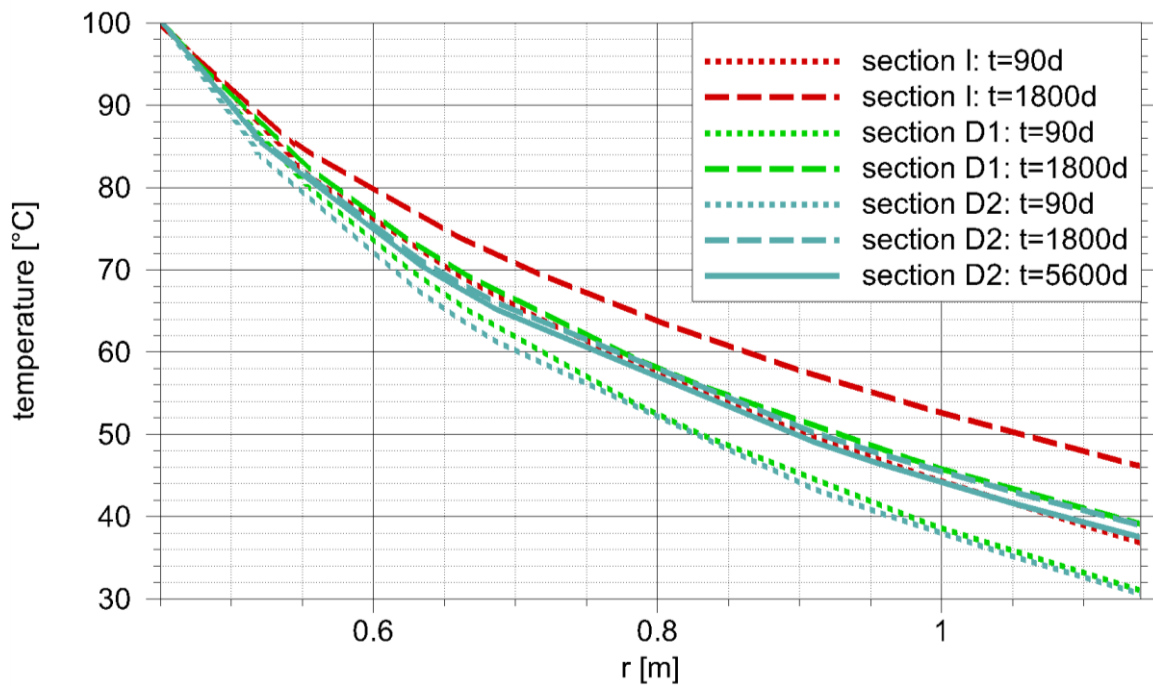


**Fig. 4.9** Temperature for sections I, D1 and D2 at 90, 1800, and 5600 days

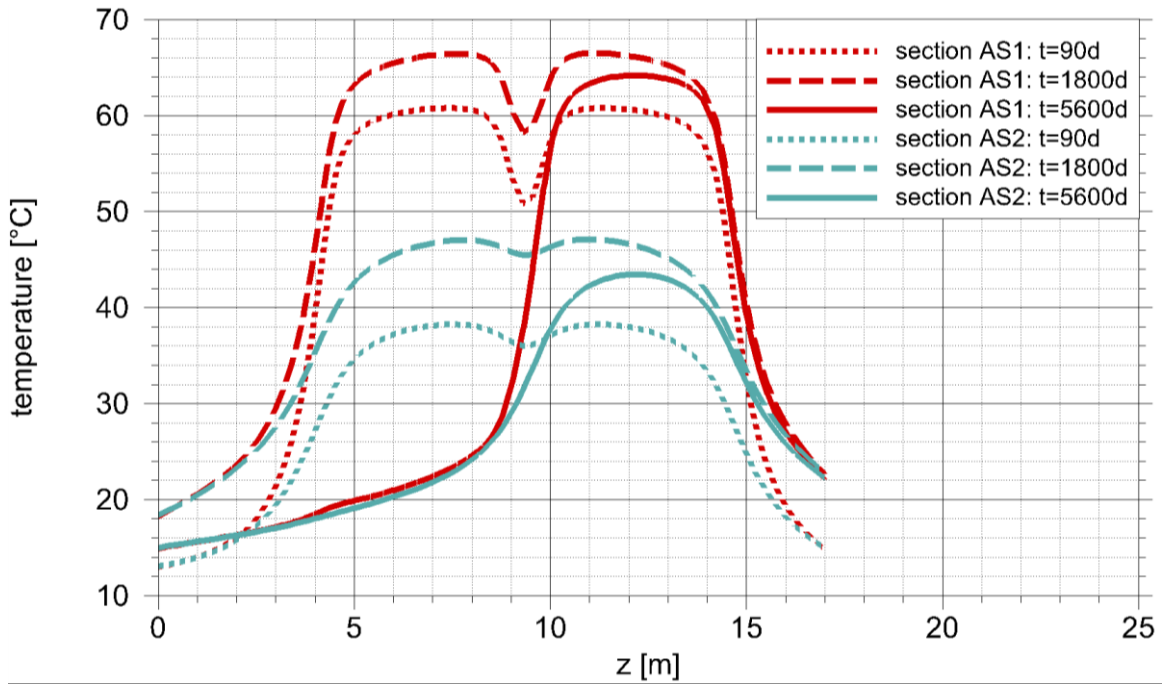


**Fig. 4.10** Temperature for axial sections AS1 and AS2 at 90, 1800, and 5600 days

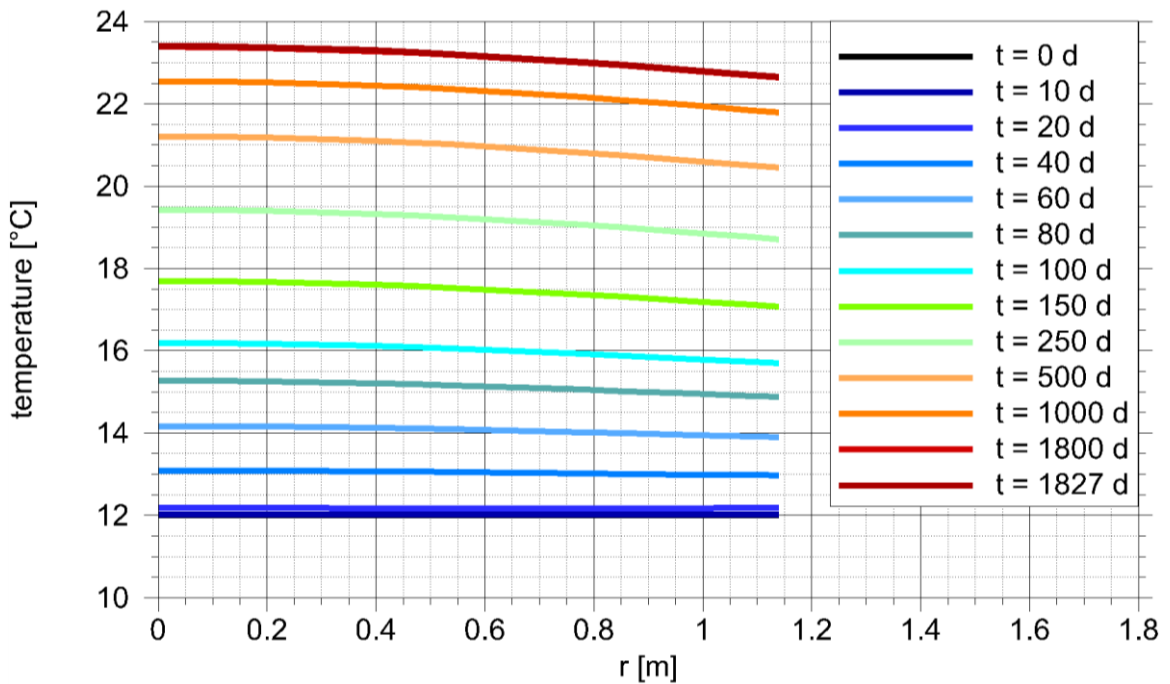


**Fig. 4.11** Transient radial temperature profiles in cross-section C

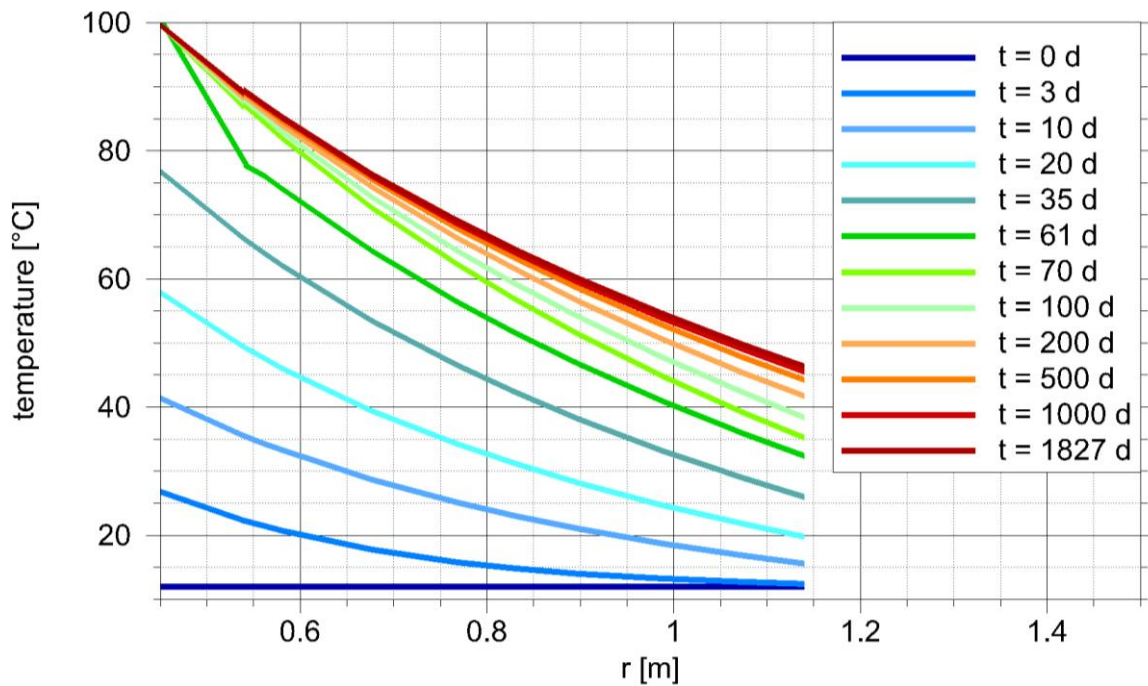


**Fig. 4.12** Transient radial temperature profiles in cross-section F2

*Evolutions of heating power*

Back calculated from the temperature gradient at the respective heater surface is the power consumption over time. It is shown for stage 1 in Fig. 4.13 and for stages 1 and 2 in Fig. 4.14.

As has to be expected, the calculations show similar curves for heaters 1 and 2 during stage 1 (see Fig. 4.13). After switching off heater 1 there is a slight increase of power consumption in heater 2 to compensate the loss of heat from previously neighbouring heater 1 (see Fig. 4.14). Contrary to the measurements, the simulations do not reproduce the increase of power consumption that results from the increase of thermal conductivity due to increasing water content because this coupling has been neglected.

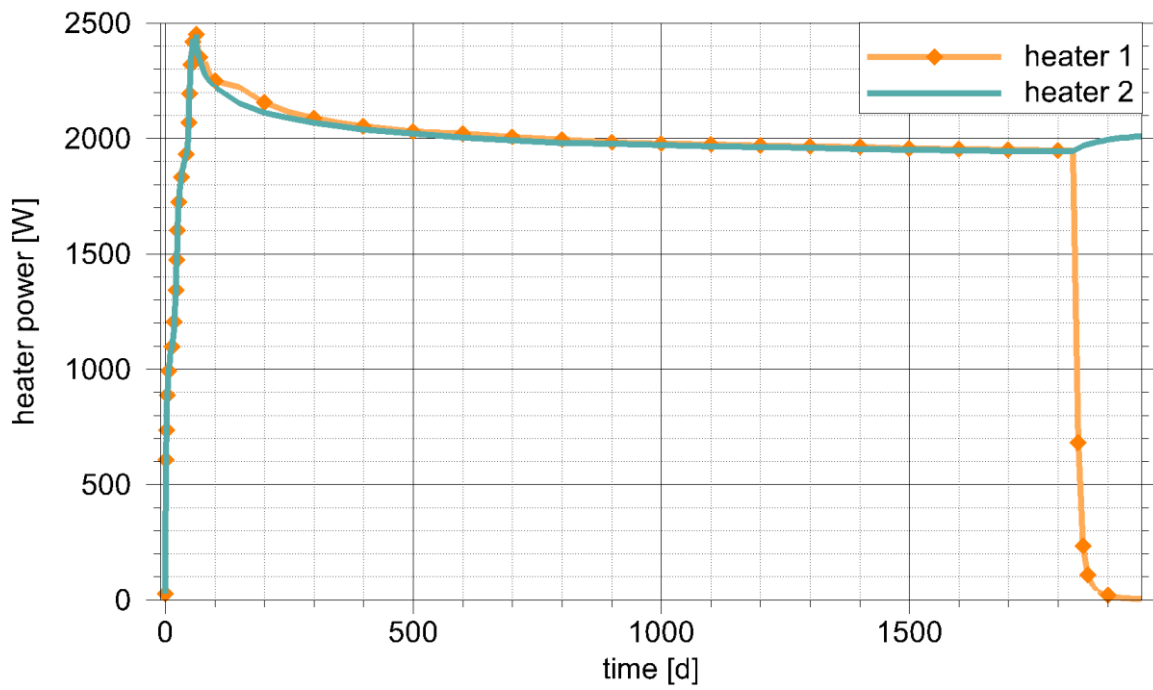


**Fig. 4.13** Evolution of power for heaters 1 and 2 during stage 1 at  $z=6.60\text{m}$

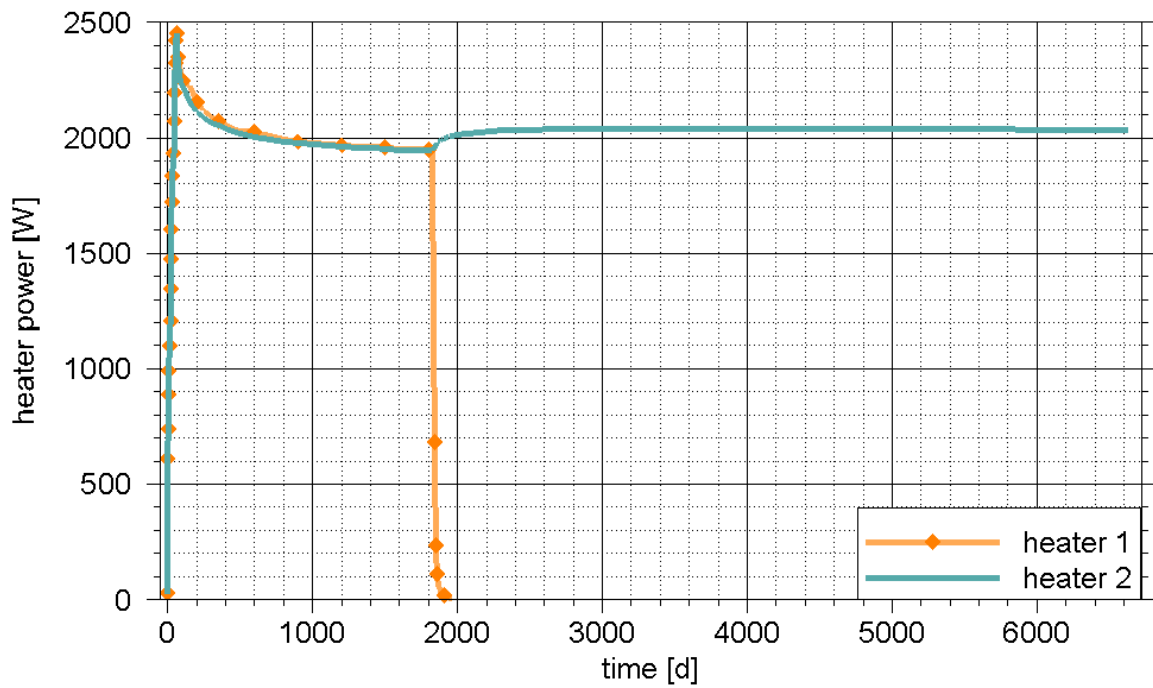


**Fig. 4.14** Evolution of power for heaters 1 and 2 during both stages at  $z=6.60\text{m}$

#### 4.1.1.4 Water uptake Model

##### Geometry

The restriction of the re-saturation simulating code VIPER to 1d-axial symmetries implies that cross-sections of the FEBEX-tunnel with axial components of heat flow are not suitable for modelling. What have been looked for are thus sections where the temperature gradient is orthogonal to the tunnel axis. As a basis for the choice of appropriate cutting planes Fig. 4.15 shows exemplarily the contour lines of the temperature field around the heaters after 1800 days. Apparently, the condition of no axial heat flux is met in the middle of the heaters, in the middle between the heaters and close to the tunnel plug.

Illustrated in Fig. 4.16 are the cross-sections of interest in the task description in relation to tunnel and heaters. Sections E1 and H do not meet the requirement of no axial heat flow but sections C and F2 do so and are thus investigated further on. Fig. 4.17 shows the geometry of the re-saturation models.

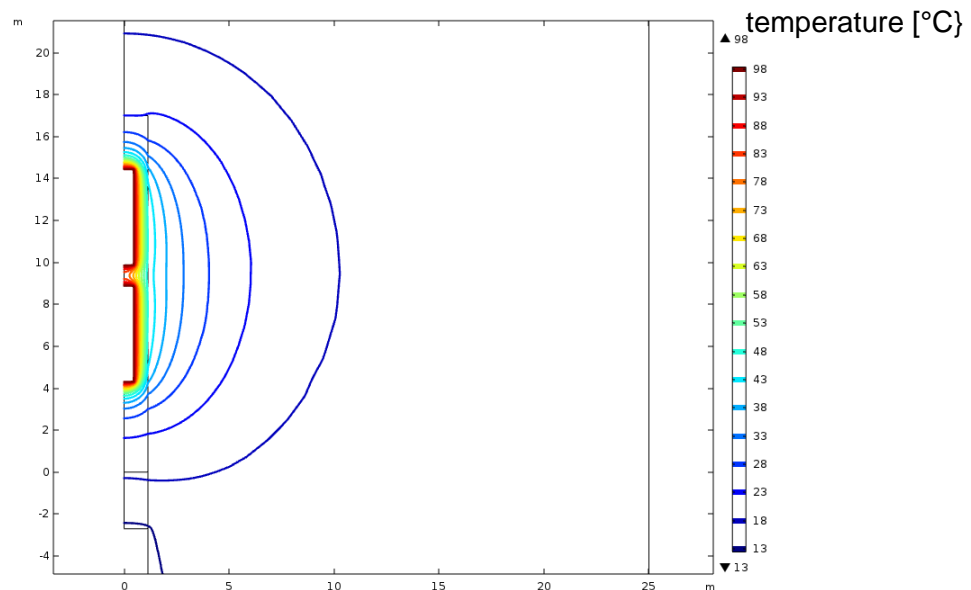


**Fig. 4.15** Temperature isolines around the heaters after 1800 days

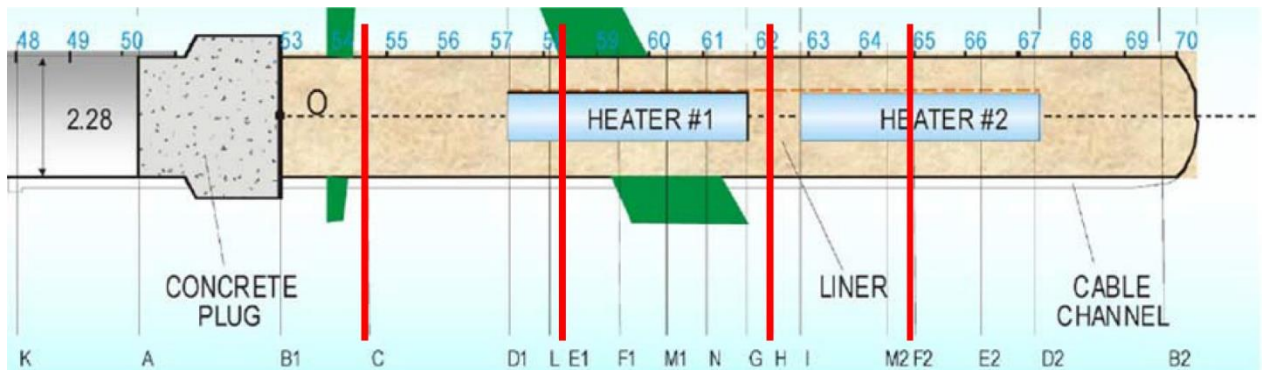


**Fig. 4.16** Experimental setup with the cross-sections of interest marked in red

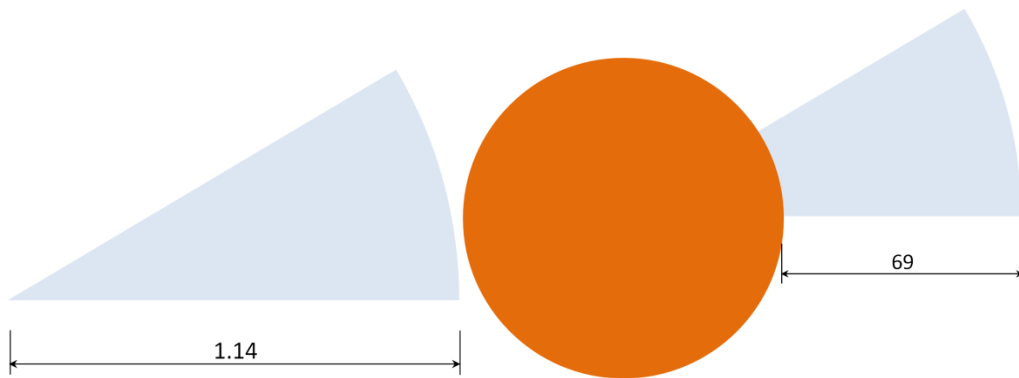


**Fig. 4.17** Model domain for the buffer in cross-sections C (left) and F2 (right)

### Code and equations

The code VIPER /KRÖ 11/, /KRÖ 17/ is used to simulate water-uptake and re-saturation of the bentonite. VIPER considers one-dimensional, axial symmetric wetting under unrestricted or restricted access to water, and includes vapour diffusion in the pore space, water diffusion in interlamellar space, and instantaneous exchange of water between these two spaces using an adsorption isotherm. Non-isothermal problems can be solved by using pre-determined transient temperature fields as input.

The conceptual background is therefore basically a double-continuum model which is composed of the intergranular pore space and the interlamellar space of the clay grains. Balance equations were set up for water vapour in the pore space as well as for hydrated water in the interlamellar space. In each balance equation, just one migration process is considered; vapour diffusion in the pore space and diffusion of hydrated water in the interlamellar space:

$$(2) \quad \frac{\partial(\Phi \rho_v)}{\partial t} - \nabla \cdot (\Phi \tau D_m \cdot \rho_v) = \rho_v \tilde{\tau} \quad (4.2)$$

$$(3) \quad \rho_d \frac{\partial w}{\partial t} - \rho_d \nabla \cdot (\tau_{hyd} D' \nabla w) = \bar{r} \quad (4.3)$$

#### Symbols

- $\Phi$  - porosity [-]
- $\rho$  - density [ $\text{kg m}^{-3}$ ]
- $t$  - time [s]
- $\tau$  - tortuosity of the pore space [-]
- $D_m$  - coefficient of binary vapour diffusion in air [ $\text{m}^2 \text{s}^{-1}$ ]
- $w$  - gravimetric water content of the bentonite [ $\text{kg}_{\text{water}} \text{kg}_{\text{solids}}^{-1}$ ]
- $\tau_{hyd}$  - tortuosity of the interlamellar space [-]
- $D'$  - coefficient of diffusion of the interlamellar water [ $\text{m}^2 \text{s}^{-1}$ ]
- $\bar{r}$  - source of interlamellar water [ $\text{kg m}^{-3} \text{s}^{-1}$ ]
- $\tilde{r}$  - source of vapour [ $\text{kg m}^{-3} \text{s}^{-1}$ ]

#### Indices

- $d$  dry state of the bentonite
- $v$  vapour

The equations are linked by the process of hydration that is idealised as an instantaneous water exchange according to an isotherm<sup>8</sup>, an equivalent to the more commonly used retention curve. Note that the isotherm changes shape with temperature, which is appropriately accounted for in the model. The model concept is schematically depicted for a horizontal two-dimensional domain in Fig. 4.18.

---

<sup>8</sup> In the context of this report, the expression “isotherm” denotes the relationship between water content and relative humidity at a constant temperature.

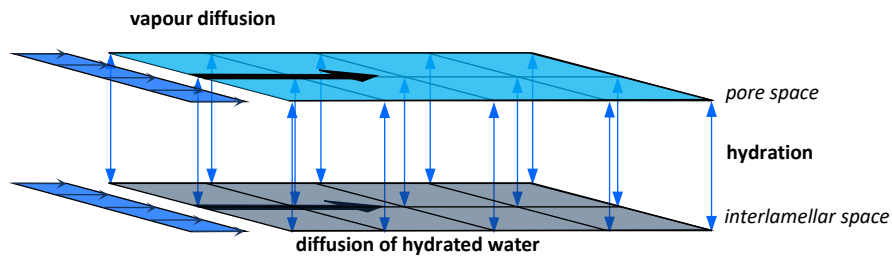


**Fig. 4.18** Processes acting according to the extended vapour diffusion model; from /KRÖ 11/

Possible boundary conditions are

- Full saturation in terms of vapour saturation density and maximum water content,
- Vapour saturation density but initial water content,
- Water inflow rate, or
- Closed boundary.

Initial conditions are given as a water content distribution.

### Material data

Crucial for the model is the temperature-dependent isotherm. The approach realised in VIPER starts with an established isotherm which is – as the name says – valid for a specific temperature. Such an isotherm for FEBEX-bentonite has been provided for Task 1 with the non-isothermal laboratory test by CIEMAT /VIL 05/. In order to provide a continuous formulation for VIPER a polynomial of degree 5 has been fitted to the discrete data points (see Fig. 4.19) /KRÖ 08/.

Dependence on temperature is then introduced by a factor depending on temperature and relative humidity that has been based on data for MX-80 bentonite /KRÖ 11/. The family of curves resulting from applying such a deviation function is depicted in Fig. 4.20. Note that the maximum influence of temperature lies in the range of 70 % relative humidity.

The remaining parameters required by the model are listed in Tab. 4.4, including their source.

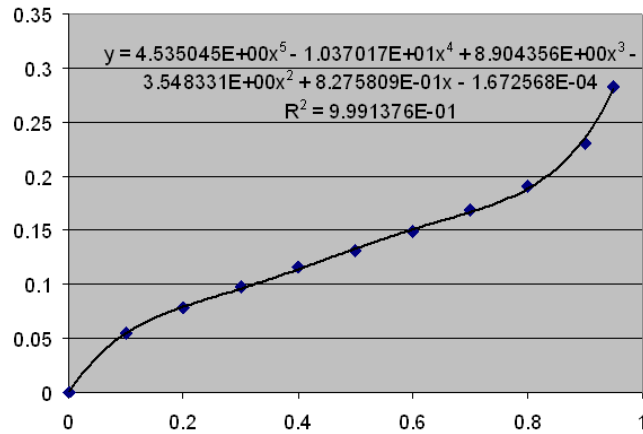


**Fig. 4.19** Mathematical approach for the isotherm for unconfined FEBEX-bentonite /KRÖ 08/

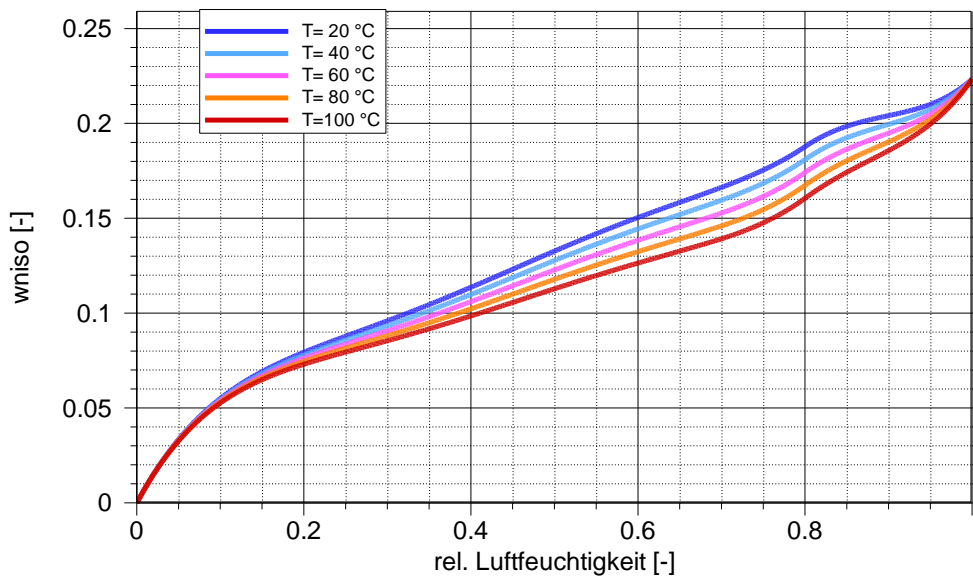


**Fig. 4.20** Temperature-dependent isotherm for confined FEBEX-bentonite /KRÖ 08/

**Tab. 4.4** Material parameters for the re-saturation model

parameter	value	unit	remarks
tortuosity $\tau$	0.65	[-]	general experience
end porosity $\Phi_e$	0.05	[-]	guess based on /PUS 90/
density of the solids	2700	[kg/m <sup>3</sup> ]	/VIL 05/
density of the interlamellar water	1000	[kg/m <sup>3</sup> ]	(Assumption)

## Initial and boundary conditions

The following boundary conditions hold for the entire modelling time:

Maximum water content at the granite contact (1.14 m): 22.3 %

Closed boundary at the axis (0 m) and at the heater surface (0.45 m), respectively

The parameters for the initial state of the re-saturation model are compiled in Tab. 4.5.

**Tab. 4.5** Parameters for the initial state of the re-saturation model

parameter	value	unit	remarks
bentonite dry density $\rho_b^9$	1600	[kg/m <sup>3</sup> ]	Task description
relative humidity $r_h$	37.9	[%]	guessed from /AIT 03/
water content	11.0	[%]	from $r_h$ and isotherm
porosity $\Phi_i$	23.1	[%]	geometric considerations

## Model performance

Re-saturation simulations are performed on a grid of 100 1D-axisymmetric elements with 101 nodes. A characteristic running time has been 186 s which includes the pre-heating stage of 135 days, stage1 and stage 2.

## Results

The results of the re-saturation modelling are given in terms of either relative humidity or water content as distributions at a specific point in time or as breakthrough curves:

Distributions of relative humidity

Section C at the end of the pre-heating stage (Fig. 4.21)

Section C at 90, 300, and 1800 days (Fig. 4.22)

Section C at 90, 300, 1800, and 4000 days (Fig. 4.23)

Evolutions of relative humidity

Section C at 0, 60.4, and 112.2 cm from the tunnel axis (Fig. 4.24)

Section F2 at 58.4, 81.5, and 105.3 cm from the tunnel axis (Fig. 4.25)

Water content and saturation after dismantling

section F2 as a proxy to section 27 at 1968 days (Fig. 4.26)

section F2 as a proxy to section 49 at 6717 days (Fig. 4.27)

---

<sup>9</sup> The dry density of the bentonite is approximated by a constant, i.e. it does not change with water content

Note that the relative humidity in section C close to the granite (Fig. 4.24) shows some strange oscillations. Unfortunately, this phenomenon could not be investigated in-depth.

*Distributions of relative humidity*

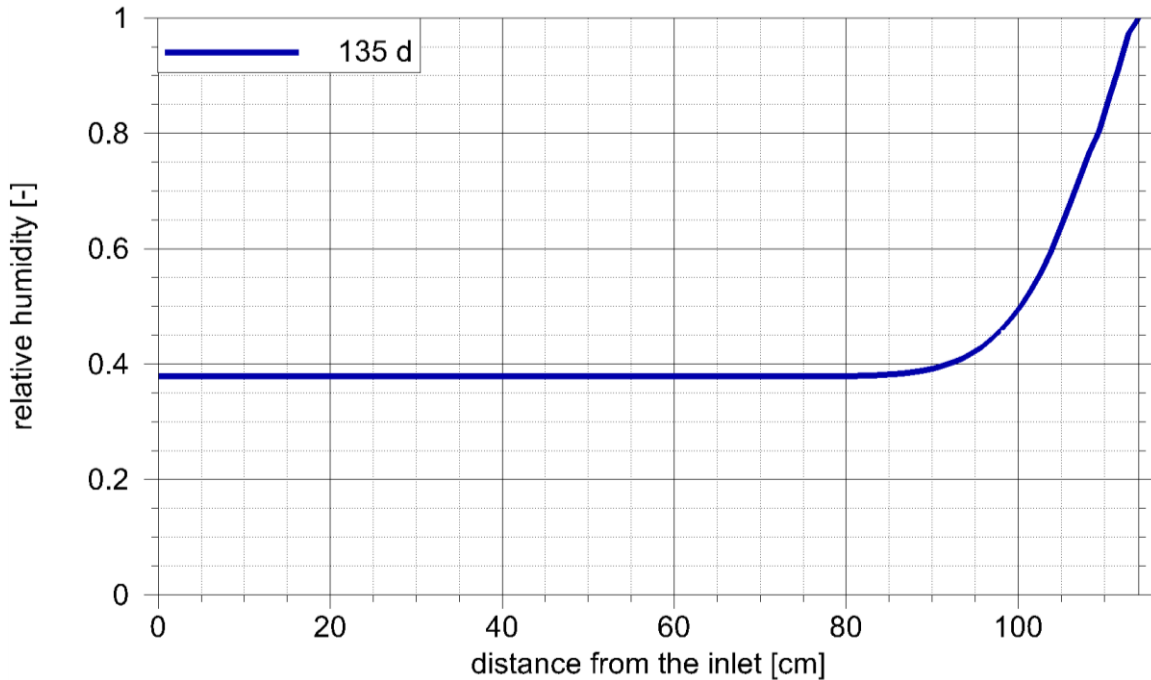


**Fig. 4.21** Isothermal water uptake after 135 days of isothermal uptake in section C

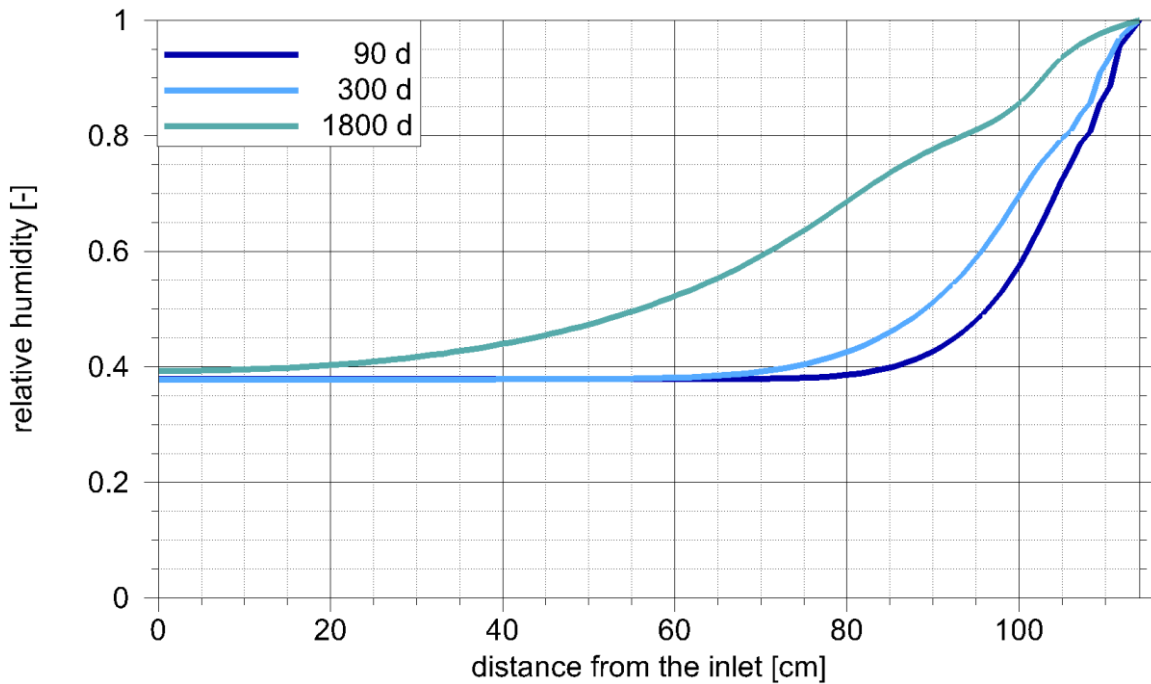


**Fig. 4.22** Distributions of relative humidity at appointed times in section C

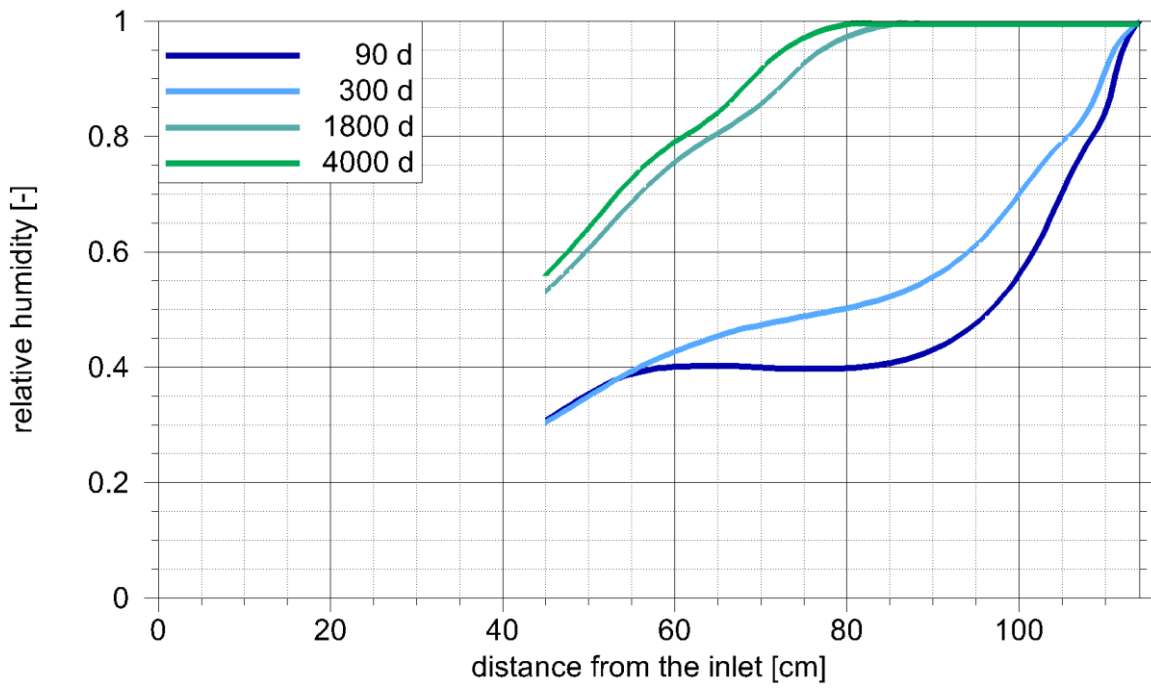


**Fig. 4.23** Distributions of relative humidity at appointed times in section F2

*Evolutions of relative humidity*

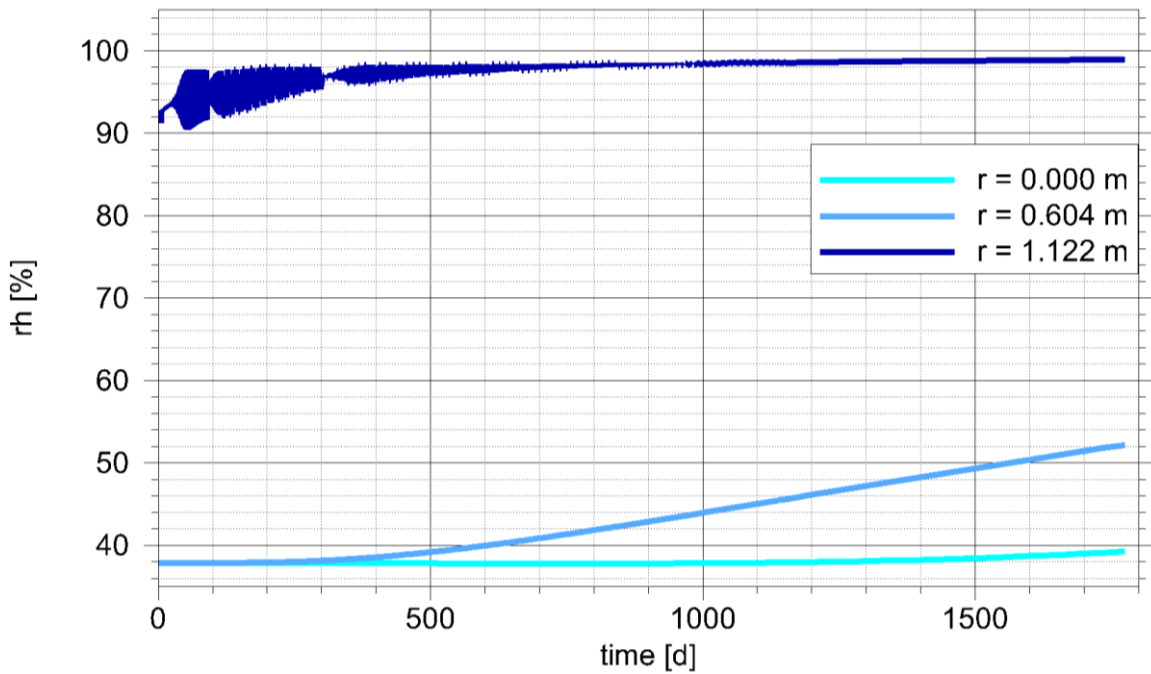


**Fig. 4.24** Evolutions of relative humidity at appointed locations in section C

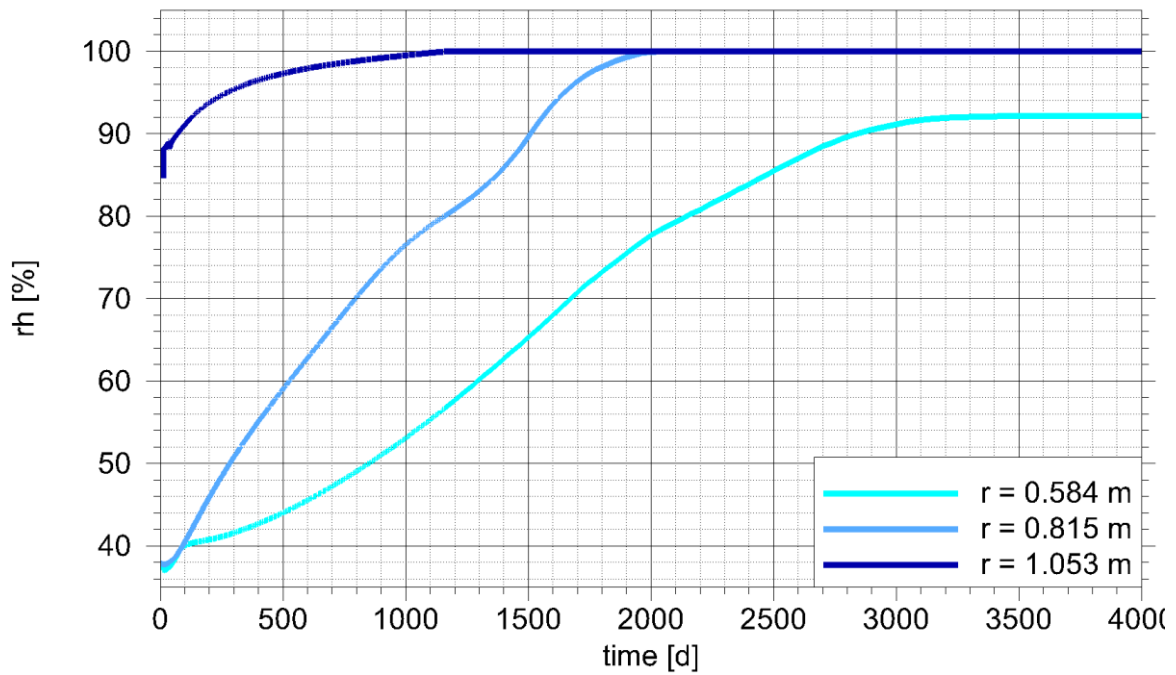


**Fig. 4.25** Evolutions of relative humidity at appointed locations in section F2

*Water content and saturation after dismantling of heater 1*

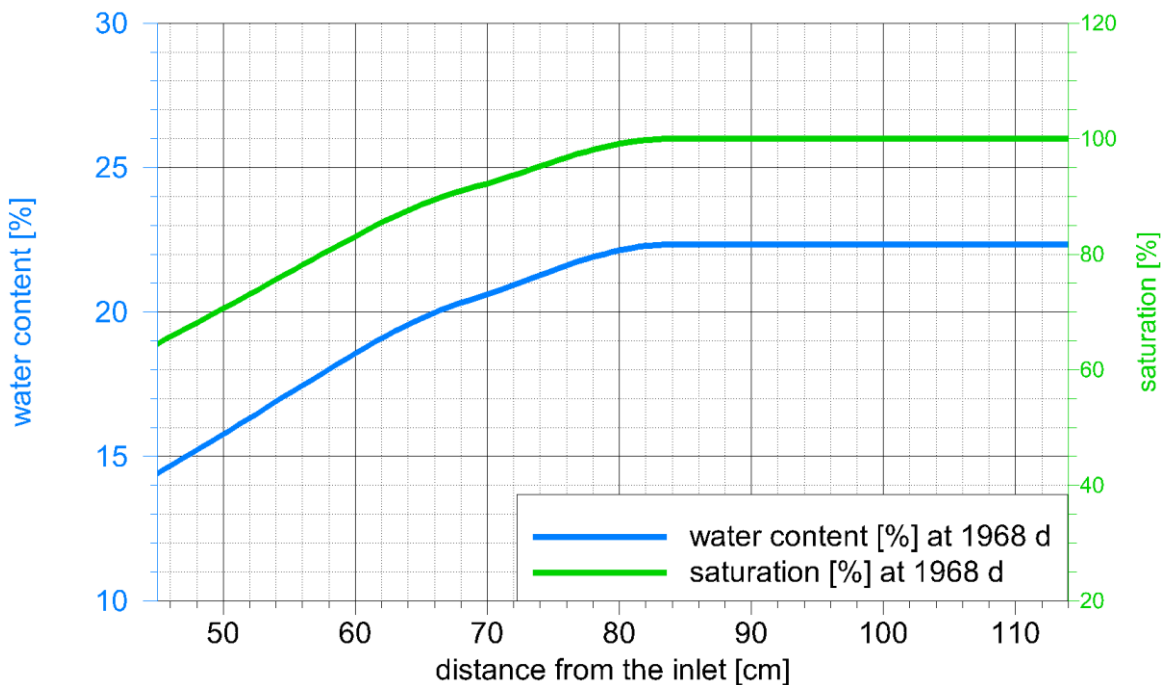


**Fig. 4.26** Water content and saturation in section F2 as a proxy to section 27

## Water content and saturation after dismantling of heater 2

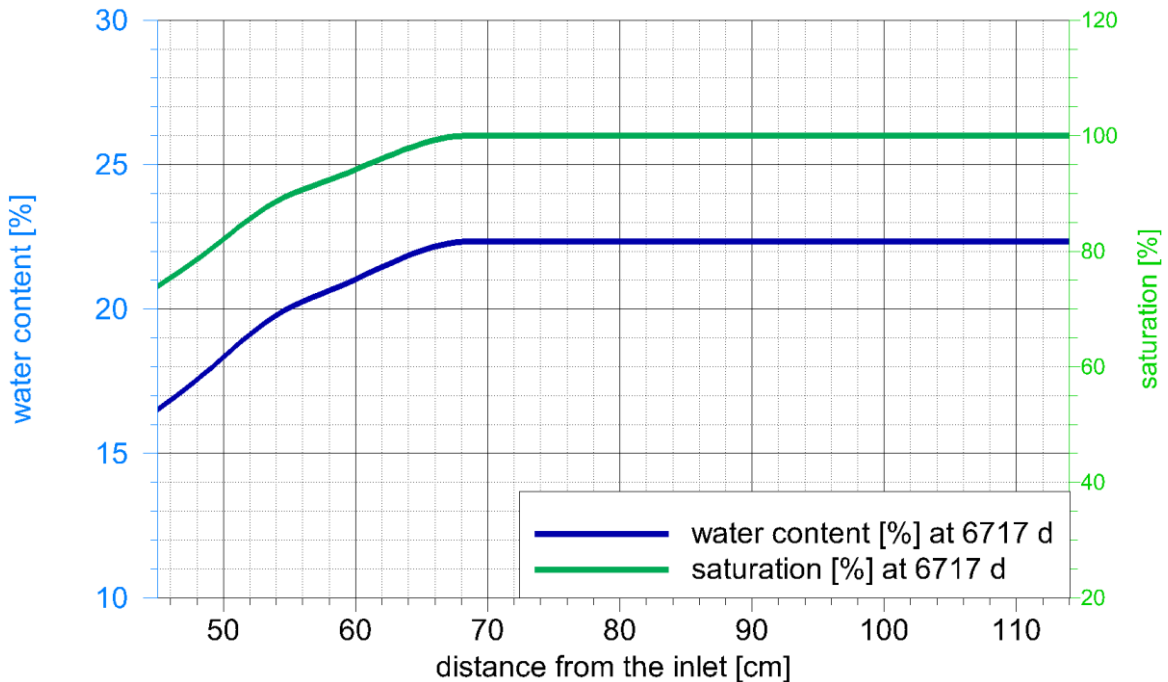


**Fig. 4.27** Water content and saturation in section F2 as a proxy to section 49

### 4.1.1.5 Provisional comparison of modelling results

At the last physical meeting of the TF EBS before the pandemic prevented such meetings temporarily, a first comparison of results from all modelling teams working in Task 9 – FEBEX in-situ test has been presented<sup>10</sup>. The overall conclusions concerning temperature and re-saturation read as follows /GEN 19b/.

Qualitatively (the) features of the performance (are) reasonably reproduced:

- Temperatures are generally well predicted.
- Heater power variation (has been) quite well predicted although power is underestimated for heater 2.
- General evolution of relative humidity across the barrier is correctly simulated (saturation close to the rock, drying followed by hydration close to the heater).

---

<sup>10</sup> A report on the comparison is presently written.

- Drying close to the heater is generally underestimated.

The modelling results concerning temperatures as presented in this report agree quite well with the data as well as, indeed, with the other modelling teams. Relative humidity simulations fit the data in general also reasonably well. Not quite as nice but still acceptable are the results for the water content and the equivalent degree of saturation. Where larger deviations from the water content data could be observed, the results of all teams tend to diverge.

#### **4.1.1.6 Summary**

The model used here for simulating the non-isothermal water uptake in the FEBEX in-situ test is based on the following assumptions:

- Rock permeability is high enough to provide as much water as the bentonite can take up.
- Buffer and heater are thus considered to be 2d-axisymmetric.
- Re-saturation of the buffer has negligible impact on heat flow.

This set of assumptions allows for dropping flow modelling for the rock and for decoupling of heat flow from bentonite re-saturation. Accordingly, heat flow is modelled first using COMSOL. Since the outer boundaries were treated as closed boundaries, the size was chosen in such a way that the increase of temperature at these boundaries did not exceed roughly 1.5°C. Unfortunately, decoupling prevented getting model results on the slow increase of power uptake over time, as this should be caused by the increase of thermal conductivity with the water content.

Using the experimental code VIPER for modelling bentonite re-saturation requires restriction to 1D-axisymmetric domains. Prerequisite for the hydraulic modelling is therefore that heat flow occurs exclusively orthogonal to the tunnel axis. Only cross-sections C and F2 thus qualify for the simulation of the relative humidity evolution. Based on symmetry considerations in the temperature field, section F2 is also taken as a proxy for sections 27 and/or 31. A pre-heating isothermal period of 135 days has been added to the calculations in the course of work on the FEBEX. Data for the bentonite have been chosen according to the non-isothermal CIEMAT test from Task 1 of the Task Force on EBS.

By and large, the modeling results appear to match the data quite well and to fit in with the results from other modeling teams. Where more pronounced deviations from the data were found, other teams had apparently also difficulties to match the measurements.

#### **4.1.1.7 Conclusions**

Decoupling of the thermal calculations from the hydraulic part, that is neglecting the dependence of thermal parameters on the degree of saturation, seems to have rather little influence on the overall temperature field as well as on the relative humidity evolution in the bentonite buffer. The same observation has been made already with the two previous non-isothermal models that have been set up by GRS within the Task Force on EBS (Task 1: Laboratory tests /KRÖ 08/, Task 2: Large-scale tests /KRÖ 11/). Assuming only a unidirectional coupling of thermal effects to hydraulic processes is quite advantageously as it accelerates modelling considerably. A drawback is, however, that simulating the increase of power uptake of the heaters is excluded by this assumption since this effect is actually caused by changes in the thermal conductivity due to an increasing water content.

With a view to re-saturation, only a quite small fraction of the performance measures that were defined in the task description could be met by code VIPER. This is of course not a flaw since VIPER has been developed to test and refine an alternative concept for simulating bentonite re-saturation. To that end, it has not been necessary, yet, to implement the capability of full 3D-modelling in the code. However, work on Task 9 – FEBEX in-situ test has shown once again that this capability will be required in the long run for concrete applications.

#### **4.1.2 Transferring code VIPER to COMSOL Multiphysics**

##### **4.1.2.1 Motivation**

An established method for numerically simulating processes in bentonite is still using thermal-hydraulic-mechanical (THM) coupled models. These models assume an uptake of liquid water by suction in the bentonite. Vapour diffusion in bentonite was also taken into account in these models at the time, but only as a propagation mechanism without influence on the saturation state of the bentonite.

Against this background, a simple, alternative saturation concept was created at the GRS, which takes into account a saturation of the bentonite by vapour. In parallel, the "experimental" one-dimensional code VIPER (**V**apour transport **I**n **P**artially saturated bentonite as **E**ngineered barrier for **R**epositories) was developed /KRÖ 05/.

Both the model ideas and the code were gradually expanded with a view to the conditions in a real repository and checked for their load-bearing capacity at every step (e.g. /KRÖ 08/, /KRÖ 11/). A significant part of the development was the participation in the Task Force on Engineered Barrier Systems (EBS) of the Svensk Kärnbrenslanhantering AB (SKB). As part of the work with the Task Force, several simulation models for bentonite saturation were investigated using benchmark cases that were based on laboratory and in-situ experiments.

One of the last benchmark cases was Task 9 "FEBEX" (see section 4.1.1). Due to the spatial nature of the experiment, there were only a few very special subtasks in Task 9 that could be simulated with VIPER. This showed once again the limitations of the "experimental code" VIPER in terms of practical application. In addition to the obvious limitation of the code to one dimension, the integration of other physical processes is also very complex.

Having reached a rather advanced stage of development and at the same time the limitations of VIPER repeatedly, it appeared to be about time to transfer the VIPER concept to COMSOL Multiphysics /COM 21/. However, due to the complexity of VIPER, this only makes sense if done stepwise. The first step in this direction has been taken with this work.

#### **4.1.2.2 Conceptual model**

In contrast to the classic THM models, the basic idea of VIPER is that the saturation of bentonite begins with a quick evolution of a thin fully saturated layer at the bentonite-water contact. This particular zone remains stable after the first few minutes. Beyond this layer, water evaporates and migrates deeper into the bentonite via vapour diffusion. The saturation then takes place by hydration of water molecules in the interlayer of the clay minerals.

Initially, it had been assumed that the hydrated water in the bentonite is immobile. Later it has been shown that a diffusive water migration process also takes place in the inter-layer. However, this process was not yet recognized in the first models.

The model concept realised in VIPER has the advantage over the classic THM models that the model requires only a few input parameters. Most of the required parameters can also be taken from textbooks.

#### 4.1.2.3 Mathematical model

To keep things simple, the influence of temperature on the re-saturation is not taken into account. It could be shown that the water balance equation under these circumstances takes a similar form to Fick's 2<sup>nd</sup> law of diffusive migration:

$$\square \quad \frac{\rho_d}{\rho_{v \text{ sat}}} w_e \frac{\partial \rho_v}{\partial t} - D_a \Delta \rho_v = 0 \quad (4.4)$$

- $\rho_d$  - bentonite dry density [kg/m<sup>3</sup>]
- $\rho_v$  - vapour partial density [kg/m<sup>3</sup>]
- $\rho_{v \text{ sat}}$  - saturation vapour density [kg/m<sup>3</sup>]
- $w_e$  - water content at full saturation [-]
- $t$  - time [s]
- $D_a$  - coefficient of the apparent diffusion [m<sup>2</sup>/s]

In equation ( 4.4 ), all quantities except the vapour partial density  $\rho_v$  are constant. However, it should be noted with a view to later models that the saturation vapor density  $\rho_{v \text{ sat}}$  and the diffusion coefficient  $D_a$  are actually temperature-dependent. In order to facilitate model advancements for non-isothermal conditions at a later date, the variables in COMSOL have already been prepared accordingly. In addition, the diffusion coefficient  $D_a$  takes the interlayer diffusion into account ( 4.5 ):

$$\square \quad D_a = D_{mol} \cdot \Phi \cdot \tau + \rho_d \cdot \frac{\partial w}{\partial r_h} \cdot \frac{1}{\rho_{v \text{ sat}}} D_{hyd} \quad (4.5)$$

- $D_{mol}$  - coefficient of the molecular diffusion [m<sup>2</sup>/s]
- $\Phi$  - porosity [-]
- $\tau$  - tortuosity [-]
- $w$  - water content [-]

$r_h$  - relative humidity [-]

$D_{hyd}$  - coefficient of the interlayer diffusion [m<sup>2</sup>/s]

The coefficient of interlayer diffusion depends on the water content /SKI 06/. This dependency can be implemented as a step function in COMSOL which determines the diffusion coefficient according to the water content:

$$\begin{aligned} \square \quad D_{hyd} &= 1 \cdot 10^{-11} \frac{m^2}{s} && \text{for } w < 7.5\% \\ \square \quad D_{hyd} &= 1 \cdot 10^{-10} \frac{m^2}{s} && \text{for } 7,5 \% < w < 18 \% \\ \square \quad D_{hyd} &= 2 \cdot 10^{-10} \frac{m^2}{s} && \text{for } w > 18 \% \end{aligned} \quad (4.6)$$

It has turned out that the specified values for the diffusion coefficient as well as the limiting water contents should rather be specified as parameters. The clay content of the bentonite can vary between different charges, which means that the limiting water contents can vary as well.

#### 4.1.2.4 Transfer

In its simplest form, the model concept describes bentonite re-saturation by the processes of binary vapour diffusion in the free pore space and the instantaneous uptake of water vapor by the clay particles. Hydrated water is considered to be immobile then. Mathematically, this can be represented by balance equation ( 4.4 ) if the second summand of the diffusion coefficient in equation ( 4.5 ) is dropped. This form of balance equation has been derived from Reynolds transport theorem and was implemented first in COMSOL, using the PDE node.

Next, the calculation of the interlayer diffusion coefficient was added. A difficulty arose then from the fact that this diffusion coefficient depends on the water content. The water content in turn depends on the partial vapour density. This causes the balance equation ( 4.4 ) to become non-linear. To circumvent this problem the calculated partial vapour density from the previous time step was stored to be used as input for the calculation of the diffusion coefficient in the next time step. Storage was initially implemented by using the nojac operator in COMSOL. This caused repeatedly premature termination of model runs, though. During the work, a COMSOL version 5.5 was released that offered the

Previous Solution Operator as an alternative to the nojac operator which made the model much more robust.

#### 4.1.2.5 Verification

As part of the EBS project /KRÖ 04/, several water uptake tests had been carried out in the years 2001 to 2003. For these tests, cylindrical bentonite samples were compacted in a steel form to a diameter of 50mm and a length of 100mm. The samples were then installed in cylindrical steel cells, which prevented the samples from expanding (see Fig. 4.28). At one end of the cell, water vapor was then passed into the sample, while the other end of the cylinder was closed with a lid. After defined periods of 4, 13, 20, 56, 90, 120, and 185 days, the individual tests were terminated, the samples were removed from the cells and sliced to determine the water distribution in the sample.

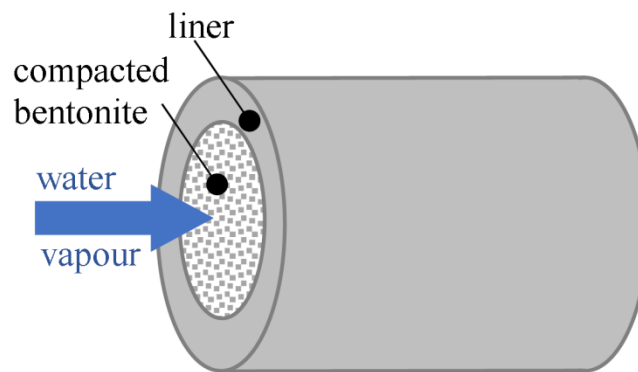


**Fig. 4.28** Sketch of the test set-up; from /KRM 20/

This experiment had already been simulated with an early version of the VIPER code /KRÖ 05/, so that experimental data as well as modelling results from VIPER were available for a comparison with the results of the new COMSOL-model. The COMSOL-model was formulated in 1D to provide a maximum degree of comparability with the VIPER-model. Both models describe the water content along the sample axis at the running times of the individual tests. Inflow of steam was ascribed to the left-hand side and a no-flow boundary condition was set on the right-hand side. The plot depicted in Fig. 4.29 shows all three results.

The results generated with COMSOL correspond almost perfectly to the results from VIPER. Like the results from the VIPER-model, they match the experimental results satisfyingly well.

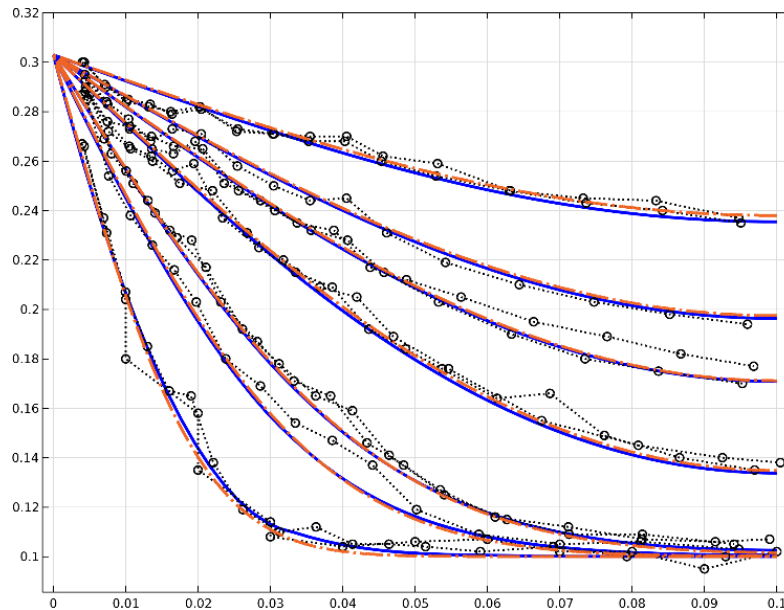


**Fig. 4.29** Water content distributions; from the experiment (black), from COMSOL (blue), from VIPER (orange); from /KRM 20/

#### 4.1.2.6 Demonstration of multidimensional modelling

Based on the successful one-dimensional model, an experimental extension of the model into the second dimension was carried out. The model domain consisted then of a square with an edge length of 10 cm, in which one side was defined as an inflow side and the other 3 sides as impermeable. Thus, the one-dimensional model was raised to the second dimension. In order to optimize the comparison of the results with those of the 1D-calculation, a section line was placed in the middle through the model area. As expected, the results of the one-dimensional and the two-dimensional calculations were congruent /KRM 20/.

In order to check whether the model actually calculates in two dimensions, the inflow boundary condition for the whole edge was changed to a pointwise inflow and the rest of the edge was defined as impermeable. These changes introduce diffusion in the y-direction, which means that it takes much longer time for the water to reach the right end of the sample.

Next, the model was extended into the third dimension, now with a cube-shaped geometry that also had an edge length of 10 cm. As with the previous calculations, one side of the cube was defined as an influx side and the other as impermeable. Thus, the comparability to the first 1D case is still given. As with the comparison between the one-

dimensional and the two-dimensional case, the calculated results matched each other well /KRM 20/. Finally, the scenario of a pointwise inflow into a 3D-domain was simulated. As expected, the saturation took even longer than in the 2D-case as shown in Fig. 4.30, since the vapour could now also fill up the model in the z-direction.

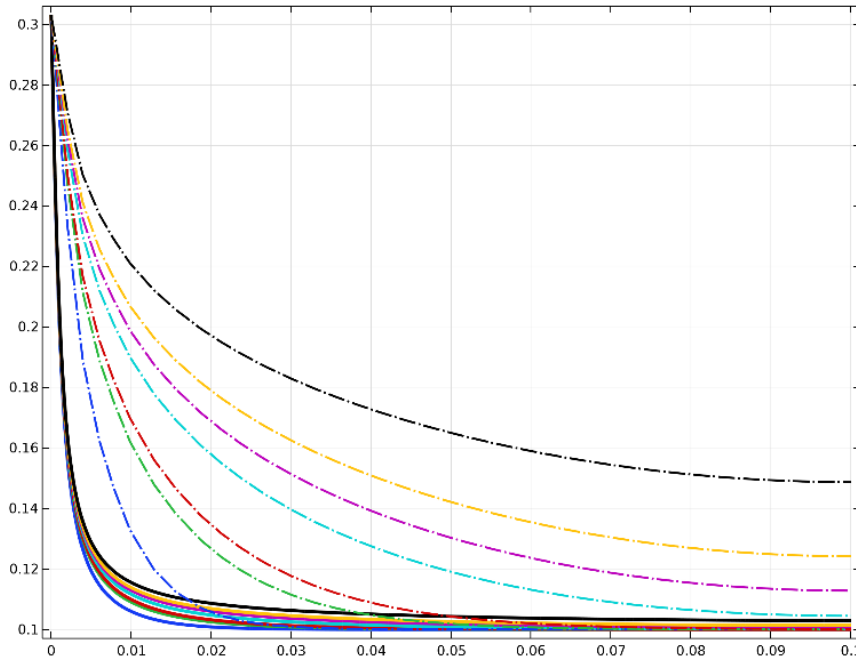


**Fig. 4.30** Axial water content distributions after pointwise water inflow; 2D-domain (dashed lines), 3D-domain (solid lines); from /KRM 20/

As a pure demonstration model, water uptake from a point source in a cuboid model with side lengths of  $0.5 * 0.5 * 1.0$  m was finally simulated. The calculated water content distribution at 75 years simulation time is shown in Fig. 4.31 by contour planes. This representation depicts clearly the three-dimensional characteristics of the water content distribution in the vicinity of the point-shaped inflow while it shows the results converging to the characteristics of an essentially one-dimensional migration with distance to the inflow boundary. In terms of shapes of the contour planes it says that there is a transition from hemispherical contour planes to planar ones.

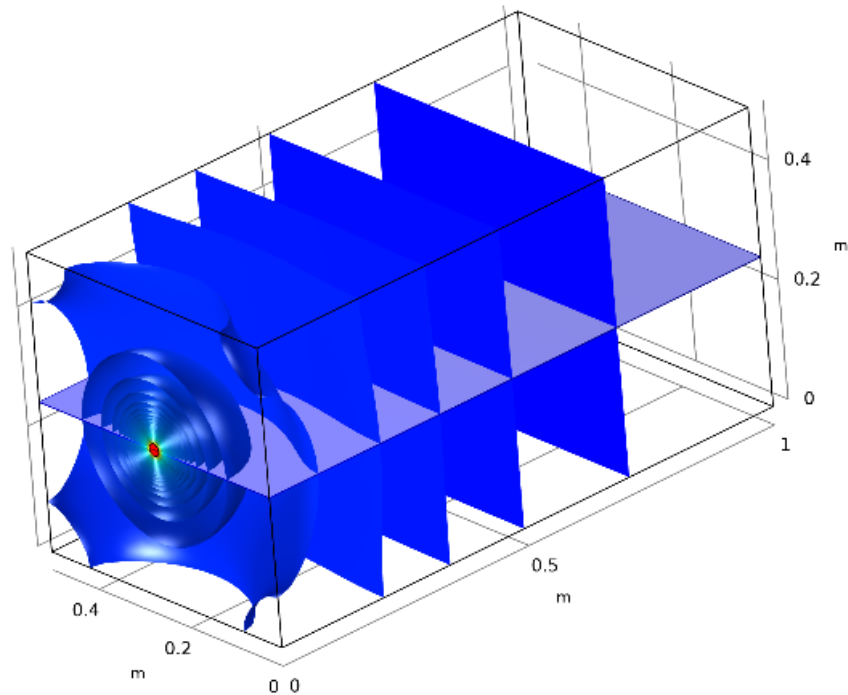


**Fig. 4.31** Water content distribution in a 3D-domain after 75 years; from /KRM 20/

#### 4.1.2.7 Outlook

The first step in transferring the VIPER concept to COMSOL Multiphysics has successfully been carried out and the feasibility of the transfer was demonstrated using a simple form of isothermal re-saturation. Sensible next steps would be on the one hand the extension of the COMSOL-VIPER model to the full complexity of isothermal saturation. This would involve the import of measured isotherms as well as the whole range of possible boundary conditions. A further step could be the implementation of all temperature dependencies of secondary variables and parameters in preparation for a non-isothermal model. The heat flow module of COMSOL can then be coupled to the equation-based model. Among other things, this also enables a systematic investigation of the influence of feedback from the hydraulic to the thermal model part. However, this influence is often estimated to be very low on the basis of the model calculations with the classic THM models.

In addition to the implementation of the VIPER model, the COMSOL model can of course also be extended by other functionalities that would be much more difficult to implement in the original VIPER code. For example, the calculation of swelling pressures or the influence of saline solutions on the saturation and the swelling pressure could comparatively easy be supplemented in the COMSOL model. Furthermore, approaches to

erosion of bentonite in fractured porous media, such as granite, could also be integrated into the model. New approaches for the swelling of bentonite into a free or a limited free space are currently being investigated and developed. These could also be incorporated into the COMSOL model in the future.

Research on the performance of a bentonite buffer in a geologic repository is still ongoing. With a view to possible further developments, the set-up of a simulation tool for bentonite saturation within the framework of a multiphysics code appears to be a sensible move to facilitate advancements of the re-saturation model in the future.

## **4.2 Permafrost**

### **4.2.1 Motivation**

Deep geological disposal of nuclear waste implies (1) storage at a depth of several hundred metres below surface and (2) a safety assessment that covers a long period of time. In Germany a time span of 1 Million years has to be considered /STA 17/. One of the main concerns for such a repository is the detrimental effect of groundwater on the technical and geotechnical barriers, e.g. waste canisters. For the design of the repository, knowledge of the local and regional groundwater system is therefore required to a considerable extent. This knowledge forms also the basis for predicting a possible radionuclide migration in case of leakage from a damaged waste canister.

Potential sites in Germany have been identified in the North German lowlands, in Southern Germany within or adjacent to the Alpine foothills and in the range of the Erzgebirge (see Fig. 4.32, left) /BGR 12/, /BGE 20/. During recent cold stages like the Weichselian glacial (Würm glacial stage for the Alpine region) these sites experienced partly permafrost conditions<sup>11</sup>, partly coverage by an ice shield (see Fig. 4.32, right; e.g. /VAN 93/ and /REN 03/). Ground freezing to a large lateral as well as vertical extent has thus to be assumed under these conditions independently from the eventually selected site. Please see also chapter 4.4.2 for a more detailed description of permafrost including information from natural analogues.

---

<sup>11</sup> The term “permafrost” refers to any type of ground in the subsurface that has experienced temperatures below 0°C for at least two years without interruption. At that, the top of the permafrost might be located at any depth below the surface.

Under permafrost conditions, radically different groundwater flow systems compared to those prevailing during warm climate stages may evolve as freezing grounds provide an efficient flow barrier. However, the degree to which lower groundwater systems are affected by freezing depends of course on the thickness of the permafrost.

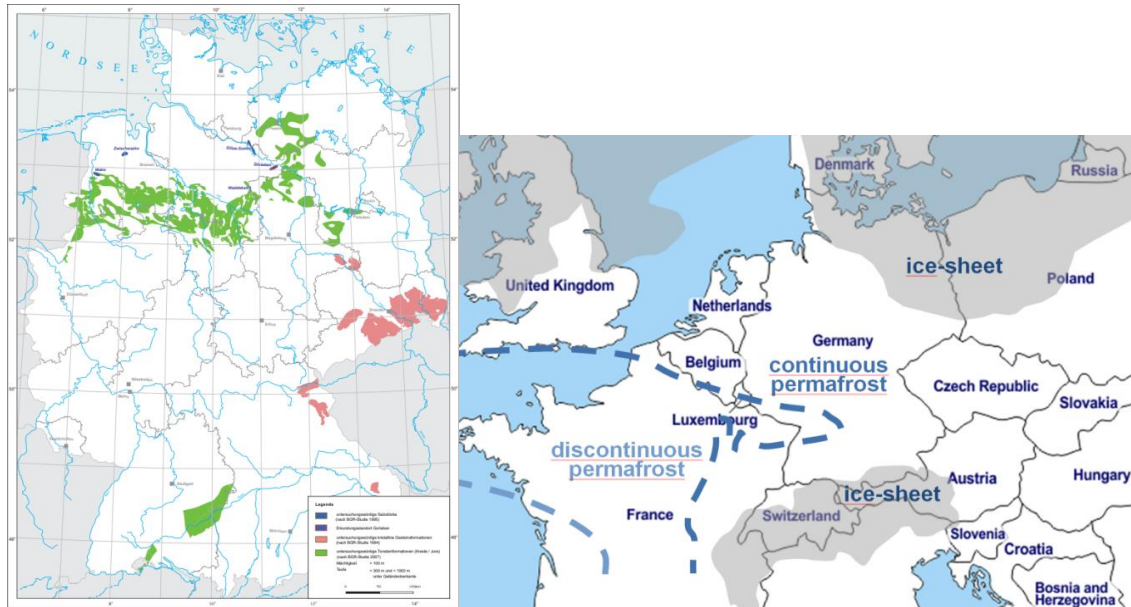


**Fig. 4.32** Potential repository-sites worthy of investigation /BGR 12/ (left) and maximum permafrost coverage during the Weichselian/Würm glacial after /VAN 93/ and /REN 03/ (right).

The difficulties concerning the prediction of groundwater flow under permafrost conditions are aggravated by the occurrence of taliki, unfrozen zones in the permafrost affected underground. There are several types of taliki (see Fig. 4.33):

- Open taliki: unfrozen zones at the top of the frozen underground
- Closed taliki: unfrozen zones that are fully enclosed in the frozen underground
- Through taliki: unfrozen zones that penetrate the whole depth of the frozen ground

While open as well as closed taliki are not really of concern, through-taliki can form hydraulic shortcuts between deep unfrozen aquifers and ground surface. Consequences for the potential migration paths of radionuclides in case of a canister breach are therefore presently hard to predict. Highly adverse appears to be the possibility that contaminated waters may be able to reach the surface via through taliki while remaining highly concentrated with pollutants. The possible impact of a change from temperate to periglacial climate on radionuclide migration is graphically illustrated in Fig. 4.34. Conditions

for the development and persistence of taliki are still only partly known, though (e.g. /PAR 18/).

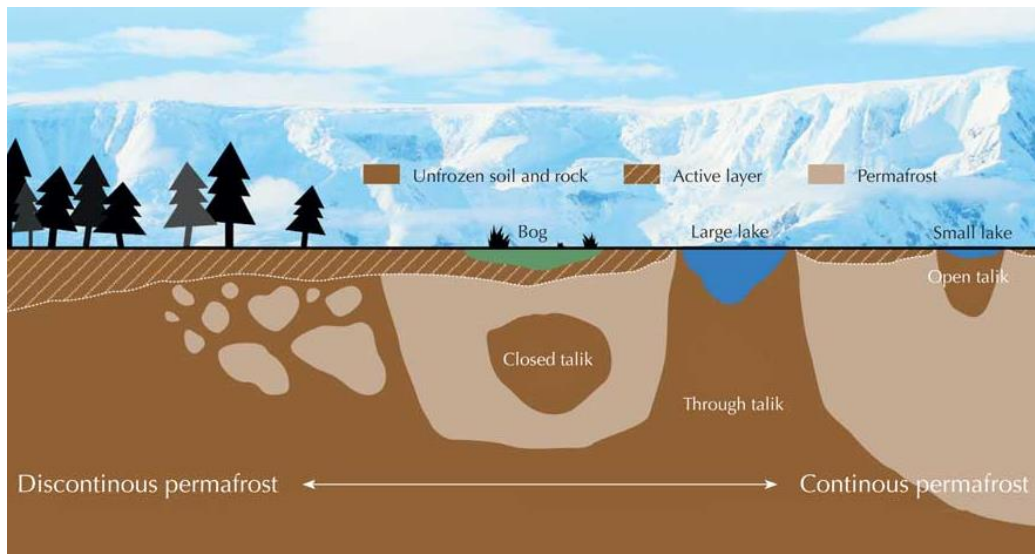


**Fig. 4.33** Types of taliki; from /PAB 12/

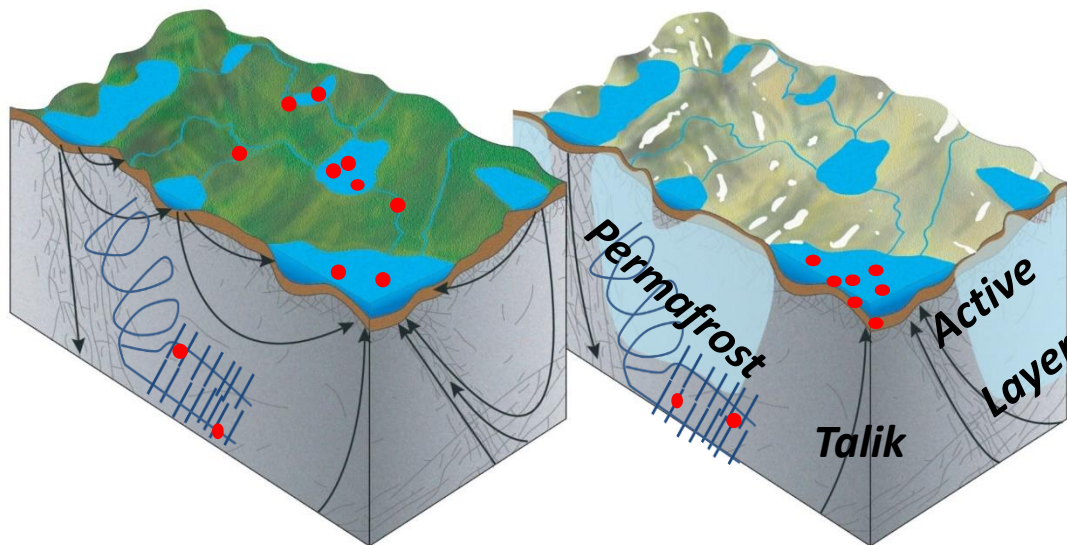


**Fig. 4.34** Influence of climate change on the hydrological flow system; from /LIN 19/ (modified from /JOH 16/)

Further complexity is introduced by the fact that the macroscopic phenomenon of freezing and melting is actually influenced by the microscopic process of surface melting on pore scale. For thermodynamic reasons, a „liquid-like“ layer (LLL) evolves at the surface of ice (e.g. /BLU 00/). The thickness of the LLL depends on temperature and is increased

by a concave surface of the ice (e.g. /DAS 06/) so that ice can coexist with water even below  $-10^{\circ}\text{C}$ . The pore space in the underground does therefore not become abruptly impermeable when the temperature decreases below  $0^{\circ}\text{C}$ . Macroscopic porosity and effective water permeability rather show a gradual monotonic decrease for temperatures below the freezing point.

For porous media, this behaviour can be characterized by the soil freezing characteristic curve (SFCC) that describes the volumetric fraction occupied by ice in the pore space as a function of temperature. In terms of the classic two-phase flow, the SFCC could also be called a temperature-dependent saturation with ice. It has already been investigated for porous media and prepared for implementation in numerical models (e.g. /AUK 16/).

For fracture media, however, no such relation exists yet. There are several adverse circumstances that have kept so far from work on determining an analogous relation which could be called “fracture freezing characteristic curve” (FFCC). Fractures are more diverse than common soils as soils can rather easily be characterized by grain size distributions while fractures may differ not only in terms of mean aperture and size, but also in terms of aperture distribution and surface roughness. Assigning an FFCC to a whole fracture might prove to be questionable. An analogy to the representative elementary volume (REV) for porous media that applies to a fracture – something like a representative elementary area (REA) – would be required.

One way to solve these problems in the long run is to start with visualizing the process of freezing in fractures. The classic approach to hydraulic tests in fractures is to form replicas the two opposing surfaces with transparent epoxy. This is a somewhat tedious task that also requires the physical presence of original fracture surfaces (e.g. /WIN 20/).

A rather new alternative has come up with the technology for 3D-scanning and 3D-printing. Also, with this technology, the process of producing physical models of a fracture begins with the original fracture surfaces as they have to be scanned first. However, once the surface has been scanned, a digital model can be constructed that is suitable for 3D-printing with transparent resins. Physical presence of the original fracture is thus not required from that point on because the digital model suffices. Furthermore, a theoretically infinite number of copies can be produced. And finally, using CAD-tools, the digital model can be enhanced by additional features to facilitate hydraulic tests in the laboratory.

However, application of this new technique to freezing groundwater in fractures must be ascertained with respect to several details. The technique must allow for clear observation of the freezing of water and thereby for delimiting the local boundaries of the evolved ice. In order to derive an appropriate FFCC, also the aperture of the fracture must be known to a maximum degree of accuracy. Additionally, the experimental set-up must enable measurements of the effective permeability and ensure a sufficiently accurate temperature control.

#### **4.2.2 Plans and realisation**

Against this background, a feasibility study has been performed as an orientating exercise with limited resources in terms of time and material that is also intended to demonstrate the potential of the 3D-printing technique for investigating freezing processes of groundwater in fractured rock.

The intended approach to this task had been to start out with the observation of freezing in a 3D-printed fracture. When successful, the ice content and the related temperature were to be measured as well as the relative permeability for water. These measurements were then to be repeated at different temperatures. The resulting FFCC data were finally envisioned to reproduce the freezing experiment by means of numerical modelling. The foreseen code was COMSOL Multiphysics /COM 21/ because only moderate effort had been expected to set up a specific but meaningful model.

However, several unforeseen difficulties have delayed the experiment to the extent that only the observation of freezing in a simplified fracture could be achieved. The plan for subsequent modelling that would have required simulating of the freezing process of water with the associated changes of the thermal properties, did therefore not make sense. As a substitute, a model for determination of the growth of permafrost depending on the surface temperature has been set up since it comprised many of the physical aspects of the originally envisaged model. It was furthermore expected that the model would prepare ground for investigations beyond the present project, serving as preparatory work for studies on groundwater flow under permafrost conditions such as the conditions for talik development.

## 4.2.3 Observing freezing groundwater in fractures

### 4.2.3.1 Test components and preparation

In this subsection, the components of the test setup are listed and described, followed by an account of their assembly.

#### Artificial fracture (printed)

As a basis for the feasibility study, a parallel plate model has been chosen for the fracture that is subdivided into five channels with rectangular cross-sections and equal widths (see Fig. 4.35). The channels have an increasing aperture towards the inner channel, following the sequence 0.5, 1.0, 1.5, 1.0, and 0.5 mm. The fracture is realised as two plates representing opposing fracture surfaces. The bottom plate is planar while the counterpart has recesses giving shape to the five channels.



**Fig. 4.35** Artificial printed fracture

#### Liquids

Three different liquids for different purposes are utilized:

- A cooling liquid is intended to remove heat from the test set-up.
- The fracture is brought to a low temperature by bringing it into contact with a cooling medium. Initially, tap water was envisaged to get frozen, thereby ensuring sub-zero temperatures in the fracture and fixing the position of the fracture plates as well as sealing them at the same time. Later tap water has been exchanged with a 50% NaCl-solution because damage of the cooling coils from expanding ice was feared.

- Tap water has been injected into the fracture with the help of a syringe pump. In order to determine different stages of freezing, the water in the syringes has been blended with different water colours to enable relation to the injection sequence.

### Cooling unit (printed)

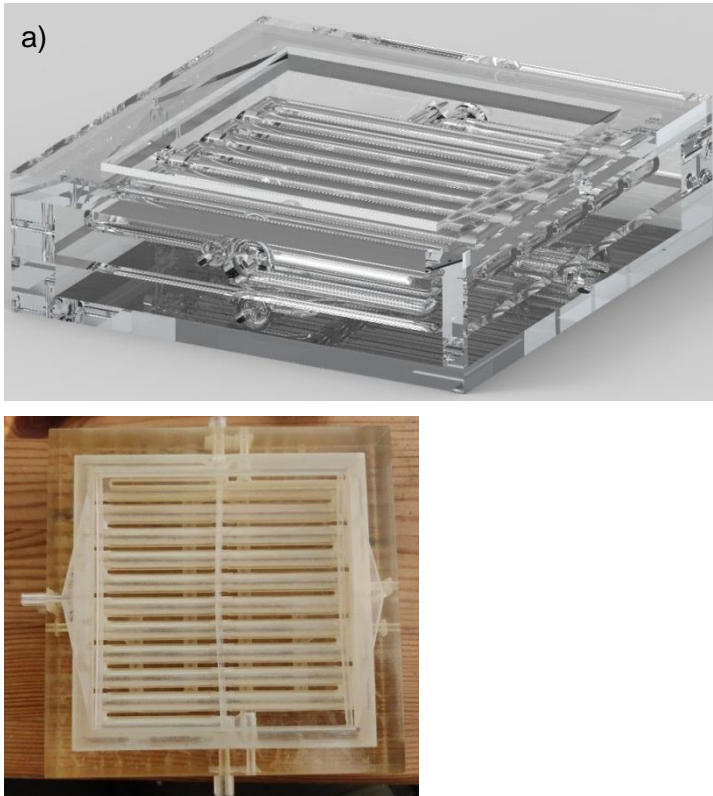


**Fig. 4.36** Cooling unit; a) construction, b) print

A cooling unit has been constructed (see Fig. 4.36 a)) and printed with a transparent resin (see Fig. 4.36 b)). It combines several functions:

- Holding the two fractures plates.
- Providing contact of the bottom fracture plate to a cooling medium.
- Allowing for an inflow into the fracture at constant pressure across one whole side of the fracture.
- Ditto at the outflow side with atmospheric pressure.
- Cooling the cooling medium.
- Precooling the coloured water.

- Providing recesses for temperature sensors.
- Providing connectors for inflow and outflow for flexible tubes containing cooling liquid and coloured water.

Note that CAD-construction and 3D-printing has allowed for a quick production of the cooling unit at a minimum of effort while at the same time fulfilling a couple of quite different requirements. Such a construction could not have been achieved by conventional methods.

### **Auxiliary cooling unit (printed)**

At an early planning stage, a comparatively simple cooling unit has been printed. It is basically a flat board with a cooling coil inside and connectors at two opposing ends to attach the flexible tubes transporting the cooling fluid. To increase efficiency, a heat sink with cooling fins on both sides of the plate has additionally been installed as shown in Fig. 4.37. This has later been used as an auxiliary cooling unit.



**Fig. 4.37** Auxiliary cooling unit (top view)

### **Cooling aggregate (from stock)**

The cooling aggregate depicted in Fig. 4.38 is a central part of the test set-up that has been used already for laboratory tests in the framework of the projects WiGru-6 and WiGru-7 /NOS 18/, /KRÖ 19/. It provides the cooling unit and the auxiliary cooling unit, if applicable, with the cooling fluid. The temperature can be pre-set to two-digit negative values with an accuracy of  $\pm 0.02^{\circ}\text{C}$ . The pump rate amounts to approximately 20 l/min, thus providing a stable and controlled cooling environment.



**Fig. 4.38** Cooling aggregate

### **Syringe pump (from stock)**

Also already used for laboratory tests with bentonite in the project WiGru-7 was the syringe pump /NOS 18/, /KRÖ 19/. It allows for injection of water at variable rates up to 100 ml/h. The pump is depicted in Fig. 4.39 while it is injecting magenta coloured water.



**Fig. 4.39** Syringe pump

### **Temperature sensors (from stock)**

As with the cooling aggregate, the temperature sensors have been available from tests in projects WiGru-6 and WiGru-7. In order to avoid influences on the flow, the sensors

were positioned in recesses in the frame of the cooling unit close to the fluid. Fig. 4.40 shows the arrangement of the temperature sensors after installation.

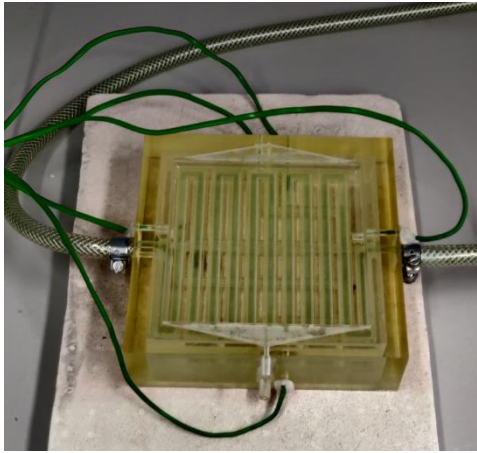


**Fig. 4.40** Temperature sensors installed in the cooling unit

#### **Data acquisition system (from stock)**

Temperature data have been collected by the data acquisition system that is shown in Fig. 4.41. It stores data from up to 10 sensors at pre-set intervals.



**Fig. 4.41** Data acquisition system

#### **Cool box (ad hoc constructed)**

During the experiment it became clear that the cooling unit with the fracture required better insulation against ambient climate conditions. A box has therefore been built from an insulating slab, see Fig. 4.42. It consists of a top and a bottom slab with a connecting ring in between. The top part includes a cut-out observation duct that is closed at the

bottom by an acrylic glass pane. The duct has been introduced to allow for an observation of the fracture without letting ambient air entering the box. The cut-out part of the duct has always been re-installed for thermal insulation except for the very short observation periods.

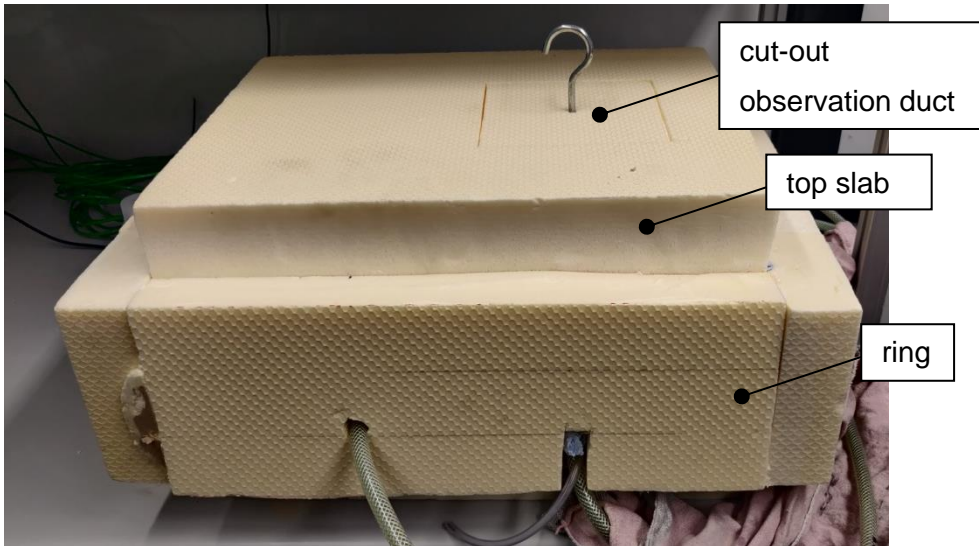


**Fig. 4.42** Cool box

### **Test preparation**

A list of all necessary steps for setting up a test is given below. Note that some steps have not to be taken for every new test.

- Emplacing the cooling medium in the cooling unit
- Emplacing and sealing the fracture plates
- Connection the cooling aggregate with the cooling coils of the cooling unit(s)
- Connecting the sensors with a data acquisition system
- Inserting the temperature sensors in the provided recesses in the cooling unit
- Connection of the syringe pump with the precooling coils of the cooling unit

#### 4.2.3.2 Experimental procedure

Several attempts at the test configuration have been made to establish some positive results in the end. The set-up used as well as the knowledge gained from each attempt are documented in this section.

##### First attempt

The cooling unit has been set up according to the procedure described in the previous sub section and was just put on a thermally insulating plate as shown in Fig. 4.43. Water has been used as a cooling medium, but this water did not freeze, even after several hours.

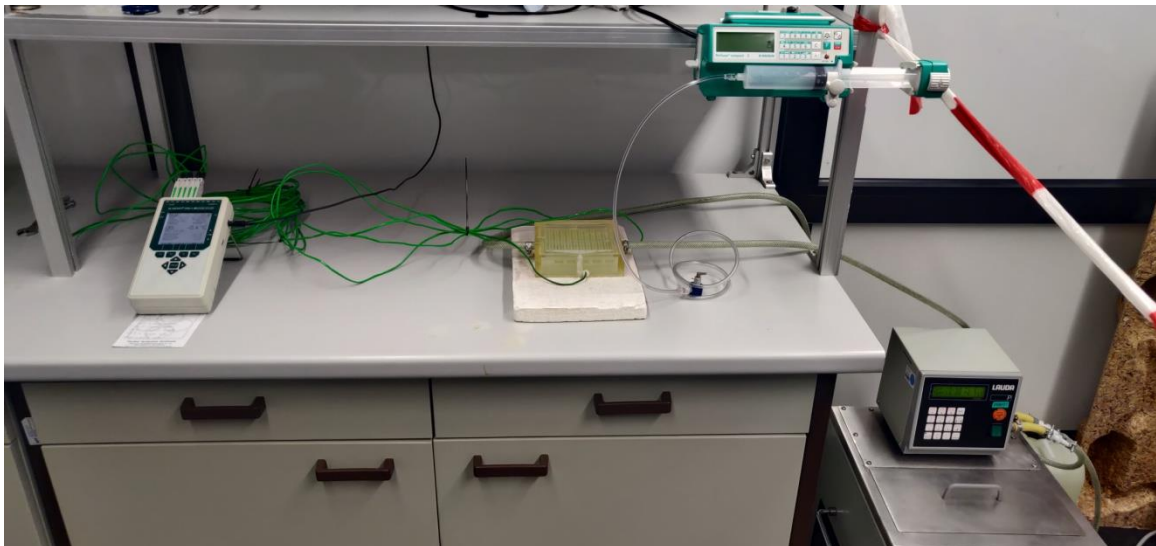


**Fig. 4.43** Setup for the first attempt

In order to find out when freezing could be expected in the test and possibly to optimise the test conditions, it has been tried to set up a model with simplified physics in COMSOL Multiphysics /COM 21/. Particularly, the change of water to ice and the referring changes in the thermal properties are not considered in this model. The CAD construction file for printing the cooling unit has been intended to be a basis for the model geometry. However, steering clear of difficulties at importing the CAD-file appeared became too time consuming. A simplified geometry has therefore been chosen instead where the cooling coil is unwound to a straight line. In Fig. 4.44, the components of the model are depicted.

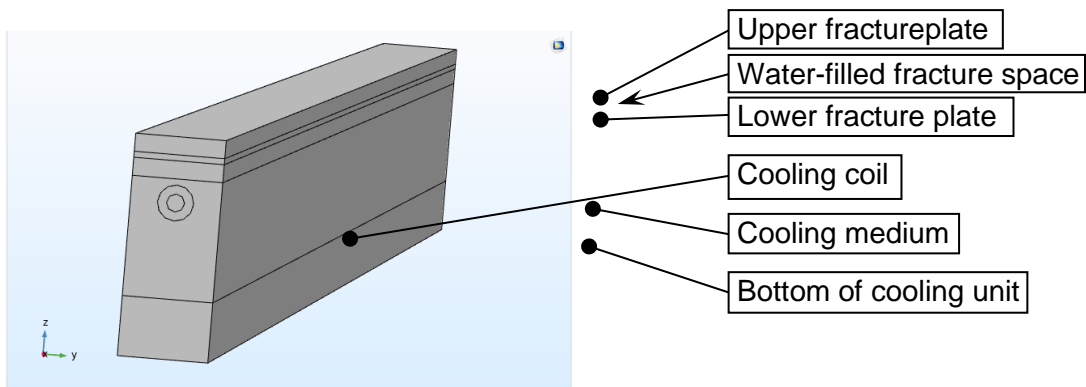


**Fig. 4.44** Principal sketch of the numerical model

When setting the cooling fluid to  $-2^{\circ}\text{C}$  at the inflow and the surface of the upper fracture plate at a temperature of  $20^{\circ}\text{C}$ , the climate-controlled room temperature, not even the temperature at the surface of the cooling coil falls below the freezing point according to the model. It is thus not surprising that no freezing could be observed in this attempt.

Taking into account that there might be a certain cooling at the fracture surface by slight movement of the air in the room or by heat radiation, another model run has been performed with temperature of only  $5^{\circ}\text{C}$  at the top of the upper fracture plate. In this case, about two hours are required to cool the temperature at the surface of the cooling coil down to the freezing point. Additional four hours model time pass until approaching steady state. The contour planes are depicted in Fig. 4.45. However, even at steady state, the contour plane for  $0^{\circ}\text{C}$  indicating the boundary of frozen water barely touches the bottom of the lower fracture, meaning that freezing conditions are still not yet reached in the fracture. How far sub-zero temperatures reach from the bottom into the fracture plates depends strongly on the temperature that is assigned to the top of the upper fracture plate. Variations of this boundary condition indicate that the top temperature should not exceed  $+1^{\circ}\text{C}$  in order to ensure freezing conditions in the fracture.

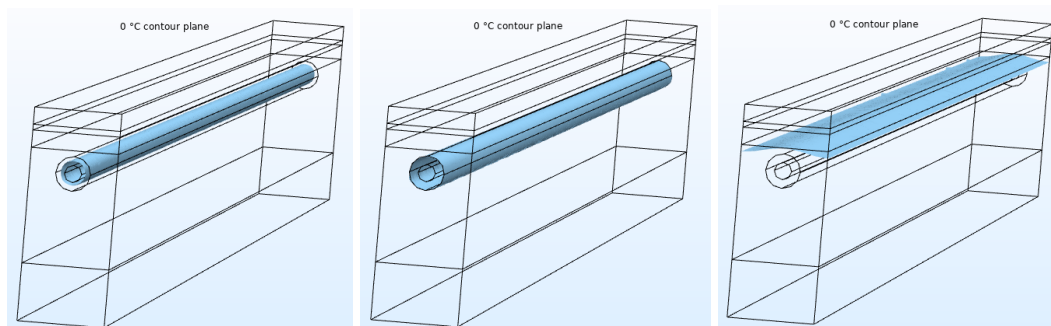


**Fig. 4.45** Contour planes indicating  $0^{\circ}\text{C}$  in the model with a top temperature of  $5^{\circ}\text{C}$ ; from left to right: after 0.5 h, 1.5 h and 6 h

In parallel to the model calculations, a simplified version of the cooling unit relating to the geometry of the COMSOL-models has been 3D-printed. Initially, it has been intended as a reality check for the COMSOL calculations. However, when paying closer attention to the details of freezing in the cooling unit, it was realised that freezing would start out at the cooling coils and the freezing front would then move downwards in the cooling medium towards the bottom of the cooling unit. The volumetric expansion of water when freezing would then lead to an upward movement of the ice because the unfrozen water below cannot significantly be compressed. As a result, the volumetric expansion would exert upwards directed forces on the cooling coil thus possibly compromising its mechanical integrity.

This understanding has been put to test by filling the reservoir of the simplified cooling unit with water and putting it overnight into a deep freeze. When taken out, the water has been completely frozen and the printed model was indeed broken, confirming insufficient stiffness of the printed material against expansion due to freezing.

For safety reasons, the cooling medium has therefore been changed from water to a 50 % NaCl-solution with a freezing point of about  $-10^{\circ}\text{C}$ . This solved the problem of possible damage of the cooling coils but introduced at the same time new difficulties concerning the emplacement of the fracture plates. Sealing of the fracture as well as of the volume of the cooling medium required now a tedious process of gluing and lacquering.

Note that after each test, successful or unsuccessful, the cooling unit as well as the fracture has to be defrosted, if applicable, cleaned, and dried before a new test can be started. This is necessary in order to avoid damage to the tubing system when freezing for a new test commences and to establish well defined initial test conditions. However, sealing of the fracture had proved to be difficult to the extent that it was not dismantled after each test but alternatively flushed with air in some cases. This technique could not remove all the water, though, so that some water remained in the fracture and larger air bubbles evolved later in the beginning of the subsequent test.

### **Second attempt**

Failing to reach freezing conditions in the fracture in the first attempt as well as the results of the numerical models had indicated the necessity to insulate the cooling unit thermally. A cool box has therefore been built to contain the cooling unit as well as the auxiliary cooling unit. The new test set-up including the cool box (that has been used further on)

is depicted in Fig. 4.46. Following an unfortunate last-minute decision, the auxiliary cooling unit has not been installed for this attempt. Instead, the space designated for this unit has been used to pre-cool some water in small plastic bottles for later injection into the fracture.

Freezing temperatures have not been reached even after a week, though. Insufficient tightness against ambient air has been suspected afterwards as well as a considerable buffering of heat by the stored water.

Furthermore, difficulties with condensation became apparent. Condensing water formed on the acrylic glass pane in the observation duct and on the top of the upper fracture plate. This called repeatedly for undesirable unscheduled removing the top slab of the box for cleaning. About 200 g of MX-80 bentonite for dehumidifying purposes have been exchanged for the water bottles but did subsequently not really help to avoid condensation and were therefore removed again in all further attempts.

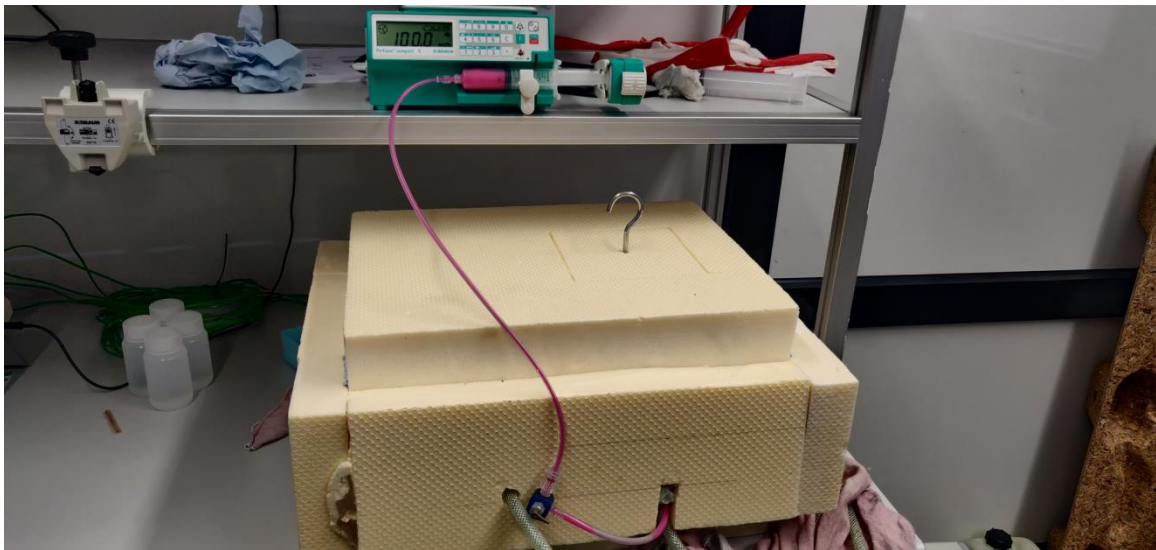


**Fig. 4.46** Setup for the second and following attempts

### **Third attempt**

For the third attempt, the auxiliary cooling unit has been added in the box as shown in Fig. 4.47 a). Again, it took some time until the condensing water in the box started to freeze. But then it turned out that the power from the cooling aggregate had been overestimated. The syringe pump gave a warning signal indicating that a counter pressure was building up in the tubing. As freezing in the tubing was suspected and for fear of

damage by expanding ice, the test was immediately aborted. Checking on the tubing system confirmed the suspicion that the injected coloured water had become frozen within the precooling coils in the cooling unit.

This has been the first time that water has been injected into the fracture. Preceding the coloured water, the fracture had initially been flooded with clear tap water. This needed to be flushed out again, so that injecting air has been tried. This proved to be only partially successful as water remained in the fracture, particularly in the outer channels with the smallest aperture (see Fig. 4.47 b)).

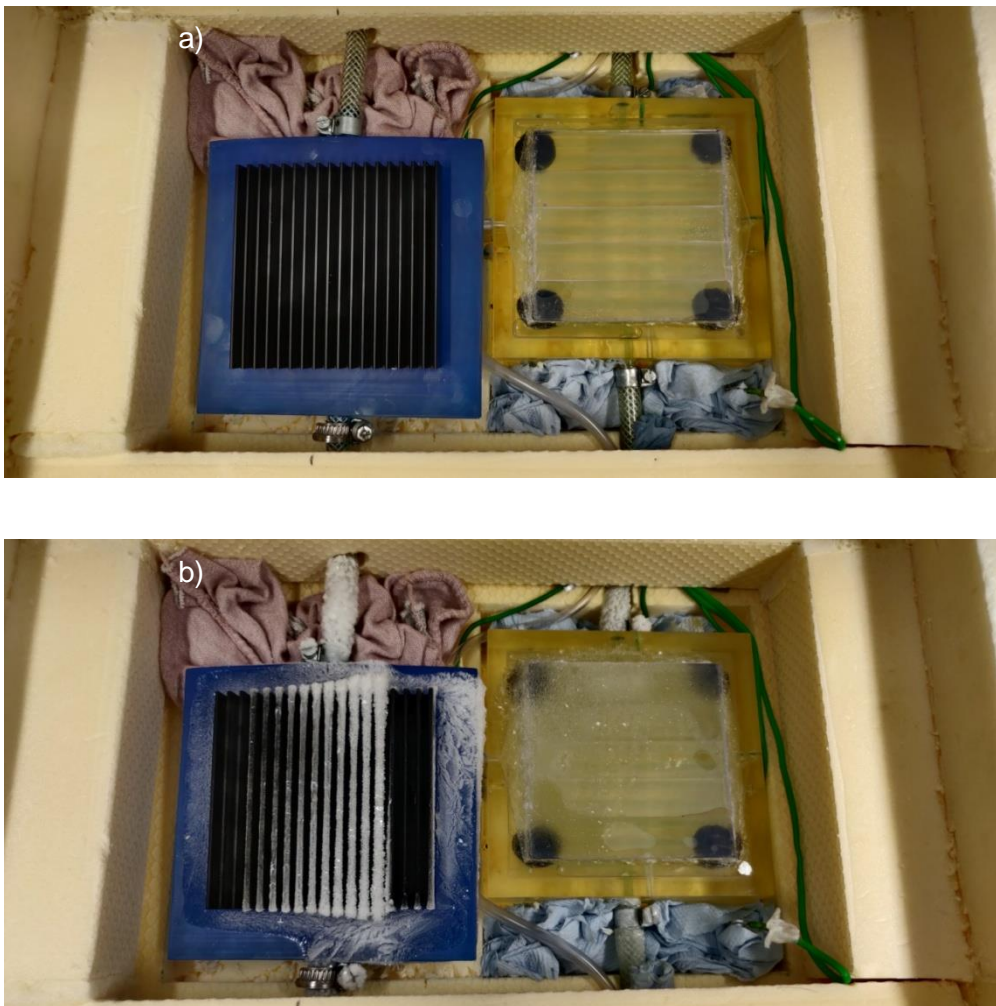


**Fig. 4.47** Cooling unit (right) and auxiliary cooling unit (left) inside the cool box; a) before the test, b) after cleaning of the test

In doing so, a hydraulic connection of the fracture to the cooling medium, i.e. the saline solution, has been detected. This should not have posed a problem during the injection as neither type of water, injected water, and saline water, had escaped the cooling unit.

When trying to dry the fracture by slightly pressurized air, however, the air was forced also into the saline solution, thereby locally preventing a direct contact of the cooling medium with the bottom plate of the fracture. Full dismantling, cleaning and new assembly of the set-up was therefore required.

#### **Fourth attempt**

For the fourth attempt, the temperature of the cooling fluid from the cooling aggregate has been adjusted. When reaching a reasonable constant temperature in the cool box, the fracture has been flushed with clear tap water. Subsequently, water has been injected from 20 ml syringes at a rate of 100 ml/min. Each syringe contained water with a different colour which has been injected in the sequence magenta, silver, green, and gold. The idea behind this colouring scheme has been to identify areas of ice forming in the fracture by its colour because differently coloured water would not be able to enter this area after freezing.

Pictures have been taken after each injection revealing some difficulties with the lighting. There has been hardly sufficient illumination from the surroundings so that a flashlight had to be used. This resulted in serious reflections on the acrylic glass. The final photographs from the test have undergone a post-processing with GIMP to remove these reflections. Based on the photographs, the course of the test is described in detail in the following.

The conditions before the test without the top slab installed yet are shown in Fig. 4.48. The picture is orientated in such a way that the inflow side is located at the top. Visible are the artificial fracture with the five parallel plate channels and the triangular openings that distribute the inflowing water over the whole fracture side and collect the water at the outflow side. The black circular structures at the corners of the fracture are actually ad hoc supports for the fracture plates and do thus not interfere with the flow. The fracture is largely free of water except in the top right corner and at the bottom at the border between the two outer right channels. Only at the end of the experiment, it has been realised that the supports might have had an influence on the thermal response of the fracture to water that has not been at exactly the temperature of the fracture.

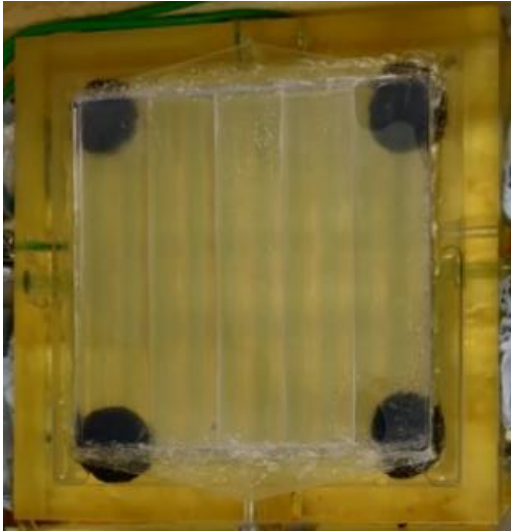


**Fig. 4.48** Cooling unit before the test

The picture of the conditions in the fracture after injecting the magenta colour is of poor quality as shown in Fig. 4.49. Visible are, though, three major air bubbles, one in the middle channel and one each in the outer channels.

A fourth bubble blocks almost completely the inflow into the large middle channel except in the top left corner. The remaining open inflow area of the middle channel covered only about 17 % of the total inflow area. According to the cubic law, the permeability in the middle fracture amounts to 2.25 times the permeability of the medium size channel. This results in an effective volumetric flow into the middle channel of only about 40 % compared to that into one of the medium sized channels. However, water flowing into the medium sized channels quickly sought a flow path directed towards less resistance as posed by the middle channel.

The right outer channel appears to be only slightly coloured, the left one not at all. Despite the bubble in the middle channel, main outflow occurs via the middle channel.

Moreover, something appears to impede outflow at the bottom of the medium sized channel to the left. The water directly adjacent to the air bubbles in the outer channels seems to be slightly darker than further away. If this is actually coloured water or simply an optical effect at the water-air interface is not entirely clear at this point.



**Fig. 4.49** Fracture after injection of magenta coloured water

The occurrence of the air bubbles is most unfortunate. They have possibly been introduced either by the flushing of the fracture with tap water or by air in the tubing between the syringe pump and the cooling unit. The latter possibility has popped up during close inspection of a photograph as shown in Fig. 4.50.



**Fig. 4.50** Air in the injection tubing

After the injection of silver water, the silver can hardly be recognized in Fig. 4.51. However, the reddish colour has been replaced at the whole upper part of the fracture as well as mostly in both medium sized channels. Main inflow appears to have occurred over the two medium sized channels. A somewhat reddish colour can be observed in the right narrow channel. The left narrow channel still appears to be void of colour.



**Fig. 4.51** Fracture after injection of silver coloured water

The two photographs in Fig. 4.52 showing the situation at the end of injection of green water are particularly blurred. However, the green water appears to have largely replaced silver and red. Exceptions are reddish tints in the right narrow channel, particularly around the large bubble. While the left photograph lets this also appear to be the case in the left outer channel, this cannot be confirmed from the right photo.

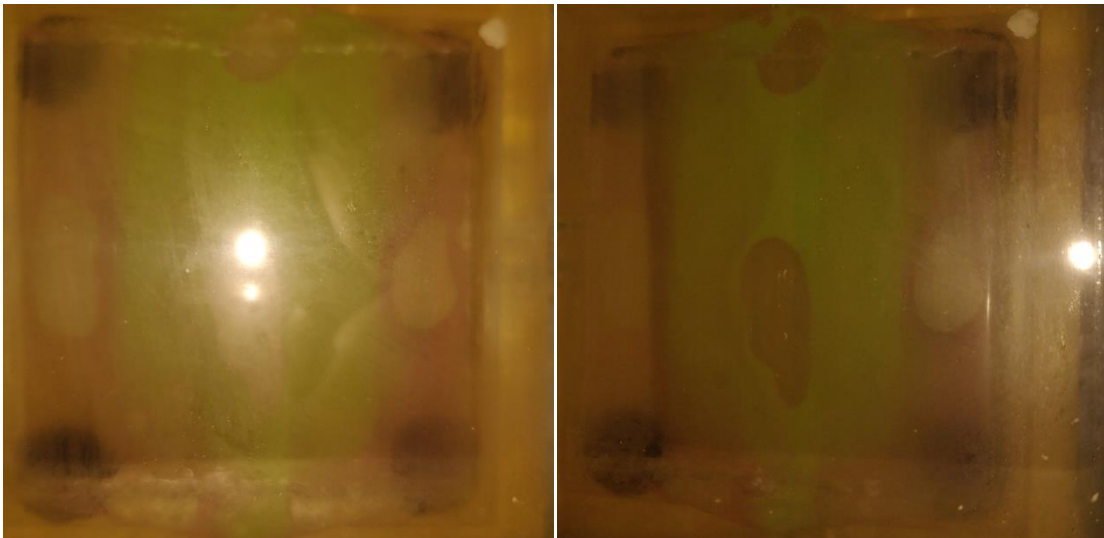


**Fig. 4.52** Fracture after injection of green coloured water

After injection of golden coloured water, the gold has replaced much of the previously injected waters in the three middle channels (see Fig. 4.53). There are also accumulations of gold at both borders of the left medium sized channel and below the large bubble in the middle. From the right medium sized channel, the gold coloured water has

apparently also advanced into the right outer channel. This effect is not symmetrical as the left narrow channel does not seem to contain golden water at all. While entering the right narrow channel from the medium sized right channel, the golden water has not been able to replace the previously prevailing green water completely. Instead, a thin green ribbon stretches from the top to the bottom of the narrow channel, enclosed by gold on the left and magenta at the right-hand side.

All in all, most of the water entered the fracture via the two medium sized channels as the entrance into the thick channel in the middle has been blocked by an air bubble. Due to the relatively low flow resistance in the middle channel, the entering water was then drawn towards the middle channel but diverted back again to the medium sized channels because the large air bubble in the middle blocked the flow in this channel again.

The area of roughly the last 2 cm towards the outlet of the **left medium sized channel** seems to have been blocked right from start, seemingly caused by local freezing. The water coming down from the top has therefore been squeezing back into the thick middle channel as is also suggested by the form of the air bubble in the middle channel.

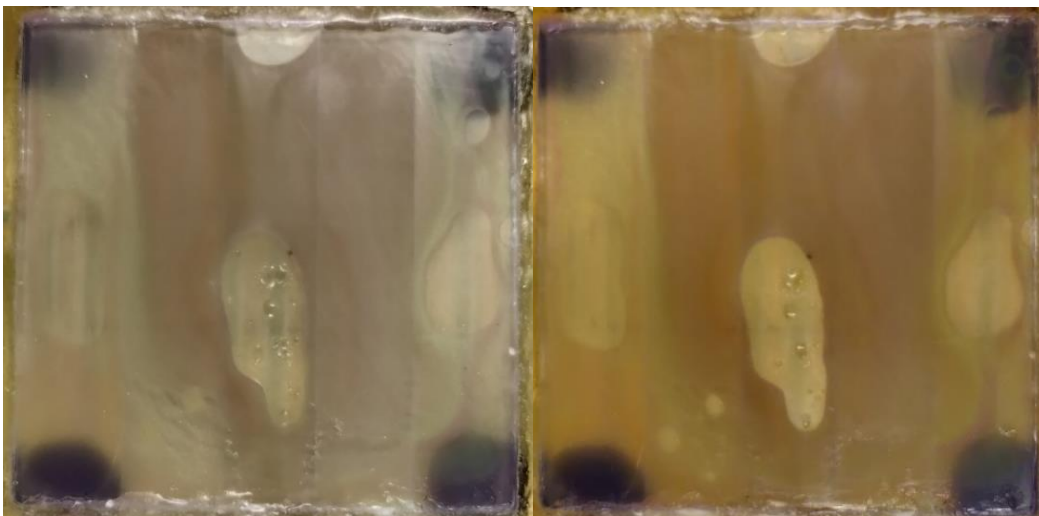


**Fig. 4.53** Fracture after injection of golden coloured water

It appears that also the **left narrow channel** had been frozen from the beginning on as no coloured water has been detected here at any stage. Since the dark lining around the large air bubble is not visible in all pictures, it is concluded that this observation is probably an optical effect caused by the water-air interface.

By comparison, the evolution in the **right narrow channel** is more complex. Here, freezing progressed during the test from the right-hand side of the channel towards the adjacent medium sized channel. It immobilized first the magenta coloured water, and subsequently the green and the golden water, leaving ribbons of these colours along the way.

The final photographs have been processed with the GIMP-software. Initially, the intention has simply been to remove the reflections from the flashlight. But subsequently it was also tried to draw additional information from the picture since the photographs in Fig. 4.49 through Fig. 4.53 from which the conclusions have been drawn so far, are of low quality.

The result for removing the reflections is shown in Fig. 4.54 a)<sup>12</sup>. Visibility of the colour tracers have then been enhanced by changes in the weighing of the colour channels which lead to Fig. 4.54 b). Also, a process that reduced the number of colours in the pictures was tentatively applied. The results for two differently drastic reductions are depicted in Fig. 4.54 c) and d).

These manipulations are clearly successful when removing the annoying reflections. They also confirm nicely the conclusions from the plane pictures by the enhanced visibility of structures such as the boundaries of the sedimented areas. The colours themselves become quite misleading, though. What has clearly been golden has become rather red with the postprocessing which would have led to entirely wrong conclusions about the test evolution.

---

<sup>12</sup> This goes also for the photographs in Fig. 4.53.

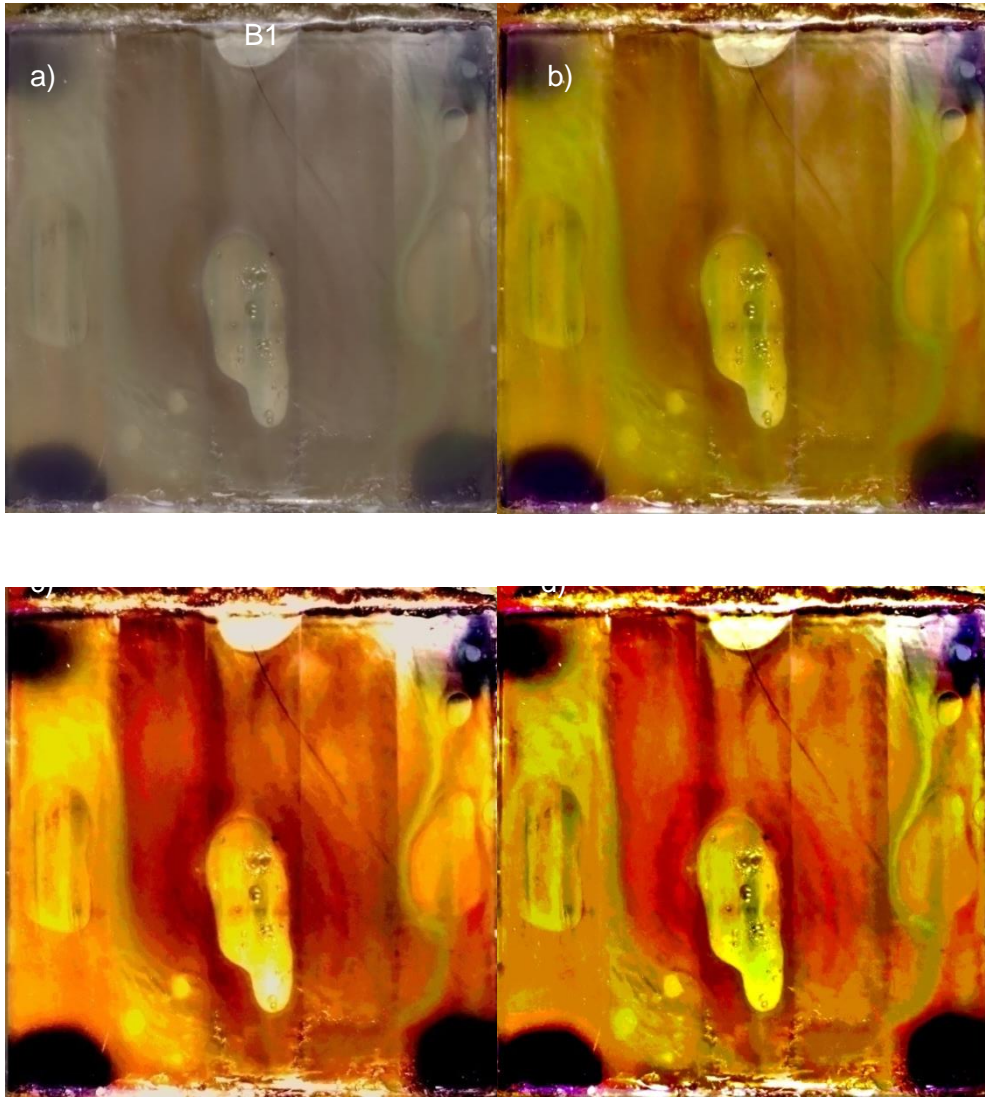


**Fig. 4.54** Colour distribution in the fracture at the end of test; a) original photograph, b) modified colour channels, c) reduced number of colours, d) stronger reduced number of colours

The result from the final flushing of the fracture with tap water and with air afterwards, as depicted in Fig. 4.55, allows for two more direct observations. Firstly, the colour pigments could be removed to the extent that they are not visible anymore. Secondly, the pressure applied by quickly squeezing air from a syringe into the system does not build up enough pressure to clean the narrow-sized channels. Interestingly, the impediment at the bottom of the left medium sized channel could be cleared which substantiates the notion that it had been formed by ice.

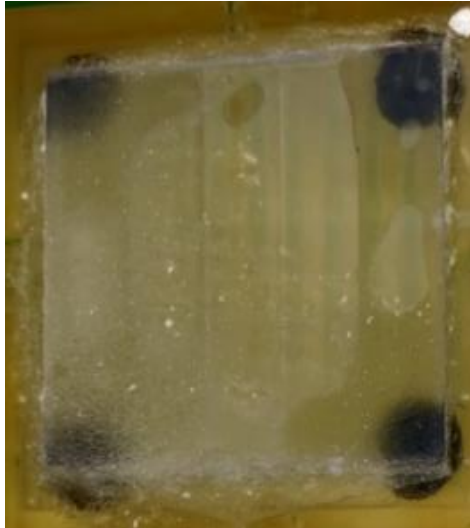


**Fig. 4.55** Fracture after final flushing with tap water and with air

During cleaning it has been noticed that a red hue had remained on the surface of the fracture plates. It was formed by the reddish particles that had coloured the magenta water. The particles have thus been suspected either to have a particular affinity to the printed resin or to be particularly heavy causing sedimentation of some sort. However, if there had been an effect like bonding of the particles to the resin, they should have remained visible everywhere in the fracture except where ice was present right from start. However, differently coloured water had been able to replace the red water. This contradicts the idea of bonding of the magenta particles to the resin, leaving only the interpretation of sedimentation of particles happening to such a low extent that they have not been observable in the photographs.

#### **Fifth attempt**

In the fifth and final attempt, the test set-up has been improved again. The backside of the fracture has been painted white to improve visibility of the colours. A better camera technology has been used for taking pictures at the end of each injection phase. The fracture was filled with a salt solution at assembly which minimised number and size of the initial air bubbles and allowed at the same time for precooling without the danger of premature freezing in the system that could be threatening the structural integrity of the cooling unit. Finally, a different sequence of colours was used as well as 50 ml per colour instead of 20 ml to ensure longer testing times as well as better distinction between the injection phases.

The test has been run according to the following list:

- Starting the cooling aggregate providing a temperature of  $-7^{\circ}\text{C}$  in the cooling fluid<sup>13</sup>
- Cooling over 54 h
- Quick injection of clear tap water to replace the salt solution<sup>14</sup>
- Increasing temperature of the cooling fluid to  $-6^{\circ}\text{C}$
- Injection of about 50 ml coloured water at 100 ml/h in the sequence blue, red, and green
- Several quick flushes with clear water in rapid succession
- Stopping the cooling aggregate
- End of test

This time, the fluid temperatures in the cooling unit during the envisaged test have been simulated with an updated numerical model in hope of better test controlling. Particularly the cool box has been added in the model (see Fig. 4.56). The change in the temperature of the cooling fluid at 54 h has been accounted for as well as commencing the injection at 55 h which implies beginning of flow and change of the inflow temperature. During precooling, the immobile injection fluid has been cooled down with the cooling unit but was then set to an inflow temperature of  $+3^{\circ}\text{C}$ <sup>15</sup> and a flow velocity according to the injection rate.

---

<sup>13</sup> A slightly lower temperature than intended for the test has been chosen for precooling to ensure an appropriate temperature in the cool box

<sup>14</sup> Pictures were taken at the end of this and each of the following injection phases. Note that focussing through the acrylic glass was difficult and has led to somewhat blurry photographs in some cases.

<sup>15</sup> The syringes filled with coloured water had been stored and transported at approximately refrigerator conditions.

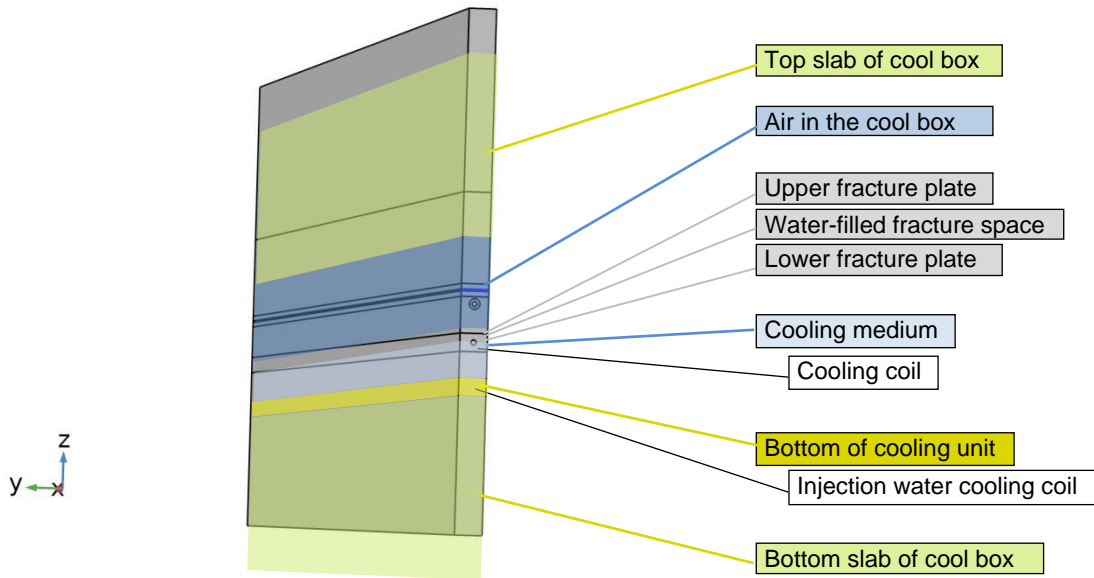


**Fig. 4.56** Updated domain of the numerical model

The air temperature in the cool box was monitored in the model. Predicted was an air temperature of  $+0.4^{\circ}\text{C}$  (see Fig. 4.57, left) which has been somewhat less than the measured air temperature of  $+2.7^{\circ}\text{C}$  at the beginning of the test. A close-up of the plot to the left in Fig. 4.57 is depicted at the right-hand side. It shows the effect of the temperature increase in the cooling fluid at 54 h and of the injection at 55 h model time on the air temperature in the box. Note that the mean air temperature was still decreasing at 54 h.

Due to the simplifications in the model, some care had to be taken when looking at the temperatures of the injection cooling coil and the fracture as these structures did of course not have the length of the unwound coil for the cooling fluid. The inflow temperature for the fracture was therefore taken from the point at 40 cm into to cooling coil for the injection fluid. In the same way, the temperatures monitored in the fracture were taken from 0, 5 and 10 cm into the fracture.

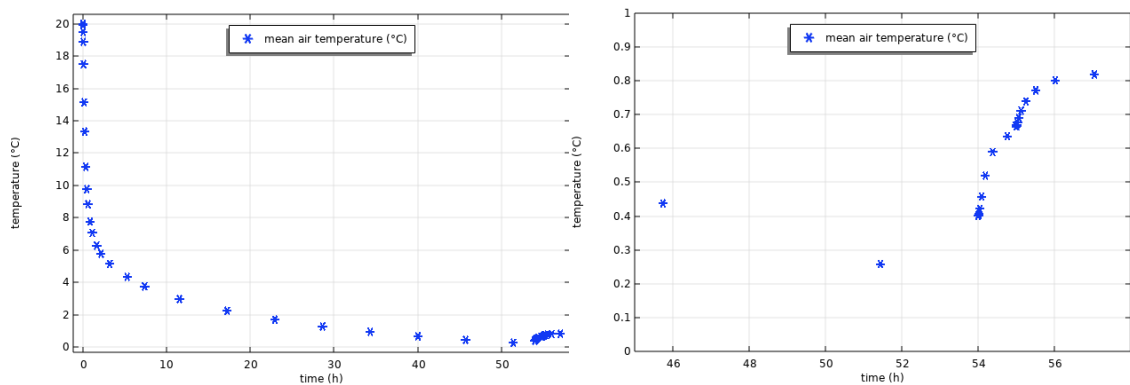


**Fig. 4.57** Mean air temperature in the cool box; left: full test, right: final phase

The temperature evolution in the fracture that has been expected from the model calculation is depicted in Fig. 4.58 for three locations, at the inflow side (green line), in the middle of the fracture (red line) and at the outflow side (blue line). It suggests that contrary to the temperature in the cool box, the fluids have been more or less at steady state at the beginning of the test. From the curves for the middle and the outflow side of the fracture it can be concluded that water in the fracture should have been frozen in this region. However, it turned out in the actual test that this has not been the case.

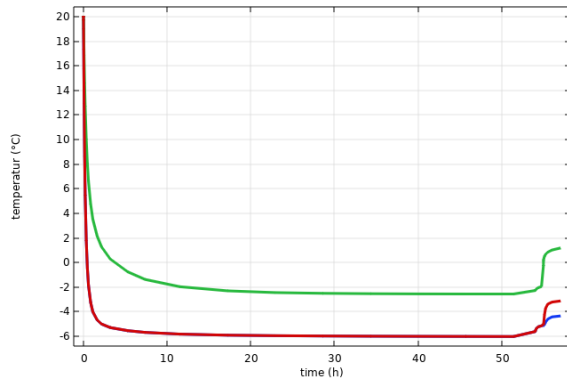


**Fig. 4.58** Temperature in the fracture; inflow: green, middle: red, outflow: blue

As with the fourth attempt, the developments in the test are described based on the photographs taken. Fig. 4.59 shows that the procedure has initially been successful in that no air bubbles have developed.

The photograph at the end of the first injection phase is depicted in Fig. 4.60. Despite it being quite blurred, it can be seen that seemingly, air bubbles have emerged even if much smaller than in the previous attempt. They appear mostly in the middle channel, and a few can be found in the medium sized channels. But none are present in the narrow outer channels.

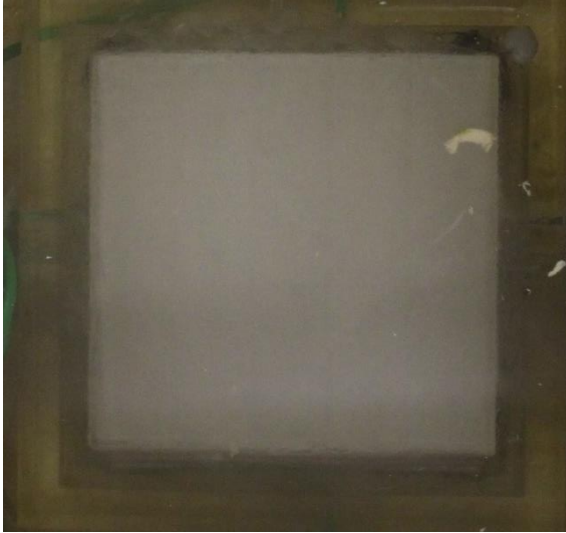


**Fig. 4.59** Fracture after injection of tap water

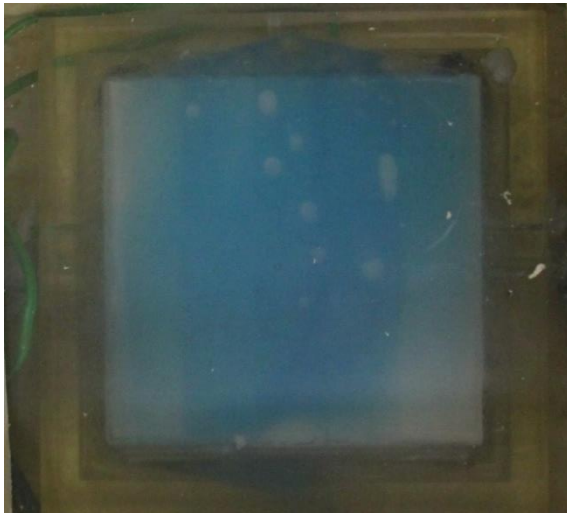


**Fig. 4.60** Fracture after injection of blue water

The blue hue is less pronounced in the outer channels than in the middle three channels because they show the smallest aperture. However, the hue is even less pronounced at the inflow and outflow side of the left channel and at the outflow side of the right channel. The same applies to the outflow side of the right medium sized channel and the middle channel where a large bubble similar to the one at the top in the previous attempt can be surmised.

After injection of the magenta-coloured water as depicted in Fig. 4.61 the overall colour is rather violet than reddish. The position of the small bubble-like features has not changed, there colour appears to be also slightly violetly tinted. The brighter patches are

still visible. The notion of a large bubble at the outflow of the thick, middle channel appears to be confirmed.

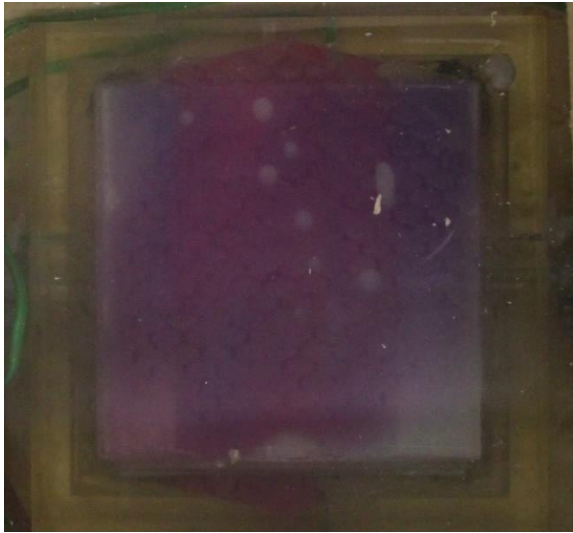


**Fig. 4.61** After injection of red water

The picture is influenced by condensing water which can be recognized by the honeycombed pattern superimposed on the picture. These were the places where the cut-out part of the duct has been in contact with the acrylic glass pane and has locally prevented from condensation. This observation raises the suspicion that the blurring might at least partly be caused by condensing water on the acrylic glass pane.

In comparison with Fig. 4.60, the brightness of the area in the top left corner appears to have decreased. Probably due to a better focus, the bright areas at the bottom corners of the fracture seem to be rather sharply delineated from the adjacent medium sized channels.

The pictures taken after the injection of green water have been quite dark. The best one depicted left in Fig. 4.62 is complemented by a version of increased brightness by post-processing. Quite unexpected, the dominant colour is blue and not a bit greenish and does also not show clear signs of the magenta colour which also goes for the bubble-like features. The bright area in the top left corner has disappeared while the bright areas in the bottom corners prevail. Almost the complete middle channel appears now at the same brightness as the bottom corner areas. Also, triangular areas at the top of the medium sized channels appear to be affected in the same way



**Fig. 4.62** After injection of green water; left: original photo, right: increased brightness

After the injection of green water, the fracture was flushed ten times in rapid succession just taking time between consecutive flushings to take a photograph. The ten photos are compiled in Fig. 4.63. They show that the big bubble at the outlet of the thick middle channel could apparently not be flushed out at all. Nevertheless, a large bubble has formed in the middle of this channel during the first flush which is gone again after the second flush. By contrast, what had appeared to be bubbles after the injection of the blue water (cp. Fig. 4.60) does not vanish even after all ten flushes. They just show a decreasing contrast to the surrounding area.

A bright line-like feature has started downwards from the bright triangle in the left medium sized channel during the third flush getting longer during the sixth flush and then again during the eighth flush. Others appear after the sixth flush and even more after the eighth to tenth flush. It could be observed that they are the result of small air bubbles pushing blue particles out of the way.

The bright area at the top of the right medium sized channel widens with the flushes and becomes brighter. Below, close to the boundary to the right narrow channel, two vertical narrow ovals form. They grow until they connect during the eighth flush (a) with each other, (b) at the top with the large area above and (c) at the bottom with the thick channel in the middle. Connection (c) becomes particularly thick after the tenth flush.

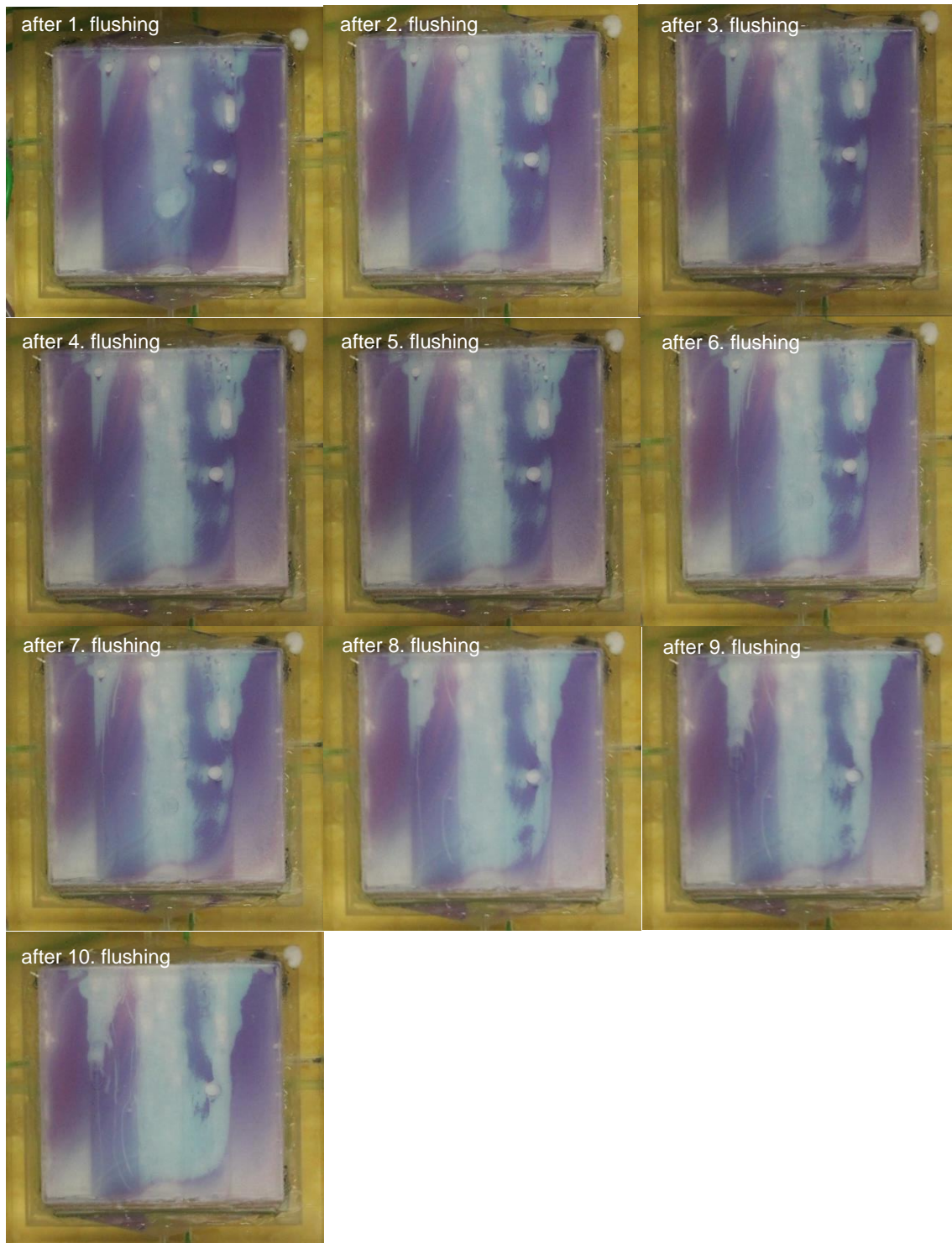


**Fig. 4.63** Fracture after the first to tenth flush with tap water

Cleaning cooling unit and tubings revealed a lot of “sediments“, formed by particles from the water colours. It thus appears that the blue hues that have been dominating the pictures, resulted from prevailing blue particles. It can be speculated here that the coloured waters have been blended differently in the fourth and fifth attempt, letting red be

dominant in the fourth attempt and blue in the fifth one. Unfortunately, this confirms also the notion that there has been no freezing in the fifth attempt and the dynamics observed during the flushings are the consequence of moving particles with the flow like the little bubbles forming the bright lines.

The bubble-like structures that have appeared after injecting the blue water are quite difficult to understand as they prevail even after the final flush of tap water. The best explanation found so far – even if somewhat speculative – is that these features are indeed initiated by air bubbles which prevented the affected areas from most of the sedimentation of blue particles. They must have moved away towards the end of the injection of blue water, though, as they nevertheless appear to be slightly blue. The later injected differently coloured waters should have been more clearly identifiable here. Unfortunately, this cannot be substantiated due to the poor quality of the photographs. During flushing, however, they prevail but loose contrast to the surrounding areas which can be interpreted as slowly removing the surrounding particles.

#### **4.2.4 Modelling growth of permafrost**

Since numerical simulation of the experiment described in the previous section did not make sense at this stage, a model for calculating the thickness of permafrost as a function of surface temperature has been developed instead. This work can be considered to prepare grounds for an investigation of the development of taliki by numerical models as the environmental background for this development must be known first.

The development of permafrost requires an environment that is characterized by decreasing surface temperatures, leading to downward growth of permanently frozen ground. This growth is counteracted by heat flow from earth's interior. In order to set up a credible model for talik development, the interplay between surface temperature and heat flux from earth must be simulated reasonably well first.

A simple performance measure for such a model can be the thickness of the permafrost at steady-state conditions. The thickness can be defined as the depth where the temperature of 0°C is found in the model. Therefore, the increase of permafrost thickness due to different constant surface temperatures is modelled. An interesting graph showing this thickness as a function of surface temperature for different locations in the world can be found in /JNC 00/ (see Fig. 4.64 and section 4.4.2). Unfortunately, it is not entirely clear to which locations the four entries refer. It is assumed here that the data from Canada

have been taken from somewhere in the Canadian shield. Where not enough data have been available for the present model, advantage was taken from the similarity to the granitic underground in Greenland or Scandinavia.

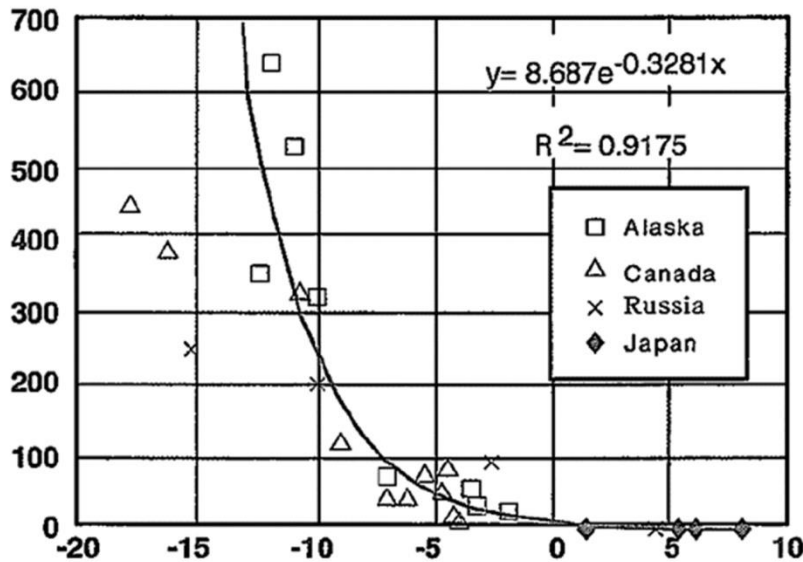


Fig. 4.64 Permafrost thickness over surface temperature; from /JNC 00/

According to the purpose of the model as defined above, it is sufficient to set up a steady-state model. However, since the time for reaching steady state provides information on the response time of the system to temperature changes, a transient model was set up exemplarily as well.

The components of both models are discussed in the following.

### Surface temperature

Permafrost is defined as any type or part of the underground that has experienced continuously sub-zero temperatures for two or more years (e.g. /MAR 00/). Relevant here is the ground temperature at the surface which is generally a few degrees lower than the near-surface air temperature (e.g. /KJE 09/).

In principle, the ground surface is subject to different cycles of varying temperatures. There are daily, seasonal and climatical variations. The influence of these cycles on a vertical temperature profile is that the temperatures are oscillating around a mean temperature. The amplitude of these oscillations decreases with depth. The depth at which the oscillations become negligible is directly related to the length of the temperature

cycle. The daily variations become unnoticeable at a depth of about 1 m, the seasonal variations at about 10 – 15 m /MAR 00/. This much deeper than the zone of freezing and thawing in the topsoil associated with seasonal changes, called “active layer”, whose thickness can be found in the range of decimetres to several meters (e.g. /YI 20/).

Daily and seasonal variations are ignored in the model as they are comparatively quick and thus do not reach deep into the subsurface. By contrast, climatic cycles are assumed here to take much longer than the related temperature changes in the underground. A constant temperature is therefore assigned to the surface in the present model. In order to draw up a graph of permafrost thickness over surface temperature, several model runs are performed with surface temperatures that decrease in steps of 4°C.

### **Heat flow from earth’s interior**

There are several causes for earth’s heat production such as radioactive decay which is believed to account for half of the heat production if not even somewhat more, residual heat from planetary accretion, and latent heat from core crystallization. The hottest spot is expected to be found at the centre of the earth but decrease of temperature towards the surface conditions as we know them forms a complex curve. Only in earth’s very upper part of the crust down to about 400 km depth, the curve is linear and well described by the geothermal gradient as heat flow is basically due to conduction here.

In principle, the geothermal gradient is a constant, but it varies to a certain extent over earth’s surface. The generally accepted mean value of the geothermal gradient amounts to 3°C/100 m but values as high as 9°C/100 m and as low as 1°C/100 m have been found also. The actual value depends on different local factors like geology, mineralogy, morphology and, if applicable, volcanic activity. Ultimately, however, the local thermal conductivity of earth’s crust decides about the steepness of the geothermal gradient. As a rule, the steepness is inversely related to the conductivity.

Basically, the heat flux entering the model can be calculated as the product of the effective thermal conductivity<sup>16</sup> and the geothermal gradient. Consequentially, the model must reach down deep enough, though, to avoid significant influence of the permafrost

---

<sup>16</sup> That is the porosity weighed sum of the thermal conductivity for water and the rock.

building at the top of the model on the heat inflow at the lower boundary. When the model was set up, tentative model runs with a surface temperature of  $-2^{\circ}\text{C}$  showed, that the calculated permafrost depth differed by half a metre when setting the model depth to 1500 and to 2000 m and only by less than 2 cm for model depths of 2000 and 2500 m. It was therefore set to 2000 m.

### **Phase state of the water**

Essentially, water changes the phase state from solid to liquid by melting or vice versa by freezing at  $0^{\circ}\text{C}$ . A temperature of  $0^{\circ}\text{C}$  is therefore assumed to be a marker for the boundary of frozen ground that is the permafrost thickness.

### **Thermal properties of water**

The thermal conductivities of water and ice are in principle temperature dependent. However, the value of the thermal conductivity at  $60^{\circ}\text{C}$  differs from that at  $0^{\circ}\text{C}$  only by approx. 15 % (cp. /KRÖ 10/) and even less for water and ice below  $0^{\circ}\text{C}$  (cp. /KRÖ 21/). Constant values for the thermal conductivity of water and ice are therefore considered to be sufficient for the purpose at hand<sup>17</sup>. Different values for water and ice are required, though, as they differ by a factor of approximately 4. Adopted are  $569 \text{ W}/(\text{m K})$  for water and  $2220 \text{ W}/(\text{m K})$  for ice.

Also, for the specific heat that decides about the response time of the system to temperature changes, constant values suffice according to /KRÖ 21/. Adopted are  $4219 \text{ J}/(\text{kg K})$  for water and  $2050 \text{ J}/(\text{kg K})$  for ice.

### **Properties of geological units**

Most simple is the geology in Scandinavia, Greenland or Canada as the prevailing granite has a thickness in the range of kilometres. Any geological surface features such as topsoil, regolith or aquatic features are assumed here to form a quite thin layer. In analogy to the situation at Äspö, Sweden the thickness of surface features is assumed to be about 40 m.

---

<sup>17</sup> The tentatively added temperature dependence for water according to /KRÖ 10/ changed the inflow temperature only in the third decimal place.

The granite is characterized by a porosity of 0.01, a density of 2400 kg/m<sup>3</sup>, a thermal conductivity of 3600 W/(m K) and a specific heat of 686 J/(kg K). By contrast, the overlying thin layer is assumed to show one third of the thermal conductivity.

### Numerical simulation

For modelling heat flow in the rock-water system, the numerical simulator COMSOL Multiphysics /COM 21/ is used, employing the interface “heat transfer in porous media”. The partial differential equation that is solved there reads

$$- \left( \rho c_p \right)_{eff} \frac{\partial T}{\partial t} + \rho c_p \mathbf{v} \cdot \nabla T + \lambda_{eff} \nabla T = q_0 \quad (4.7)$$

- $\rho$  – water density [kg/m<sup>3</sup>]
- $c_p$  – specific heat capacity of water [J/(kg K)]
- $T$  – temperature [K]
- $t$  – time [s]
- $\mathbf{v}$  – vector of the fluid velocity [m/s]
- $\lambda_{eff}$  – effective thermal conductivity [W/(m K)] (cp. ( 4.8 ))
- $q_0$  – heat flux over a boundary of a 2d-model [W/m<sup>2</sup>]
- $\left( \rho c_p \right)_{eff}$  – effective volumetric heat capacity [J/(m<sup>3</sup> K)] (cp. ( 4.9 ))

with

$$- \lambda_{eff} = \Phi \rho \lambda + (1 - \Phi) \rho_p \lambda_p \quad (4.8)$$

- $\Phi$  – porosity [-]
- $\lambda$  – thermal conductivity of water [W/(m K)]
- $\rho_p$  – rock density [kg/m<sup>3</sup>]
- $\lambda_p$  – thermal conductivity of the rock [W/(m K)]

and

$$- \left( \rho c_p \right)_{eff} = \Phi \rho c_p + (1 - \Phi) \rho_p c_{p,p} \quad (4.9)$$

- $c_{p,p}$  – specific heat capacity of the rock [J/(kg K)]

Note that the velocity vector is set to be a zero vector for this investigation.

## Results

The permafrost thickness was determined with the steady-state model for 5 different surface temperatures. The data are listed in Tab. 4.6 and graphically compared with the data from /JNC 00/ in Fig. 4.65. The calculated thickness is slightly too high, but the trend is sufficiently well matched. The results leave room for parameter adjustments in order to match the data even better. Because of the data uncertainty, this option has not been pursued, though.

Clearly visible in Fig. 4.65 is the influence of the thin top layer with reduced thermal conductivity by a different gradient in the plot. The lower thermal conductivity requires higher temperature gradients to conduct the same amount of heat as the granite beneath. The permafrost boundary (depth with 0°C) thus moves slower with decreasing surface temperature in the top layer than below, in other words, the top layer impedes the permafrost growth.

**Tab. 4.6** Depth of permafrost as a function of the surface temperature

Surface temperature [°C]	Calculated permafrost depth [m]
-1	11
-2	22
-3	33
-4	54
-6	121
-8	188
-10	254
-12	321
-14	388
-16	454
-18	521

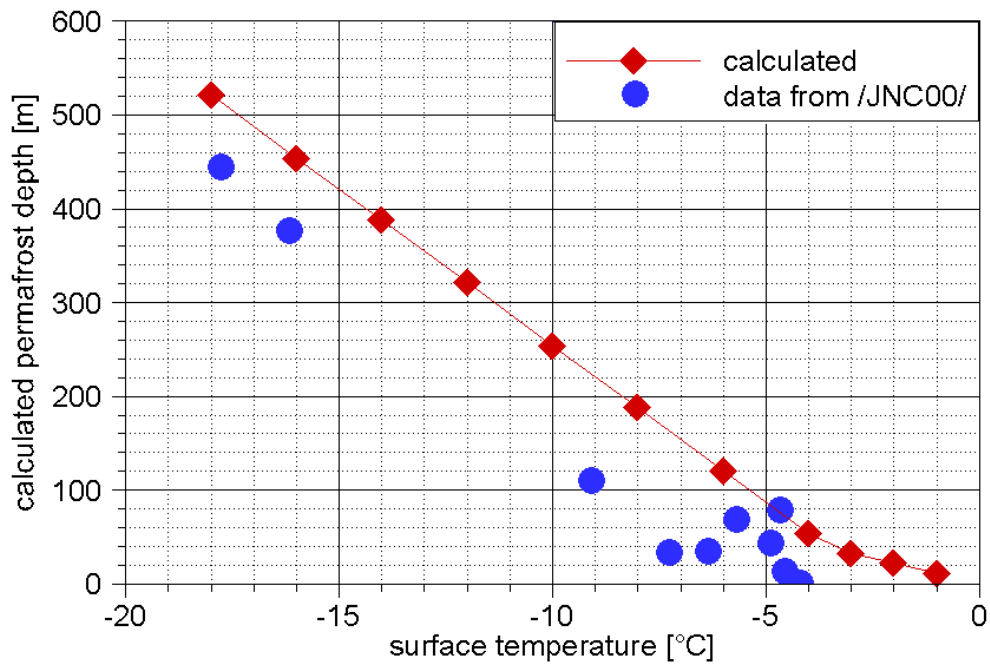


**Fig. 4.65** Permafrost depth depending on surface temperature for the Canadian shield; modelling results and data from /JNC 00/

In order to estimate the time until steady-state conditions are reached, an equivalent transient model was run exemplarily for a surface temperature of  $-2^{\circ}\text{C}$  and  $-10^{\circ}\text{C}$ . Mathematically, the transient freezing process converges but never reaches steady state. Steady-state conditions are therefore ad hoc considered to be reached at the time when the simulated temperature drop amounts to 95 % of the difference between initial and steady-state temperature. Referring to this definition, steady-state conditions are reached after about 6800 years at a surface temperature of  $-2^{\circ}\text{C}$  and after about 46000 years at  $-10^{\circ}\text{C}$  (see Fig. 4.66).

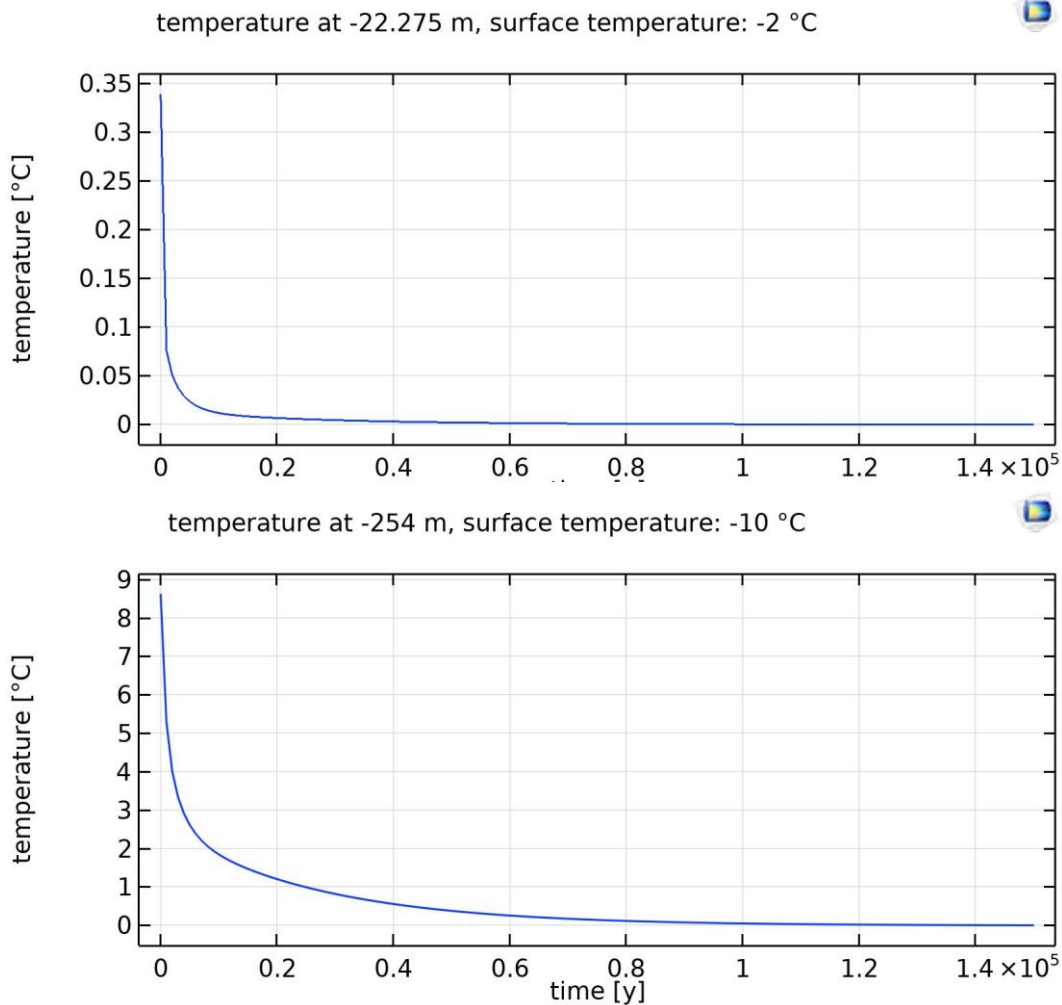


**Fig. 4.66** Convergence of temperature at the steady-state permafrost boundary; top plot: surface temperature of -2°C, observation level -22.275 m, bottom plot: surface temperature of -10°C, observation level -254 m

#### 4.2.5 Conclusions and outlook

The experiment with respect to freezing water in fractures will be continued. Several difficulties have been encountered during the present study that will be addressed and circumvented in the future:

- (1) Visibility of the colour tracers in the fracture still needs to be enhanced to avoid tedious postprocessing of the photographs. Using water colours as colour tracers has been proven to be an unfortunate choice. Other marker fluids will thus be checked for practicality.

(2) The cool box needs to be reconstructed.

(a) Too much air in the cool box has been impeding the cooling process throughout the whole study. Minimising the available space in the cool box should be improving the test conditions considerably.

(b) The observation duct has been a weak point in the construction as it still allowed for ambient heat to enter the box and to heat the air in the box surprisingly quick. Instead, a suitable camera including an internal lighting is to be installed in the box.

(c) Condensing water required repeatedly opening of the cool box and was thus disturbing the tests. This can be avoided – at least to a certain degree – by a better sealing of the cool box to ambient air humidity. Furthermore, alternative desiccants emplaced in the cool box might help to reduce the air humidity. And the potential for improvement by a treatment of the surfaces of the acrylic glass pane and the top fracture plate should be checked.

(3) The construction of the cooling unit can be optimised in at least two aspects.

(a) First of all, it should be adapted to facilitate installation of the fracture plates when using saline solutions as a cooling medium. This had not been foreseen in the planning stage and has caused later quite some additional work with respect to installation and sealing of the fracture plates.

(b) Mechanically, the connectors for the tubing are a weak point as they can rather easily break off when connecting the tubings with the cooling unit. In this case, the form as well as the position should be changed in order to minimise the strain during installation as well as during dismantling.

(c) With respect to inflow and outflow from the fracture, the present construction is highly adapted to the parallel plate model for the fracture. Positioning the fracture in such a way that the outflow opening at the cooling unit coincides with the inflow side of the fracture requires quite some accuracy during installation. A construction that allows for a more robust installation while being flexible enough to accommodate a natural course of a fracture is therefore advisable.

(5) The numerical heat flow model should be improved along with the other test components as it has the potential to be a more targeted test control. To begin with, this concerns the expected time for precooling of the setup before the actual test. More important, though, is the prediction of the fluid temperatures at various locations in the test setup as the injection fluid must be supercooled by movement in the cooling coil in order to freeze in the fracture. A good prediction would be an enormous help for this is a meticulous task.

The envisaged strategy for further work in general is to improve the tests with a parallel plate fracture with respect to the technique itself as well as to the interpretation of the results. Having reached control over the tests with a parallel plate fracture, realistic printed replicas of fractures are intended to be used.

A numerical model for granitic formations that explains growth of permafrost thickness with decreasing surface temperatures has been set up. The input parameters have been chosen to be in accordance to the Canadian shield, one of the largest and oldest crystalline formations on earth. As a performance measure, the steady-state thickness of the permafrost was calculated as a function of the surface temperature. A comparison with referring data from the field confirms the viability of the model. Next step is the inclusion of large aquatic features at the surface to study the impact of such features on freezing ground.

The times for reaching steady state are rather long and come into the range of climatic changes. Modelling talik development will therefore require well set initial conditions as well as transient modelling.

### **4.3 Gas transport in clay stone**

Claystone is one of the potential host rocks considered for nuclear waste disposal of high-level, heat-generating radioactive waste in Germany. The repository concepts currently discussed for nuclear waste repositories in claystone formations in Germany /JOB 17a/ are considering the disposal of the waste in cast iron containers either in disposal drifts or boreholes. In the latter case the boreholes are supported by cast iron borehole liners to achieve retrievability of the containers.

Due to the natural water content of the porous claystone host rock and the hydrostatic boundary conditions, it is expected that the backfilled emplacement areas of the repository are re-saturated with water within a few hundreds of years /JOB 17b/ by water inflow according to the Darcy law. The contact of the cast iron containers and liners with water in absence of oxygen leads to anaerobic corrosion resulting in a production of about 19 moles of hydrogen gas per kilogram iron by anaerobic corrosion /MÜL 92/. The volume of gases produced are typically too large to be stored in the pore space of the backfill in the emplacement areas and therefore lead to a gas pressure build-up /JOB 16b/. The resulting pressure gradients induce an advective movement of gas and potentially also of water in the drift system of the repository, but also in the clay host rock.

Due to this reason, the gas transport mechanisms in claystone host rocks were studied for quite a long time as part of the scientific research carried out in the nuclear waste disposal programmes of Nagra in Switzerland /NAG 02/, /MAR 05/ and ANDRA in France /AND 05/. The state of art of the international research for gas transport in consolidated claystone formations was reviewed in 2008 as a part of a previous project /NOS 08/. The review was mainly carried out to evaluate the knowledge in terms of the possibility to incorporate the gas transport processes in integrated performance assessment modelling.

Due to the ongoing scientific research since that time, for example as part of the research project FORGE (Fate of Repository Gases) in the Euratom 7<sup>th</sup> framework programme /JAC 14/, the current advanced knowledge is reviewed again with an emphasis on new developments since 2008.

In water saturated clay formations, the following gas transport processes are considered to dissipate the gas pressure in the waste repository:

- A fraction of the gas can be **dissolved** in the pore water corresponding to its gas solubility. It can be transported by **diffusion** or by **advection** with the water flow.
- If the gas generation rate exceeds the potential dissipation rate of gas by diffusion in the dissolved state, the gas pressure in the gas phase of the emplacement areas rises continuously. Once the gas pressure in the emplacement area exceeds a certain threshold pressure (gas entry pressure), the gases can enter into the claystone pore space by displacement of water, resulting in a partial desaturation of the claystone. The gas entry pressure shows a distinct dependence from the intrinsic permeability. Therefore, the gas entry pressure is expected to show a similar

heterogeneity in a claystone formation than the permeability, resulting in gas to enter the formation first in areas with higher permeability.

While the degree of saturation changes, the porosity of the claystone remains unchanged by the entry of the gas into the pore space. The entry of gas into the pore space brings water and gas into joint motion. The simultaneous flow of gaseous and liquid phases is called **two-phase flow**. Two-phase flow is the most likely gas-transport mechanism if the gas pressure is below the minimal principal normal stress.

- If the gas pressure in the waste repository exceeds the minimal principal stress of the host rock in the repository depth, it is not expected that claystone formations can withstand the pressure over long time scales because they usually have a rather low tensile strength. Therefore, if the gas pressure exceeds the principal stress, microfractures are formed in the claystone formation. These microfractures do not only increase the pore space but also the gas permeability of the formation leading to a notable increase in the gas transport. This effect is called pathway dilation. The penetration of the gas into the newly created pore space is causing only minor desaturation and the gas pathways are believed to be resealed as soon as the gas flow decreases and water re-saturates the pore space. Since the porosity of the claystone is changed by the pathway dilation and the porosity therefore becomes a function of gas pressure, the classical models for the two-phase flow like van Genuchten are not valid for the description of the **dilatancy controlled gas flow**.
- An additional transport mechanism could occur in claystone formations if stress on the rock matrix is exceeding the claystone rupture strength; namely the creation of fractures, which includes the disturbance of the claystone matrix. Models for fracturing caused by fluid injection, so called **hydraulic fracturing**, are available.

One main emphasis of the research performed since 2008 was to study in more detail the effect of dilatancy controlled gas transport in consolidated claystone using either drill core samples in laboratory experiments, in-situ experiments in underground research laboratories (URL) and numerical modelling of those experiments. The most important latest in-situ experiments are HG-C / HG-D experiments at Mont Terri URL and the PGZ experiment at Bure URL. Those in-situ experiments consist of groups of boreholes, in which one borehole is used for gas and water injection and others are to monitor water and gas pressures in the rock. The PGZ experiment uses two boreholes (Fig. 4.67), while the HG-C experiment uses four boreholes. Fig. 4.68 exemplarily shows the pressure measurements at the three measurement intervals in PGZ1201 and the gas flowrate

imposed between January 2010 and January 2011. Gas flow clearly already occurs at low pressure states.

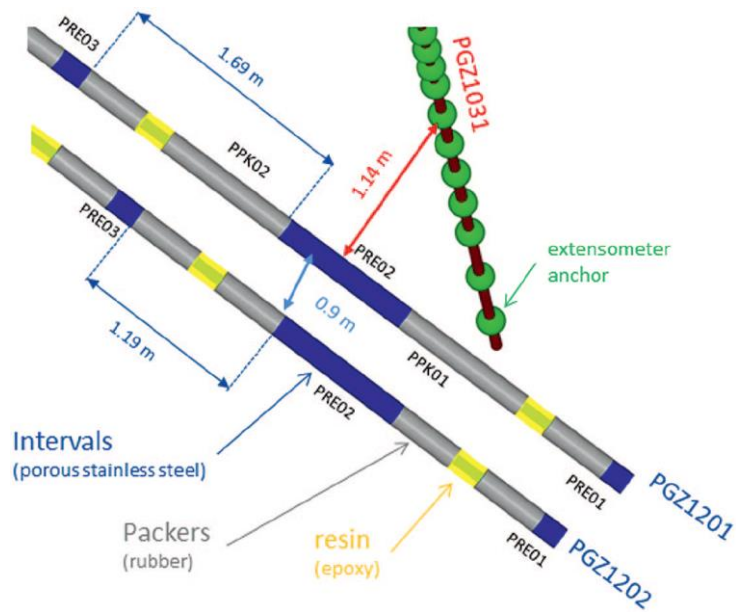


**Fig. 4.67** Set-up of the PGZ experiment /HAR 12a/

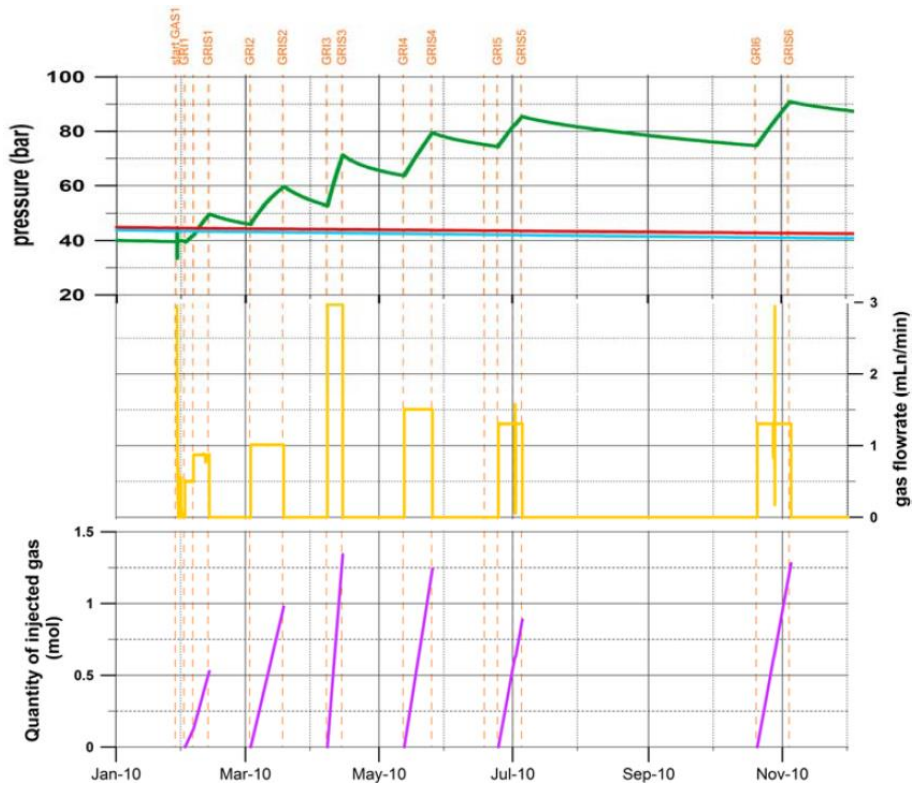


**Fig. 4.68** Pressure measurements, gas flowrate and gas quantity injected in PGZ1201 over one year /JAC 14/

The results of these experiments are interpreted differently. The reason for that is that for in-situ experiments the interpretation mainly results from inverse modelling of the obtained results, not from direct observation. For the long-term in-situ experiment PGZ 1201 Cuss et al. /JAC 14/ state that *there is no evidence of dilatant pathways formation during the gas injection, even if the gas pressure reached is high (9.1 MPa) considering the gas fracturing pressure (about 12 MPa) in Bure site*. The reason for the latter interpretation is the fact that the results of the experiment could be reproduced by modelling using classical two-phase flow numerical codes. The HG experiments from Mont Terri have been modelled with both, classical two-phase flow codes according to the van Genuchten model, but also with different new models assuming pressure dependent permeability and capillary strength /JAC 14/ and /NAV 13/. All approaches allow to some extent to describe the achieved results from the experiments. The same applies to new modelling of the older BG experiment /CRO 06/ and /SON 16/. Therefore, the interpretation of the in-situ experiments to some extent is still under discussion.

Laboratory experiments allowed to have a closer look to the effects of the gas flow on the claystone samples. Cuss et al. /CUS 14/ were able to measure dilatational volumetric deformation resulting from the gas flow in two independent experiments (see Fig. 4.69) using different set-ups, *suggesting that gas flow occurs along micro-fissures rather than in major conductive features* and that this allows to *demonstrate the movement of gas is accompanied by dilation of the clay fabric*. Alike is true for experiments reported by Senger et al. /SEN 18/ who were able to model the experiments using a code regarding dilatancy of the sample. Some insight could also be achieved by direct observation of the flow paths by Nano imaging techniques /HAR 12b/ and /SON 16/.

From the direct observation of the mechanical behaviour of the claystone samples in laboratory experiments it can be sufficiently well concluded that dilatancy driven gas transport in claystone is a fact. However, there still does not exist a commonly accepted theory of the mechanical behaviour during dilatant gas flow consistently describing the porosity and permeability changes of the claystone as a function of gas pressure. In /BIR 16/ it is additionally noted that *It is worth noting that the general literature lacks information on system responses during unloading and that elasticity theory is primarily concerned with material deformation during loading. The issue of hysteresis in such systems is complex and poorly understood*.

However, it must be clearly noted that the re-closure of the microfractures are not an issue of major concern. Claystone is known to reseal and achieve its initial permeability

when the mechanical load is decreasing under the principal stress even if fractures were created /BOC 10/ and /ZHA 17/.

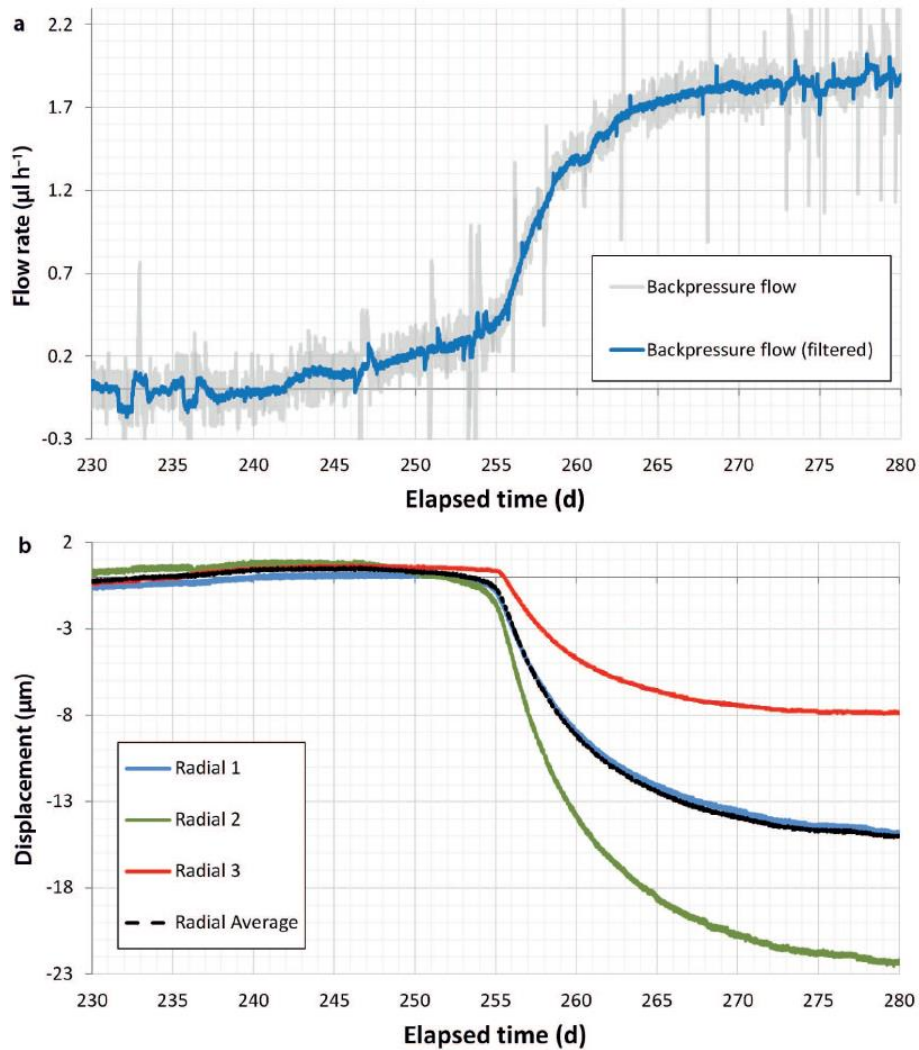


**Fig. 4.69:** Time dependent evolution of gas flux out of a claystone core sample and sample dilatation in response of the gas flow /CUS 14/

The open questions in the principal understanding of the claystone dilatation process also results in the lack of a mathematical description of the phenomenological net mass transfer of gas through the claystone under dilatant conditions. The literature often uses classical van Genuchten two-phase flow codes to model the gas transport, e. g. TOUGH2, which are only applicable if the gas pressure stays below the minimal principal stress of the rock. The use of this approach for dilatant pressure conditions is not expected to be valid, although even still applied here and there. Different modifications have been programmed into the TOUGH2 code to model dilatant gas flow e. g. /JAC 14/, /NAV 13/, /PAP 14/. A comprehensive comparison of the different approaches or a code

benchmark of the resulting codes has not yet been performed. Although these codes were able to model the results from gas transport experiments, from our point of view none of these modifications seems to be justified enough to be used for reliable long-term predictions needed for long-term safety assessment. The reason for this judgement is twofold. First, the use of the modified code was in some cases not significantly better than the classical van Genuchten models applied and second, the reproduction of the experimental results was obtained by parameter fitting, while it was not tested if predictions could be made for experiments under different conditions using the same or a deduced parameter set. This conclusion was also expressed within the FORGE project /JAC 14/.

As long as neither the physical equations of the mechanical behaviour during gas transport by dilation of the claystone rock are sufficiently well described nor a validated phenomenological description of the net mass gas transfer exists, we would suggest to prefer a repository design concept that does not rely on the dilatant gas transport in the expected evolution of the system, but is expected to develop gas pressure in the system which always stays well below the minimal principal stress of the rock. This can be either achieved by a repository concept that implicates low amounts of iron in the system or that results in low corrosion rates of the iron under the expected chemical conditions.

#### **4.4 Natural analogues for repositories in crystalline rock formations**

##### **4.4.1 Background**

Due to the safety requirements /DEU 20/ the safe containment of the radioactive waste shall be reached by essential barriers, namely one or more containment-providing rock zones. However, in the case of the potential host formation crystalline rock, provided that no containment-providing rock zone can be identified, technical and geotechnical barriers suitable for the respective geological environment, can be the essential barriers. Safe containment must take place within the essential barriers in such a way that the radionuclides from the radioactive waste largely remain at the place of their original emplacement /DEU 20/.

In the past, the research and host-rock-specific investigations in Germany were focused on rock salt and clay/claystone formations. The compilation of state of knowledge and the basics for the formulation of a safety concept in crystalline formations in Germany

mainly took place during the last decade, e.g. /JOB 16a,b/. In this context FEP catalogues for different concepts for repositories in crystalline formations in Germany have been developed /MRU 21/. The catalogue distinguishes between features or components on the one hand and processes / events on the other hand. Using the FEP catalogue a comprehensive compilation of parameters for crystalline host rocks and a description of correlations and dependencies of repository relevant (coupled) processes is possible. FEP catalogues are the basis to derive scenarios in a traceable, objective and representative manner enabling the integrity and long-term safety analyses for a repository in a crystalline rock formation.

Because of the complexity and the geological time frame to be considered (assessment period of 1 million years) deep insights into relevant “natural” geological processes may contribute substantially to system understanding and finally to the description and underpinning of FEP. Furthermore, since the properties of the crystalline formations in Germany considerably vary in dependence of the structural geological properties, diagenesis and geological boundary conditions it is considered as helpful to compile bandwidths of key features relevant for the integrity of and the long-term safety analysis for repositories in crystalline formations.

Therefore, in this work an approach is developed to compile and evaluate natural analogue studies based on the FEP catalogue, which was developed for crystalline formations in Germany /MRU 21/. In a first step selected key components and processes from the FEP catalogue, where the contribution of analogue knowledge is expected to be useful, have been identified and used for this approach. It was the objective to exemplarily illustrate which information and data from natural analogue studies are of use in a safety case and where analogue information is lacking. In the study /FAH 21/ summarized here the component FEP “Host Rock”, “Faults and Fractures within Host Rock”, as well as the process FEP “Permafrost”, “Microbial Processes”, “Metal Corrosion”, “Alteration of Fuel Matrix” and “Diffusion” have been considered. For each FEP the most important characteristics are adopted in form of a summarized data sheet. These characteristics are deduced from the FEP descriptions in the FEP catalogue which has been developed for three different concepts in crystalline formations. Following this, for each FEP characteristic information from NA studies have been gathered from literature. For the component FEP typical key parameters for crystalline rock were compiled in order to illustrate the bandwidth for each parameter obtained from the natural analogue studies. This is – of course – analogue information, which can also be seen as part of the

geological characterization. However, since the knowledge about crystalline rock is so far very limited, it was decided to include it in this report. For the process FEP all characteristics, where analogue information is available, have been described. For each FEP the most important characteristics are adopted in form of a summarized data sheet.

A detailed description of this study can be found in /FAH 21/. In the following the content is exemplarily shown for the FEP “Permafrost” and key outcomes are summarized.

#### 4.4.2 NA information related to FEP Permafrost

Permafrost is defined as a subsurface that remains continuously frozen over a minimum of two years /BRO 97/. Its development starts with a mean annual temperature of  $-1^{\circ}\text{C}$  or below /RUS 02/. It is classified by extent /BRO 97/, which is correlated to the annual mean temperatures illustrated in Tab. 4.7.

**Tab. 4.7** Correlation between permafrost extent and mean annual temperature /BRO 97/, /RUS 02/

Kind of Permafrost per Extent	Permafrost Extent <sup>/BRO 97/</sup>	Mean Annual Temperature <sup>/RUS 02/</sup>
sporadic permafrost	less than 50% of an area	between $-1$ and $-4^{\circ}\text{C}$
discontinuous permafrost	50 - 90% of an area	below $-4^{\circ}\text{C}$
continuous permafrost	more than 90% of an area	between $-6$ and $-8^{\circ}\text{C}$

The generation of permafrost depends on low surface air temperatures. These can be found in front of an ice-shield, caused by cold downslope winds from the glacier. Increasing surface temperatures or ice load leads to a decrease of permafrost /CLA 16/.

Rock and groundwater properties influence the permafrost growth. Parameter values of heat conductivity for water and different crystalline hard rocks are summarized in Fig. 4.70. The heat conductivity of hard rock is influenced by its porosity, density and the surrounding temperature. It becomes obvious that the heat conductivity increases from water over basalt, gneiss and granite up to quartzite. The heat conductivity of water-ice is about  $2.2 - 2.35 [\text{W}\cdot\text{m}^{-1}\cdot\text{K}^{-1}]$  /YEN 81/, /CLA 06/, /RAS 16/. In contrast the differences in heat capacity are small. The rock values are between  $0.72$  for Basalt and  $1.22 [\text{W}\cdot\text{m}^{-1}\cdot\text{K}^{-1}]$  for Granite. Water-ice has a value about  $2.03 [\text{W}\cdot\text{m}^{-1}\cdot\text{K}^{-1}]$ , fresh water has the highest value of  $4.12 [\text{W}\cdot\text{m}^{-1}\cdot\text{K}^{-1}]$ .

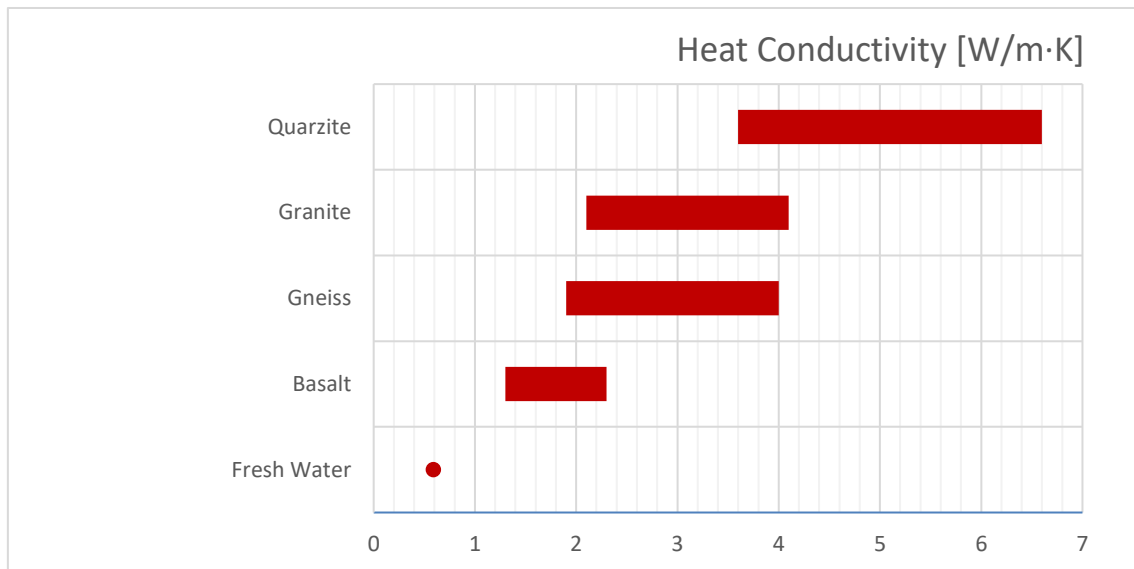


**Fig. 4.70** Heat conductivity for different rocks and fresh water

It is supposed that Germany was covered with continuous permafrost during the last ice-age /LIN 16/. Indications are the distribution of filled ice-wedges all over the area of Germany. They were generated during alternating freezing and thawing conditions and were filled afterwards. Fig. 4.71 shows locations of filled ice-wedges generated during Weichsel-/Würm glaciation and ice-covers during different glaciations (Weichsel, Saale, Elster, Würm, Riß Hoßkirch, Mindel). In northern Europe there are expected cold and dry periods during the next million years. These climate conditions will lead to cycles of stepwise formation of permafrost in the future.

It is assumed that permafrost takes indirectly influence to erosion processes beneath the ice shield. Hence many of the erosion structures in northern Germany called buried valleys are associated to permafrost conditions. The erosion was caused by subglacial meltwater flow and coupled on the thickness of the glacier and the solidity of the ground sediments. Within areas which had been only covered with ice thicknesses of a few hundred meters and crystalline bedrock, only flat valleys had been generated. Unfortunately, the formation history of buried valleys is not completely understood since now. In the reviewed literature of the natural analogues Lupin and Greenland no subglacial meltwater flow or erosion processes had been mentioned.

In Germany the highest erosion depths had been reached during the Elster Ice Age with often 200 m to 300 m and more than 500 m at maximum with a broadness of several

kilometers and a length of more than 100 kilometer /KLA 13/. Buried valleys of younger glaciations are rare and erosion depths are between 100 m and 200 m, s. Fig. 4.72.

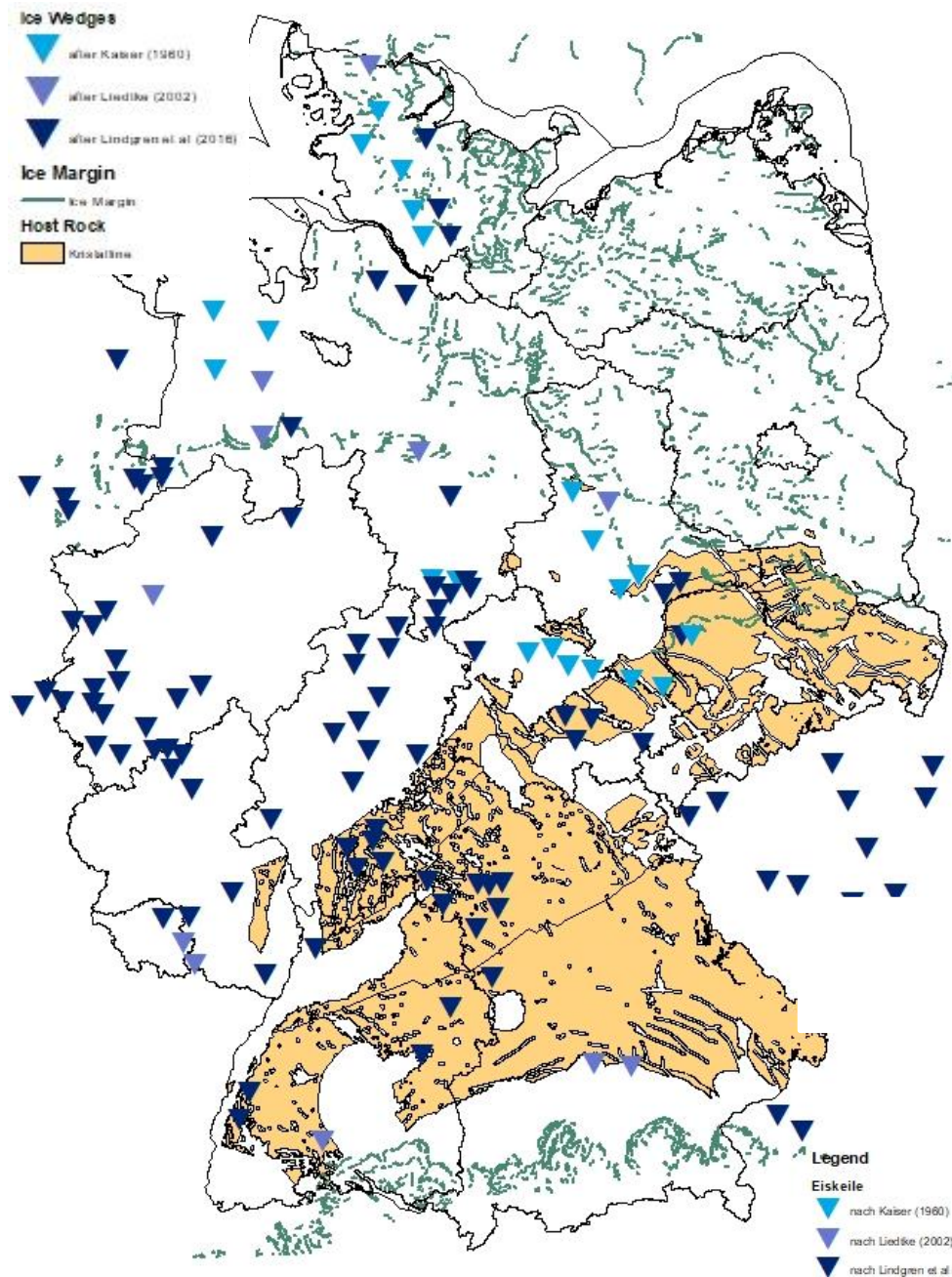


**Fig. 4.71** Ice wedges generated during Weichsel and Würm, maximum ice margins and crystalline formations potential suitable for a repository in Germany.

<https://www.bge.de/de/endlagersuche/wesentliche-unterlagen/zwischenbericht-teilgebiete/>

<https://www.bgr.bund.de/DE/Themen/Endlagerung/Projekte/Langzeitsicherheit/abgeschlossen/Permafrostprognose.html/>

<https://opendata-esri-de.opendata.arcgis.com/datasets/esri-de-content::gk1000-eis-rand?geometry=-5.918%2C46.206%2C47.163%2C55.834/>

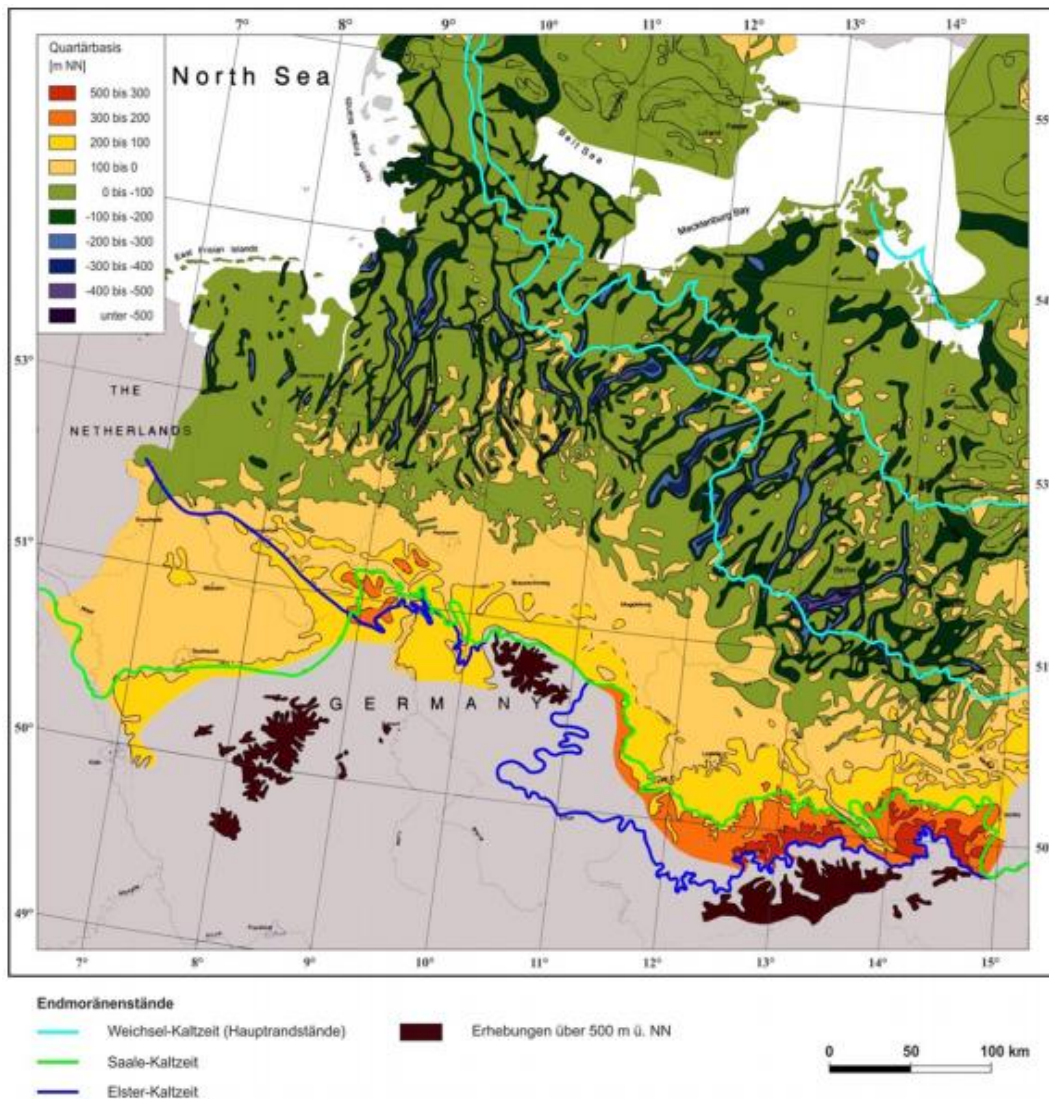


**Fig. 4.72** Buried Valleys and Ice Margins in Northern Germany /WEI 17/

However, the effects of (dis)continuous / sporadic permafrost have to be included in the performance assessment and long-term safety analysis. And the question is, how permafrost causes subsurface changes that may affect the integrity of natural and engineered barriers, as well as the fact how far permafrost will affect the ability of the repository to retard and retain radionuclides in case of radionuclide release from the waste containers /RUS 02/. For the component FEP “Host Rock” and „Faults and Fractures within Host Rock” changes are expected in the fracture frequency (aperture, filling material, porosity) and the occurrence and alteration of minerals within fractures matrix.

The considered natural analogue studies can help the safety assessment by defining the variation of rock and fracture parameters, expected groundwater changes in flow and chemistry and changes in radionuclide transport and sorption. A consequence could be,

that long-term safety analysis will give more reliable information, due to the changing parameter values of different scenarios (permafrost, distance to glacier margin). Natural analogues which yield information about permafrost effects to the deep rock are Greenland and Lupin. Their areas are covered by continuous permafrost in different distances to the glacier margin. In the following data sheet, relevant information of the FEP “Permafrost” are summarized.

<b>Process FEP: „Permafrost“</b>			
<u>Characteristic of Permafrost</u> Formation, Variation of permafrost depths and extension is a combination of interaction between soil and rock temperatures, rock and fracture parameter values (e.g. porosity, density, heat conductivity, heat capacity) and groundwater chemistry			
<u>Available Parameter Values of Permafrost of the Natural analogue studies so far</u>			
Natural Analogue	Kind	Depths [m]	Distance to glacier margin
Greenland	continuous	350 – 400	2km
Lupin	continuous	541	Not influenced by glacier
<ul style="list-style-type: none"> <li>- Information about Through Taliki (necessary size of the lake)</li> <li>- Correlation between permafrost depth and near-surface temperatures</li> <li>- Appearance of gases in Greenland</li> </ul>			
<u>Consequences</u>			
<u>Primary</u>		<u>Secondary</u>	
Amount of Pore Water during - Freezing of Permafrost and Glacier - Thawing of Permafrost and Glacier		Changes in Groundwater Flow: - velocity - pathway	
Existence of Taliki		<ul style="list-style-type: none"> <li>- Changes in Groundwater Flow (velocity, pathway, chemistry)</li> <li>- Changes in Fracture Filling (Alteration)</li> <li>- Changes in Radionuclide Transport / Sorption</li> </ul>	
Accumulation of High Salinar Fluids (Cryopecs) due to Mineral Accumulation		<ul style="list-style-type: none"> <li>- Changed Freezing Point</li> <li>- Changes in Radionuclide Retention (Sorpton / Precipitation)</li> </ul>	
Existence of Gas Hydrates e.g. Chlathrates (Methane Hydrates) (Genesis, Destabilisation)		Possibility of 2 -Phase Flow	
Thermally Induced Strain Changes within the Hard Rock		<ul style="list-style-type: none"> <li>- Fracture Formation, Reactivation, Changes (frequency, aperture, filling / porosity)</li> <li>- Changes in Groundwater Flow</li> <li>- Changes in Radionuclide Transport / Sorption</li> </ul>	
Barriere for Groundwater and Subglacial Meltwater		<ul style="list-style-type: none"> <li>- Reduction of Infiltration Water</li> <li>- Reduction of Ascending Groundwater</li> <li>- Support Confined Groundwater</li> <li>- Support Subglacial Erosion Processes</li> </ul>	

Benefit for Long-Term Safety Analysis / Assessment Criteria:

- Comprehensive and reliable data variation of Fracture Frequency, Aperture, Permeability, Mineralogy based on different scenarios (growth, persistent, decay of permafrost with different distance to ice-margin)
- Assessment of the 2-Phase Flow Relevance

Impacts, e.g. the following FEP:

- Faults and Fractures within Host Rock (Permeability)
- Groundwater flow (direction, velocity, chemistry, Radionuclide transport)
- Erosion
- Sorption and Desorption
- Heat Flow

## **Permafrost depth**

Permafrost extent and thickness is related to stable near-surface temperature and the host rocks and groundwaters heat-capacity (possibility of heat accumulation) and heat conductivity (possibility of heat transfer). Differences in porosity and water content of the rock causes fluctuation of the depth of permafrost's base /RUS 02/. In addition, the heat input from the earth's mantle / lower crust and the coverage of the crystalline rock (sediment, snow) impacts the permafrost depth. The highest permafrost values are assumed for rocks with a weathering horizon on top and without any coverage of sediment, snow or ice.

Permafrost depths for German crystalline formations are estimated by means of models in NW-Europe, because there are no model results for this purpose. In this way permafrost depths between 100 m up to 300 m have been supposed within a German low mountain range reference area /MRU 21/. The natural analogue studies mentioned a permafrost depth about 350-400m in Greenland /CLA 16/ and of 541m in Lupin /PAA 03/. In addition, Fig. 4.73 illustrates the depth of zero degree and therefore permafrost depth in different parts of Canada. The attempt for a correlation between mean annual surface temperature and permafrost thickness for different sites on the world is illustrated in Fig. 4.74 /JNC 00/.

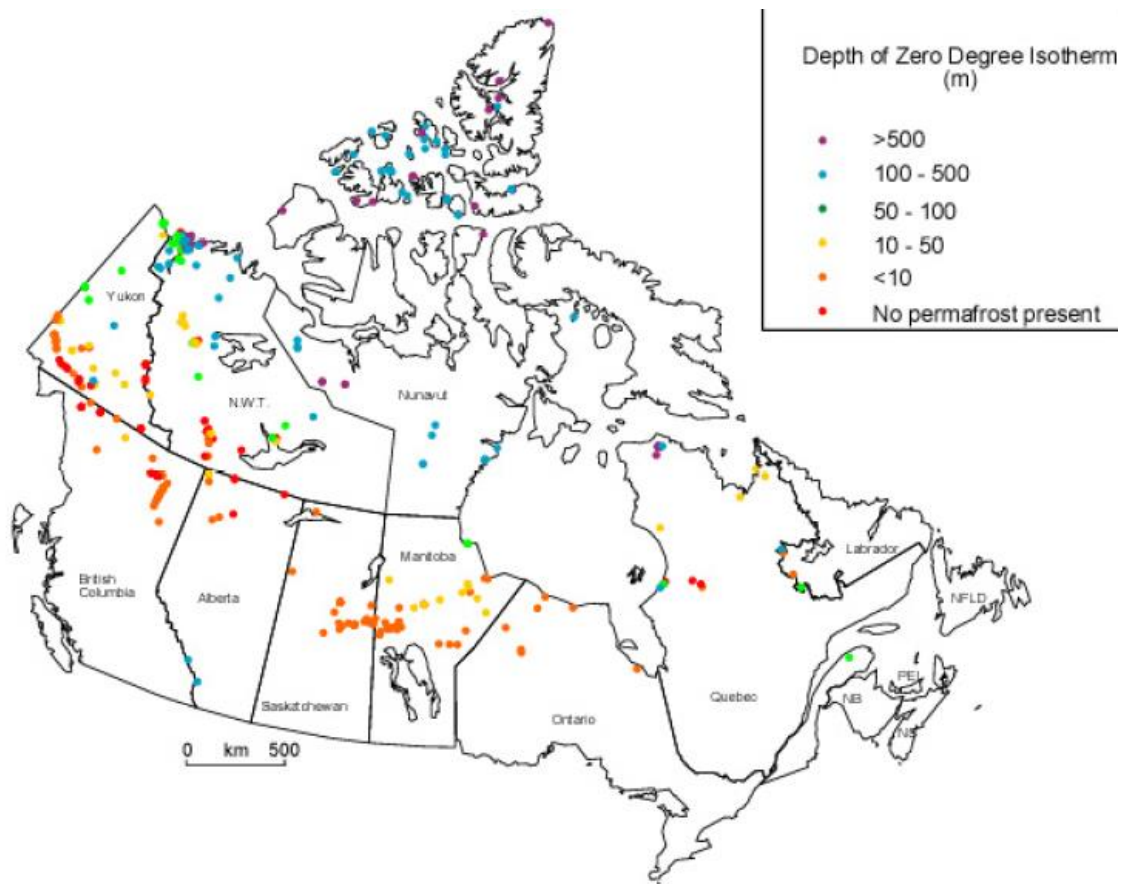


**Fig. 4.73** Permafrost depth in the territory of Canada. (National Permafrost Data-base, GSC, [http://sts.gsc.nrcan.gc.ca/tsdweb/geoserv\\_permafrost.asp](http://sts.gsc.nrcan.gc.ca/tsdweb/geoserv_permafrost.asp) /RUS 02/.

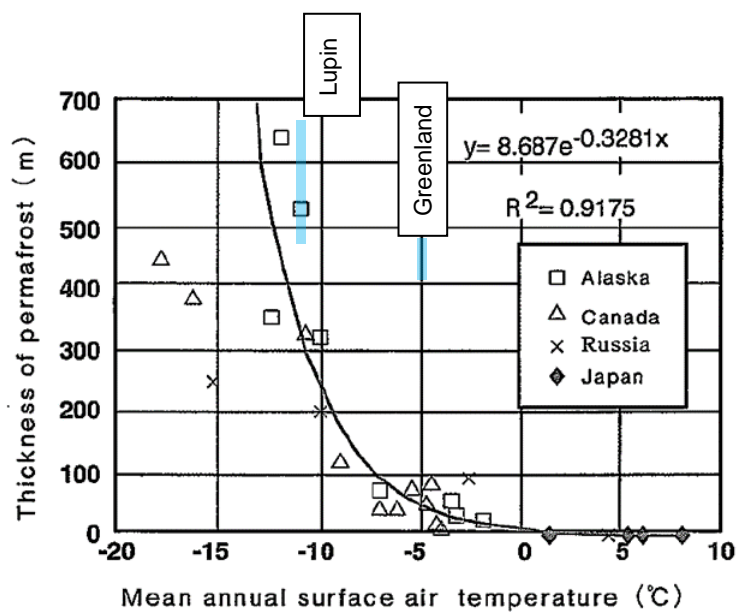


**Fig. 4.74** Correlation between permafrost thickness and mean annual surface temperature /JNC 00/

## Unfrozen Areas within the Permafrost

Taliks are unfrozen areas (gaps) within the permafrost. In general, they are localized in the vicinity of deep lakes, but can also be formed by a thermal or chemical anomaly. Due to the diameter and depth of the lake or anomaly, different kinds of taliks are defined, namely “open” or “through” talik, s. Fig. 4.75. Both are open to the surface but the open talik is confined by permafrost, whereas through taliks have a constantly unfrozen area beneath. That means, that the open talik has no contact to the groundwater, whereas the through talik provides an opportunity for water exchange between surface- and groundwater. Therefore, during continuous permafrost the recharge and exchange between surface and deep groundwater is interrupted with the exception of through taliks.

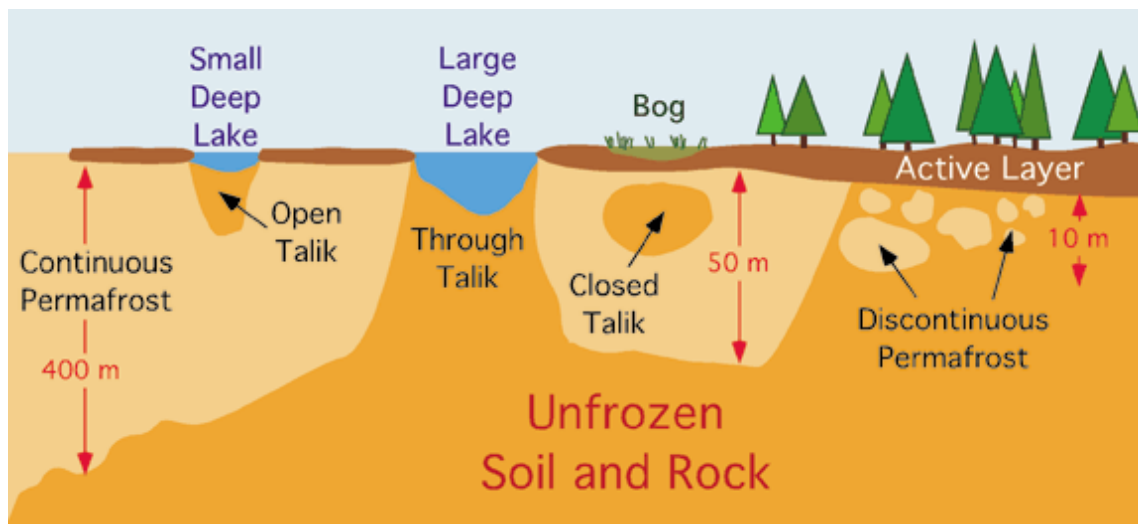


**Fig. 4.75** Kinds of unfrozen areas (taliks) within permafrost

[www.physicalgeography.net/fundamentals/10ag.html](http://www.physicalgeography.net/fundamentals/10ag.html) (25.02.2021)

Under the conditions of the investigation site in Greenland a permafrost depth of approximately 300 to 350 m a lake diameter of approximately 360–420 m is required to maintain through taliks /CLA 16/. Geothermal modelling suggests, that, through taliks can be formed in a 300 m deep layer of permafrost in less than 500 years if the lake is wider than about 200 m /CLA 16/, /HAR 11/.

In the natural analogue of Greenland the investigated “through talik lake” is situated approximately 800 m away from the ice sheet margin, has a diameter of  $\geq 400\text{m}$ , a surface area of  $0.37\text{ km}^2$ , an average water depths of 11.3 m and a maximum depth of 29.9 m /CLA 16/. About 20% of several hundreds of pro-glacial lakes (6% of the land surface

area) have a diameter larger than 400 m, which suggests that the permafrost in this area is perforated by through taliks.

In the natural analogue of Lupin there is no solid information about the existence of taliks. But it could be possible, that Lake Contwoyto supports a through talik. The water body in the lake is large enough to insulate the underlying bedrock from the cold air. The lake is more than 100 km long and between 2 and 5 km wide /RUS 02/.

### **Fracture generation, release and filling**

The development of permafrost causes thermally induced strain changes within the hard rock. The consequence is the formation and reactivation of fractures and changes in their permeability. Unfortunately, the reviewed Natural Analoga of Greenland and Lupin give no detailed information about the processes of fracture formation and reactivation.

However, the Natural Analogue of Greenland gives information about the fracture filling with pyrite, FeOOH and gypsum and their distribution in depth, s. Fig. 4.76 /CLA 16/.

- The presence of FeOOH is an indication to minerals oxidation in shallow depth up to 260m within permafrost.
- Pyrite shows reducing conditions and promotes anoxic, sulphidic conditions below permafrost between 25 m and ~650 m.
- Gypsum is only observed in the third borehole. It is the major filling mineral below 300m depth, but also occurs in the first 300 m. Its mineralogical texture suggests a high temperature origin (hydrothermal/metamorphic). The widespread presence of highly soluble gypsum beneath 300 m is interpreted by rather small volumes of melt-water infiltration and groundwater flow (continuously for hundreds of thousands of years). During warmer climate conditions, recharge in the upper section up to 300 m could have dissolved it /CLA 16/.

The slow groundwater flow in the deeper rock would be a consequence of permafrost, geology (more vertical fractures in the upper 300 m, more sub-horizontal fractures below 300 m) and hydrogeology (i.e. groundwater flow) /CLA 16/.

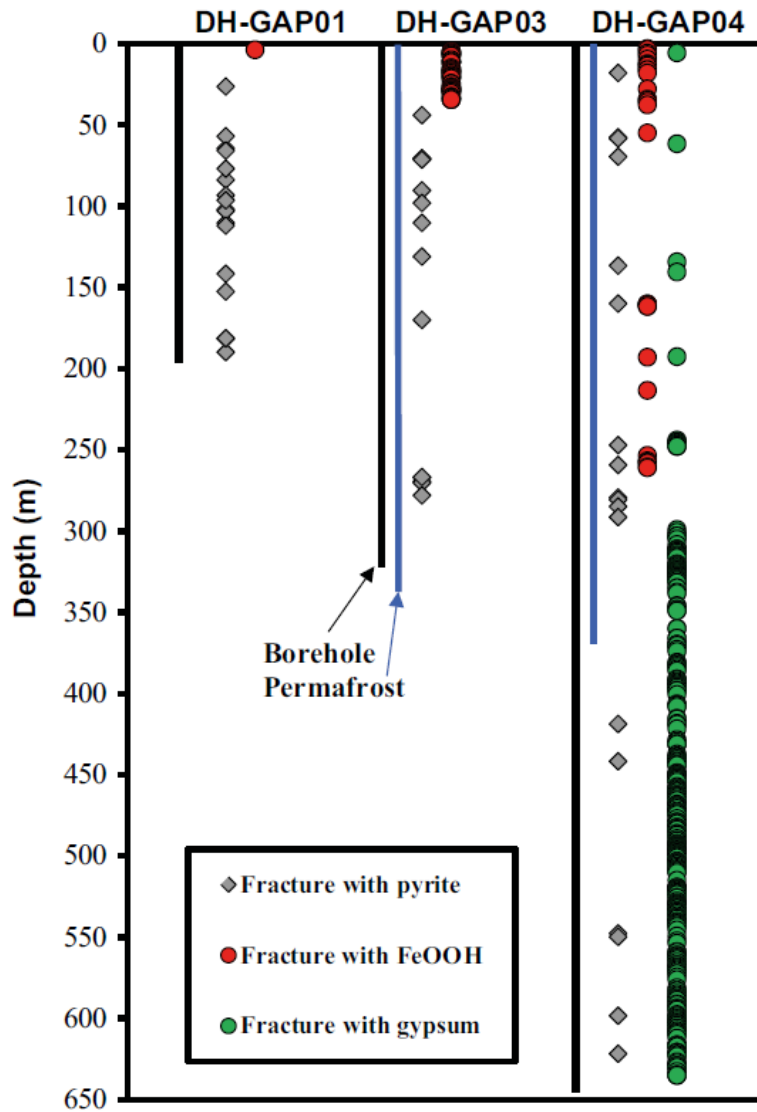


**Fig. 4.76** Distribution of pyrite, FEOOH and gypsum in fracture fillings within permafrost in Greenland /CLA 16/

### Appearance and release of gases

The different gases and gas compositions in the subsurface have different solubilities, but in overall the gas solubility is controlled by the groundwaters temperature and pressure, to a lesser part by its salinity. The solubility increases with depth, due to the increase in hydrostatic pressure, but is reduced by an increase in groundwater temperature and salinity. Hence, depending on the physical, thermal and chemical boundary conditions the gases are either free, solved in the groundwater or part of the mineral texture of crystalline rock /POS 12/.

A free gas phase will form during their upwards movement if the aggregate partial pressure of the dissolved gases exceeds the hydrostatic pressure /POS 12/. Once a free gas phase has formed in the groundwater, a two-phase (water and gas) system is created. In a fractured crystalline rock, the free gas will migrate upwards through the fracture network towards the surface. The radionuclide transport in form of free gas bubbles can lead to a faster transport than the mean groundwater flow rate. Mainly affected are radionuclides which can be incorporated into gases (e.g. C-14 in CH<sub>4</sub> or CO<sub>2</sub>) or colloids, which are often preferentially attached to the gas-water interface. Therefore, in deep, saline groundwater the most important consideration after waste disposal is the high CH<sub>4</sub> concentration /POS 12/.

Dissolved gases occur in most deep groundwater systems and are of varying composition /SKB 01/. They are generated during

- recharge dependent on atmospheric and hydrogeochemical conditions,
- radioactive decay in the bedrock,
- crustal degassing and diffusion,
- thermogenic and microbial processes like respiration and decay of organic debris, which catalyze redox processes by consuming or producing gases.

Free Gas may be generated in different parts of the repositories near field and during the transport, if the partial pressure of the dissolved gases exceeds the hydrostatic pressure /POS 12/:

- radiolysis of the canister water,
- anaerobic corrosion of the iron insert of the canister and
- microbial activity (buffer / tunnel backfill, bedrock). For Example, typical metabolism products of bacteria are CH<sub>4</sub> and CO<sub>2</sub>, s. Fig. 4.77. Subsequently both gases can be used by microbes in sulphate reduction processes.

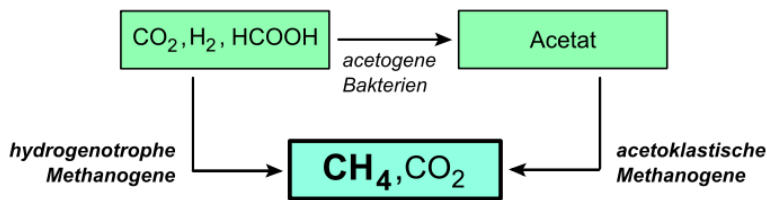


**Fig. 4.77** Microbial Production of CH<sub>4</sub> and CO<sub>2</sub>

[https://de.wikipedia.org/wiki/Datei:Anaerobic\\_food\\_chain.svg](https://de.wikipedia.org/wiki/Datei:Anaerobic_food_chain.svg)

The distribution of radionuclides in the surface environment depends on their release after canister failing and their transport and retention on their way to surface area (buffer, geosphere). They are dissolved into surface and groundwaters and trapped as free gas within pores in soils and sediments. Radionuclide transport in the geosphere as dissolved gas depends on the groundwater movement. Hence, in shallow groundwaters and surface waters it may be transported by advection, within the bedrocks in the fracture system (geometry). This transport may be retarded or even restricted, if gas bubbles become trapped and accumulate within kinks and bends in fractures, forming an airlock /POS 12/.

Uncertainties persist concerning the

- volumes of repository-derived gases,
- the rate of gas generation, which will be sufficient for two-phase and whether it will be significant in controlling radionuclide transport processes,
- kinetics of microbiological formation,
- accumulation rate of microbiological or abiogenic methane,
- mechanism in the very long term (future geological / climate variability).

During permafrost conditions a change of the groundwater temperature, salinity and pressure occurs, which influence some of the gas generation processes and the ratio of free and dissolved gas within underground, s. also Tab. 4.8. No or less impacts are expected to the radioactive decay in the bedrock and crustal degassing processes in the far field and the near-field processes of the radiolysis, the anaerobic corrosion of the canisters iron insert and the microbial activity in buffer and tunnel backfill.

**Tab. 4.8** Impact of Permafrost on gas generating processes

	<b>Permafrost growth</b>	<b>Permafrost occurrence</b>	<b>Permafrost decay</b>
Near-surface process: Recharge	decreasing with increasing permafrost extent / depth	in talik areas	High (O <sub>2</sub> rich surface groundwater)
Deep-surface process: thermogenic / microbial processes (respiration / decay of organic debris)	Decreasing (decreasing temperature and O <sub>2</sub> content)	low (low temperature, low O <sub>2</sub> )	Increasing (increasing temperature and O <sub>2</sub> content)

In the context of performance assessment and gas occurrence in permafrost areas, methane hydrates are in the focus of investigation. They can lead to a rapid generation of free gas in the geosphere /POS 12/ and offer a fast transport way for some radionuclides. For instance, C-14 could be transported as CH<sub>4</sub> (or CO<sub>2</sub>) nearly without retention to the near-field.

Clathrates (methanhydrates) are solid crystalline compounds of methane, trapped within hydrogen-bonded water molecules, with small molecular size, and can be found abundantly on the sea floor and in the Arctic permafrost areas. When CH<sub>4</sub> dissolves in water they can be also found in fluid inclusion within quartz grains, formed at very high temperatures (up to 400°C) and pressures /POS 12/. Permafrost growth and decay take influence on the generation and destabilization of gas hydrates, especially clathrates, which are stable under high pressure and low temperature, occurring between 100 and 2000 m depth /POS 12/.

An important precondition of their formation is the separation of CH<sub>4</sub> gas from groundwater. For this to happen, methane content must be close to its solubility limit (super-saturated condition in groundwater), temperature decrease is required, and the hydrostatic pressures has to be below 200 m depth, s. Fig. 4.78 /POS 12/. Pressure release or temperature increase make the hydrate structure unstable and vast amounts of methane may be released. Even in the fluid inclusions separation of gas and water during cooling leads to a high gas pressure within the quartz grains. A rapid gas overpressure in the rock may cause a mechanical disruption. In addition, methane hydrate formation directly affects the aqueous solubility / speciation, (co-) precipitation, groundwater flow, advective transport and gas transport /POS 12/.

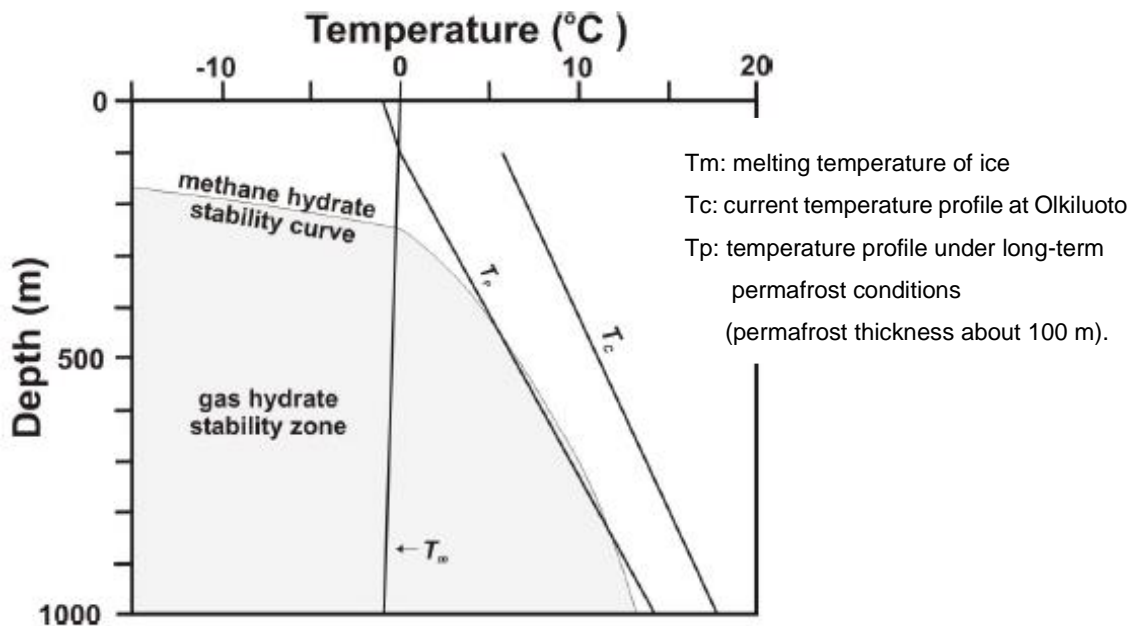


**Fig. 4.78** Phase diagram for a methane-water mixture as a function of depth and temperature (10 bar = 100 m) /POS 12/

$\text{CH}_4$  is a common feature in the northern gas fields of North Alaska and western Siberia. In shield areas the amounts of methane are much less but some methane is often present in deep groundwaters, as was also observed in Lupin /RUS 02/. In Greenland methane origin is microbial, either from the fermentation of organic matter or perhaps from methanogenesis sustained by deep crustal  $\text{H}_2$  /CLA 16/. For both natural sites information about gas occurrence is available. In the boreholes of Lupin, the gas volumes are between 0.4 and 1.0 L in depth of 890 to 1130 m /RUS 04/

At Olkiluoto, the most abundant naturally occurring dissolved gases are  $\text{CO}_2$ ,  $\text{H}_2$ ,  $\text{N}_2$ ,  $\text{O}_2$  and He. In addition, the deep saline groundwater contains methane in solution close to its saturation point and methane clathrates have been also observed in a few microscopic fluid inclusions within quartz grains /POS 12/.

In Lupin gases found in the deep groundwater systems beneath the permafrost, are apparently thermogenic in origin. The gas composition and age would most likely be the age of the metamorphic event in the originally deep ocean sediments (i.e. hundreds of millions to billions of years). In most cases, the gases, matrix fluids and many of the saline groundwaters have similar evolutionary histories /RUS 04/. The observation in the permafrost-holes show, that many fractures produce gas bubbles /RUS 02/.

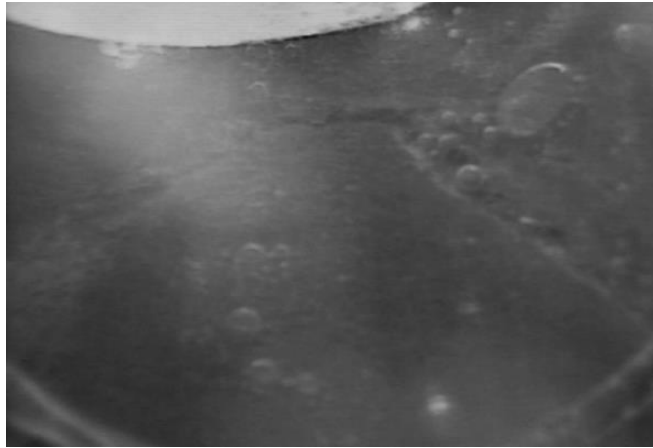


**Fig. 4.79** Lupin: Methan bubbles emanating from a fracture (aperture is 1-2 mm) in 890m depth /RUS 02/

In Greenland, gas samples in upper 300m contain  $\text{CH}_4$  and  $\text{H}_2$  are consistent with reducing conditions in the groundwater /CLA 16/. The relatively high He concentration observed in two samples from the upper section (1.0 and 3.3 mL/L), are probably crustal in origin (from radioactive decay of U and Th). The He data suggest that groundwaters have been isolated for long periods from the atmosphere and that they may have residence times exceeding hundreds of thousands of years.

In a similar way the existing analogue information has been compiled for the FEP “Host Rock”, “Faults and Fractures within Host Rock”, “Microbial Processes”, “Metal Corrosion”, “Alteration of Fuel Matrix” and “Diffusion” for a repository in crystalline rock. The respective information can be found in /FAH 21/.

#### **4.5           Uncertainties in geochemical behaviour of relevant fission and activation products in the repository near-field in rock salt**

In /MOO 17/ geochemical model calculations on the solubility of relevant elements in high saline brines in the near-field of a repository for heat-generating radioactive waste have been performed aiming to derive the state of the art of thermodynamic data for each element and to identify the need for further research for dose relevant radionuclides. One key result was that particularly for the elements C, Cl, I, Nb, Ni, Se and Sn high uncertainties exist with respect to their geochemical behaviour in highly saline conditions and therewith for the determination of solubilities. Open questions to the elements Se und I are already addressed in the research project VESPA II, FKZ 02E11607 (BMW). The objective of the task described here was to evaluate the results for carbon

yielded in the European project CAST and to develop a strategy for further experiments to derive a substantiated basis for geochemical modelling in high saline conditions for the elements Cl, Ni, Sn und Nb.

#### **4.5.1 Nickel**

The transition element Nickel is a metal. Under conditions relevant for the disposal of radioactive waste it occurs in the oxidation state +II. Under natural conditions, it forms poorly soluble compounds with arsenic, antimony, and sulfur. Examples are the minerals NiS (millerite), NiAs, NiSb, NiAs<sub>2</sub>, or NiSbS /COT 80/. Nickel is a component of stainless steel alloys used for specific waste containers, from which it may be released in the course of corrosion.

##### **4.5.1.1 Oxidation states**

In the absence of bulky organic ligands that may stabilize higher oxidation states, nickel occurs in aqueous solutions only as Ni<sup>2+</sup>. Aerobic corrosion of nickel or nickel alloys may lead to the development of passivating films that may contain Ni(III) and Ni(IV) oxides, such as Ni<sub>3</sub>O<sub>4</sub> and NiO<sub>2</sub> /PAV 18/.

Under reducing conditions, Ni<sup>2+</sup> may be reduced by metallic iron to elemental Nickel, which is virtually insoluble. Whether this process predicted by thermodynamic calculations may take place under the conditions of a repository needs to be investigated further.

##### **4.5.1.2 Hydrolysis**

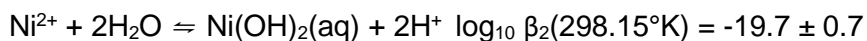
The five hydrolysis products Ni(OH)<sup>+</sup>, Ni(OH)<sub>2</sub>(aq), Ni(OH)<sub>3</sub><sup>-</sup>, Ni<sub>2</sub>OH<sup>3+</sup> and Ni<sub>4</sub>(OH)<sub>4</sub><sup>4+</sup> are considered most important /GAM 05/. Due to the comparatively low solubility of Nickel hydroxide compounds, it is difficult to quantify these species, some of which occur simultaneously. Circumstances get even more difficult in that the formation of oligomeric species doesn't happen instantaneously but proceeds according to reaction kinetics subject to various conditions. /GAM 05/ estimated that at pH>6.9 only Ni(OH)<sup>+</sup> is relevant beside Ni<sup>2+</sup>. However, a more detailed analysis reveals that Ni(OH)<sup>+</sup> at pH-values up to ~8 contributes only 1% to the total concentration of nickel, being superseded by carbonate complexes at pH>8. The tetramer, on the other hand, predominates at a total nickel concentration of >0.005 M only. However, this concentration is several orders of magnitude higher than the expected Ni concentration in equilibrium with nickel

hydroxides or -carbonates. If no carbonate is present, nickel hydroxide equilibrates with  $\text{Ni(OH)}^+$  or  $\text{Ni(OH)}_2(\text{aq})$ . For the reaction



Gamsjäger et al. /GAM 05/ provided  $\log_{10}K(T = T_0) = -9.54 \pm 0.140$ . The value given by Brown and Ekberg is significantly lower ( $\log_{10}K(T = T_0) = -9.90 \pm 0.03$ , /BRO 16/), but takes into account more recent solubility studies by Palmer and Gamsjäger /PAL 10/. The latter value indicates that at pH values below ~10 the formation of complexes with hydroxide might be neglected

According to recent reviews of nickel hydroxide complexation, up to pH 13, only the complex  $\text{Ni(OH)}_2(\text{aq})$  has a significant stability /BRO 16/, /GON 18/. The stability constants proposed by the NEA database /GAM 15/ include a very high stability of the anionic species  $\text{Ni(OH)}_3^-$  which would lead to increasing solubilities in alkaline solutions. Such behavior was not observed in solubility experiments /PAL 11/, /GON 18/. Because /GAM 05/ believed in  $\text{Ni(OH)}_3^-$  to be the only relevant species in alkaline systems, they did not derive a value for the stability of  $\text{Ni(OH)}_2(\text{aq})$ . A recent estimate is provided by /GON 18/



#### 4.5.1.3 Complex formation with chloride

With nickel, several chloro complexes were established or postulated:  $\text{NiCl}^+$ ,  $\text{NiCl}_2(\text{aq})$ ,  $\text{Ni}_2\text{Cl}^{3+}$ ,  $\text{NiCl}_3^-$  und  $\text{NiCl}_4^{2-}$ . At ambient temperature, the first complex,  $\text{NiCl}^+$  is weak. /GAM 05/ derived an equilibrium constant of

$\log_{10}K^0(298.15^\circ\text{K}) = 0.08 \pm 0.6$  for the reaction



The quite high uncertainty originates from the disparity between measurements in perchlorate and potassium chloride media. /HAG 15/ pointed to the fact that it was difficult to calculate equilibria in mixed aqueous KCl-NiCl<sub>2</sub> systems. This may be an indication of stronger complex formation systems with bulkier cations than sodium. Because of this,

the complex formation constant of  $\log K = -0.37$  derived from measurements in perchlorate systems seems to be more reliable.

The stability of the second complex,  $\text{NiCl}_2(\text{aq})$  is even lower and almost impossible to determine. /GAM 05/ did not recommend a value. /LIU 12/ measured the stability of  $\text{NiCl}_2(\text{aq})$  and  $\text{NiCl}_3^-$  in a broad temperature range estimated  $\log_{10} \beta_2 = -0.93$  and  $\log_{10} \beta_3 = -2.48$ . On the other hand, /ZHA 15a/, /ZHA 15b/ concluded based on UV spectrophotometry and EXAFS measurements that at  $25^\circ\text{C}$  the second complex becomes predominant only in saturated  $\text{MgCl}_2$  solutions. No trace of  $\text{NiCl}_3^-$  was found. The authors derived a stability constant of  $\log \beta_2 = -6.6$ . It should be noted that different thermodynamic models were employed to calculate activity coefficients, but the difference is too high to allow a definite conclusion on the stability of  $\text{NiCl}_2(\text{aq})$ .

#### 4.5.1.4 Complex formation with sulfate

In analogy to  $\text{Fe}^{2+}$ ,  $\text{Ni}^{2+}$  forms stable complexes with sulfate.  $\text{NiSO}_4(\text{aq})$  is probably the most important for conditions of interest here. The formation constant for the reaction



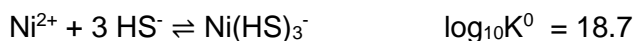
was selected as  $\log K((4.11), T = 298.15\text{K}) = 2.35 \pm 0.03$  /GAM 05/. This value indicates that the uncharged complex might be predominant in invariant solutions in the system of oceanic salts.

#### 4.5.1.5 Complex formation with sulfide

With hydrogen sulfide nickel form a series of complexes that were investigated by /ZHA 94/ and /LUT 96/. These and other sources were evaluated by /GAM 05/. They derived the following formation constants:

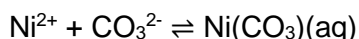


The latter two complexes only play a role in solutions with a total nickel concentration higher than  $10^{-4}$  mol/l and a  $H_2S$  pressure of 1 bar. In a solution in equilibrium with  $\alpha$ -NiS and a total sulfide concentration of 0.001 m, only the complexes  $NiHS^+$  and  $Ni(HS)_3^-$  were important. For  $Ni(HS)_3^-$  they found:

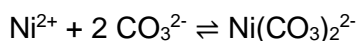


#### 4.5.1.6 Complex formation with carbonate

With carbonate, nickel forms the carbonato complexes  $NiCO_3(aq)$  and  $Ni(CO_3)_2^{2-}$ . In systems, where the carbonate concentration is controlled by the presence of calcite, the neutral complex  $NiCO_3(aq)$  may occur. For this species /GAM 05/ recommended a formation constant of  $\log_{10}\beta_1 (209.15^\circ K) = 4.2$  for the reaction



High carbonate concentrations that may result from the degradation of organic material could lead to the formation of the dicarbonato complex  $Ni(CO_3)_2^{2-}$ . Due to insufficient data neither /GAM 05/ nor /THO 14/ selected a value for its stability. They only identified an upper stability limit ( $\log \beta_2 < 6$ ) for the reaction.



#### 4.5.1.7 Relevant solid phases

##### **NiO(cr) (bunsenite) and $\beta$ -Ni(OH)<sub>2</sub>(cr) (theophrastite)**

The mineral bunsenite, NiO is rarely encountered under natural conditions. At temperatures relevant for nuclear waste disposal no equilibrium with aqueous solutions is observed /GAM 05/. There are contradicting statements as to the transition of bunsenite to theophrastite. According to Gamsjäger, this transition happens at 503 K /GAM 05/. Brown and Akberg give a temperature of 373 K /BRO 16/, while Palmer and Gamsjäger report a temperature of 350 K /PAL 10/.

Interestingly, solubility studies with bunsenite extend to temperatures as low as 25°C. Actually, at this temperature theophrastite should be stable. The most recent study to this respect comes from Palmer et al. /PAL 11/. The authors used measured solubilities

for the derivation of equilibrium constants for the formation of bunsenite and the neutral complex  $\text{Ni}(\text{OH})_2(\text{aq})$ .

Fig. 4.80 shows the solubility of bunsenite at 25°C. For the dissolution reaction



Palmer et al. assumed a temperature function for the solubility constant /PAL 11/. For 25°C this function yields  $\log_{10} K^0(298.15\text{K}) = -12.40$ . This model represents experimental data well, see Fig. 4.80. In the same figure, two calculations for the solubility of bunsenite in NaCl-solution (1.0M and 6.0 M) are presented. No real solubility data are available for these data. However, in the pH-range up to  $\sim 10$   $\text{Ni}^{2+}$  should be the dominant species. For the interaction between  $\text{Ni}^{2+}$  and NaCl Pitzer coefficients are available, which were used for these calculations, see section 4.5.1.9. As expected, calculated solubility in 1.0 or 6.0 M NaCl-solution is higher than in pure water.

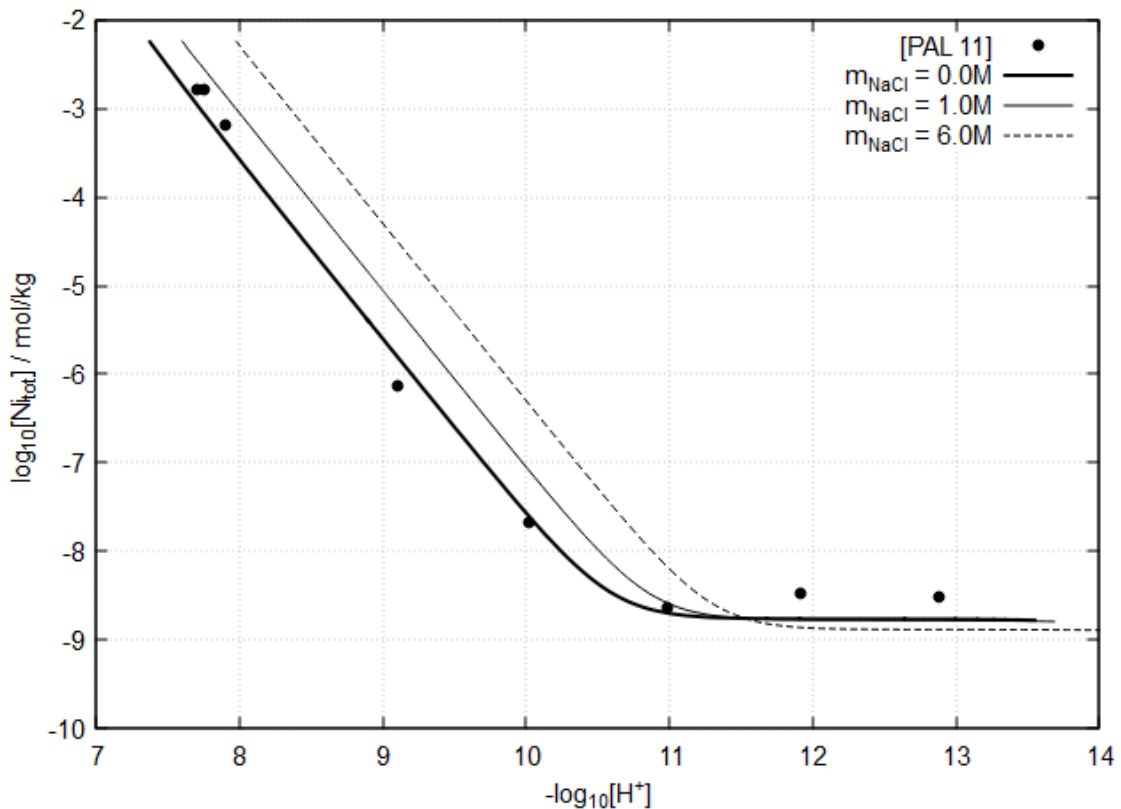


**Fig. 4.80** Nickel concentrations in solutions in equilibrium with bunsenite

Palmer et al. investigated the solid phase at the end of their experiment and identified Nickel oxide as the dominant fraction. However, XRD results indicate the presence of

Nickel hydroxide. That being said, it remains unclear whether the overserved Nickel concentration is to be attributed to bunsenite or theophrastite.

For the given reasons it remains questionable whether bunsenite should be part of a thermodynamic database for nuclear waste disposal, even though reliable thermodynamic data from thermochemical measurements exist. In contrast, Ni(OH)<sub>2</sub>(cr) has to be regarded as relevant, even more, as reliable solubility studies exist (e. g. /GAY 49/). Note, that two modifications exist, from which β-Ni(OH)<sub>2</sub>(cr) only can be regarded as thermodynamically stable. Contrary to β-Ni(OH)<sub>2</sub>(cr), there is no evidence for α-Ni(OH)<sub>2</sub>(cr) under natural conditions /GAM 05/. Within the frame of a future project it should be checked if a solid solution is formed with Brucite Mg(OH)<sub>2</sub>(cr). It is known that Nickel forms solid solutions of the type Ni<sub>2x</sub>Mg<sub>2-2x</sub>Cl(OH)<sub>3</sub> /BET 15/.

### **Nickel chlorides and sulfates**

Nickel forms highly soluble salts with chlorides and sulfates: NiCl<sub>2</sub>·6H<sub>2</sub>O(cr) and NiSO<sub>4</sub>·7H<sub>2</sub>O(cr) along with some double salts. Their solubility can be calculated using existing Pitzer coefficients, see chapter 4.5.1.9. However, these solid phases are only relevant in solutions with high nickel concentrations (>> 0.1 mol/kg) that are not likely to occur under neutral or alkaline conditions.

/MAK 69/ observed the formation of Ni<sub>2</sub>(OH)<sub>3</sub>Cl in dilute NaCl solutions. In the chosen pH range (7 to 9.5) the fresh precipitate converted into Ni(OH)<sub>2</sub>. They found the following stabilities:



The compounds seem to be stable if prepared from moderately concentrated NiCl<sub>2</sub> solutions (>0.5 mol/kg) /BET 17/. Other nickel hydroxy chlorides that initially form during hydrolysis are not thermodynamically stable (such as NiClOH, Ni<sub>3</sub>Cl<sub>2+x</sub>(OH)<sub>4-x</sub>·4H<sub>2</sub>O) but transform only very slowly into more stable /FEI 36/, /BET 17/.

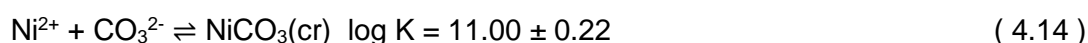
### **NiCO<sub>3</sub>(cr) (gaspéite) and NiCO<sub>3</sub>·5.5H<sub>2</sub>O(cr) (hellyerite)**

Two Nickel carbonates are known to exist in nature, the minerals gaspéite, NiCO<sub>3</sub>(cr) and hellyerite, NiCO<sub>3</sub>·5.5H<sub>2</sub>O.

Gamsjäger et al. derived an equilibrium constant for the following reaction with gaspéite /GAM 05/:



Adding the carbonic acid equilibrium yields

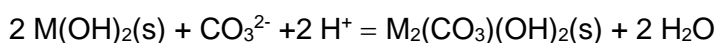


NiCO<sub>3</sub> (gaspéite) may be the thermodynamically more stable phase if carbonate is present, but hydrated NiCO<sub>3</sub> (NiCO<sub>3</sub>·5.5H<sub>2</sub>O) is the primarily forming phase under ambient conditions. The existence of the hydrate as a naturally occurring mineral (hellyerite, /ISA 63/) shows that transformation into gaspéite may be very slow if taking place at all at ambient temperatures. In that case, it must be assumed that hellyerite would be the solubility limiting phase and the solubility of Ni could be five to six orders of magnitude higher if no other nickel phases were allowed, /GAM 01/. The solubility constant for this phase was taken from /GAM 05/, but taking into account the water content (5.5 instead of 6) as described by /BET 16/.

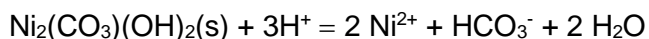


Numerous compounds have been described in the literature, including the minerals nullaginite, Ni<sub>2</sub>(CO<sub>3</sub>)(OH)<sub>2</sub> (Nickel and Berry 1981), otwayite, Ni<sub>2</sub>(CO<sub>3</sub>)(OH)<sub>2</sub>·H<sub>2</sub>O /NIC 77/ paraotwayite, Ni(OH)<sub>2-x</sub>(SO<sub>4</sub>,CO<sub>3</sub>)<sub>0.5x</sub> /NIC 87, kambaldaite, Na<sub>2</sub>Ni<sub>8</sub>(CO<sub>3</sub>)<sub>6</sub>(OH)<sub>6</sub>·6H<sub>2</sub>O /NIC 85/, zaratite (doubtful), Ni<sub>3</sub>(CO<sub>3</sub>)(OH)<sub>4</sub>·4H<sub>2</sub>O, and widgiemoolthalite, Ni<sub>5</sub>(CO<sub>3</sub>)<sub>4</sub>(OH)<sub>2</sub>·4-5 H<sub>2</sub>O /NIC 93/. Another basic nickel carbonate, Ni<sub>12</sub>(CO<sub>3</sub>)<sub>8</sub>(OH)<sub>8</sub>·(x-1)H<sub>2</sub>O, was characterized by /RIN 15/.

For none of these solids, thermodynamic data could be found. The nickel mineral nullaginite is an analog of the iron(II) mineral chukanovite. Because the chemistry of nickel(II) and iron(II) is quite similar /HAG 21/ guessed that the equilibrium constant for the reaction



is the same for nickel and iron(II). In that case the equilibrium constant for nullaginite



would be  $\log_{10}K(209.15^\circ\text{K}) = -0.24$ .

### **NiFe<sub>2</sub>O<sub>4</sub> (nickel ferrite)**

It is conceivable that nickel ferrite forms upon corrosion of nickel-containing steel. But so far, this compound has only been observed as a product of high-temperature solid-state reactions /ELW 96/. There is no evidence that this phase might be formed reversibly from aqueous solutions, for which reason it has not been selected for the PSI/NAGRA database.

### **Nickel Sulfide**

Several nickel sulfide minerals are known. They include Ni<sub>3</sub>S<sub>2</sub> (heazlewoodite), Ni<sub>7</sub>S<sub>6</sub> (godlevskite), NiS (millerite), Ni<sub>3</sub>S<sub>4</sub> (polydymite), NiS<sub>2</sub> (vaesite), but also mixed iron-nickel sulfides such as (Ni,Fe)<sub>9</sub>S<sub>8</sub> (pentlandite), FeNi<sub>2</sub>S<sub>4</sub>(violarite), and (Fe,Ni)S<sub>2</sub> (bravoite). Many of these phases have never been found to precipitate at ambient temperatures. Although thermodynamic data exist for many of these compounds, these have to be regarded with some doubt as are mostly based on high-temperature calorimetric measurements. Inclusion of these data into thermodynamic databases may lead to a serious underestimation of nickel solubilities /THO 99/. /WIL 10/ found that the precipitation of nickel in sulfidic solutions always leads to the formation of hexagonal α-NiS. Rhombohedral millerite (β-NiS) was never observed. In the presence of elemental sulfur α-NiS transformed into polydymite and vaesite. They derived the following solubility constant for α-NiS



#### **4.5.1.8 Speciation model**

Conditional to future findings, the following species would be adopted as a working hypothesis for the speciation of nickel in aqueous solution: Ni<sup>2+</sup>, Ni(OH)<sub>2</sub>(aq), Ni(CO<sub>3</sub>)(aq), NiHS<sup>+</sup>, and Ni(HS)<sub>3</sub><sup>-</sup>. All other species are regarded as either irrelevant or compensable by interaction coefficients. This is valid also for sulfate-containing solutions where the

neutral complex  $\text{NiSO}_4(\text{aq})$  exists. Inclusion in a thermodynamic model would be problematic as available data (solubilities, isopiestic measurements) don't deliver any information on the speciation. On the other hand, a more complex speciation scheme being fully parametrized after an extended research program wouldn't lead to an improved calculation of solubilities. Inclusion of at least one nickel chloride complex,  $\text{NiCl}^+$ , would probably lead to an improvement of solid/solution modeling in systems with very high chloride concentration ( $> 5 \text{ mol/kg}$ ). But for the time being, it seems sufficient to express the complexation in terms of a strong ion interaction.

For an explicit inclusion of more complexes with nickel into an extended Pitzer model more spectroscopic investigations are necessary. Such a model would pay off for applications where the real speciation must be known precisely, e. g. for the consideration of the retention of Nickel on charged surfaces.

#### 4.5.1.9 Modeling in high-saline solutions

Plenty of experimental data are available for lower pH-values which allow the calculation of Pitzer coefficients for  $\text{Ni}^{2+}$ , see Tab. 4.9.

**Tab. 4.9** Pitzer coefficients for  $\text{Ni}^{2+}$  in the six-component seawater system. Experimental data used are mostly related to weakly acidic and neutral solutions.

System			PC	log°K
Ni	Cl		x	$\text{NiCl}_2 \cdot 6\text{H}_2\text{O}$ , $\text{NiCl}_2 \cdot 4\text{H}_2\text{O}$
Ni	SO4		x	$\text{NiSO}_4 \cdot 7\text{H}_2\text{O}$
Ni	Cl	Na	x	
Ni	Cl	K	x	
Ni	Cl	Mg	x	
Ni	Cl	Ca		
Ni	Cl	SO4		
Ni	SO4	Na	x	$\text{Na}_2\text{Ni}(\text{SO}_4)_2 \cdot 4\text{H}_2\text{O}$
Ni	SO4	K	x	$\text{K}_2\text{Ni}(\text{SO}_4)_2 \cdot 6\text{H}_2\text{O}$
Ni	SO4	Mg	~	(solid solution)
Ni	SO4	Ca		

PC = Pitzer-Coefficients, log°K = Solubility constants for mineral phases; mineral phases from the system of oceanic salts are omitted, x = reliable data, ~ = questionable data

Two reports shall be mentioned here representatively in which the state of knowledge valid at the time of publication was compiled and supplemented by own data. Bremer

and Christov evaluated data from the literature and processed solubility- and isopiestic data /BRE 98/. Their work was improved by Hagemann et al. /HAG 15/, who considered data from a larger number of sources. For the complex  $\text{Ni}(\text{OH})_2(\text{aq})$  /HAG 21/ derived an interaction coefficient from the ionic strength dependence of  $\text{Ni}(\text{OH})_2(\text{s})$  solubility in NaCl solutions.

As part of the project LÖVE<sup>18</sup> /HAG 21/, the solubility of nickel was determined in several high-saline solutions. The study delivered reliable boundary values for solubility to be used in integrated near field models for safety analysis. Fig. 4.81 shows experimental values for the solubility of nickel in a halite/ anhydrite saturated brine over a broad pCH range. The predicted solubility coincides with the experimental values very well.

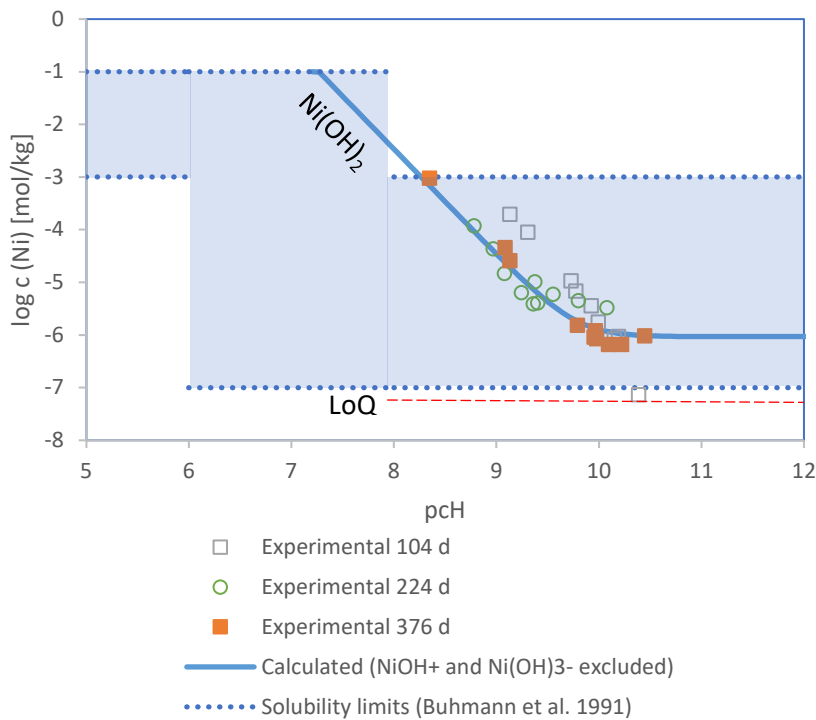


**Fig. 4.81** Solubility of nickel in a solution saturated with halite and anhydrite (from /HAG 21/)

<sup>18</sup> Förderkennzeichen 02 E 11365

#### 4.5.1.10 Suggestions for further work

Future work should focus on solid phases which might limit the overall solubility of nickel, especially in alkaline solutions. The transition between bunsenite and theophrastite should be closely inspected as well as the overall solubility at pH values > 8. Such experiments should be done with NaCl-, MgCl<sub>2</sub>- and CaCl<sub>2</sub>-solutions of various ionic strengths. These would allow the identification of solubility limiting phases and the estimation of Pitzer interaction coefficients for relevant nickel species.

In the case of CaCl<sub>2</sub> containing solutions, the formation and relevance of ternary calcium nickel hydroxide complexes should be tested as these could drastically increase the solubility of nickel. Additional efforts are needed to measure the stability of nickel carbonates, such as Ni<sub>2</sub>(CO<sub>3</sub>)(OH)<sub>2</sub> (Nullaginite), NaNi<sub>4</sub>(CO<sub>3</sub>)<sub>3</sub>(OH)<sub>3</sub>·3H<sub>2</sub>O (Kambaldaite) and Ni<sub>2</sub>(CO<sub>3</sub>)(OH)<sub>2</sub>·H<sub>2</sub>O (Otwayite). Numerous phases are known to exist in nature but too few thermodynamic investigations exist to allow assessing which of these are relevant for repository systems.

In the presence of Mg and Fe(II), it is probably that nickel is bound in solid solutions with these elements. Little is known about their stability. Whether or not mixed compounds such as hibbingite (Ni,Fe)(OH)<sub>3</sub>Cl may be regarded as ideal solutions should be tested.

Because of its potential for lowering the solubility to extremely low values, the formation of elemental nickel, as well as nickel sulfide, should be inspected. The latter poses a special challenge because for its implementation in a database a thermodynamic model for H<sub>2</sub>S(aq) in high saline solution had to be established first. Relevant efforts were already undertaken but require some additional work to cover the interactions of the important HS<sup>-</sup> species /MOO 14/.

#### 4.5.2 Carbon

The speciation of carbon strongly depends on its chemical form in the waste and the release process. Carbon-14 is present in important amounts in the inventory of different components of spent fuel element waste, and particularly in activated steel and zircaloy. Carbon-14 differs in its chemical behaviour from the other elements, since it can be released as an organic species, i.e. carboxylic acids, alcohols, aldehydes, alkenes and alkanes or as an inorganic species i.e. carbonate, bicarbonate and carbon dioxide. The mobility of C-14 strongly depends on whether it occurs in inorganic or organic form. As

carbonate, C-14 shows retention characteristics in cementitious and clay environments due to isotopic exchanges or precipitation. As organic species it can be very mobile and even transferred into the gaseous phase.

Therefore, here the state of the art with respect to the release and subsequent speciation of C-14 is presented, namely the outcome of the European project CAST (CARbon-14 Source Term) is summarized. The primary focus of the CAST project was thus to develop a source term for C-14 and to discriminate experimentally between these two different forms (organic / inorganic) and to more precisely characterize the speciation of the C-14 bearing compounds released from the waste /CAP 18/.

Since the half life of C-14 is 5730 years and many concepts for high-level waste and spent fuel consider a long-containment in the engineered barrier system a radioactive decay down to insignificant inventory amounts is expected under undisturbed conditions. Investigation of the in CAST is therefore of more interest for the Low and Intermediate Level Waste (LILW) than for HLW for many countries. Experiments to measure the release of carbon-14 and carbon-14 speciation have thus been mainly performed at room temperature and in many cases under cementitious conditions, namely high pH values /NEE 18/. With respect to a high-level waste repository in rock salt this limits the direct transferability of the results from the CAST project, since there more neutral and highly mineralized solutions are expected. However, in the following the key results from CAST with respect to C-14 release and speciation are described. Since spent ion exchange resins and neutron activated graphite are not in the focus the description is restricted to the results on neutron irradiated steel (WP2) and neutron irradiated Zircaloy (WP3).

#### 4.5.2.1 Redox and speciation

The release of  $^{14}\text{C}$  **from activated steel** in the early phase after the first contact of the metal surface with water is dominated by dissolved species, mainly carbonate and carboxylic acids, accompanied by a significantly smaller fraction of the gaseous species CO and methane. These compounds will be released from the metal oxide layer or surface contaminations /MIB 18/. A high variation of this fraction between  $10^{-6}$  and 3.6 % is found in the experiments.

After release of C-14 compounds from the metal oxide layer, the C-14 from the bulk material will be released upon further steel corrosion /CAP 18/. It is still unclear what the source of oxygen for the formation of carbonate or organic compounds with oxygen-

containing functional groups will be. Radiolysis with subsequent formation of oxidants may enable the formation of these species. Under real repository conditions it is expected that after water saturation of the near field large amounts of H<sub>2</sub> will form by anaerobic corrosion and will likely consume oxidants from radiolysis. The speciation under real repository conditions can then be expected to shift towards hydrocarbons without oxygen containing functional groups such as methane implying the formation of gaseous species instead of dissolved /MIB 18/, /CAP 18/. As a consequence, the formation of gaseous hydrocarbons can be expected to increase during the long-term release. In addition, the impact of irradiation and radiolysis on the chemical conditions in solution in the repository will decrease with the decay of relatively short-lived gamma emitters like <sup>60</sup>Co. It can be expected that then the influence of radiolysis on the formation of oxygen-containing <sup>14</sup>C species will be diminished.

New publications seem to support this picture. In general, small compounds containing less than seven C atoms were observed both in the gas and liquid phase in leaching experiments with carbon-containing zero-valent iron (ZVI) powders /GUI 20/. More specifically, methane in the gas phase and formic and acetic acids in the liquid phase were the carbon compounds with the highest concentrations. The hydrocarbons and carboxylic acids are produced by two distinct processes. The hydrocarbons are continuously released from the iron surface during corrosion. Their concentration increases with the progress of the anoxic corrosion of iron, in line with H<sub>2</sub> production, while this relationship does not exist with carboxylic acids. The latter compounds are formed during exposure of ZVI powders to oxic conditions, accommodated by the corrosion layer and instantaneously released in contact with solution by desorption.

In summary, it could thus be expected that the C-14 speciation will be dominated by reduced organic compounds, such as – gaseous – hydrocarbons. After mobilization of an instant release fraction the C-14 release is expected to occur with the corrosion rate of the steel in alkaline conditions rather low, corrosion rates down to 0.4 nm yr<sup>-1</sup> were measured in experiments performed at 30°C. However, for a HLW repository in rock salt, where – in case of water ingress to the waste – neutral conditions and saturated salt brines will occur, higher corrosion rates are expected.

With respect to the **Zircaloy cladding** C-14 is found either in the metal part of the Zircaloy cladding due to the neutron activation of <sup>14</sup>N impurities by <sup>14</sup>N(n,p) <sup>14</sup>C reaction, or in the oxide layer (ZrO<sub>2</sub>) formed at the metal surface by the neutron activation of <sup>17</sup>O

by  $^{17}\text{O}(n,\alpha)^{14}\text{C}$  reaction /NEC 18/. The C-14 content determined by modelling agrees well with experimentally determined C-14 contents.

Zirconium alloys show a high resistance against uniform corrosion at low or moderate temperatures. Various studies have shown that the uniform corrosion rates of zirconium alloys are very low in anaerobic neutral or alkaline waters at low temperature with an envelope value of  $20\text{ nm yr}^{-1}$  /NEC 18/. A significant part of the work carried out in CAST was devoted to the analytical development, since the C-14 concentrations in the experiments are very low and measuring needed highly sensitive techniques and particular precaution to handle the samples /NEC 18/. The results from the experimental work in the CAST project showed that for irradiated Zircalloys, the corrosion rates seem to be around  $1\text{-}2\text{ nm yr}^{-1}$  on the longer term (experimental time was 6.5 years), but initially higher over the first year (up to  $100\text{ nm yr}^{-1}$ ).

The vast majority of C-14 inventory (90%) is released as gaseous organic compounds during dissolution of Zircaloy. The gas samples were analysed by a gas chromatograph (GC). The results revealed the production of methane, ethene and  $\text{CO}_2$ . C-14 speciation in solution showed that the organic fraction is more important than the inorganic fraction. Carboxylic acids and oxalate were identified. However, the authors state that the release mechanisms of C-14 are still not very well understood /NEC 14/.

The results highlight a fast release fraction of C-14. From a safety assessment point of view, the instant release fraction (IRF) was determined on irradiated Zircaloy-2 based on inventory measurements. The results showed that the C-14 inventory in the oxide was around 7.5% /NEC 18/. Unfortunately, there are not enough data and currently no consensus over the release mechanism of C-14 from the oxide layer to abstract these very low fractions in quantitative safety assessments. In addition, the influence of hydrides on the corrosion behaviour on the long term in disposal conditions remains uncertain /CAP 18/.

C-14 from Zircaloy shows the same behaviour in terms of speciation: The liquid phase is shared between inorganic and small oxygenated organic compounds. Methane, ethene and  $\text{CO}_2$  were mainly detected in the gas phase. Precise distribution as an input to safety assessment is still challenging at this stage, nevertheless, it can be concluded that the organic form of C-14 released from Zircaloy and steel is present in non-negligible fractions /CAP 18/.

As discussed above these results stem from experiments performed for LLW/ILW conditions repositories in clay environment, performed in rather alkaline conditions.

### **4.5.3 Chloride**

#### **4.5.3.1 Oxidation states**

In natural systems, chlorine only occurs in the oxidation state -I in the form of chloride, Cl<sup>-</sup>. Other oxidation states, such as +I, +III, +V, VII are stable only under extremely oxidizing conditions that are not relevant for the near-field of a geological repository.

#### **4.5.3.2 Speciation**

Chloride forms complexes with many metal cations such as Fe<sup>2+</sup>, Fe<sup>3+</sup>, Ni<sup>2+</sup>, Pb<sup>2+</sup>, Sn<sup>2+</sup>. For most of these metals, hydroxo complexes predominate under alkaline conditions (less so for some heavy metals). Moreover, under typical conditions and in naturally-occurring solutions the concentration of chloride in solution is much higher than that of all complexing metals so that only a small part of chloride is bound in complexes.

#### **4.5.3.3 Relevant solid phases**

In crystalline and clay rocks, pore or formation waters are typically not saturated with any chloride phase. However, at least for some regions in Lower Cretaceous and Jurassic clay formation, a saturation with halite cannot be excluded /HAG 21/. The same may apply to certain crystalline rock formations that are located in the vicinity of salt rock formations. More analytical field data are needed to verify this assumption.

In salt rock, several different chloride minerals may occur. They include halite, NaCl, sylvite, KCl and carnallite, KMgCl<sub>3</sub>·6H<sub>2</sub>O, bischofite, MgCl<sub>2</sub>·6H<sub>2</sub>O and tachyhydrite, CaCl<sub>2</sub>·6H<sub>2</sub>O.

Furthermore, secondary phases may occur that are produced by container corrosion and the interaction of solutions with the waste matrix. In systems with moderate to high chloride concentrations, basic chloride may occur as corrosion products, e.g. Fe<sub>2</sub>(OH)<sub>3</sub>Cl (Fe-hibbingite) or Fe(OH,Cl)<sub>3</sub> (akaganeite), but the vast majority of chloride will be provided by pore and formation waters from the host rock. For all relevant host rock types, the supply of chloride from the host rock may be regarded as unlimited, so that the total

chloride concentration will likely be constant or at least many orders of magnitude higher. If the available chloride content of the near field solution should drop too strong, chloride-containing corrosion phases will become unstable thus stabilizing a certain level of chloride.

Except for AgCl, TlCl, Hg<sub>2</sub>Cl<sub>2</sub>, and PbCl<sub>2</sub> /GAM 97/, /KHO 91/, /HAG 15/, /HAG 12/, all metal chlorides are rather well soluble. Mercury and thallium are not expected to be present in the nearfield of a repository. Minor amounts of silver may be present as a fission product in spent fuel or vitrified waste, but these are expected to be much too low to have a relevant effect on chloride retention. Lead could be a component in radioactive waste types. In neutral to alkaline solutions, it is precipitated in the form of PbCl<sub>2</sub> (cotunnite) and basic chlorides such as laurionite, PbClOH or blixite, Pb<sub>8</sub>O<sub>5</sub>(OH)<sub>2</sub>Cl<sub>4</sub> if sufficient chloride levels are present /HAG 12/. Under very alkaline conditions ~pH 10-12, the formation of 6PbO·PbCl<sub>2</sub>·2H<sub>2</sub>O is predicted (Fig. 4.82). This solid may bind chloride even at very low chloride levels.

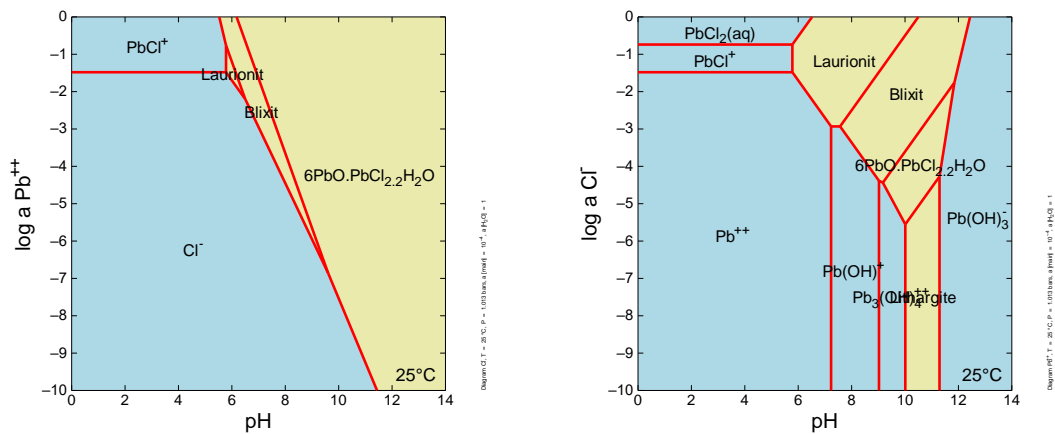


**Fig. 4.82** Stability of lead chloride phases (left:  $a_{Cl}=10^{-4}$ ; right:  $a_{Pb}=10^{-4}$ ) calculated with the database in /HAG 12/

However, all groundwaters that are expected in potential deep host rock formations in Germany as well as in other countries already contain significant levels of chloride, so that <sup>36</sup>Cl released from the waste matrix will have to compete with the chloride already present. Assuming an ideal ion exchange between <sup>35</sup>Cl, <sup>36</sup>Cl, and <sup>37</sup>Cl, the maximum relative amount of <sup>36</sup>Cl bound in secondary phases will not exceed the ratio <sup>36</sup>Cl/(<sup>35</sup>Cl+<sup>37</sup>Cl) in the near-field system, which is extremely low.

The situation is somewhat different in salt rock. Chloride-containing minerals, especially halite are abundant. Any  $^{36}\text{Cl}$  leaving the waste container will enter into intensive contact with the halite mineral surfaces. No information could be found on the speed of ion exchange between  $^{36}\text{Cl}$  and  $^{35/37}\text{Cl}$  but it may significant amounts of  $^{36}\text{Cl}$  will be temporarily exchanged between solution and solid surface and/ or permanently bound. In that case, the ratio  $^{36}\text{Cl}/(^{35}\text{Cl}+^{37}\text{Cl})$  in solution will drop until it achieves a level close to the overall  $^{36}\text{Cl}/(^{35}\text{Cl}+^{37}\text{Cl})$  ratio in the nearfield system.

#### **4.5.3.4 Suggestions for further work**

As discussed above the main retention mechanism for  $^{36}\text{Cl}$  in salt rock is probably the isotopic substitution between solution and halite. The kinetics of this process should be investigated. Poorly soluble chloride-containing secondary phases are not likely to control the mobility of  $^{36}\text{Cl}$ . Nevertheless, for some specific waste types and under the assumption of limited chloride resupply from the host rock (in case of ultrafiltration effects) as observed in some highly compacted smectite-rich clay rocks, /HAG 21/, the retention of chloride from the waste container may cause a relevant limitation of chloride release. Such cases should be considered more deeply.

#### **4.5.4 Tin**

##### **4.5.4.1 Oxidation states**

In aqueous systems, tin occurs in the oxidation states Sn(II) and Sn(IV). Only at high temperatures ( $> 500^\circ\text{K}$ ), tin(II) oxide disproportionates into Sn(IV) and metallic tin so that this process plays no relevant role under moderate conditions in a repository ( $<100^\circ\text{C}$ ). Direct reduction of Sn(II) with hydrogen to metallic tin would require hydrogen pressures and/or temperatures that are also not likely to occur. Metallic tin corrodes in water. Even though the process is enhanced by the presence of chloride, corrosion may be slow enough so that tin objects may survive centuries or millennia if in contact with seawater /DUN 03/, /BER 19/.

##### **4.5.4.2 Speciation of tin(II) in aqueous solutions**

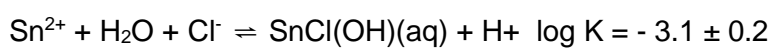
Tin(II) forms mononuclear and polynuclear complexes with hydroxide. Mononuclear species include  $\text{SnOH}^+$ ,  $\text{Sn}(\text{OH})_2(\text{aq})$ , and  $\text{Sn}(\text{OH})_3^-$ . A higher complex does not exist, similar to the homologous  $\text{Pb}^{2+}$ . In the presence of larger  $\text{Sn}^{2+}$  concentrations, the occurrence

of polynuclear hydroxo complexes is possible. Only the existence of the species  $\text{Sn}_3(\text{OH})_4^{2+}$  can be regarded as certain. For the also postulated species  $\text{Sn}_2(\text{OH})_2^{2+}$  the evidence is too weak /GAM 12/. Stability data for hydroxo and other complexes are summarized in Tab. 4.10.

/PET 81/ reported on the formation of ternary  $\text{MSn}(\text{OH})_3^+$  complexes, where M= mixture of Ca, Mg, Sr). Only a few measurements were conducted, but a rough assessment showed that at metal concentrations of 0.065 the ternary complex dominated at  $\text{pH} > 10$  in seawater.

With chloride tin(II) forms a series of chloro complexes  $\text{SnCl}_n^{2-n}$  with  $n=1-4$ . A critical evaluation of the stabilities of these compounds has been made by Gamsjäger (2012).

So far, one mixed chloro hydroxo complex is described for Sn(II),  $\text{Sn}(\text{OH})\text{Cl}(\text{aq})$ . No stability constant was accepted by /GAM 12/ because the only source reported high uncertainties. But /HUM 02/ included the species in their database and found its way into the Thermochemie database as well.



/CIG 12/ estimated the stability of this mixed complex based on the statistical method of /BEC 90/ and derived  $\log K = - 1.5 \pm 0.1$ . The data in /HUM 02/ is preferred because it is based on experimental work. Moreover, it is reasonable to assume that mixed complexes with three or four ligands also exist as has been found for the similar compound Pd(II), e.g.  $\text{SnCl}_y(\text{OH})_x^{2-x-y}$  ( $x=1-2$ ,  $y=1-3$ ) /VAN 99/. The stability and relevance of some of these complexes could be estimated by the statistical methods method of /BEC 90/. Taking into account the data available, binary chloro complexes, especially  $\text{SnCl}_4^-$  play an important role up to slightly alkaline conditions if the chloride activity is sufficiently high ( $\log a_{\text{Cl}^-} > -2$ , Fig. 4.83). The stability field of mixed chloro hydroxo complexes may extend much farther into the alkaline region and need to be explored further.

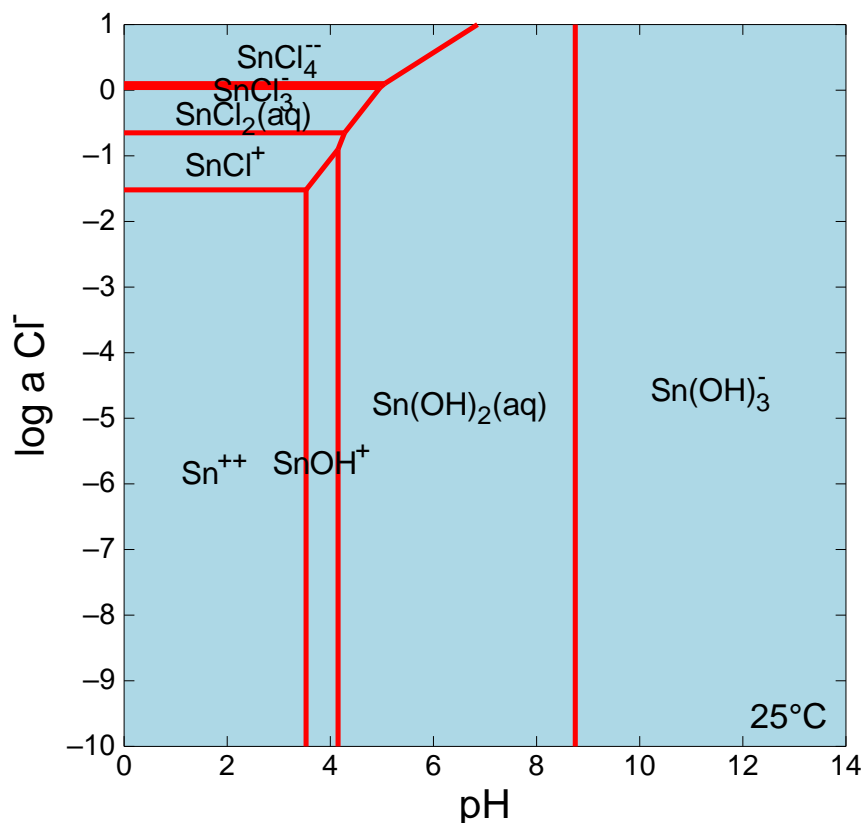


**Fig. 4.83** Relative stability of tin(II) chloro and hydroxo complexes

With sulfate, the two complexes  $\text{SnSO}_4(\text{aq})$  and  $\text{Sn}(\text{SO}_4)_2^{2-}$  are obtained. Gamsjäger et al. /GAM 12/ derived a stability constant of  $\log K = 3.4$  for the neutral complex, while Hummel et al. /HUM 02/ gave a value of 2.6 in agreement with other M(II) sulfato complexes. Both groups of authors were unable to reliably evaluate the few available data on the stability of the complex  $\text{Sn}(\text{SO}_4)_2^{2-}$ . Gamsjäger et al. noted that the value ( $\log \beta_2$ ) for the second complex may be in the order of 3.3. /CIG 12/ derived the values 2.47 and 3.55 for the two sulfato complexes. A comparison with the stability of the analogous complexes of Pb(II) (2.78 and 3.13, /HAG 99/, shows that the proposed value for the second complex is probably in the correct order of magnitude. No attempt is made to re-evaluate the few available experimental investigations. The stability diagram demonstrates that the first sulfato complex is dominant in weakly acidic solutions (Fig. 4.84). It is probably of low importance in alkaline solutions.

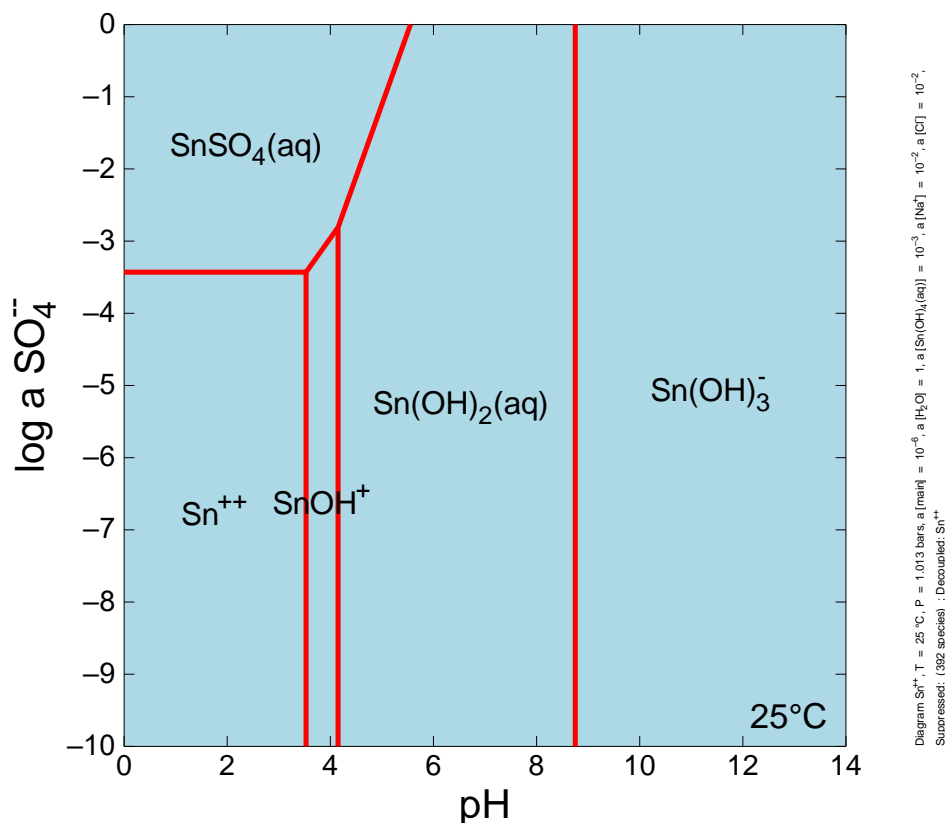
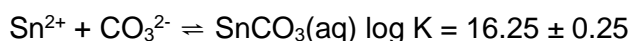


**Fig. 4.84** Relative stability of tin(II) sulfato and hydroxo complexes

Like other divalent cations,  $\text{Sn}^{2+}$  forms complexes with carbonate. So far, there has been only one determination of the formation constants of Sn(II) carbonato complexes /CIG 12/. However, their value for the reaction



is very high in comparison to other  $\text{M}^{2+}$  carbonato complexes. It would cause  $\text{SnCO}_3(\text{aq})$  to be the dominating species at all relevant p<sub>c</sub>H levels, even in the presence of up to 10 mol/kg chloride and low carbonate concentration. Using a correlation method, /BRO 87/ estimated  $\log K = 9.72$ . In that case,  $\text{SnCO}_3(\text{aq})$  would have a negligible impact on the solubility. The data from /CIG 12/ for  $\text{SnCO}_3(\text{aq})$  and  $\text{Sn}(\text{OH})\text{CO}_3^-$  are not used.

No information could be found on sulfido complexes of tin(II), e.g.  $\text{SnS}(\text{aq})$  or  $\text{SnS}_2^{2-}$ . They are likely to exist as they have been documented for other M(II) cations, such as  $\text{Pb}^{2+}$ ,  $\text{Fe}^{2+}$ , or  $\text{Cd}^{2+}$  /ALF 99/, but so far no thermodynamic data are available. It appears that so far only polynuclear complexes were investigated /RIC 06/.

**Tab. 4.10** Stability of tin(II) complexes

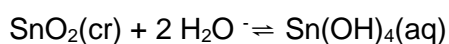
Reaction	log K	Source
$\text{Sn}^{2+} + \text{H}_2\text{O} \rightleftharpoons \text{SnOH}^+ + \text{H}^+$	-3.53	1
$\text{Sn}^{2+} + 2 \text{H}_2\text{O} \rightleftharpoons \text{Sn(OH)}_2(\text{aq}) + 2 \text{H}^+$	-7.68	1
$\text{Sn}^{2+} + 3 \text{H}_2\text{O} \rightleftharpoons \text{Sn(OH)}_3^- + 3 \text{H}^+$	-16.43	1
$3\text{Sn}^{2+} + 4 \text{H}_2\text{O} \rightleftharpoons \text{Sn}_3(\text{OH})_4^{2+} + \text{H}^+$	-5.6	1
$\text{Sn}^{2+} + \text{Cl}^- \rightleftharpoons \text{SnCl}^+$	1.52	1
$\text{Sn}^{2+} + 2\text{Cl}^- \rightleftharpoons \text{SnCl}_2(\text{aq})$	2.17	1
$\text{Sn}^{2+} + 3\text{Cl}^- \rightleftharpoons \text{SnCl}_3^-$	2.13	1
$\text{Sn}^{2+} + 4\text{Cl}^- \rightleftharpoons \text{SnCl}_4^{2-}$	2.03	1
$\text{Sn}^{2+} + \text{H}_2\text{O} + \text{Cl}^- \rightleftharpoons \text{SnCl(OH)}^+ + \text{H}^+$	3.1	2
$\text{Sn}^{2+} + \text{SO}_4^{2-} \rightleftharpoons \text{SnSO}_4(\text{aq})^-$	3.43	1
$\text{Sn}^{2+} + \text{CO}_3^{2-} \rightleftharpoons \text{SnCO}_3(\text{aq})^-$	9.72	3

1: /GAM 12/, 2: /HUM 02/, 3: /BRO 87/

#### 4.5.4.3 Speciation of tin(IV) in aqueous solutions

In comparison with  $\text{Sn}^{2+}$ , the complexation of  $\text{Sn}^{4+}$  with hydroxide is much stronger. To suppress the formation of hydroxo complexes high acid concentrations, e.g. 5 M  $\text{HClO}_4$  are required /FAT 78/. At lower acidities, hydrolysis occurs and leads to the formation of  $\text{Sn(OH)}_x^{4-x}$  with  $n=1..6$  (Tab. 4.11). Only one weakly documented study has been published on the hydrolysis under acidic conditions /NAZ 71/ that was not considered as reliable by /GAM 12/. However, /RAI 11/ evaluated the information from that study and derived a model that was able to explain their own experimental data at low pH (<pH 2). According to this model, only four species need to be considered between pH 0 and pH12:  $\text{Sn(OH)}_3^+$ ,  $\text{Sn(OH)}_4(\text{aq})$ ,  $\text{Sn(OH)}_5^-$ , and  $\text{Sn(OH)}_6^{2-}$ . The complex  $\text{Sn(OH)}_3^+$  is the only complex not included in the NEA database. It occurs only at  $\text{pH} < 1.5$  and is of no relevance for naturally occurring fluids. Because of this and the inconsistency between the two models the species is not included in Tab. 4.11.

The stability of the species  $\text{Sn(OH)}_4(\text{aq})$  is still uncertain. It is expected to be the predominant complex in a broad pH range (1.5 to 8) but its concentration in equilibrium with  $\text{SnO}_2(\text{am})$  or  $\text{SnO}_2(\text{cr})$  (cassiterite) is so low so that in most studies the analytical results were close or at the detection limit. For the reaction



/GAM 12/ derived an equilibrium constant of  $-8.06$ , but the experimental data of /RAI 11/ indicate a constant of  $<-8.7$ . The difference may have been caused by insufficient filtering or centrifugation or different water content of the solid phase.

In their solubility study, /RAI 11/ observed an increase of the total Sn(IV) concentration above pH 7 which could be attributed to the formation of  $\text{Sn}(\text{OH})_5^-$  and  $\text{Sn}(\text{OH})_6^{2-}$ . Above pH 11.7 the solubility remained constant. The authors assumed that above this value  $\text{Na}_2\text{Sn}(\text{OH})_6(\text{aq})$  abruptly predominates and is in equilibrium with solid  $\text{Na}_2\text{Sn}(\text{OH})_6(\text{s})$ . This compound is known from the literature but the authors did not prove it by XRD or chemical analysis.

For other M(IV) cations ternary calcium and magnesium complexes have been reported, e.g.  $\text{Ca}_3\text{Zr}(\text{OH})_6^{4+}$ . So far, no such species have been reported for Sn(IV), but the similar ionic radii of  $\text{Sn}(\text{OH})_6^{2-}$  and  $\text{Zr}(\text{OH})_6^{2-}$  suggest that they may be similarly stable.

For tin(IV) a complete series of chloro complexes from  $\text{SnCl}^{3+}$  to  $\text{SnCl}_6^{2-}$  is documented. Due to the high stability of hydroxo complexes even at low pH values, pure chloro complexes can only be formed in concentrated HCl solutions. At 1 M HCl, the dominating Sn(IV) species already contain hydroxide /GAM 12/. Under slightly acidic conditions chloro complexes won't play any role (Fig. 4.85).

However, the formation of mixed hydroxo chloro complexes with a high OH/Cl ratio cannot be fully excluded under slightly acidic conditions, but a concise thermodynamic treatment of these species is still lacking.

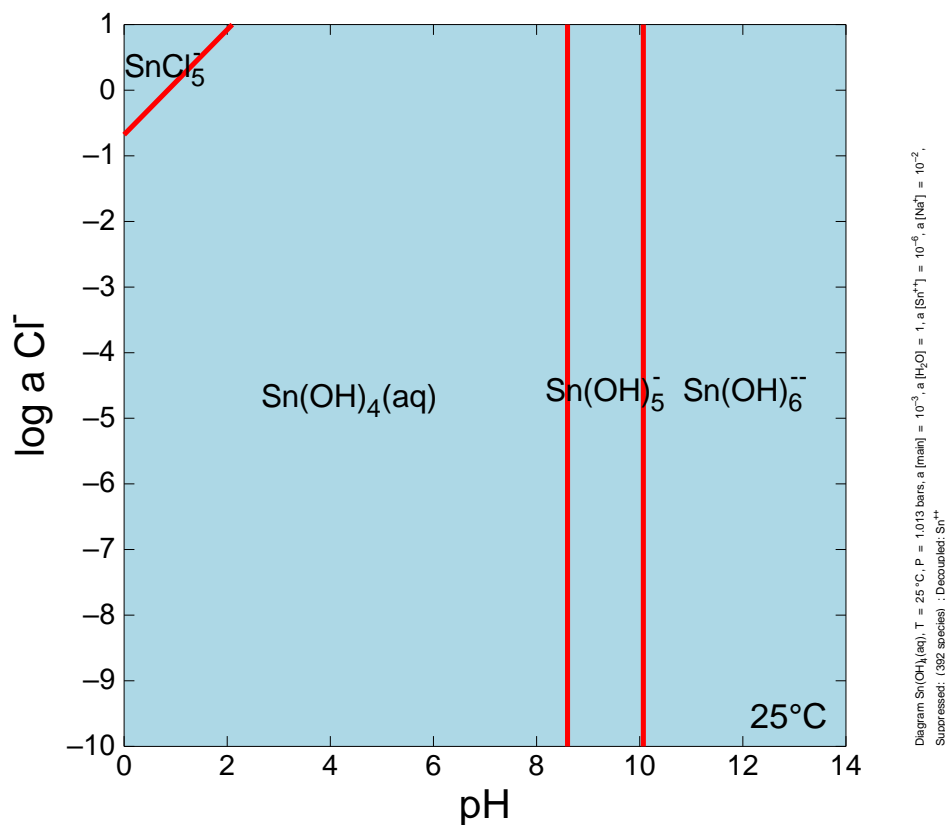
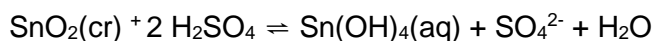


**Fig. 4.85** Relative stability of tin(IV) chloro and hydroxo complexes

Tin(IV) forms a complex with sulfate in sulfuric acid. Its stability is rather weak. For the reaction



a constant  $\log K = -1.3$  was reported /GAM 12/. In neutral solutions the complexation with sulfate is negligible.

Tin(IV) sulfide,  $\text{SnS}_2$ , is soluble in aqueous  $\text{Na}_2\text{S}$  where it forms the complex  $\text{SnS}_3^{2-}$ . Only a few experimental determinations of its stability were conducted. They did not allow a reliable determination of the equilibrium constant /GAM 12/

No information is available on carbonato complexes of tin(IV).

**Tab. 4.11** Stability of tin(IV) complexes

Reaction	log K	Source
$\text{Sn(OH)}_4(\text{aq}) + \text{H}_2\text{O} \rightleftharpoons \text{Sn(OH)}_5^- + \text{H}^+$	-8.6	1
$\text{Sn(OH)}_4(\text{aq}) + 2 \text{H}_2\text{O} \rightleftharpoons \text{Sn(OH)}_6^{2-} + 2 \text{H}^+$	-18.67	1

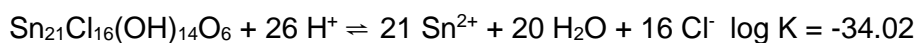
1; /GAM 12/

**4.5.4.4 Solid phases of Tin(II)**

Romarchite, SnO, is the most simple oxo compound of Sn(II). Its solubility has been critically discussed by /GAM 12/ (Tab. 4.12).

Thermodynamic data for the important tin(II) hydroxide  $\text{Sn}_3\text{O}_2(\text{OH})_2$ , the mineral hydroromarchite is still lacking. It was found on ancient tin ingots that have corroded in seawater for centuries. It occurs together with romarchite and abhurite,  $\text{Sn}_{21}\text{O}_6(\text{OH})_{14}\text{Cl}_{16}$  /DUN 03/. A solubility constant is reported for amorphous “ $\text{Sn(OH)}_2$ ”, but the real composition was not determined /CIG 12/. It may well be close to the composition of hydroromarchite,  $\text{Sn}_3\text{O}_2(\text{OH})_2$ , but the reported value is assumed to apply to a solid with the composition  $\text{Sn(OH)}_2(\text{am})$ .

Tin(II) forms the neutral chloride  $\text{SnCl}_2 \cdot 2\text{H}_2\text{O}$ , but it can only be prepared from hydrochloric acid. Mixing with water leads to hydrolysis and precipitation of basic tin(II) chlorides. Its formula was debated for a long time. Often referred to as “ $\text{Sn(OH)Cl} \cdot \text{H}_2\text{O}$ ”, the correct formulation seems to be  $\text{Sn}_{21}\text{Cl}_{16}(\text{OH})_{14}\text{O}_6$ , which represents the naturally occurring mineral abhurite/SCH 81/, /EDW 92/. Thermodynamic data for ‘ $\text{Sn(OH)Cl} \cdot \text{H}_2\text{O}$ ’ in /GAM 12/ was transformed into the formula for the above mentioned mineral:



The relative stability of tin(II) chlorides and hydroxides is shown in Fig. 4.87.

Similar to the neutral chloride, tin(II) sulfate,  $\text{SnSO}_4$  hydrolyses if not in contact with acid. Corrosion of tin or bronze in sulfate-containing media may lead to the formation of basic sulfates, such as  $\text{Sn}_2\text{OSO}_4$ ,  $\text{Sn}_3\text{O}_2\text{SO}_4$ , or  $\text{Sn}_3(\text{OH})_2\text{OSO}_4$  /MCL 91/, /MUL 10/. Only for  $\text{Sn}_3(\text{OH})_2\text{OSO}_4$  a solubility has been determined /EDW 96/. The value has not been selected by /GAM 12/ because some experimental details were lacking in the original publication. Nevertheless, the data from /EDW 96/ seem to be well elaborated and we feel it would be better to include than to omit them. The relative stability of tin(II) hydroxides

and sulfates is depicted in Fig. 4.86. With sulfide, tin(II) forms the compound SnS, also known as the mineral herzenbergite. No information could be found on solid tin(II) carbonates.

**Tab. 4.12** Stability of solid tin(II) phases

Reaction	log K	Source
$\text{SnO} + 2 \text{H}^+ \rightleftharpoons \text{Sn}^{2+} + \text{H}_2\text{O}$	1.59	1
$\text{Sn}(\text{OH})_2(\text{am}) + 2\text{H}^+ \rightleftharpoons \text{Sn}^{2+} + 2\text{H}_2\text{O}$	1.74	2
$\text{Sn}_{21}\text{Cl}_{16}(\text{OH})_{14}\text{O}_6 + 26 \text{H}^+ \rightleftharpoons 21 \text{Sn}^{2+} + 20 \text{H}_2\text{O} + 16 \text{Cl}^-$	-34.02	1
$\text{Sn}_3(\text{OH})_2\text{OSO}_4 + 4 \text{H}^+ \rightleftharpoons 3 \text{Sn}^{2+} + 3 \text{H}_2\text{O} + \text{SO}_4^{2-}$	-5.01	3
$\text{SnS} + \text{H}^+ \rightleftharpoons \text{Sn}^{2+} + \text{HS}^-$	-16.21	1

1: /GAM 12/, 2: /CIG 12/, 3: /EDW 96/

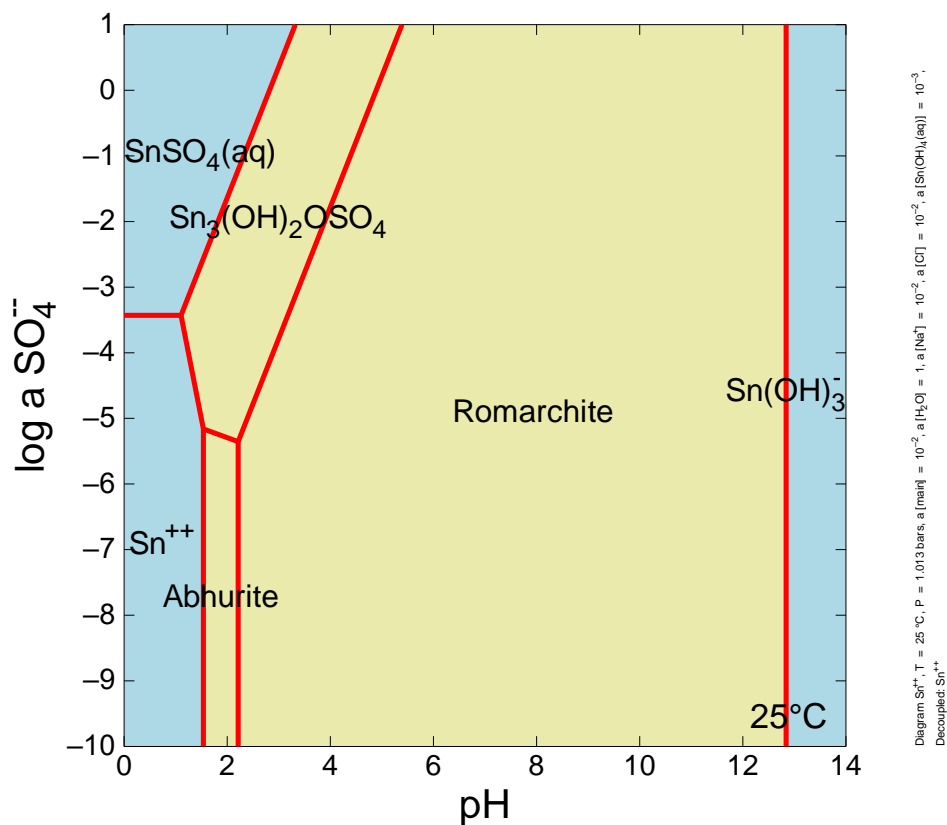


**Fig. 4.86** Relative stability of solid tin(II) hydroxide and sulfate compounds in the presence of chloride ( $a_{\text{Sn}}=0.01$ ,  $a_{\text{Cl}}=0.01$ )

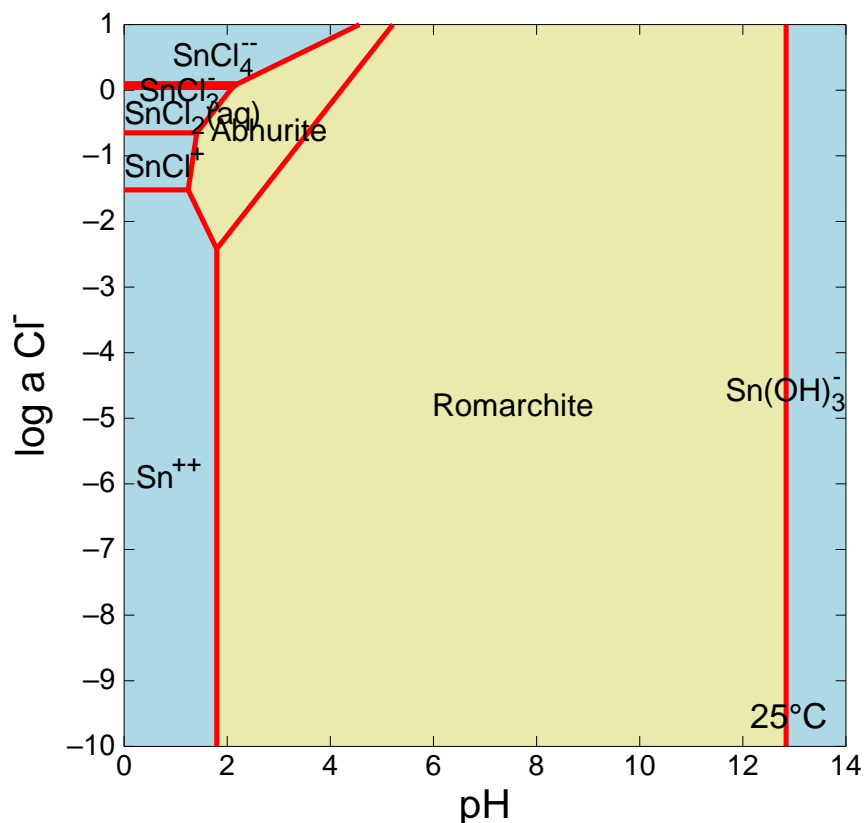


Diagram  $\text{Sn}^{++}$ ,  $T = 25^\circ\text{C}$ ,  $P = 1.013\text{ bars}$ ,  $a[\text{H}_2\text{O}] = 1$ ,  $a[\text{Na}^+] = 10^{-2}$ ,  $a[\text{Sn}(\text{OH})_4(\text{aq})] = 10^{-3}$ , Decoupled:  $\text{Sn}^{++}$

**Fig. 4.87** Relative stability of solid tin(II) hydroxide and chloride compounds ( $a_{\text{Sn}}=0.01$ )

#### 4.5.4.5 Solid phases of Tin(IV)

According to the strong tendency of tin(IV) to hydrolyze, the oxide compounds are particularly stable. The least soluble is the dioxide  $\text{SnO}_2$ , which also occurs in nature as cassiterite. However, if  $\text{Sn}(\text{IV})$  is precipitated from the solution, an amorphous compound with changing water content is formed, which is alternatively called  $\text{SnO}_2(\text{am})$  or  $\text{SnO}_2 \cdot x\text{H}_2\text{O}$ . It does not transform into cassiterite even after a long period of experimental time (180 days) /CIG 12/. Recommended solubility constants for cassiterite and  $\text{SnO}_2(\text{am})$  may be found in /GAM 12/.

The database was supplemented by a solubility constant for fresh and crystalline burtite,  $\text{CaSn}(\text{OH})_6$ , which /LOT 00/ found in alkaline cement systems. The compound occurs under alkaline conditions (Fig. 4.88).

An analogous compound with magnesium,  $\text{MgSn}(\text{OH})_6$ , known as the mineral schoenfliesite /FAU 71/ can be synthesized by grinding a 1:1 mixture of  $\text{MgCl}_2 \cdot 6\text{H}_2\text{O}$  and

$\text{Na}_2\text{Sn}(\text{OH})_6$  at room temperature /KRA 10/. The solid is obviously very poorly soluble as it can be used to prepare coatings. It was also found in contact with seawater in ancient shipwrecks /BAS 98/, but solubility data are not available.

Potassium stannate is very soluble in water (about 87 wt.-%, /ROS 68/) and would precipitate only in concentrated KOH media. The same applies to sodium stannate,  $\text{Na}_2\text{Sn}(\text{OH})_6$  (> 400 g/l, /REI 39/, /UZA 59/. However, /RAI 11/ stated that sodium stannate would have a very low solubility (<  $10^{-5}$  mol/kg) which is obviously in sharp contrast to earlier results.

Solid tin(IV) chloride is of no relevance as it decomposes quickly when getting into contact with water. A tin(IV) sulfate is unknown. Several sulfides are known that contain Sn(IV). They include  $\beta\text{-SnS}_2$  (berndtite), and the mixed tin(II)/tin(IV) compound  $\text{Sn}_2\text{S}_3$  (ottemannite). /GAM 12/ provides stability data for berndtite but could not find any reliable thermodynamic data for ottemannite. Log K values are summarized in Tab. 4.13.

**Tab. 4.13** Stability of solid tin(IV) phase

Reaction	log K	Source
$\text{SnO}_2(\text{cr}) + 2 \text{H}_2\text{O} \rightleftharpoons \text{Sn}(\text{OH})_4(\text{aq})$	-8.06	1
$\text{SnO}_2(\text{am}) + 2 \text{H}_2\text{O} \rightleftharpoons \text{Sn}(\text{OH})_4(\text{aq})$	-7.22	1
$\text{CaSn}(\text{OH})_6(\text{cr}) + 2 \text{H}^+ \rightleftharpoons \text{Sn}(\text{OH})_4(\text{aq}) + \text{Ca}^{2+} + 2\text{H}_2\text{O}$	7.74	2
$\text{CaSn}(\text{OH})_6(\text{fresh}) + 2 \text{H}^+ \rightleftharpoons \text{Sn}(\text{OH})_4(\text{aq}) + \text{Ca}^{2+} + 2\text{H}_2\text{O}$	8.82	2
$\text{SnS}_2 + 4 \text{H}_2\text{O} \rightleftharpoons \text{Sn}(\text{OH})_4(\text{aq}) + 2 \text{HS}^- + 2 \text{H}^+$	-30.02	1

1: /GAM 12/; 2: /LOT 00/

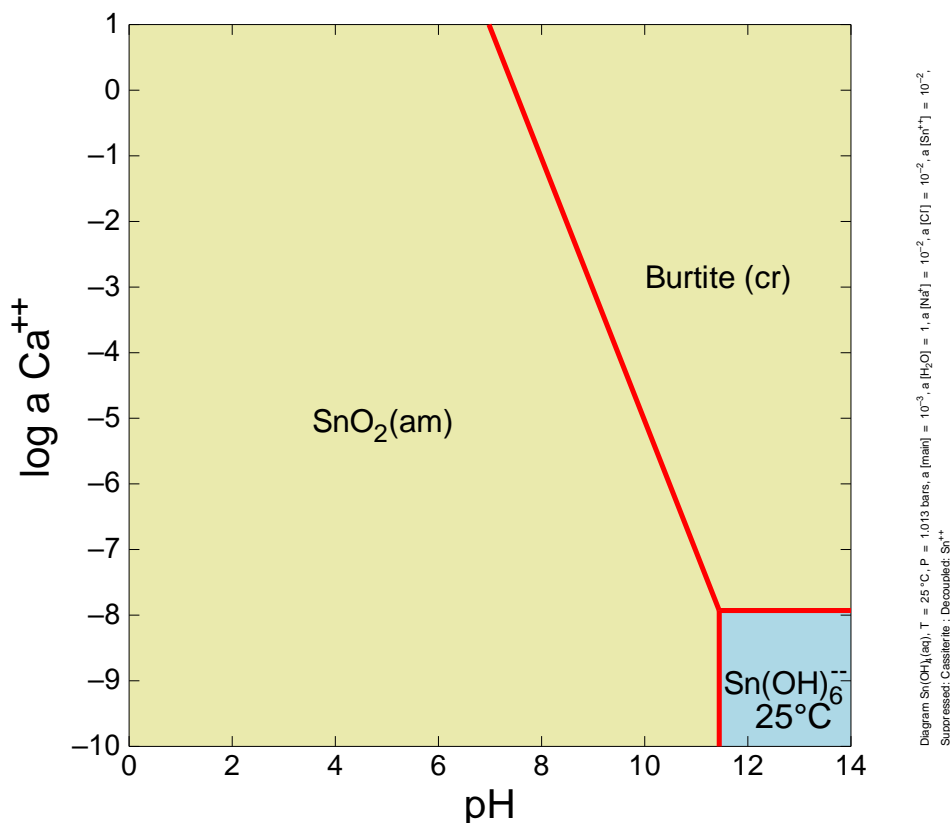


**Fig. 4.88** Relative stability of tin(IV) solids in the presence of calcium

#### 4.5.4.6 Speciation model

Based on the discussion above the following tin species seem to be relevant in slightly acidic to alkaline solutions.

Tin(II):  $\text{Sn(OH)}_2(\text{aq})$ ,  $\text{Sn(OH)}_3^-$ ,  $\text{SnCl}_2(\text{aq})$ ,  $\text{SnCl}_4^{2-}$

Tin(IV):  $\text{Sn(OH)}_4(\text{aq})$ ,  $\text{Sn(OH)}_5^-$ ,  $\text{Sn(OH)}_6^{2-}$

#### 4.5.4.7 Modeling in high-saline solutions

So far, no models have been published that would allow the modeling of tin(II) or tin(IV) in saline solutions. /RAI 11/ as well as /CIG 12/ published extended sets of SIT interaction coefficients that would allow the prediction of solution properties in moderately concentrated solutions of NaCl. /HAG 21/ undertook an attempt to estimate Pitzer ion interaction coefficients for many relevant ion combinations. Their approach is based on the method of /SIM 16/ and /SIM 17/, who provided empirical formula to estimate the ionic

radii of anionic and cationic complex species and ion interaction coefficients. The derived database was mainly intended as a proof of concept that estimation methods can be used to fill gaps in the thermodynamic database. Fig. 4.89 shows the solubility of tin(II) in a solution that is nearly saturated with halite and anhydrite. If the formation of Sn(IV) is not allowed the calculated solubility of SnO is within 1 to 1.5 orders of magnitude within the experimental values. The difference under alkaline conditions may have been caused by ternary calcium tin hydroxo complexes.

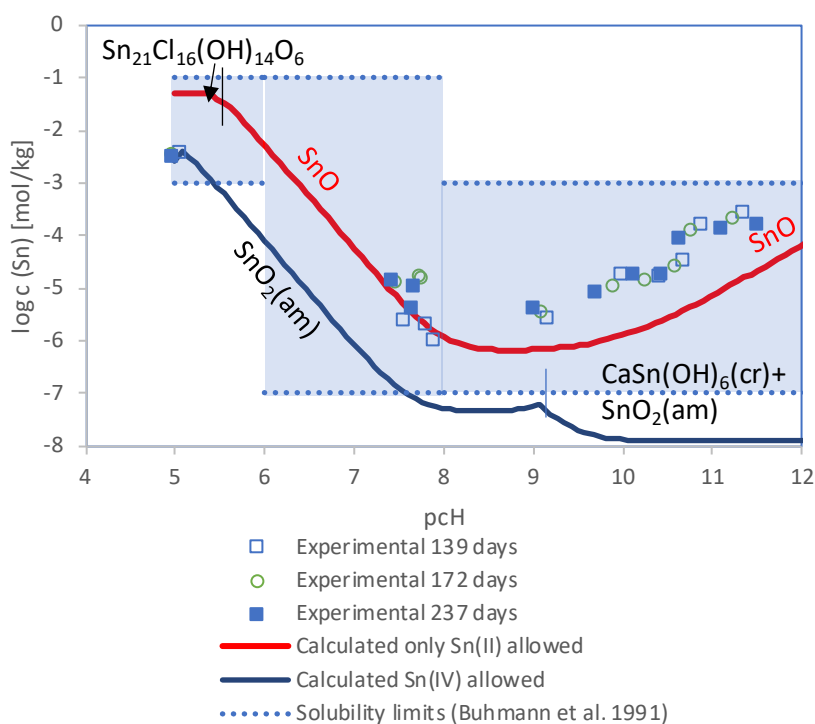


**Fig. 4.89** Solubility of tin(II) in a solution saturated with halite and anhydrite

A similar experiment was conducted with Sn(IV) with  $\text{SnO}_2 \cdot x\text{H}_2\text{O}$  as a starting material. In this case, the equilibrium solids could not be identified by XRD, but their composition was assumed based on the solution concentrations and their change. Below approximately pcH 9.5 the original  $\text{SnO}_2 \cdot x\text{H}_2\text{O}$  was probably present. At higher pcH, calcium was removed from the solution while the sulfate concentration increased. That was an indication that calcium was bound with tin in burtite,  $\text{CaSn}(\text{SnOH})_6$ . Calculated and observed solubilities agreed well (within one order of magnitude) (Fig. 4.90). However, the scattering of data was quite high, possibly due to insufficient filtration ( $0,2 \mu\text{m}$ ) that may not have removed very fine particles or colloidal tin.

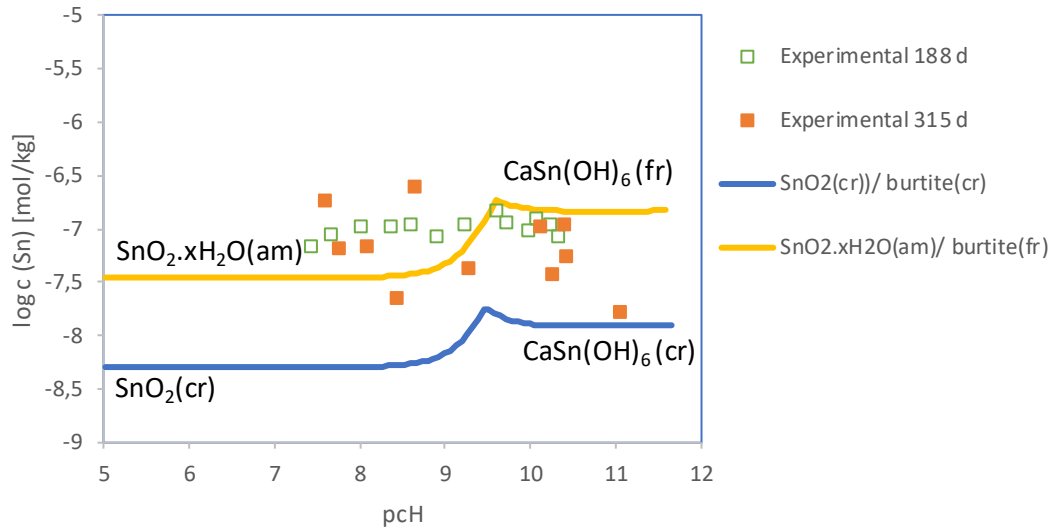


**Fig. 4.90** Solubility of tin(IV) in a solution saturated with halite and anhydrite

Both cases show that the approach of estimating data is justified where experimental results for minor species are missing. Further work is needed to test estimated interaction coefficients and to investigate whether ternary hydroxo complexes with calcium and possibly magnesium account for some of the observed differences.

#### 4.5.4.8 Identification of knowledge gaps

The discussion of available information on tin(II) chemistry revealed a couple of knowledge gaps that mandate further scientific investigations. These include:

- Relevance and stability of ternary calcium and magnesium tin(II) hydroxo complexes
- Stability of  $\text{Sn}(\text{OH})_4(\text{aq})$
- Solubility of hydromarchite,  $\text{Sn}_3\text{O}_2(\text{OH})_2$  and schoenfliesite,  $\text{MgSn}(\text{OH})_4$
- Ion interaction coefficients of the main tin species in alkaline solutions:  $\text{Sn}(\text{OH})_3^-$ ,  $\text{Sn}(\text{OH})_5^-$  and  $\text{Sn}(\text{OH})_6^{2-}$

#### 4.5.5 Niob

Recently, the Paul-Scherrer-Institute (PSI) issued a report about the selection of thermodynamic data for aqueous species and solid phases containing niobium /THO 21/. Many references are given to earlier reviews from Lothenbach et al. /LOT 99/, Wood 2005 /WOO 05/, and Kitamura et al. /KIT 10/, mostly motivated by the relevance of Niobium for radioactive waste disposal. After the finalization of Thoenen's report, another review

appeared by Filella and May (2020) /FIL 20/. This report aims to summarize findings in the above-mentioned reports and publications.

#### 4.5.5.1 Speciation

Niobium is known to form compounds where it exhibits oxidation numbers ranging from -I to +V and +VII. Aqueous species are only known for the pentavalent state. Depending on the coordination number Nb(+V) has ionic radii between 0.74 and 0.48°Å. This in combination with its high charge qualifies it as hard Lewis acid being inclined to combine with hard Lewis bases such as O<sup>2-</sup> or OH<sup>-</sup>. Like ferric iron which exhibits smaller charge to radius ratios complexes with hydroxide predominate the speciation of niobium in aqueous solution: Nb(OH)<sub>4</sub><sup>+</sup>, Nb(OH)<sub>5</sub><sup>0</sup>, Nb(OH)<sub>6</sub><sup>-</sup>, and Nb(OH)<sub>7</sub><sup>2-</sup>. Even at pH=0, no free Nb<sup>5+</sup> is found. Thoenen points out that the exact composition of these complexes is subject to discussion. For example Nb(OH)<sub>5</sub><sup>0</sup> is also referred to as NbO(OH)<sub>3</sub><sup>0</sup> or NbO<sub>2</sub>(OH)<sup>0</sup>.

There is experimental evidence for the existence of polynuclear species. Well established hexaniobate species are Nb<sub>6</sub>O<sub>19</sub><sup>8-</sup>, HNb<sub>6</sub>O<sub>19</sub><sup>7-</sup>, H<sub>2</sub>Nb<sub>6</sub>O<sub>19</sub><sup>6-</sup>, and H<sub>3</sub>Nb<sub>6</sub>O<sub>19</sub><sup>5-</sup>. Thermodynamic data for these species were only selected as supplemental data by Thoenen because of a general lack of experimental reaction data between mononuclear and hexaniobate species. This is also reflected in the fact, that in /FIL 20/ no equilibrium constant is given for the formation of a hexaniobate species from mononuclear ones. It is interesting to note that in /SPI 68/ studies are cited which propose the formation of Nb<sub>2</sub>O<sub>5</sub>(s) via the intermediary formation of hexaniobate anions. Tetranibate species are expected to be formed at pH>13.97 only and are therefore not considered to be relevant for waste repository conditions. Experimental data (spectrophotometry, pH-titrations) indicate the existence of dodecaniobates. Two sets of formation constants exist which are completely inconsistent. Potentiometric data by Spinner (1968) indicate that at pH ≤ 7 hexaniobate may transform into dodecaniobate. This reaction doesn't seem to proceed instantaneously though, and it is reported that colloids form upon acidification. Thus, it remains unclear whether dodecaniobates constitute thermodynamically stable species.

Thermodynamic data for Niobium species as given in /THO 21/ and /FIL 20/ are compiled in Tab. 4.14. Contrary to Thoenen, Filella and May didn't select a formation constant for Nb(OH)<sub>7</sub><sup>2-</sup>.

**Tab. 4.14** Thermodynamic data for niobium species. Numbers underlined were calculated for this report. All data are valid for 298.15 K.

	$\log_{10} K^0$	$\log_{10} K^0$	$\Delta_f G_m^0$	$\Delta_f G_m^0$	$\Delta_r H_m^0$	Reaction
	/FIL 20/	/THO 21/	/FIL 20/(b)	/THO 21/		/THO 21/
			[kJ · mol <sup>-1</sup> ]			
Nb(OH) <sub>4</sub> <sup>+</sup>			-1197	-1196		
Nb(OH) <sub>5</sub> (aq)	-1.60	-1.89	-1425	<u>-1422</u>	9	Nb(OH) <sub>4</sub> <sup>+</sup> + H <sub>2</sub> O(l) = Nb(OH) <sub>5</sub> (aq) + H <sup>+</sup>
Nb(OH) <sub>6</sub> <sup>-</sup>	<u>-6.56</u>	-6.69	-1634	<u>-1632</u>	26	Nb(OH) <sub>4</sub> <sup>+</sup> + 2H <sub>2</sub> O(l) = Nb(OH) <sub>5</sub> (aq) + 2H <sup>+</sup>
Nb(OH) <sub>7</sub> <sup>2-</sup>		-16.09		<u>-1816</u>	63	Nb(OH) <sub>4</sub> <sup>+</sup> + 3H <sub>2</sub> O(l) = Nb(OH) <sub>5</sub> (aq) + 3H <sup>+</sup>
Nb <sub>6</sub> O <sub>19</sub> <sup>8-</sup>		<u>-70.54</u>	-5609	<u>-5588</u>		6Nb(OH) <sub>4</sub> <sup>+</sup> = Nb <sub>6</sub> O <sub>19</sub> <sup>8-</sup> + 14H <sup>+</sup> + 5H <sub>2</sub> O(l)
HNb <sub>6</sub> O <sub>19</sub> <sup>7-</sup>		<u>-56.54</u>	-5695	<u>-5668</u>		6Nb(OH) <sub>4</sub> <sup>+</sup> = HNb <sub>6</sub> O <sub>19</sub> <sup>7-</sup> + 13H <sup>+</sup> + 5H <sub>2</sub> O(l)
H <sub>2</sub> Nb <sub>6</sub> O <sub>19</sub> <sup>6-</sup>		<u>-43.54</u>	-5770	<u>-5742</u>		6Nb(OH) <sub>4</sub> <sup>+</sup> = H <sub>2</sub> Nb <sub>6</sub> O <sub>19</sub> <sup>6-</sup> + 12H <sup>+</sup> + 5H <sub>2</sub> O(l)
H <sub>3</sub> Nb <sub>6</sub> O <sub>19</sub> <sup>5-</sup>		<u>-31.94</u>	-5837	<u>-5808</u>		6Nb(OH) <sub>4</sub> <sup>+</sup> = H <sub>3</sub> Nb <sub>6</sub> O <sub>19</sub> <sup>5-</sup> + 11H <sup>+</sup> + 5H <sub>2</sub> O(l)

(b) in in /FIL 20/ no value was given for  $\Delta_f G_m^0(\text{H}_2\text{O}(\text{l}), 298.15\text{K})$  but assumed to be the same as in /THO 21/.

An application of Thoenens data is shown in the following Fig. 4.91. The most relevant species for pH-conditions met in underground waste repositories are  $\text{Nb}(\text{OH})_6^-$  and  $\text{Nb}(\text{OH})_7^{2-}$ . Note that hexaniobates were considered in this calculation but didn't turn out in orders of magnitude covered by the figure.

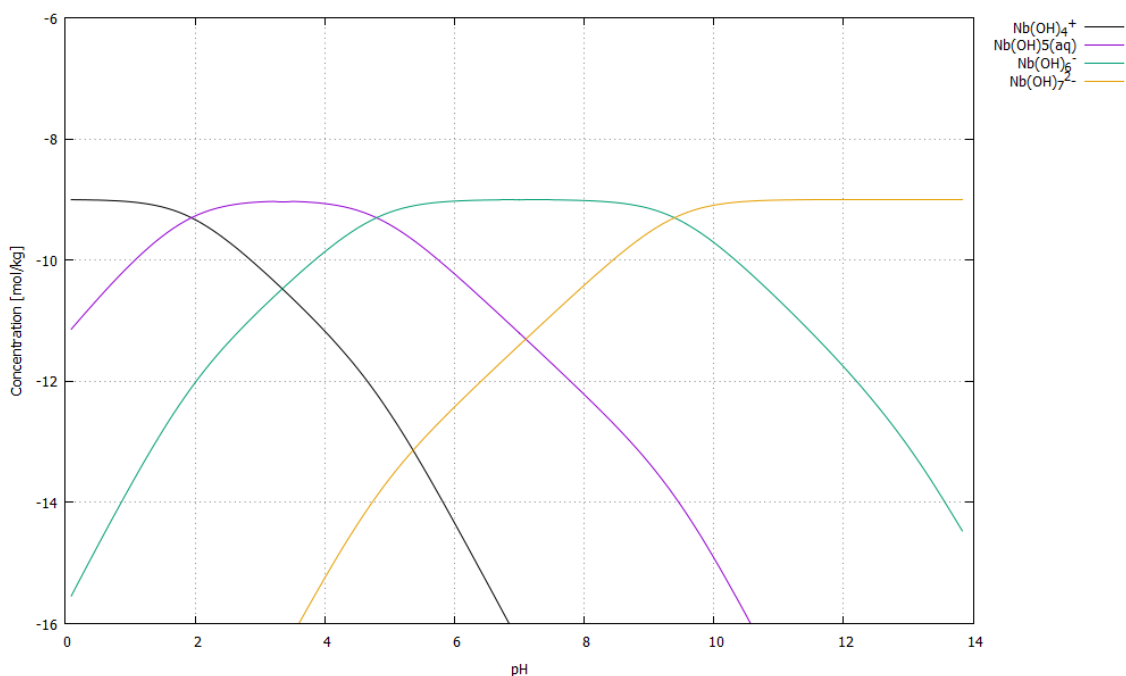


**Fig. 4.91** Hydrolysis of Nb with  $[\text{Nb}]_{\text{tot}} = 10^{-9}\text{M}$

Complex formation with other ligands than  $\text{OH}^-$  is known but appears to be irrelevant for conditions likely to be met in an underground repository for nuclear waste. Complexation with chloride was observed in extremely high concentrated  $\text{HCl}$ -solutions. The formation of mixed hydroxo-sulfato complexes, even polynuclear  $\text{Nb}(+\text{V})$ -sulfato-complexes is reported. Complexes with fluoride were observed under very acid conditions and very high fluoride concentrations, higher than in equilibrium with Fluorite. The situation is similar for complexes with carbonate whose formation is indicated by solubility experiments of  $\text{Nb}_2\text{O}_5 \cdot n\text{H}_2\text{O}(\text{s})$  in  $\text{KHCO}_3/\text{KCl}$  and  $\text{K}_2\text{CO}_3/\text{KCl}$  solutions under high pressure-temperature conditions.

While the publication of Filella and May /FIL 20/ is very much founded on the same publications used by Thoenen, it is interesting to note that Filellas and May included a compilation of formation constants with organic ligands. The potential for organic ligands to form stable complexes with niobate is reflected in their traditional use to stabilize niobium solutions. Despite numerous studies going back to as early as 1950 Filellas and May

concluded that a reliable set of constants for modeling calculations cannot yet be selected.

#### 4.5.5.2 Relevant solid phases

Thoenen (2021) discarded the inclusion of crystalline oxides such as  $\text{NbO}_2(\text{cr})$  or  $\text{Nb}_2\text{O}_5(\text{cr})$ . Instead hydrous, amorphous Nb(+V)-oxide  $\text{Nb}_2\text{O}_5(\text{hyd,am})$  was considered as solubility limiting phase. Accepting solubility data by Yajima et al. (1992) /YAJ 92/ and Yajima (1994) /YAJ 94/ he adopted a solubility constant yielding a conservative estimate for the total niobium concentration. Applying formation constants and the solubility constant for  $\text{Nb}_2\text{O}_5(\text{hyd,am})$  from Thoenen (2021) yields the solubility curve shown Fig. 4.92.

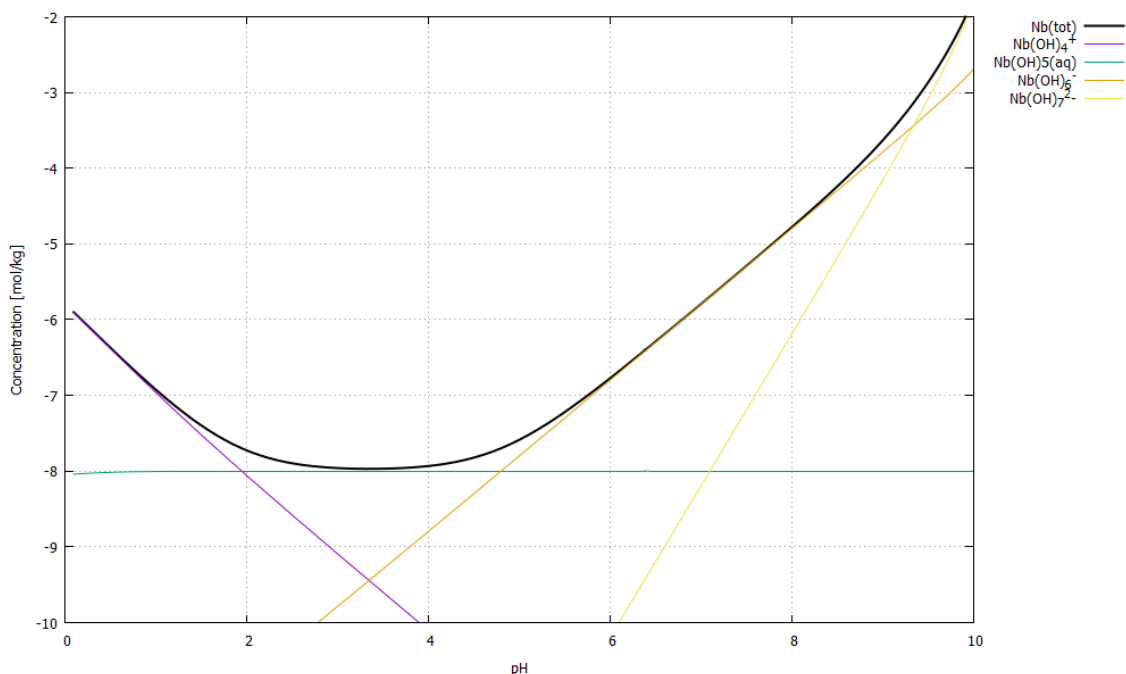


**Fig. 4.92** Solubility of  $\text{Nb}_2\text{O}_5(\text{hyd,am})$  as a function of pH

The result disagrees with the solubility curve shown in Thoenen (2021). Obviously, the species  $\text{Nb}(\text{OH})_4^+$  and  $\text{Nb}(\text{OH})_7^{2-}$  were omitted in the calculation, even though they are marked as being part of TDB 2020. Regarding the solubility data from Yajima et al. (1992) /YAJ 92/ and Yajima (1994) /YAJ 94/ the increasing solubility at  $\text{pH} < 3$  is not backed by experimental data. The same can be said for the upward curvature of the solubility curve at  $\text{pH} > 9$ . The inclusion of hexaniobate species led to numerical problems; these had to be eliminated from the calculation.

The calculated solubility curve of what Filella and May call "Nb<sub>2</sub>O<sub>5</sub>(s)" looks different: they included Nb(OH)<sub>4</sub><sup>+</sup> and didn't select a formation constant for Nb(OH)<sub>7</sub><sup>2-</sup>. Thus, their calculated solubility for "Nb<sub>2</sub>O<sub>5</sub>(s)" increases below pH=2 and extends to pH=10 only. Given the fact that above pH=10 solubility data scatter by about four orders of magnitude and considering that under these conditions other solid phases might exist (see below) this approach seems plausible.

In alkaline Ca-solutions resembling cement-equilibrated systems a different solid phase forms whose formula has been tentatively identified as CaNb<sub>4</sub>O<sub>11</sub>·8H<sub>2</sub>O, which corresponds to the mineral Hochelagaite. For the solubility between pH 9.5 and 13.2 and [Ca] between 0.1 and 20 mmol/l only an empirical relation from Talerico et al. (2004) exists /TAL 04/:

$$[\text{Nb}]_{\text{tot}} = 1.4643e^{-1.3402\text{pH}}[\text{Ca}]_{\text{tot}}^{-0.8922}/10^{2.6766} \quad (4.16)$$

The evaluation of equation ( 4.16 ) is shown in Fig. 4.93. Comparison with Fig. 4.92 indicates that the total Nb concentration in cement pore waters is probably not limited by Nb<sub>2</sub>O<sub>5</sub>(hyd,am).

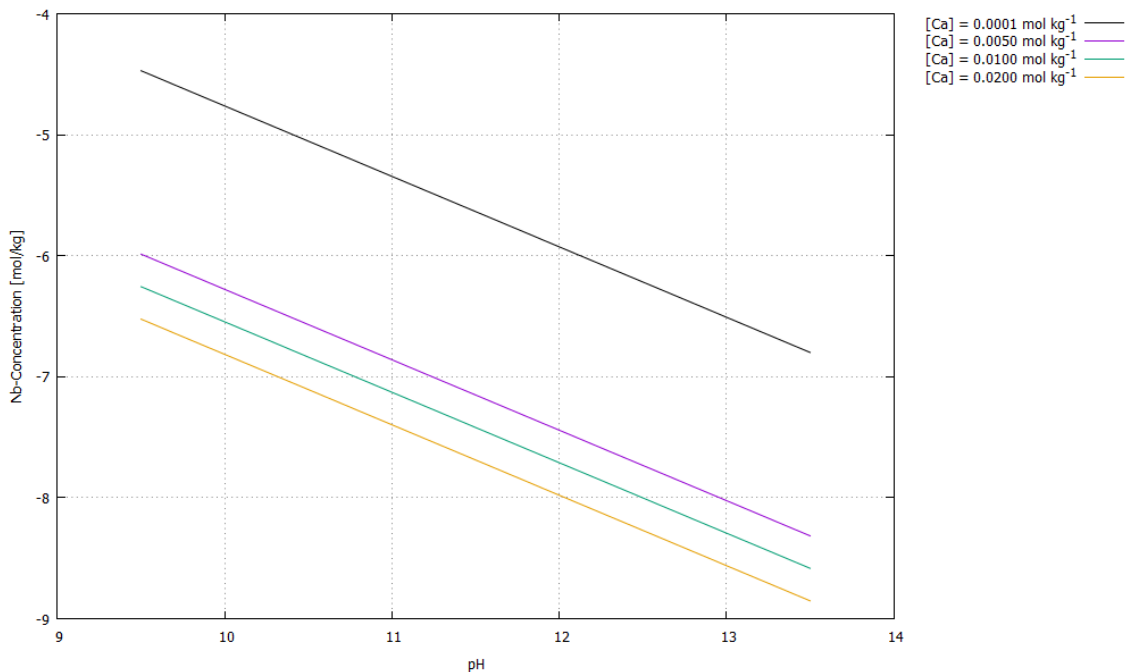


**Fig. 4.93** Solubility of Hochelagaite as a function of pH at different Ca-concentrations

Another series of experiments in 0.12M NaCl/Na<sub>2</sub>CO<sub>3</sub>/NaOH solution indicates that beginning at pH~8 hydrous amorphous Nb(+V)-oxide transforms into a hexaniobate salt with varying composition /DEB 15/. Under these conditions, Nb-concentrations in the order magnitude of 10<sup>-2</sup>M were detected. This concentration is considerably higher than indicated in Fig. 4.92 and may be attributed to the formation of ion pairs between alkali ions and hexaniobate anions. This assumption is supported by solubility experiments of Na<sub>7</sub>HNb<sub>6</sub>O<sub>19</sub>·15H<sub>2</sub>O(cr) in KCl solutions.

Due to the poor thermodynamic link between hexaniobate ions and mononiobate hydroxo complexes, and because of numerical problems, perhaps caused by the very high charge of hexaniobate anions, the modeling of these experimental results is not going to be straightforward. However, this predicament could be circumvented using a speciation scheme where hexaniobate – alkali ion pairs are implemented instead of the very high charged hexaniobate anions. Thoenen remarks that the ion pairs K<sub>8</sub>Nb<sub>6</sub>O<sub>10</sub>(aq) and K<sub>10</sub>Nb<sub>6</sub>O<sub>19</sub><sup>2+</sup> were indeed observed /ANT 09/.

Concerning the solubility of Nb<sub>2</sub>O<sub>5</sub>(hyd,am) as calculated in Fig. 4.92 it should be kept in mind that the solubility curve beyond pH~9 probably doesn't depict realistic conditions. For this to be understood it should be noted that for the retention of electroneutrality acid and alkaline conditions come with increasing ionic strength. For example, for the calculation illustrated in Fig. 4.92 Na concentration at pH~10 was about 1M. This means that at conditions where the solubility of Nb<sub>2</sub>O<sub>5</sub>(hyd,am) increases so does the concentration of cations. As a rule of thumb, it may be stated that the formation of hexaniobates is furthered by an increasing total concentration of Nb at pH>7. In conjunction with an increasing concentration of cations such as Na<sup>+</sup> or Ca<sup>2+</sup>, this leads to an increased formation of ion pairs and eventually to the formation of other solid phases like Na<sub>7</sub>HNb<sub>6</sub>O<sub>19</sub>·15H<sub>2</sub>O(cr) or CaNb<sub>4</sub>O<sub>11</sub>·8H<sub>2</sub>O. Thermodynamic data for solid Nb phases are compiled in Tab. 4.15.

**Tab. 4.15** Thermodynamic data for niobium solid phases as given in /THO 21/. Numbers in *italic* were marked as supplementary. Numbers underlined were calculated for this report. All data are valid for 298.15 K.

	$\log_{10}K^0$	$\log_{10}K^0$	$\Delta_f G_m^0$	$\Delta_f G_m^0$	$\Delta_f H_m^0$	$\Delta_f G_m^0$	$\Delta_f H_m^0$	$S_m^0$	$C_{p,m}^0$	Reaction
	/FIL 20/	/THO 21/	/FIL 20/ <sup>(b)</sup>	/THO 21/						/THO 21/
			[kJ · mol <sup>-1</sup> ]				[J · mol <sup>-1</sup> · K <sup>-1</sup> ]			
Nb(cr)				0			0	36.40	24.60	
Nb(OH) <sub>4</sub> <sup>+</sup>				-1196			- <i>1375</i>	42.4	179	
Nb <sub>2</sub> O <sub>5</sub> (hyd,am) <sup>(a)</sup>		12.22	-1768	<u>-1750</u>						2Nb(OH) <sub>4</sub> <sup>+</sup> = Nb <sub>2</sub> O <sub>5</sub> (hyd,am) + 3H <sub>2</sub> O(l) + 2H <sup>+</sup>

(a) in /FIL 20/ this phase was referred to as Nb<sub>2</sub>O<sub>5</sub>(s), but from the sources cited and the values given it seems plausible that it is equivalent to Nb<sub>2</sub>O<sub>5</sub>(pr) in /THO 21/, referred in this report as to Nb<sub>2</sub>O<sub>5</sub>(hyd,am).

(b) in /FIL 20/ no value was given for  $\Delta_f G_m^0$ (H<sub>2</sub>O(l), 298.15K) but assumed to be the same as in /THO 21/

#### 4.5.5.3 Speciation model

As discussed above other complexes than those with hydroxide are not likely to be relevant for conditions relevant to underground waste repositories. Thus  $\text{Nb}(\text{OH})_4^+$ ,  $\text{Nb}(\text{OH})_5^0$ ,  $\text{Nb}(\text{OH})_6^-$ , and  $\text{Nb}(\text{OH})_7^{2-}$  should be considered first. Depending on the presence of other cations such as  $\text{Na}^+$  or  $\text{Ca}^{2+}$  it remains to be investigated to which extent the complex  $\text{Nb}(\text{OH})_7^{2-}$  is predominant. To avoid unfavorable numerical conditions due to the high charge of hexaniobates, and because of strong experimental indications, ion pairs with Na, K, Mg, and Ca should be considered as a replacement for Pitzer coefficients and other hexaniobates such as  $\text{Nb}_6\text{O}_{19}^{8-}$ ,  $\text{HNb}_6\text{O}_{19}^{7-}$ ,  $\text{H}_2\text{Nb}_6\text{O}_{19}^{6-}$ , and  $\text{H}_3\text{Nb}_6\text{O}_{19}^{5-}$  avoided.

#### 4.5.5.4 Modeling in high saline solutions

At present no Pitzer model exists for the modeling of niobium solubility in high saline solutions.

#### 4.5.5.5 Suggestions for further work

Two lines of investigation should be followed for future work. First, the solubility of Nb(+V)-oxide should be investigated between pH=6 and pH=13 with different background concentrations of NaCl,  $\text{MgCl}_2$ , and  $\text{CaCl}_2$ . These experiments must be accompanied by a detailed inspection of the solid phase formed. Under conditions where the formation of other phases as  $\text{Nb}_2\text{O}_5(\text{s})$  is evident, it should be checked if these phases can be synthesized and used for experiments. From the shift of the solubility curve Pitzer coefficients for interactions between  $\text{Nb}(\text{OH})_6^-$  and  $\text{Na}^+$  could be deduced.

Second, the formation of hexaniobate ion pairs at  $7 < \text{pH} < 13$  must be investigated. It is hypothesized that the precipitation of  $\text{Nb}_2\text{O}_5(\text{s})$  is progressively inhibited as the hexaniobate precursors are stabilized as ion pairs eventually leading to the formation of other phases. Ion pair formation with potassium had been observed by Antonio et al. /ANT 09/ using Small-angle X-ray scattering (SAXS) and it is proposed to use this technique for the identification of other ion pairs. The determination of formation constants had to be conducted using potentiometric measurements in solutions of different ionic strength.

## 5 Summary and conclusions

The R&D work presented here has contributed to further development of different aspects of a safety case for radioactive waste repositories, namely to the assessment basis (process understanding) to the methods and strategies in developing a safety case, to the qualification of long-term safety assessment models and data, to the use of additional arguments in a safety case as well as to societal questions like communication with and information of today's and future generations. National projects as well as developments in other countries and on the international level were followed. Active participation occurred in international committees as the Radioactive Waste Management Committee (RWMC), the Integration Group for the Safety Case (IGSC), the working party Information, Data and Knowledge Management (IDKM) and its subgroups, the Salt Club, Crystalline Club as well as activities of the IAEA for treatment of the biosphere in a safety case. The thereby improved knowledge contributes to the creation and further development of appropriate strategies, methods and approaches in Germany.

With respect to long-term safety assessment significant work was performed regarding uncertainty and sensitivity analyses. Probabilistic analysis is a well-proven tool for investigating the overall uncertainty of the results of a computational model (uncertainty analysis) as well as its sensitivities against variation of input parameters (sensitivity analysis). Such analysis can provide deeper insight into the behaviour of performance assessment models and can therefore increase model understanding and confidence. The work presented here on this topic comprises, on the one hand, detailed sensitivity analyses, specifically focused on the influences of parameter interactions, using sophisticated meta-modeling methods. On the other hand, GRS is involved in an informal international working group (Joint Sensitivity Analysis Exercise, JOSA), which consists of a number of organisations dealing with radioactive waste disposal and was founded in order to exchange model results and to test different sensitivity analysis approaches. The work presented here is still going on; therefore, the outcomes can be regarded as interim results. In summary, it was found that variance-based methods, which today belong to the main sensitivity analysis approaches, can be easily applied using effective mathematical approaches and numerical tools. Correlation coefficients and regression approaches continue to be used and are informative. Other approaches like density-based methods show results mostly consistent with simpler methods, but in case of more complex models they might identify clearly different sensitivities, which may lead to enhanced understanding of the model behaviour. Graphical methods such as CUSUNORO provide

additional visualization and can show influences over the range of a variable. It might be advisable to start an analysis by applying such methods.

General consistency was found between the linearisation-based sensitivity measures calculated by the different partners. Variance-based methods, however, showed considerable differences, though theoretically, they should calculate the same sensitivity indices, but on the basis of different mathematical approaches using different methods of analysis, approximation or interpolation. It was often found that the sensitivity analyses of the partners agreed with regard to the significance of the one or two most influential parameters but calculated different orders for the less relevant ones, specifically if they vary over many orders of magnitude. It can be concluded that such rankings should not be overvalued. There is also a certain lack of consensus between participants on the delineation between sensitivity measure values that indicate secondary sensitivity versus sensitivity measure values that indicate negligible sensitivity. This highlights a need for development of consensus methods for testing or justifying conclusions regarding lower-ranked parameters.

With respect to biosphere modelling in performance assessment a comparison of biosphere dose conversion factors (BDCFs) calculated by the Czech and the German biosphere model showed significant differences, for some radionuclides by more than three orders of magnitude. In order to identify reasons for these differences the modelling approaches and data used in biosphere models from Czech Republic and Germany are compared and the impact of differences on the BDCFs are described. The benchmark was focused on the radionuclide treatment in the soil, the pathways from soil to plant and the external radiation from soil. The benchmark has been successfully performed. In general, it was shown that soil transport modelling yield mostly similar results although different models have been used. Some differences in the description of the radionuclide transport in the soil could be explained by different parameter values. Furthermore, the models for external irradiation are rather different and their impact on BDCFs was evaluated. However, the very large differences in biosphere dose conversion factors could be mainly reduced to two errors, one caused by a unit error, and a second one by including a non-realistic pathway. Both have occurred during transferring the new German biosphere model into Excel. In addition, the need to calculate BDCFs for radionuclides separately have been identified by UJV. This benchmark looking only into two sub parts of the biosphere model was an important contribution to the quality assurance of both models.

Since for most of the radionuclides the soil pathway with subsequent exposition pathways contributes most to the radiation exposition, a study to identify the state of the art in radionuclide sorption modeling in soils was initiated. For the respective model calculations the component additive model UNiSeCs II was applied, which has been designed and validated for moderate climatic conditions and, therefore, should be applicable for the majority of the German and Western European soils. It could be validated for the radionuclides Am, Pu, Se, Ni, Cs, Ra and U with the help of data from batch experiments. However, it was emphasized that in some cases, parameters had to be estimated or additional assumptions had to be made. Consequently, it is desirable to further validate the model, preferably with data from the field. By application of the model the most important soil solution parameters have been identified for each radionuclide by single parameter variations for two Refesol soils within ranges that are frequently occurring in the soil as e.g. given by IAEA data compilations. Particularly for Cs and Ra, where differences between the Czech and German model are highest, the bandwidth of the sorption calculations are also rather high. The values used in the biosphere models for performance assessment are also in the calculated ranges. To estimate ranges of  $K_d$  that may occur under field conditions, the element-specific distribution coefficient has been calculated for a number of parameter combinations and has been classified by its frequency of occurrence (“ $K_d$  distribution density”). In most cases, the median value of the distribution is close to the value deterministically calculated for defined reference conditions. However, again, it has to be noticed that some soil parameters (e.g. pH and  $p_e$ ) are usually correlated and thus not all combinations of soil parameters in the field will be equally probable as assumed in the calculations. Further limitations of the model, particularly for each of the considered elements are described.

On the topic bentonite re-saturation has been worked at from two different angles. Firstly, GRS actively participated in the Task Force on Engineered Barrier Systems which implied working on Task 9 – FEBEX in-situ test. Secondly, a first step for transferring the model concept for bentonite re-saturation realized in code VIPER to the COMSOL Multiphysics code was implemented.

The FEBEX in-situ test was a full-scale test conducted over 18.4 years in the Grimsel URL (Switzerland) managed by NAGRA. A 70.4 m long drift with a circular section 2.28 m in diameter was excavated in the Grimsel granite. In the last 17.4 m of the gallery, two electrical heaters were emplaced and in the remaining space compacted bentonite blocks were emplaced. The test zone was closed with a concrete plug. The experiment was instrumented with sensors monitoring the thermo-hydro-mechanical processes

taking place in the clay barrier and in the surrounding Grimsel granite. The experiment was in operation for 5.0 years. Thereafter, the outer heater was switched off and the outer half of the experiment was dismantled, whereby samples were taken from various points of the rock, the concrete and the bentonite buffer. During this first dismantling, the remaining half of the experiment, including the second heater, continued in operation. This remaining half of the experiment was in operation for additional 13.2 years. Thereafter, the experiment was completely dismantled and, as before, samples from various points were taken.

The conclusions from the modelling approach with code VIPER are as follows: By and large, the modelling results appear to match the data quite well and to fit in with the results from other modelling teams. Where more pronounced deviations from the data were found, other teams had apparently also difficulties to match the measurements. Decoupling of the thermal calculations from the hydraulic part, that is neglecting the dependence of thermal parameters on the degree of saturation, seems to have rather little influence on the overall temperature field as well as on the relative humidity evolution in the bentonite buffer. The same observation has been made already with the two previous non-isothermal models that have been set up by GRS for Task 1 and Task 2 within the Task Force on EBS. Assuming only unidirectional coupling of thermal effects to hydraulic processes is quite advantageously as it accelerates modelling considerably. A drawback is, however, that simulating the increase of power uptake of the heaters is excluded by this assumption since this effect is actually caused by changes in the thermal conductivity due to an increasing water content. With a view to re-saturation, only a quite small fraction of the performance measures that were defined in the task description could be met by code VIPER. This is of course not a flaw, since VIPER has been developed to test and refine an alternative concept for simulating bentonite re-saturation. To that end, it has not been necessary, yet, to implement the capability of full 3D-modelling in the code. However, this work has shown once again that this capability will be required in the long run for concrete applications. In addition to the obvious limitation of the code to one dimension, the integration of other physical processes is also very complex. As a consequence, it was decided to transfer the VIPER concept to COMSOL Multiphysics. However, due to the complexity of VIPER, this only makes sense if done stepwise. The first step in transferring the VIPER concept to COMSOL Multiphysics has successfully been carried out –enabling the application on 3D problems – and the feasibility of the transfer was demonstrated using a simple form of isothermal re-saturation. Sensible next steps would be on the one hand the extension of the COMSOL-VIPER model to the full complexity of isothermal saturation. This would involve the import of measured isotherms as

well as the whole range of possible boundary conditions. A further step could be the implementation of all temperature dependencies of secondary variables and parameters in preparation for a non-isothermal model.

The existence of permafrost is a topic to be considered in a safety case since it can extend several 100 m below the surface and therewith effect processes occurring in the near and far field of a deep geological repository. Under permafrost conditions, radically different groundwater flow systems compared to those prevailing during warm climate stages may evolve as freezing grounds provide an efficient flow barrier. However, the degree to which lower groundwater systems are affected by freezing depends of course on the thickness of the permafrost. The difficulties concerning the prediction of groundwater flow under permafrost conditions are aggravated by the occurrence of taliki, unfrozen zones in the permafrost affected underground. While open as well as closed taliki are not really of concern, through-taliki can form hydraulic shortcuts between deep unfrozen aquifers and ground surface and therewith, crucially impact radionuclide migration in case of RN release from the waste. For fracture media, as regarded here, no relation describing the volumetric fraction occupied by ice in the pore space as a function of temperature exists yet. Such a curve, a fracture freezing characteristic curve, is necessary to simulate the changing hydraulic conditions during temporal evolution of permafrost in fractured media.

Therefore, it was intended to establish and test a new approach to derive such data starting out with a freezing experiment in a 3D-printed, water-saturated fracture. When successful, the ice content and the related temperature were to be measured as well as the relative permeability for water. These measurements were then to be repeated at different temperatures. A high effort was put into the set-up and observation of the experiments. However, it turned out that these experiments are rather challenging, and several unforeseen difficulties have delayed the experiment to the extent that only the observation of freezing in one simplified fracture could be achieved. Several difficulties and challenges with respect to the use of coloured tracers and the optimization of the cooling box have been encountered. An improved construction that allows for a more robust installation while being flexible enough to accommodate a natural course of a fracture is therefore advisable. which will be addressed and circumvented in future experiments. The envisaged strategy for further work in general is to improve the tests with a parallel plate fracture with respect to the technique itself as well as to the interpretation of the results. Having reached control over the tests with a parallel plate fracture, realistic printed replicas of fractures are intended to be used.

The plan for subsequent modelling that would have required simulating of the freezing process of water with the associated changes of the thermal properties, did therefore not work. As a substitute, a numerical model for granitic formations that explains growth of permafrost thickness with decreasing surface temperatures has been set up, since it comprised many of the physical aspects of the originally envisaged model. The input parameters have been chosen to be in accordance to the Canadian shield, one of the largest and oldest crystalline formations on earth. As a performance measure, the steady-state thickness of the permafrost was calculated as a function of the surface temperature. A comparison with referring data from the field confirms the viability of the model. Next step is the inclusion of large aquatic features at the surface to study the impact of such features on freezing ground. Furthermore, this model prepares ground for investigations beyond the present project, serving as preparatory work for studies on groundwater flow under permafrost conditions such as the conditions for talik development.

Claystone is foreseen as one potential host rock formation for a deep geological repository in Germany. Due to the natural water content of porous claystone host rock and the hydrostatic boundary conditions, it is expected that the backfilled emplacement areas of the repository are re-saturated with water within a few hundreds of years. The contact of the cast iron containers and liners with water in absence of oxygen leads to anaerobic corrosion producing hydrogen. The volume of gases produced are typically too large to be stored in the pore space of the backfill in the emplacement areas and therefore lead to a gas pressure build-up. The resulting pressure gradients induce an advective movement of gas and potentially also of water in the drift system of the repository, but also in the clay host rock. Due to this reason, the gas transport mechanisms in claystone host rocks were studied for quite a long time and the objective of the study presented here was to review the state of the art to incorporate the gas transport processes in integrated performance assessment modelling, since the last review in 2008.

Generally, gas transport in claystone can be described by four different mechanisms, depending on the amount of gases built, namely (i) dissolution and diffusive transport through the clay, (ii) two-phase flow (if the gas pressure is below the minimal principal normal stress), (iii) dilatancy controlled gas flow and (iv) hydraulic fracturing, if stress on the rock matrix is exceeding the claystone rupture strength. A main emphasis of the research performed since 2008 was to study in more detail the effect of dilatancy controlled gas transport in consolidated claystone using either drill core samples in laboratory experiments, in-situ experiments in underground research laboratories and

numerical modelling of those experiments. From the direct observation of the mechanical behaviour of the claystone samples in laboratory experiments it can be sufficiently well concluded that dilatancy driven gas transport in claystone is a fact. However, there still does not exist a commonly accepted theory of the mechanical behaviour during dilatant gas flow consistently describing the porosity and permeability changes of the claystone as a function of gas pressure.

However, it must be clearly noted that the re-closure of the microfractures is not an issue of major concern. Claystone is known to reseal and achieve its initial permeability when the mechanical load is decreasing under the principal stress even if fractures were created. The open questions in the principal understanding of the claystone dilatation process also results in the lack of a mathematical description of the phenomenological net mass transfer of gas through the claystone under dilatant conditions. The literature often uses classical van Genuchten two-phase flow codes to model the gas transport, e. g. TOUGH2, which are only applicable if the gas pressure stays below the minimal principal stress of the rock. The use of this approach for dilatant pressure conditions is not expected to be valid, although even still applied here and there. Different modifications have been programmed into the TOUGH2 code to model dilatant gas flow. A comprehensive comparison of the different approaches or a code benchmark of the resulting codes has not yet been performed. Although these codes were able to model the results from gas transport experiments, from our point of view none of these modifications seems to be justified enough to be used for reliable long-term predictions needed for long-term safety assessment. As long as neither the physical equations of the mechanical behaviour during gas transport by dilation of the claystone rock are sufficiently well described nor a validated phenomenological description of the net mass gas transfer exists, it is suggested to choose a repository design concept that does not rely on the dilatant gas transport in the expected evolution of the system, but is expected to develop gas pressure in the system which always stays well below the minimal principal stress of the rock. This can be either achieved by a repository concept that implicates low amounts of iron in the system or that results in low corrosion rates of the iron under the expected chemical conditions.

A safety case for a deep geological repository is based on performance assessment calculations but also considers additional quantitative and qualitative arguments underpinning the calculation results as well as the safety case itself. More quantitative arguments are derived from safety and performance indicators, qualitative arguments are mainly derived from observations of natural archeological or geological features and

processes, which are similar to those expected to occur in the evolution of the repository system. These types of studies are called natural analogues. One objective of this project was to compile analogue studies to be used for a safety case for a potential repository in crystalline formations, which have not been a research focus in Germany, so far. Because of the complexity and the geological time frame to be considered (assessment period of 1 million years) deep insights into relevant “natural” geological processes may contribute substantially to system understanding and particularly to the description and underpinning of FEP. Therefore, in this work an approach is developed to compile and evaluate natural analogue studies based on the FEP catalogue, which was developed for crystalline formations in Germany. In a first step selected key components and processes from the FEP catalogue, where the contribution of analogue knowledge is expected to be useful, have been identified and used for this approach. In the study the component FEP “Host Rock”, “Faults and Fractures within Host Rock”, as well as the process FEP “Permafrost”, “Microbial Processes”, “Metal Corrosion”, “Alteration of Fuel Matrix” and “Diffusion” have been considered. For each FEP the most important characteristics are deduced from the FEP descriptions in the FEP catalogue and adopted in form of a summarized data sheet. Following this, for each FEP characteristic information from NA studies have been gathered from literature, as well as compiled and structured with respect to the characteristics of each considered FEP. Here, the approach is illustrated for the FEP “Permafrost”, respective information for all other FEP can be found in a separate report /FAH 21/. For permafrost, key analogue information on (i) extent and depths including impacting parameters, (ii) unfrozen areas within the permafrost (taliki) – also used in the permafrost study described above –, (iii) fracture generation, release and filling and (iv) appearance and release of gases have been compiled and documented. In general, this approach worked out to be useful in preparing and structuring various and diverse information from existing analogue studies to be used in a safety case. It is emphasized to continue this work applying additional key FEP for potential repositories in crystalline formations to those considered so far.

One key result of a recent study on geochemical speciation calculations of relevant elements in the repository near field in rock salt was that particularly for the elements C, Cl, I, Nb, Ni, Se and Sn high uncertainties exist with respect to their geochemical behaviour in highly saline conditions and therewith for the determination of solubilities. Since open questions to Se und I are already addressed in other research projects, the objective of the task described here was to evaluate the results for carbon yielded in the European project CAST and to develop a strategy for further experiments to derive a substantiated basis for geochemical modelling in high saline conditions for the elements Cl, Ni, Sn und

Nb. For each of these four elements a description of its speciation with relevant oxidation states, formation of key complexes in solution with inorganic and organic ligands, most relevant solid species and status of geochemical modelling including the limitations and open questions is presented. Finally, for each element most crucial future work to increase confidence in speciation modelling is proposed. For Ni future work should focus on solid phases which might limit the overall solubility of nickel, especially in alkaline solutions yielding in the identification of solubility limiting phases and the estimation of Pitzer interaction coefficients for relevant nickel species. In the case of  $\text{CaCl}_2$  containing solutions, the formation and relevance of ternary calcium nickel hydroxide complexes should be tested as these could drastically increase the solubility of nickel. In the presence of magnesium and iron(II), nickel may be bound in solid solutions with these elements. Little is known about their stability. Furthermore, because of its potential for lowering the solubility to extremely low values, the formation of elemental nickel, as well as nickel sulfide, should be inspected. The main retention mechanism for  $^{36}\text{Cl}$  in salt rock is probably the isotopic substitution between solution and halite. The kinetics of this process should be investigated. Poorly soluble chloride-containing secondary phases are not likely to control the mobility of  $^{36}\text{Cl}$ . The discussion of available information on tin chemistry revealed a couple of knowledge gaps that mandate specific further scientific investigations. These include (i) the relevance and stability of ternary calcium and magnesium tin(II) hydroxo complexes, (ii) the stability of the  $\text{Sn}(\text{OH})_4(\text{aq})$  complex, (iii) the solubility of the mineral phase hydroromarchite,  $\text{Sn}_3\text{O}_2(\text{OH})_2$  and schoenfliesite,  $\text{MgSn}(\text{OH})_4$  as well as (iv) ion interaction coefficients of the main tin species in alkaline solutions:  $\text{Sn}(\text{OH})_3^-$ ,  $\text{Sn}(\text{OH})_5^-$  and  $\text{Sn}(\text{OH})_6^{2-}$ . For Nb it is proposed to follow two lines of investigation for future work. First, the solubility of Nb(+V)-oxide should be investigated in the neutral to alkaline range with different background concentrations of  $\text{NaCl}$ ,  $\text{MgCl}_2$ , and  $\text{CaCl}_2$  to evaluate whether under any conditions the formation of other phases as  $\text{Nb}_2\text{O}_5(\text{s})$  is evident. Pitzer coefficients for interactions between  $\text{Nb}(\text{OH})_6^-$  and  $\text{Na}^+$  should be deduced. Second, the formation of hexaniobate ion pairs must be investigated. It is hypothesized that the precipitation of  $\text{Nb}_2\text{O}_5(\text{s})$  is progressively inhibited as the hexaniobate precursors are stabilized as ion pairs eventually leading to the formation of other phases.



## References

- /AIT 03/ AITEMIN: Sensors Data Report (In Situ Experiment), Project Deliverable D8-d. Report 70-AIT-L-6-07, AITEMIN, 2003.
- /ALE 15/ Alexander, R., Reijonen, H.M., McKinley, I.G. (2015): Natural analogues: studies of geological processes relevant to radioactive waste disposal in deep geological repositories. *Swiss Journal of Geosciences* 108 (1), 75-100, DOI 10.1007/s00015-015-0187-y.
- /ALE 19/ Alexanderian, A., Gremaud, P.A., Smith, R.C.: Variance-based sensitivity analysis for time-dependent processes. <https://arxiv.org/pdf/1711.08030.pdf>
- /ALF99/ Al-Farawati, R.; van den Berg, C. M. G. (1999) Metal-sulfide complexation in seawater. *Marine Chem.* 63, p. 331–352.
- /AND 05/ ANDRA: Dossier 2005 Argile, Tome, Évolution phénoménologique du stockage géologique, 2005.
- /ANT 09/ Antonio, M.R., Nyman, M. & Anderson, T.M. (2009): Direct observation of contact ion-pair formation in aqueous solution. *Angewandte Chemie International Edition*, 48, 6136–6140.
- /APP 05/ Appelo, C.A.J., Postma, D.: *Geochemistry, groundwater and pollution*. 2. Edition, 649 pages, ISBN 04-1536-428-0, A.A. Balkema Publishers: Rotterdam (2005).
- /AUK 16/ Aukenthaler, M., Brinkgreve, R., Haxaire, A.: A practical approach to obtain the soil freezing characteristic curve and the freezing/melting point of a soil-water system. In *Proceedings of the GeoVancouver 2016: the 69th Canadian Geotechnical Conference*, Vancouver, Canada (pp. 1-8), 2016.
- /BAN 16/ Banik, N.L., Marsac, R., Lützenkirchen, J., Diacorn, A., Bender, K., Marquardt, C.M., Geckeis, H.: Sorption and Redox Speciation of Plutonium at the Illite Surface. *Environ Sci Technol* 50 (2016) 2092-2098.

- /BÁR 03/ Bárcena I., Fuentes-Cantillana J.-L. and García-Siñeriz J.L. (2003) Dismantling of heater No. 1 at the FEBEX in situ test. Description of operations. DRAFT. AITEMIN, 29.9.2003.
- /BAR 06/ Barton, R.R, Meckesheimer, M.: Handbooks in Operations Research and Management Science, Chapter 18 Metamodel-Based Simulation Optimization, 13: 535-574.
- /BAS 98/ Basciano, L. C.; Peterson, R. C.; Roder, P. L.; Swainson, I. (1998) Description of schoenfliesite,  $\text{MgSn}(\text{OH})_6$ , and roxbyite,  $\text{Cu}_{1.72}\text{S}$ , from a 1375 BC shipwreck, Rietveld neutron-diffraction refinement of synthetic schoenfliesite, wickmanite,  $\text{MnSn}(\text{OH})_6$ , and burtite,  $\text{CaSn}(\text{OH})_6$ . *Can. Min.* 36, p. 1203–1210.
- /BBO 99/ Bundes-Bodenschutz- und Altlastenverordnung, Verordnung vom 12.7.1999, BGBl. I 1999, S. 1554 (1999).
- /BEC 90/ Beck, M. T.; Nagypal, I. (1990) Chemistry of complex equilibria. Chichester: Ellis Horwood, 410p.
- /BER 19/ Berger, D.; Soles, J. S.; Giunlia-Mair, A. R.; Brüggmann, G.; Galili, E.; Lockhoff, N.; Pernicka, E. (2019) Isotope systematics and chemical composition of tin ingots from Mochlos (Crete) and other Late Bronze Age sites in the eastern Mediterranean Sea: An ultimate key to tin provenance? *PloS one* 14 (6), e0218326.
- /BET 15/ Sebastian Bette, Robert E. Dinnebier, Christian Röder, Daniela Freyer (2015): *Journal of Solid State Chemistry* (228), 131-140. DOI <https://doi.org/10.1016/j.jssc.2015.04.015>.
- /BET 17/ Bette, S.; Pannach, M.; Dinnebier, R. E.; Freyer, D. (2017) Phase formation and solubilities in the ternary System  $\text{Ni}(\text{OH})_2$  -  $\text{NiCl}_2$  -  $\text{H}_2\text{O}$  at 25 and 200 °C. *Eur. J. Inorg. Chem.* 2017 (11), p. 1488–1497.
- /BET 16/ Bette, S.; Rincke, C.; Dinnebier, R. E.; Voigt, W. (2016) Crystal structure and hydrate water content of synthetic hellyerite,  $\text{NiCO}_3 \cdot 5 \cdot 5\text{H}_2\text{O}$ . *Z. Anorg. Allg. Chem.* 642 (9-10), p. 652–659.

- /BGE 20/ BGE (Bundesgesellschaft für Endlagerung): Sub-areas Interim Report pursuant to Section 13 StandAG. As per 28/09/2020.  
[https://www.bge.de/fileadmin/user\\_upload/Standortsuche/Wesentliche\\_Unterlagen/Zwischenbericht\\_Teilgebiete/Zwischenbericht\\_Teilgebiete - Englische Fassung barrierefrei.pdf](https://www.bge.de/fileadmin/user_upload/Standortsuche/Wesentliche_Unterlagen/Zwischenbericht_Teilgebiete/Zwischenbericht_Teilgebiete_-_Englische_Fassung_barrierefrei.pdf). Date of access. 02. December 2021
- /BGR 12/ BGR: Karte der untersuchungswürdigen Wirtsgesteinsformationen - Ergebnisse der regionalen BGR-Studien. Web-Seiten der BGR, 2012.  
[https://www.bgr.bund.de/DE/Themen/Endlagerung/Downloads/Charakterisierung\\_Wirtsgesteine\\_geotech\\_Barrieren/4\\_Wirtsgesteinsuebergreifend/Karte\\_Wirtsgesteinsformationen\\_Dtl.html](https://www.bgr.bund.de/DE/Themen/Endlagerung/Downloads/Charakterisierung_Wirtsgesteine_geotech_Barrieren/4_Wirtsgesteinsuebergreifend/Karte_Wirtsgesteinsformationen_Dtl.html)
- /BIR 16/ Birchall, D. J.; Harrington, J. F.; Noy, D. J.; Cuss, R.J.: Laboratory study examining permeability evolution along an isotropic unloading stress path. British Geological Survey Open Report, OR/07/016, 2016.
- /BLA 15/ BLA-GEO & LAWA: Hydrogeochemische Hintergrundwerte im Grundwasser und ihre Bedeutung für die Wasserwirtschaft. Länderarbeitsgemeinschaft Wasser (LAWA) 2015
- /BLU 00/ Bluhm, H., Inoue, T., Salmeron, M.: Friction of ice measured using lateral force microscopy. The American Physical Society, Physical Review B, Volume 61, Number 11, 2000.
- /BLU 16/ Blume, H.P., Brümmer G.W., Fleige H., Horn R., Kandeler E., Kögel-Knabner I., Kretzschmar R., Stahr K., Wilke B.M.: Scheffer/Schachtschabel soil science, Springer-Verlag Berlin Heidelberg (2016).
- /BMU 12/ Allgemeine Verwaltungsvorschrift zu §47 Strahlenschutzverordnung: Ermittlung der Strahlenexposition durch die Ableitung radioaktiver Stoffe aus Anlagen oder Einrichtungen. Bundesanzeiger, 28.08.2012.
- /BOC 10/ Bock, H.; Dehandschutter, B.; Martin, C. D.; Mazurek, M.; de Haller, A.; Skoczylas, F.; Davy, C.: Self-sealing of fractures in argillaceous formations in the context of geological disposal of radioactive waste. NEA Report 6184, Paris (OECD/NEA), 2010.

- /BOG 11/ Boggs, M.A., Minton, T., Dong, W., Lomasney, S., Islam, M.R., Gu, B., Wall, N.A.: Interactions of Tc(IV) with Humic Substances. *Environ Sci Technol* 45 (2011) 2718-2724.
- /BRA 17/ Bradbury, M.H., Baeyens B.: The development of a thermodynamic sorption data base for illite and the application to argillaceous rocks (NTB--17-14). Switzerland (2017).
- /BRE 98/ M. Bremer, C. Christov (1998): (InstErstellung einer Datenbasis zur Modellierung der Wechselwirkung von chrom-, kupfer- und nickelhaltigem Deponegut mit Lösungen des Salzgesteins einer UTD. Abschlussbericht im Auftrag des BMBF, Förderkennzeichen: 02 C 0405.
- /BRO 16/ Brown, P.L.; Ekberg, C. (2016): *Hydrolysis of Metal Ions*. Wiley-VCH. ISBN 9788-3-527-33010-2.
- /BRO 87/ Brown, P. L.; Wanner, H. (1987) Predicted formation constants using the unified theory of metal ion complexation. Hg. v. OECD Nuclear Energy Agency. Paris.
- /BRO 97/ Brown, J.; Ferrians, O.J.; Heginbottom, J.A.; Melnikov, E.S.: *Circum-Arctic Map of Permafrost and Ground Ice Conditions*, International Permafrost Association, published by U.S. Geological Survey, ISBN 0-607-88745-1, 1997.
- /CAP 18/ Capouet, M.; Necib, S.; Schumacher, S.; Mibus, J.; Neeft, E.A.C.; Norris, S.; Nummi, O.; Rübél, A.: *CArbon-14 Source Term. CAST outcomes in the context of the safety case: WP6 Synthesis report (D6.4)*, 2018.
- /CIG 12/ Cigala, R. M.; Crea, F.; Stefano, C. d. (2012) The inorganic speciation of tin(II) in aque-ous solution. *Geochim. Cosmochim. Acta* 87, p. 1–20.
- /CLA 06/ Clauser, C: "Advanced Materials and Technologies", *Geothermal Energy*, In: K. Heinloth (Ed), *Landolt-Börnstein, Group VII, Vol. 3 "Energy Technologies"*, Subvol. C, "Renewable Energies", 480 – 595, Springer Verlag, Heidelberg-Berlin, 2006.

- /CLA 16/ Claesson Liljedahl, L.; Kontula, A.; Harper, J.; Näslund, J-O.; Selroos, J-O; Pitkänen, P.; Puigdomenech, I.; Hobbs, M.; Follin, S.; Hirschorn, S.; Jansson, P.; Kennell, L.; Marcos, N.; Ruskeenieniemi, T.; Tullborg, E.-L; Vidstrand, P.: The Greenland Analogue Project -Final report: Technical Report SKB TR-14-13, ISSN 1404-0344, 2016.
- /COM 21/ COMSOL: Documentation. 2021. <https://www.comsol.com/documentation/>
- /COT 80/ Cotton, F. A.; Wilkinson, G. (1980): Advanced Inorganic Chemistry. Fourth edition. John Wiley & Sons, Inc. ISBN 0-471-02775-8.
- /CRO 06/ Croisé, J.; Mayer, G.; Marschall, P.; Matray, J. M.; Tanaka, T.; Vogel, P.: Gas Threshold Pressure Test Performed at the Mont Terri Rock Laboratory (Switzerland): Experimental Data and Data Analysis. Oil & Gas Science and Technology – Rev. IFP, Vol. 61, No. 5, pp. 631-645, 2006.
- /CUS 14/ Cuss, R.; Harrington, J.; Giot, R.; Auvray, C.: Experimental observations of mechanical dilation at the onset of gas flow in Callovo-Oxfordian claystone. From: Norris, S., Bruno, J., Cathelineau, M., Delage, P., Fairhurst, C., Gaucher, E. C., Hoehn, E. H., Kalinichev, A., Lalieux, P. & Sellin, P. (eds) 2014. Clays in Natural and Engineered Barriers for Radioactive Waste Confinement. Geological Society, London, Special Publications, 400, 507–519.
- /DAS 06/ Dash, J. G., Rempel, A. W., Wettlaufer, J. S.: The physics of premelted ice and its geophysical consequences. American Physical Society, Rev. Mod. Phys. 78, 695, 2006.
- /DEB 15/ Deblonde, G.J.P., Chagnes, A., Bélair, S. & Cote, G. (2015): Solubility of niobium(V) and tantalum(V) under mild alkaline conditions. Hydrometallurgy, 156, 99–106.
- /DEU 17/ Deutscher Bundestag: Gesetz zur Suche und Auswahl eines Standortes für ein Endlager für hochradioaktive Abfälle (Standortauswahlgesetz - StandAG). Decision of the Deutscher Bundestag, 2017.

- /DEU 20/ Deutscher Bundestag (2020): Verordnung des Bundesministeriums für Umwelt, Naturschutz und nukleare Sicherheit: Verordnung über Sicherheitsanforderungen und vorläufige Sicherheitsuntersuchungen für die Endlagerung hochradioaktiver Abfälle, Deutscher Bundestag, Drucksache 19/19291 vom 18.05.2020.
- /DIN 17/ Dinh, Q.T., Li, Z., Tran, T.A.T., Wang, D., Liang, D.: Role of organic acids on the bioavailability of selenium in soil: A review. *Chemosphere* 184 (2012) 618-635.
- /DUI 08/ Duijnsveld, W.H.M., Godbersen, L., Dilling, J., Gäbler, H.-E., Utermann, J., Klump, G., Scheeder, G.: Ermittlung flächenrepräsentativer Hintergrundkonzentrationen prioritärer Schadstoffe im Bodensickerwasser. Forschungsbericht des Umweltbundesamtes. Bundesanstalt für Geowissenschaften und Rohstoffe, Hannover, S. 163 (2008).
- /DUN 03/ Dunkle, S.; Craig, J. R.; Rimstidt, J. D.; Lusardi, W. (2003) Romarchite, hydromarchite and abhurite formed during the corrosion of pewter artifacts from the Queen Anne's Revenge (1718). *Can. Min.* 41, p. 659–669.
- /DZO 90/ Dzombak, D.A., Morel, F.M.M.: Surface complexation modeling: hydrous ferric oxide. Wiley-Interscience, New York (1990).
- /EDW 92/ Edwards, R.; Gillard, R. D.; Williams, P. A. (1992) The stabilities of secondary tin minerals: abhurite and its relationships to Sn(II) and Sn(IV) oxides and oxyhydroxides. *Mineral. Mag.* 56 (383), p. 221–226.
- /EDW 96/ Edwards, R.; Gillard, R. D.; Williams, P. A. (1996) The stabilities of secondary tin minerals. Part 2: The hydrolysis of tin(II) sulphate and the stability of  $\text{Sn}_3\text{O}(\text{OH})_2\text{SO}_4$ . *Mineral. Mag.* 60 (400), p. 427–432.
- /ELW 66/ Elwell, D.; Parker, R.; Tinsley, C. J. (1966) The formation of nickel ferrite. *Solid State Communications* 4 (1), p. 69–71.
- /ENR 00/ ENRESA: FEBEX project. Full-scale engineered barriers experiment for a deep geological repository for high level radioactive waste in crystalline host rock. Final report. ENRESA, Madrid, 2000.

- /EPRI 02/ EPRI: Evaluation of the Proposed High-Level Radioactive Waste Repository at Yucca Mountain Using Total System Performance Assessment, Phase 6. - EPRI, Palo Alto, 2002.
- /FAH 21/ Fahrenholz, Ch., Meleshyn, A., Noseck, U. (2021): Natural analogues for repositories in crystalline formations. Correlation to key FEP. FKZ 02 E 11647 (BMW), Report GRS-644, Gesellschaft für Anlagen- und Reaktorsicherheit (GRS) mbH, Braunschweig, 2021. ISBN: 978-3-949088-33-9.
- /FAT 78/ Fatouros, N., Rouelle, F.; Chemla, M. (1978) Influence de la formation de complexes chlorures sur la réduction électrochimique de Sn IV en milieu perchlorique acide. *J. Chim. Phys. Phys. Biol.* 75, p. 476–483.
- /FAU 71/ Faust, G. T.; Schaller, W. T. (1971) Schoenfliesite, MgSn(OH)<sub>6</sub>. *Zeitschrift für Kristallographie - Crystalline Materials* 134 (1-2).
- /FEI 36/ Feitknecht, W.; Collet, A. (1936) Über die Konstitution der festen basischen Salze zweiwertiger Metalle. II Basische Nickelhalogenide mit "Einfachschichtengittern". *Helv. Chim. Acta* 19, p. 831–841.
- /FRE 20/ Freeze, G., Sevougian, S.D., Kuhlman, K., Gross, M., Wolf, J., Buhmann, D., Bartol, J., Leigh, C., Mönig, J.: Generic FEP Catalogue and Salt Knowledge Archive, SANDIA REPORT SAND2020-13186, Printed November 2020.
- /FIL 20/ Montserrat Filella, Peter M. May (2020): The aqueous solution thermodynamics of niobium under conditions of environmental and biological interest. *Applied Geochemistry* 122 (2020) 104729.  
<https://doi.org/10.1016/j.apgeochem.2020.104729>
- /FUL 15/ Fuller, A. J., Shaw, S., Ward, M. B., Haigh, S. J., Mosselmans, J. F. W., Peacock, C. L., ... Burke, I. T.: Caesium incorporation and retention in illite interlayers. *Applied Clay Science* 108 (2015) 128–134.
- /GAM 97/ Gammons, C. H.; Yu, Y. (1997) The stability of aqueous silver bromide and iodide complexes at 25–300°C: Experiments, theory and geologic applications. *Chem. Geol.* 137 (3-4), p. 155–173.

- /GAM 05/ Gamsjäger, H. (Chairman): Chemical Thermodynamics of Nickel. Chemical Thermodynamics 6. OECD, Elsevier, ISBN 0-444-51802-9 (2005).
- /GAM 12/ Gamsjäger, H.; Gajda, T.; Sangster, J.; Saxena, S. K.; Voigt, W. (2012) Chemical thermodynamics of tin: OECD (Chemical Thermodynamics, 12), 646p.
- /GAM 01/ Gamsjäger, H.; Preis, W.; Wallner, H. (2001) Solid-solute phase equilibria in aqueous solutions XIV [1]. Thermodynamic analysis of the solubility of hellyrite in Water. *Monatsh. Chem.* 132, p. 411–415.
- /GAY 49/ Gayer, K. H., Garrett, A. B., The equilibria of nickel hydroxide, Ni(OH)<sub>2</sub>, in solutions of hydrochloric acid and sodium hydroxide at 25°C, *J. Am. Chem. Soc.*, 71, (1949), 2973-2975.
- /GEN 19a/ Gens, A.: Task Force on Engineered Barrier System (EBS) – Task 1: Laboratory Tests. International Report TR-14-24, Swedish Nuclear Fuel and Waste Management (SKB), Solna, 2019.
- /GEN 19b/ Gens, A.: Task 9: The FEBEX in situ test. Presentation at the 30th meeting of the Task Force on EBS, Baden, Switzerland, 2019.
- /GIL 08/ Gil-García, C.J., Rigol, A., Rauret, G., Vidal, M.: Radionuclide sorption–desorption pattern in soils from Spain, *Applied Radiation and Isotopes* 66 (2008) 126-138.
- /GON 18/ González-Siso, M. R.; Gaona, X.; Duro, L.; Altmaier, M.; Bruno, J. (2018) Thermodynamic model of Ni(II) solubility, hydrolysis and complex formation with ISA. *Radiochim. Acta* 106 (1), p. 31–45.
- /GRA 88/ Graves, P. R., C. Johnston, and J. J. Campaniello: Raman scattering in spinel structure ferrites. *Materials Research Bulletin* 23.11 (1988): 1651-1660.
- /GRI 15/ Grivé, M., Duro, L., Colàs, E., Giffaut, E.: Thermodynamic data selection applied to radionuclides and chemotoxic elements: An overview of the ThermoChimie-TDB. *Appl Geochem* 55 (2015) 85-94.

- /GRO 10/ Groenenberg, J.E., Koopmans, G.F., Comans, R.N.J.: Uncertainty Analysis of the Nonideal Competitive Adsorption–Donnan Model: Effects of Dissolved Organic Matter Variability on Predicted Metal Speciation in Soil Solution. *Environ Sci Technol* 44 (2010) 1340-1346.
- /GUI 20/ Guillemot, T.; Cvetkovi, B.Z.; Kunz, D.; Wieland, E.: Processes leading to reduced and oxidised carbon compounds during corrosion of zero-valent iron in alkaline anoxic conditions. *Chemosphere* 250 (2020) 126230.
- /HAG 15/ Sven Hagemann, Tina Scharge, Thomas Willms (2015): Entwicklung einer thermodynamischen Datenbasis für ausgewählte Schwermetalle. Abschlussbericht zu einem vom BMBF geförderten Projekt, Förderkennzeichen 02 C 0983. GRS-244, ISBN 978-3-939355-18-2.
- /HAG 99/ Hagemann, S. (1999) Thermodynamische Eigenschaften des Bleis in Lösungen der ozeanischen Salze. Online verfügbar unter <http://entw-server.grs.de/7390/>.
- /HAG 12/ Hagemann, S. (2012) Entwicklung eines thermodynamischen Modells für Zink, Blei und Cadmium in salinaren Lösungen. GRS-Bericht 219.
- /HAG 14/ Hagemann, S.; Bischofer, B.; Scharge, T. (2014) Entwicklung von Methoden und Modellen zur Bestimmung des Redoxpotentials salinärer Lösungen. GRS-Bericht 260.
- /HAG 15/ Hagemann, S.; Scharge, T.; Willms, T. (2015) Entwicklung einer thermodynamischen Datenbasis für ausgewählte Schwermetalle. GRS-Bericht 244.
- /HAG 21a/ Hagemann, S.; Meyer, T.; Mönig, H.; Bischofer, B.; Jantschik, K. (2021) Solubility limits of fission and activation products in saline near field solutions (In Vorbereitung) (GRS-Bericht).
- /HAG 21b/ Hagemann, S.; Mönig, H. (2021) Stability of iron corrosion phases expected in a repository in Lower Cretaceous clay (in preparation) (GRS-Bericht, 587).

- /HAR 11/ Harper, J.; Hubbard, A.; Ruskeeniemi, T.; Claesson Liljedahl, L.; Lehtinen, A.; Booth, A.; Brinkerhoff, D.; Drake, H.; Dow, C.; Doyle, S.; Engström, J.; Fitzpatrick, A.; Frape, S.; Henkemans, E.; Humphrey, N.; Johnson, J.; Jones, G.; Joughin, I.; Klint, K.E.; Kukkonen, I.; Kulesa, B.; Landowski, C.; Lindbäck, K.; Makahnouk, M.; Meierbachtol, T.; Pere, T.; Pedersen, K.; Pettersson, R.; Pimentel, S.; Quincey, D.; Tullborg, E.; van As, D.: The Greenland Analogue Project - Yearly Report 2010, SKB R-11-23, ISSN 1402-3091, ID 1334696, 2011.
- /HAR 12a/ Harrington, J. F.; de la Vassière, R.; Noy, D. J.; Cuss, R. J.; Talander, J.: Gas flow in Callovo-Oxfordian claystone (COx): results from laboratory and field-scale measurements, *Mineralogical Magazine*, Vol. 76(8), pp. 3303–3318, 2012.
- /HAR 12b/ Harrington, J. F.; Mildodowski, A.E.; graham, C. C., Rushton, C.; Cuss, R. J.: Evidence for gas-induced pathways in clay using a nanoparticle injection technique. *Mineralogical Magazine*, December 2012, Vol. 76(8), pp. 3327–3336.
- /HOR 02/ Hormann V., Kirchner G.: Prediction of the effects of soil-based countermeasures on soil solution chemistry of soils contaminated with radiocesium using the hydrogeochemical code PHREEQC. *Sci Total Environ* 289 (2002) 83-95.
- /HOR 13/ Hormann, V., Fischer H.W.: Estimating the distribution of radionuclides in agricultural soils - dependence on soil parameters. *J Environ Radioact.* 124 (2013) 278-86.
- /HOR 15/ Hormann, V.: Modelling Speciation and Distribution of Radionuclides in Agricultural Soils. In: Walther C, Gupta D (eds) *Radionuclides in the Environment*. Springer, Cham (2015).
- /HOR 21a/ Hormann, V.: Modellierung von Speziation, Sorption und Migration von Radionukliden für repräsentative bewirtschaftete Böden, Abschlussbericht des Teilprojekts D des BMBF-Verbundprojekts TRANS-LARA (02NUK051D), Bremen (2021).

- /HOR 21b/ Hormann, V.: A consistent model for estimating the partitioning of Am, Pu and Se in agricultural soils. *J Radioanal Nucl Chem* (2021).  
<https://doi.org/10.1007/s10967-021-07839-0>
- /HUM 02/ Hummel, W.; Berner, U.; Curti, E. (2002) NAGRA / PSI Chemical Thermodynamic Data Base 01/01. Nagra, Technical Report 02 (16).
- /HUS 13/ Husson, O.: Redox potential (Eh) and pH as drivers of soil/plant/microorganism systems: a transdisciplinary overview pointing to integrative opportunities for agronomy. *Plant and Soil* 362 (2013) 389-417.
- /ISA 63/ Isaacs, T. (1963) The mineralogy and chemistry of the nickel carbonates. *Mineral. mag. j. Mineral. Soc.* 33 (263), p. 663–678.
- /IAEA 03a/ "Reference Biospheres" for Solid Radioactive Waste Disposal, Report of BIOMASS Theme 1 of the BIOSphere Modelling and ASSESSment Programme, IAEA-BIOMASS-6, International Atomic Energy Agency, Vienna, 2003.
- /IAEA 03b/ IAEA Derivation of activity limits for the disposal of radioactive waste in near surface disposal facilities. - IAEA-TECDOC-1380, Vienna, 2003.
- /IAEA 10/ IAEA: Handbook of Parameter Values for the Prediction of Radionuclide Transfer in Terrestrial and Freshwater environments. - IAEA Technical Reports Series No. 472, IAEA, Vienna, 2010.
- /IAEA 20/ Development Of A Common Framework For Addressing Climate And Environmental Change In Post-Closure Radiological Assessment Of Solid Radioactive Waste Disposal - Report Of Working Group 6 Common Framework For Addressing Environmental Change In Long Term Safety Assessments Of Radioactive Waste Disposal Facilities Modaria Topical Heading Uncertainties And Variability - Modelling And Data For Radiological Impact Assessments (Modaria) Programme. IAEA-TECDOC-1904, International Atomic Energy Agency, Vienna 2020.
- /JAC 14/ Jacops et al., WP5 Final Report: Experiments and modelling of gas migration processes in undisturbed rocks. FORGE Report D5.19, 2014.

- /JNC 00/ Japan Nuclear Cycle Development Institute (JNC): H12: Project to Establish the Scientific and Technical Basis for HLW Disposal in Japan, Supporting Report 1: Geological Environment in Japan. Report JNC TN 1410 2000-002, JNC, Tokai-Mura, 2000.
- /JOB 16a/ Jobmann, M. (Editor); Becker, D.-A., Hammer, J.; Jahn, S.; Lommerzheim, A.; Müller-Hoeppe, N.; Noseck, U.; Krone, J.; Müller, Chr.; Weber, J. R.; Weitkamp, A.; Wolf, J.: Projekt CHRISTA - Abschlussbericht, Machbarkeitsuntersuchung zur Entwicklung einer Sicherheits- und Nachweismethodik für ein Endlager für Wärme entwickelnde radioaktive Abfälle im Kristallingestein in Deutschland, TEC-20-2016-AB, 2016.
- /JOB 16b/ Jobmann, M.; Burlaka, V.; Meleshyn, A.; Rübel, A.: Spezifische Prozessanalysen. FKZ 02E11061A/B, TEC-13-2016-B, DBE TECHNOLOGY, Peine, 2016.
- /JOB 17a/ Jobmann, M.; Bebiolka, A.; Jahn, S.; Lommerzheim, A.; Maßmann, J.; Meleshyn, A.; Mrugalla, S.; Reinhold, K.; Rübel, A.; Stark, L.; Ziefle, G.: Sicherheits- und Nachweismethodik für ein Endlager im Tongestein in Deutschland – Synthesebericht. FKZ 02E11061A/B, TEC-19-2016-AB, DBE TECHNOLOGY, Peine, 2017.
- /JOB 17b/ Jobmann, M.; Burlaka, V.; Herold, P.; Kuate Simo, E.; Maßmann, J.; Meleshyn, A.; Rübel, A.; Ziefle, G.: Systemanalyse für die Endlagerstandortmodelle - Methode und exemplarische Berechnungen zum Sicherheitsnachweis. TEC-29-2016-TB, DBE TECHNOLOGY, Peine, 2017.
- /JOH 16/ Johansson, E.: The influence of climate and permafrost on catchment hydrology. Thesis, Department of Physical Geography, Stockholm University, 2016.
- /KAR 10/ Karamalidis, A. K., Dzombak, D.A.: Surface Complexation Modeling: Gibbsite. John Wiley & Sons (2010).
- Khoo, K. H.; Fernando, K. R. (1991) Solubility and activity coefficient of thallium (I) chloride in the system TlCl+HCl+NaCl+H<sub>2</sub>O at 25C. J. Solution Chem. 20 (12), p. 1199–1211.

- /KIT 10/ Kitamura, A., Fujiwara, K., Doi, R., Yoshida, Y., Mihara, M., Terashima, M., Yui, M., 2010. JAEA Thermodynamic Database for Performance Assessment of Geological Disposal of High-Level Radioactive and TRU-Wastes. Report JAEA-Data/Code 2009-024. Japan Atomic Energy Agency, p. 84.
- /KJE 09/ Kjellström E., Strandberg G., Brandefelt J., Näslund J.-O., Smith B., Wohlfarth B.: Climate conditions in Sweden in a 100,000-year time perspective. Report SKB TR-09-04, Svensk Kärnbränslehantering AB, 2009.
- /KLA 13/ Klaus, R.; Jahn, St.; Kühnlenz, T.; Ptock, L.; Sönnke, J.: Endlager-standortmodell Nord (AnSichT), Teil I: Beschreibung des geologischen Endlager-standortmodells, Zwischenbericht, 9Y3207000000, 2013.
- /KOE 09/ Kördel W., Peijnenburg W., Klein C.L., Kuhnt G., Bussian B.M., Gawlik B.M., The reference-matrix concept applied to chemical testing of soils, Trends Analyt. Chem. 28 (2009) 51–63.
- /KRA 10/ Kramer, J.; Kelly, B.; Manivannan, V. (2010) Synthesis of  $M\text{Sn}(\text{OH})_6$  (where M = Mg, Ca, Zn, Mn, or Cu) materials at room temperature. Open Chemistry 8 (1), p. 65–69.
- /KRI 07/ Kristensson, O. and Börgesson, L.: CRT – Canister Retrieval Test; EBS Task Force Assignments. Clay Technology, 2007.
- /KRM 20/ Kröhn, M. and Fromme, L.: An alternative equation-based model in COMSOL Multiphysics® for bentonite re-saturation. Paper and poster. Virtual Conference 'COMSOL Conference 2020', 2020.
- /KRÖ 04/ Kröhn, K.-P.: Modelling the re-saturation of bentonite in final repositories in crystalline rock. Final report, FKZ 02 E 9430 (BMWA), Gesellschaft für Anlagen- und Reaktorsicherheit (GRS) mbH, GRS-199, Köln, 2004.
- /KRÖ 05/ Kröhn, K.-P.: New Evidence for the Dominance of Vapour Diffusion During the Re-saturation of Compacted Bentonite. Engineering Geology, Volume 82, Issue 2, 2005.

- /KRÖ 08/ Kröhn, K.-P.: Simulating water uptake of compacted bentonite under non-isothermal conditions, decoupled from the mechanics and without feedback of hydraulics to heat transport. Proceedings of the Workshop on “Long-term performance of smectitic clays embedding canisters with highly radioactive waste” held in Lund, 2007, Applied Clay Science, Vol. 47, pp. 28-35, 2010; Online: <http://dx.doi.org/10.1016/j.clay.2008.06.004>, 2008; printed version: 2010.
- /KRÖ 10/ Kröhn, K.-P.: State Variables for Modelling Thermohaline Flow in Rocks. FKZ 02 E 10336 (BMW), Gesellschaft für Anlagen- und Reaktorsicherheit (GRS) mbH, GRS-268, Köln, 2010.
- /KRÖ 11/ Kröhn, K.-P.: Code VIPER - Theory and Current Status. Statusreport, FKZ 02 E 10548 (BMW), Gesellschaft für Anlagen- und Reaktorsicherheit (GRS) mbH, GRS-269, Köln, 2011.
- /KRÖ 17/ Kröhn, K.-P.: Hydraulic Interaction of Engineered and Natural Barriers – Task 8b-8d,8f of SKB. Summary report, FKZ 02 E 10336, 02 E 10548, 02 E 10558, 02 E 11102, and 02 E 11213 (BMW), Gesellschaft für Anlagen- und Reaktor-sicherheit (GRS) mbH, GRS-430, Köln, 2017.
- /KRÖ 19/ Kröhn, K.-P.: Bentonite Re-saturation – limited Access to Water and high Temperature Gradients. FKZ 02 E 10548 and FKZ 02 E 11102 (BMW), Report GRS-503, Gesellschaft für Anlagen- und Reaktorsicherheit (GRS) mbH, Braunschweig, 2019.
- /KRÖ 21/ Kröhn, K.-P.: Groundwater flow under permafrost conditions. FKZ 02 E 11809A (BMW), Gesellschaft für Anlagen- und Reaktorsicherheit (GRS) mbH, Braunschweig, 2021. (in preparation)
- /KUC 17/ Kucherenko, S., Song, S.: Different numerical estimators for main effect global sensitivity indices. Reliab Eng Syst Saf, 165: 222–238.

- /LIN 18/ Lindborg, T.; Pröhl, G.; Thorne, M.; Andersson, E.; Becker, J.; Brandefelt, J.; Cabianca, T.; Gunia, M.; Ikonen, A. T. K.; Johansson, E.; Kangasniemi, V.; Kautsky, U.; Kirchner, G.; Klos, R.; Kowe, R.; Kontula, A.; Kupiainen, P.; Lahdenperä, A-M; Lord, N. S.; Lunt, D. J.; Näslund, J-O.; Nordén, M.; Norris, S.; Pérez-Sánchez D.; Proverbio, A.; Riekkki, K.; Rübél, A.; Sweeck, L.; Walke, R.; Xu. S.: Climate Change and Landscape Development in Post-Closure Safety Assessment of Solid Radioactive Waste Disposal: Results of an Initiative of the IAEA. *Journal of Environmental Radioactivity* 183 (2018) 41–53, 2018.
- /LIN 19/ Lindborg, E.: Introduction. Presentation on the First Annual Meeting of the CatchNet Group, Vienna, 2019.
- /LIN 16/ Lindgren, A; Hugelius, G.; Kuhry, P.; Christensen, T.R., Vandenberghe, J.: GIS-based Maps and Area Estimates of Northern Hemisphere Permafrost Extent during the Last Glacial Maximum- Permafrost and Periglacial Processes, 27: 6-16. DOI:10.1002/ppp.1851, 2016.
- /LIU 12/ Liu, W.; Migdisov, A.; Williams-Jones, A. (2012) The stability of aqueous nickel(II) chloro-complexes in hydrothermal solutions. Results of UV–Visible spectroscopic experiments. *Geochim. Cosmochim. Acta* 94, p. 276–290.
- /LOF 02/ Lofts, S., Tipping, E.W., Sanchez, A.L., Dodd, B.A.: Modelling the role of humic acid in radiocaesium distribution in a British upland peat soil. *J Environ Radioact.* 61 (2002) 133-47.
- /LOT 99/ Lothenbach, B., Ochs, M., Wanner, H. & Yui, M. (1999): Thermodynamic Data for the Speciation and Solubility of Pd, Pb, Sn, Sb, Nb and Bi in Aqueous Solution. Japan Nuclear Cycle Development Institute (JNC), TN8400 99-011.
- /LOT 00/ Lothenbach, B.; Ochs, M.; Hager, D. (2000) Thermodynamic data for the solubility of tin (IV) in aqueous cementitious environments. *Radiochimica Acta* 88, p. 521–526.

- /LUT 96/ Luther, G. W.; Rickard, D. T.; Theberge, S. (1996) Determination of metal (bi)sulfide stability constants of Mn<sup>2+</sup>, Fe<sup>2+</sup>, Co<sup>2+</sup>, Ni<sup>2+</sup>, Cu<sup>2+</sup>, and Zn<sup>2+</sup> by voltammetric methods. *Env. Sci. Tech.* 30, p. 671–679.
- /MAH 09/ Mahoney, J.J., Cadle, S.A., Jakubowski, R.T.: Uranyl adsorption onto hydrous ferric oxide-A re-evaluation for the diffuse layer model database. *Environ Sci Technol.* 43 (2009) 9260-9266.
- /MAK 69/ Makovskaya, G. V.; Spivakovskii, V. B. (1969) Nickel(II) and cobalt(II) hydroxides and hydroxide chlorides and the conditions for their precipitation from chloride solutions. *Russ. J. Inorg. Chem.* 14 (773-776).
- /MAR 00/ Martin, C and Eiblmaier, E. (eds.): *Lexikon der Geowissenschaften: Band 2.* Spektrum Akademischer Verlag, 2000.
- /MAR 05/ Marschall, P.; Horseman, S.; Gimmi, T.: Characterisation of Gas Transport Properties of the Opalinus Clay, a Potential Host Rock Formation for Radioactive Waste Disposal. *Oil & Gas Science and Technology*, Vol. 60, No. 1, pp. 121-139, 2005.
- /MCB 94/ McBride, M.B.: *Environmental Chemistry of Soils.* Oxford University Press, New York (1994).
- /MCL 91/ McLeod, I. D. (1991) Identification of corrosion products on non-ferrous metal artifacts recovered from shipwrecks. *Studies in Conservation* 36, p. 222–234.
- /MIB 18/ Mibus, J.; Diomidis, N.; Wieland, E.; Swanton S.: Release and speciation of <sup>14</sup>C during the corrosion of activated steel in deep geological repositories for the disposal of radioactive waste. *Radiocarbon*, Vol 60, Nr 6, 2018, p 1657–1670. DOI:10.1017/RDC.2018.138.
- /MIJ 19/ Mijndonckx, K., Small, J., Abrahamsen-Mills L., Pedersen, K., & Leys, N. (2019): Final integration and evaluation report. MIND project, Euratom research and training programme 2014-2018, Deliverable 3.7, 2019.

- /MIL 00/ Miller, W.; Alexander, R.; Chapman, N.; McKinley, I.; Smellie, J.: Geological Disposal Of Radioactive Wastes and Natural Analogues, Waste Management Series, Volume 2, Pergamon Verlag, ISBN-10 0080438539, ISBN-13 978-0080438535, 2000.
- /MIL 06/ Miller, B.; Hooker, P.; Smellie, J., Dalton, J.; Degnan, P.; Knight, L.; Noseck, U.; Ahonen, L.; Laciok, A.; Trotignon, L.; Wouters, L.; Hernán, P.; Vela, A.: Network to review natural analogue studies and their applications to repository safety assessment and public communication (NAnet), Synthesis Report, EUR 21919, 2006.
- /MIS 09/ Missana, T., Alonso, U., García-Gutiérrez, M.: Experimental study and modelling of selenite sorption onto illite and smectite clays. J Colloid Interface Sci 334 (2009) 132-138.
- /MOO 04/ Moog, H. C.; Hagemann, S. (2004) Thermodynamische Modellierung hochsalinärer Lösungen. GRS-Bericht 195.
- /MOO 17/ Moog, H.; Noseck, U.; Hagemann, S.; Wolf, J.; Buhmann, D.: Geochemical modelling in the near field of a HLW repository in a high-saline environment. Gesellschaft für Anlagen- und Reaktorsicherheit (GRS) gGmbH, GRS-419 (BMW, FKZ: 02E10719), Köln, 2017.
- /MRU 21/ Mrugalla, S.; Frenzel, B.; Jobmann, M.; Lommerzheim, A.; Meleshyn, A.; Noseck, U.; Rübel, A.; Stark, L.; Weitkamp, A.; Wolf, J.: CHRISTA-II FEP-Katalog zur Einlagerungsoption „multipler ewG“, BGE TEC 2021, To be published.
- /MÜL 92/ Müller, W., Morlock, G., Gronemeyer, C.: Produktion und Verbleib von Gasen im Grubengebäude eines salinaren Endlagers, Statusbericht, GSF-Bericht 3/92, GSF-Forschungszentrum für Umwelt und Gesundheit, Neuherrberg, 1992.
- /MUL 10/ Muller, J. (2010) Etude électrochimique et caractérisation des produits de corrosion formés à la surface des bronzes Cu-Sn en milieu sulfate. Thesis. Université Paris Est, Paris.

- /NAG 02/ NAGRA: Projekt Opalinuston - Synthese der geowissenschaftlichen Untersuchungsergebnisse. Entsorgungsnachweis für abgebrannte Brennelemente, verglaste hochaktive sowie langlebige mittelaktive Abfälle. NAGRA, NTB 02-03, Wettingen, 2002.
- /NAV 13/ Navarro, M.: Modelling Gas and Water Flow through Dilating Pathways in Opalinus Clay - The HG-C and HG-D Experiments. Gesellschaft für Anlagen- und Reaktorsicherheit (GRS) gGmbH, GRS-306, 2013.
- NAZ 71/ Nazarenko, V. A.; Antonovich, V. P.; Nevskaya, E. M. (1971) Spectrophotometric determination of the hydrolysis constants of tin(IV) ions. Russ. J. Inorg. Chem. 15, p. 980–982.
- /NEA 17/ OECD/NEA: Communication on the Safety Case for a Deep Geological Repository. Radioactive Waste Management, NEA No. 7336, OECD 2017.
- /NEA 19a/ OECD/NEA: Managing uncertainty in siting and implementation – Creating a dialogue between science and society. Second Joint Workshop of FSC and IGSC, 9 October 2019, Flyer.  
[https://www.oecd-nea.org/upload/docs/application/pdf/2021-05/fsc\\_igsc\\_workshop\\_flyer.pdf](https://www.oecd-nea.org/upload/docs/application/pdf/2021-05/fsc_igsc_workshop_flyer.pdf)
- /NEA 19b/ OECD/NEA: The 21st Meeting of the NEA Integration Group for the Safety Case (IGSC). 8-10 October 2019, Paris, France. Summary of the Topical Session on “Considerations for Updating a Safety Case”. [https://www.oecd-nea.org/upload/docs/application/pdf/2021-07/summary\\_record\\_of\\_the\\_topical\\_session\\_of\\_the\\_21st\\_meeting\\_of\\_the\\_igsc.pdf](https://www.oecd-nea.org/upload/docs/application/pdf/2021-07/summary_record_of_the_topical_session_of_the_21st_meeting_of_the_igsc.pdf)
- /NEA 20a/ OECD/NEA: Two decades of Safety Case Development: An IGSC Brochure. Paris, 2020.
- /NEA 20b/ OECD/NEA: Programme of Work of the Expert Group on Repositories in Rock Salt Formations (Salt Club) 2021-2022. NEA/RWM/IGSC(2020)7, OECD/NEA, Paris.

- /NEA 22/ OECD/NEA: Proceedings of IGSC Safety Case Symposium “Current Understanding and Future Direction for the Geological Disposal of Radioactive Waste” 2018 in Rotterdam. OECD/NEA, Paris 2022.
- /NEE 18/ Neef, E.A.C.: CARbon-14 Source Term. Final overview of CAST (D7.23) Version 2. 2018.
- /NIC 87/ Nickel, E.; Graham, J. (1987) Paraotwayite, a new nickel hydroxide mineral from Western Australia. *Canadian Mineralogist* 25, p. 409–411.
- /NIC 85/ Nickel, E.; Robinson, B. W. (1985) Kambaldaite - a new hydrated Ni-Na carbonate mineral from Kambalda, Western Australia. *Am. Mineral.* 70, p. 419–422.
- /NIC 77/ Nickel, E.; Robinson, B. W.; Davis, C. E. S. (1977) Otwayite, a new nickel mineral from Western Australia. *Am. Mineral.* 62, p. 999–1002.
- /NIC 93/ Nickel, E. H.; Robinson, B. W.; Mumme, W. G. (1993) Widgiemootthalite: The new Ni analogue of hydromagnesite from Western Australia. *Am. Mineral.* 78, p. 819–821.
- /NOS 08/ Noseck, U.; Becker, D.; Fahrenholz, C.; Fein, E.; Flügge, J.; Kröhn, K.-P.; Mönig, J.; Müller-Lyda, I.; Rothfuchs, T.; Rübel, A.; Wolf, J.: Assessment of the long-term safety of repositories - Scientific basis. FKZ 02E9954, GRS-237, Gesellschaft für Anlagen und Reaktorsicherheit (GRS) mbH, Braunschweig, 2008.
- /NOS 12/ Noseck, U., Brendler, V., Flügge, J., Stockmann, M., Lampe, M., Britz, S., Schikora, J., Schneider, A.: Realistic integration of sorption processes in transport codes for long-term safety assessments. BMWi-FKZ 02E 10518, Gesellschaft für Anlagen- und Reaktorsicherheit (GRS) mbH, GRS-297. Braunschweig (2012).

- /NOS 18/ Noseck, U., Becker, D., Brassler, T., Buhmann, D., Fahrenholz, C., Flügge, J., Kröhn, K.-P., Meleshyn, A., Mönig, J., Moog, H., Rübel, A., Spießl, S., Wolf, J.: Scientific Basis for a Safety Case of Deep Geological Repositories. Final Report, FKZ 02E11102 (BMW), GRS-501, GRS Braunschweig, 2018.
- /OLS 99/ Olsen, E., and J. Thonstad: Nickel ferrite as inert anodes in aluminium electrolysis: Part I Material fabrication and preliminary testing. Journal of Applied Electrochemistry 29.3 (1999): 293-299.
- /PAA 03/ Paananen, M.; Ruskeeniemi, T.: Permafrost at Lupin - Interpretation of SAMPO electromagnetic soundings at Lupin, Geological Survey of Finland (Nuclear Waste Disposal Research), Report YST-117, ISBN 951-690-871-3, ISSN 0783-3555, 2003.
- /PAB 12/ de Pablo, M.Á., Ramos, M., Viaira, G., Molina, A.: Revealing the secrets of permafrost. Science in School, The European journal for science teachers, issue 22, 2012, <https://www.scienceinschool.org/2012/issue22/permafrost> (as of 9th June 2021).
- /PAL 10/ Donald A. Palmer & Heinz Gamsjäger (2010) Solubility measurements of crystalline  $\beta$ -Ni(OH)<sub>2</sub> in aqueous solution as a function of temperature and pH, Journal of Coordination Chemistry, 63:14-16, 2888-2908, DOI: 10.1080/00958972.2010.492215.
- /PAL 11/ Donald A. Palmer, Pascale Bénézech, Caibin Xiao, David J. Wesolowski, Lawrence M. Anovitz (2011) Solubility Measurements of Crystalline NiO in Aqueous Solution as a Function of Temperature and pH. J. Solution Chem. (40), 680–702. DOI 10.1007/s10953-011-9670-x
- /PAP 14/ Papafotiou, A.; Senger, R.: Sensitivity analyses of gas release from a SF/HLW repository in the Opalinus Clay in the candidate siting regions of Northern Switzerland. Nagra Arbeitsbericht NAB 14-10, 2014.

- /PAR 99/ Parkhurst, D.L., and Appelo, C.A.J., User's guide to PHREEQC (Version 2) - A computer program for speciation, batch-reaction, one-dimensional transport, and inverse geochemical calculations: U.S. Geological Survey Water-Resources Investigations Report 99-4259 (1999) 312 p.
- /PAR 13/ Parkhurst, D.L., Appelo, C.A.J.: Description of input and examples for PHREEQC version 3—A computer program for speciation, batch-reaction, one-dimensional transport, and inverse geochemical calculations. U.S. Geological Survey Techniques and Methods, Vol. 6 (2013).
- /PAV 18/ Pavapootanont, G.; Wongpanya, P.; Viyanit, E.; Lothongkum, G. (2018) Corrosion behavior of Ni steels in aerated 3.5-wt.% NaCl Solution at 25°C by potentiodynamic method. Eng. J. (Engineering Journal) 22 (4), p. 1–12.
- /PET 81/ Pettine, M.; Millero, F. J.; Macchi, G. (1981) Hydrolysis of tin(II) in aqueous solutions. Anal. Chem. 53, p. 1039–1043.
- /PLI 09/ Plischke, E., Röhlig, K.-J.: Sensitivity Analysis Benchmark Based on the Use of Synthetic PA Cases (Topic Report). PAMINA Milestone M 2.1.D.11.
- /POS 12/ Posiva Oy: Safety Case for the Disposal of Spent Nuclear Fuel at Olkiluoto - Features, Events and Processes 2012, ISBN 978-951-652-188-9, ISSN 1239-3096, 2012.
- /PRO 02/ Pröhl, G., Gering, F.: Dosiskonversionsfaktoren zur Berechnung der Strahlenexposition in der Nachbetriebsphase von Endlagern nach dem Entwurf der Allgemeinen Verwaltungsvorschrift zu §47 Strahlenschutzverordnung in Anlehnung an die Vorgehensweise im Rahmen des Planfeststellungsverfahrens des geplanten Endlagers Konrad, GSF-Forschungszentrum für Umwelt und Gesundheit, Institut Strahlenschutz, Neuherberg, 15.12.2002.
- /PUS 90/ Pusch, R., Karnland, O., Hökmark, H.: GMM - A general microstructural model for quantitative studies of smectite clays. SKB, Technical Report 90-43, 1990.

- /RAI 11/ Rai, D.; Yui, M.; Schaef, H. T.; Kitamura, A. (2011) Thermodynamic model for SnO<sub>2</sub>(cr) and SnO<sub>2</sub>(am) solubility in the aqueous Na<sup>+</sup>-H<sup>+</sup>-OH<sup>-</sup>-Cl-H<sub>2</sub>O system. *J. Solution Chem.* 40, p. 1155–1172.
- /RAS 16/ Rashid, T.; Khawaja, H.; Edvardsen, K.: Determination of Thermal Properties of Fresh Water and Sea Water Ice using Multiphysics Analysis; *Int. Jnl. of Multiphysics*, Volume 10, Number 3, 277, 2016.
- /REI 39/ Reiff, F.; Toussaint, S. M. (1939) Stability and solubility of sodium stannates. *Z. Anorg. Allg. Chem.* 241, p. 372–380.
- /REN 03/ Renssen, H. and Vandenberghe, J., 2003: Investigation of the relationship between permafrost distribution in NW Europe and extensive winter sea-ice cover in the North Atlantic Ocean during the cold phases of the Last Glaciation. *Quaternary Science Reviews* 22, 209-223, 2003.
- /RIC 06/ Rickard, D.; Luther, G. W. (2006) 8. Metal sulfide complexes and clusters. In: David J. Vaughan (Hg.): *Sulfide Mineralogy and Geochemistry*. Berlin, Boston: De Gruyter (Reviews in Mineralogy et Geochemistry, 61), p. 421–504.
- /RIG 02/ Rigol, A., Vidal, M., Rauret, G.: An overview of the effect of organic matter on soil-radiocaesium interaction: implications in root uptake. *J Environ Radioact* 58 (2002) 191-216.
- /RIN 15/ Rincke, C.; Bette, S.; Dinnebier, R. E.; Voigt, W. (2015) Nickel bicarbonate revealed as a basic carbonate. *European Journal of Inorganic Chemistry* (36), p. 5913–5920.
- /RIN 17/ Rinklebe, J., Shaheen, S.M.: Redox chemistry of nickel in soils and sediments: A review. *Chemosphere* 179 (2017) 265-278.
- /ROS 68/ Rosenblum, P. (1968) Solubility in the potassium stannate – potassium hydroxide – water system at 0 to 95.0 °C. *Can. J. Chem.* 46 (16), p. 2715–2719.
- /ROU 05/ Roussel-Debet, S.: Experimental values for <sup>241</sup>Am and <sup>239+240</sup>Pu K<sub>d</sub>'s in French agricultural soils. *J Environ Radioact.* 79 (2005) 171-85.

- /RUE 07/ Rübél, A., Becker, D.-A., Fein, E.: Radionuclide transport modelling to assess the safety of repositories in clays. GRS-228.
- /RUS 02/ Ruskeeniemi, T.; Paananen, M.; Ahonen, L.; Kaija, J.; Kuivamäki, A.; Frape, S.; Moren, L.; Degnan, P.: Permafrost at Lupin, Report of Phase I, Report YST-112, Geological Survey of Finland (Nuclear Waste Disposal Research), ISBN 951-690-846-2, ISSN 0783-3555, 2002.
- /RUS 04/ Ruskeeniemi, T., Ahonen, L.; Paananen, M.; Frape, S.; Stotler, R.; Hobbs, M.; Kaija, J.; Degnan, P. Blomquist, R.; Jensen, M.; Lehto, K.; Moren, L.; Puigdomenech, I.; Snellmann, M.: Permafrost at Lupin – Report of Phase II, Geological Survey of Finland (Nuclear Waste Disposal Research), Report YST-119, ISBN 951-690-890-X, ISSN 0783-3555, 2004.
- /SAJ 14/ Sajih, M., Bryan, N., Livens, F., Vaughan, D., Descostes, M., Phrommavanh, V., Nos, J., Morris, K.: Adsorption of radium and barium on goethite and ferrihydrite: A kinetic and surface complexation modelling study. *Geochimica et Cosmochimica Acta* 146 (2014) 150-163.
- /SAL 99/ Saltelli, A., Tarantola, S., Chan, K.A.: Quantitative, model independent method for global sensitivity analysis of model output. *Technometrics* 1999, 41(1): 39-56.
- /SAL 04/ Saltelli, A., Tarantola, S., Campolongo, F., Ratto, M.: *Sensitivity Analysis in Practice: A Guide to Assessing Scientific Models*. Wiley, ISBN-10: 0470870931, ISBN-13: 978-0470870938.
- /SCH 81/ Schnering, H. G. v.; Nesper, R.; Pelshenke, H. (1981)  $\text{Sn}_{21}\text{Cl}_{16}(\text{OH})_{14}\text{O}_6$ , das sogenannte basische Zinn(II)-chlorid [1] /  $\text{Sn}_{21}\text{Cl}_{16}(\text{OH})_{14}\text{O}_6$ , the So-called Basic Tin(II) Chloride. *Zeitschrift für Naturforschung B* 36 (12), p. 1551–1560.
- /SCH 97/ Schulten H.R., Schnitzer, M.: Chemical Model Structures for Soil Organic Matter and Soils. *Soil Science* 162 (1997) 115-130.

- /SEN 18/ Senger, R.; Romero, E.; Marschall, P.: Modeling of Gas Migration Through Low-Permeability Clay Rock Using Information on Pressure and Deformation from Fast Air Injection Tests. *Transp Porous Med* 123:563–579, 2018.
- /SHA 17/ Shao, Q., Younes, A., Fahs, M., Mara, T.A.: Bayesian sparse polynomial chaos expansion for global sensitivity analysis. *Computer Methods in Applied Mechanics and Engineering*, 318: 474-496.
- /SIM 16/ Simoes, M. C.; Hughes, K. J.; Ingham, D. B.; Ma, L.; Pourkashanian, M. (2016) Estimation of the Pitzer parameters for 1–1, 2–1, 3–1, 4–1, and 2–2 single electrolytes at 25 °C. *J. Chem. Eng. Data* 61 (7), p. 2536–2554.
- /SIM 17/ Simoes, M. C.; Hughes, K. J.; Ingham, D. B.; Ma, L.; Pourkashanian, M. (2017) Estimation of the thermochemical radii and ionic volumes of complex ions. *Inorg. Chem.* 56 (13), p. 7566–7573.
- /SKI 06/ Skipper, N.T., Lock, P.A., Titiloye, J.O., Swenson, J., Mirza, Z.A., Howells, W.S., Fernandez-Alonso, F., The structure and dynamics of 2-dimensional fluids in swelling clays. *Chemical Geology* 230, 182-196, 2006).
- /SKB 01/ SKB: Programme for research, development and demonstration of methods for the management and disposal of nuclear waste - RD&D Programme 2001- , TR-01-30, 2001.
- /SOB 21/ SobolGSA software. Imperial College London, User manual, <http://www.imperial.ac.uk/process-systems-engineering/research/free-software/sobol-gsasoftware/>.
- /SOB 01/ Sobol', I.M.: Global sensitivity indices for nonlinear mathematical models and their Monte Carlo estimates. *Mathematics and Computers in Simulation*, 55: 271-280.
- /SON 16/ Song, Y.; Davy, C. A.; Troadec, D.: Gas Breakthrough Pressure (GBP) through Claystones: Correlation with FIB/SEM Imaging of the Pore Volume. *Oil & Gas Science and Technology – Rev. IFP Energies nouvelles* 71, 51, 2016.

- /SPI 17/ Spiessl, S.M., Becker, D.-A.: Investigation of Modern Methods of Probabilistic Sensitivity Analysis of Final Repository Performance Assessment Models (MOSEL). FKZ 02E 10941 (BMW), GRS-412, ISBN 978-3-944161-94-5.
- /SPI 18/ Spiessl, S.M., Kucherenko, S., Becker, D.-A., Zaccheus, O.: Higher-order sensitivity analysis of a final repository model with discontinuous behaviour. Reliability Engineering and System Safety, doi: <https://doi.org/10.1016/j.ress.2018.12.004>.
- /SPI 68/ Spinner, B. (1968): Étude quantitative de l'hydrolyse des niobates de potassium. Revue de Chimie minérale, 5, 839–868.
- /STA 03/ Staven L.H., Rhodas K., Napier B. A., Strenge D. L.: A Compendium of Transfer Factors for Agricultural and Animal Products. - Pacific Northwest National Laboratory, USA, June 2003, PNNL-13421.
- /STA 04/ Staunton, S.: Sensitivity analysis of the distribution coefficient,  $K_d$ , of nickel with changing soil chemical properties, Geoderma 122 (2004) 281-290.
- /STE 02/ Steelink, C.: Investigating Humic Acids in Soils. Anal Chem 74 (2002) 326A–333A.
- /SUA 92/ Suarez, D. L., Wood J. D., Ibrahim, I.: Reevaluation of Calcite Supersaturation in Soils, Soil Sci. Soc. Am. J. 56 (1992) 1776-1784.
- /SWI 21/ Swiler, L. P.; Becker, D.-A.; Brooks, D.; Govaerts, J.; Koskinen, L.; Kupiainen, P.; Plischke, E.; Röhlig, K.-J.; Saveleva, E.; Spiessl, S. M.; Stein, E.; Svitelman, V.: "Sensitivity Analysis Comparisons on Geologic Case Studies: An International Collaboration." Sandia National Laboratories Technical Report SAND2021-11053. Albuquerque, NM. Sept. 2021.
- /TAL 04/ Talerico, C., Ochs, M. & Giffaut, E. (2004): Solubility of niobium(V) under cementitious conditions: Importance of Ca-niobate. Materials Research Society Symposium Proceedings, 824, CC8.31.1-CC8.31.6.

- /THO 99/ Thoenen, T. (1999) Pitfalls in the use of solubility limits for radioactive waste disposal: the case of nickel in sulfidic groundwaters. *Nuclear Technology* 126 (1), p. 75–87.
- /THO 14/ Thoenen, T.; Hummel, W.; Berner, U. (2014) The PSI/Nagra Chemical Thermodynamic Database 12/07. PSI-Report 14 (04).
- /THO 21/ Tres Thoenen (2021): The PSI Chemical Thermodynamic Database 2020: Data Selection for Niobium. TM-44-18-10.
- /TIP 11/ Tipping, E., Lofts, S., Sonke, J.E.: Humic Ion-Binding Model VII: a revised parameterisation of cation-binding by humic substances. *Environ Chem* 8 (2011) 225-235.
- /URS 19/ Urso, L., Hormann, V., Diener, A., Achatz, M.: Modelling partition coefficients of radium in soils. *Applied Geochemistry* 105 (2019) 78–86.
- /UZA 59/ Uzarov, G. G.; Lipshits, B. M.; Lovchikov, V. S. (1959) Izotermiy rastvorimosti v sisteme Na<sub>2</sub>O-H<sub>2</sub>O-SnO<sub>2</sub> pri 25 i 75°. *Zh. Neorg. Khim.* 4, p. 2380–2383.
- /VAN 93/ Vandenberghe, J. and Pissart, A.: Permafrost changes in Europe during the Last Glacial. *Permafrost and Periglacial Processes* 4, 121–135, 1993.
- /VAN 99/ van Middlesworth, J. M.; Wood, S. A. (1999) The stability of palladium(II) hydroxide and hydroxy–chloride complexes: an experimental solubility study at 25–85°C and 1 bar. *Geochim. Cosmochim. Acta* 63 (11-12), p. 1751–1765.
- /VAN 07a/ Vandenhove, H., Van Hees M.: Predicting radium availability and uptake from soil properties. *Chemosphere* 69 (2007) 664-74.
- /VAN 07b/ Vandenhove, H., Hees, M. van, Wouters, K., Wannijn, J: Can we predict uranium bioavailability based on soil parameters? Part 1: Effect of soil parameters on soil solution uranium concentration. *Environmental Pollution* 145 (2007) 587-595.

- /VIL 05/ Villar, M.V., Martín, P.L., Barcala, J.M.: Infiltration test at isothermal conditions and under thermal gradient. Technical Report CIEMAT/DMA/M2140/1/05, CIEMAT, Madrid, 2005.
- /WEI 17/ Weitkamp, A.; Bebiolka, A. C.: Subglaziale Rinnen – Darstellung und Bewertung des Kenntnisstandes, Abschlussbericht, 9Y2013040000, 2017.
- /WIL 10/ Wilkin, R. T.; Rogers, D. A. (2010) Nickel sulfide formation at low temperature: initial precipitates, solubility and transformation products. *Environ. Chem.* 7 (6), p. 514.
- /WIN 20/ WINBERG WANG, H.: Water density impact on waterflow and mass transport in rock fractures. Doctoral thesis, KTH Royal Institute of Technology, School of Engineering Sciences in Chemistry, Biotechnology and Health, Department of Chemical Engineering, Stockholm, 2020.
- /WOO 05/ WOOD, S.A. (2005): The aqueous geochemistry of zirconium, hafnium, niobium, and tantalum. In: LINNEN, R.L. & SAMSON, I.M. (eds.): Rare-element geochemistry and mineral deposits. Geological Association of Canada, GAC Short Course Notes, 17, 217–268.
- /YAJ 94/ YAJIMA, T. (1994): Solubility measurements of uranium and niobium, Report of Yayoi Kenkyukai, UTNL-R 0331, University of Tokyo, pp. 127–144 [in Japanese] (as cited by KITAMURA et al. 2010).
- /YAJ 92/ YAJIMA, T., TOBITA, S. & UETA, S. (1992): Solubility measurements of niobium in the system Nb-O-H under CO<sub>2</sub>-free condition, presented at 1992 Fall Meeting of Atomic Energy Society of Japan, F33, p. 341 [in Japanese] (as cited by KITAMURA et al. 2010).
- /YEN 81/ Yen, Y.-C.: Review of thermal properties of snow, ice and sea ice, CRREL Report 81-10, June 1981, ISBN 92056733, 1981.
- /YI 20/ Yi, Y., and Kimball, J.S.: ABoVE: Active Layer Thickness from Remote Sensing Permafrost Model, Alaska, 2001-2015. ORNL DAAC, Oak Ridge, Tennessee, USA, 2020. <https://doi.org/10.3334/ORNLDAAC/1760>.
- /ZAC 15/ Zaccheus, O., Kucherenko, S.: SobolGSA Version 2.0 TUTORIAL.

- /ZAV 04/ Zavarin M., Bruton C.J.: A Non-Electrostatic Surface Complexation Approach to Modeling Radionuclide Migration at the Nevada Test Site: I. Iron Oxides and Calcite. United States (2004).
- /ZHA 94/ Zhang, J. -Z.; Millero, F. J. (1994) Investigation of metal sulfide complexes in sea water using cathodic stripping square wave voltammetry. *Analytica Chimica Acta* 284, p. 497–504.
- /ZHA 15a/ Zhang, N.; Brugger, J.; Etschmann, B.; Ngothai, Y.; Zeng, D. (2015) Thermodynamic modeling of poorly complexing metals in concentrated electrolyte solutions: an X-ray absorption and UV-Vis spectroscopic study of Ni(II) in the NiCl<sub>2</sub>-MgCl<sub>2</sub>-H<sub>2</sub>O system. *PloS one* 10 (4), e0119805.
- /ZHA 15b/ Zhang, N.; Zeng, D.; Brugger, J.; Zhou, Q.; Ngothai, Y. (2015) Effect of Solvent Activity on Solute Association: The Formation of Aqueous Nickel(II) Chloride Complexes Studied by UV–Vis and EXAFS Spectroscopy. *J. Solution Chem.* 44 (6), p. 1320–1338.
- /ZHA 17/ Zhang, C.-L.: Sealing Performance of Fractured Claystone and Clay-Based Materials. FKZ 02E10377, Gesellschaft für Anlagen- und Reaktorsicherheit (GRS) gGmbH, GRS-451, 2017.
- /ZUN 13/ Zuniga, M., Kucherenko, S., Shah, N.: Metamodelling with independent and dependent inputs. *Computer Physics Communications*, 184 (6): 1570-1580.

## List of Figures

Fig. 2.1	Pointwise approach: SI1 and SIT of $X_1$ of the Ishigami function with Sobol' sampling and different number of simulations, calculated using the direct Sobol' formula .....	14
Fig. 2.2	Pointwise approach: SI1 of $X_1$ of the Ishigami function with Sobol' sampling and different number of simulations and coefficients, calculated using the RS-HDMR method.....	15
Fig. 2.3	Pointwise approach: SI2 of the Ishigami function with Sobol' sampling and different number of simulations and coefficients, calculated using the RS-HDMR method.....	16
Fig. 2.4	Pointwise approach: SIT of $X_1$ of the Ishigami function with Sobol' sampling and different number of simulations and coefficients, calculated using the RS-HDMR method.....	17
Fig. 2.5	Pointwise approach: SI1 of and SIT of $X_1$ of the Ishigami function with Sobol' sampling and different number of simulations, calculated using the BSPCE method .....	18
Fig. 2.6	Pointwise approach: SI1 of <i>DiffClay3</i> , SI2 of [ <i>DiffClay3</i> ][ <i>DiffClay2</i> ] and SIT of <i>DiffClay3</i> with 8192 runs (random sampling) and 4096 runs (LpTau sampling), calculated using RS-HDMR with different pairs of polynomial orders.....	19
Fig. 2.7	Generalised approach: Si1 of <i>DiffClay3</i> , SI2 of [ <i>DiffClay3</i> ][ <i>DiffClay2</i> ] and SIT of <i>DiffClay3</i> with 8192 runs (random sampling) and 4096 runs (LpTau sampling), calculated using RS-HDMR with different pairs of polynomial orders.....	21
Fig. 2.8	Pointwise approach: SI1 of <i>DiffClay3</i> and SIT of <i>DiffClay3</i> and <i>KdClay2</i> for random and LpTau sampling with different sample sizes, calculated with BSPCE .....	23
Fig. 2.9	Pointwise approach: SI1 of <i>DiffClay3</i> and SIT of <i>DiffClay3</i> and <i>KdClay2</i> for random and LpTau sampling with different sample sizes, calculated with BSPCE .....	24
Fig. 2.10	Pointwise and generalised approach: SIT of the clay system with random and lptau sampling calculated using RS-HDMR and BSPCE .....	25
Fig. 2.11	Pointwise and generalised approach: SI1, SI2 and SIT indices of the LILW20 model with 8192 and 16384 simulations and coefficients of 10-4 and 10-5 using the RS-HDMR method.....	27

Fig. 2.12	Pointwise approach: SI1 and SIT of <i>AEBCConv</i> and <i>IniPermSeal</i> with LpTau sampling and different number of simulations, computed using BSPCE .....	29
Fig. 2.13	Generalised approach: SI1 and SIT of <i>AEBCConv</i> and <i>IniPermSeal</i> with LpTau sampling and different number of simulations, computed using BSPCE .....	30
Fig. 2.14	Pointwise and generalised approach: SI1 and SIT of the LILW6 model with LpTau sampling and 4096, 8192 and 16384 runs calculated using BSPCE .....	31
Fig. 2.15	Pointwise approach: SI1 and SI2 of the influential parameters and sum of SI1 of the case <i>AEBCConv-IniPermSeal-1D</i> of the LILW model with 8192 simulations using RS-HDMR with different coefficients and EASI .....	32
Fig. 2.16	Pointwise approach: comparison of RS-HDMR and BSPCE methods for SI1 (left) and SIT (right) .....	33
Fig. 2.17	Pearson correlation coefficients of the GRS clay system (SNL results).....	40
Fig. 2.18	Spearman rank correlation coefficients of the GRS clay system (SNL results).....	41
Fig. 2.19	Sensitivity analysis of GRS Clay case (8192 runs): PAWN method, dummy parameter subtracted (IBRAE results) .....	42
Fig. 2.20	CUSUNORO analysis of the SNL shale system (GRS results) .....	44
Fig. 2.21	Sensitivity measures for RF1 (upper), RF4 (middle) and RF6 (lower) of the SNL Shale calculation case (SNL results).....	45
Fig. 2.22	Sensitivity analysis of the Dessel model with different transformation parameters (GRS results) .....	46
Fig. 2.23	Sum of first order effects and absolute contribution to total output variance (results of SCK-CEN) .....	47
Fig. 2.24	Direct (left) and rank-based (right) sensitivity analysis of the IBRAE groundwater model (GRS results).....	48
Fig. 2.25	First-order sensitivity indices of the IBRAE groundwater model, calculated with different surrogate models for all sample sizes (SNL results).....	49
Fig. 2.26	Czech conceptual biosphere model (local version for the site Kravi Hora) .....	51

Fig. 2.27	Czech transport model in GoldSim .....	52
Fig. 2.28	Scheme for the treatment of contaminated soils and resulting pathways with key parameters differing for the respective components.....	56
Fig. 2.29	Time dependence of radionuclide concentration in agriculture soil calculated by UJV model and GRS.....	59
Fig. 2.30	Time dependence of dose from external irradiation from irrigated agricultural soil calculated by UJV and GRS.....	66
Fig. 2.31	Simulations vs. experimental data for Cs from /GIL 08/.....	71
Fig. 2.32	Simulations vs. experimental data for Ni from /STA 04/ .....	72
Fig. 2.33	Simulations vs. experimental data for Ra from /VAN 07a/.....	73
Fig. 2.34	Simulations vs. experimental data for U from /VAN 07b/.....	74
Fig. 2.35	Normal ranges of Eh-pH in soil (from /HUS 13/) .....	76
Fig. 2.36	Calculated pH dependence of $K_d$ for americium (Refesol 01A) .....	84
Fig. 2.37	Calculated pH dependence of $K_d$ for uranium (Refesol 03G).....	85
Fig. 2.38	Calculated DOC dependence of $K_d$ for americium (Refesol 01A).....	86
Fig. 2.39	Calculated ammonium dependence of $K_d$ for cesium (Refesol 01A) .....	87
Fig. 2.40	Calculated cyanide dependence of $K_d$ for nickel (Refesol 01A).....	88
Fig. 2.41	Calculated phosphate dependence of $K_d$ for selenium (Refesol 03G) .....	89
Fig. 2.42	Dependence of $\log K_d$ for Pu on pe and pH .....	90
Fig. 2.43	Dependence of $\log K_d$ for Se on pe and pH .....	90
Fig. 2.44	Dependence of $\log K_d$ for Tc on pe and pH.....	91
Fig. 2.45	Screenshot of the batch program „KdMultigrid“ .....	93
Fig. 2.46	$K_d$ distribution of Am for Refesol 01A .....	95
Fig. 2.47	$K_d$ distribution of Cs for Refesol 01A .....	96
Fig. 2.48	$K_d$ distribution of Ni for Refesol 01A .....	96
Fig. 2.49	$K_d$ distribution of Pu for Refesol 01A.....	97
Fig. 2.50	$K_d$ distribution of Ra for Refesol 01A.....	98
Fig. 2.51	$K_d$ distribution of Se for Refesol 01A.....	99

Fig. 2.52	$K_d$ distribution of Tc for Refesol 01A .....	100
Fig. 2.53	$K_d$ distribution of U for Refesol 01A.....	100
Fig. 3.1	Timeline of IGSC activities and selected publications /NEA 20a/ .....	108
Fig. 3.2	Structure of the IDKM with the four expert groups. Figure is internally used by the IDKM Bureau.....	124
Fig. 4.1	FEBEX "in situ" test layout; from /ENR 00/.....	146
Fig. 4.2	General layout for stage 1 of the FEBEX in situ test; from /BÁR 03/ .....	147
Fig. 4.3	General layout for stage 2 of the FEBEX in situ test; from /BÁR 03/ .....	147
Fig. 4.4	Position of axial segments AS1 (left) and AS2 (right) /BÁR 03/.....	148
Fig. 4.5	Domain of the thermal model; left: full model in 3D, right: cut-out in 2D.....	151
Fig. 4.6	Numerical grid; left: opened whole domain, right: close-up .....	152
Fig. 4.7	Temperature field after 18 years of heating; left: contour lines and temperature observation point (red dot) right: breakthrough temperature at observation point .....	154
Fig. 4.8	Temperature evolution at point P1 on sections D1, D2, and I.....	155
Fig. 4.9	Temperature for sections I, D1 and D2 at 90, 1800, and 5600 days.....	155
Fig. 4.10	Temperature for axial sections AS1 and AS2 at 90, 1800, and 5600 days.....	156
Fig. 4.11	Transient radial temperature profiles in cross-section C.....	156
Fig. 4.12	Transient radial temperature profiles in cross-section F2.....	157
Fig. 4.13	Evolution of power for heaters 1 and 2 during stage 1 at z=6.60m.....	158
Fig. 4.14	Evolution of power for heaters 1 and 2 during both stages at z=6.60m ..	158
Fig. 4.15	Temperature isolines around the heaters after 1800 days .....	159
Fig. 4.16	Experimental setup with the cross-sections of interest marked in red ....	160
Fig. 4.17	Model domain for the buffer in cross-sections C (left) and F2 (right) .....	160
Fig. 4.18	Processes acting according to the extended vapour diffusion model; from /KRÖ 11/.....	162
Fig. 4.19	Mathematical approach for the isotherm for unconfined FEBEX-bentonite /KRÖ 08/ .....	163

Fig. 4.20	Temperature-dependent isotherm for confined FEBEX-bentonite /KRÖ 08/.....	163
Fig. 4.21	Isothermal water uptake after 135 days of isothermal uptake in section C .....	165
Fig. 4.22	Distributions of relative humidity at appointed times in section C .....	165
Fig. 4.23	Distributions of relative humidity at appointed times in section F2.....	166
Fig. 4.24	Evolutions of relative humidity at appointed locations in section C.....	166
Fig. 4.25	Evolutions of relative humidity at appointed locations in section F2 .....	167
Fig. 4.26	Water content and saturation in section F2 as a proxy to section 27.....	167
Fig. 4.27	Water content and saturation in section F2 as a proxy to section 49.....	168
Fig. 4.28	Sketch of the test set-up; from /KRM 20/ .....	174
Fig. 4.29	Water content distributions; from the experiment (black), from COMSOL (blue), from VIPER (orange); from /KRM 20/ .....	175
Fig. 4.30	Axial water content distributions after pointwise water inflow; 2D-domain (dashed lines), 3D-domain (solid lines); from /KRM 20/.....	176
Fig. 4.31	Water content distribution in a 3D-domain after 75 years; from /KRM 20/ .....	177
Fig. 4.32	Potential repository-sites worthy of investigation /BGR 12/ (left) and maximum permafrost coverage during the Weichselian/Würm glacial after /VAN 93/ and /REN 03/ (right).....	179
Fig. 4.33	Types of taliki; from /PAB 12/.....	180
Fig. 4.34	Influence of climate change on the hydrological flow system; from /LIN 19/ (modified from /JOH 16/)	180
Fig. 4.35	Artificial printed fracture .....	183
Fig. 4.36	Cooling unit; a) construction, b) print.....	184
Fig. 4.37	Auxiliary cooling unit (top view).....	185
Fig. 4.38	Cooling aggregate .....	186
Fig. 4.39	Syringe pump .....	186
Fig. 4.40	Temperature sensors installed in the cooling unit .....	187
Fig. 4.41	Data acquisition system.....	187

Fig. 4.42	Cool box .....	188
Fig. 4.43	Setup for the first attempt.....	189
Fig. 4.44	Principal sketch of the numerical model.....	190
Fig. 4.45	Contour planes indicating 0°C in the model with a top temperature of 5°C; from left to right: after 0.5 h, 1.5 h and 6 h .....	190
Fig. 4.46	Setup for the second and following attempts.....	192
Fig. 4.47	Cooling unit (right) and auxiliary cooling unit (left) inside the cool box; a) before the test, b) after cleaning of the test.....	193
Fig. 4.48	Cooling unit before the test .....	195
Fig. 4.49	Fracture after injection of magenta coloured water .....	196
Fig. 4.50	Air in the injection tubing.....	196
Fig. 4.51	Fracture after injection of silver coloured water .....	197
Fig. 4.52	Fracture after injection of green coloured water .....	197
Fig. 4.53	Fracture after injection of golden coloured water .....	198
Fig. 4.54	Colour distribution in the fracture at the end of test; a) original photograph, b) modified colour channels, c) reduced number of colours, d) stronger reduced number of colours.....	200
Fig. 4.55	Fracture after final flushing with tap water and with air.....	201
Fig. 4.56	Updated domain of the numerical model.....	203
Fig. 4.57	Mean air temperature in the cool box; left: full test, right: final phase .....	203
Fig. 4.58	Temperature in the fracture; inflow: green, middle: red, outflow: blue ....	204
Fig. 4.59	Fracture after injection of tap water.....	205
Fig. 4.60	Fracture after injection of blue water .....	205
Fig. 4.61	After injection of red water .....	206
Fig. 4.62	After injection of green water; left: original photo, right: increased brightness.....	207
Fig. 4.63	Fracture after the first to tenth flush with tap water.....	208
Fig. 4.64	Permafrost thickness over surface temperature; from /JNC 00/ .....	210

Fig. 4.65	Permafrost depth depending on surface temperature for the Canadian shield; modelling results and data from /JNC 00/ .....	215
Fig. 4.66	Convergence of temperature at the steady-state permafrost boundary; top plot: surface temperature of -2°C, observation level - 22.275 m, bottom plot: surface temperature of -10°C, observation level -254 m .....	216
Fig. 4.67	Set-up of the PGZ experiment /HAR 12a/ .....	221
Fig. 4.68	Pressure measurements, gas flowrate and gas quantity injected in PGZ1201 over one year /JAC 14/ .....	221
Fig. 4.69:	Time dependent evolution of gas flux out of a claystone core sample and sample dilatation in response of the gas flow /CUS 14/ .....	223
Fig. 4.70	Heat conductivity for different rocks and fresh water .....	227
Fig. 4.71	Ice wedges generated during Weichsel and Würm, maximum ice margins and crystalline formations potential suitable for a repository in Germany. / <a href="https://www.bge.de/de/endlagersuche/wesentliche-unterlagen/zwischenbericht-teilgebiete/">https://www.bge.de/de/endlagersuche/wesentliche-unterlagen/zwischenbericht-teilgebiete/</a> / <a href="https://www.bgr.bund.de/DE/Themen/Endlagerung/Projekte/Langzeit_sicherheit/abgeschlossen/Permafrostprognose.html/">https://www.bgr.bund.de/DE/Themen/Endlagerung/Projekte/Langzeit_sicherheit/abgeschlossen/Permafrostprognose.html/</a> / <a href="https://opendata-esri-de.opendata.arcgis.com/datasets/esri-de-content::gk1000-eisrand?geometry=5.918%2C46.206%2C47.163%2C55.834/">https://opendata-esri-de.opendata.arcgis.com/datasets/esri-de-content::gk1000-eisrand?geometry=5.918%2C46.206%2C47.163%2C55.834/</a> .....	228
Fig. 4.72	Buried Valleys and Ice Margins in Northern Germany /WEI 17/ .....	229
Fig. 4.73	Permafrost depth in the territory of Canada. (National Permafrost Data-base, GSC, <a href="http://sts.gsc.nrcan.gc.ca/tsdweb/geoserv_permafrost.asp">http://sts.gsc.nrcan.gc.ca/tsdweb/geoserv_permafrost.asp</a> ) /RUS 02/....	232
Fig. 4.74	Correlation between permafrost thickness and mean annual surface temperature /JNC 00/ .....	232
Fig. 4.75	Kinds of unfrozen areas (taliks) within permafrost.....	233
Fig. 4.76	Distribution of pyrite, FeOOH and gypsum in fracture fillings within permafrost in Greenland /CLA 16/ .....	235
Fig. 4.77	Microbial Production of CH <sub>4</sub> and CO <sub>2</sub> .....	237
Fig. 4.78	Phase diagram for a methane-water mixture as a function of depth and temperature (10 bar = 100 m) /POS 12/ .....	239
Fig. 4.79	Lupin: Methan bubbles emanating from a fracture (aperture is 1-2 mm) in 890m depth /RUS 02/.....	240

Fig. 4.80	Nickel concentrations in solutions in equilibrium with bunsenite.....	245
Fig. 4.81	Solubility of nickel in a solution saturated with halite and anhydrite (from /HAG 21/) .....	250
Fig. 4.82	Stability of lead chloride phases (left: $a_{Cl}=10^{-4}$ ; right: $a_{Pb}=10^{-4}$ ) calculated with the database in /HAG 12/ .....	256
Fig. 4.83	Relative stability of tin(II) chloro and hydroxo complexes .....	259
Fig. 4.84	Relative stability of tin(II) sulfato and hydroxo complexes .....	260
Fig. 4.85	Relative stability of tin(IV) chloro and hydroxo complexes.....	263
Fig. 4.86	Relative stability of solid tin(II) hydroxide and sulfate compounds in the presence of chloride ( $a_{Sn}=0.01$ , $a_{Cl}=0.01$ ).....	265
Fig. 4.87	Relative stability of solid tin(II) hydroxide and chloride compounds ( $a_{Sn}=0.01$ ) .....	266
Fig. 4.88	Relative stability of tin(IV) solids in the presence of calcium .....	268
Fig. 4.89	Solubility of tin(II) in a solution saturated with halite and anhydrite.....	269
Fig. 4.90	Solubility of tin(IV) in a solution saturated with halite and anhydrite .....	270
Fig. 4.91	Hydrolysis of Nb with $[Nb]_{tot} = 10^{-9}M$ .....	273
Fig. 4.92	Solubility of $Nb_2O_5(hyd,am)$ as a function of pH .....	274
Fig. 4.93	Solubility of Hochelagaite as a function of pH at different Ca- concentrations .....	275

## List of Tables

Tab. 2.1	Parameters of the clay model .....	12
Tab. 2.2	Parameters of the LILW model (LILW-6: only red parameters, LILW-7: red and green, LILW-11: red, green and blue, LILW-20: all parameters) .....	13
Tab. 2.3	Toolboxes for sensitivity analysis .....	37
Tab. 2.4	Main features of the model cases .....	38
Tab. 2.5	Parameters for calculation of RN uptake via root, Czech model.....	53
Tab. 2.6	Soil to plant transfer factors $[(\text{Bq kg}_{\text{fm}}^{-1})/(\text{Bq kg}_{\text{dm}}^{-1})]$ used in the Czech model.....	54
Tab. 2.7	Parameters for calculation of RN uptake via foliage, Czech model .....	54
Tab. 2.8	Interception parameters .....	55
Tab. 2.9	Parameters for calculation of external contamination of crops, Czech model.....	55
Tab. 2.10	Parameters and parameter values used in the German model for root uptake into the plant for the irrigation pathway. Note that values for pasture soil are in brackets. ....	56
Tab. 2.11	RN-specific parameters and parameter values used in the German model for root uptake into the plant for the irrigation pathway. Note that values for pasture soil are in brackets. ....	57
Tab. 2.12	Parameters and parameter values used in the German model for foliar uptake into the plant for the irrigation pathway, s. also Tab. 2.10 and Tab. 2.11. ....	57
Tab. 2.13	Radionuclide concentrations in soil ( $\text{Bq kg}_{\text{dm}}^{-1}$ ) calculated by Czech and German biosphere models for different points in time. For GRS concentration values differ for soil (top) and pasture soil (bottom). The bold numbers are the values used in the reference case by UJV and GRS.....	58
Tab. 2.14	Radionuclide concentrations in plants ( $\text{Bq/kg}$ fresh mass) calculated by German biosphere model for different points in time .....	59
Tab. 2.15	Radionuclide concentrations in agriculture crops ( $\text{Bq/kg}$ fresh mass) calculated by Czech biosphere model for different points in time .....	60
Tab. 2.16	Biosphere dose conversion factors (BDCF) in $[(\text{mSv year}^{-1}) / (\text{Bq m}^{-3})]$ .....	61

Tab. 2.17	Parameters for calculation of loss rate in the Czech model.....	61
Tab. 2.18	$K_d$ values, corresponding $R_i$ values and $\lambda_{il}$ for the Czech model compared to $\lambda_{M,r}$ of the German model (values in brackets are for pasture soil) .....	61
Tab. 2.19	Comparison of concentration in soil [Bq kg <sup>-1</sup> ]. For GRS concentration after 50 years (reference value) and after 10 <sup>5</sup> years are shown. ....	62
Tab. 2.20	Concentration in leafy vegetables, calculated dose for this single pathway (ingestion of leafy vegetables) and ratio of dose rates for UJV/GRS. For GRS the data are based on soil concentrations after 50 years.....	63
Tab. 2.21	Parameters for calculation of external radiation from residence time on agricultural soil, Czech model .....	64
Tab. 2.22	Dose coefficients for external radiation for Czech and German model.....	64
Tab. 2.23	Parameters for calculation of external radiation from residence time on agricultural soil, German model .....	65
Tab. 2.24	Dose from external irradiation from the soil (radionuclide contributions) (Sv year <sup>-1</sup> ) calculated by Czech and German biosphere models for different points in time .....	66
Tab. 2.25	Comparison of radiation exposures [Sv/ year) for different external radiation pathways calculated with the German model (for irrigation on agricultural soils accumulation time of 50 y is considered) .....	67
Tab. 2.26	Species for which sorption submodels have been implemented in the extended UNiSeCs model.....	70
Tab. 2.27	Characteristics of the two Refesols as far as relevant for PHREEQC modeling (ox = oxalate extractable hydrous oxides).....	75
Tab. 2.28	Calculated distribution coefficients for Refesol 01A under the standard conditions defined in Section 2.3.2.2.....	78
Tab. 2.29	Calculated distribution coefficients for Refesol 03G under the standard conditions defined in Section 3.2.....	78
Tab. 2.30	Ranges of parameter values used in the sensitivity analysis.....	80
Tab. 2.31	The most significant parameters for Am, Cs, Ni and Pu.....	82
Tab. 2.32	The most significant parameters for Ra, Se, Tc and U.....	83
Tab. 2.33	Ranges of $K_d$ values calculated by „KdMultigrid“ .....	94

Tab. 4.1	Characteristic periods of the experiment.....	149
Tab. 4.2	Characteristic periods for the models.....	149
Tab. 4.3	Material parameters for the thermal model.....	153
Tab. 4.4	Material parameters for the re-saturation model .....	163
Tab. 4.5	Parameters for the initial state of the re-saturation model .....	164
Tab. 4.6	Depth of permafrost as a function of the surface temperature.....	214
Tab. 4.7	Pitzer coefficients for Ni <sup>2+</sup> in the six-component seawater system. Experimental data used are mostly related to weakly acidic and neutral solutions.....	249
Tab. 4.8	Stability of tin(II) complexes .....	261
Tab. 4.9	Stability of tin(IV) complexes.....	264
Tab. 4.10	Stability of solid tin(II) phases .....	265
Tab. 4.11	Stability of solid tin(IV) phase.....	267
Tab. 4.12	Thermodynamic data for niobium species. Numbers underlined were calculated for this report. All data are valid for 298.15 K. ....	272
Tab. 4.13	Thermodynamic data for niobium solid phases as given in /THO 21/. Numbers in italic were marked as supplementary. Numbers underlined were calculated for this report. All data are valid for 298.15 K. ....	277

**Gesellschaft für Anlagen-  
und Reaktorsicherheit  
(GRS) gGmbH**

Schwertnergasse 1  
**50667 Köln**  
Telefon +49 221 2068-0  
Telefax +49 221 2068-888

Forschungszentrum  
Boltzmannstraße 14  
**85748 Garching b. München**  
Telefon +49 89 32004-0  
Telefax +49 89 32004-300

Kurfürstendamm 200  
**10719 Berlin**  
Telefon +49 30 88589-0  
Telefax +49 30 88589-111

Theodor-Heuss-Straße 4  
**38122 Braunschweig**  
Telefon +49 531 8012-0  
Telefax +49 531 8012-200

[www.grs.de](http://www.grs.de)